(2)

GL-TR-90-0175

The Magnetopause Boundary Layer

Bengt U. Ö. Sonnerup
W. Lotko

Dartmouth College
Thayer School of Engineering
Hanover, NH 03755

29 June 1990

Final Report
19 February 1987 - 18 May 1990

Approved for public release; distribution unlimited

GEOPHYSICS LABORATORY
AIR FORCE SYSTEMS COMMAND
UNITED STATES AIR FORCE
HANSCOM AIR FORCE BASE, MASSACHUSETTS 01731-5000

"This technical report has been reviewed and is approved for publication"

PAUL L. ROTHWELL
Contract Manager

NELSON C. MAYNARD
Branch Chief

FOR THE COMMANDER

RITA C. SAGALYN
Division Director

This report has been reviewed by the ESD Public Affair Office (PA) and is releasable to the National Technical Information Service (NTIS).

Qualified requestors may obtain additional copies from the Defense Technical Information Center. All others should apply to the National Technical Information Center.

If your address has changed, or if you wish to be removed from the mailing list, or if the addressee is no longer employed by your organization, please notify GL/IMA, Hanscom AFB, MA 01731. This will assist us in maintaining a current mailing list.

Do not return copies of this report unless contractual obligations or notices on a specific document requires that it be returned.

Unclassified

SECURITY CLASSIFICATION OF THIS PAGE

REPORT DOCUMENTATION PAGE

Form Approved OMB No. 0704-0188

1a REPORT SECURITY CLASSIFICATION: Unclassified	1b RESTRICTIVE MARKINGS
2a SECURITY CLASSIFICATION AUTHORITY	3 DISTRIBUTION/AVAILABILITY OF REPORT: approved for public release; distribution unlimited
2b DECLASSIFICATION/DOWNGRADING SCHEDULE	
4 PERFORMING ORGANIZATION REPORT NUMBER(S)	5 MONITORING ORGANIZATION REPORT NUMBER(S): GL-TR-90-0175
6a NAME OF PERFORMING ORGANIZATION: Dartmouth College; 6b OFFICE SYMBOL (If applicable)	7a NAME OF MONITORING ORGANIZATION: Geophysics Laboratory
6c ADDRESS (City, State, and ZIP Code): Thayer School of Engineering, Hanover, NH 03755	7b ADDRESS (City, State, and ZIP Code): Hanscom AFB, Massachusetts 01731-5000
8a NAME OF FUNDING/SPONSORING ORGANIZATION; 8b OFFICE SYMBOL (If applicable)	9 PROCUREMENT INSTRUMENT IDENTIFICATION NUMBER: F19628-87-K-0026
8c ADDRESS (City, State, and ZIP Code)	10 SOURCE OF FUNDING NUMBERS: PROGRAM ELEMENT NO 61102F; PROJECT NO 2311; TASK NO G5; WORK UNIT ACCESSION NO BB

11 TITLE (Include Security Classification)

The Magnetopause Boundary Layer

12 PERSONAL AUTHOR(S)

Bengt U. O. Sonnerup; W. Lotko

13a TYPE OF REPORT	13b TIME COVERED	14 DATE OF REPORT (Year, Month, Day)	15 PAGE COUNT
Final Report	FROM 2/19/87 TO 5/18/90	1990 June 29	228

16 SUPPLEMENTARY NOTATION

17 COSATI CODES		
FIELD	GROUP	SUB-GROUP

18 SUBJECT TERMS (Continue on reverse if necessary and identify by block number)

Magnetopause; Flux Transfer Events; Low Latitude Boundary Layer; Intermediate Shocks; Reconnection

19 ABSTRACT (Continue on reverse if necessary and identify by block number)

SEE REVERSE SIDE FOR ABSTRACT

20 DISTRIBUTION/AVAILABILITY OF ABSTRACT: ☐ UNCLASSIFIED/UNLIMITED ☐ SAME AS RPT ☐ DTIC USERS	21 ABSTRACT SECURITY CLASSIFICATION: Unclassified
22a NAME OF RESPONSIBLE INDIVIDUAL: Paul Rothwell	22b TELEPHONE (Include Area Code); 22c OFFICE SYMBOL: GL/PHG

DD Form 1473, JUN 86 — Previous editions are obsolete — SECURITY CLASSIFICATION OF THIS PAGE: Unclassified

Theoretical models have been developed to describe the structure of, and dynamical processes in the magnetopause current layer and the adjoining low latitude boundary layer (LLBL), including coupling of the latter to the dayside auroral ionosphere. Also a pilot study has been performed to demonstrate how information about magnetopause and boundary layer structure can be extracted from in-situ measurements of magnetic fields and plasma velocities. (1) Simple two-dimensional dynamic models of the LLBL and other shear flows have been developed and used to study the decay of shear layers, and the breakup of driven unstable shear flows, such as the LLBL, into quasisteady vortex rows similar to those observed in the post-noon auroral-zone ionosphere, or into turbulence. A steady-state viscous LLBL model has also been generated in which the magnetic field deformation caused by the currents is included in a self consistent manner. (2) A viscous-resistive model of magnetic field annihilation at the magnetopause has been developed which allows for plasma flow along the reconnection line. (3) The structure of resistive and resistive-dispersive MHD intermediate shocks has been determined and their possible role as part of the magnetopause structure assessed. (4) Certain geometric and dynamic properties of the magnetopause/LLBL have been extracted from AMPTE/IRM data with special emphasis on magnetic-field reconnection and flux transfer events.

Contents

THE MAGNETOPAUSE BOUNDARY LAYER
Final Technical Report
AFGL Contract F19628-87-K-0026
Summary

The research conducted under this contract has been concerned with the structure of, and dynamical processes in the earth's magnetopause/boundary layer regions. The work has been concentrated in four areas:

1. Theoretical modeling of the low-latitude boundary layer.
2. Theoretical modeling of the magnetic-field reconnection process.
3. Theoretical modeling of the magnetopause structure during reconnection in terms of intermediate MHD shocks.
4. Observational studies of the magnetopause during reconnection, including flux transfer events and low-latitude boundary layer structure.

The following sections of the report contain a brief summary and discussion of the results obtained in each of these areas. Details of the research are provided in a total of eight published papers, one paper in press, and three papers submitted for publication. These articles are appended to, and form an integral part of this final report. The research described in these papers has been supported partially by the present contract; partial support has also been obtained from other sources, as indicated in the acknowledgment section of each paper.

1. Theory of the Low-Latitude Boundary Layer

The low-latitude boundary layer (LLBL) is a narrow region, located in the low latitutde region immediately inside the outer boundary of the magnetosphere, the magnetopause. The LLBL contains plasma, mostly of magnetosheath origin, that flows along the layer in the antisolar direction at a speed comparable to the magnetosheath flow speed. This plasma flow is at an angle — in the simplest model at a 90° angle — to the geomagnetic field in the vicinity of the equatorial plane and thus it has an associated electric field, $\mathbf{E}_e$, which is projected, in part at least, into the ionosphere at the footpoints of the geomagnetic field lines threading the LLBL. This impressed electric field, $\mathbf{E}_i$, drives a horizontal Pedersen current, $\mathbf{J}_i$, in the ionosphere; the divergence in $\mathbf{E}_i$ gives rise to a corresponding divergence in this horizontal current, i.e., it gives rise to a corresponding magnetic-field-aligned current into or out of the ionosphere. This field-aligned current connects the ionosphere to the LLBL, where it is again deflected to form a current $\mathbf{J}_c$ that flows across the geomagnetic field. In the ionosphere, the product $\mathbf{E}_i \bullet \mathbf{J}_i > 0$, whereas in the LLBL the product $\mathbf{E}_e \bullet \mathbf{J}_c < 0$; thus the former acts as an electrical load and the latter as an electrical

generator, connected to the ionospheric load via the field-aligned currents. In the simplest conceptual model, the projection of the equatorial electric field into the ionosphere occurs by assuming the geomagnetic field lines to be equipotentials. In more realistic modeling such as ours, a potential drop, $\Delta\Phi_{||}$, along the field lines is incorporated via a field-aligned conductance K, so that $J_{||} = K\Delta\phi_{||}$. In the post-noon LLBL, the field-aligned current, $J_{||}$, flows out of the post-noon ionosphere so that the potential drop $\Delta\Phi_{||}$ can accelerate electrons precipitating into the ionosphere to energies comparable to those needed to explain auroral emissions. On the pre-noon side, a potential drop $\Delta\Phi_{||}$ will accelerate electrons upwards and ions downwards instead. A schematic drawing of the dawnside LLBL configuration and its coupling to the ionosphere is shown in Fig. 1. Note that the main field-aligned current associated with the LLBL provides the portion of the so-called Region 1 current that is observed to flow into the pre-noon (8 - 12 LT, say) and out of the post-noon (12 - 16 LT, say) sides of the dayside auroral oval. Any field-aligned return current, at the outer edge of the LLBL, i.e., at the magnetopause itself, could correspond to the so-called NBZ currents, observed at low altitudes during conditions of northward interplanetary magnetic field (IMF). Note also that the actual local time extent of the LLBL projection into the ionosphere remains uncertain at present, since no accurate geomagnetic-field mapping is available for the region immediately adjacent to the magnetopause.

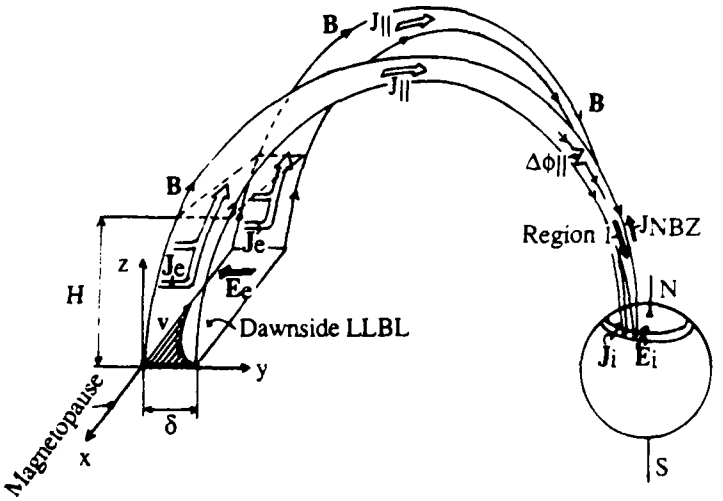

Fig. 1. View from the sun of dawnside low-latitude boundary layer and its coupling to the dayside auroral oval. Coordinates (x,y,z) are the usual GSM coordinates.

Under the AFGL contract, we have developed two distinct models of the LLBL and its coupling to the dayside auroral ionosphere. The first of these models is described in detail in Lotko et al. [1987, Appendix 1]. In this model, the magnetic field threading the boundary layer is taken to be uniform within the region, $|z| < H$, $0<y<\delta$, occupied by the layer. The plasma motion

within the layer is incompressible and confined to planes perpendicular to the magnetic field (xy planes). The equation of motion includes inertia effects, pressure gradients, the $\mathbf{J}_e \times \mathbf{B}$ force, and a viscous force; the current $\mathbf{J}_e$ is determined via coupling to the ionosphere as described in the previous paragraph. A principal result of the formal theory is the identification of the appropriate characteristic time and length scales which should be used, along with two nondimensional groups, in describing the structure and dynamic evolution of the boundary layer. These quantities are defined in Eq. (22) of Appendix 1.

A result of particular interest is the finding that, in our model, the LLBL is characterized by a so-called Hartmann number, M, which is a measure of the relative importance of resistive drag in the ionosphere and viscous drag in the boundary layer itself. Important findings are that the coupling of the LLBL to the ionosphere creates the possibility of spatially anisotropic temporal decay of large-scale disturbances in the boundary layer and that the field-aligned potential drops promote long-lived fluctuations on the inverted "V" scale length. The Lotko et al. [1987] paper also provides a complete analytical treatment of one-dimensional ($\partial/\partial x = 0$), time-dependent boundary-layer structures. It is shown that, as time increases, arbitrary initial boundary-layer velocity profiles, $v_x(y,0)$, and current profiles, $J_{ey}(y,0)$ asymptotically approach a one-dimensional steady state, in which viscous forces and $\mathbf{J}_e \times \mathbf{B}$ are in exact balance. Finally, the one-dimensional time-dependent theory is applied to describe the evolution (decay) of shear layers in the magnetosphere and their possible relationship to inverted "V" structures.

The simple model in Appendix 1 has also been used to examine two-dimensional dynamical processes of relevance to the LLBL. A particular application to post-noon auroral shear layers is described in the paper by Lotko and Shen [1990, Appendix 2]. The approach taken by Lotko and Shen is to treat the distribution of field-aligned current generated in the LLBL proper as given, and ask what are the dynamical consequences of such currents in the lower altitude, low β region extending along magnetic field lines from the top of the LLBL (at z=H) to the ionosphere. Although the distinction between the LLBL region and this adjoining tenuous plasma region is somewhat artificial, the fact that $\mathbf{E} \times \mathbf{B}$ shear flow instabilities tend to be supressed by the strong magnetic shear (see Appendix 3) that accompanies field-aligned currents in the higher-β, LLBL region, and that the generation of currents by an enhanced viscous interaction is substantial in the LLBL relative to the tenuous plasma region, suggests that such a distinction is qualitatively meaningful. Given this distinction, the stability of the shear layer can be readily evaluated. As shown in Fig. 2 of Appendix 2, the neutral curves depend on three nondimensional parameters related to the amplitude of the field-aligned current (or $\mathbf{E} \times \mathbf{B}$ velocity amplitude) required by the LLBL, the scale size of the current distribution and the Hartmann number. Numerical simulations of unstable cases show (1) that 2D quasi-steady rotational states arise when the shear layer is weakly unstable, (2) that eddy-shedding turbulent states can arise when the shear layer is more

strongly unstable, and (3) that the flow kinetic energy and the energy dissipation, by ionospheric Joule heating, by production of field-aligned particle fluxes, and by viscous heating are all reduced as a consequence of the instability. Power spectral densities are also evaluated along selected 'satellite' cuts through the shear layer. The results of the study are consistent with the tendency for 2D rotational motion and periodic bright spots in post-noon auroral forms, found in satellite images [Lui et al., 1989] and radar measurements [Robinson et al., 1984].

Our second model of the low-latitude boundary layer [Phan et al., 1989, Appendix 3] concerns the time-asymptotic, steady-state, one-dimensional structures mentioned earlier, in which a balance between $\mathbf{J}_e \times \mathbf{B}$ forces and viscous forces is maintained in the layer. In this new model, the magnetic field in the LLBL is no longer taken to be uniform. Rather, it is determined self consistently from Ampère's law. From the requirement that the total pressure, $p + B^2/2\,\mu_o$, be constant everywhere in the layer, one can then find the variations in pressure and from it, assuming isothermal conditions, the variations in density within the boundary layer. In this way, the model actually describes the diamagnetic depression of the **B** field within the layer, caused by currents J_{ex}, as well as the bending of the field lines into parabolic shape caused by the presence of currents J_{ey} in the layer.

Although certain qualitative and even quantitative comparisons can be made, and have been made, between the models discussed above and actual observations of the LLBL and its ionospheric footprints, we believe that the models need to be improved rather substantially before extensive comparisons with observations become meaningful and before the models can be used to make realistic quantitative predictions. A number of physical effects such as mass diffusion, inertia, and pressure gradients need to be included in the steady-state model and the one-dimensional flow assumption must then be abandoned. Furthermore, the geometrical mapping along magnetic field lines into the ionosphere needs to be incorporated in a more realistic and self-consistent way. In our view, the greatest significance of the model calculations performed to date is that they have helped identify a number of important parameters and effects associated with a magnetospheric boundary-layer or shear layer coupled to the ionosphere, thus providing a systematic framework for thinking about these problems and for developing new more realistic models. It is noted that recently we have collaborated with Dr. G. Siscoe in an attempt to place the simple model described in Appendix 1 in the context of the global magnetospheric electric current circuit [Siscoe et al., 1990]. This application has required certain changes in the boundary conditions at the magnetopause used by Lotko et al., changes that have led to the appearance of NBZ currents at the magnetopause edge of the LLBL projected into the ionosphere,i.e., at the poleward edge of the Region 1 currents, during conditions of northward IMF. This work provides a good example of the kind of conceptual use to which our models can be put.

2. Theory of Steady Magnetic Field Reconnection

Magnetic field reconnection is known to occur at the dayside magnetopause during conditions of southward IMF. However, parameters other than the IMF direction also appear to control the onset of the process or the rate at which it occurs. In fact, a southward or nearly southward directed IMF may not in itself be a guarantee that reconnection takes place [Paschmann et al., 1986]. Our work on the theory of reconnection has been concerned with the case where the reconnection rate is sufficiently small so that the process can be described as magnetic-field annihilation rather than reconnection. In this situation, the magnetopause is modeled as a plane current sheet centered at $x = 0$. Plasmas containing nearly frozen-in magnetic fields flow towards the current sheet from both sides. The magnetic field direction is different for $x<0$ and $x>0$, but the field lines are confined to lie in planes parallel to the plan $x = 0$. The model, which can be either two dimensional or three dimensional, is described by the incompressible, resistive, viscous MHD equations. We have found a rather wide class of exact solutions of these equations for the type of configurations just described. The two-dimensional solutions, for which $\partial/\partial z = 0$, are described in detail in a draft paper by Phan and Sonnerup [1990, Appendix 4]; the 3D case is still under study.

Among the exact solutions, one finds, as a special case, the irrotational, resistive stagnation point flows discussed by Sonnerup and Priest [1975]. However, rotational flows of the same type can also be obtained, some of which display less of the troublesome large magnetic flux pile-up that tends to occur in these models but is not seen at the subsolar magnetopause (see Figs. 1-3 in Appendix 4).

Another new feature of the exact solutions we have found is that they permit of a flow velocity component $v_z(x,y)$ and a magnetic field component $B_z(x,y)$ along the invariant (z) direction. Except near the subsolar point, such a flow component of large magnitude is always present at the magnetopause. In that application, there is usually also a large amount of shear in the flow along the magnetopause, i.e., $v_z(x,y)$ decreases rapidly with the coordinate, x, as one crosses the magnetopause and LLBL from the magnetosheath, where the flow speed is large, into the magnetosphere where the flow is small or absent. In our model of this shear flow, viscosity plays an important role. The configuration is shown schematically in Fig. 2. This diagram shows that the model contains an electric current component, J_x, which flows from the magnetosheath, across the magnetopause and into the magnetosphere where it is deflected to become field aligned (with the correct sense of the Region 1 currents, although the model in its present form does not have coupling to the ionosphere built into it). As a result of this current, the magnetic field lines in the magnetosheath are bent into parabolas with their vertices pointing in the upstream (sunward) direction. The field lines in the LLBL immediately inside the magnetopause are also bent into

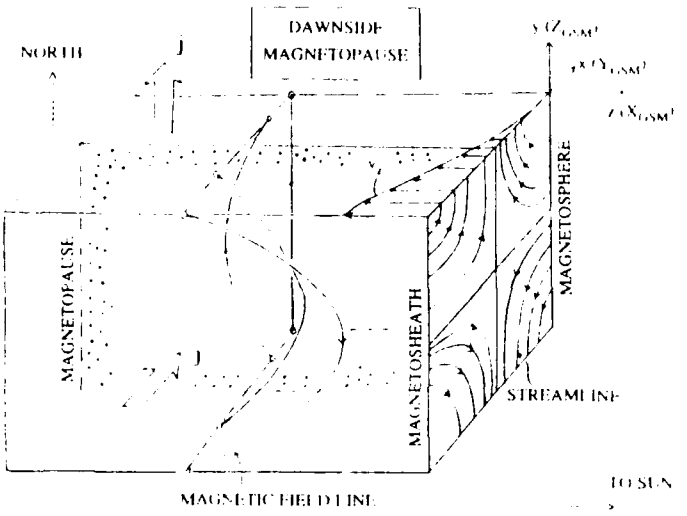

Fig. 2. Magnetic field annihilation at a current sheet with shear flow along the sheet. Coordinates: $x=Y_{GSM}$, $y=Z_{GSM}$, $z=X_{GSM}$.

parabolas but with their vertices pointing in the downstream (antisunward) direction, just as in the model by Phan et al. [1989, Appendix 3]. This type of reversal of the field curvature across the magnetopause, in the vicinity of a reconnection line (the z axis in Fig. 2) with plasma flow along it, has also been observed in the global numerical MHD simulation of the solar-wind magnetosphere-ionosphere system performed by Fedder and Lyon at NRL.

The various field-annihilation models described in Appendix 4 need to be improved by allowing different plasma properties on the two sides of the magnetopause current sheet before they can be applied to the real magnetopause situation. In our view, they will ultimately prove useful in providing a qualitatively correct local description of flow near the magnetopause subsolar point as well as flow (in the magnetosheath and in the LLBL) along a magnetopause reconnection line during weak reconnection.

Two more pieces of work on the reconnection problem have been performed under the AFGL contract: a review article has been written by Sonnerup et al.[1990, Appendix 5] and a comment has been generated and published on an incorrect paper concerned with MHD stagnation point flows (Sonnerup and Phan [1990, Appendix 6]).

3. Theory of Intermediate Shock Structure

Since the early theoretical work by Levy et al. [1964], it has been a commonly held view that, during conditions of steady or quasisteady reconnection, the magnetopause should contain a rotational discontinuity (RD) as the dominant part of its structure. Indeed, attempts to find in-situ evidence of reconnection at the magnetopause have been strongly focused on this feature of the

magnetopause structure [see for example Appendix 9]. However, recently C. C. Wu [1987; 1988a; 1988b; 1990] has proposed that, rather than containing a rotational discontinuity, the magnetopause may consist mainly of a weak intermediate shock. The tangential magnetic field always rotates by exactly 180° across a steady-state intermediate shock. To accommodate the real situation at the magnetopause, where the field rotation angle seldom is exactly 180°, Wu proposes and shows by numerical simulation that intermediate-mode pseudoshocks exist, across which the field can rotate by an arbitrary angle. These psuedo-shock structures evolve in time, that evolution being more rapid the more the field rotation angle deviates from 180°.

Since the structure of intermediate shocks had not been studied in detail, we found it desirable to investigate this topic so that one could come to understand what predictions, in terms of observable features of the magnetopause structure, could be extracted from C. C. Wu's proposal. The results of our study are contained in two papers by Hau and Sonnerup [1989, Appendix 7; 1990, Appendix 8]. In the first of these papers, the purely resistive, steady-state structure of intermediate shocks is investigated; in the second paper, dispersive effects, associated with the Hall term in Ohm's law, are included as well.

It has been known since the late fifties that two intermediate shock branches exist: a "weak" branch and a "strong" branch. In other words, for one and the same superalfvénic upstream condition, two possible downstream states exist. For the weak branch, the downstream state is weakly subalfvénic but superslow while for the strong branch, it is more strongly subalfvénic and also subslow. By downstream superslow (subslow) is meant that the downstream normal flow speed, in the shock frame, is faster (slower) than the local small-amplitude slow-mode wave speed. What is found in our work is that the structure of intermediate shocks is not always unique: more than one structure can sometimes connect the same pair of given upstream and downstream states. And, as the upstream or downstream states change from being subsonic to being supersonic, rather different structures are obtained. In the two papers, the shock structures are presented in terms of magnetic hodograms, i.e., they are shown as plots of one tangential magnetic field component, B_z, versus the other, B_y. In the purely resistive case, all possible structures of intermediate shocks (as well as fast and slow shocks) are contained within three types of hodogram topology (shown in Fig. 8 of Appendix 7). When dispersive effects are included, a total of 13 distinct topologies (some having several subcases) were found (see Appendix 8). We believe we have documented all possible structures described by the resistive/dispersive nonviscous MHD model. Included are many cases where the shock contains a substructure consisting of a discontinuous isomagnetic jump. Such a jump involves a transition from supersonic to subsonic flow in which the magnetic field remains unchanged: it is an ordinary gasdynamic shock, the structure of which is determined by viscosity and heat

conductivity. For zero viscosity and heat conductivity, as assumed in our model, the width of such a substructure collapses to zero, i.e., it becomes a discontinuity.

The question arises whether any of the many intermediate shock structures found in our study could provide an acceptable explanation for observed magnetopause structures. At present, the answer to this question remains somewhat ambiguous. One fundamental property of intermediate shocks is that they always involve a transition from upstream superalfvénic to downstream subalfvénic flow. In the most detailed observational studies of magnetopause reconnection events that have been performed to date [Sonnerup et al., 1987; 1990, Appendix 9], the ratio of flow speed (in the deHoffmann-Teller frame) to Alfvén speed as the spacecraft AMPTE/IRM crosses the magnetopause is calculated from the spacecraft data. The results contain no indication of a transition from superalfvénic to subalfvénic flow. But these results are not sufficiently accurate to allow one to exclude the possibility that the upstream (magnetosheath) state could have been slightly superalfvénic and the downstream (magnetospheric) state could have been slightly subalfvénic. The smallest-amplitude members of the weak intermediate shock branch have exactly that property and, furthermore, the magnetic field magnitude also changes very little (while the tangential field direction is reversed) across such a weak shock. It would be difficult to distinguish a shock of this type from a rotational discontinuity (RD) with a tangential field rotation of 180° since, for isotropic pressure, the field magnitude is exactly constant in a laminar, one-dimensional RD. It should also be said that many observed magnetopause structures appear very complicated, indicating the presence of turbulent processes in the current layer.

There are isolated magnetopause crossings by earlier spacecraft, where plasma measurements were not made, which fit the model of a laminar weak intermediate shock reasonably well. An example is shown in Fig. 3. In that figure, a comparison is made between the observed magnetic hodogram and one predicted from our purely resistive model. It is noted that the tangential field rotates by almost exactly 180° in the main "circular" part of the observed structure and that there is a modest decrease in magnetic field strength as the field rotates from its upstream to its downstream state. These are the exact properties of a weak intermediate shock. As can be seen, the details of the field rotation obtained from the resistive model do not match the observations so well. We have found that inclusion of dispersive and other effects (viscosity, gyroviscosity) does not lead to an improvement in this regard. Thus, this event, while suggestive, does not provide entirely convincing evidence for the occurrence of a weak intermediate shock as part of the magnetopause structure.

As mentioned already, the magnetic-field rotation angle across the magnetopause usually differs substantially from 180°. In such cases, comparison between observations and theory should focus on time-dependent pseudoshocks of the type discussed and simulated by C. C. Wu rather than on the time-independent structures analyzed in Appendices 7 and 8.

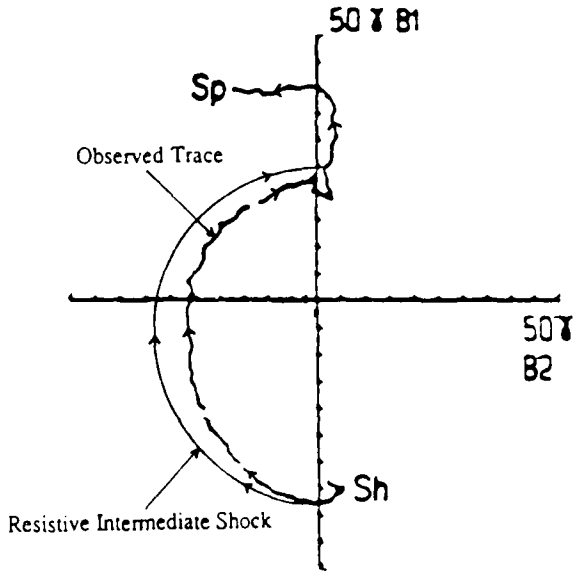

Fig. 3. OGO-5 crossing of the magnetopause on March 27, 1968 (from Sonnerup and Ledley [1979]).

4. Observations in the Magnetopause/LLBL Regions

The AFGL contract has also provided partial support for a data-analysis effort in which plasma and magnetic-field data, collected by the spacecraft AMPTE/IRM in the magnetopause and in the adjoining low-latitude boundary layer, are interpreted. This portion of the project has been carried out in close collaboration with Dr. G. Paschmann and his research group at the Max-Planck-Institute for Extraterrestrial Physics (MPE) in Garching, F. R. G..

The studies that have been performed are based on a somewhat novel technique for analyzing magnetopause data. This technique, which has some of its origins in the work by Aggson et al. [1983] on the existence of deHoffmann-Teller frames, has been described in detail by Sonnerup et al. [1987]. It is based on the use of the convection electric fields, $\mathbf{E}_c = -\mathbf{v}\times\mathbf{B}$, calculated from measured plasma velocities, $\mathbf{v}$, and magnetic fields, $\mathbf{B}$, for the determination of the magnetopause normal, $\mathbf{n}$, as well as for finding a moving frame of reference, a so-called deHoffmann-Teller (HT) frame, in which the plasma flow is field aligned or nearly field aligned.

Sonnerup et al. [1990, Appendix 9] have applied the new electric-field-based analysis to a number of magnetopause crossings having large magnetic field shear (i.e., having a large rotation angle of the tangential component of the magnetic field across the current layer). In agreement with Aggson et al., they have found that for many of these cases, excellent HT frames (moving with velocity, $\mathbf{v}_{HT}$, and acceleration $\mathbf{a}_{HT}$) can be found. However, contrary to Aggson et al., they have also found that the existence of a good HT frame does not guarantee that the

magnetopause has the properties of a rotational discontinuity (or a weak intermediate shock), i.e., it does not guarantee that the magnetopause has structure associated with quasisteady reconnection. One excellent example of this situation is shown in Figs. 13 - 16 of Appendix 9. The field-aligned plasma flow in the HT frame is small or absent in this case (Fig. 15 of Appendix 9), indicating that the current sheet was a 2D or 3D tangential-discontinuity structure carried in a frozen fashion with the plasma flow along the magnetopause. The absence of a measurable normal magnetic field component (Fig. 13 of Appendix 9) is consistent with this conclusion.

A second important result, described in Appendix 9, is that the acceleration, $\mathbf{a}_{HT}$, of the HT frame, first calculated on a trial basis by Sonnerup et al [1987], appears to be physically meaningful, at least in some cases. There are two types of evidence to support this statement. First, the normal component of $\mathbf{a}_{HT}$, which should represent the acceleration of the magnetopause normal to itself, has been found to slow down the normal motion of the magnetopause in every case where it is known, from the presence of a subsequent crossing (caused by flapping of the magnetopause), that the normal motion must ultimately reverse itself. Second, inclusion of the tangential component of $\mathbf{a}_{HT}$ sometimes leads to a dramatic improvement in the tangential stress balance (the Walén relation, $\Delta \mathbf{v} = \pm \Delta \mathbf{v}_A$, see Fig. 11 of Appendix 9). Thus it appears that the tangential components of $\mathbf{v}_{HT}$ and $\mathbf{a}_{HT}$ characterize the velocity and acceleration of actual 2D and 3D spatial magnetopause substructures in their motion along the magnetopause.

A third significant result, described in Appendix 9, is that the Walén relation, while occasionally nearly exactly satisfied, more often is satisfied only to about 70 - 80%. In other words, the observed field-aligned plasma flow speed in the HT frame is only 70 - 80% of the local Alfvén speed. While this discrepancy could perhaps be accounted for by assuming a small admixture of heavy ions (O^+, say) in the magnetopause plasma (the AMPTE/IRM plasma analyzer has no mass discrimination), an equally plausible explanation may be that pressure gradients along the magnetopause cause actual systematic deviations from the Walén relation.

Recently, Paschmann et al. [1990, Appendix 10] have used the analysis methods based on the convection electric field on one magnetopause crossing having small rather than large magnetic shear, i.e., on a case where the **B** fields external and internal to the magnetopause have nearly the same direction. It is found that, provided a substantial plasma boundary layer (LLBL) containing strong velocity shear is present, the analysis method works: an accurate normal vector can be found, a good HT frame exists, and, finally, the Walén relation is found to be rather well satisfied. This may therefore be an example of reconnection (above the cusps) for northward IMF. Furthermore, knowledge of the magnetopause normal vector, **n**, allows one to calculate the fluctuations in the measured boundary-layer plasma velocity component along **n**. If these fluctuations are interpreted as inward-outward motion of the magnetopause and boundary layer, the measured time series of, for example, plasma density, $\rho(t)$, in the LLBL can be converted to a

spatial profile (Fig. 4 in Appendix 10). In the example examined, a thickness of the LLBL of ~ 1.3 R_E was found. This is a rather large value, but it is qualitatively consistent with a number of other studies that indicate the presence of thick boundary layers for northward IMF.

Finally, the analysis based on $\mathbf{E}_c$ has also been applied successfully to flux transfer events (FTEs), as described by Sonnerup [1988, Appendix 11] and by Papamastorakis et al. [1989, Appendix 12]. The study deals with three FTEs, observed in the magnetosheath immediately prior to a set of three crossings of the magnetopause by AMPTE/IRM, all of which displayed unambiguous signatures of quasisteady reconnection and all of which are discussed in Appendix 9 (see also Sonnerup et al. [1987]). Each FTE was found to have a very good HT frame and, furthermore, to a good approximation, all three FTEs, *and* the three magnetopause crossings following them, have one and the same HT frame, suggesting that they were all part of the same dynamic reconnection event. These results are consistent with the idea that FTEs as well as quasisteady reconnection events are manifestations of large-scale reconnection with a reconnection rate that sometimes fluctuates and sometimes remains approximately steady. Theoretical and numerical models of this type have been discussed extensively by Lee and Fu [1985], by Scholer [1988], and by Southwood et al. [1988]. Another important finding that is consistent with these models was obtained for the first (outermost) of the three FTEs. This event appears to have corresponded to a traversal of magnetic fields draped around an FTE flux tube (a so-called distant encounter). The observed field structure was found to be quasi two-dimensional in the sense that spatial variations across the structure occurred on a substantially shorter length scale than variations along it. In fact, the observations agree rather well with a model proposed by Farrugia et al. [1987] in which the FTE flux tube is a cylinder of semicircular cross section, around which an irrotational **B** field is draped and around which a corresponding irrotational field-aligned flow occurs in the HT frame.

The number of magnetopause crossings and FTEs studied to date by use of $\mathbf{E}_c$ analysis is relatively small. The effort supported by AFGL should therefore be viewed mainly as a pilot project in which the feasibility of extracting detailed results concerning spatial structure and physical processes (reconnection) in the magnetopause region from single-spacecraft data is demonstrated.

REFERENCES

Aggson, T.L., P.J. Gambardella, and N.C. Maynard, Electric field measurements at the magnetopause 1. Observation of large convective velocities at rotational magnetopause discontinuities, *J. Geophys. Res.*, **88**, 10,000, 1983.

Farrugia, C.J., R.C. Elphic, D.J. Southwood, and S.W.H. Cowley, Field and flow perturbations outside the reconnected field line region in flux transfer events: Theory, *Planet. Space Sci.*, **35** 227, 1987.

Hau, L.-N., and B.U.Ö. Sonnerup, On the structure of resistive MHD intermediate shocks, *J. Geophys. Res.*, **94**, 6539, 1989.

Hau, L.-N., and B.U.Ö. Sonnerup, The structure of resistive-dispersive intermediate shocks, *J. Geophys. Res.*, **95**, in press, 1990.

Lee, L.C., and Z.F. Fu, A theory of magnetic flux transfer at the Earth's magnetopause, *Geophys. Res. Lett.*, **12**, 105, 1985.

Levy, R.H., H.E. Petschek, and G.L. Siscoe, Aerodynamic aspects of the magnetospheric flow, *AIAA J.*, **2**, 2065, 1964.

Lotko, W., B.U.Ö. Sonnerup, and R.L. Lysak, Nonsteady boundary layer flow including ionospheric drag and parallel electric fields, *J. Geophys. Res.*, **92**, 8635, 1987.

Lotko, W., and M.-M. Shen, On large scale rotational motion and energetics of auroral shear layers, Thayer School of Engg., preprint, 1990.

Lui, A.T.Y., D. Venkatesan, and J.S. Murphree, Auroral bright spots on the dayside auroral oval, *J. Geophys. Res.*, **94**, 5515, 1989.

Papamastorakis, I., G. Paschmann, W. Baumjohann, B.U.Ö. Sonnerup, and H. Lühr, Orientation, motion, and other properties of flux transfer event structures on September 4, 1984, *J. Geophys. Res.*, **94**, 8852, 1989.

Paschmann, G., I. Papamastorakis, W. Baumjohann, N. Sckopke, C.W. Carlson, B.U.Ö. Sonnerup, and H. Lühr, The magnetopause for large magnetic shear: AMPTE/IRM observations, *J. Geophys. Res.*, **91**, 11,099, 1986.

Paschmann, G., B.U.Ö. Sonnerup, I. Papamastorakis, W. Baumjohann, N. Sckopke, and H. Lühr, The magnetopause and boundary layer for small magnetic shear: Convection electric fields and reconnection, *Geophys. Res. Lett.*, **17**, submitted, 1990.

Phan, T.-D., B.U.Ö. Sonnerup, and W. Lotko, Self-consistent model of the low latitude boundary layer, *J. Geophys. Res.*, **94**, 1281, 1989.

Phan, T.-D., and B.U.Ö. Sonnerup, MHD stagnation point flows at a current sheet, including viscous and resistive effects: General two-dimensional solutions, Thayer School of Engg., preprint, 1990.

Robinson, R.M., D.S. Evans, T.A. Potemra, and J.D. Kelley, Radar and satellite measurements of an F-region ionization enhancement in the post-noon sector, *Geophys. Res. Lett.*, **11**, 899, 1984.

Scholer, M., Magnetic flux transfer at the magnetopause based on single X-line bursty reconnection, *Geophys. Res. Lett.*, **15**, 291, 1988.

Siscoe, G.L., W. Lotko, and B.U.Ö. Sonnerup, A high-latitutde, low-latitude boundary layer model of the convection current system, UCLA, preprint, 1990.

Sonnerup, B.U.Ö., Experimental tests of FTE theories, *Adv. Space Sci.*, **8**, (9)263, 1988.

Sonnerup, B.U.Ö., and E.R. Priest, Resistive MHD stagnation point flows at a current sheet, *J. Plasma Phys.*, **14**, 283, 1975.

Sonnerup, B.U.Ö., and B.G. Ledley, OGO5 magnetopause structure and classical reconnection, *J. Geophys. Res.*, **84**, 399, 1979.

Sonnerup, B.U.Ö., I. Papamastorakis, G. Paschmann, and H. Lühr, Magnetopause properties from AMPTE/IRM observations of the convection electric field: Method development, *J. Geophys. Res.*, **92**, 12,137, 1987.

Sonnerup, B.U.Ö., and T.-D. Phan, Comment on "MHD stagnation point flows in the presence of resistivity and viscosity" by F.T. Gratton, M.F. Heyn, H.K. Biernat, R.P. Rijnbeek, and G. Gnavi, *J. Geophys. Res.*, **95**, 259, 1990.

Sonnerup, B.U.Ö., J. Ip, and T.-D. Phan, Steady magnetic field reconnection, in *Physics of Flux Ropes*, AGU Monograph, in press, 1990.

Sonnerup, B.U.Ö., I. Papamastorakis, G. Paschmann, and H. Lühr, The magnetopause for large magnetic shear: Analysis of convection electric fields from AMPTE/IRM, *J. Geophys. Res.*, **95**, in press, 1990.

Southwood, D.J., C.J. Farrugia, and M.A. Saunders, What are flux transfer events?, *Planet. Space Sci.*, **36**, 503, 1988.

Wu, C.C., On MHD intermediate shocks, *Geophys. Res. Lett.*, **14**, 668, 1987.

Wu, C.C., The MHD intermediate shock interaction with an intermediate wave: Are intermediate shocks physical?, *J. Geophys. Res.*, **93**, 987, 1988a.

Wu, C.C., Effects of dissipation on rotational discontinuities, *J. Geophys. Res.*, **93**, 3969, 1988b.

Wu, C.C., Formation, structure, and stability of MHD intermediate shocks, *J. Geophys. Res.*, **95**, 8149, 1990.

APPENDICES

Articles generated under AFGL Contract F19628-87-K-0026

1. Theory of the Low-Latitude Boundary Layer

Appendix 1 (in print)
Lotko, W., B.U.Ö. Sonnerup, and R.L. Lysak,
Nonsteady boundary layer flow including ionospheric drag and parallel electric fields, *J. Geophys. Res.*, **92**, 8635, 1987.

Appendix 2 (submitted)
Lotko, W., and M.-M. Shen,
On large scale rotational motions and energetics of auroral shear layers, *J. Geophys. Res.*, 1990.

Appendix 3 (in print)
Phan, T.-D., B.U.Ö. Sonnerup, and W. Lotko,
Self-consistent model of the low-latitude boundary layer, *J. Geophys. Res.*, **94**, 1281, 1989.

2. Theory of Steady Magnetic Field Reconnection

Appendix 4 (submitted)
Phan, T.-D., and B.U.Ö. Sonnerup,
MHD stagnation-point flows at a current sheet including viscous and resistive effects: general two-dimensional solutions, *J. Plasma Phys.*, 1990.

Appendix 5 (in print)
Sonnerup, B.U.Ö., J. Ip, and T.-D. Phan,
Steady magnetic field reconnection, in *Physics of Magnetic Flux Ropes*, \GU Geophys.Monograph 58, pp. 63-75, 1990.

Appendix 6 (in print)
Sonnerup, B.U.Ö., and T.-D. Phan,
Comment on "MHD stagnation point flows in the presence of resistivity and viscosity" by F.T. Gratton, M.F. Heyn, H.K. Biernat, R.P. Rijnbeek, and G. Gnavi, *J. Geophys. Res.*, **95**, 259, 1990.

3. Theory of Intermediate Shock Structure

Appendix 7 (in print)
Hau, L.-N., and B.U. Ö. Sonnerup,
On the structure of resistive MHD intermediate shocks, *J. Geophys. Res.*, **94**, 6539, 1989.

Appendix 8 (in press)
Hau, L.-N., and B.U.Ö. Sonnerup,
The structure of resistive-dispersive intermediate shocks, *J. Geophys. Res.*, **95**, 1990.

4. Observations in the Magnetopause/LLBL Regions

Appendix 9 (in print)
Sonnerup, B.U.Ö., I. Papamastorakis, G. Paschmann, and H. Lühr,
The magnetopause for large magnetic shear: Analysis of convection electric fields from AMPTE/IRM, *J. Geophys. Res.* **95**, 10,541, 1990.

Appendix 10 (submitted)
Paschmann, G., B.U.Ö. Sonnerup, I. Papamastorakis, W. Baumjohann, N. Sckopke, and H. Lühr,
The magnetopause and boundary layer for small magnetic shear: Convection electric fields and reconnection, *Geophys. Res. Lett.*, **17**, 1990.

Appendix 11 (in print)
Sonnerup, B.U.Ö.,
Experimental tests of FTE theories, *Adv. Space Sci.*, **8**, (9)263, 1988.

Appendix 12 (in print)
Papamastorakis, I., G. Paschmann, W. Baumjohann, B.U.Ö. Sonnerup, and H. Lühr,
Orientation, motion, and other properties of flux transfer event structures on September 4, 1984, *J. Geophys. Res.*, **94**, 8852, 1989.

Appendix 1

JOURNAL OF GEOPHYSICAL RESEARCH, VOL. 92, NO. A8, PAGES 8635-8648, AUGUST 1, 1987

Nonsteady Boundary Layer Flow Including Ionospheric Drag and Parallel Electric Fields

W. LOTKO AND B. U. Ö. SONNERUP

Thayer School of Engineering, Dartmouth College, Hanover, New Hampshire

R. L. LYSAK

School of Physics and Astronomy, University of Minnesota, Minneapolis

A simple two-dimensional model is developed for the perpendicular flow dynamics of boundary layers located on closed magnetic field lines in the equatorial magnetosphere. In addition to viscous damping in the equatorial region, nonlocal dissipation associated with the closure of field-aligned currents in the ionosphere and field-aligned potential drops is included and is shown to have two consequences: (1) coupling to the ionosphere causes large-scale disturbances to decay anisotropically and (2) field-aligned potential drops promote long-lived fluctuations at scale lengths that can be comparable to the "inverted V" scale but which vary with the local Hartmann number (a measure of the ratio of ionospheric resistive friction to magnetospheric viscous friction). Depending on the degree of anisotropy, the combined effect is a tendency for the two-dimensional flow to organize into either relatively isotropic eddies or essentially one-dimensional striations. The limiting case of a one-dimensional flow is considered with applications to the low-latitude boundary layer and internal magnetospheric shear layers. A particular boundary layer equilibrium state is compared with observations of an ionospheric boundary layer region and is found to be in fair agreement with the observed properties for reasonable values of the model parameters. It is also shown, under certain conditions, that a monotonically varying internal shear layer can form paired oscillations in the electric field, which are characteristic of the so-called "V shocks" that occur in and above the auroral acceleration region.

1. INTRODUCTION

The dynamics of the high-latitude ionosphere are governed largely by nonlocal processes in which magnetic or mechanical energy of the outer magnetosphere is transferred to and eventually dissipated by the ionosphere. A particular process of this type occurs in association with sheared convection in low-latitude regions of the magnetosphere, for example, in the low-latitude boundary layer separating the shocked solar wind and magnetospheric plasma [*Coleman*, 1971; *Eastman et al.*, 1976, 1985; *Sckopke et al.*, 1981] or the evening equatorial region where sunward flows encounter the more slowing convecting or corotating plasma of the inner magnetosphere [*Wolf and Harel*, 1980; *Olsen et al.*, 1986]. Intense field-aligned currents, broadband turbulence, and auroral precipitation are generally associated with these velocity shear layers, and, for this reason, they are thought to be of central importance in magnetospheric and ionospheric dynamics.

In this paper a two-dimensional model for time-dependent coupling between magnetospheric shear layers and the ionosphere is developed. It describes the horizontal flow dynamics in each of the two regions and differs in at least one important respect from other MHD [*Lysak and Dum*, 1983; *Watanabe et al.*, 1986] or electrostatic [*Lyons*, 1980; *Chiu and Cornwall*, 1980] models of magnetosphere-ionosphere coupling: The magnetospheric convection pattern is not imposed as a boundary condition but is allowed to evolve through self-consistent interaction with the ionosphere. In effect, the model provides a measure of the time scale over which such boundary conditions are meaningful. It predicts, for example, that a free internal shear layer in the equatorial plane of the hyberbolic tangent type can, under certain conditions, evolve toward a "V shock" structure [*Mozer et al.*, 1977; *Temerin et al.*, 1981] on a time scale of 10 min and persist up to an hour. This behavior differs significantly from local analyses of equatorial shear flows (no ionospheric coupling or parallel electric fields), which yield a simple turbulent relaxation of the shear profile [*Miura*, 1984; *Pritchett and Coroniti*, 1984; *Wu*, 1986]. The model also predicts that semibounded flows, as occur near the low-latitude magnetopause, form relatively narrow boundary layers where nearly all of the flow variation is confined [*Sonnerup*, 1980].

The emphasis of the paper is on mesoscale processes occurring at scales of a few kilometers up to a few hundreds of kilometers in the ionosphere (hundreds of kilometers to a few earth radii in the equatorial plane). Dynamic phenomena occurring on such scales are not resolvable in current global MHD simulations of the magnetosphere [see *Ogino*, 1986] for a recent study and survey of previous work) or of the auroral oval [*Miura and Sato*, 1980; *Watanabe et al.*, 1986]. It is also unlikely that any proposed advances in computer technology will be able to accommodate two- or three-dimensional simulations spanning scales of kilometers to hundreds of earth radii. The present study therefore complements global studies by providing detailed information on magnetospheric boundary layer phenomena and their relation to mesoscale auroral processes.

The principal elements of the model include: (1) an ionospheric response characterized by an Ohm's law and current continuity, (2) an equatorial magnetospheric region supporting nonsteady, incompressible viscous flow across a static magnetic field, in which current continuity is also maintained, and (3) a lumped (linear) current-voltage relation [*Lyons et al.*,

Paper number 6A8763
0148-0227/87/006A-8763$05.00

1979] characterizing the plasma response in the intervening region along the magnetic field. In addition, a geomagnetic field model is required to map flux tube elements between the ionosphere and equatorial plane. Elements 1 and 3 are the basis for the electrostatic models proposed by *Lyons* [1980] and *Chiu and Cornwall* [1980]. They are intrinsically passive and incapable of generating dynamical behavior without external forcing. When combined, they define an Ohmic scale length for magnetosphere-ionosphere coupling. *Weimer et al.* [1985] recently concluded, based on DE 1 and 2 data taken at times of approximate magnetic conjunction, that low-frequency electric field fluctuations map between the two spacecraft in accordance with these relations. Element 2 above, together with boundary and initial conditions, governs the dynamics of the system; it is one of the primary mechanisms for generating field-aligned currents in the magnetosphere [*Vasyliunas*, 1970], including currents generated by viscous forces [*Sonnerup*, 1980] and time-varying vorticity [*Hasegawa and Sato*, 1980]. The model differs in this regard from the nonviscous, steady state model described by *Kan and Lee* [1980], in which field-aligned currents are generated by a deceleration and accompanying expansion of the boundary layer flow. The main contribution of this paper is to bring the above ideas together and thereby analyze the interplay between boundary layer and auroral dynamics.

The model is, of course, not without limitations. Self-consistent magnetic fields are neglected, which may be important for applications to the low-latitude boundary layer where the local currents often produce large deformations of the magnetic field. Consequently, it is difficult to assess the relative importance of MHD processes such as flux transfer events [*Russell and Elphic*, 1979; *Cowley*, 1982; *Gosling et al.*, 1985] and the essentially electrostatic processes described here. The passive ionospheric response implied by element 1 precludes any description of small-scale ionospheric irregularities associated with $\mathbf{E} \times \mathbf{B}$ gradient drift or current convective instabilities [*Keskinen and Ossakow*, 1983; *Mitchell et al.*, 1985] or of propagating ionospheric disturbances [*Sato*, 1978; *Rothwell et al.*, 1984; *Lysak*, 1986]. The linear current-voltage relation used in element 3 is known to be inaccurate near the edges of auroral forms [*Lotko*, 1986] and becomes wholly inadequate for large downward field-aligned currents. Since it is a lumped relation, it also eliminates the possibility of describing transit time effects between the ionosphere and equatorial region. Finite Larmor radius effects are also neglected, which become important at transverse scale lengths less than a few kilometers (referenced to 1 R_E), and which influence the behavior of auroral electric fields associated with small scale electrostatic shocks [*Swift*, 1975; *Temerin et al.*, 1981] and kinetic Alfvén waves [*Hasegawa*, 1976; *Goertz and Boswell*, 1979; *Lysak and Carlson*, 1981]. The model described here does not apply to kilometer scale structure in the transverse electric field. Finally, the structure of the magnetic field is not well known and indeed may vary with time, especially near the magnetopause and in the magnetotail. This leads to uncertainty in the scale factors used to map electric fields from the outer magnetosphere to the ionosphere. Although a resolution to these problems will not be of immediate concern for this study, it does underly the ability to forecast ionospheric dynamics in the presence of nonsteady magnetospheric flows. We prefer to view the present study as one step in a progression toward a comprehensive theory encompassing all such phenomena.

The article is organized as follows. In section 2 the basic model equations are developed. In section 3 the spectral representation of these equations is presented, and the behavior of nonlocal damping effects as a function of wave number is discussed. Section 4 contains an analysis of one-dimensional flows with applications to the low-latitude boundary layer and the dynamics of an internal magnetospheric shear layer. A comparison between a particular boundary layer equilibrium state and observations of an ionospheric boundary layer region is also presented in section 4. Finally, section 5 contains a summary and further discussion of the results.

2. Basic Equations

In this section a closed set of equations is derived for the flow dynamics in a low-latitude region of the magnetosphere. The equations include electrodynamic coupling to the ionosphere through field-aligned currents and parallel electric fields. The derivation merges several ideas that have been proposed independently by *Chiu and Cornwall* [1980], *Hasegawa and Sato* [1980], *Lyons* [1980], *Sato and Iijima* [1979], and *Sonnerup* [1980]. The notation is for the most part the same as that used by *Sonnerup* [1980].

We first consider the ionospheric response. The ionosphere is characterized by Pedersen (σ_P) and Hall (σ_H) conductivities, which depend on the electron density, the electron neutral and ion neutral collision frequencies, and the electron and ion gyro frequencies [*Bostrom*, 1973]. The current, electric field, and neutral wind velocity perpendicular to the magnetic field are denoted as $\mathbf{j}_{\perp i}$, $\mathbf{E}_{\perp i}$, and $\mathbf{v}_n$, respectively. These quantities are related by an Ohm's law:

$$\mathbf{j}_{\perp i} = \sigma_P(\mathbf{E}_{\perp i} + \mathbf{v}_n \times \mathbf{B}_i) + \sigma_H \hat{\mathbf{z}} \times (\mathbf{E}_{\perp i} + \mathbf{v}_n \times \mathbf{B}_i) \tag{1}$$

The quantity $\mathbf{B}_i$ is the magnetic field in the ionosphere, and a local slab geometry is considered in which $\mathbf{B}_i = B_i\hat{\mathbf{z}}$.

The field-aligned current $j_{\parallel i}$ in the ionosphere is related to $\mathbf{j}_{\perp i}$ through the current continuity relation:

$$\nabla_i \cdot \mathbf{j}_i = 0 \tag{2}$$

For simplicity the neutral wind velocity, electron and ion densities, and collision frequencies will be taken to be constant in time and space. At high latitudes the magnetic field may also be considered to be constant over the effective height of the ionosphere. In this case, the Pedersen and Hall conductivities are also constant; consequently, neither the Hall nor neutral wind terms in (1) enter (2). Neglecting any vertical stratification in the horizontal fields, we obtain from (1) and (2), after integrating over the height of the ionosphere

$$j_{\parallel i} = -\Sigma_P \nabla_{\perp i} \cdot \mathbf{E}_{\perp i} \tag{3}$$

Here Σ_P is the height-integrated Pedersen conductivity, and

$$\nabla_{\perp i} = \hat{\mathbf{x}}\partial_{x_i} + \hat{\mathbf{y}}\partial_{y_i} \tag{4}$$

where x_i and y_i are ionospheric coordinates perpendicular to the magnetic field. The $\hat{\mathbf{x}}_i$ direction is defined to be locally tangent to a meridian of magnetic latitude (east-west aligned); the $\hat{\mathbf{y}}_i$ direction is locally tangent to a meridian of magnetic longitude or local time (north-south aligned). Throughout this paper, $j_{\parallel i}$ is chosen to be positive for field-aligned currents directed away from the earth.

In treating the ionospheric conductivity as constant we are effectively neglecting auroral conductivity enhancements that

occur in regions of strong upward field-aligned currents. This important quantitative effect may influence the relationship between gradients in the ionospheric electric field and the field-aligned current and therefore in the structure of inverted V precipitation regions. Given this assumption, the model probably applies better to the sunlit and summer ionosphere than to the nightside and winter ionosphere, since, in the former cases, the increased ionization makes auroral enhancements proportionately less dramatic.

Defining an ionospheric potential through the relation $\mathbf{E}_{\perp i} = -\nabla_{\perp i}\phi_i$, we can relate $j_{\parallel i}$ to ϕ_i:

$$j_{\parallel i} = \Sigma_P \nabla_{\perp i}^2 \phi_i \tag{5}$$

The variables $j_{\parallel i}$ and ϕ_i may vary with x_i, y_i, and time t. Once the field-aligned current density is specified the ionospheric potential distribution can be found from (5).

Following *Lyons* [1980] and *Chiu and Cornwall* [1980], we assume that the field-aligned current at the ionosphere is related to the potential drop between the equatorial region and the ionosphere through

$$j_{\parallel i} = K(\phi_i - \phi_e) \tag{6}$$

where $\phi_e(x_e, y_e, t)$ is the potential distribution in the equatorial region in the plane perpendicular to the magnetic field and K is a constant conductance density. The subscript "e" will be used to denote variables in the equatorial region. Note that the divergence of the flux tube implies that $\nabla_{\perp e} \neq \nabla_{\perp i}$.

The phenomenological relation (6) applies primarily to currents in "inverted V" precipitation regions [*Lyons et al.*, 1979], where the net field-aligned current is directed out of the ionosphere. In these regions the current is carried primarily by accelerated kilovolt electrons, and the parameter K lies in the range 0.1–1 $(\mu A/m^2)/kV$ [*Fridman and Lemaire*, 1980]. Currents near the edges of auroral precipitation regions or in narrow channels may not, however, be adequately described by this relation [*Lotko*, 1986]. It is also not clear that it applies in regions of downward field-aligned current, although *Lysak and Dum* [1983] and *Chiu et al.* [1981] have described two special cases where such a relation may have some validity. In addition, kinetic analyses by *Knight* [1973] and *Fridman and Lemaire* [1980] indicate that the linear relationship implied by (6) becomes nonlinear at very small and large potential differences. This "nonlocal Ohm's law" is clearly an oversimplification of the problem; its use here should be regarded as a first step toward a more detailed analysis.

The field-aligned current in the ionosphere can be related directly to the magnetospheric potential by eliminating ϕ_i from (5) and (6). This provides

$$(1 - \lambda_i^2 \nabla_{\perp i}^2) j_{\parallel i} = \Sigma_P \nabla_{\perp i}^2 \phi_e \tag{7}$$

where

$$\lambda_i = (\Sigma_P / K)^{1/2} \tag{8}$$

is the resistive scale length for magnetosphere-ionosphere coupling introduced by *Chiu and Cornwall* [1980] and *Lyons* [1980]. By Fourier transforming (7), *Weimer et al.* [1985] have shown that the current density $j_{\parallel i}$ induced by a given ϕ_e is larger when the gradient scale length of ϕ_e is smaller. This enhancement in current density is attributed to the finite value of K in (6) and, consequently, to accelerated electrons.

One may also eliminate $j_{\parallel i}$ between (5) and (6) to obtain a similar relation between ϕ_i and ϕ_e. On the basis of this latter relation, *Lyons* [1980] and *Chiu and Cornwall* [1980] observed that (1) the high-altitude potential ϕ_e maps (almost) perfectly to the ionosphere if its scale is large compared to λ_i, while (2) a parallel potential drop of magnitude $|\phi_e|$ occurs when the scale of ϕ_e is small compared to λ_i, in which case ϕ_e is not transmitted to the ionosphere. This spatial-filtering effect was recently verified by *Weimer et al.* [1985] by comparing electric field spectral intensities from the DE 1 and 2 satellites at times of approximate magnetic conjunction. The results imply that auroral zone turbulence in the plane perpendicular to the magnetic field is quasi-static at scales exceeding 10 km (that is, it apparently maps electrostatically in accordance with (5) and (6) above). Although the relation could not be tested at smaller scales owing to the measurement technique, other experimental studies using different techniques [*Temerin*, 1978; *Weimer et al.*, 1987] suggest that smaller-scale two-dimensional turbulence also has a rather long correlation time.

Another manifestation of (7) can be found in electric and magnetic fluctuation data from the HILAT satellite, as reported recently by *Vickrey et al.* [1986]. For scale sizes in the range 3–80 km the magnetic fluctuation levels and therefore presumbably the field-aligned current densities $j_{\parallel i}$ are observed to be about the same in the summer and winter hemispheres. Thus they are insensitive to the value of Σ_P. This effect is consistent with (7) for scale sizes that are sufficiently small so that the second term on the left side of the equation dominates the first term, in which case Σ_P can be eliminated from the equation. The observed seasonal dependence of the horizontal velocity or electric field fluctuations reported by Vickrey et al. is also consistent with (5) and (6). When $j_{\parallel i}$ is eliminated between these relations and λ_i is of the order of or larger than 80 km, one finds that the 3- to 80-km scale ionospheric electric fields should vary inversely with Σ_P for a given magnetospheric electric field spectrum. In the absence of any seasonal dependence in the magnetospheric electric fields it follows that the velocity fluctuation intensity in the ionosphere should be larger in winter than summer as observed.

Equation (7) alone provides no insight into the generation of turbulence or fluctuations and must be supplemented by a dynamical equation for $\phi_e(x_e, y_e, t)$. This equation is obtained by extending the one-dimensional, laminar model of *Sonnerup* [1980] to include two-dimensional, time-dependent flow in the plane perpendicular to the magnetic field [cf. *Sato and Iijima*, 1979; *Hasegawa and Sato*, 1980]. If the flow is taken to be incompressible ($\nabla \cdot \mathbf{v} = 0$) and is not allowed to perturb the magnetic field ($\mathbf{B} = \hat{\mathbf{z}} B_e$ with $B_e \simeq$ const in the low-latitude region, and $\hat{\mathbf{z}}$ is directed away from the equatorial plane), then the curl of the MHD momentum equation, together with current continuity ($\nabla_e \cdot \mathbf{j}_e = 0$), provides

$$\rho(\partial_t + \mathbf{v} \cdot \nabla_{\perp e} - \nu \nabla_{\perp e}^2)\Omega = B_e \partial_z j_z \simeq -\frac{B_e j_{\parallel e}}{H} \tag{9}$$

where ρ is the constant plasma density,

$$\mathbf{v} = \frac{\mathbf{E}_e \times \hat{\mathbf{z}}}{B_e} \tag{10}$$

is the magnetospheric convection velocity, $\mathbf{E}_e = -\nabla_{\perp e}\phi_e$, and

$$\Omega = (\nabla \times \mathbf{v}) \cdot \hat{\mathbf{z}} = \frac{\nabla_{\perp e}^2 \phi_e}{B_e} \tag{11}$$

is the scalar vorticity field. Furthermore, $2H$ is the effective

height of the equatorial flow region, and $j_{\parallel e}$ is the field-aligned current at its lower-altitude boundary, that is at $z = H$.

A kinematic viscosity ν has been introduced in (9) to allow for dissipation at small scales. Since the plasma is effectively collisionless, this dissipation should be attributed either to wave-particle interactions occurring at scale lengths comparable to the ion gyro radius or to an enhanced eddy viscosity as discussed by *Sonnerup* [1980] and *Sato* [1982]. A scalar form is used here to assess, in a simple way, the consequences of viscosity in the flow dynamics and structure. As an example, *Tsurutani and Thorne* [1982] have deduced an anomalous particle diffusion rate in the low-latitude boundary layer that is of the order of one-tenth of the Bohm diffusion rate. Using their diffusion rate to estimate the viscosity, one finds that $\nu \sim 100$ km^2 s, which is about a factor of 10 less than estimates of large-scale eddy viscosity [*Miura*, 1984]. It is fair to say that the precise value of the enhanced viscosity is not known and is likely to vary considerably from one region of the equatorial magnetosphere to another.

To close (7) and (9)–(11), we require relationships between $j_{\parallel i}$ and $j_{\parallel e}$ and $\nabla_{\perp e}$ and $\nabla_{\perp i}$. In the intermediate altitude region the plasma is both collisionless and strongly magnetized (plasma pressure much less than magnetic pressure, that is, low β). The amount of field-aligned current diverted into perpendicular current in this region is therefore minimal in comparison to that in the higher β equatorial magnetosphere or the collisional ionosphere. Neglecting any diversion in the intermediate altitude region, conservation of magnetic flux and field-aligned current implies

$$j_{\parallel i} = \frac{B_i}{B_e} j_{\parallel e} \tag{12}$$

For a dipolar magnetic field the relationship between the length element dx_e in the equatorial plane and the corresponding east-west element dx_i in the ionosphere is given by

$$\frac{dx_i}{dx_e} = \frac{\cos \Lambda}{L} = \frac{1}{L^{3/2}} \tag{13}$$

where Λ is the latitude of the foot of the field line in the ionosphere and L is the radial distance, measured in earth radii R_E, to the intersection of a field line with the equatorial plane. It should be noted, however, that the precise value of dx_i/dx_e can deviate significantly from that given by (13). For more realistic magnetic field models one can expect this ratio to depend on both L and the azimuthal coordinate in some complicated manner. Given a value of dx_i/dx_e, conservation of magnetic flux can be used to determine a relation between the orthogonal length elements:

$$\frac{dy_i}{dy_e} = \frac{B_e}{B_i} \frac{dx_e}{dx_i} \tag{14}$$

For the simple type of mapping considered here these relations provide the scale factors required to convert derivatives in the ionosphere to derivatives in the low-latitude magnetosphere:

$$\hat{c}_{x_i} = \frac{dx_e}{dx_i} \hat{c}_{x_e}$$
$$\hat{c}_{y_i} = \frac{dy_e}{dy_i} \hat{c}_{y_e} \tag{15}$$

The mapping implied by (15) assumes both the ionosphere and the equatorial magnetospheric coordinates are locally orthogonal. While this is true for "orange segment" mapping, the mapping relations suggested by empirical magnetic field models are generally nonorthogonal. For example, in these models, ionospheric magnetic latitude and local-time meridians map to curves in the equatorial plane which are nearly parallel in the vicinity of the magnetopause. However, empirical models also become inaccurate in the outer magnetosphere, so the exact mapping relations remain somewhat uncertain. It is fair to say that the orthogonal mapping used here is a reasonable approximation in the inner magnetosphere and perhaps in the outer magnetosphere except in the immediate vicinity of the magnetopause or in the magnetotail current sheet.

The system of (7)–(15), together with appropriate boundary conditions, are sufficient to determine the flow dynamics. When a solution $\phi_e(x_e, y_e, t)$ is given, the ionospheric fields can be determined by making use of (5), (7), and (13)–(15).

It is emphasized that transit time effects between the ionosphere and magnetosphere are not included here. In reality, the ionospheric response to changes in magnetospheric convection will be delayed by the travel time of an Alfven wave to the ionosphere and back, which is the order of a few minutes on the dayside, although it can be significantly longer on the nightside [*Singer et al.*, 1981]. Neglect of this delay allows the use of the lumped relation (6) to couple the two regions. This model is therefore appropriate when the time scale for evolution of the low-latitude flow exceeds the Alfvén wave travel time. As disucssed in the following section, large- and intermediate-scale motions have lifetimes that are long compared with the Alfvén travel time and will therefore be adequately described by this model, whereas the very small-scale motions have the shortest lifetimes and, consequently, will be damped before the ionosphere has time to respond. Whether these small-scale motions are dynamically important will depend on the Reynolds number for the magnetospheric flow and the relative dissipation associated with mechanical viscosity (finite ν) and particle acceleration (finite K).

3. Spectral Representation

In this section the flow model described in the previous section is analyzed under conditions where the flow is either localized or periodic. The objective here is to derive a spectral representation for the flow dynamics, which can be used to analyze the dissipative processes and to exhibit similarities to two-dimensional, incompressible Navier-Stokes flow.

First, (7) and (9) are combined by operating on (9) with $(1 - \lambda_i^2 \nabla_{\perp i}^2)$, using (7) and (12) to eliminate $j_{\parallel i}$ and $j_{\parallel e}$. This provides

$$(1 - \lambda_i^2 \nabla_{\perp i}^2)(\partial_t + \mathbf{v} \cdot \nabla_{\perp e} - \nu \nabla_{\perp e}^2)\Omega = -\frac{\Sigma_P}{H\rho} \frac{B_e^2}{B_i} \nabla_{\perp i}^2 \phi_e \tag{16}$$

where $\mathbf{v}$, Ω, and ϕ_e are related through (10) and (11), and the derivatives in $\nabla_{\perp e}$ and $\nabla_{\perp i}$ are related by (15). In the limit $\Sigma_P \to 0$, where the ionospheric drag is eliminated and $\lambda_i \to 0$, (16) becomes equivalent to the two-dimensional (incompressible) Navier-Stokes equations.

Using the two-dimensional Fourier transform with respect to the equatorial spatial coordinate $\mathbf{x}_e$,

$$F_{\mathbf{k}}(t) = \int F(\mathbf{x}_e, t) \exp(-i\mathbf{k}\cdot\mathbf{x}_e)\, d^2x$$
$$F(\mathbf{x}_e, t) = \int F_{\mathbf{k}}(t) \exp(i\mathbf{k}\cdot\mathbf{x}_e) \frac{d^2k}{(2\pi)^2} \tag{17}$$

Equation (16) can be represented as

$$\frac{d}{dt}\Omega_{\mathbf{k}}(t) = \int M(\mathbf{k}, \mathbf{p})\Omega_{\mathbf{p}}(t)\Omega_{\mathbf{k}-\mathbf{p}}(t)\frac{d^2p}{(2\pi)^2} - \Gamma_{\mathbf{k}}\Omega_{\mathbf{k}}(t) \tag{18}$$

where

$$M(\mathbf{k}, \mathbf{p}) = \frac{\hat{\mathbf{z}}\cdot(\mathbf{k}\times\mathbf{p})}{p^2} \tag{19}$$

The linear damping term in (18) has the form

$$\Gamma_{\mathbf{k}} = \Gamma(k, \theta) = \gamma\left[\frac{k^2\lambda_e^2}{M^2} + \frac{A(\theta)}{1 + k^2\lambda_e^2 A(\theta)}\right] \tag{20}$$

with $k^2 = k_x^2 + k_y^2$, $\theta = \arctan(k_y, k_x)$, and

$$A(\theta) = \delta\cos^2\theta + \sin^2\theta \tag{21}$$

The angles $\theta = 0$ and $\theta = \pi/2$ correspond, respectively, to wave vectors $\mathbf{k}$ that map into the ionosphere in the east-west (k_x) and north-south (k_y) directions. Other parameters in (20) are defined as follows:

$$\gamma = \frac{\Sigma_P}{H\rho}\frac{B_e^2}{B_i}\frac{dx_e^2}{dx_i^2} \qquad \lambda_e = \lambda_i\frac{dy_e}{dy_i}$$
$$M^2 = \frac{\gamma\lambda_e^2}{\nu} \qquad \delta = \left(\frac{dx_e}{dx_i}\frac{dy_i}{dy_e}\right)^2 \tag{22}$$

Here γ is a resistive decay rate associated with ionospheric drag on the convecting magnetic field lines, λ_e is the resistive scale length scaled by the magnetospheric (north-south) length element, M is an effective Hartmann number, and δ is a flux tube anisotropy factor. The flux tube anisotropy factor is a measure of the relative stretching of the east-west and north-south ionospheric flux tube dimensions in the equatorial plane. It is less than 1 when the north-south dimension is stretched more than the east-west dimension. The Hartmann number is a measure of the relative dissipation associated with (ionospheric) resistive drag and (magnetospheric) viscous friction at the scale length λ_e [cf. *Cowling*, 1976]. The ionospheric drag or "magnetic friction" is dominant when $M \gg 1$ and vice versa when $M \ll 1$. It is noted that the Hartmann number and the mechanical Reynolds number Re are not independent parameters. The relation is $M^2 = Re\gamma\tau_{eddy}$ where $\tau_{eddy} = \lambda_e/v_0$ is the eddy turnover time and v_0 is a characteristic flow velocity.

The first term on the right side of (18) describes the nonlinear coupling between Fourier modes and is identical to the Navier-Stokes nonlinearity; the second term describes the modal damping. This system does not support normal modes (waves) since the linearized equation does not admit a real part to the frequency. The hydrodynamic limit follows by setting $\gamma = 0$ in (20). This shows that the effects of ionospheric drag (finite Σ_P) and particle acceleration at intermediate altitudes (finite K and λ_i) enter only the linear damping of the flow. These are nonlocal effects which become dynamically important at large and intermediate scales. Consequently, the flow may be characterized as hydrodynamic only at small scales where viscosity is the primary dissipative process.

In the absence of any dissipation, that is, with $\Gamma_{\mathbf{k}} = 0$, (18) possesses an infinite number of invariants. Only two of these, the mean square vorticity or enstrophy $\langle\Omega^2\rangle$ and the mean square velocity or energy $\langle v^2\rangle$, survive a truncation in k space when the continuum limit is replaced by a discrete Fourier expansion. These are the so-called "rugged invariants." When the dissipation is finite and is produced by viscosity alone, Kolmogorov type cascades are known to arise in which enstrophy is transferred from "externally driven wave numbers" to higher wave numbers, while energy is transferred to smaller wave numbers through an inverse cascade. The dimensionally determined inertial range spectra are $k^{-5/3}$ for the energy cascade and k^{-3} for the enstrophy cascade [*Kraichnan and Montgomery*, 1980]. The effects of nonlocal damping described by the second term in (20) on these cascade processes and inertial range spectra have not been analyzed. To the extent that both inertial ranges are a consequence of the (quadratic) mode-coupling term in (18), it follows from (20) for $\Gamma_{\mathbf{k}}$ that the inversely cascading energy is dissipated nonlocally in the ionosphere and acceleration region, whereas the directly cascading enstrophy is dissipated locally in the boundary layer through viscous damping. The precise shape of the power spectrum may depend, however, in some complicated manner on both the flux tube anisotropy parameter and the Hartmann number and on whether the spectrum is observed in the equatorial magnetosphere or ionosphere. In this regard, it is worth mentioning that *Kelley and Kintner* [1978] have reported experimental evidence for both of the above spectral indices, based on electric field spectra obtained in auroral shear flow regions at altitudes below several thousand kilometers.

Depending on the value of the flux tube anisotropy parameter δ, the dissipation at large scales may be highly anisotropic. This behavior is illustrated in Figure 1, where the decay time, $\tau_d = 1/\Gamma(k, \theta)$, multiplied by γ, has been plotted as a function of $k\lambda_e$ for $\theta = 0$ and $\theta = \pi/2$ for a Hartmann number $M = 35$. The $\theta = \pi/2$ curve is independent of the flux tube anisotropy factor δ. The middle and upper ($\theta = 0$) curves are plotted for $\delta = 0.35$ (dipolar mapping) and $\delta = 0.028$, respectively. (As discussed below, the value of δ may deviate significantly from the dipole value in the outer magnetosphere.) At small wave numbers the decay time for "east-west variations" ($\theta = 0$) is seen to be considerably larger than that for "north-south variations" ($\theta = \pi/2$). A maximum occurs in the decay time at the angle-dependent modal number

$$k_*(\theta)\lambda_e = [M - 1\ A(\theta)]^{1/2} \tag{23}$$

If $M < 1\ A(\theta)$, the maximum occurs at $k = 0$ as for the upper curve in Figure 1. At the smallest scales the local viscosity, which is assumed to act isotropically in the equatorial region, dominates the flow dynamics. Also indicated in Figure 1 are the three wave number regimes for north-south variations where ionospheric drag (finite Σ_P), particle acceleration (finite K), and viscous damping (finite ν) are the dominant dissipative mechanisms.

The scale-dependent and anisotropic dissipation illustrated in Figure 1 suggests that relatively isotropic eddies should develop in the flow pattern in regions of the magnetosphere where the relative maximum in the decay time is nearly isotropic, as for the lower and middle curves in Figure 1. In regions where the maximum in the decay time is highly anisotropic, as for the lower and upper curves in Figure 1, one

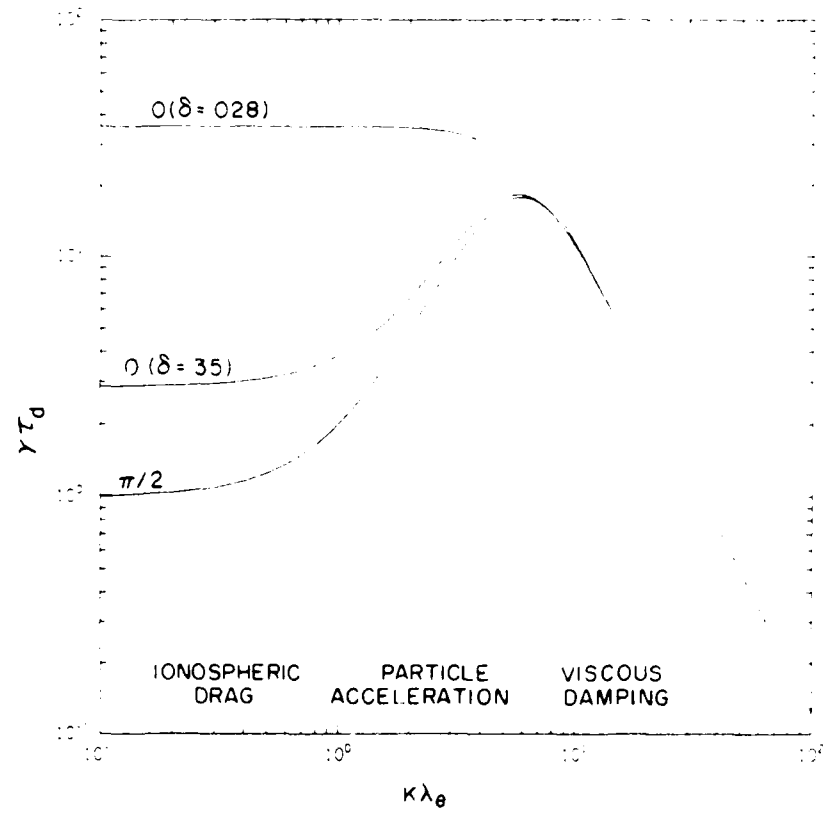

Fig. 1. Normalized damping time ($\gamma\tau_d$ versus $k\lambda_e$ for wave vectors lying in the longitudinal ($\theta = 0$) and latitudinal ($\theta = \pi/2$) directions in the ionosphere for $M = 35$. The parameter $\delta = 0.028$ (0.35) for the upper (lower) $\theta = 0$ curves. Dissipation due to particle acceleration dominates (for latitudinal perturbations) at wave numbers $1 < k\lambda_e < 6$. Ionospheric drag and viscous damping are dominant to the left and right of this interval.

would expect the flow pattern to become striated or filamentary. In either case, the eddy size or striation spacing will be determined by the wavelength $2\pi k_*$ of the slowest decaying mode. When striations occur, their orientation ($\hat{x}$ or $\hat{y}$ aligned) will depend on the orientation of the minimally damped mode, that is, on whether the decay time is maximum for $\theta = \pi/2$ or $\theta = 0$.

The two sets of curves in Figure 1 (lower middle and lower upper) illustrate only two of six distinct regimes in the M-δ parameter space defined by (20) and (23). These include the cases 1, $M < 1$ $\delta < 1$; 2, $1 \delta < M < 1$; 3, $1 \delta < 1 < M$; 4, $M < 1 < 1 \delta$; 5, $1 < M < 1 \delta$; and 6, $1 < 1 \delta < M$. The last two inequalities are represented in Figure 1. The other cases lead to modal decay curves similar to those in Figure 1 but with different types of anisotropy. For example, case 4 implies that both the $\tau_d(\pi/2)$ and $\tau_d(0)$ curves have a maximum at $k = 0$, like the upper curve in Figure 1, with $\tau_d(\pi/2) < \tau_d(0)$ for all k as in Figure 1. Cases 1–3 lead to modal decay curves analogous to those for cases 4–6, respectively, but with the $\tau_d(0)$ and $\tau_d(\pi/2)$ labels interchanged.

It is possible that all six parameter regimes may be realized within the magnetospnere. For dipolar magnetic field lines the flux tube anisotropy parameter depends only on the magnetic latitude and lies in the range $\frac{1}{4} < \delta < 1$. This range of values (or a subset of it) is expected in the inner magnetosphere. In the outer magnetosphere the field line topology deviates significantly from the dipole model, and more extreme values can be expected. For example, the local value of dx_e/dx_i may be much larger than the dipole value near the magnetopause, so δ may be greater than 1 near the magnetopause. In the nightside plasma sheet the field lines are stretched tailward, so both dy_i/dy_e and δ should be smaller than the dipole value. The Hartmann number is expected to be large in low-latitude regions of the inner magnetosphere where the field-aligned current flows out of the ionosphere and where the magnetic field geometry is fairly well known (see Table 1 for some numerical estimates). The value of M is more uncertain in the outer magnetosphere. It is probably also large in the nightside plasma sheet owing to the larger value of dy_e/dy_i in the plasma sheet; it may be less than 1, however, near the magnetopause if dx_e/dx_i becomes much larger than the dipole value. (Note: For orange segment mapping, dy_e/dy_i and therefore M are inversely proportional to dx_e/dx_i.) The Hartmann number may also be small in regions where the large scale field-aligned current flows into the ionosphere and, consequently, where both the "field-aligned resistance" $1/K$ and resistive scale length λ_* become much smaller than what is expected in regions of large-scale outward field-aligned current.

4. One-Dimensional Convection

The principal difficulty with constructing exact solutions to (16) or (18) is due to the convective nonlinearity, $\mathbf{v} \cdot \nabla_\perp \Omega$. When the flow is one-dimensional with $\mathbf{v} = v\hat{x}$ (along lines of constant latitude in the ionosphere) and has a gradient only in

TABLE 1 Data for Illustrative Numerical Examples

Parameter	Value
Basic Parameters	
Height-integrated Pedersen conductivity	$\Sigma_P = 6$ mho
Field line conductance density	$K = 10^{-9}$ mho m^2
Ionospheric latitude	$\Lambda = 73$
Equatorial distance*	$L = 12$
Ionospheric magnetic field*	$B_i = 6 \times 10^{-5}$ t
Equatorial magnetic field*	$B_e = 2 \times 10^{-8}$ t
Equatorial height	$H = 10\ R_E$
Maximum boundary layer speed ($y = 0$)	$v_0 = 200$ km/s
Kinematic viscosity	$\nu = 10^8$ m^2/s
Boundary layer density	$n_0 = 10^7$ protons/m^3
Derived Parameters	
Longitudinal-stretching factor	$dx_e/dx_i = 42$
Latitudinal-stretching factor	$dy_e/dy_i = 71$
Flux tube anisotropy factor	$\delta = 0.35$
Resistive-coupling length (at ionosphere)	$\lambda_i = 80$ km
Resistive-coupling length (at equator)	$\lambda_e = 5700$ km
Resistive-damping rate	$\gamma = 3.8 \times 10^{-3}$/s
Maximum boundary layer electric field ($y = 0$)	$E_0 = 4$ mV/m
Effective Hartmann number	$M = 35$

*Calculated for a dipolar magnetic field.

the $\hat{y}$ direction (along meridians of longitude in the ionosphere), the convective derivative is identically zero. We now consider this case which may pertain to ionospheric structures elongated in the east-west direction. For simplicity the neutral wind velocity appearing in (1) is taken to be zero.

With normalizations,

$$\tau = \gamma t \qquad y = y_e/\lambda_e = y_i/\lambda_i \tag{24}$$

Equation (16) becomes

$$(1 - \partial_y^2)L\{\Omega\} + \Omega = 0 \tag{25}$$

where

$$L\{\Omega(y, \tau)\} = \left(\partial_\tau - \frac{1}{M^2}\partial_y^2\right)\Omega(y, \tau)$$

M is the effective Hartmann number defined in (22). Using the relation between Ω and the equatorial electric field E_e, a first integral of (25) provides

$$(1 - \partial_y^2)L\{E_e\} + E_e = E_x \tag{26}$$

where E_x is an integration constant depending on the boundary conditions. With periodic boundary conditions, it is easy to show that the solutions to (26) always decay to the uniform state, $E_e = E_x$ as $\tau \to \infty$. Nontrivial equilibrium or time asymptotic solutions require finite boundary conditions, either on a doubly bounded interval or a semibounded interval.

Given a solution $E_e(y, \tau)$, which is either periodic or bounded, the ionospheric electric field E_i, the equatorial perpendicular current density j_{ye}, averaged over the height of the equatorial region H, and the field-aligned potential drop $\Delta\phi_\parallel(y, \tau) \equiv j_\parallel(y, \tau)/K$ are given in terms of $E_e(y, \tau)$ as

$$E_i(y, \tau) = \frac{dy_e}{dy_i}\left[E_x - L\{E_e(y, \tau)\}\right] \tag{27}$$

$$j_{ye}(y, \tau) = j_x + \sigma_0 L\{E_e(y, \tau)\} \tag{28}$$

$$\Delta\phi_\parallel(y, \tau) = \lambda_e L\{\partial_y E_e(y, \tau)\} \tag{29}$$

where

$$\sigma_0 = \frac{\Sigma_P}{H}\frac{B_e}{B_i}\frac{dy_e^2}{dy_i^2} \tag{30}$$

Relations (27) and (29) follow from the developments in section 2. Relation (28) is obtained using $j_{\parallel e} = H\hat{c}_e j_{ye}$. The integration constant j_x is determined by the boundary conditions on the force balance equation in the equatorial region, which may include a constant pressure gradient in the $\hat{x}$ direction.

Notice that j_{ye} is proportional to E_i and therefore to j_{yi}. The relation is

$$j_{ye} + \frac{h}{H}\frac{dx_i}{dx_e}j_{yi} = j_x + \sigma_0 E_x \tag{31}$$

where h is the effective height of the ionosphere. Evaluating (31) at two boundaries determines j_x and E_x in terms of the boundary conditions on j_{ye} and j_{yi}. Relations (26)–(29) also imply that $j_{ye} = j_x - \sigma_0(E_e - E_x - \hat{c}_e\Delta\phi_\parallel)$. Therefore, in contrast to the earlier model described by *Sonnerup* [1980], we find that $j_{ye} = j_x - \sigma_0(E_e - E_x)$ only if the field-aligned potential drop is zero.

4.1. *Boundary Layer Flows*

We now consider nonsteady flow in a semibounded domain with $0 \le y \le \infty$. When the flow velocity is fixed at a boundary, in this case at $y = 0$, the velocity variation is confined to a relatively narrow layer near the boundary, as occurs near the low-latitude magnetopause.

The general solution to (26) on the interval $0 \le y \le \infty$ may be obtained by taking a Laplace transform in y, solving the resulting ode in τ, and then inverting the Laplace transform. This yields four integration constants at $y = 0$ (in addition to E_x). Since the solution is required to be finite at $y = \infty$, only two of the four constants are independent. A simpler approach is to use a sine or cosine Fourier transform [*Erdélyi et al.*, 1954] in y rather than a Laplace transform. In this case, only two integration constants are obtained, but the solution is explicitly finite at $y = \infty$. The latter approach is less flexible than the former because the types of boundary conditions that can be treated in the time-dependent problem are restricted; only even derivatives of E_e can be specified at $y = 0$ when the sine transform is used, whereas the cosine transform yields odd derivatives of E_e at the boundary. Using either approach, one can show that a unique time-independent boundary layer state results as $\tau \to \infty$ if the boundary conditons are also time-independent. In this section we will demonstrate this statement using the simpler sine transform method and subsequently analyze the properties of the equilibrium state.

Making use of the Fourier sine transform, the solution to (26) is

$$E_e(y, \tau) = E_x + \tilde{E}_e(y, \infty) + \frac{2}{\pi}\int_0^\infty [\tilde{E}_{ek}(0) - \tilde{E}_{ek}(\infty)]e^{-\tau_k}\sin ky\, dk \tag{32}$$

where

$$\tilde{E}_{ek}(\infty) = \frac{k}{k^4 + k^2 + M^2}\left[(1 + k^2)E_0 - E_x - E_{0k}\right] \tag{33}$$

contains the boundary information at $y = 0$. $\tilde{E}_e(y, \infty)$ is the inverse sine transform of $\tilde{E}_{ek}(\infty)$, and $\tilde{E}_{ek}(0) = E_{ek}(0) - E_x$.

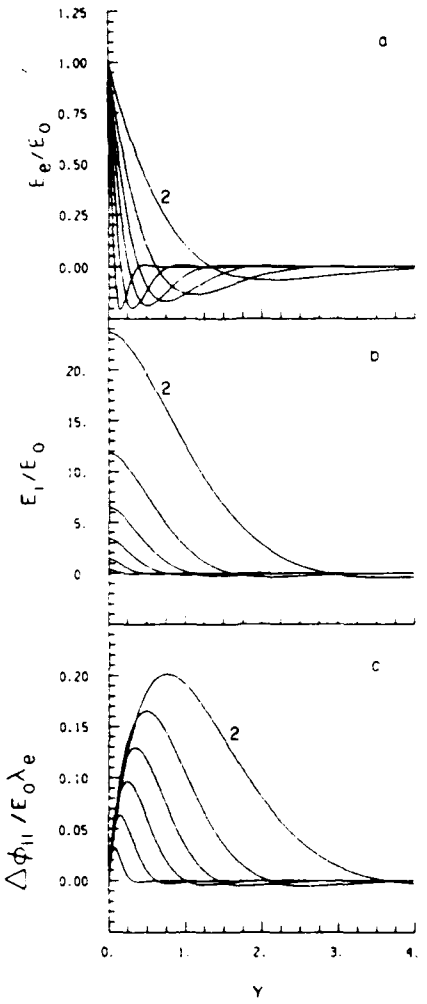

Fig. 2. Variation of the equilibrium state with the Hartmann number for (*a*) the equatorial electric field, (*b*) the ionospheric electric field, and (*c*) the field-aligned potential drop versus $y = y_i/\lambda_i = y_e/\lambda_e$. In each panel the six curves (upper to lower, respectively) correspond to $M = 2$, 5, 10, 20, 50, and 200. Other parameters are $\Delta\phi_{\parallel 0} = 0$, $E_x = 0$, and $dy_e/dy_i = 71$.

where $E_{ek}(0)$ is the sine transform of the initial state. The damping rate for mode k is

$$\Gamma_k = \frac{k^2}{M^2} + \frac{1}{1 + k^2} \tag{34}$$

Here k is the wave number multiplied by λ_e.

As $\tau \to \infty$, the integral term in (32) approaches zero. The time asymptotic solution is

$$E_e(y, \infty) = \frac{E_0 - E_x}{\cos \psi} e^{-k_- y} \cos (k_- y + \psi) + E_x \tag{35}$$

with

$$k_\pm = \tfrac{1}{2}(2M \pm 1)^{1/2} \tag{36}$$

$$\psi = \arctan\left(\frac{2E_0'' E_0 - 1}{(4M^2 - 1)^{1/2}}\right) \tag{37}$$

When $M \gg 1$, the oscillation length and exponential decay length in (35) are nearly equal since $k_+ \simeq k_-$. When $M < \frac{1}{2}$, k_- becomes imaginary, and the equilibrium field decreases monotonically from its value at $y = 0$. This case corresponds to a viscous dominated boundary layer.

Equations (32) and (35) show that a unique boundary layer state $E_e(y, \infty)$, depending only on the boundary conditions and the Hartmann number M and independent of the initial conditions, is approached as $\tau \to \infty$. The flow variation or vorticity in the boundary layer extends over a distance of order $\lambda_e k_+$. This result applies only to one-dimensional flows, however, and cannot be extended to two-dimensional flows for which nonlinear mode coupling may be important.

An example of a boundary layer equilibrium state is shown in Figure 2 when (1) the flow velocity (or electric field) is specified at $y = 0$, (2) the field-aligned current or potential drop is zero at $y = 0$, and (3) $E_x = 0$. The first condition determines the integration constant E_0. The second condition determines the integration constant E_0''. From (29) and (35) we find $E_0'' = M^2 E_0/(M + 1)$. A finite E_x simply adds a constant offset to electric fields. The six curves in each panel of Figure 2 correspond to different Hartmann numbers: $M = 2$, 5, 10, 20, 50, and 200. The equatorial and ionospheric electric fields and the field-aligned potential drop are shown in the top, middle, and bottom panels. The electric fields are normalized to E_0. With this normalization, an equatorial electric field with amplitude 1 would produce an ionospheric electric field with amplitude dy_e/dy_i if the conductivity along magnetic field lines were infinite (no field-aligned potential drop). The value of dy_e/dy_i used to evaluate E_i in Figure 2 is 71 (from the dipole magnetic field parameters in Table 1). $\Delta\phi_{\parallel}$ is normalized to $E_0\lambda_e$. For reference the illustrative parameters given in Table 1 are $E_0 = 4$ mV/m and $\lambda_e = 5700$ km.

Since the scale length of the boundary layer varies as k_+^{-1}, which varies approximately as $M^{-1/2}$ for large M, the boundary layer width in Figure 2 is smaller for larger Hartmann numbers. It is also apparent that the magnitudes of the field-aligned potential drop (and current) and ionospheric electric field are smaller for large Hartmann numbers. At $y = 0$ the ionospheric electric field is reduced by a factor of $1/(M + 1)$ from its perfectly mapped value, and for large Hartmann numbers, is substantially less than the perfectly mapped value. This effect is a consequence of the field-aligned potential drop.

For $E_0 > 0$ (duskside) a perpendicular magnetospheric current flows out of the boundary layer at $y = 0$ while a perpendicular ionospheric current flows into the boundary layer at $y = 0$. When $j_x = E_x = 0$, (31) implies that the net current flowing into the ionospheric boundary (at $y = 0$) leaves the system at the magnetospheric boundary. Consequently, there must be a net field-aligned current out of the ionosphere as shown in Figure 2*c*. Since there is essentially no return current (that is, into the ionosphere) in Figure 2*c*, this example applies to the higher-latitude, region 1 current system versus the lower-latitude, region 2 current system. When $E_0 < 0$ (dawnside), the sense of the boundary currents and net field-aligned current is reversed. Finite values of j_x and E_x change the partition of incoming and outgoing perpendicular currents at $y = 0$ and $y = \infty$ but do not alter the current continuity of the system or the inferred direction of the field-aligned current.

Given that the equatorial perpendicular current is proportional to the ionospheric electric field including a sign reversal, a comparison of Figures 2*a* and 2*b* shows that this current acts, through a $\mathbf{j} \times \mathbf{B}$ force, to brake the tailward flow. As discussed by *Vasyliunas* [1979], this force is a consequence

of the finite ionospheric Pedersen conductivity. The impressed ionospheric electric field induces a perpendicular ionospheric current. As is the case for a duskside boundary layer, field-aligned currents flow out of the ionosphere where gradients exist in the ionospheric perpendicular current. Perpendicular boundary layer currents are then generated at the associated gradients in the field-aligned current. It is emphasized that the perpendicular boundary currents discussed above do not drive the boundary layer flow; when $\Delta\phi_{\parallel} = 0$ at $y = 0$ as in Figure 2, the energy dissipated by Ohmic and viscous processes is supplied entirely by a mechanical shear stress at the boundary.

The average transport of magnetic flux in the boundary layer is proportional to the integral of E_e over the interval $0 \le y \le \infty$. Figure 2*a* exhibits a net transport in the anti-sunward direction, although the average value and direction will vary with the offset electric field E_x. For large M the average flow relative to the offset value is proportional to $M^{-3/2}$ and therefore negligible in large Hartmann number boundary layers. In such cases, the average convection is determined almost entirely by the offset electric field. The occurrence of the sunward convecting "overshoot" region in Figure 2*a* suggests that in addition to the general sunward flow in the interior of the magnetosphere there should be a stronger sunward flow just earthward of the tailward flow region. *Eastman et al.* [1985] have, in fact, shown two examples from ISEE 1 data of dusk side boundary layer regions exhibiting such overshoots. (It is noted, however, that the more or less uniform flow located earthward of the observed overshoots is in the tailward rather than sunward direction in these data; this may be due to a (physical) offset electric field as discussed above.) In the context of the present model the observed overshoots are interpreted as evidence for field-aligned potential drops. As pointed out by *Sonnerup* [1980], there is no overshoot region for a viscous-dominated boundary layer, corresponding to $M < \frac{1}{2}$ in the present model. It is clear in Figure 2*a* that the effect of the field-aligned potential drop, that is, the overshoot region, becomes more prominent at large Hartmann numbers.

4.2. *Comparison With Data*

We have attempted to fit a particular equilibrium solution to observations of the ionospheric boundary layer region extending between the poleward and equatorward edges of the region 1 current system (current away from the earth on the duskside). The polar cap boundary (or magnetopause projection) may be regarded as the poleward edge of the region 1 current system. To put the model in the context of other work, the equatorward edge of the region 1 current system is usually taken to be a given boundary condition in the Rice convection model [*Harel et al.*, 1981] which applies at latitudes below this boundary.

Figure 3 shows a comparison between the model and observations reported by *Smiday et al.* [1980] for the summer hemisphere near 1700 MLT at an altitude of a few hundred kilometers between about 73° and 71° invariant latitude (S3-2 data). The asterisks and plus signs in the top panel of the figure are data points inferred from *Smiddy et al.* [1980, Figure 4] for the observed magnetic deflection and ionospheric electric field, respectively. The dotted line is the reference geomagnetic field given by *Smiddy et al.* [1980, Figure 4]. The upper and lower solid curves in the top panel are the magnetic deflection ΔB_x and the ionospheric electric field E_{yi} predicted by the one-

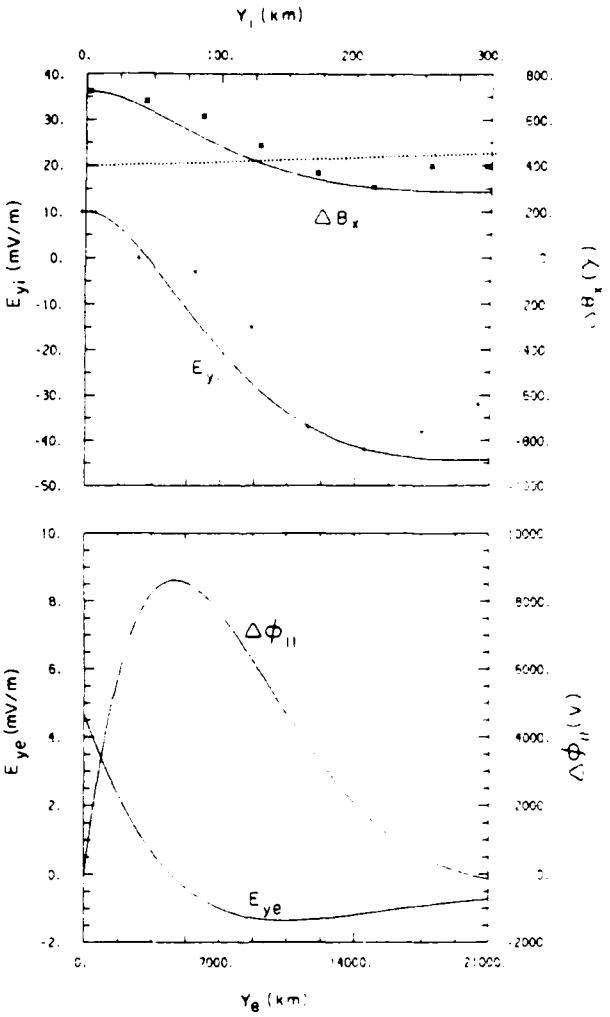

Fig. 3. Comparison between a boundary layer equilibrium state and ionospheric electric field (plus sign) and magnetic deflection (asterisk) data inferred from *Smiddy et al.* [1980, Figure 4]. The dotted line is the reference geomagnetic field from Smiddy et al. The solid curves in the top panel are an approximate fit to the data. The predicted field-aligned potential drop and equatorial electric field are shown in the bottom panel. The horizontal axis in the top panel is the ionospheric distance (in kilometers) from the poleward edge of the region 1 current system; in the bottom panel it is the equatorial distance (in kilometers) from the magnetopause. A one-to-one correspondence between these distances is assumed so that the magnetopause maps into the poleward edge of the region 1 current system in the ionosphere. The equatorward edge of the region 1 current system is located at the minimum in the observed magnetic deflection.

dimensional boundary layer model. (Smiddy et al. used a different coordinate system in which their $\hat{x}$ and $\hat{y}$ correspond to our $\hat{y}$ and $\hat{x}$, respectively.

The observed amplitude of the electric field at the polar cap boundary and its observed peak-to-peak value from the poleward to equatorward edges of the region 1 current system are used to constrain two of four model parameters required to calculate $E_{yi}(y)$. These are $E_0 = 4.6$ mV m and $E_x(dy_e/dy_i) = -42$m V m. The other two parameters of the solution are the Hartmann number and the Ohmic scale length λ_i. In principle, the Pedersen conductivity and "field-aligned conductance" K

required to calculate λ_i can be determined as follows. The parameter K may be estimated following the procedure described by *Lyons et al.* [1979], wherein the field-aligned potential drop and current are determined from the observed characteristics of the electron precipitation. (This assumes that most of the field-aligned current is carried by accelerated electrons, which is usually a good approximation in regions where the potential drop exceeds a few kilovolts.) The Pedersen conductivity (in mhos) can be estimated from the relation between the magnetic deflection (in nanoteslas) and electric field (in millivolts per meter) derived by Smiddy et al., which also follows from our model:

$$\Delta B_x - 1.256\Sigma_P E_{yi} = \text{const}$$

This relation assumes that ΔB_x may be calculated from $\mathbf{j}_{\|i}$ in the infinite current sheet approximation. Two paired data values for ΔB_x and E_{yi} are required to determine Σ_P and the constant. This relation is also used to calculate the predicted magnetic direction shown in Figure 3 from the predicted electric field. Unfortunately, Smiddy et al *did not provide enough* details of the associated electron precipitation to estimate the parameter K as described above, although they did note that a rather intense inverted V event occurred slightly to the right (that is, equatorward) of the ionospheric convection reversal.

A reasonably good fit to the data was obtained by choosing $M = 6.0$ and $\lambda_i = 150$ km. This value for the Hartmann number is a factor of 6 less than the illustrative value given in Table 1. The difference is probably due primarily to deviations from dipolar magnetic field mapping since M is directly proportional to dy_e^2/dy_i^2; a larger viscosity would also reduce the Hartmann number but less so since $M \sim \nu^{-1/2}$. The value of the Ohmic scale length used in Figure 3 is also larger by a factor of 2 than the illustrative value given in Table 1. Since the Pedersen conductivity inferred from the above relation between ΔB_x and E_{yi} is 6.43 and therefore not appreciably different from the value of 6 in Table 1, this difference is attributed to a smaller value of the field line conductance K. Its inferred value is 2.86×10^{-10} mho/m^2, which is in the range of values estimated by *Fridman and Lemaire* [1980] for typical inverted V electron events.

The two curves in the bottom panel of Figure 3 show the predicted equatorial field and field-aligned potential drop. In order to generate these curves it is necessary to specify the value of dy_e, dy_i, which is taken here to be the dipole magnetic field value of 70 for an invariant latitude of 73°. Although there are no points for comparison with the observations of *Smiddy et al.* [1980], both curves have profiles and amplitudes within the range of expected values. It is interesting that the fit predicts a maximum field-aligned potential drop of about 8.5 kV. It is also worth noting that the peak in the field-aligned potential drop and therefore in the energy flux in the associated inverted V precipitation occurs equatorward of the ionospheric convection reversal as discussed by Smiddy et al. The predicted equatorial convection reversal also occurs on a magnetic field line that is equatorward of that on which the ionospheric convection reversal occurs. This feature seems to be consistent with the observation that soft magnetosheathlike precipitation was found only on the poleward side of the ionospheric convection reversal. Note that if the equatorial convection reversal had occurred poleward of the ionospheric convection reversal, this would put some of the magnetosheath precipitation on sunward convecting field lines, which would be inconsistent with in situ particle observations in the equatorial boundary layer region [*Eastman et al.*, 1985].

4.3. *Flow Dynamics in an Internal Shear Layer*

As discussed earlier, equilibrium solutions other than a uniform flow do not exist when the vorticity distribution is either periodic or vanishes at the boundaries. We now consider the latter case in an infinite domain with boundary conditions $\Omega(\pm\infty, \tau) = 0$. Since there are no fixed boundaries for this case, we do not expect to find boundary layer phenomena as in the previous section. Rather, the velocity field develops as a free internal shear layer.

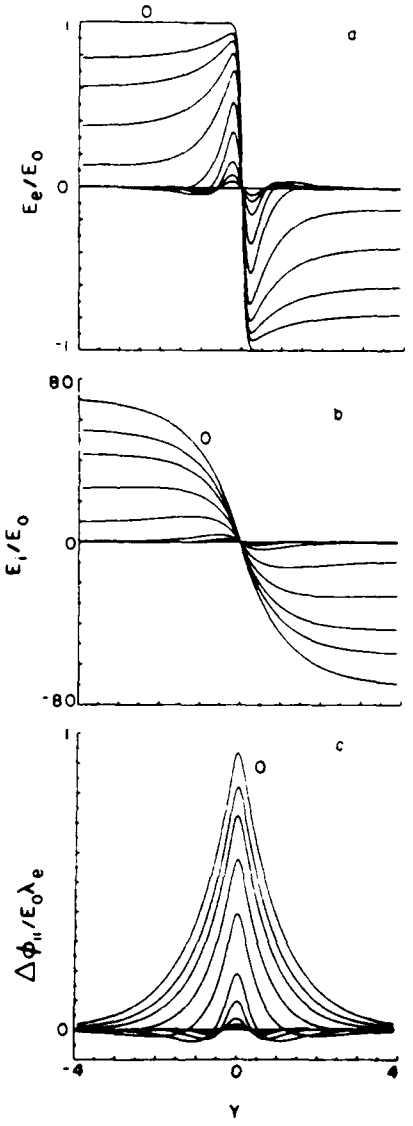

Fig. 4. Dynamics of a small-scale internal shear layer for (*a*) the equatorial electric field, (*b*) the ionospheric electric field, and (*c*) the field-aligned potential drop versus $y = y_i/\lambda_i = y_e/\lambda_e$. The 11 curves for each field variable correspond to times $\gamma t = 0, \frac{1}{4}, \frac{1}{2}, 1, 2, 5, 10, 20, 30, 40$, and ∞. All fields are zero at $t = \infty$, and E_i is essentially zero at $\gamma t > 10$. The initial condition is given by (40) with $L_v = 0.1$

Equation (25) for the vorticity field is first solved using exponential Fourier transforms. The vorticity distribution is then integrated from $y' = 0$ to $y' = y$ to obtain the electric field. This yields

$$E_e(y, \tau) = E_e(0, \tau) - \frac{B_e \lambda_e}{2\pi} \int_{-\infty}^{\infty} \Omega_k(0) e^{-\Gamma_k \tau} \frac{e^{iky} - 1}{ik} dk \qquad (38)$$

where $\Omega_k(0)$ is the Fourier transform of the initial vorticity distribution, Γ_k is defined by (34), and $E_e(0, \tau)$ is an integration constant specifying the value of E_e at $y = 0$. The particular choice of $E_e(0, \tau)$ does not affect the internal structure of the shear layer, which is described by the integral term in (38). For simplicity it will be set to zero.

As an example, we consider an initial vorticity distribution of the form

$$\Omega(y, 0) = \frac{E_0}{B_e \lambda_e L_s} \operatorname{sech}^2 \frac{y}{L_s} \qquad (39)$$

The shear scale length L_s is normalized to λ_e. The initial electric field distribution is

$$E_e(y, 0) = E_0 \tanh \frac{y}{L_s} \qquad (40)$$

Choosing $E_e(0, \tau) = 0$ allows the electric field distribution to relax to zero at both $y = \pm \infty$ as $\tau \to \infty$. If instead, $E(0, \tau) = E_\infty (1 - \exp(-\tau))$, the electric field would remain at E_∞ at $y = -\infty$. As $\tau \to \infty$, it would then become uniform and approach the constant value E_∞.

The evolution of the equatorial and ionospheric electric fields (normalized to E_0) and the parallel potential distribution (normalized to $E_0 \lambda_e$) are shown in Figure 4 for $L_s = 0.1$ and $M = 35$ (the Hartmann number given in Table 1). Eleven curves are plotted for each field variable corresponding to times $\gamma t = 0, \frac{1}{4}, \frac{1}{2}, 1, 2, 5, 10, 20, 30, 40$, and ∞. For reference the value of γ^{-1} given in Table 1 is 4.4 min.

The time scale for evolution of the fields shown in Figure 4 clearly depends on the scale length of the variation. The large- and small-scale length variations are more rapidly damped than the intermediate scale variations. This is particularly apparent in Figure 4*a* and is consistent with the damping characteristics depicted in Figure 1. After the large- and small-scale variations have died away a localized (intermediate scale) oscillation remains on a rather long time scale. This oscillation has the characteristic waveform of a so-called "V shock" and is accompanied by the development of small (downward) return currents in Figure 4*c*. While the overall structure of the equatorial electric field changes dramatically in the course of time, the parallel potential profile does not. It resembles a slowly decaying "inverted V" precipitation region that becomes increasingly narrow with time, particularly at early times.

The small and intermediate scales are mostly filtered out of the ionospheric electric field (Figure 4*b*). This is a consequence of the relation [*Weimer et al.*, 1985]

$$E_{ik}(t) = \frac{dy_e}{dy_i} \frac{E_{ek}(t)}{1 + k^2}$$

which shows that $E_{ik} \to 0$ as $k \to \infty$. Since the Fourier spectrum of the equatorial field (compare (42) below) contains significant energy at large scales ($k \to 0$), the amplitude (though not the profile) of the ionospheric electric field at early times is very close to its perfectly mapped value of $(dy_e/dy_i)E_e$. It decays at approximately an exponential rate given by $\Gamma_{ik} \approx \gamma$.

Similarly, (6) and (7) imply

$$\Delta\phi_{ik}(t) = -\frac{k^2}{1 + k^2} \Phi_{ek}(t)$$

For $k \simeq 0$ the field-aligned potential drop is $\Delta\phi_{ik} \simeq 0$, so this relation also implies that large-scale variations map almost perfectly between the ionosphere and magnetosphere. In addition, it indicates that the scale length of the largest field-aligned potential drops should occur at the smallest scale lengths present in the equatorial spectrum. The field-aligned potential in Figure 4*c* exhibits this behavior. Finally, noting that $j_{ye} = -\sigma_0 (dy_e/dy_i) E_i$, a comparison of Figures 4*a* and 4*b*

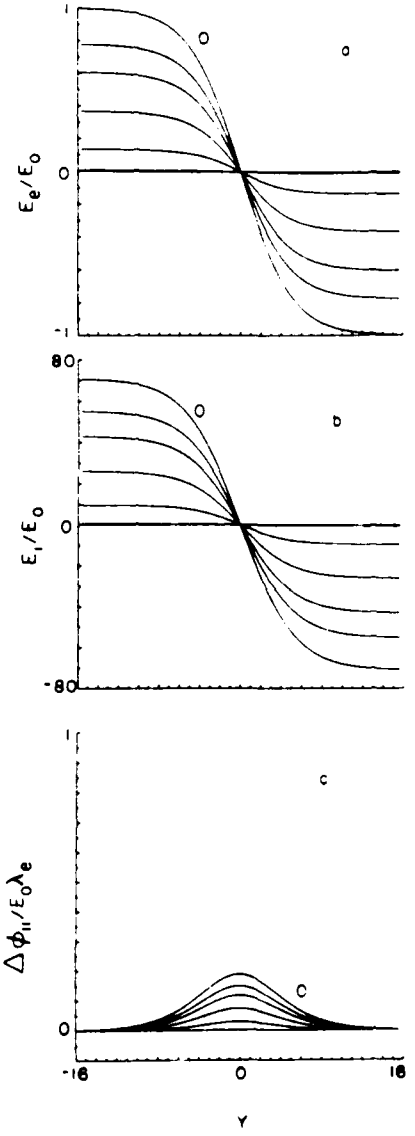

Fig. 5. Dynamics of a large-scale internal shear layer. Same format as Figure 4. The initial condition is given by (40) with $L_s = 5.0$. All fields are essentially zero at $\gamma t \geq 5$.

shows that the equatorial shear layer acts as a dynamo ($\mathbf{j} \cdot \mathbf{E} < 0$) except to the left and right of the primary oscillation in Figure 4*a*. Return flows and currents occur where $\mathbf{j} \cdot \mathbf{E} > 0$.

For comparison a solution with $L_\parallel = 5$ is shown in Figure 5. In this case, the equatorial shear profile simply relaxes at approximately an exponential rate equal to γ. Furthermore, the shear layer acts as a dynamo throughout the entire equatorial region. Since the initial state now contains very little energy at small or intermediate scales, the oscillatory and "nonideal" behavior attributable to parallel electric fields is essentially absent. These results extend those obtained by *Lysak* [1985], in which oscillatory flow occurred for small-scale but not large-scale imposed flows in a model where the equatorial response was described by a simple lumped conductance.

Although it has been shown above that a free internal shear layer of the hyperbolic tangent type can, under certain conditions, evolve toward a V shock structure, it is emphasized that this behavior is not a consequence of the initial hyperbolic tangent state. Rather, one can expect V shock signatures in the evolving electric field distribution whenever there is significant power at the wavelength $2\pi k_*$ of the most weakly damped mode. For $y \lesssim 2\pi k_*$ and $M \gg 1$, where $k_* \simeq M^{1/2}$ is the wave number when Γ_k is a minimum, one can derive the following expression for the time asymptotic electric field:

$$E_z(y, \tau) \sim E_{zk_*}(0) \frac{M}{(4\pi\tau)^{1/2}} \exp\left(-\frac{2}{M}\tau\right) \sin k_* y \qquad (41)$$

$$\tau \to \infty$$

The initial electric field spectrum is defined as $E_{zk}(0) = -B_z \lambda_\parallel \Omega_k(0)\, k$. For comparison with Figures 4 and 5 we have taken $\Omega(y, 0)$ to be symmetric as in (39). Relation (41) clearly shows that the oscillatory behavior, present in Figure 4*a* and absent in Figure 5*a*, is governed primarily by the initial spectrum. The spectrum associated with (39) is

$$E_{zk}(0) = \frac{2L_\parallel E_0}{\sinh\left[(\pi/2) k L_\parallel\right]} \qquad (42)$$

Evaluating at $k = k_*$ and using $M = 35$, we find $E_{zk_*}(0) \simeq 0.19 E_0$ when $L_\parallel = 0.1$, while $E_{zk_*}(0) \simeq 1.7 \times 10^{-19} E_0$ when $L_\parallel = 5$.

5. SUMMARY

Although the model and results described in this paper should be viewed as illustrative rather than as applicable in detail to the magnetosphere, they do indicate a number of interesting effects of relevance to the low-latitude boundary layer and internal magnetospheric shear layers. The spectral analysis described in section 3 shows that while magnetospheric flows are nonlocally dissipated by the ionosphere, the dissipation becomes less effective at smaller scales in the presence of parallel electric fields, leading, under certain conditions, to a minimum in the decay rate at an ionospheric scale length of $\lambda_\parallel M^{1/2}$. M is an effective Hartmann number which measures the ratio of (ionospheric) resistive friction to (magnetospheric) viscous friction, and $\lambda_\parallel$ is the resistive scale length for magnetosphere-ionosphere coupling defined by *Lyons* [1980] and *Chiu and Cornwall* [1980]. For large Hartmann numbers the scale length at minimum damping is therefore less than the inverted V scale (essentially $\lambda_\parallel$). Large Hartmann number flows are expected in low-latitude regions of the inner magnetosphere where the field-aligned current is dissipated out of the ionosphere and where the magnetic field geometry is fairly well known. In the outer magnetosphere the value of the Hartmann number is somewhat uncertain owing to the uncertainty in the magnetic field mapping. It may be less than 1 in the immediate vicinity of the magnetopause or in regions where the field-aligned current is directed into the ionosphere and consequently where the "field-aligned conductance" is much larger than what is expected in regions of outward field-aligned current.

For parameters illustrative of the low-latitude boundary layer and the high-latitude ionosphere the decay time for fluctuations at the wave number $k = M^{1/2} \lambda_\parallel$ may be as large as 1 hour. In contrast, the decay time for large-scale ($k \to 0$) fluctuations may be as small as a few minutes, which is comparable to the time scale for the transverse Kelvin-Helmholtz (K-H) instability that is thought to occur at the magnetopause [cf. *Miura*, 1984; *Wu*, 1986]. One can therefore expect nonlocal ionospheric dissipation to be an important factor in anomalous transport processes occurring near the low-latitude magnetopause, especially those involving large-scale eddy motion. The modal decay rate can also be anisotropic in $\mathbf{k}$ owing to the anisotropic mapping of flux tube elements between the ionosphere and equatorial magnetosphere. For dipolar magnetic field mapping at auroral latitudes the decay time for north-south variations ($\mathbf{k}$ directed along ionospheric meridians of magnetic LT or longitude) is smaller by a factor of $\delta \simeq 0.35$ than the decay time for east-west variations ($\mathbf{k}$ directed along ionospheric meridians of magnetic latitude). For more accurate magnetic field models, δ is likely to be larger than this value on field lines near the low-latitude magnetopause but smaller on field lines threading the nightside plasma sheet. The modal decay times, which depend on both δ and M, may therefore vary significantly in different regions of the magnetosphere. It is suggested that these differences will lead in some cases to the formation of more or less isotropic eddies and in others to striated or filamentary flows.

As a preliminary step toward a fully nonlinear, two-dimensional analysis, the limiting case of a one-dimensional flow, mapping onto lines of constant latitude in the ionosphere, was considered. This special case extends the one-dimensional steady state model described by *Sonnerup* [1980] and includes time-dependent effects and a more realistic current-voltage relation for the field-aligned current. The evolution of all one-dimensional states involves relaxation either to a uniform state (effectively unbounded systems) or to a particular equilibrium state (bounded systems) that depends on the boundary conditions. It is not yet known whether these equilibrium states are stable in two dimensions. The large velocity shear in the equilibrium flow profile suggests a K-H instability, although nonlocal dissipation at large scales resulting from ionospheric drag and field-aligned potential drops can be expected modify the K-H instability threshold inferred from numerical studies of (ionospherically) decoupled magnetospheric shear flows [*Miura and Pritchett*, 1982].

In the case of one-dimensional, semibounded flows, as occur in the low-latitude boundary layer region, the flow eventually forms a narrow boundary layer. The boundary layer flow is "viscous dominated" when $M < \frac{1}{2}$ and "current limited" [*Sonnerup*, 1980] when $M > \frac{1}{2}$. The distinction is in the flow profile. In the viscous-dominated boundary layer the flow profile varies monotonically (overdamped), whereas it has an overshoot region (underdamped) in the current-limited boundary

layer. The convection overshoot is a direct consequence of the field-aligned potential drop. Evidence for such overshoots in the low-latitude, duskside boundary layer can be found in the data reported by *Eastman et al.* [1985, Figures 2 and 3]. When $M \gg 1$, the thickness of the current-limited boundary layer is independent of the ionospheric Pedersen conductivity and varies as $(\nu K)^{1/4}$. It is therefore relatively narrow if the viscosity ν is small or the field-aligned "conductance" K is large. When $M \ll 1$, the thickness of the viscous-dominated boundary layer is independent of the field-aligned conductance and varies as $(\nu \Sigma_P)^{1/2}$, as discussed previously by *Sonnerup* [1980].

The current-limited boundary layer model appears to be consistent with convection profiles observed in the ionosphere within the duskside region 1 current system. (Detailed properties of the dawnside boundary layer and region 1 current system have not yet been examined.) For example, the main features in Figure 4 of the low-altitude data reported *Smiddy et al.* [1980] are reproduced by a boundary layer equilibrium state characterized by a Hartmann number of 6. In one sense, such comparisons provide an independent method of determining the Hartmann number. The model, as presently configured, does not give a good fit to the data of Smiddy et al. at latitudes below the equatorward edge of the region 1 current system. This region is probably strongly influenced by field-aligned currents associated with the diversion of the ring current and other sources of perpendicular magnetospheric currents. There are also likely to be large gradients in the ionospheric conductivity near the duskside boundary between the region 1 and 2 current systems as discussed by Smiddy et al. These effects are not included in the present model. One can view the boundary layer model, as applied to the region 1 current system, as providing a boundary condition for global convection models of the inner magnetosphere, which apply at latitudes within and below the region 2 current system [cf. *Harel et al.*, 1981].

A free internal shear layer that is separated from the boundary and therefore that is not constrained by fixed boundary conditions decays on a time scale that depends on the Hartman number as well as the initial state. If the wave number spectrum of the initial state rolls off at a wave number less than $k_* \simeq M^{1/2}/\lambda_e$, the entire flow pattern, at least for large Hartmann number flows, decays more or less uniformly at an approximately exponential rate determined by the ionospheric resistive decay time γ^{-1}. For parameters characteristic of the low-latitude boundary layer region, γ^{-1} is estimated to be roughly several minutes. If the initial spectrum extends beyond k_* or contains significant energy at k_*, then the disturbed flow decays at a much slower rate and develops localized oscillations at a wavelength $2\pi/k_*$. In the example depicted in Figure 4 these oscillations persist for about 1 hour. They resemble the so-called "V shocks" that have been identified on the S3-3 satellite at altitudes of about 1 R_E [*Mozer et al.*, 1977; *Temerin et al.*, 1981] and on the ISEE 1 satellite at altitudes between 2.5 and 7 R_E [*Mozer*, 1981]. This suggests that the observed V shocks are a natural progesssion in the evolution of free magnetospheric shear flows containing energy at scales of order $2\pi/k_*$. It is worth emphasizing that even though the electric field (or flow) profile undergoes substantial redistribution during its evolution, the field-aligned current profile does not (although it decays similarly). This suggests, for example, that a V shock may or may not be associated with an inverted V precipitation region depending on the time of observation.

The two-dimensional nature of the flow dynamics has received very little attention in this paper and is left for future study. As in Navier-Stokes flow, turbulent behavior can be expected at sufficiently large Reynolds numbers. However since ordinary viscous damping must be augmented by nonlocal damping, which produces dissipation at both small and large scales, a new class of phenomena can also be expected. A study of two-dimensional turbulence including these effects is currently underway.

Acknowledgments. This work was supported at Dartmouth College by National Science Foundation grants ATM-8445010 and ATM-8507192 and the Air Force Geophysics Laboratory grant F19628-87-K-0026 and at the University of Minnesota by the National Science Foundation grant ATM-8508949. We would like to acknowledge the helpful and perceptive comments of one of the anonymous referees.

The Editor thanks A. Hasegawa and another referee for their assistance in evaluating this paper.

REFERENCES

Bostrom, R., Electrodynamics of the ionosphere, in *Cosmical Geophysics*, edited by A. Egeland, O. Holter, and A. Omholt, p. 181, Universitetsforlaget, Oslo, Norway, 1973.

Chiu, Y. T., and J. M. Cornwall, Electrostatic model of a quiet auroral arc, *J. Geophys. Res.*, *85*, 543, 1980.

Chiu, Y. T., A. L. Newman, and J. M. Cornwall, On the structures and mapping of auroral electrostatic potentials, *J. Geophys. Res.*, *86*, 10,029, 1981.

Coleman, P. J., Jr., A model of the geomagnetic cavity, *Radio Sci.*, *6*, 321, 1971.

Cowley, S. W. H., The causes of convection in the earth's magnetosphere: A review of developments during the IMS, *Rev. Geophys.*, *20*, 531, 1982.

Cowling, T. G., *Magnetohydrodynamics*, p. 11, Adam Hilger Ltd., Bristol, England, 1976.

Eastman, T. E., E. W. Hones, Jr., S. J. Bame, and J. R. Asbridge, The magnetospheric boundary layer: Site of plasma, momentum and energy transfer from the magnetosheath into the magnetosphere, *Geophys. Res. Lett.*, *3*, 685, 1976.

Eastman, T. E., B. Popielawska, and L. A. Frank, Three-dimensional plasma observations near the outer magnetospheric bounary, *J. Geophys. Res.*, *90*, 9519, 1985.

Erdélyi, A., W. Magnus, F. Oberhettinger, and F. G. Tricomi, *Tables of Integral Transforms*, vol. 1, McGraw-Hill, New York, 1954.

Fridman, M., and J. Lemaire, Relationship between auroral electron fluxes and field-aligned electric potential differences, *J. Geophys. Res.*, *85*, 664, 1980.

Goertz, C. K., and R. W. Boswell, Magnetosphere-ionosphere coupling, *J. Geophys. Res.*, *84*, 7239, 1979.

Gosling, J. T., M. F. Thomsen, S. J. Bame, R. C. Elphic, and C. T. Russell, The post-terminator low-latitude boundary layer: Multiple flux transfer events?, *Eos Trans. AGU*, *66*, 1031, 1985.

Harel, M., R. A. Wolf, P. H. Reiff, R. W. Spiro, W. J. Burke, F. J. Rich, and M. Smiddy, Quantitative simulation of a magnetospheric substorm, 1, Model logic and overview, *J. Geophys. Res.*, *86*, 2217, 1981.

Hasegawa, A., Particle acceleration by MHD surface wave and formation of aurora, *J. Geophys. Res.*, *81*, 5083, 1976.

Hasegawa, A., and T. Sato, Generation of field-aligned current during substorm, in *Dynamics of the Magnetosphere*, edited by S.-I. Akasofu, p. 529, D. Reidel, Hingham, Mass., 1980.

Kan, J. R., and L. C. Lee, Theory of imperfect magnetosphere-ionosphere coupling, *Geophys. Res. Lett.*, *7*, 633, 1980.

Kelley, M. C., and P. M. Kintner, Evidence for two-dimensional inertial turbulence in a cosmic-scale low-β plasma, *Astrophys. J.*, *220*, 339, 1978.

Keskinen, M. J., and S. L. Ossakow, Theories of high-latitude ionospheric irregularities: A review, *Radio Sci.*, *18*, 1077, 1983.

Knight, S., Parallel electric fields, *Planet. Space Sci.*, *21*, 741, 1973.

Kraichnan, R. H., and D. Montgomery, Two-dimensional turbulence, *Rep. Prog. Phys.*, *43*, 547, 1980.

Lotko, W., Diffusive acceleration of auroral primaries, *J. Geophys. Res.*, *91*, 191, 1986.

Lyons, L. R., Generation of large-scale regions of auroral currents, electric potentials, and precipitation by the divergence of the convection electric field, *J. Geophys. Res.*, *85*, 17, 1980.

Lyons, L. R., D. S. Evans, and R. Lundin, An observed relation between magnetic field aligned electric fields and downward electron energy fluxes in the vicinity of auroral forms, *J. Geophys. Res.*, *84*, 457, 1979.

Lysak, R. L., Auroral electrodynamics with current and voltage generators, *J. Geophys. Res.*, *90*, 4178, 1985.

Lysak, R. L., Coupling of the dynamic ionosphere to auroral flux tubes, *J. Geophys. Res.*, *91*, 7047, 1986.

Lysak, R. L., and C. W. Carlson, The effect of microscopic turbulence on magnetosphere-ionosphere coupling, *Geophys. Res. Lett.*, *8*, 269, 1981.

Lysak, R. L., and C. T. Dum, Dynamics of magnetosphere-ionosphere coupling including turbulent transport, *J. Geophys. Res.*, *88*, 365, 1983.

Mitchell, H. G. Jr., J. A. Fedder, M. J. Keskinen, and S. T. Zalesak, A simulation of high latitude F-layer instabilities in the presence of magnetosphere-ionosphere coupling, *Geophys. Res. Lett.*, *12*, 283, 1985.

Miura, A., Anomalous transport by magnetohydrodynamic Kelvin-Helmholtz instabilities in the solar wind-magnetosphere interaction, *J. Geophys. Res.*, *89*, 801, 1984.

Miura, A., and P. L. Pritchett, Nonlocal stability analysis of the MHD Kelvin-Helmholtz instability in a compressible plasma, *J. Geophys. Res.*, *87*, 7431, 1982.

Miura, A., and T. Sato, Numerical simulation of global formation of auroral arcs, *J. Geophys. Res.*, *85*, 73, 1980.

Mozer, F. S., ISEE-1 observations of electrostatic shocks on auroral zone field lines between 2.5 and 7 earth radii, *Geophys. Res. Lett.*, *8*, 823, 1981.

Mozer, F. S., C. W. Carlson, M. K. Hudson, R. B. Torbert, B. Parady, J. Yatteau, and M. C. Kelley, Observations of paired electrostatic shocks in the polar magnetosphere, *Phys. Rev. Lett.*, *38*, 292, 1977.

Ogino, T., A three-dimensional MHD simulation of the interaction of the solar wind with the earth's magnetosphere: The generation of field-aligned currents, *J. Geophys. Res.*, *91*, 6791, 1986.

Olsen, R. C., T. L. Aggson, and B. G. Ledley, Observations of electric fields near the plasmapause at midnight, *J. Geophys. Res.*, *91*, 12,017, 1986.

Pritchett, P. L., and F. V. Coroniti, The collisionless macroscopic Kelvin-Helmholtz instability, 1, Transverse electrostatic mode, *J. Geophys. Res.*, *89*, 168, 1984.

Rothwell, P. L., M. B. Silevitch, and L. P. Block, A model for propagation of the westward travelling surge, *J. Geophys. Res.*, *89*, 8941, 1984.

Russell, C. T., and R. C. Elphic, ISEE observations of flux transfer events at the dayside magnetopause, *Geophys. Res. Lett.*, *6*, 33, 1979.

Sato, T., A theory of quiet auroral arcs, *J. Geophys. Res.*, *83*, 1042, 1978.

Sato, T., Auroral physics, in *Magnetospheric Plasma Physics*, edited by A. Nishida, p. 197, D. Reidel, Hinghan, Mass., 1982.

Sato, T., and T. Iijima, Primary sources of large-scale Birkeland currents, *Space Sci. Rev.*, *24*, 347, 1979.

Sckopke, N., G. Paschmann, G. Haerendel, B. U. O. Sonnerup, S. J. Bame, T. G. Forbes, E. W. Hones, Jr., and C. T. Russell, Structure of the low-latitude boundary layer, *J. Geophys. Res.*, *86*, 2099, 1981.

Singer, H. J., D. J. Southwood, R. J. Walker, and M. G. Kivelson, Alfvén wave resonances in a realistic magnetospheric magnetic field geometry, *J. Geophys. Res.*, *86*, 4589, 1981.

Smiddy, M., W. J. Burke, M. C. Kelley, N. A. Saflekos, M. S. Gussenhoven, D. A. Hardy, and F. J. Rich, Effects of high-latitude conductivity on observed convection electric fields and Birkeland currents, *J. Geophys. Res.*, *85*, 6811, 1980.

Sonnerup, B. U. O., Theory of the low-latitude boundary layer, *J. Geophys. Res.*, *85*, 2017, 1980.

Swift, D. W., On the formation of auroral arcs and acceleration of auroral electrons, *J. Geophys. Res.*, *80*, 2096, 1975.

Temerin, M., The polarization, frequency, and wavelengths of high-latitude turbulence, *J. Geophys. Res.*, *83*, 2609, 1978.

Temerin, M., M. H. Boehm, and F. S. Mozer, Paired electrostatic shocks, *Geophys. Res. Lett.*, *8*, 799, 1981.

Temerin, M., C. Cattell, R. Lysak, M. Hudson, R. B. Torbert, F. S. Mozer, R. D. Sharp, and P. M. Kintner, The small-scale structure of electrostatic shocks, *J. Geophys. Res.*, *86*, 11,278, 1981.

Tsurutani, B. T., and R. M. Thorne, Diffusion processes in the magnetopause boundary layer, *Geophys. Res. Lett.*, *9*, 1247, 1982.

Vasyliunas, V. M., Mathematical models of magnetospheric convection and its coupling to the ionosphere, in *Particles and Fields in the Magnetosphere*, edited by B. M. McCormac, p. 60, D. Reidel, Hingham, Mass., 1970.

Vasyliunas, V. M., Interaction between the magnetospheric boundary layers and the ionosphere, in *Magnetospheric Boundary Layers, Eur. Space Agency Spec. Publ. 148*, p. 387, European Space Research and Technology Center, Noordwijk, Holland, 1979.

Vickrey, J. F., R. C. Livingston, N. B. Walker, T. A. Potemra, R. A. Heelis, M. C. Kelley, and F. J. Rich, On the current-voltage relationship of the magnetospheric generator at intermediate spatial scales, *Geophys. Res. Lett.*, *13*, 495, 1986.

Watanabe, K., M. Ashour-Abdalla, and T. Sato, A numerical model of magnetosphere-ionosphere coupling: Preliminary results, *J. Geophys. Res.*, *91*, 6973, 1986.

Weimer, D. R., C. K. Goertz, D. A. Gurnett, N. C. Maynard, and J. L. Burch, Auroral zone electric fields from DE 1 and 2 at magnetic conjunctions, *J. Geophys. Res.*, *90*, 7479, 1985.

Weimer, D. R., D. A. Gurnett, C. K. Goertz, J. D. Menietti, J. L. Burch, and M. Sugiura, The current-voltage relationship in auroral current sheets, *J. Geophys. Res.*, *92*, 187, 1987.

Wolf, R. A., and M. Harel, Dynamics of the magnetospheric plasma, in *Dynamics of the Magnetosphere*, edited by S.-I. Akasofu, p. 143, D. Reidel, Hingham, Mass., 1980.

Wu, C. C., Kelvin-Helmholtz instability at the magnetopause boundary, *J. Geophys. Res.*, *91*, 3042, 1986.

W. Lotko and B. U. O. Sonnerup, Thayer School of Engineering, Dartmouth College, Hanover, NH 03755.

R. L. Lysak, School of Physics and Astronomy, University of Minnesota, 116 Church Street SE, Minneapolis, MN 55455.

(Received September 24, 1986,
revised April 6, 1987,
accepted April 8, 1987.)

Appendix 2

On Large Scale Rotational Motions and Energetics of Auroral Shear Layers

W. Lotko and M.-M Shen
Thayer School of Engineering, Dartmouth College, Hanover, NH 03755

ABSTRACT

The stability, dynamics and energetics of an auroral shear layer are considered in the framework of incompressible, one-fluid magnetohydrodynamics, under conditions where current flow through the system is limited by a resistive boundary condition. The model includes a magnetospheric region where currents resulting from polarization electric fields and viscous forces are important, an ionospheric substrate of uniform conductivity, and a force-free acceleration region, characterized by a linear current-voltage relation and located at an intermediate altitude between the magnetospheric viscous/polarization layer and the ionosphere. It is assumed that the Alfvén wave transit time across the viscous/polarization layer is small compared with the eddy time. Neutral stability of the model system is determined for a class of one-dimensional equilibria in which a specified current distribution at the upper boundary of the viscous/polarization layer produces a potential structure with convergent, localized reversals in the transverse ($\mathbf{E} \times \mathbf{B}$) electric field. The calculated neutral curves depend on three nondimensional parameters related to the intensity of the imposed field-aligned current, the shear layer scale size, and the ratio of resistive to viscous drag at equilibrium. Numerical simulations of unstable configurations shows that (1) 2D quasi-steady rotational states arise when the equilibrium is weakly unstable; (2) eddy shedding turbulent states can arise when the equilibrium is strongly unstable; and (3) the flow kinetic energy and energy input/dissipation rates in the model system are reduced as a consequence of the instability. Power spectral densities for the electric and magnetic fields are also evaluated along sample 'satellite' cuts through the shear layer. An application to post-noon auroral forms confirms the tendency for 2D rotational motion and periodic bright spots, although the observed intensity of the upward field-aligned current suggests that magnetoinductive effects such as Alfvén waves may be more important than is implied by the assumed condition for resistive current limitation.

1. Introduction

The term auroral shear layer, as used in this paper, refers to an extended region of horizontal $\mathbf{E} \times \mathbf{B}$ shear, typically observed in the topside polar and auroral ionosphere and lower magnetosphere. An auroral shear layer entails both velocity and magnetic shear because current conservation at the ionosphere requires field-aligned current at locations of electric field divergence or convergence; the average current in the layer is directed out of or into the ionosphere when the transverse ($\mathbf{E} \times \mathbf{B}$) electric field has a local convergence or divergence, respectively [cf. Burke et al., 1984]. Satellite observations show that strongly convergent electric fields are associated with the precipitation of kilovolt electrons [Gurnett and Frank, 1973; Burch et al., 1976], and it is now evident that the energetic electrons in such precipitation regions are produced by a field-aligned potential drop, located at a nominal altitude of 1 R_E [e.g., Mozer et al., 1980; Weimer et al., 1985]. It is also evident from ground-based and satellite images of auroral luminosity [Davis, 1978; Oguti, 1981; Lui et al., 1989] that auroral shear layers frequently exhibit some form of two-dimensional rotational motion. In addition, *in situ* measurements of small-scale vortices [Burke et al., 1983] and broadband, low frequency turbulence [Kintner, 1976; Kelley and Carlson, 1977; Gurnett et al., 1984; Basu et al., 1988] in and near auroral shear layers indicate that they are sites of considerable energy dissipation and variability in the lower magnetosphere and ionosphere.

The observed rotational motions are apparently a consequence of two different types of macroscopic instabilities, originally identified [Webster and Hallinan, 1973] as the charge sheet instability and the current sheet instability. The charge sheet instability discussed is a prototype of the electrostatic Kelvin-Helmholtz or shear flow instability; the current sheet instability [Murty, 1961] is a type of electromagnetic tearing instability [Furth et al., 1963; White, 1986] of a strongly magnetized sheet current with zero flow in the unperturbed state. Webster and Hallinan [1973] suggested that the large scale motions identified by them as auroral spirals [see also Oguti, 1974; Davis and Hallinan, 1976; Hallinan, 1976] evolve from the current sheet instability. They also suggested, and numerical simulations [Miura and Sato, 1978; Wagner et al., 1981; 1983] of various 2D charge sheet configurations seem to confirm, that the small scale rotational motions called curls and folds [Hallinan and Davis, 1970] evolve from a charge sheet instability.

The simulations are noteworthy, not only for their successes in reproducing many features of observed rotational motions, but also because they do so in the framework of a local model, i.e., effects resulting from the closure of field-aligned currents in the ionosphere are not included. The implication is that finite transit-time effects, associated with the propagation of shear Alfvén waves between the

magnetospheric location of the instability and the ionosphere, are negligible. A local approximation is reasonable if, for example, the instability is initiated in a strong shear layer located far from the ionosphere. If the linear growth time (proportional to the eddy time = shear scale length/velocity jump) is small compared to the Alfvén transit time, then the linear phase of the instability should proceed locally, uninhibited by any knowledge of the ionosphere. The eventual fate of the instability cannot be discerned from a local model, however, because information about the ionosphere is eventually communicated to the distant plasma by returning Alfvén waves. In addition, a local model gives no information on the stability of configurations for which the eddy/linear growth time is on the order of or larger than the Alfvén transit time; nor can it be used to address the issue of whether, or under what conditions, a mixed magnetic/velocity shear layer can be regarded primarily as a charge sheet configuration or primarily as a current sheet configuration, if such distinctions are even meaningful in the time-asymptotic limit.

Some recent 3D numerical studies by Seyler [1988], based on reduced equations of two-fluid magnetohydrodynamics, provide some insights into these questions. In a simple model, the ionosphere may be represented either as an infinitely conducting boundary or a nonconducting boundary. Not surprisingly, the electrical current and potential within the shear layer are regulated very differently in the two cases. When the ionosphere is represented as a short circuit boundary (infinite conductivity), Seyler reports that a type of collisionless tearing instability dominates the shear layer dynamics because large field-aligned currents and magnetic shear exist with minimal cross-field potential drops. The shear layer in this configuration resembles an electromagnetic current sheet. Alternatively, when the ionosphere is represented as an open circuit boundary (zero conductivity), the shear flow instability dominates because a large electric potential and velocity shear can be maintained across magnetic field lines with minimal current flow through the system. In this configuration, the current density and, therefore, the induced magnetic field are limited, so the shear layer more closely resembles an electrostatic charge sheet. Neither of these two rather extreme boundary conditions is realized exactly in the ionosphere, however, and to improve upon Seyler's model, it is necessary to model the ionospheric plasma as a distributed medium with finite conductivity.

Open and short circuit boundary conditions correspond to the respective limits, $\mu\Sigma_P v_A \ll 1$ and $\mu\Sigma_P v_A \gg 1$, where μ is the permeability of free space, Σ_P is the height-integrated ionospheric Pedersen conductivity and v_A is the characteristic Alfvén speed at the *magnetospheric* end of the flux tube [Lysak, 1990]. Both limits, as well as the intermediate regime, are of interest because Σ_P can be very low in the nightside winter ionosphere, very high in the dayside summer ionosphere, and anywhere in between depending on season and diurnal location [Vickrey et al., 1981]. A hydromagnetic model,

including magnetoinductive feedback in the flow dynamics, as well as the finite ionospheric conductivity, is required to treat the full range of values. Some progress has been made in developing such a model [Seyler, private communication]. Results from a more restrictive electrostatic model [Keskinen et al., 1988], appropriate to the low conductivity limit, show that the finite Pedersen conductivity, in conjunction with a neutral wind and plasma density dynamics, reduces the growth rate of the shear flow instability in the linear phase and inhibits the formation of eddies, which are supplanted by nonlinear structures resembling breaking waves. The calculated power spectral densities of the electric field and plasma density fluctuations in the model shear layer appear to be consistent with spectral densities measured in the vicinity of relatively small scale shear layers [Basu et al., 1988].

The study reported in this paper is also concerned with the dynamics of an auroral shear layer in the electrostatic approximation, but under somewhat less severe conditions than are implied by the inequality $\mu v_A \Sigma_P \ll 1$. In particular, it is shown that when a field-aligned potential drop exists above the ionosphere, this inequality should be replaced by the less restrictive condition $\mu v_A \Sigma_P \ll 1 + \lambda_\parallel^2 / L_s^2$. Here, L_s is the horizontal scale size of the shear layer, and $\lambda_\parallel = (\Sigma_P/K)^{1/2}$ is a resistive scale length [Lyons, 1980; Chiu and Cornwall, 1980] based on Σ_P and a field-aligned conductance density K that characterizes the effects of the field-aligned potential drop. An expression for the parameter K can be derived, under certain restrictions, from an adiabatic particle model [Knight, 1973; Lyons et al., 1979; Fridman and Lemaire, 1980]; an alternative expression can also be derived from a local Ohm's law involving an enhanced resistivity (cf. the Appendix; Lysak and Hudson, 1987). When $L_s > \lambda_\parallel$, the more general condition given above is approximately equivalent to $\mu v_A \Sigma_P \ll 1$. However, if $L_s < \lambda_\parallel$, current limitation and an electrostatic response is expected when $\mu v_A (K L_s^2) \ll 1$, which is independent of the Pedersen conductivity. In this case, the low effective conductance KL_s^2 of an enhanced resistive layer in the lower magnetosphere promotes the shear flow instability.

The model to be analyzed here is similar in some respects with the one proposed by Keskinen et al. [1988]. In both models, the field-aligned current closes via Pedersen currents in the ionosphere and via electric polarization currents in the magnetosphere. Keskinen et al. also include the effects of a constant inhomogeneous neutral wind and incompressible density dynamics (which are neglected here), but do not include the effects of either a field-aligned potential drop or microscopically enhanced viscosity (which are included here). In addition, the boundary conditions implemented by Keskinen et al. correspond to a boundary shear layer, i.e., a transition from one flow state to another at large horizontal distances from the shear layer. In the present study, as well as in the one reported by Seyler [1988], a spatially localized, $\mathbf{E} \times \mathbf{B}$ flow reversal is maintained by fixing the field-aligned current distribution on the upper boundary plane of the magnetospheric region. (Two examples of observed shear

layers of this type are shown in Fig. 1.) While this type of boundary condition is not entirely satisfactory because, in reality, one would expect the current distribution to evolve self-consistently at distances beyond this somewhat artificial upper boundary, we have found it difficult to understand how an internal layer, containing spike-like flow reversals, can be maintained without some type of forcing at the upper boundary. In cases where the shear layer is not maintained by boundary conditions, Lotko et al. [1987] show that an initial 1D boundary shear layer can decay into an internal shear layer, while Lotko and Schultz [1988] show that anisotropic magnetic field mapping can cause decaying $\mathbf{E} \times \mathbf{B}$ turbulence to organize into turbulent internal shear layers. We comment briefly in the concluding remarks on similarities and differences in the two-dimensional dynamics of decaying and forced auroral shear layers.

The basic equations of the model are discussed in the following Section 2, and its linear stability properties are analyzed in the subsequent Section 3. The effect of the field-aligned potential drop is demonstrated in Fig. 2, which shows that an auroral shear layer is, in fact, more unstable than one would otherwise conclude from the numerical results reported by Keskinen et al. [1988] or from the scaling argument given by Cornwall [1988]. Numerical solutions of the fully nonlinear, time-dependent equations are discussed in Section 4, which also includes an analysis of the energetics of the model system and the power spectra that would be observed by a satellite traversing the shear layer at different locations. Owing to the one-fluid approximation employed here, the results of the study apply primarily to relatively 'large scale' auroral shear layers with characteristic transverse scale sizes exceeding the ion gyroradius and the electron inertial length. While this includes certain classes of fields associated with 'inverted V' precipitation regions [Gurnett and Frank, 1973; Burch et al., 1976], the approximation is perhaps marginal for applications to 'paired electrostatic shocks' [Temerin et al., 1981] which are often observed with scale sizes comparable to the ion gyroradius or electron inertial length. It is worth emphasizing, however, that paired electrostatic shocks and 'inverted V' precipitation regions are rather extreme examples of an auroral shear layer. Many other observed auroral shear layers, to which our results may also apply, are not particularly striking in terms of the associated electron energization. For example, the electron precitation may be either sub-luminous or at background levels, especially when the field-aligned current in the layer is directed into the ionosphere. In the final Section 5, we illustrate how the model may be applied to observed shear layers by comparing the results to observed properties of post-noon auroral forms exhibiting periodic bright spots [e.g., Robinson et al., 1984; Lui et al., 1989; Potemra et al., 1990; Bruning et al., 1990].

2. Model Formulation

Physical description

The main elements of the model have been described previously by Lotko et al. [1987] and Lotko and Schultz [1988]. Briefly, three distinct regions along a magnetic flux tube are modeled: (1) a low β magnetospheric region where viscosity and the divergence of magnetic field-aligned currents into polarization currents are important. We refer to this region as the viscous/polarization layer; (2) an ionospheric substrate characterized by a height-integrated Pedersen conductivity Σ_P, assumed to be uniform and constant (the Hall conductivity and neutral wind velocity are also assumed to be uniform and constant and therefore do not explicitly enter the formulation), and (3) a force-free region, intermediate in altitude between the ionosphere and the viscous/polarization layer, where a field-aligned potential drop may exist. This region is refered to as the acceleration region. The field-aligned potential drop is assumed to be linearly proportional to the field-aligned current evaluated at the ionospheric substrate (cf. the Appendix); the proportionality constant K has the units of mho/m^2. The field-aligned current at the ionospheric substrate is diverted entirely into a Pedersen current when the neutral wind velocity and ionospheric conductivities are uniform.

The ionospheric substrate together with the intermediate region provide a lower boundary condition on the magnetospheric flow. This boundary condition relates the field-aligned current at the boundary to the electric potential there. Above this boundary, the electric potential does not vary with z, the coordinate along the magnetic field; however, the field-aligned current density varies linearly with z in this region. This type of variation (or lack of variation with z) may be formally demonstrated from the MHD equations under conditions where the field-aligned current in the system is limited by the boundary conditions and when the Alfvén Mach number $M_A = v_0/v_A$ for the flow is small and of the same order as $(L_\perp/L_\parallel)^2$. $L_\perp$ and $L_\parallel$ are characteristic scale lengths for variation perpendicular and parallel to the d. c. magnetic field $\mathbf{B}_0 = B\hat{\mathbf{z}}$ assumed to be uniform in the magnetospheric region; v_0 is a characteristic velocity for the flow; $v_A = B/\sqrt{\mu\rho_0}$ is the Alfvén speed, and ρ_0 is the characteristic mass density of the magnetospheric region. The small Mach number limit and the assumed relation between M_A and $L_\perp/L_\parallel$ imply that the Alfvén wave transit time along the magnetic field in the magnetospheric region is small compared to the characteristic eddy time $L_\perp/v_0$. Alfvén waves therefore do not enter the formulation to lowest order in the small parameter $\varepsilon \sim (L_\perp/L_\parallel)^2 \sim M_A$. It can be shown, with appropriate scaling, that current flow is limited by the lower boundary condition when the nondimensional parameter $\mu\Sigma_P v_A$ based on the Alfvén speed in the viscous/polarization layer is much smaller than $1 + \lambda^2/L_\perp^2$,

where $\lambda \equiv (B_i\Sigma_P/BK)^{1/2}$ is the resistive length scaled by the ratio $(B_i/B)^{1/2}$ of the flux tube dimension in the viscous/polarization layer to that in the ionosphere. (Throughout this paper, the subscript 'i' will be used to denote a value at the ionospheric substrate; unsubscripted variables denote values in the viscous/polarization layer.) Current limitation implies that magnetic induction is weak, so the model is essentially electrostatic when the MHD equations are expanded to O(1) in ε.

Basic Equations

The dynamical variables used to characterize the viscous/polarization layer include the stream function ψ, mass density ρ, magnetic field-aligned velocity $v_\parallel$, and magnetic field-aligned current $j_\parallel$. The stream function is related to the electric potential through the relation $\psi = -\phi/B$. The perpendicular velocity is defined in terms of the stream function as $v_\perp = \nabla_\perp\psi \times \hat{z}$. Subject to the above restrictions, the reduced equations describing the magnetospheric flow are

$$\frac{d}{dt}\rho \equiv (\partial_t + v_\perp \cdot \nabla_\perp)\rho = 0 \tag{1}$$

$$(\frac{d}{dt} - \nu\nabla_\perp^2)v_\parallel = 0 \tag{2}$$

$$\frac{d}{dt}\nabla_\perp \cdot \rho\nabla_\perp\psi = -B\partial_z j_\parallel + \nu\nabla_\perp \cdot \rho\nabla_\perp\nabla_\perp^2\psi \tag{3}$$

$$\partial_z\psi = \partial_z\rho = 0 \tag{4}$$

The parameter ν is an effective kinematic viscosity, and $\nabla_\perp = \hat{x}\partial_x + \hat{y}\partial_y$. The effective viscosity should be regarded as an enhanced viscosity attributed to kinetic or fluid processes occurring on time and spatial scales smaller than those considered here.

Relations (3) and (4) imply that $j_\parallel$ is at most a linear function of z, i.e., it is uniquely determined by its values at the z boundaries of the magnetospheric region, which we take to be z = 0 (upper boundary) and z = H (lower boundary). The field-aligned current density is therefore given by

$$j_\parallel = j_H\frac{z}{H} + j_0(1 - \frac{z}{H}) \tag{5}$$

where $j_0(x, y, t)$ and $j_H(x, y, t)$ are the values of $j_\parallel$ at z = 0 and z = H, respectively. At this point, we identify the length H with the characteristic scale size $L_\parallel$.

Current continuity at the ionospheric substrate, the ionospheric Ohm's law, and the linear current-voltage relation, $j_{\parallel i} = K(\phi_i - \phi)$ where ϕ_i is the electric potential at the ionospheric substrate, imply the following relation between j_H and ψ (Chiu and Cornwall, 1980; Lyons, 1980):

$$(1 - \lambda^2 \nabla_\perp^2) j_H = B\Sigma_P \nabla_\perp^2 \psi \qquad (6)$$

It is noted that perpendicular spatial derivatives in the ionosphere generally do not map into isotropic spatial derivatives in the magnetospheric region owing to the anisotropic mapping of flux tube dimensions [cf. Lotko et al., 1987; Lotko and Schultz, 1988). This anisotropy would enter the formulation in equation (6) but will not be included in the present study. See Sec. 5 for additional comments on this effect.

Once the field-aligned current density j_0 at $z = 0$ is specified, and the initial and x–y boundary conditions on ρ and ψ are given, the stream function ψ (x, y, t) is completely determined by equations (1) and (3) - (6). Note that $v_\parallel$ is an 'enslaved' variable and can be evaluated directly from (2) once ψ, and therefore $v_\perp$, is known. If $j_0 = 0$, the system is undriven, and any initial state will decay as $t \rightarrow \infty$. Numerical studies of undriven systems have been described by Lotko and Schultz [1988]. A nonzero value of j_0 permits energy to flow into the system through the boundary at $z = 0$. Examples of driven systems will be analyzed in detail below. Henceforth, it is assumed that ρ is constant initially and, as a consequence of (1), ρ remains constant for all time. Periodic boundary conditions will be implemented in the x–y plane.

3. Equilibrium and Stability

Method

The equilibrium states considered here are assumed to have a flow in the $\hat{y}$ direction which varies in the $\hat{x}$ direction, i.e, $v = (0, v_y(x), 0)$. As a consequence, the divergence of the polarization current represented by the left side of (3) is zero in equilibrium; in the viscous/polarization layer, the equilibrium field-aligned current is therefore locally diverted into a transverse current resulting solely from the viscous force. If the viscous force were zero, then any 1D velocity profile is an equilibrium, as in the Lyons [1980] and Chiu and Cornwall [1980] models.

Specification of the equilibrium state and its stability are facilitated by making use of the assumed periodic boundary conditions in the x–y plane. The equilibrium stream function is denoted as ψ_{eq} and will be specified in terms of its Fourier amplitudes and the Fourier amplitudes of the boundary current $j_0(k)$. Equations (3), (5) and (6) imply

$$j_0(k) = - B\Sigma_p \, k^2 \, \Gamma_k \psi_{eq}(k) \qquad (7)$$

where

$$\Gamma_k = \frac{k^2\lambda^2}{M^2} + \frac{1}{1 + k^2\lambda^2} \tag{8}$$

The composite parameter M is an effective Hartmann number defined by the relation

$$M^2 = \frac{\gamma\lambda^2}{\nu} = \frac{\Sigma_P^2 B B_i}{\rho\nu HK} \tag{9}$$

The Hartmann number is a measure of the ratio of resistive or magnetic friction to viscous friction. Magnetic friction dominates when M is large (cf. Lotko et al., [1987] and Lotko and Schultz [1988] for additional discussion of the significance of the Hartmann number and the effects of nonlocal dissipation represented by the factor Γ_k). The parameter $\gamma = \Sigma_P B^2/\rho H$, defined implicitly in (9), is the RC decay rate. This is the rate at which an initially imposed but unsustained transverse potential drop decays by discharging currents through the resistive ionosphere. As defined by Mitchell et al. [1975], the effective capacitance of the viscous/polarization layer is $C_m = \int(\rho/B^2)\,ds \approx \rho H/B^2$.

We now consider the effect of small perturbations ψ_p about the equilibrium state ψ_{eq}. The Fourier amplitudes for the stream function are represented as $\psi(k, q, t) = \psi_{eq}(k) + \psi_p(k, q, t)$. Linearizing (3) with respect to ψ_p and using (5) and (6) results in the following eigenvalue equation for the Fourier amplitudes of the perturbed stream function:

$$\partial_t\psi_p(k, q, t) = \sum_{k'} C(k, q, k')\psi_{eq}(k-k')\psi_p(k', q, t) - \gamma\Gamma_\kappa\psi_p(k, q, t) \tag{10}$$

Here, $\kappa = (k^2 + q^2)^{1/2}$ is the magnitude of the 2D wavevector (k, q), and

$$C(k, q, k') = \frac{q(k - k')}{k^2 + q^2}(q^2 - k^2 + 2kk') \tag{11}$$

is a mode coupling coefficient.

The eigenvalues s of the truncated system (10) are determined by letting $\psi_p(k, q, t) = e^{st}\psi_p(k, q, 0)$. The system is stable if for all eigenvalues $Re(s) < 0$. The system is unstable if for at least one eigenvalue $Re(s) > 0$. The system is neutrally stable if $Re(s) = 0$ for one or more eigenvalues with $Re(s) < 0$ for the remaining eigenvalues. Non-dimensionalizing (10) by letting $\psi \rightarrow \psi/\lambda v_0$ and $(k, k', q) \rightarrow (k, k', q)\lambda$ shows that the linear stability of the system depends on the three parameters, M, $v_0/\gamma\lambda$, and $L_\perp/\lambda$, as well as the functional form of $j_0(k)$.

Neutral stability

The field-aligned current density at z = 0 is chosen so that the equilibrium stream function has a Gaussian profile. The equilibrium flow velocity is then a derivative Gaussian resembling two adjacent, localized and oppositely flowing streams. The spike-like, oppositely directed electric fields accompanying this reversed flow configuration are similar to the observed electric field structures shown in Fig 1.

In coordinate space, the equilibrium stream function is chosen to be

$$\psi_{eq} = v_0 \sigma \exp(-x^2/\sigma^2) \tag{12}$$

The characteristic scale length $L_\perp$ introduced in the previous section should now be identified as σ. The Fourier transformed boundary current $j_0(k)$ required to produce this ψ_{eq} is

$$j_0(k) = - \frac{B\Sigma_p v_0}{2\sqrt{\pi}} k^2\sigma^2 \Gamma_k e^{-k^2\sigma^2/4} \tag{13}$$

Neutral stability curves resulting from this boundary current are shown in Figure 2 for several values of the Hartmann number M. The system is unstable when the velocity v_0 is sufficiently large (parameter values above each curve); the critical velocity decreases as the Hartmann number increases, which reduces the stabilizing influence of viscous dissipation. For any finite Hartmann number, the vortex layer is stable when the scale size σ is sufficiently large or sufficiently small. Stabilization at small scale sizes is due to viscous drag, whereas at large scale sizes, ionospheric resistive drag on the feet of the magnetic field lines impedes the instability.

Scaling relations

Qualitative features of the neutral stability curve can be understood by considering the competition between the various dissipative forces and the nonlinear inertial force in (3), which drives the perturbing modes. The inertial force acts on the eddy time scale, $\tau_e = \sigma/v_0$. Instability occurs when the driver acts more rapidly than resistive and viscous relaxation, i.e., when τ_e is smaller than both the resistive decay time γ^{-1} and the viscous decay time $\tau_\nu = \sigma^2/\nu$.

At large scale lengths, when viscous relaxation is negligible, the condition for instability is $\gamma\tau_e \le 1/b_1$, where b_1 is a number of order unity. This implies

$$\frac{v_0}{\gamma\lambda} \ge b_1 \frac{\sigma}{\lambda}$$

On a log-log plot (as in Figure 1), the threshold is a line with slope 1 and a y-intercept at log b_1. This is the asymptote at large v_0 and σ in the figure. The value of b_1 deduced from the figure is

approximately 2.5. The neutral curves for a wall bounded shear layer (cf. Fig. 3 in the paper by Keskinen et al. [1988]) also obey this scaling relation if allowance is made for a different value of the parameter b_1.

At small scale lengths, when resistive relaxation is negligible, the condition for instability is $\tau_e/\tau_v \leq b_2$, where b_2 is another number of order unity. Note that τ_e/τ_v is the inverse of the mechanical Reynolds number. This condition implies

$$\frac{v_0}{\gamma\lambda} \geq \frac{b_2}{M^2}\frac{\lambda}{\sigma}$$

On a log-log plot, the viscous dominated threshold is a line with slope -1 and y-intersept log (b_2/M^2). This is the M-dependent family of asymptotes at large v_0 and small σ. The zero viscosity limit corresponds to $M \rightarrow \infty$. The value of b_2 deduced from the figure is approximately 6. Of course, the precise values of b_1 and b_2 depend on the particular form of the equilibrium state, but the asymptotic behavior predicted by this scaling analysis is general.

The deviation of the large M neutral curves from the dotted line in Fig. 2 illustrates the influence of the field-aligned potential drop. The dotted line is the neutral curve predicted by the scaling relation given above in the zero viscosity and zero field-aligned potential drop limits. At relatively small v_0, the calculated threshold occurs at larger scale sizes than the threshold predicted by the simple scaling analysis, i.e., the actual neutral curve lies below the zero viscosity, zero field-aligned potential neutral curve. Because the field-aligned potential increases at smaller scale sizes, which effectively reduces the electric field impressed on the ionosphere and, therefore, Ohmic dissipation, the marginal stability threshold is lower than what would be expected from equipotential mapping. A better predictor of the neutral curve is obtained if, in the above scaling relations, γ is replaced by $\gamma/(1 + 4\lambda^2/\sigma^2)$, which represents the denominator in the second term in the dissipation rate Γ_k given by (8) with $k = 2/\sigma$.

4. Shear Layer Dynamics

Simulation method and parameters

We now consider the dynamics of an unstable shear layer, including nonlinear effects. Equations (3), (5) and (6) with ρ constant are solved in discrete Fourier space using a pseudo-spectral method. The initial Fourier amplitudes for the stream function have a Gaussian spectrum generated from the discrete Fourier transform of (12). Superimposed on this 1D Gaussian spectrum is an isotropic white

noise spectrum with random phases. The power spectral density of the white noise has the form $2\pi\kappa|\kappa\psi(\kappa)|^2$ = constant; the intensity of the constant white noise spectral density is generally smaller than the peak value of the equilibrium Gaussian spectrum by a factor of 10^{-3} or less. The algorithm for time-advancing the Fourier amplitudes is a variable time-step Adams-Moulton predictor-corrector scheme. Aliasing terms resulting from the nonlinear term in (3) are removed using Orszag's [1971] pseudo-spectral method. The numerical solutions described below are constructed from relatively low resolution, truncated Fourier expansions of size 64×64 or 128×128 ($k_{max} = 32$ or 64, respectively).

Parameters for the four cases examined in detail are listed in Table 1. In all cases, the effective Hartmann number defined by Eq. (9) is fixed at M = 10. At Hartmann numbers somewhat larger than 10, we began to encounter significant truncation errors for comparable spatial resolutions (64^2 or 128^2). This numerical effect is typical of nonlinear spectral algorithms and can always be minimized by appropriately increasing k_{max} to resolve the dissipation range.

The four runs identified in Table 1 differ primarily in the scale size of the shear layer (σ/λ) and the velocity amplitude ($v_0/\gamma\lambda$). It was necessary to use different values of $2\pi\sigma/L$, the ratio of the shear layer scale size to box size, in each run to adequately resolve both the driver spectrum, which is determined by σ/λ (cf. Eq. 13) and the scale dependent dissipation rate Γ_k defined by relation (8). The scale size of the shear layer determines the primary dissipation processes, as follows:

Run (1) — Small scale shear layer ($\sigma/\lambda = .1$, $v_0/\gamma\lambda = 2$).

The energy flux incident at the upper boundary z = 0 is dissipated almost completely in the magnetospheric region by local viscous heating. The flow dynamics are practically decoupled from the ionosphere and acceleration region, and the magnetospheric electric field maps very imperfectly to the ionosphere.

Runs (2), (3) — Sub-intermediate scale shear layers ($\sigma/\lambda = .5$, $v_0/\gamma\lambda = 2, 10$).

The dissipation rates for viscous heating and fast particle production by the the field-aligned potential drop are initially comparable (though not time-asymptotically) and are substantially greater than the ionospheric Ohmic heating rate. The magnetospheric flow is weakly coupled to the ionosphere in these runs.

Run (4) — Intermediate scale shear layer ($\sigma/\lambda = 1$, $v_0/\gamma\lambda = 2$).

Ionospheric Ohmic heating and fast particle production by the field-aligned potential drop are roughly comparable initially, as well as time-asymptotically, and are much larger than the viscous heating rate. The magnetospheric flow is moderately influenced by coupling to

the ionosphere.

Run 1, which has a relatively small mechanical Reynolds number, and Run 4, which has a relatively large ratio of eddy time to RC decay time, are more weakly driven than Runs 2 and 3. Run 3 is most strongly driven owing to the large driving amplitude, $v_0/\gamma\lambda = 10$, as compared with 2 for the other three cases. Runs 2 and 3 will be described in detail below. Similarities and differences in the flow dynamics for the other two cases will be indicated by comparison.

Referring to Table 1, it is seen that the linearly most unstable mode number is slightly larger than $2\pi/\sigma$ for all cases considered (determined by the product of q_m and $2\pi\sigma/L$ in Table 1). The growth rate of the linearly most unstable mode scales roughly with the eddy time. The mode number and growth rate of the linearly most unstable mode, as well as the linear regime bandwidth predicted by the linear analysis in the previous section, have been verified by the numerical simulations. Several linearly stable cases were also simulated to verify, at least qualitatively, the marginal stability curves indicated in Figure 1. The energy and mean square vorticity (enstrophy), as well as their sources and sinks (cf. Eq. 14 below), were monitored throughout the runs. The energy budget balanced to within about 0.1%; the enstrophy budget, which is typically more sensitive to truncation errors than energy, balanced to within about 1%.

Energetics

The overall dynamics of an unstable shear layer is best appreciated by considering the energetics of the model system. The equations given in Sec. 2 can be combined to form the following energy equation (cf. Lotko and Schultz [1988] for a derivation including all terms except the forcing term containing j_0):

$$\frac{d}{dt}\int \tfrac{1}{2}\rho v_\perp^2 \, H dx dy = -\int \rho\nu\omega^2 \, H dx dy - \frac{1}{K}\int j_{\parallel i}^2 dx_i dy_i - \frac{1}{\Sigma_C}\int I_{\perp i}^2 dx_i dy_i - \int \phi j_0 \, dx dy \qquad (14)$$

Energy flux sources at the x–y boundaries, which are included in the derivation by Lotko and Schultz [1988], do not appear in (14) owing to the periodic boundary conditions. The equation also does not include effects resulting from a nonzero neutral wind velocity in the ionosphere. Notations include the z-component of vorticity ($\omega = -\nabla_\perp^2\psi$), the field-aligned current density at the ionospheric substrate ($j_{\parallel i} = j_H B_i/B$), the height-integrated perpendicular current at the ionospheric substrate ($I_{\perp i}$), and the Cowling conductivity defined in terms of the Pedersen and Hall conductivities as $\Sigma_C = \Sigma_P + \Sigma_H^2/\Sigma_P$. H is the

height of the viscous/polarization layer as discussed in Sec 3, and $dx_i dy_i$ is an area element at the ionospheric substrate. The term on the left is the time rate of change in flow kinetic energy. The first three terms on the right are negative definite and represent, in order of appearance, power dissipation by viscous friction (P_ν), the production of particle energy flux attributed to the field-aligned potential drop ($P_{||}$), and Ohmic heating in the ionosphere (P_Ω). The last term on the right can be shown to be the integral of the Poynting flux (P_S) over the upper boundary surface of the magnetospheric region at $z = 0$. The field-aligned current density $j_0(x, y)$ is fixed at this boundary, which sustains the system energy. The Poynting flux at the boundary and its integral are not constant in time, however, because the electric potential there may vary with time.

Figure 3 shows time-histories for Runs 2 and 3 of the magnitude of each term on the right side of equation (14) normalized to the initial value of the input power at $z = 0$ (the boundary integrated Poynting flux, P_S). The flow kinetic energy normalized to its initial value is also plotted. The net run time displayed in Figs. 3 (i.e., $t = 100$ on the horizontal axis) corresponds to 680 τ_e (eddy time) for Run 2 and 426 τ_e for Run 3. The input power at $z = 0$, flow kinetic energy, and energy dissipation rates shown in the figure all decrease as a consequence of the instability. As shown below, this decrease is accompanied by the formation eddies within the shear layer. Most of the system energy resides in the eddies, which are also the principal sites of dissipation within the layer. The input Poynting flux is reduced because the flow velocity and, therefore, the electric field and potential are substantially reduced from their initial values in the regions between eddies (cf. the following discussion of power spectral densities).

Near the end of Runs 2 and 3, the energy dissipation attributed to the field-aligned potential drop exceeds both the viscous and Ohmic heating rates. Note, however, that the viscous heating rate is initially largest in both runs. In contrast, Ohmic heating and fast particle production are negligible for the duration of Run 1 of Table 1, which is dominated by viscous heating; in Run 4 of Table 1, the Ohmic heating and fast particle production rates are comparable throughout the run and are much larger than the viscous heating rate. The relative energy dissipation rates for all four runs, evaluated at the end of each run, are compared in the last column of Table 2.

A somewhat more detailed examination of the simulations shows that in all four cases, the system undergoes an initial transient phase in which the 1D equilibrium flow breaks up into eddies; the number of eddies present during the initial transient phase is determined by the linearly most unstable mode number. This primary transient phase is clearly evident in Fig. 3 when the energy and dissipation rate rapidly decrease. The primary transient phase is followed by a secondary transient phase in which

spectral energy is distributed to other perturbing modes, principally to integral harmonics of the linearly most unstable mode. Most of the excited harmonics are linearly stable modes. The secondary transient phase is exemplified in Figs. 3 by a slower rate of decrease in the flow kinetic energy. During and subsequent to the secondary transient phase in Fig. 3, irregular oscillations appear the flow kinetic energy and dissipation rates. These oscillations are associated with eddy merging and splitting. Owing to the finite run time, we cannot say whether eddy merging and splitting is a statistically-steady process, similar to hunting in a nonlinear control system, or whether it is a longer time-scale transient process involving some type of damped oscillatory motion. The more weakly driven cases 1 and 4 identified in Table 1 (but not shown in Fig. 3) show no evidence of eddy merging or splitting for the duration of the runs which extend to 190 τ_e and 167 τ_e, respectively. In both cases, the flow kinetic energy and dissipation rates are practically constant during the last half of the run, indicating that Runs 1 and 4 may have actually reached a time-asymptotic steady-state.

A curious feature of the nonlinear dynamics, which is correlated with the relative linear growth rate and, therefore, with how strongly the system is initially driven, is the ratio of final to initial flow kinetic energy in the system. This ratio is given in column 2 of Table 2; the ratio of the final to initial dissipation rate (which is also equal to the ratio of final to initial input power at the upper boundary) is also tabulated in column 3. In all four cases, the net result of the instability is to cause the system to undergo a transition from a one-dimensional state of relatively high energy and high rate of dissipation to a two-dimensional, vortex flow state of lower energy with a correspondingly lower dissipation rate. The reduction in energy and dissipation rate becomes more severe when the system is more strongly unstable, as in Run 3 where the final energy is only 24% of the initial energy.

Flows and currents

Time sequences for the velocity field in the viscous/polarization layer and contours of constant field-aligned current density at z = H (i.e., at the bottom of the magnetospheric region) are shown for Run 2 in Figures 4 and 5. The current density at the ionosphere is identically distributed but is larger in amplitude by the constant scaling factor B_i/B. In both figures, the dc magnetic field points into the plane of the figure. The numerical time-step is indicated at the right side of the figures. Only the central region of the simulation box containing the shear layer is shown at each sample time-step. Outside the central region, the field amplitude is significantly reduced, with little apparent activity on the linear contour level scale used in the plots.

The initial flow field depicted in Fig. 4 is generated by the Gaussian stream function given in Eq. (12). Since the velocity is the derivative of the stream function, the initial velocity field consists of a reversed flow moving to the right above the midplane and to the left below it (the arrow directions for velocity are not very well-resolved in Fig. 4). The corresponding electric field is orthogonal to the flow velocity and dc magnetic field and initially points toward the midplane. The initial field-aligned current density in Fig. 5 is maximum at the midplane, falls off exponentially and symmetrically away from it, and changes sign at the transition from solid contours (positive values) to dotted contours (negative values). However, the bulk of the current resides near the midplane, so the flow channel sustains a net current out of the figure.

Recalling that one numerical time unit in Run 2 is equivalent to 6.80 τ_e, we see that the unstable shear layer in Fig. 4 starts to break up within a few eddy times; by 30 τ_e, eight eddies, corresponding to the linearly most unstable mode 8, are well-formed. At later times nonlinear mode couplings become increasingly important, and two pairs of eddies merge, leaving 6 eddies at one point; after t = 100 the last time-step shown in Fig. 4, one eddy subsequently splits, leaving 7 eddies. (The final eddy splitting can be seen in the current density contours in Fig. 5 which is a slightly longer record than Fig. 4.) The eddy structure is also apparent in the field-aligned current density contours shown in Fig. 5, which shows concentrated current filaments near the center of the eddies.

Figure 6 shows the field-aligned current density at z = H for the more strongly driven Run 3. The eddy structure is less well-ordered than in Run 2, and more fluctuation activity appears on the eddy periphery. The dominance of the linearly most unstable mode 5 is apparent at time steps 2 and 4 (9.3 and 18.6 τ_e), but subsequent nonlinear couplings (eddy merging) eventually produce a larger scale order dominated by mode 3 at time step 100. Another difference between Run 3 and the previous Run 2 is that free eddies are created when the driving amplitude is sufficiently large. Notice in Fig. 6 that the rightmost eddy at time step 10 has moved out of and below the main shear layer by time step 20. After time step 20, it continues to move away from the shear layer while convecting to the left in the direction of the average flow velocity. This free eddy decays as it moves away from the shear layer, and between time steps 20 and 30 another eddy forms in the shear layer to take its place. The phenomenon of eddy shedding is somewhat better resolved in the flow field shown in Figure 7.

The flows and current densities in the more weakly driven Runs 1 and 4 (not shown) exhibit much less activity than those in Runs 2 and 3. A linear array of vortices forms in the main shear layer, and the number of vortices, corresponding to the linearly most unstable mode, remains constant throughout both runs (no splitting or merging).

Power spectral density

Since a vortex shear layer is very inhomogeneous, the power spectral density that would be recorded by a spacecraft traversing the shear layer will depend on its particular path through the layer. To give some idea of the possible variations, power spectral densities have been evaluated for six different "satellite" trajectories as indicated in Figure 8. The vortex layer shown in the figure is a snapshot of Run 3 at time step 80. At this time the shear layer is evolving very slowly, in terms of a 'satellite' crossing time (10 sec or so for a layer of 10-50 km across and a satellite velocity of 5 km/sec), so the 'measured' frequency spectrum is primarily a result of Doppler shifted spatial variations [e.g. Kintner, 1976].

Figures 9 and 10 show the electric field spectral density in the magnetospheric and the ionospheric regions, respectively. Figure 11 shows the magnetic spectral density. The spectral densities for the x and y components of the fields are identified in each figure. Significant harmonic structure is apparent in the streamwise spectra (generated from x-cuts) in all three figures. The mode number of the fundamental corresponds to the number of eddies in the simulation box, three in this case. The origin of the harmonic structure is due to nonlinear coupling between the fundamental and higher order modes, most of which are otherwise linearly stable. Note that the intensity tends to decrease as the satellite trajectory moves from $x = 0$ to $x = 15$. Furthermore, the harmonic structure has disappeared in the $x = 15$ cut, which is outside the main shear layer region.

In contrast with the streamwise spectra, the spanwise spectra (generated from y-cuts) exhibit no harmonic structure. The lack of harmonic structure is a consequence of the essentially exponential decay of the field transverse to the shear layer, a remnant of the spatial distribution of the forcing current imposed at the upper boundary of the viscous polarization layer. The spanwise spectra in E_x and B_y closely resemble the exponential forcing spectrum represented by Eq. (13), especially through a vortex center (e.g., near $y = 0$). However, the power in these two field components decreases in the regions between eddies (compare the spectrum generated along $y = 0$ with the one generated at $y = 15$). At small spatial scales, in the viscous dissipation range, the spectrum tends to become relatively isotropic and homogeneous. The spanwise spectra for E_y and B_x are significantly augmented relative to the their initial values as a consequence of the instability. Recall that the initial spectrum is composed of a 1D Gaussian spectrum for E_x and B_y, corresponding to the 1D equilibrium shear layer, and a superimposed, isotropic noise spectrum with an initial intensity that is smaller than the Gaussian part by a factor of 10^{-3}.

A comparison of Figs. 9 and 10 shows that the electric field spectrum is less intense in the ionospheric substrate than in the magnetospheric region and contains less power at large wavenumbers. This effect is a direct consequence of the field-aligned potential drop; as discussed by Weimer et al. (1985) and Lotko and Schultz (1988), the effect is analogous to a low pass filter when electric fields are mapped from the magnetosphere to the ionosphere in the wavenumber domain. Other than this filtering effect the electric field spectra in the ionosphere and magnetosphere are qualitatively similar. By construction, the magnetic field spectra in Fig. 11 are identical in the magnetospheric and ionospheric regions, except for an amplitude scaling factor of B_i/B_e which results from mapping the field-aligned current density between the two regions.

5. Discussion

Summary of Results

At this point it is worth reiterating one of the basic assumptions of the model: a temporally constant or slowly varying field-aligned current is produced in some outer region of the magnetosphere, and any feedback between this outer region and the highly tenuous, low β plasma region below it does not appreciably modify the source distribution of field-aligned current flowing through the outer boundary. Whether this assumption makes sense for a given application depends on the particular processes that produce the field-aligned current, the spatio-temporal scales of interest, etc. The application described below, to post-noon auroral forms resulting from field-aligned currents generated in the low latitude boundary layer, is an example where it seems reasonable to distinguish between the current source region and the plasma load region modeled here.

Given this assumption, and a 1D form for the field-aligned current entering the upper boundary of the viscous/polarization layer, e.g., equation (7), then the neutral stability diagram of Fig. 2, together with the simulation results of Sec. 4, suggest the following interpretation for the structure and dynamics of an auroral shear layer. If all of the field-aligned current entering (or leaving) the upper boundary of the layer can be closed through the combined action of ion-neutral drag, leading to ionospheric Pedersen currents, and viscous body forces in the viscous/polarization layer, then there is no need to close any of the current via polarization currents. In this case, the configuration will remain in equilibrium as a 1D flow state. If all of the current at the upper boundary cannot be closed in this way, then the configuration is unstable, and polarization currents will develop in the viscous/polarization layer in

order to close the unbalanced portion of the field-aligned current. The resulting 2D configuration, in the unstable case, is either a quasi-steady rotational state, when the field-aligned current is weakly unbalanced, or a turbulent state, when the field-aligned current is strongly unbalanced.

Turbulent and quasi-steady rotational states arise when the field-aligned current density is sufficiently large or, equivalently, when the associated **E×B** velocity is sufficiently large. How large is sufficient depends on the shear layer scale size σ, as well as three intrinsic parameters, as indicated in Fig. 2: the RC decay rate $\gamma = \Sigma_p/C_m$, where Σ_P is the height-integrated Pedersen conductivity of the ionosphere and $C_m = \int(\rho/B^2)\,ds$ is the effective capacitance of the viscous/polarization layer; the resistive scale length $\lambda_i = \sqrt{\Sigma_p/K}$, where K is the effective field-aligned conductance density of the acceleration region; and an effective Hartmann number $M = \sqrt{\gamma\lambda^2/\nu}$, where ν is the effective kinematic viscosity of the viscous/polarization layer. When polarization currents develop as a consequence of the instability, both the flow kinetic energy and energy input/dissipation rates of the system are reduced relative to the 1D equilibrium configuration, by a large margin for turbulent states, and more modestly for 2D quasi-steady rotational states (cf. Fig. 3 and Table 2). Turbulent shear layers shed free eddies, which are dissipated in the formerly unperturbed region outside the shear layer.

The power spectral densities computed along sample spanwise 'satellite' cuts through an unstable shear layer are characteristic of the power spectral density of the imposed distribution of field-aligned current density imposed at the upper boundary of the viscous/polarization layer. For streamwise cuts, the spectrum exhibits peaks at the dominant wavelength and its harmonics when the shear layer is weakly unstable. The valleys between spectral peaks become progressively shallower when the system is more strongly driven. The fundamental wavenumber of a harmonic spectrum corresponds to the linearly most unstable mode in the case of weakly unstable shear layers and is apparently smaller than the linearly most unstable mode when the shear layer is more strongly unstable; in the latter case, however, non-steady effects associated with merging and splitting of vortices results in a dynamic spectrum, for which a fundamental mode may not be well-defined. For streamwise cuts outside the region of large velocity shear, the power spectral density is reduced relative to that within the large shear region, and sufficiently far from the shear layer, it becomes broadbanded with no spectral peaks. The field fluctuations in the exterior region may be characterized as spatially decaying turbulence. Owing to the spatial filtering effect of field-aligned potential drops [Weimer et al., 1985; Lotko and Schultz, 1989], the electric field spectral density at scale lengths smaller than the resistive scale length λ defined above is reduced in the ionospheric substrate relative to that in the viscous/polarization layer.

Relation to Decaying Shear Layers

For comparison, we also considered the dynamics of an initial state that is identical to one of the unstable equilibrium states described in Sec. 4, but with the boundary source current $j_0(x)$ turned off. Such a state can never be in static equilibrium and will decay to a zero flow/current state as $t \rightarrow \infty$. However, relative to the initial configuration of the decaying state, one finds that the system may still be unstable (using Liapunov's definition of the stability of phase space paths), because the approach to the zero flow state becomes qualitatively different as one crosses a neutral stability curve in Fig. 2. On the stable side of the neutral curve, the initially 1D state is a decaying 1D state for all time, similar in form to the decaying 1D shear layers analyzed by Lotko et al. [1987]; on the unstable side, the otherwise 1D decaying shear layer, develops 2D rotational motion similar to the driven unstable shear layer. The difference between driven and decaying unstable shear layers is a lack of organization of the eddies in the latter case. Once formed, the eddies tend to move away from the original region of large velocity shear, in more or less random directions as they decay. A similar situation arises if one abruptly turns off the driving current $j_0(x)$ after the shear layer has developed eddies; the eddies decay as they move away from the original location of the shear layer. One can envision (and examine with this model) a continuum of related configurations in which the distribution of boundary current density varies dynamically throughout the period of interest.

In the study reported by Lotko and Schultz [1988], decay turbulence developed striated flows with time that resemble 1D shear layers. This organizing effect is a consequence of anisotropic magnetic field mapping between the ionosphere and magnetosphere. It is not clear exactly what effect such anisotropy would have on the driven systems examined in this paper. If the anisotropic mapping tends to reinforce the one-dimensionality of the driven shear layer, then the configuration may be more stable than indicated by the neutral curves in Fig. 2; alternatively, it may be more unstable if the mapping tends to counteract the one-dimensionality of the equilibrium state.

Application to Post-Noon Auroral Forms

Nearly all images from the Viking satellite show dynamic dayside auroral luminosity with frequent occurrences of spatially periodic bright spots distributed in magnetic local time in the 1400 to 1600 MLT region [Lui et al., 1989; Potemra et al., 1990]. Similar features have also been identified in electron density maps inferred from the Sondrestrom radar [Robinson et al., 1984]. These bright spots resemble the current filaments and vortices shown in Figs. 4-7; moreover, the meridional electric field measured over post-noon auroral forms [e.g., Bruning et al., 1990] exhibits localized, spike-like

reversals that also resemble the derivative Gaussian initial condition implied by equation (12). It is therefore natural to ask whether the model under consideration here actually predicts periodic bright spots. Because dayside auroral forms are produced by relatively soft electron precipitation, the Hall and Pedersen conductivities are relatively uniform [cf. Robinson et al., 1984], and our simple ionospheric model is reasonably well-justified.

The observed periodic forms are typically located in the post-noon ionosphere at an invariant magnetic latitude of about 75°. Lui et al. and Potemra et al. note that such auroral forms are most likely the ionospheric projection of **E×B** plasma flows that map along field lines to the low latitude boundary layer region. We therefore apply the model, in this case, at points along field lines from the F-region ionosphere up to the effective lower boundary of the LLBL. This effective boundary is defined as the transition from the higher altitude, higher β plasma of the outer magnetospheric region to the lower altitude, lower β plasma of the middle magnetosphere. The transition occurs roughly at a distance of ½ the length of the field line, as measured from its ionospheric foot to the point where it crosses the equatorial plane. Above this effective boundary, field-aligned currents are produced by processes that are still not well-understood; an enhanced viscous interaction between the magnetosheath and magnetospheric plasmas and an enhanced resistive interaction between merging magnetosheath and magnetospheric magnetic fields are possible mechanisms. The mechanism that generates field-aligned currents in the LLBL region will not actually be specified here; rather we assume that some quasi-steady process generates the field-aligned current and that it is sufficient to model its distribution on the effective boundary at $z = 0$ by the 1D Gaussian function $j_0(x)$ given by the inverse transform of (13). Below the effective boundary, the flow state is initially characterized by the 1D equilibrium state (12), although it may not remain in this state if the configuration is unstable. While this model does not allow feedback to the LLBL processes that produce the field-aligned current, one might expect an instability of the configuration to occur first in the middle magnetospheric layer where the stabilizing effects of magnetic shear are comparatively weak.

We now estimate the parameters $v_0/\gamma\lambda$ and σ/λ that are needed to determine the stability of the 1D flow state. Using the approximate formula $C_m \approx 10F(n/1\,cm^{-3})(L/10)^7$ for the capacitance of the viscous/polarization layer, we estimate a minimum capacitance of a few 10's F, corresponding to L = 15 (75° invariant latitude in the ionosphere) and a density of a few particles/cm^3. The height-integrated Pedersen conductivity in the 1400 to 1600 MLT auroral oval is about 5-10 mho [Robinson et al., 1984]. The RC decay rate $\gamma = \Sigma_P/C_m$ is therefore estimated to be of order $\gamma \approx 0.02$/sec. Potemra et al. [1990] report an average field-aligned current density in the region of periodic auroral forms of about $2\mu A/m^2$, projected to the ionospheric altitude, a value that is also consistent with the estimates reported by

Bruning et al. and Robinson et al. Electron and ion velocity distributions measured over the post-noon aurora show evidence of acceleration by a field-aligned potential drop of 1-3 kV [Bruning et al., 1990; Robinson et al., 1984]. Assuming 1 kV for the field-aligned potential drop and $2\mu A/m^2$ for the field-aligned current density, we estimate a field-aligned conductance density of $K \approx j_{\parallel}/\Delta\phi_{\parallel} \approx 2\times10^{-9}$mho/m^2. This value, together with $\Sigma_P \approx 7$mho, implies a resistive scale length of $\lambda_i = \sqrt{\Sigma_P/K} \approx 50$km, projected to the ionospheric reference altitude. Potemra et al. report an average bright spot separation of about ½ hour of MLT corresponding to about 200 km at 75° invariant latitude. This distance should be approximately equal to the wavelength q_m of the linearly most unstable mode. Because $2\pi\sigma/q_m \approx 1$, this implies that $\sigma \approx 30$km. Thus σ/λ is in the range 0.5 to 1. This value is also consistent with the measured north-south electric field profile reported by Bruning et al., which has a peak electric field of about 100 mV/m when a sliding 20 sec average is applied to the data or about 400 mV/m when the field is examined at the instrument resolution of 0.4 sec. The measurement reported by Bruning et al. was made at a geocentric distance of $3R_E$ at 75.5° invariant latitude, where the inferred east-west **E×B** flow maximum is about 5 km/sec or 20 km/sec, depending on whether average or instantaneous data is used. At the ionospheric reference altitude, ignoring field-aligned potential drops in the mapping, the reference velocity is 1-4 km/sec. Our estimate for the parameter $v_0/\gamma\lambda$ is therefore in the range 1 to 4 because $\gamma\lambda_i \approx 1$km/sec.

Referring now to Fig. 2, the neutral stability curves at $\sigma/\lambda = 1$ predict an unstable shear layer if $v_0/\gamma\lambda > .6$ at a Hartmann number M = 10 and $v_0/\gamma\lambda > 5$ at M = 1.5. Since $M^2 = \gamma\lambda^2/\nu$, these two values for the Hartmann number imply an effective viscosity at the bottom of the LLBL (i.e., the top of the polarization layer) of 5×10^8m^2/sec and 2×10^{10}m^2/sec, respectively. Although the effective viscosity is the least certain parameter of the model, the higher value surpasses by an order of magnitude the eddy viscosity estimate $\nu_{eff} \approx .02\sigma v_0 \approx 10^9$m^2/sec deduced from numerical simulations [Miura and Sato, 1978; Miura, 1984]. From these estimates, and using the neutral stability calculation, it is therefore very plausible that 2D rotational states should occur in the post-noon sector of the auroral zone.

In concluding this section, we ask whether the values estimated above are consistent with the assumption of resistive current limitation, i.e., is the inequality $\mu\Sigma_P v_A/(1 + 4\lambda^2/\sigma^2) \ll 1$, where v_A is the Alfvén speed near the top of the polarization layer, satisfied? Using the previous estimates, this condition requires that $v_A \ll 600$km/sec. At the top of the polarization layer at a geocentric distance of 9 R_E we estimate $v_A \approx 650$ km/sec for a density of a few cm^{-3}. Thus, the electrostatic approximation appears to be marginal. As proposed by Potemra et al. [1990], this would indicate that magnetoinductive effects involving Alfvén waves are very likely an important part of the structure and dynamics of post-noon auroral systems.

Acknowledgments. We wish to acknowledge helpful discussions with R. L. Lysak, B. U. O. Sonnerup, and M. Temerin, as well as the hospitality of the research staff at the University of California, Space Sciences Laboratory where portions of the work by WL were completed. Funding for this research was provided by NASA under grants NAGW-1169, 1824, NAG 5-1098; NSF under grant ATM-8619019; and the Air Force Geophysics Laboratory under contract F19628-87-K-0026. The computationally intensive calculations were made possible by a grant in computer time from the San Diego Supercomputer Center.

Appendix

The local Ohm's law in the acceleration region is

$$E_{\parallel}(s) = \eta(s) j_{\parallel}(s) \tag{A1}$$

where s is the coordinate along the magnetic field. If the acceleration region is force-free then

$$j_{\parallel}(s) = B(s) \frac{j_{\parallel i}}{B_i} \tag{A2}$$

Now express $E_{\parallel}$ in terms of an electrostatic potential, $E_{\parallel}(s) = -\partial_s \phi(s)$; use (A2) for $j_{\parallel}(s)$; and integrate (A1) from the bottom of the acceleration region, denoted by s_i, to the top, denoted by s_e (i.e., from the ionospheric substrate to the bottom of the viscous polarization layer) to obtain

$$\phi_i - \phi = \frac{j_{\parallel i}}{B_i} \int_{s_i}^{s_e} B(s)\eta(s)\, ds \tag{A3}$$

The proportionality constant in the linear current-voltage relation (A3) determines the field-aligned conductance density K:

$$K^{-1} = \frac{1}{B_i} \int_{s_i}^{s_e} B(s)\eta(s)\, ds \tag{A4}$$

For the application to post-noon auroral forms discussed in Sec 5., K was estimated as 2×10^{-9} mho/m^2. To see what this implies for a resistivity, we approximate (A4) as $K \approx B_i/(\overline{B}\,\overline{\eta}\Delta s)$ where Δs is the effective length of the acceleration region, and an overbar signifies mean value in the acceleration region. For a nominal acceleration region located at high latitude (75° in the post-noon application), at about 1 R_E altitude, extending along the magnetic field a distance of about 1 R_E, the estimate of 2×10^{-9} mho/m^2 for K requires a mean resistivity $\overline{\eta} \approx 600$ ohm-m.

References

Basu, S., S. Basu, E. Mackenzie, P. F. Fougere, W. R. Coley, N. C. Maynard, J. D. Winningham, M. Sugiura, W. B. Hanson, and W. R. Hoegy, Simultaneous density and electric field fluctuation spectra associated with velocity shears in the auroral oval, *J. Geophys. Res.* **93**, 115, 1988.

Brüning, K., L. P. Block, G. T. Marklund, L. Eliasson, R. Pottelette, J. S. Murphree, T. A. Potemra, and S. Perraut, Viking observations above a postnoon aurora, *J. Geophys. Res.* **95**, 6039, 1990.

Burch, J. L., W. Lennartsson, W. B. Hanson, R. A. Heelis, J. H. Hoffman, and R. A. Hoffman, Properties of spikelike shear flow reversals observed in the auroral plasma by the Atmosphere Explorer C, *J. Geophys. Res.* **81**, 3886, 1976.

Burke, W. J., M. Silevitch, and D. A. Hardy, Observations of small-scale auroral vortices by the S3-2 satellite, *J. Geophys. Res.* **88**, 3127, 1983.

Burke, W. J., D. A. Hardy, F. J. Rich, R. C. Sagalyn, B. Shuman, M. Smiddy, R. Vancour, P. J. L. Wildman, M. C. Kelley, M. A. Doyle, M. S. Gussenhoven, and N. A. Saflekos, High latitude electrodynamics: Observations from S3-2, *Space Sci. Rev.* **37**, 161, 1984.

Chiu, Y. T. and J. M. Cornwall, Electrostatic model of quiet auroral arcs, *J. Geophys. Res.* **85**, 543, 1980.

Cornwall, J. M., Exact solutions and low-frequency instability of the adiabatic auroral arc model, *J. Geophys. Res.* **93**, 11429, 1988.

Davis, T. N., Observed characterisitics of auroral forms, *Space Sci. Rev.* **22**, 77, 1978.

Davis, T. N. and T. J. Hallinan, Auroral Spirals 1. Observations, *J. Geophys. Res.* **93**, 3953, 1976.

Fridman, M. and J. Lemaire, Relationship between auroral electron fluxes and field-aligned electric potential differences *J. Geophys. Res.* **85**, 664, 1980.

Furth, H. P., J. Killeen, and M. N. Rosenbluth, Finite-resistivity instabilities of a sheet pinch, *Phys. Fluids* **6**, 459, 1963.

Gurnett, D. A. and L. A. Frank, Observed relationships between electric fields and auroral particle precipitation, *J. Geophys. Res.* **78**, 145, 1973.

Gurnett, D. A., R. L. Huff, J. D. Menietti, J. L. Burch, J. D. Winningham, and S. D. Shawhan, Correlated low-frequency electric and magnetic noise along auroral field lines, *J. Geophys. Res.* **89**, 8971, 1984.

Hallinan, T. J., Auroral spirals 2. Theory, *J. Geophys. Res.* **81**, 3959, 1976.

Hallinan, T. J. and T. N. Davis, Small-scale auroral arcs distortions, *Planet Space Sci.* **18**, 1735, 1970.

Kelley, M. C. and C. W. Carlson, Observations of intense velocity shear and associated electrostatic waves near and auroral arc, *J. Geophys. Res.* **82**, 2343, 1977.

Keskinen, M. J., H. G. Mitchell, J. A. Fedder, P. Satyanarayana, S. T. Zalesak, and J. D. Huba, Nonlinear evolution of the Kelvin-Helmholtz instability in the high-latitude ionosphere, *J. Geophys. Res.* **93**, 137, 1988.

Kintner, P. M. Jr., Observations of velocity shear driven plasma turbulence, *J. Geophys. Res.* **81**, 5114, 1976.

Kintner, P.M. and C. E. Seyler, The status of observations and theory of high latitude ionospheric and magnetospheric turbulence, *Space Sci. Rev.* **41**, 91, 1985.

Knight, S., Parallel electric fields *Planet. Space Sci.* **21**, 741, 1973.

Lotko, W., B. U. O. Sonnerup, and R. L. Lysak, Nonsteady boundary layer flow including ionospheric drag and parallel electric fields, *J. Geophys. Res.* **92**, 8635, 1987.

Lotko, W. and C. G. Schultz, Internal shear layers in auroral dynamics, in *Magnetosphere-Ionosphere Plasma Models, Geophys. Monogr. Ser.*, v. **44**, ed. by T. E. Moore and J. H. Waite, Jr., p. 121, AGU, Washington D. C., 1988.

Lui, A. T. Y., D. Venkatesan, and J. S. Murphree, Auroral bright spots on the dayside auroral oval, *J. Geophys. Res.* **94**, 5515, 1989.

Lyons, L. R., Generation of large-scale regions of auroral current, electric potential, and precipitation by divergences of convective electric fields, *J. Geophys. Res.* **85**, 17, 1980.

Lyons, L. R., D. S. Evans, and R. Lundin, An observed relation between magnetic field-aligned electric fields and downward electron energy fluxes in the vicinity of auroral forms *J. Geophys. Res.* **84**, 457, 1979.

Lysak, R. L., Feedback instability of the ionospheric resonant cavity, submitted to *J. Geophys. Res.*, *1990*.

Lysak, R. L. and M. K. Hudson, Effect of double layers on magnetosphere-ionosphere coupling, *Laser and Particle Beams* **5**, 351, 1987.

Mitchell, H. G., Jr., J. A. Fedder, M. J. Keskinen, and S. T. Zalesak, A simulation of high latitude F-layer instabilities in the presence of magnetosphere-ionosphere coupling, *Geophys. Res. Lett.* **12**, 283, 1985.

Miura, A., Anomalous transport by magnetohydrodynamic Kelvin-Helmholtz instabilities in the solar wind-magnetosphere interaction, *J. Geophys. Res.* **89**, 801, 1984.

Miura, A. and T. Sato, Shear instability: auroral arc deformation and anomalous momentum transport, *J. Geophys. Res.* **83**, 2109, 1978.

Mozer, F. S., C. A. Cattell, M. K. Hudson, R. L. Lysak, M. Temerin, and R. B. Torbert, Satellite measurements and theories of auroral acceleration mechanisms, *Space Sci. Rev.* **27**, 155, 1980.

Murty, G. S., Instability of a conducting fluid slab carrying uniform current in the presence of a homogeneous magnetic field, *Ark. Fys.* **19**, 499, 1961.

Oguti, T., Rotational deformations and related drift motions of auroral arcs, *J. Geophys. Res.* **79**, 3861, 1974.

Oguti, T., TV observations of auroral arcs, in *Physics of Auroral Arc Formation, Geophys. Monogr. Ser.*, v. **25**, ed. by S.-I Akasofu and J. R. Kan, p. 31, AGU, Washington, D.C., 1981.

Orszag, S. A., Numerical simulation of incompressible flows with simple boundaries. I. Galerkin (spec-

tral) representation, *Studies in Appl. Math* **50**, 293, 1971.

Potemra, T.A., H. Vo, D. Venkatesan, L. L. Cogger, R. E. Erlandson, L. J. Zanetti, P. F. Bythrow, and B. J. Anderson, Periodic auroral forms and geomagnetic field oscillations in the 1400 MLT region, *J. Geophys. Res.* **95**, 5835, 1990.

Robinson, R. M., D. S. Evans, T. A. Potemra, and J. D. Kelly, Radar and satellite measurements of an F-region ionization enhancement in the post-noon sector, *Geophys. Res. Lett.* **11**, 899, 1984.

Seyler, C. E., Nonlinear 3-D evolution of bounded kinetic Alfvén waves due to shear flow and collisionless tearing instability, *Geophys. Res. Lett.* **15**, 756, 1988.

Temerin, M., M. H. Boehm, and F. S. Mozer, Paired electrostatic shocks, *Geophys. Res. Lett.* **8**, 799, 1981.

Temerin, M., C. Cattell, R. Lysak, M. Hudson, R. B. Torbert, F. S. Mozer, R. D. Sharp, and P. M. Kintner, The small-scale structure of electrostatic shocks, *J. Geophys. Res.* **86**, 11278, 1981.

Temerin, M. and P. M. Kintner, Review of ionospheric turbulence, in *Plasma Waves and Instabilities at Comets and in Magnetospheres, Geophys. Monogr. Ser.*, v. **53**, ed. by B. T. Tsurutani and H. Oya, p. 65, AGU, Washington, D.C., 1989.

Vickrey, J. F., R. R. Vondrak, and S. J. Matthews, The diurnal and latitudinal variation of auroral zone ionospheric conductivity, *J. Geophys. Res.* **86**, 65, 1981.

Wagner, J. S., J. R. Kan, S.-I Akasofu, T. Tajima, J. N. Leboeuf, and J. M. Dawson, A simulation study of V-potential double layers and auroral arc deformations, in *Physics of Auroral Arc Formation, Geophys. Monogr. Ser.*, v. **25**, ed. by S.-I Akasofu and J. R. Kan, p. 304, AGU, Washington, D.C., 1981.

Wagner, J.S., R. D. Sydora, T. Tajima, T. Hallinan, L.C. Lee, and S.-I Akasofu, Small-scale auroral arc deformations, *J. Geophys. Res.* **88**, 8013, 1983.

Webster, H. F. and T. J. Hallinan, Instabilities in charge sheets and current sheets and their possible occurrence in the aurora, *Rad. Sci.* **8**, 475, 1973.

Weimer, D. R., C. K. Goertz, D. A. Gurnett, N. C. Maynard, and J. L. Burch, Auroral zone electric fields from DE 1 and DE 2 at magnetic conjunctions, *J. Geophys. Res.* **90**, 7479, 1985.

Weimer, D. R., D. A. Gurnett, C. K. Goertz, J. D. Menietti, J. L. Burch, and M. Sugiura, The current-voltage relationship in auroral current sheets, *J. Geophys. Res.* **92**, 187, 1987.

White, R. B., Resistive reconnection, *Rev. Mod. Phys.* **58**, 183, 1986.

TABLE 1. Simulation Parameters

Run	σ/λ	$v_0/\gamma\lambda$	q_m	$s_m\tau_e$	$\gamma\tau_e$	R	$2\pi\sigma/L$	τ_n/τ_e	Box
1	0.1	2.	4	.21	.05	20	.263	3.80	64^2
2	0.5	2.	8	.33	.25	100	.147	6.80	128^2
3	0.5	10.	5	.38	.05	500	.235	4.26	64^2
4	1.0	2.	4	.24	.50	200	.300	3.33	128^2

Glossary

σ/λ	ratio of shear layer scale size to resistive scale length
$v_0/\gamma\lambda$	nondimensional shear layer velocity amplitude; γ is the inverse of the RC decay time.
q_m	mode number of the most unstable linear mode (wavenumber scaled to σ is $q_m \cdot 2\pi\sigma/L$).
$s_m\tau_e$	growth rate of linear mode q_m scaled to the eddy time $\tau_e = \sigma/v_0$.
$\gamma\tau_e$	ratio of eddy time to RC decay time.
R	mechanical Reynolds number ($R = \sigma^2/\nu\tau_e$, the ratio of viscous decay time to eddy time).
$2\pi\sigma/L$	ratio of shear layer scale size to box size.
τ_n/τ_e	ratio of numerical time unit to eddy time (=*romanL*$/2\pi\sigma$).
Box	box size.

For all cases, the effective Hartmann number is $M = \sqrt{R\,\gamma\tau_e}\,\lambda/\sigma = 10$.

TABLE 2. Comparison of Simulation Results

Run	E_f/E_0	P_f/P_0	Relative dissipation rates
1	.52	.48	$P_v \gg P_\parallel \gg P_\Omega$
2	.45	.48	$P_v \approx P_\parallel/2 \approx P_\Omega$
3	.24	.30	$P_v \approx P_\parallel/4 \approx P_\Omega/2$
4	.78	.84	$P_v \ll P_\parallel \approx P_\Omega$

E_f/E_0 is the ratio of final to initial flow kinetic energy. P_f/P_0 is the ratio of final to initial dissipation rate, also equal to the ratio of final to initial input power at the upper boundary. P_v, $P_\parallel$ and P_Ω are, respectively, the final dissipation rates attributed to viscous heating, fast particle porduction by the field-aligned potential drop and ionospheric Ohmic heating.

Table 3. Nominal Parameters for Post-Noon Aurora

MLT sector	1400-1600
Invariant latitude	75°
L shell	15
Mean periodicity of bright spots in local time (km)	200
Peak east-west $\mathbf{E}\times\mathbf{B}$ velocity projected to $1\,R_E$ (km/sec)	1-4
Meridional scale size projected to $1\,R_E$ (km)	30
Field-aligned current density projected to $1\,R_E$ ($\mu A/m^2$)	2
Field-aligned potential drop (kV)	1
Ionospheric Pedersen conductivity (mho)	7
Estimated particle density above acceleration region (m^{-3})	3×10^6
Capacitance of the viscous/polarization layer $C_m = \int(\rho/B^2)\,ds$ (Farad)	300
RC decay rate $\gamma = \Sigma_P/C_m$ (sec^{-1})	.02
Field-aligned conductance density $K = j_\parallel/\Delta\phi_\parallel$ (mho/m^2)	2×10^{-9}
Resistive scale length at ionosphere $\lambda_i = \sqrt{\Sigma_P/K}$ (km)	50

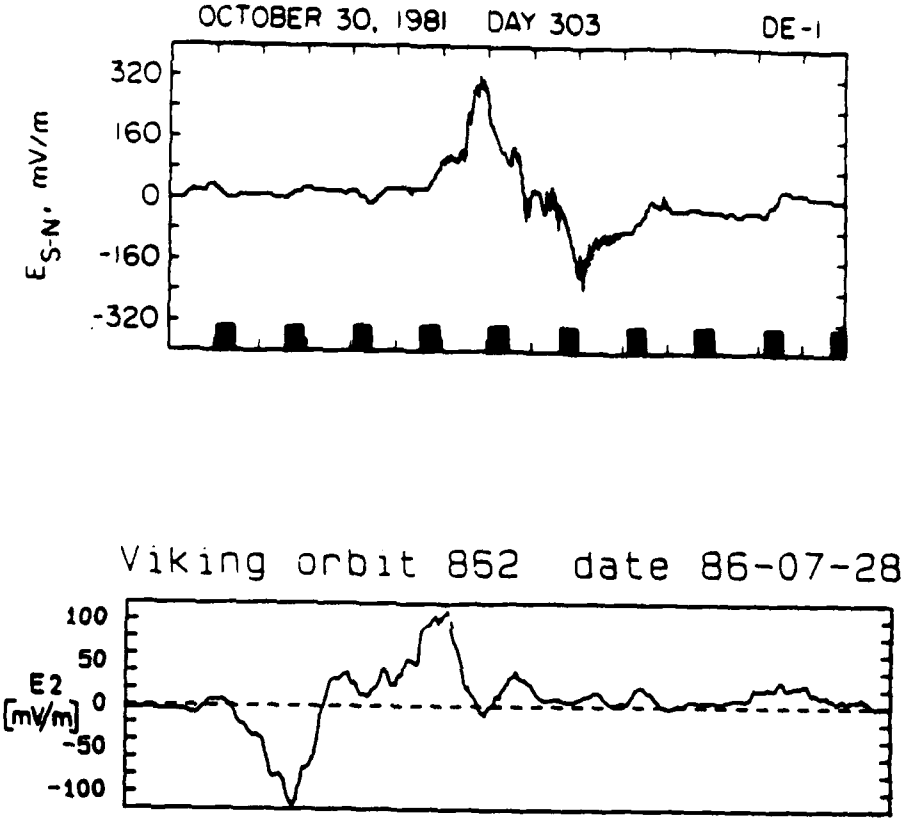

Figure 1. Examples of the meridional electric field distribution in an auroral shear layer from the DE-1 satellite in the evening auroral oval [from Weimer et al., 1987] and from the Viking satellite in the post-noon auroral oval [from Bruning et al., 1990].

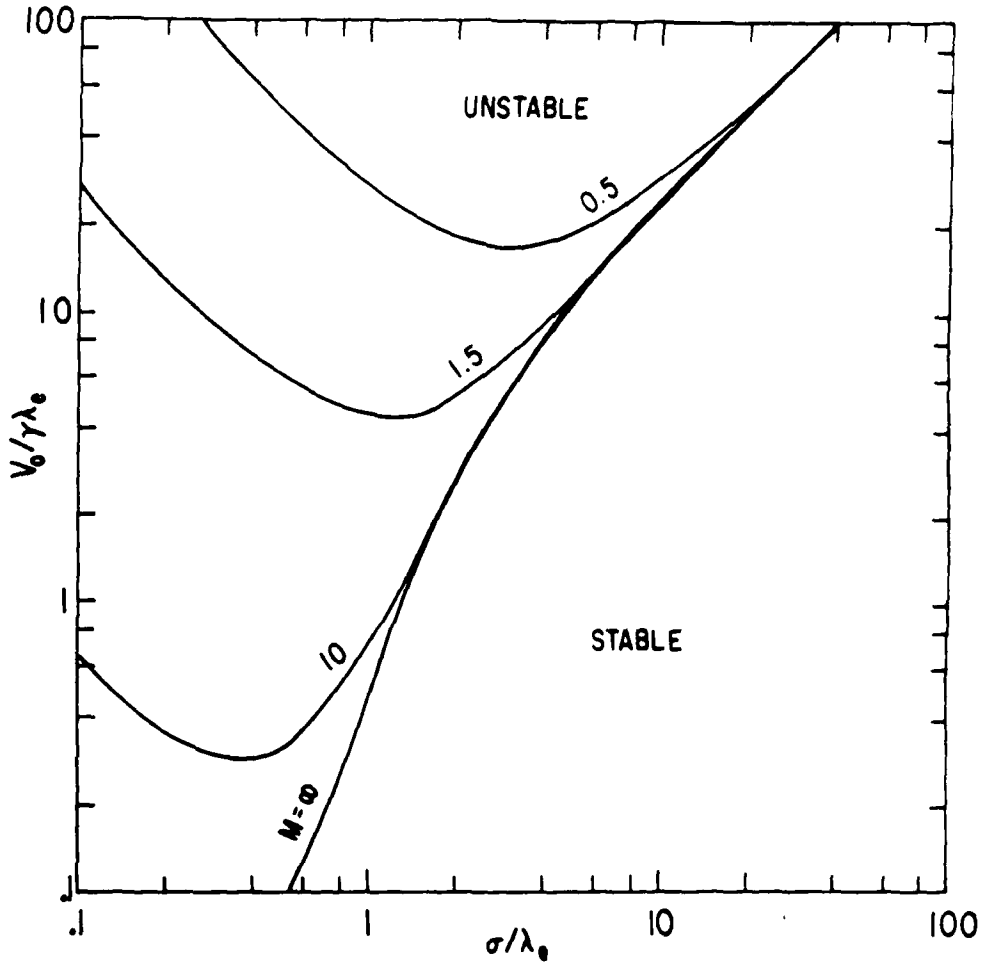

Figure 2. Neutral stability curves for M = 0.5, 1.5, 10, and 10^5 (marked ∞). M is the effective Hartmann number. For a given value of M, the shear layer is linearly stable below the curve corresponding to that value of M and unstable above it.

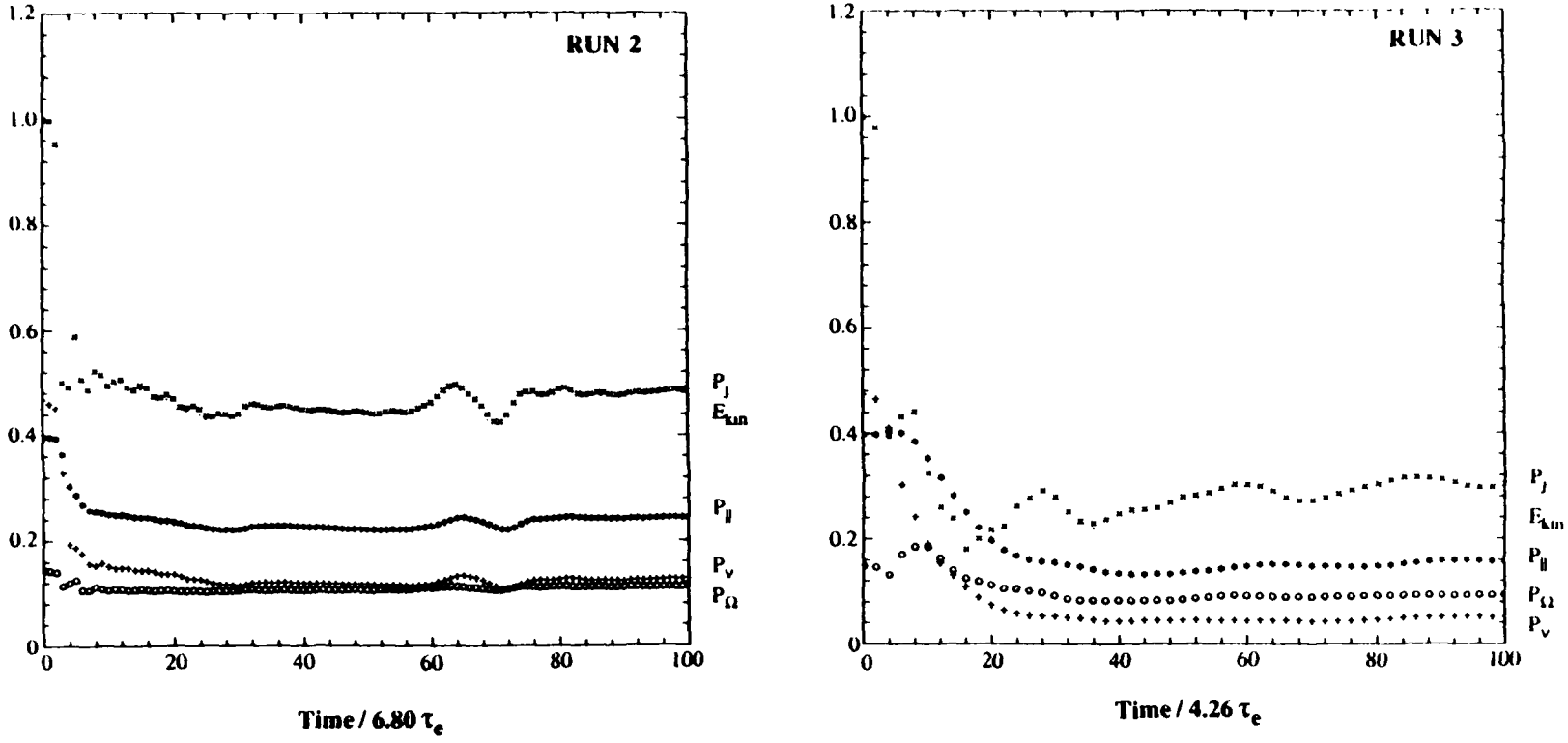

Figure 3. Time histories for the flow kinetic energy E_{kin} (dotted line), power input P_j at the upper boundary of the viscous/polarization layer (x symbol), and power dissipation attributed to viscous heating P_v in the viscous/polarization layer (plus signs), Ohmic heating P_Ω in the ionosphere (circles), and field-aligned particle energy flux $P_\parallel$ in the acceleration region (asterisks). Flow kinetic energy is normalized to its initial value; power input/dissipation is normalized to the intial value of the power input. Plots are for Runs 2 and 3 in Table 1. Note that 1 unit of run time corresponds to 6.80 τ_e for Run 2 and 4.26 τ_e for Run 3.

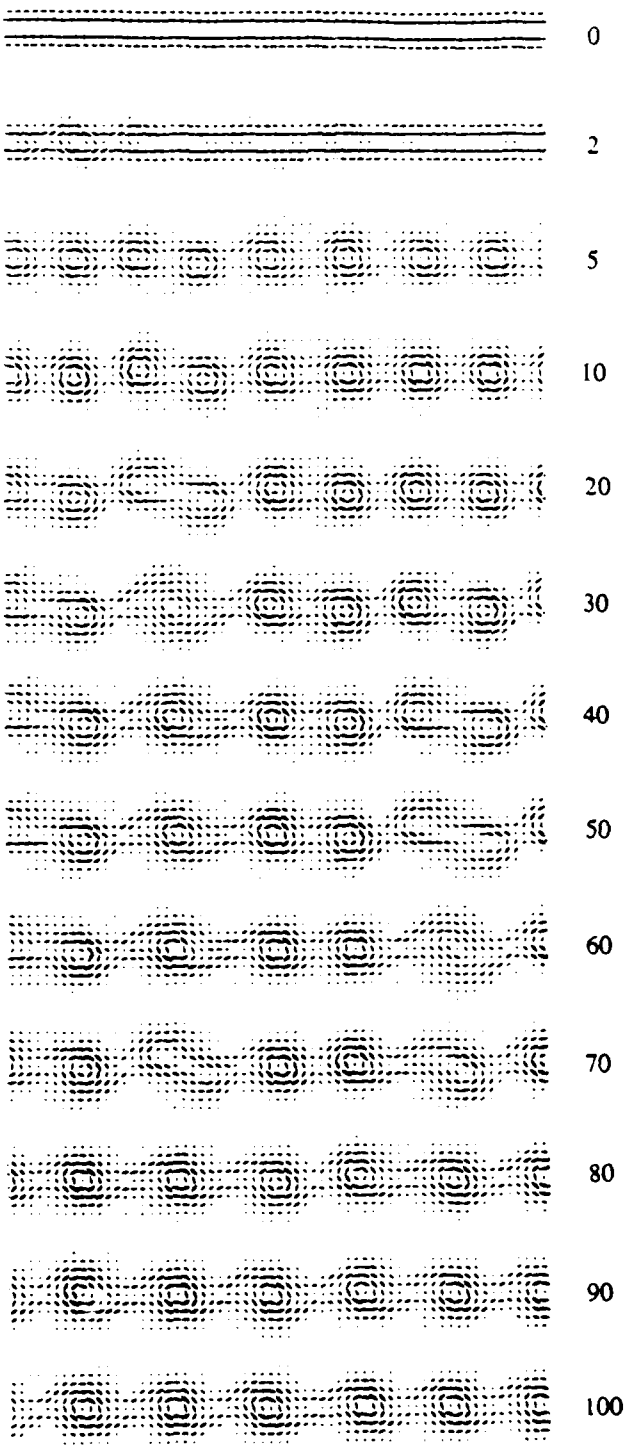

Figure 4. Time-sequence snapshots of the velocity field in the viscous/polarization layer for Run 2. The not very well-resolved arrows represent the direction of velocity; their length represents the relative magnitude of velocity. The dc magnetic field points into the plane of the figure. Numbers to the right of each snapshot represent the run time (1 unit = 6.80 τ_d).

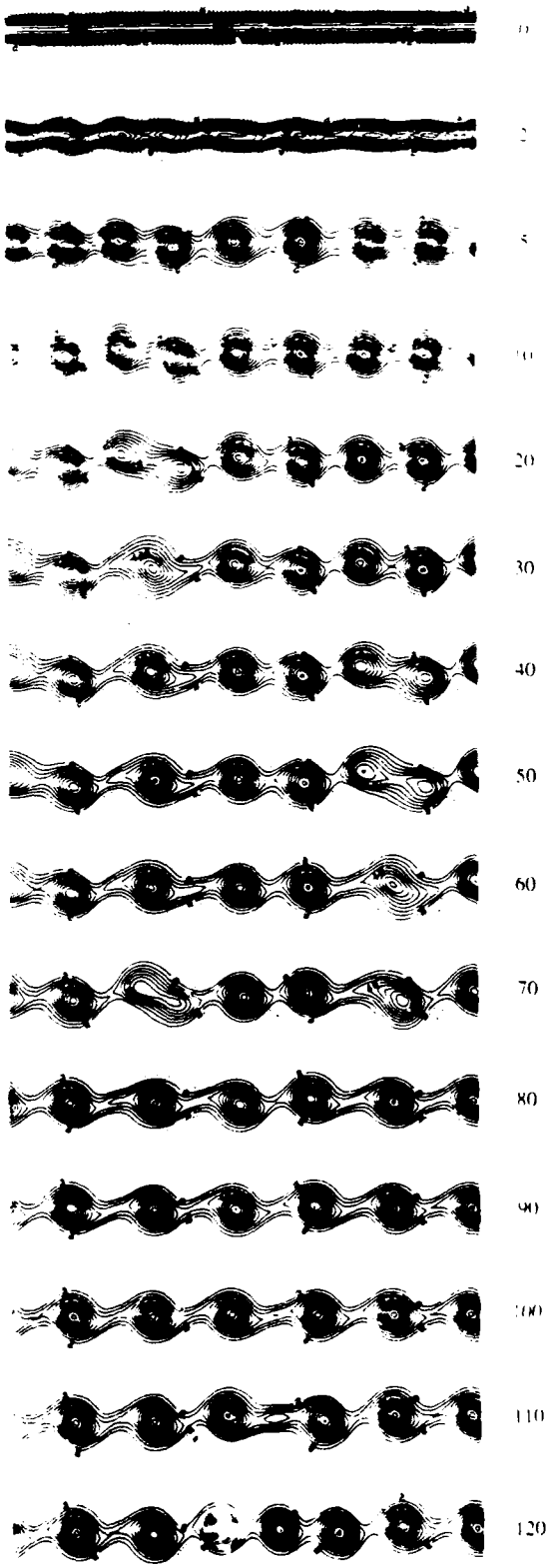

Figure 5. Time-sequence snapshots of the current density at the bottom of the viscous/polarization layer for Run 2. Solid contours represent current out of the ionosphere; dotted contours represent current into the ionosphere.

Figure 6. Same as Figure 5 for Run 3 except that 1 unit of run time now corresponds to 4.26 τ_e.

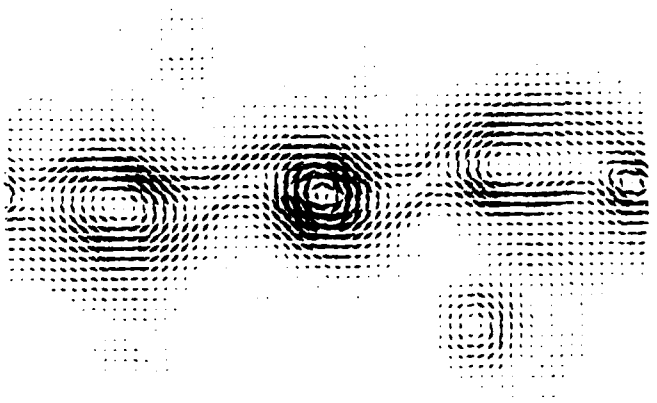

Figure 7. Eddy Shedding. The snapshot of the velocity field for Run 3 at time step 30 shows the full simulation plane. The free eddy is apparent below the shear layer and to the right side.

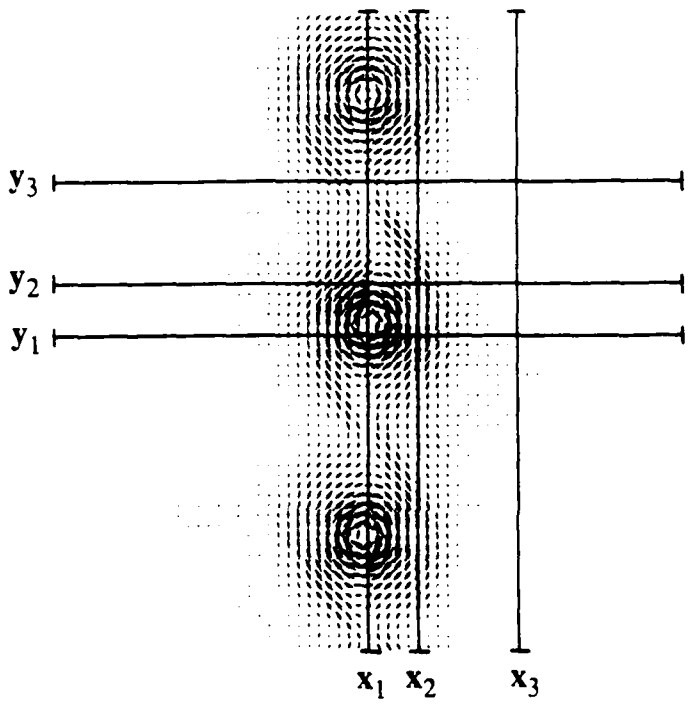

Figure 8. Sample 'satellite' cuts for evaluating power spectral densities. The velocity field for Run 3 at time step 80 is used to illustrate spectral features.

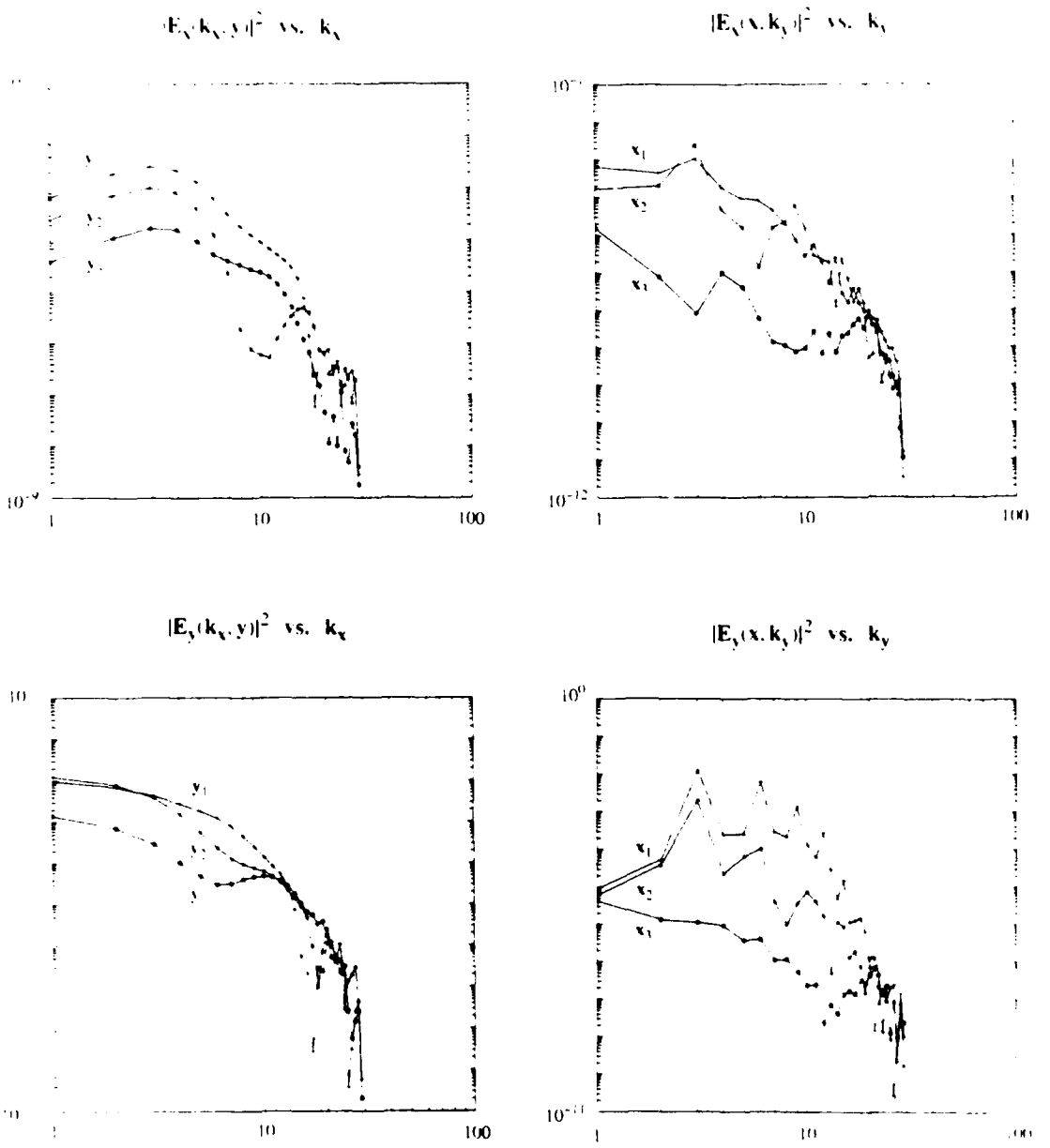

Figure 9. Spectral density for the magnetospheric electric field in the viscous/polarization layer. Clockwise from upper left are the spectral densities for the spanwise electric field (E_x) for three streamwise cuts (y_1, y_2 and y_3), the spanwise electric field for three spanwise cuts (x_1, x_2 and x_3), the streamwise electric field for streamwise cuts, and the streamwise electric field for spanwise cuts.

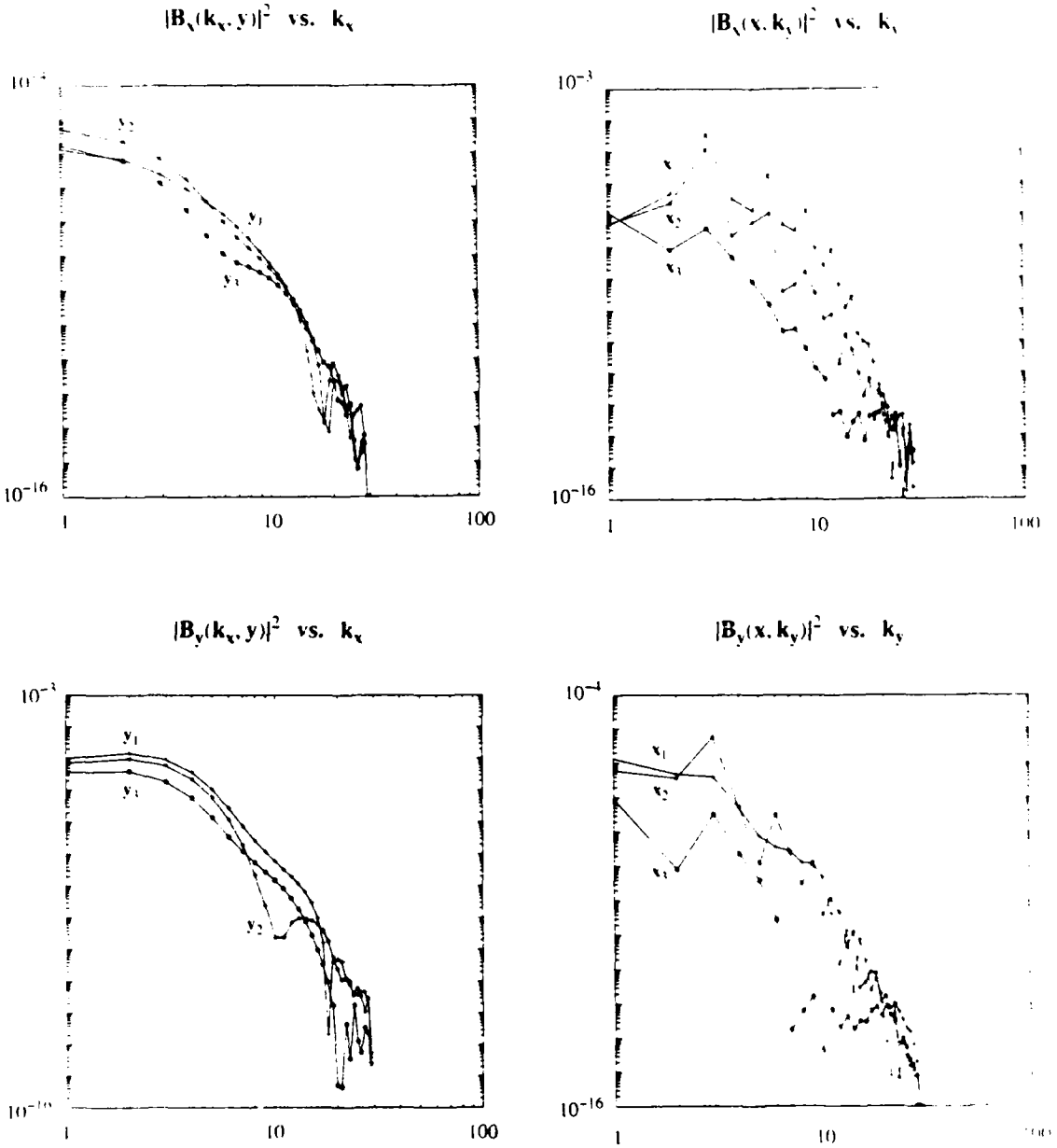

Figure 10. Spectral density for the magnetospheric magnetic field at the bottom of the viscous/polarization layer. Same format as Figure 9.

IONOSPHERE

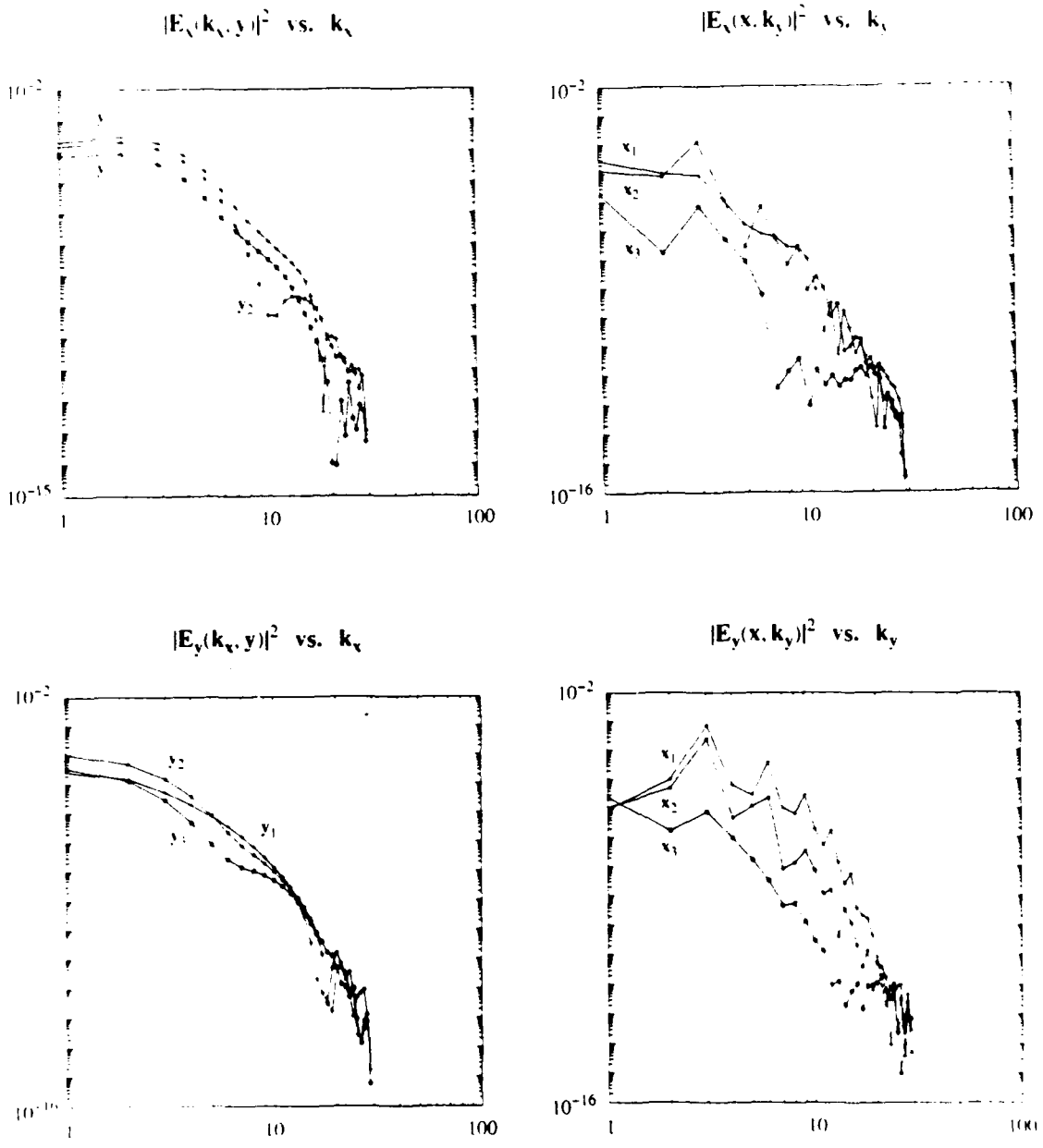

Figure 11. Spectral density for the electric field at the ionospheric substrate. Same format as Figure 9.

Appendix 3

JOURNAL OF GEOPHYSICAL RESEARCH, VOL. 94, NO. A2, PAGES 1281-1293, FEBRUARY 1, 1989

Self-Consistent Model of the Low-Latitude Boundary Layer

T. D. PHAN, B. U. Ö. SONNERUP, AND W. LOTKO

Thayer School of Engineering, Dartmouth College, Hanover, New Hampshire

A simple two-dimensional, steady state, viscous model of the dawnside and duskside low-latitude boundary layer (LLBL) has been developed. It incorporates coupling to the ionosphere via field-aligned currents and associated field-aligned potential drops, governed by a simple conductance law, and it describes boundary layer currents, magnetic fields, and plasma flow in a self-consistent manner. Slab geometry is assumed, with no variations along the flow direction $-x$ and with the layer on closed field lines. The currents in the layer are regulated by coupling to the ionosphere. The magnetic field induced by these currents leads to two effects: (1) a diamagnetic depression of the magnetic field in the equatorial region and (2) bending of the field lines into parabolas in the xz plane with their vertices in the equatorial plane, at $z = 0$, and pointing in the flow direction, i.e., tailward. Both effects are strongest at the magnetopause edge of the boundary layer and vanish at the magnetospheric edge. The diamagnetic depression corresponds to an excess of plasma pressure in the equatorial boundary layer near the magnetopause. This pressure drops off both with increasing distance z from the equatorial plane and with increasing distance y from the magnetopause. It reaches the magnetospheric level for $z = \pm H$ as well as for $y \rightarrow \infty$. The boundary layer structure is governed by a fourth-order, nonlinear, ordinary differential equation in which one nondimensional parameter, the Hartmann number M, appears. A second parameter, introduced via the boundary conditions, is a nondimensional flow velocity v_o^* at the magnetopause. It is shown that for large M values the coupling to the ionosphere is weak; in that limit, or when v_o^* is small, the model reduces to that discussed by Lotko et al. (1987) in which induced magnetic fields are neglected. Numerical results from the model are presented and the possible use of observations to determine the model parameters is discussed. The general predictions of the model in terms of region 1 currents and associated ionospheric signatures are similar to those obtained earlier by Lotko et al. and by Sonnerup (1980). Those predictions are in qualitative and approximately quantitative agreement with a number of observations. The main new contribution of the study is to provide a better description of the field and plasma configuration in the LLBL itself and to clarify in quantitative terms the circumstances in which induced magnetic fields become important. In particular, it appears that for the low values of the field-aligned conductance expected on the duskside of the magnetosphere, these fields may remain relatively unimportant, at least in the noon to dusk segment of the LLBL.

1. INTRODUCTION

The low-latitude boundary layer (LLBL) is a narrow magnetospheric region, located on the earthward side of, and immediately adjacent to, the magnetopause at low to moderate geomagnetic latitudes and containing magnetosheath like plasma streaming across geomagnetic field lines in the general antisolar direction. This plasma layer was first observed along the flanks of the geomagnetic tail [*Hones et al.*, 1972] but subsequently has been found to be present, at least intermittently, inside the entire low-latitude portion of the dayside magnetopause. Its thickness is difficult to determine from single-satellite observations but appears to increase with increasing longitudinal distance from the subsolar point, at least in the local-time segment of $\pm 6h$ from local noon [*Haerendel et al.*, 1978; *Eastman and Hones*, 1979; *Mitchell et al.*, 1987]; beyond that segment along the magnetospheric flanks, the change of thickness with distance down the tail is less apparent. Typical average thicknesses there may be of the order 0.5-1 R_E, and there is an indication that the thicknesses may be greater for the northward than for the southward interplanetary magnetic field [*Mitchell et al.*, 1987].

The plasma in the LLBL has properties similar to those observed in the adjacent magnetosheath [*Eastman et al.*, 1976, 1985; *Eastman and Hones*, 1979] although sometimes with a significant contribution of magnetospheric or ionospheric particles [*Sckopke et al.*, 1981; *Peterson et al.*, 1982; *Lundin et al.*, 1987]. The flow speed is comparable to, but on average somewhat less than, the speed in the adjacent magnetosheath [*Eastman et al.*, 1985]. Although the data are highly variable, indicating the possible presence of turbulence in the layer, the plasma density and velocity generally decrease with increasing distance from the magnetopause, sometimes with a velocity reversal near the magnetospheric edge of the layer. The LLBL appears to be located principally on closed field lines [*Eastman and Hones*, 1979], although there is also evidence that, at times, part of the layer may be on open field lines, i.e., on field lines with only one foot in the ionosphere [*Mitchell et al.*, 1987].

Theoretical models of the LLBL have been discussed in the literature, starting with the early qualitative work by *Coleman* [1971] and *Eastman et al.* [1976] in which the coupling of the layer to the dayside auroral region ionosphere plays a prominent role. This coupling produces what is known as the region 1 field-aligned currents [*Iijima and Potemra*, 1976*a*, *b*] with the correct sense, namely into the ionosphere on the dawnside and out of it on the duskside. On the basis of the ideas contained in those early papers, *Sonnerup* [1980] developed an illustrative quantitative model in which the LLBL consists of a slab-shaped region containing steady state viscous plasma flow at right

Paper number 88JA03628.
0148-0227/89/88JA-03628$05.00

angles to a uniform magnetic field so that the layer acts as a viscously driven MHD generator. Field-aligned currents $j_\parallel$ connect the generator to the resistive load provided by the auroral ionosphere, and field-aligned potential drops are allowed for in an ad hoc manner in order to limit the magnitude of the field-aligned currents to values commensurate with observations. The ionospheric signatures of the LLBL predicted by this model are not unlike those observed near the convection reversal [e.g., *Bythrow et al.*, 1981]. In particular, broad inverted V structures containing field-aligned potential drops of a few kilovolts and widths of the order of 50-100 km are predicted on the eveningside of the magnetosphere. Similar results were obtained by *Kan and Lee* [1980], who discussed a nonviscous model in which the coupling to the ionosphere causes the boundary layer plasma to slow down gradually as it moves in the antisolar direction.

More recently, *Lotko et al.* [1987] have reexamined and improved the viscous model discussed above. In particular, these authors incorporated field-aligned potential drops $\Delta\phi_\parallel$ in a more satisfactory manner by use of a simple conductance model [*Lyons*, 1980; *Chiu and Cornwall*, 1980] in which $\Delta\phi_\parallel$ is proportional to $j_\parallel$. They obtained one-dimensional steady state LLBL structures similar, on the whole, to those found by *Sonnerup* [1980] but also discussed one-dimensional time-dependent shear layers and outlined some of the spectral properties of the basic equations in two dimensions and time. Numerical simulations of decaying turbulence have also been performed [*Lotko and Schultz*, 1988].

The present paper contains an extension of the one-dimensional steady viscous model by *Lotko et al.* [1987], the extension consisting of incorporating the induced magnetic field in the boundary layer in a self-consistent manner. The presentation is organized as follows. Section 2 contains a qualitative description of the model. In section 3, the basic model equations and the boundary conditions are developed. Section 4 contains results obtained by numerical integration of the model equations, along with discussion of those results. In particular, the problem of determining the model parameters by use of observations is discussed. Finally, section 5 contains a brief discussion of results obtained from the study.

2. MODEL

The following basic features of the model to be analyzed here are the same as in the work of *Sonnerup* [1980]: the LLBL is assumed to be located on closed field lines, to be time independent, and to have slab geometry in which an equilibrium exists between viscous forces driving the flow in the antisolar direction $-x$ and $\mathbf{j} \times \mathbf{B}$ forces. The viscous forces are transmitted across the magnetopause from the streaming magnetosheath plasma. No inertia forces are present, and the plasma moves in a unidirectional manner with $\partial/\partial x \equiv 0$. As in the earlier model, we also have $B_y \equiv 0$, y being the coordinate orthogonal to the slab (and to the magnetopause), and thus a boundary layer thickness that is independent not only of x but of z, the coordinate due *north*, as well. In reality, the boundary layer has curvature in the equatorial and meridional planes but, as for ordinary fluid mechanical boundary layers, modest curvature of this type is not expected to influence the results in an important manner as long as the boundary layer thickness is much less than the radius of curvature. However, other simplifying assumptions are more restrictive: in reality the boundary layer thickness is expected to increase in the flow direction, at least on the front lobe of the magnetosphere where the force equilibrium discussed above has not been reached. This effect may be counterbalanced to some extent by a spreading out of the boundary layer flow in the z direction as the distance from the subsolar region increases. On the other hand, mass addition to the boundary layer by diffusion across the magnetopause, an effect discussed by *Sonnerup* [1980], is likely to lead to an increase of the boundary layer thickness with increasing distance from the subsolar point. This latter effect is not included in our model. Rather it is assumed that such mass diffusion occurs only upstream of the region analyzed. On the whole, it seems that the best potential region of applicability for our model is on the low-latitude flanks of the magnetosphere where existing gradients $\partial/\partial x$ may be small. Even there, some of the assumptions to be made, for example, those of a steady state and of symmetry between the northern and southern hemispheres, represent an oversimplification of the real situation. For this reason, the model should be considered mainly as illustrative. It has the advantage of permitting precise mathematical analysis, identification of significant dimensionless groups governing the system, and insight into the main effects to be expected in the interaction between a rapidly moving viscous layer in the magnetosphere and the auroral ionosphere. However, future detailed comparisons with observations are likely to show the need for substantial improvements in the model assumptions.

A schematic drawing of the geometry in Figure 1 shows the dawnside of the magnetosphere and its coupling to the ionosphere. The system is divided into three parts: the LLBL region, the high-latitude (auroral) ionosphere, and

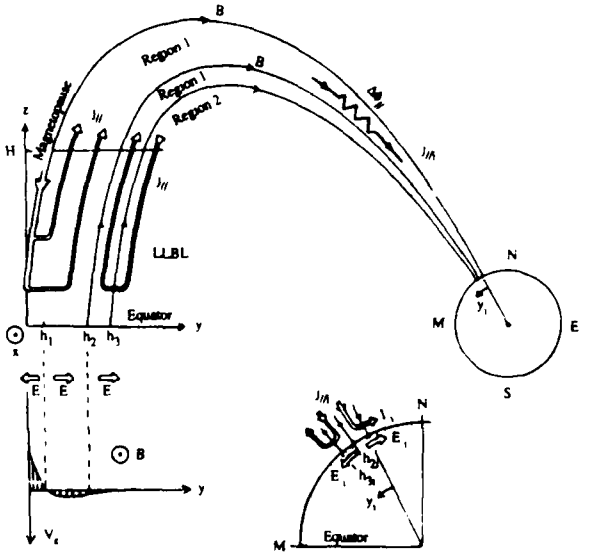

Fig. 1. Schematic drawing of the dawnside low-latitude boundary layer (LLBL) and its coupling to the auroral ionosphere including a field-aligned potential drop $\Delta\phi_\parallel$, in the so-called acceleration region. The boundary layer occupies the region $|z| < H$ in which the plasma velocity $v_x(y)$ is as shown. Pedersen currents and electric fields in the auroral ionosphere are shown in the insert. Regions 1 and 2 correspond to the field-aligned current regions found by *Iijima and Potemra* [1976a, b].

the intermediate-altitude region, or particle acceleration region, connecting the above two parts. Since the plasma in the LLBL is practically collisionless, the viscosity is assumed to be produced by wave-particle interactions occurring on scale lengths comparable to the ion gyroradius, as in the work of *Lotko et al.* [1987], or possibly by macroscopic turbulence, as discussed by *Sonnerup* [1980], *Sato* [1982], and *Miura* [1987]. In the latter case, the equations to be developed here describe the time-averaged behavior of the boundary layer.

As mentioned above, the basic force balance in the flow direction for a fluid element in the boundary layer has two terms: viscous forces which act to accelerate the element in the downstream direction and Maxwell stresses associated with magnetic field lines, curved in the xz plane, which oppose the viscous forces. The field line curvature is produced via Ampère's law by currents j_y flowing across the layer; the associated Maxwell stresses can be expressed as a net force $j_y B_z$ per unit volume opposing the flow. As one moves from the magnetopause edge of the LLBL toward the inner edge of that layer, the plasma velocity and, with it, the velocity gradients decrease, the result being a decreasing value of the net viscous force on a fluid element. The Maxwell stresses opposing the flow must also decrease proportionately, which requires the current j_y to be deflected gradually to join currents in the xz plane. The latter currents have components perpendicular to **B** which produce a force component $\mathbf{j} \times \mathbf{B}$ in the negative y direction. This component serves to balance the decreasing plasma pressure in the LLBL as one moves toward its inner edge. There is also a field-aligned component of the current which flows into the ionosphere in the northern and southern hemispheres. The ionosphere is treated as a resistive load, characterized by an Ohm's law and the requirement of current continuity. In the absence of electric field components along the magnetic field, the ionospheric electric field can be obtained from the equatorial field $-\mathbf{v} \times \mathbf{B}$ in the LLBL by mapping of potentials along the magnetic field from the LLBL to the ionosphere. However, the coupling between the two regions is not perfect in the model: an electric field component along **B**, related to the field-aligned current via a simple conductance law, is incorporated.

3. Basic Model Equations

3.1. *Low-Latitude Boundary Layer*

We assume the boundary layer flow, located within a distance H north and south of the equatorial plane as shown in Figure 1, to be steady, unidirectional, and independent of the coordinate x, i.e., $\mathbf{v} = \hat{\mathbf{x}} v_x(y, z)$. The magnetic field is assumed to be confined to the xz plane, i.e., $B_y = 0$. To satisfy $\nabla \cdot \mathbf{B} = 0$, the field component B_z can depend on y, but not on z. Thus the total field may be written $\mathbf{B} = \hat{\mathbf{x}} B_x(y, z) + \hat{\mathbf{z}} B_z(y)$. We also assume the frozen-field condition to hold in the LLBL. It then follows that the velocity v_x must be independent of the z coordinate, i.e., $\mathbf{v} = \hat{\mathbf{x}} v_x(y)$. In a velocity field of this type, mass conservation is automatically satisfied, and one can allow the plasma density to vary in both y and z so that $\rho = \rho(y, z)$.

With the previous assumptions concerning the magnetic field and the flow velocity of the plasma, the law of conservation of momentum applied to the boundary layer yields

x component

$$0 = j_y B_z(y) + \frac{d}{dy}\eta \frac{d}{dy} v_x(y) \tag{1}$$

y component

$$0 = -\frac{\partial p(y, z)}{\partial y} - j_x B_z(y) + j_z B_x(y, z) \tag{2}$$

z component

$$0 = -\frac{\partial p(y, z)}{\partial z} - j_y B_x(y, z) \tag{3}$$

where p is the plasma pressure, assumed to obey the ideal gas law

$$p(y, z) = \rho(y, z) R T(y, z) \tag{4}$$

Also, η is the dynamic viscosity, which for simplicity we assume to be a function only of the temperature T, i.e., $\eta = \eta(T)$. A more realistic expression for the viscosity should probably include a dependence on density as well as magnetic field. However, since the mechanism responsible for creating the effective viscosity is not well understood, such an improved viscosity model is not available at present.

To describe currents and magnetic fields self-consistently, Ampère's law is used. The three components of the current are given by

$$j_x = \frac{1}{\mu_0}\frac{dB_z(y)}{dy} \tag{5}$$

$$j_y = \frac{1}{\mu_0}\frac{\partial B_x(y, z)}{\partial z} \tag{6}$$

$$j_z = -\frac{1}{\mu_0}\frac{\partial B_x(y, z)}{\partial y} \tag{7}$$

By use of these expressions, (2) and (3) may be integrated to give

$$p + \frac{(B_x^2 + B_z^2)}{2\mu_0} = c_1(z) = c_1 \tag{8}$$

$$p + \frac{B_z^2}{2\mu_0} = c_2(y) \tag{9}$$

from which it follows that $B_x^2/2\mu_0 = c_1(z) - c_2(y)$. Since we have shown that $B_z = B_z(y)$, we conclude that $c_1(z)$ is in fact independent of z, i.e., $c_1(z) = c_1$.

Finally, the potential distribution in the equatorial region can be written in terms of v_x and B_z as

$$\phi(y) = -\int E_y dy = -\int v_x(y) B_z(y) dy \tag{10}$$

3.2. *Coupling to the Ionosphere*

In the remainder of the paper, all quantities referring to the ionosphere carry the subscript i, while those without a subscript refer to the equatorial region. For simplicity, we

assume the magnetic field B_i to be constant over the effective height of the ionosphere and to be independent of y_i. The height-integrated ionospheric Hall and Pedersen conductivities, Σ_h and Σ_p, respectively, together with the neutral wind velocity are also taken to be independent of y_i. The ionospheric field-aligned current density is then related to the ionospheric potential distribution through the equation

$$j_{\parallel i}(y_i) = \Sigma_p \frac{d^2\phi_i}{dy_i^2} \tag{11}$$

It is also related to the potential drop between the equatorial region and the ionosphere through the formula

$$j_{\parallel i}(y_i) = K[\phi_i(y_i) - \phi(y)] \tag{12}$$

[*Lyons*, 1980; *Chiu and Cornwall*, 1980] where K is a conductance per unit area which we shall also take to be independent of y_i. It is seen that a large K value corresponds to good coupling between the two regions. Note also that a positive value of $j_{\parallel i}$ corresponds to current flowing from the ionosphere into the magnetosphere.

We now assume that there is no current perpendicular to the magnetic field in the intermediate-altitude region. This assumption is expected to be valid because the viscous forces as well as the plasma β values are assumed very small in this region. We can then relate the ionospheric field-aligned current to the field-aligned current at $z = \pm H$ by use of the conservation of magnetic flux and field-aligned current:

$$j_{\parallel i}(y_i) = -\frac{B_i}{B_z(y)} j_z(y, z = \pm H) \tag{13}$$

The mapping of a north-south length element in the ionosphere dy_i to a corresponding length element dy in the equatorial region is obtained by use of the law of conservation of flux in a magnetic flux tube:

$$\frac{dy_i}{dy} = \frac{B_z(y)}{B_i} \frac{dx}{dx_i} \tag{14}$$

where the ratio dx/dx_i is the mapping factor for length elements in the east-west direction, i.e., the x direction. For simplicity, we assume the ratio dx/dx_i to be independent of y. By integration of (14) the relationship between y_i and y can be obtained.

Finally, to convert derivatives in the ionosphere to derivatives in the LLBL region, the following relation will be used [*Lotko et al.*, 1987]:

$$\frac{\partial}{\partial y_i} = \left(\frac{dy}{dy_i}\right) \frac{\partial}{\partial y} \tag{15}$$

3.3. *Equations for v_x and j_y*

We have already shown that in our model, the quantities v_x and B_x, and from equation (5) therefore also j_x, have no z variation but are functions of y only. If we additionally assume the viscosity to be independent of z (which for $\eta = \eta(T)$ means that the boundary layer plasma is isothermal along field lines), it follows from (1) that j_y must be a function of y only. From (6) and (7) it is then seen that B_z and j_z must both be linear in z. For simplicity we further restrict attention to the case of symmetrical conditions in the boundary layer for $z > 0$ and $z < 0$. In this case, B_z and j_z are both zero at the equatorial plane and then increase linearly with z. Furthermore, from (9) and (4) it follows that for fixed y, the pressure p and the density ρ have one and the same quadratic variation with z, such that they decrease from their maximal values at $z = 0$ to the background levels p_∞ and ρ_∞ at $z = \pm H$. It should be noted that under the given assumptions, the z variations described above are exact. In other words, they do not represent simply the leading-order terms of a nontruncating series expansion in powers of z.

For simplicity, we now assume the plasma temperature T to be independent of y as well as of z. In other words, we consider the case of a fully isothermal boundary layer. We shall also assume that at the magnetosphere edge of the LLBL, i.e., as $y \to \infty$, the plasma pressure p and velocity v_x, as well as the magnetic field B_z, all approach constant asymptotic values p_∞, v_∞, and B_∞, respectively, and that B_x, j_y, and j_z all approach zero. Note that we take the pressure to be p_∞ both at $z = \pm H$ and along the entire inner edge of the boundary layer.

As discussed above, we now have

$$B_x = \mu_0 j_y z \tag{16}$$

and

$$j_z = -\left(\frac{dj_y}{dy}\right) z \tag{17}$$

Substitution of (16) into (9), with the constant $c_2(y)$ evaluated at $z = \pm H$, leads to

$$p = p_\infty + \frac{1}{2}\mu_0 j_y^2 (H^2 - z^2) \tag{18}$$

Furthermore, substitution of (16) and (18) into (8) leads to the formula

$$\frac{B_z}{B_\infty} = \sqrt{1 - \left(\frac{\mu_0 j_y H}{B_\infty}\right)^2} \tag{19}$$

By use of (19) and the dimensionless dependent variables v^* and j^*, to be defined presently, the equation of motion for the plasma, equation (1), becomes

$$v^{*\prime\prime} = -j^* \sqrt{1 - (j^*/M)^2} \tag{20}$$

where M is an effective Hartmann number defined by

$$M = \frac{\Sigma_p B_i^{3/2}}{\sqrt{H \eta K B_\infty}} \left(\frac{dx_i}{dx}\right)^2 \tag{21}$$

The significance of this nondimensional parameter will be discussed later. Also, in (20) a prime denotes differentiation with respect to y^*, the nondimensional y coordinate. The dimensionless variables are defined by

$$\begin{aligned} y^* &= y\sqrt{M}/\lambda_e \\ j^* &= j_y M \mu_0 H / B_\infty \\ v^* &= v_x / v_e \end{aligned} \tag{22}$$

where

$$\lambda_e = \lambda_i (dx_i/dx)(B_i/B_\infty) \tag{23}$$

is the equatorial counterpart of the characteristic ionospheric scale length λ_i introduced by *Chiu and Cornwall* [1980] and *Lyons* [1980]:

$$\lambda_i \equiv \sqrt{\Sigma_p/K} \tag{24}$$

The scaling of y and j_y with M in (22) is such that y^* and j^* remain of order unity for $M \gg 1$ (see equations (36) and (28) of *Lotko et al.* [1987]). Finally, the quantity v_e is a characteristic boundary layer velocity given by

$$v_e = \frac{1}{(\mu_0 \Sigma_p)} \left(\frac{dx}{dx_i}\right)^2 \left(\frac{B_\infty}{B_i}\right) \tag{25}$$

It can be shown that for perfect coupling to the ionosphere, this velocity represents the flow speed in the boundary layer at $y = 0$ for which the induced magnetic field at $y = 0$, $z = 0$, which opposes the ambient field B_∞, is equal to 46% of B_∞ (see section 4.1). For imperfect coupling, the flow speed needed to satisfy this condition exceeds v_e. Note that by use of (25), the nondimensional velocity v^* can be viewed as a modified magnetic Reynolds number $R_m = \mu_0 \Sigma_p v_x (dx_i/dx)^2 (B_i/B_\infty)$.

Equation (20) provides a relationship between the current j^* and the velocity v^*. A second relationship between these variables is obtained by differentiating (12) with respect to y, dividing the resulting equation by B_z, and then differentiating once more with respect to y. By use of (10), (11), (13), (14), and (17), one may then eliminate ϕ_i and ϕ in favor of j_y and v_x, the result being

$$\left\{(1-(j^*/M)^2)^{-1/2}\left[j^{*\prime}(1-(j^*/M)^2)^{-1/2}\right]'\right\}' = j^{*\prime}/M + v^{*\prime} \tag{26}$$

By one more differentiation of (26) with respect to y^* and subsequent use of (20), the velocity v^* may be eliminated to yield the following fourth-order nonlinear differential equation for j^*:

$$\left\{(1-(j^*/M)^2)^{-1/2}\left[j^{*\prime}(1-(j^*/M)^2)^{-1/2}\right]'\right\}'' = j^{*\prime\prime}/M - j^*(1-(j^*/M)^2)^{1/2} \tag{27}$$

From this equation, with appropriate boundary conditions, the current distribution $j^*(y^*)$ can be calculated. The velocity distribution $v^*(y^*)$ can then be obtained by integration of (26), which leads to

$$(1-(j^*/M)^2)^{-1/2}\left[j^{*\prime}(1-(j^*/M)^2)^{-1/2}\right]' = j^*/M + v^* - v^*_\infty \tag{28}$$

where $j^*(\infty) = 0$ has been used. The constant of integration v^*_∞ represents the nondimensional flow speed in the magnetosphere with positive values representing sunward flow. A more general version of these equations is given in the appendix.

As pointed out by *Lotko et al.* [1987], the effective Hartmann number M, defined by (21), plays an important role in the theory of viscous magnetospheric boundary layers coupled to a resistive ionosphere. The regular Hartmann number for MHD channel flows [e.g., *Cowling*, 1976] is of the form $Bd(\sigma/\eta)^{1/2}$, where d is the channel width and σ/η is the ratio of electrical conductivity to viscosity. Its square represents the ratio of $\mathbf{j} \times \mathbf{B}$ forces, estimated as $\sigma v B^2$, to viscous forces, estimated as $\eta v/d^2$, in the channel. In the present model, these two forces in fact have exactly the same magnitude. The version of M^2 used here can still be interpreted as the ratio of a $\mathbf{j} \times \mathbf{B}$ force to a viscous force, provided the former force is estimated as $\sigma_\infty v B_\infty^2$ and the latter force as $\eta v/\lambda_e^2$, where $\sigma_\infty \equiv (\Sigma_p/H)(B_i/B_\infty)(dx_i/dx)$ is the effective boundary layer conductivity derived by *Sonnerup* [1980], and λ_e is the characteristic boundary layer width given by (23). Since the actual forces in general deviate systematically from these estimates, the Hartmann number defined by (21) does not have to be equal to unity.

It is noted that, in the limit of weak coupling between the boundary layer and the ionosphere, i.e., for small values of the field-aligned conductance K, the Hartmann number M becomes large. If terms of order M^{-2} are neglected in (20), (27), and (28), these equations reduce to the steady state version of the equations analyzed by *Lotko et al.* [1987], which do not take into account the nonuniform (induced) magnetic fields in the boundary layer. Thus the simplified time-asymptotic boundary layer structures presented by *Lotko et al.* [1987] are valid for weak coupling, i.e., for large values of the Hartmann number. They are also valid in the limit of small flow speed v^*, where induced magnetic fields are again negligible.

3.4. *Boundary Conditions*

To illustrate the basic features of the model, the following boundary conditions will be used:

1. At the magnetospheric edge of the boundary layer, i.e., as $y^* \to \infty$, the current j^* and its derivatives vanish. For simplicity we also assume $v^*_\infty = 0$. It is evident from (27) and (28) that $v^*_\infty \neq 0$ merely represents a shift in the zero level of the velocity. Such a shift leaves the current distribution unchanged.

2. At the magnetopause edge of the boundary layer, i.e., at $y^* = 0$, we assume j^* to be known and $j^{*\prime}$ to vanish. It is shown below that these conditions are equivalent to the specification of the velocity and the field-aligned current at $y = 0$.

As can be seen from (17), $dj_y/dy = 0$ implies that $j_z = 0$ for all z values. Thus the condition $j^{*\prime}(0) = 0$ means that the field-aligned current is put equal to zero at $y = 0$. This condition is based on the idea that field-aligned currents are fed from a high-latitude (mantle) generator [*Siscoe and Sanchez*, 1987] along the morningside magnetopause down to the low-latitude boundary layer, $|z| \leq H$, where they cross the magnetopause and, gradually, are deflected into a field-aligned (region 1) current flowing into the ionosphere. In such a picture, the field-aligned current reverses sign at the magnetopause edge of the boundary layer.

Using the conditions $j^{*'}(0) = 0$ and $v_\infty^* = 0$, (28), evaluated at $y = 0$, becomes

$$v_0^* \equiv -v^*(0) = j^*(0)/M - j^{*''}(0)/(1 - (j^*(0)/M)^2) \quad (29)$$

Thus for a given value of $j^*(0)$, (27) can be integrated and the quantity $j^{*''}(0)$ evaluated. Equation (29) then allows one to calculate v_0^*, the nondimensional plasma velocity at $y = 0$.

4. RESULTS

In this section, results of numerical integration of (27) are presented, subject to the boundary conditions given in section 3.4. The velocity, magnetic field, density, electric potential, and field-aligned current profiles, which are related to the current j^*, will also be shown. The section is divided into two parts. Relationships between dimensionless parameters will be discussed in part one. In part two, illustrative numerical examples will be given.

4.1. *Dimensionless Parameters*

With the boundary conditions described in section 3.4, the overall boundary layer characteristics are described by the following six nondimensional parameters: M, v_0^*, B_{x0}^*, β_0, j_0^*, and h_1^*. Here $v_0^* = v_0/v_e$ and $B_{x0}^* = B_x(0)/B_\infty$ are the nondimensional plasma flow speed and equatorial field strength at the magnetopause edge of the boundary layer, respectively. Furthermore, β_0 is the ratio of plasma pressure to magnetic pressure in the equatorial plane at $y = 0$ and j_0^* is the nondimensional current density j_y at $y = 0$. Note that $2j_0^* B_\infty/\mu_0 M$ represents the total current per unit length along x fed into the boundary layer from the magnetopause within the region $|z| \le H$. Finally, we define the boundary layer thickness h_1 as the y value at which the plasma flow speed reverses from the antisunward to the sunward direction (if such a reversal occurs); the corresponding nondimensional thickness is $h_1^* \equiv h_1\sqrt{M}/\lambda_e$. We emphasize that the entire boundary layer region described by the model extends well beyond $y = h_1$. Other boundary layer thicknesses of potential interest are h_2, which is associated with the reversal of j_y, and h_3, which is associated with the reversal of $j_\parallel$ and therefore with the transition from region 1 to region 2 currents [*Iijima and Potemra*, 1976*a*, *b*]. Reversals of v_x, j_y, and $j_\parallel$ are present for $M > 1/2$ and absent for $M < 1/2$ (as in the analysis of *Lotko et al.* [1987]), and furthermore we have $h_3 > h_2 > h_1$, as shown in Figure 1.

Among the six nondimensional parameters mentioned above, M and v_0^* can be viewed as the fundamental ones from which all the others can be calculated. In Figure 2 we show the relationship $B_{x0}^*(v_0^*, M)$. It is seen that for fixed v_0^*, the magnetic field depression in the equatorial plane at $y = 0$ decreases with increasing M value. In other words, the diamagnetic effect is weaker the weaker the coupling of the LLBL to the ionosphere. This result is not surprising because weaker coupling means weaker currents, and weaker currents mean smaller deviations of the magnetic field from the magnetospheric level, $B_\infty^* = 1$. For a fixed value of B_{x0}^*, $B_{x0}^* = 0.54$ say, the velocity $v_0^* = v_0/v_e$ increases with increasing M. Again this result is expected if one remembers that v_e is the characteristic speed in the boundary layer at which, for perfect coupling ($M = \infty$), the induced magnetic field is 46% of the background field B_∞ so that $B_{x0}^* = 0.54$. When the coupling is weaker, i.e., when M is larger, the flow speed needed to maintain the same size of the induced magnetic field should increase, as indeed it does: for $M = 1$, $v_0^* \approx 2$, and for $M = 15$, $v_0^* \approx 17$ (assuming $B_{x0}^* = 0.54$). When $v_0^* \to \infty$, the curves in Figure 2 approach $B_{x0}^* = 0$ for all $M > 0$. For perfect coupling, $M = 0$, the equations may be integrated in closed form and it may be shown that $B_{x0}^* = \cos v_0^*$. Thus the curve corresponding to $M = 0$ in Figure 2 reaches $B_{x0}^* = 0.54$ at $v_0^* = 1$, and it reaches zero at $v_0^* = \pi/2$.

The plasma β in the equatorial plane at $y = 0$, denoted by β_0, can be calculated directly from B_{x0}^* and β_∞, the magnetospheric β value, from the pressure balance across the field in the equatorial plane (as noted earlier, the assumed symmetry between northern and southern hemispheres implies $B_x(z = 0) = 0$). The result is

$$\beta_0 = (1 + \beta_\infty)/B_{x0}^{*2} - 1 \quad (30)$$

It is perhaps surprising that the plasma pressure and with it the plasma density distribution in the boundary cannot be specified arbitrarily. The explanation for this lies in the condition $p = p_\infty$ at $|z| = H$ where p_∞ is assumed independent of y.

The current $j_0^*(v_0^*, M) = M(1 - B_{x0}^{*2})^{1/2}$ can also be calculated from $B_{x0}^*(v_0^*, M)$. For a given M value, it increases monotonically with increasing v_0^*. The ratio j_0^*/M approaches unity as $v_0^* \to \infty$.

The boundary layer thickness $h_1^*(v_0^*, M)$ is shown in Figure 3. For fixed v_0^*, the thickness decreases with increasing M. Given that M^2 is inversely proportional to the viscosity, this result is expected. For fixed M, the boundary layer thickness increases with increasing flow speed v_0^*, a result that is opposite to the case of ordinary viscous fluid me-

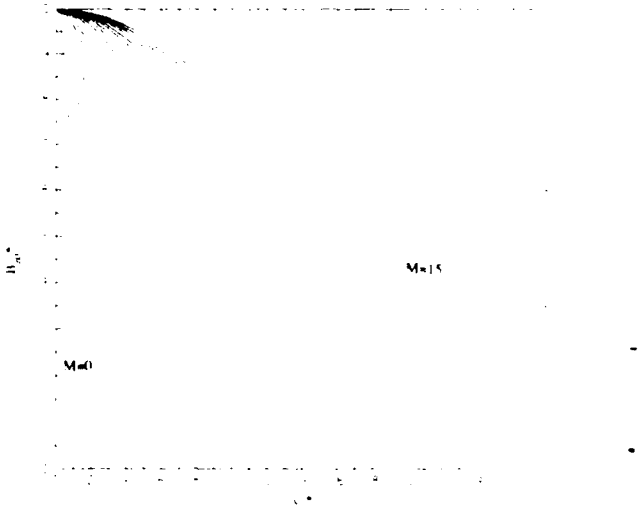

Fig. 2. Nondimensional equatorial magnetic field strength at the magnetopause edge of the boundary layer, $B_{x0}^* = B_x(0)/B_\infty$, as a function of nondimensional plasma flow speed at the magnetopause edge, $v_0^* = v_0/v_e$, and the Hartmann number M. The sixteen curves correspond to $M = 0, 1, 2, \ldots, 15$. The curve corresponding to $M = 0$ reaches zero at $v_0^* = \pi/2$, whereas for $M > 0$, B_{x0}^* approaches zero as $v_0^* \to \infty$.

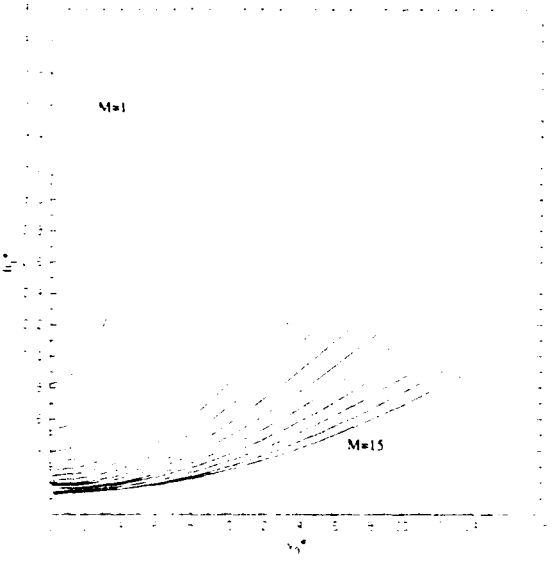

Fig. 3. Nondimensional boundary layer thickness $h_1^* = h_1/\lambda_e$, determined as the y^* value at which flow velocity reverses from the antisunward to the sunward direction, as a function of normalized speed v_0^* and Hartmann number M. The curves correspond to $M = 1, 2, 3, \ldots, 15$. All curves extend to infinity in both v_0^* and h_1^*.

chanical boundary layers. In the limit $v_0^* \to 0$, the thickness is given by

$$h_1^* = \sqrt{\frac{M}{2M+1}}\left\{\pi - 2\arctan\frac{(M-1)}{(M+1)}\sqrt{\frac{2M+1}{2M-1}}\right\} \quad (31)$$

a result that can be obtained directly from the model discussed by *Lotko et al.* [1987]. It is seen that $h_1^* \to \infty$ as $M \to 1/2$. This does not mean that the effective boundary layer width becomes infinitely large but rather that the flow reversal feature used to define h_1^* disappears. For $M \le 1/2$, a better measure of the boundary layer width might be the y^* value at half-maximum flow speed. In the same limit, $v_0^* \to 0$, it may be shown that

$$(h_2^* - h_1^*) = \sqrt{\frac{M}{2M-1}}\left\{\pi - 2\arctan\frac{1}{\sqrt{4M^2-1}}\right\} \quad (32)$$

and that

$$(h_3^* - h_1^*) = \sqrt{\frac{M}{2M-1}}\left\{\pi + 2\arctan\frac{(M-1)}{(M+1)}\sqrt{\frac{2M+1}{2M-1}}\right\} \quad (33)$$

Numerical results obtained for $v_0^* \neq 0$ indicate that $(h_2^* - h_1^*)$ and $(h_3^* - h_1^*)$ are approximately independent of v_0^* and therefore can be obtained from the above formulas, as long as B_{x0}^* remains substantially different from zero. Note that the formulas (31) to (33) as well as Figure 3 refer to the case $v_\infty^* = 0$. For $v_\infty^* \neq 0$, h_2^* and h_3^* remain the same as for $v_\infty^* = 0$. On the other hand, h_1^* decreases for increasingly positive values of v_∞^* (i.e., for increasing sunward convection at the inner edge of the LLBL).

The layer thicknesses in the ionosphere, corresponding to (h_1, h_2, h_3) and obtained by mapping along the magnetic field, are denoted by (h_{1i}, h_{2i}, h_{3i}). Because of the presence of field-aligned potential drops, the location $y_i = h_{1i}$ is not associated with any easily identifiable feature in the ionosphere. At $y_i = h_{2i}$ the ionospheric Pedersen current and, for vanishing neutral wind ($E_{i\infty} = 0$, which corresponds to the case $v_\infty^* = 0$), the associated ionospheric electric field reverse sign. For $y_i < h_{2i}$, the field-aligned current from the morningside LLBL is deflected into a northward flowing ionospheric current while for $y_i > h_{2i}$ it is deflected equatorward and forms as part of a closed current loop, as shown in Figure 1. The magnetic field line connecting the two points $y = h_2$ and $y_i = h_{2i}$ thus serves as a separatrix for the currents. Finally, the location $y_i = h_{3i}$ corresponds to the minimum in the ionospheric electric field which occurs where the field-aligned current reverses sign. The thicknesses $h_{2i}^* \equiv h_{2i}/\lambda_i$ and $h_{3i}^* \equiv h_{3i}/\lambda_i$ are shown in Figure 4 as functions of v_0^* and M. It is seen that for large M values these thicknesses become essentially independent of v_0^*.

4.2. *Illustrative Numerical Examples*

Examples of velocity, density, current, and magnetic field profiles are presented in this section. The parameter values used in these examples are listed in Table 1. Some of these values are chosen on the basis of observations. However, other parameter values, such as kinematic viscosity, field-aligned conductance, and mapping factors, are highly uncertain. For this reason, results shown in this section serve mainly as an illustration of the model. More reliable estimates of the above parameters can in principle be obtained by comparing the model results quantitatively to observations, as discussed in the next subsection.

Figure 5 shows the magnetic field configuration in the LLBL for Hartmann number $M = 0.85$ and with conductance $K = 10^{-8}$ mho/m^2, mapping factor $dx/dx_i = 100$, $\beta_\infty = 0$, and kinematic viscosity $\nu_0 = \eta/\rho_0 = 10^9$ m^2/s at $y = 0$. It is seen that field lines are bent into parabolas with their vertices pointing in the flow direction. Such curvature is compatible with the tailward distortion of field lines observed in the LLBL region [*Eastman et al.*, 1985]. As in the observations, the bending is strongest at the magnetopause edge of the layer and decreases as one approaches the magnetosphere. Other factors being equal, the bending becomes less pronounced the larger the Hartmann number and the smaller the velocity parameter v_0^*. In Figure 5, large values of K and ν_0 were chosen in order to produce significant bending. For conditions that may be representative of the duskside boundary layer ($K = 10^{-9}$ mho/m^2, $\nu_0 = 10^8$ m^2/s, $dx/dx_i = 100$), the field line deformation is found to be small. Thus the simpler analysis of *Lotko et al.* [1987] may be applicable, at least in the noon to dusk LLBL.

It may be added that for $|z| > H$ the field line slope at any chosen y value remains the same as the slope at $|z_i| = H$, shown in the figure for that y value. However, the field magnitude is constant and equal to B_∞ for $|z| > H$; the shear in the field is caused entirely by field-aligned currents.

Velocity and current profiles in the LLBL for different values of M are given in Figures 6 to 8. The four velocity distributions shown in Figure 6 illustrate the presence of a region of sunward flowing plasma on the magnetospheric side of the main boundary layer, i.e., for $y > h_1$. Such a region is present for $M > 1/2$. The magnitude of the sunward flow speed increases with increasing Hartmann number, as men-

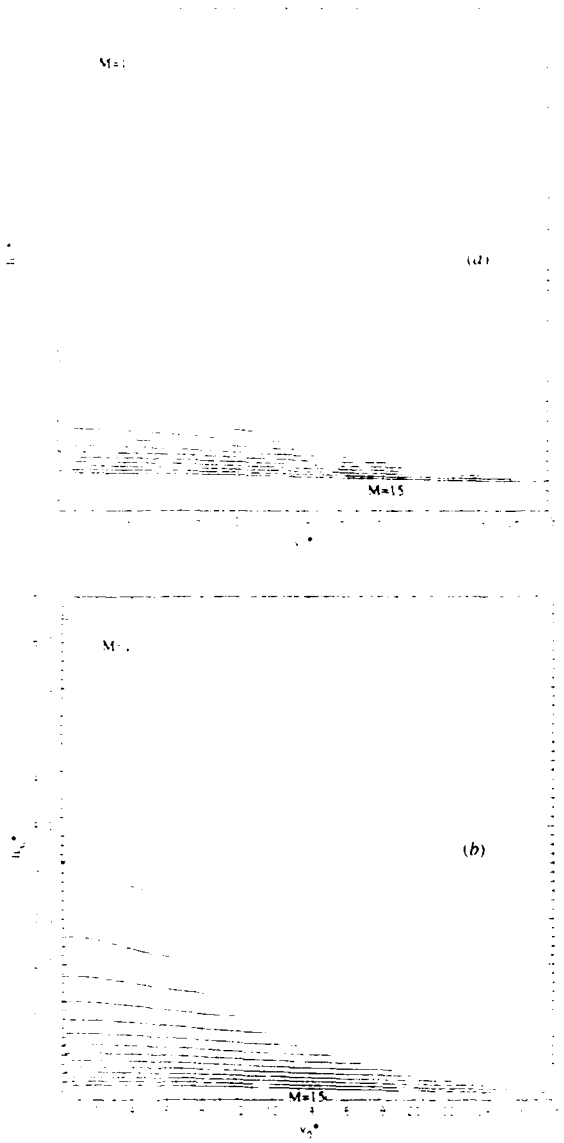

Fig. 4. (*a*) Nondimensional ionospheric boundary layer thickness $h_{2_1}^* = h_{2_1}/\lambda_1$, where the ionospheric Pedersen current and the associated ionospheric electric field reverse sign, as a function of normalized speed v_0^* and Hartmann number M. The curves correspond to $M = 1, 2, 3, \ldots, 15$. It is noted that for large values of M this thickness is essentially independent of v_0^*. (*b*) Same diagram as in Figure 4*a* but for thickness $h_{3_1}^* = h_{3_1}/\lambda_1$, where the field-aligned current reverses sign.

tioned earlier. It should be added that by allowing $v_{x\infty} \neq 0$ the maximum speed of this reverse flow may be adjusted to any desired level. The second feature apparent in Figure 6 is the thickening of the boundary layer as the kinematic viscosity increases. However, to produce h_1 values of the order of 1 R_E, a kinematic viscosity in excess of 10^{10} m^2/s would be needed, other parameters remaining unchanged.

The electric current density components j_x and j_y in the boundary layer are shown in Figure 7 for the same parameter values as those used in Figure 6. The dependence of the boundary layer thickness on the viscosity is again apparent, and it is seen that the currents increase in magnitude with increasing K value, i.e., with increasing coupling to the ionosphere. The current component j_y, but not j_x, displays a sign reversal at $y = h_2$ which is located substantially earthward of the reversal in flow speed, i.e., $h_2 > h_1$ (see Figure 6). The z component of the current density in the boundary layer reverses sign at $y = h_3$, where $h_3 > h_2$. The distribution of this current for various z values is shown in Figure 8 for one set of parameter values.

In Figure 9*a* the equatorial diamagnetic field depression in the boundary layer is shown as a function of y. As expected, the depression is larger the smaller the M value, i.e., the stronger the coupling to the ionosphere. The number density of the boundary layer plasma in the equatorial plane is shown in Figure 9*b* as a function of y for the case where the magnetospheric plasma pressure and density are assumed to be zero, i.e., $\beta_\infty = 0$. By use of the pressure balance across the layer, the plasma temperature in the LLBL can be calculated for each of the three examples in Figure 9. These temperatures are $T = 1.5 \times 10^5$ °K for the $M = 0.85$ case, $T = 4.2 \times 10^4$ °K for the two $M = 2.7$ cases, and $T = 6.2 \times 10^3$ °K for $M = 8.5$. The fact that these temperatures are very small is an indication that in reality the magnetospheric density $n_\infty \neq 0$ so that $\beta_\infty \neq 0$. For $\beta_\infty = 1$, the values are $T = 2.44 \times 10^6$ °K for $M = 0.85$, $T = 2.34 \times 10^6$ °K for $M = 2.7$, and $T = 2.30 \times 10^6$ °K for $M = 8.5$.

Field-aligned current density profiles and electric field profiles in the ionosphere are shown in Figure 10. As is seen from (11), these two diagrams are related: the field-aligned current is given by $j_{\parallel_i} = -\Sigma_p dE_x/dy$. When compared to observations [*Iijima and Potemra*, 1976*a*], the field-aligned currents are much too large for $K = 10^{-8}$ mho/m^2 but are of about the right size for $K = 10^{-9}$ mho/m^2. The field-aligned potential drops $\Delta\phi_{\parallel_i}$, obtainable as $j_{\parallel_i}/K$, have maxima of about 600 V for $K = 10^{-8}$ mho/m^2 and of 1.5-2 kV for $K = 10^{-9}$ mho/m^2. The latter values are in the range of the electron energies observed in typical inverted V events [e.g., *Lin and Hoffman*, 1982], but the potential drop has the

TABLE 1. Data for Illustrative Numerical Examples

Parameter	Value
Boundary layer density ($y = 0, z = 0$)	$n_0 = 5$ protons/cm^3
Height-integrated Pedersen conductivity	$\Sigma_p = 6$ mho
Field line conductance per unit area	$K = 10^{-7}$-10^{-9} mho/m^2
Kinematic viscosity at $y = 0$	$\eta/\rho_0 = \nu_0 = 10^8$-$10^9$ m^2/s
Ionospheric latitude	$\Lambda = 73°$
Equatorial distance	$L = 15\ R_E$
Equatorial height	$H = 10\ R_E$
Mapping factor*	$dx/dx_1 = 100$
Characteristic boundary layer speed	$v_e = 442$ km/s
Maximum boundary layer speed ($y = 0$)	$v_0 = 200$ km/s
Ionospheric magnetic field	$B_1 = 6 \times 10^{-5}$ t
Magnetospheric magnetic field ($y \to \infty$)	$B_\infty = 2 \times 10^{-8}$ t

*Orange segment map to interval $dx/dx_1 = 51.3$, which should be considered a lower limit

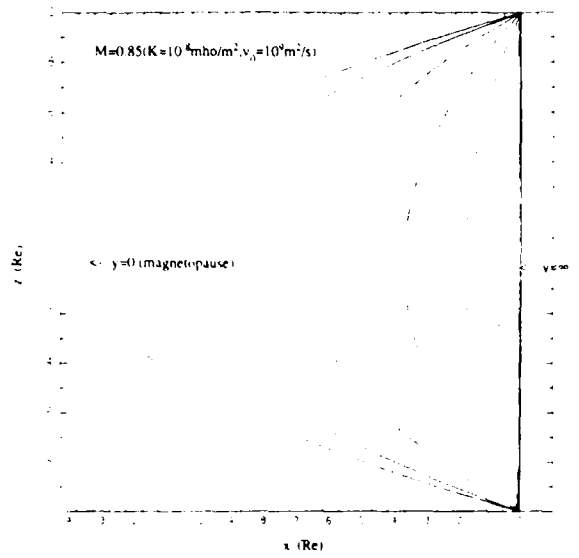

Fig. 5. Magnetic field configuration in the LLBL for $M = 0.85$ ($K = 10^{-8}$ mho/m^2; $\eta/\rho_0 = \nu_0 = 10^9$ m^2/s; $dx/dx_i = 100$; $\beta_\infty = 0$). The curves correspond to a range of y values from $y = 0$ (magnetopause edge) to $y \to \infty$ (magnetosphere edge). The bending of the magnetic field lines is strongest at $y = 0$ and decreases as $y \to \infty$.

correct sense only on the duskside where the field-aligned current flows out of the ionosphere. Thus curves 2 and 4 in Figures 6, 7, 9, and 10, for which $K = 10^{-9}$ mho/m^2, may b representative of conditions in the duskside boundary layer. (Note that these figures have been drawn for the dawnside; to adapt them to the duskside, one should replace y by $-y$ and $j_{\parallel i}$ by $-j_{\parallel i}$.) Such a small value of the field-aligned conductance is compatible with the observational study of auroral arcs by *Lyons et al.* [1979] and also with the analysis of *Fridman and Lemaire* [1980]. The situation on the dawnside where the region 1 currents flow into the ionosphere is more uncertain and will be dealt with in a separate paper. Here, we merely note that the field-aligned conductance may be far larger and the Hartmann number far smaller on the dawnside than on the duskside.

4.3. *Thought Experiment*

Finally, we illustrate how, in principle, one may determine some of the basic unknown parameters in the model from measurements in space during specific events. These unknown parameters are: the height-integrated ionospheric Pedersen conductivity Σ_p, the mapping factor dx_i/dx, the field-aligned conductance K, the viscosity η, and the boundary layer height H.

First, we note that the height-integrated conductivity Σ_p can be obtained directly from ionospheric measurements, from a polar orbiting satellite, of magnetic field deflections ΔB_{ix} caused by the field-aligned currents and of the electric field E_{iy}. For example, one may use the relation

$$\Delta B_{ix} = \text{const} + 1.256\Sigma_p E_{iy} \tag{34}$$

derived by *Smiddy et al.* [1980]. Note that this formula depends on a number of assumptions, including the neglect of neutral winds. The resulting value of Σ_p may vary a great deal depending on factors such as season and level of magnetospheric activity; the value in Table 1 may be considered representative.

We now assume that the magnetic field ratio $B^*_{z0} = B_{z0}/B_\infty$ is measured simultaneously by a spacecraft traversing the LLBL. We can then calculate $j^*_0/M = (1 - B^{*2}_{z0})^{1/2}$, and from current continuity, $I_\parallel = (j^*_0/M)(B_\infty/\mu_0)$. The latter quantity represents the total field-aligned current per unit length along x fed from the magnetopause into the boundary layer between $z = 0$ and $z = H$. However, the corresponding total current per unit length, $I_{\parallel i}$, in the ionosphere can also be measured by means of the total magnetic field deflection between $y = 0$ and $y = h_{3i}$: $I_{\parallel i} = \Delta B_{ix3}/\mu_0$. The mapping factor dx_i/dx can then be calculated as $dx_i/dx = I_\parallel/I_{\parallel i}$.

It is now possible to calculate the characteristic boundary layer velocity v_e from (25), and, if the flow speed v_0 in the boundary layer adjacent to the magnetopause is measured by the spacecraft traversing the LLBL, the ratio $v^*_0 = v_0/v_e$ may be formed. Since B^*_{z0} is also measured, the value of the Hartmann number M can now be obtained from Figure 2. Furthermore, v^*_0 and M may then be used in Figure 4 to obtain $h^*_{3i} = h_{3i}/\lambda_i$. Assuming that the width of the region 1 current system, i.e., the ionospheric boundary layer thickness h_{3i}, can be determined from the ionospheric magnetic field measurements as the y_i value where the magnetic deflection is a maximum, we may then obtain λ_i and, from (24), the field-aligned conductance K. The thickness h_{3i} rather than h_{2i} is used because, in the model, the former is independent of the electric field $E_{i\infty}$ (which is zero in the simple calculations performed here as a result of putting $v^*_\infty = 0$), whereas the latter depends on $E_{i\infty}$. A more direct method may be used on the duskside where the LLBL must generate a broad inverted V electron precipitation structure. The electron energies and field-aligned current densi-

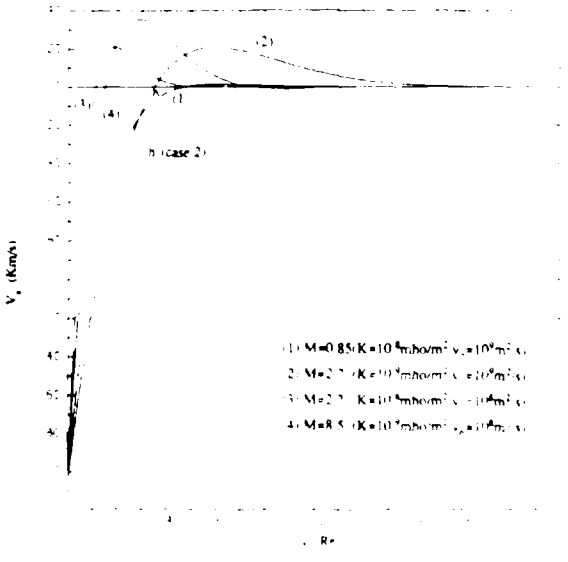

Fig. 6. Boundary layer velocity profiles for four different combinations of K and ν_0 with $dx/dx_i = 100$. Note the increase in magnitude of the sunward flow for larger Hartmann number M. The boundary layer thickness h_1 is shown for case 2.

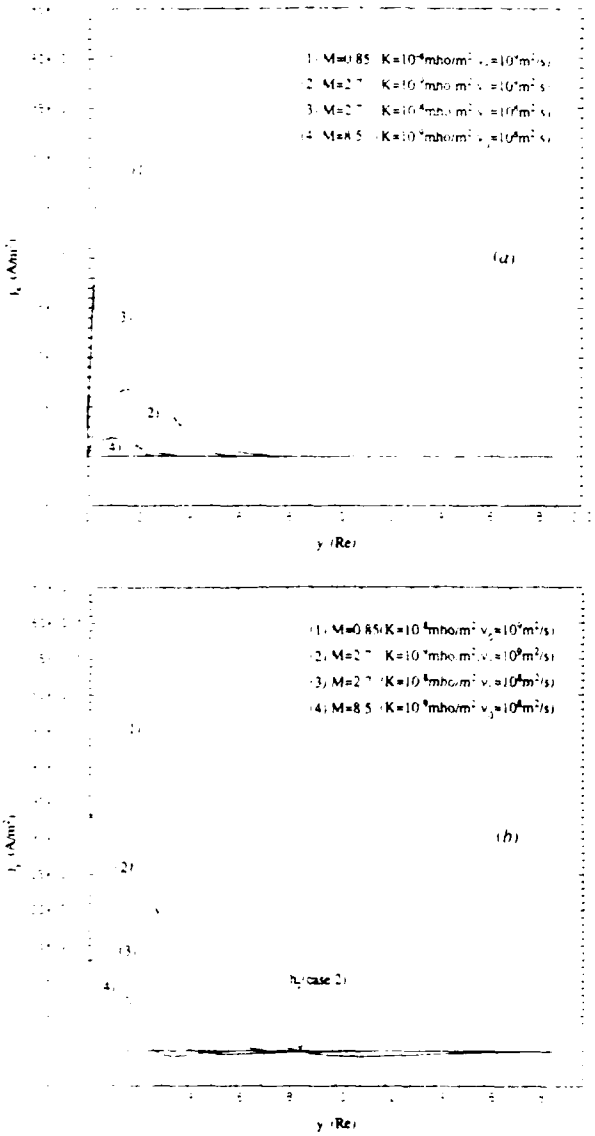

Fig. 7. Electric current density profiles in the boundary layer for (*a*) $j_x(y)$ and (*b*) $j_y(y)$ for the same cases as in Figure 6. Note that the currents increase in magnitude with increasing coupling to the ionosphere, i.e., with increasing K value. Also note the increase of the boundary layer thickness with increasing viscosity. The boundary layer thickness h_2 is shown for case 2.

ties measured in this structure will yield the conductance K directly [*Lyons et al.*, 1979].

Finally, we may insert the calculated values of M, Σ_p, K, and dx_1/dx into the definition of M, equation (21), and thus calculate the product ηH of viscosity and boundary layer height. Furthermore, a separate determination of H is possible if the elevation z_s of the equatorial spacecraft above the actual symmetry plane of the model is known. From a measured value of B_{x0}, the magnetic field x component at the magnetopause, we may then obtain H from the formula

$$B_{x0} = B_\infty j_0^* z_s / 4M \tag{35}$$

In practice, the procedure described above may be difficult to implement because of the paucity of simultaneous measurements in the ionosphere and in the corresponding portion of the low-latitude boundary layer. Furthermore, our model assumes symmetric conditions in the northern and southern hemispheres, whereas in reality rather large asymmetries may be expected as a result of the dipole tilt and the associated difference in ionospheric conductivities in the two hemispheres. Thus the model needs to be generalized to incorporate such asymmetries. Other important uncertainties in the model result from our assumption that quantities such as dx_1/dx, K, Σ_p, and the plasma pressure at $|z| = H$ are independent of y.

Finally, it is emphasized that the set of comparisons with observations described above is sufficient to determine the model parameters but, except for the possibility of determining K from duskside inverted V structures, contains no redundancy. Therefore it does not provide a test of the internal consistency of the model.

5. Discussion

In this paper, a viscous steady state slab model of the low-latitude boundary layer (LLBL) has been presented in which the magnetic field in the layer is determined from Ampère's law in a self-consistent manner. It is in this latter respect that the model provides an improvement over the analyses by *Sonnerup* [1980] and *Lotko et al.* [1987] in which a uniform field was used.

It is found that the field lines in the LLBL in general take on a parabolic shape with the vertices pointing in the downstream direction. This behavior is compatible with the tailward distortion of field lines observed by *Eastman et al.* [1985]. The field line curvature is greatest at the magnetopause edge of the layer; it vanishes at the magnetospheric edge. Associated with this field deformation is a diamagnetic field depression near the equatorial plane, this effect again being strongest at the magnetopause edge of the layer and gradually disappearing as the magnetospheric edge is

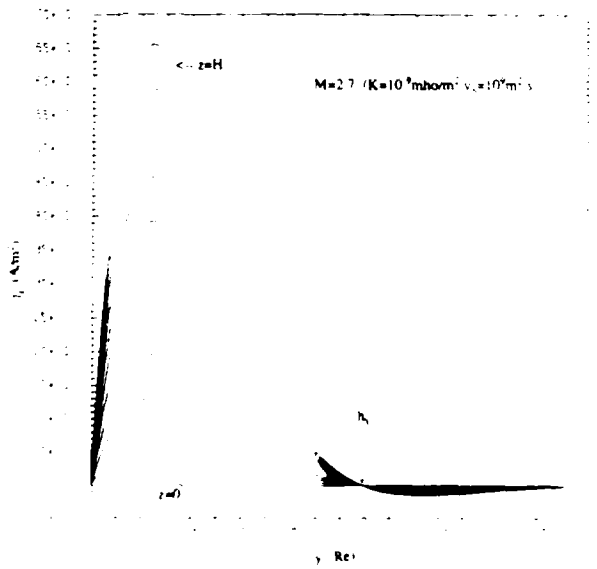

Fig. 8. Distribution of the z component of the current density in the LLBL for $M = 2.7$ (case 2 in Figure 6). The eleven curves correspond to $z = 0,\ 0.1H,\ 0.2H,\ \ldots,\ H$. The boundary layer thickness h_2 is shown.

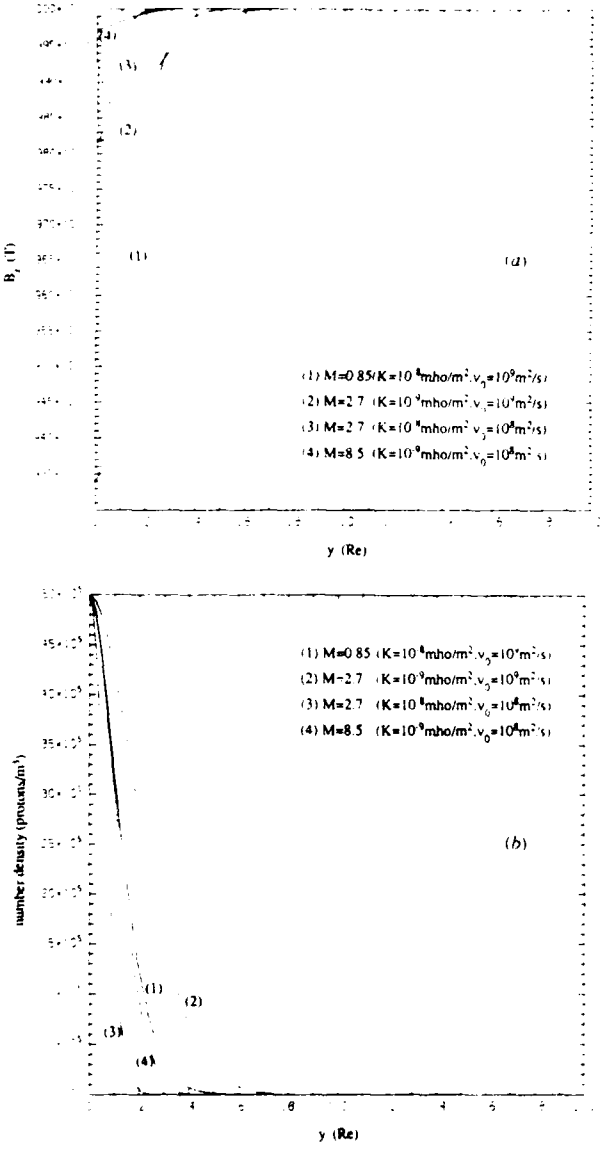

Fig. 9. (*a*) Equatorial diamagnetic field depression in the boundary layer and (*b*) number density in the equatorial plane versus y for $\beta_\infty = 0$. The curves again correspond to the cases in Figure 6. The depression is larger for stronger coupling to the ionosphere, i.e., for smaller M values.

approached. The defect in magnetic pressure is exactly balanced by the excess plasma pressure in the boundary layer.

We have shown that the field deformation is controlled by two dimensionless parameters, namely M, the Hartmann number defined by (21), and $v_0^* = v_0/v_e$, the ratio of flow speed at the magnetopause to the characteristic flow speed v_e, defined by (25). The Hartmann number serves as a measure of the coupling of the boundary layer to the ionosphere, with large M values corresponding to weak coupling. The quantity v_0^* is an effective magnetic Reynolds number, based on the ionospheric resistivity and appropriate mapping factors: for any fixed M value, the field deformation increases with increasing values of v_0^*, as shown in Figure 2.

The properties of the model are presented in a set of nondimensional diagrams (Figures 2–4) as well as in illustrative numerical examples (Figures 5–10). The model contains a number of poorly known parameters such as the boundary layer viscosity, the field-aligned conductance, and the magnetic mapping factors from the LLBL to the ionosphere. We have discussed how these parameters could in principle be determined by comparing the model to observations, but, for lack of suitable data, such a determination has not been possible. Nevertheless, for reasonable values of these parameters, the numerical examples make it plausible that like the earlier analyses by *Sonnerup* [1980] and *Lotko et al.* [1987], the model is capable of describing several features of the

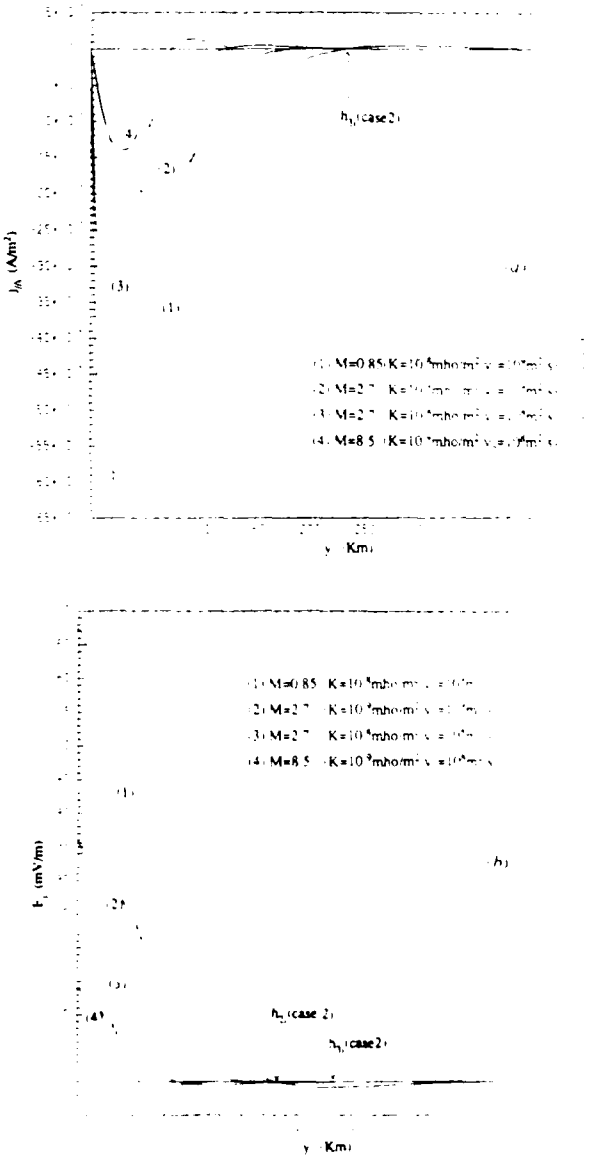

Fig. 10. (*a*) Ionospheric field-aligned current density profile and (*b*) ionospheric electric field profile for the same three cases as in Figure 6. The boundary layer thicknesses h_2, and h_1, are shown for case 2. Field-aligned potential drops may be obtained as $\Delta\Phi_\parallel = j_{\parallel_i}/K$. The total field-aligned current, obtained by integrating $j_{\parallel_i}$ from 0 to ∞, is −0.41 A/m for case 1, −0.21 A/m for cases 2 and 3, and −0.08 A/m for case 4.

morning and afternoon region 1 currents and their associated ionospheric signatures. In particular, it appears that the field line deformation in the duskside boundary layer may be relatively small, allowing the simpler straight field line model of *Lotko et al.* [1987] to be used there.

One possible discrepancy between the model and the observations is the predicted thickness of the boundary layer which, for reasonable parameter values, tends to be less than some of the observed thicknesses. The explanation for this is not clear, but it may be an indication that part of the LLBL is on open field lines at times. Any such part would be expected to display a more or less uniform plasma velocity, i.e., a velocity that is independent of the y coordinate. Such plateau effects are occasionally seen in the LLBL plasma velocity data (for example, Figure 8 of *Eastman et al.* [1985]). In such circumstances, the present model should be applied at the inner edge of the layer where the flow speed drops to its magnetospheric value in a relatively thin layer, presumably located on closed field lines. It is in this layer that the field-aligned currents would be concentrated, and therefore, even for small values of the viscosity, this portion of the LLBL is of primary importance for the magnetosphere-ionosphere coupling. However, a plateau in the boundary layer velocity profile perhaps also can be explained in a variety of other ways, including a y-dependent eddy viscosity in the boundary layer.

APPENDIX

The model equations (20) and (26) may be generalized in a straightforward manner to allow for variations of the ionospheric Pedersen conductivity Σ_p, the field-aligned conductance K, and the mapping factor dx/dx_i, with the coordinate y_i, and of the boundary layer viscosity η and the height H, with the coordinate y. As before, the relationship between y and y_i is indirect and is obtained by integration of (14). The resulting equations are

$$(\eta^* v^{*\prime})' = -j^* B^* \tag{A1}$$

$$\left[\frac{\Sigma_p^*}{B^* R^*}\left(\frac{j^{*\prime} H^*}{B^* K^*}\right)'\right]' = \frac{R^* H^*}{M_\infty} j^{*\prime} + \left(\frac{\Sigma_p^*}{R^*} v^*\right)' \tag{A2}$$

where

$$M_\infty \equiv \frac{\Sigma_{p\infty}(B_i)^{3/2}}{\sqrt{H_\infty \eta_\infty K_\infty B_\infty}}\left(\frac{dx_i}{dx}\right)_\infty^2$$

The subscript ∞ refers to values at the magnetospheric edge of the layer. In these expressions, a prime denotes differentiation with respect to the coordinate

$$y^* = y\sqrt{M}/\lambda_{e\infty}$$

in which

$$\lambda_{e\infty} = \sqrt{\Sigma_{p\infty}/K_\infty}(dx_i/dx)_\infty B_i/B_\infty$$

The nondimensional quantities carrying the * superscript in (A1) and (A2) all depend directly or indirectly on y^*. They are defined by

$$j^*(y^*) = M_\infty j_y(y)\mu_0 H_\infty / B_\infty$$

$$v^*(y^*) = v_x(y)/v_{e\infty}$$

$$B^*(y^*) = \{1 - [j^*(y^*)H^*/M_\infty]^2\}^{1/2}$$

$$R^*(y^*) = (dx/dx_i(y_i))/(dx/dx_i)_\infty$$

$$\Sigma_p^*(y^*) = \Sigma_p(y_i)/\Sigma_{p\infty}$$

$$K^*(y^*) = K(y_i)/K_\infty$$

$$\eta^*(y^*) = \eta(y)/\eta_\infty$$

$$H^*(y^*) = H(y)/H_\infty$$

The characteristic boundary layer velocity $v_{e\infty}$ is given by

$$v_{e\infty} = \frac{1}{\mu_0 \Sigma_{p\infty}}\left(\frac{dx}{dx_i}\right)_\infty \left(\frac{B_\infty}{B_i}\right)$$

Acknowledgments. The research was supported by the Air Force Geophysics Laboratory under contract F19628-87-K-0026, by the National Science Foundation, Atmospheric Sciences Division, under grant ATM-8507192, and by the National Aeronautics and Space Administration under grant NAGW-1169 to Dartmouth College.

The Editor thanks D. W. Swift and V. M. Vasyliunas for their assistance in evaluating this paper.

REFERENCES

Bythrow, P. F., R. A. Heelis, W. B. Hanson, R. A. Power, and R. A. Hoffman, Observational evidence for a boundary layer source of dayside region 1 field-aligned currents, *J. Geophys. Res.*, *86*, 5577, 1981.

Chiu, Y. T., and J. M. Cornwall, Electrostatic model of a quiet auroral arc, *J. Geophys. Res.*, *85*, 543, 1980.

Coleman, P. J., Jr., A model of the geomagnetic cavity, *Radio Sci.*, *6*, 321, 1971.

Cowling, T. G., *Magnetohydrodynamics*, p. 15, A. Hilger, Bristol, England, 1976.

Eastman, T. E., and E. W. Hones, Jr., Characteristics of the magnetospheric boundary layer and magnetopause layer as observed by IMP 6, *J. Geophys. Res.*, *84*, 2019, 1979.

Eastman, T. E., E. W. Hones, Jr., S. J. Bame, and J. R. Asbridge, The magnetopheric boundary layer: Site of plasma, momentum and energy transfer from the magnetosheath into the magnetosphere, *Geophys. Res. Lett.*, *3*, 685, 1976.

Eastman, T. E., B. Popielawska, and L. A. Frank, Three-dimensional plasma observations near the outer magnetospheric boundary, *J. Geophys. Res.*, *90*, 9519, 1985.

Fridman, M., and J. Lemaire, Relationship between auroral electron fluxes and field-aligned electric potential differences, *J. Geophys. Res.*, *85*, 664, 1980.

Haerendel, G., G. Paschmann, N. Sckopke, and H. Rosenbauer, Frontside boundary layer of the magnetosphere and the problem of reconnection, *J. Geophys. Res.*, *83*, 3195, 1978.

Hones, E. W., Jr., J. R. Asbridge, S. J. Bame, M. D. Montgomery, S. Singer, and S.-I. Akasofu, Measurements of magnetotail plasma flow made with VELA 4B, *J. Geophys. Res.*, *77*, 5503, 1972.

Iijima, T., and T. A. Potemra, The amplitude distribution of field-aligned currents at northern high latitudes observed by TRIAD, *J. Geophys. Res.*, *81*, 2165, 1976*a*.

Iijima, T., and T. A. Potemra, Field-aligned currents in the dayside cusp observed by TRIAD, *J. Geophys. Res.*, *81*, 5971, 1976*b*.

Kan, J. R., and L. C. Lee, Theory of imperfect magnetosphere-ionosphere coupling, *Geophys. Res. Lett.*, *7*, 633, 1980.

Lin, C. S., and R. A. Hoffman, Observations of inverted-V electron precipitation, *Space Sci. Rev.*, *33*, 415, 1982.

Lotko, W., and C. G. Schultz, Internal shear layers in auroral dynamics, in *Modeling Magnetospheric Plasma*, Geophys. Monogr. Ser., vol. 44, edited by T. E. Moore and J. H. Waite, p. 121, AGU, Washington, D.C., 1988.

Lotko, W., B. U. Ö. Sonnerup, and R. L. Lysak, Nonsteady boundary layer flow including ionospheric drag and parallel electric fields, *J. Geophys. Res.*, *92*, 8635, 1987.

Lundin, R., K. Stasiewicz, and B. Hultqvist, On the interpretation of different flow vectors of different ion species in the magnetospheric boundary layer, *J. Geophys. Res.*, *92*, 3214, 1987.

Lyons, L. R., Generation of large-scale regions of auroral currents, electric potential, and precipitation by the divergence of the convection electric field, *J. Geophys. Res.*, *85*, 17, 1980.

Lyons, L. R., D. S. Evans, and R. Lundin, An observed relation between magnetic field aligned electric fields and downward electron energy fluxes in the vicinity of auroral forms, *J. Geophys. Res.*, *84*, 457, 1979.

Mitchell, D. G., F. Kutchko, D. J. Williams, T. E. Eastman, L. A. Frank, and C. T. Russell, An extended study of the low-latitude boundary layer on the dawn and dusk flanks of the magnetosphere, *J. Geophys. Res.*, *92*, 7394, 1987.

Miura, A., Simulation of Kelvin-Helmholtz instability at the magnetospheric boundary, *J. Geophys. Res.*, *92*, 3195, 1987.

Peterson, W. K., E. G. Shelley, G. Haerendel, and G. Paschmann, Energetic ion composition in the subsolar magnetopause and boundary layer, *J. Geophys. Res.*, *87*, 2139, 1982.

Sato, T., Auroral physics, in *Magnetospheric Plasma Physics*, edited by A. Nishida, p. 197, D. Reidel, Hingham, Mass., 1982.

Sckopke, N., G. Paschmann, G. Haerendel, B. U. Ö. Sonnerup, S. J. Bame, T. G. Forbes, E. W. Hones, Jr., and C. T. Russell, Structure of the low-latitude boundary layer, *J. Geophys. Res.*, *86*, 2099, 1981.

Siscoe, G. L., and E. Sanchez, An MHD model for the complete open magnetotail boundary, *J. Geophys. Res.*, *92*, 7405, 1987.

Smiddy, M., W. J. Burke, M. C. Kelley, N. A. Saflekos, M. S. Gussenhoven, D. A. Hardy, and F. J. Rich, Effects of high-latitude conductivity on observed convection electric field and Birkeland currents, *J. Geophys. Res.*, *85*, 6811, 1980.

Sonnerup, B. U. Ö., Theory of the low-latitude boundary layer, *J. Geophys. Res.*, *85*, 2017, 1980.

W. Lotko, T. D. Phan, and B. U. Ö. Sonnerup, Thayer School of Engineering, Dartmouth College, Hanover, NH 03755.

(Received December 10, 1987;
revised August 18, 1988;
accepted September 8, 1988.)

Appendix 4

MHD Stagnation-Point Flows at a Current Sheet Including Viscous and Resistive Effects: General Two-Dimensional Solutions

T. D. PHAN and B. U. Ö. SONNERUP

Thayer School of Engineering, Dartmouth College, Hanover, New Hampshire 03755, USA

Exact solutions are presented of two-dimensional steady-state incompressible stagnation point flows at a current sheet separating two colliding plasmas. They describe the process of resistive field annihilation (zero reconnection) where the magnetic field in each plasma is strictly parallel to the current sheet, but may have different magnitudes and direction on its two sides. The flow in the x-y plane toward the current sheet, located at x=0, may have an arbitrary angle of incidence and an arbitrary amount of divergence from or convergence toward the stagnation point.We find the most general form of the solution for the plasma velocity and for the magnetic field. For the z components of the flow and field, solutions in the form of truncating power series in y are found. The cases obtained in this study contain the solutions obtained by Parker [1973], Sonnerup and Priest [1975], Gratton et al.[1988], and Besser et al.[1990] as special cases. The role of viscosity in determining the flow and field configurations is examined. When the two colliding plasmas have the same viscosity and density, it is shown that viscous effects usually are important only in strongly divergent or convergent viscous flows with viscous Reynolds number of the order of unity or smaller. For astrophysical applications, the viscous Reynolds number is usually high and the effects of viscosity on the interaction of plasmas of similar properties are small. The formulation of the stagnation point flow problem involving plasmas of different properties is also presented. Sample cases of such flow are shown. Finally, possible application of the results from this study to the Earth's magnetopause is discussed briefly.

1. INTRODUCTION

The problem of steady magnetic field annihilation in a plane current sheet has been investigated by several authors, starting with Parker's [1973] study of a simple case in which the magnetic field is of the form $\mathbf{B}=\hat{y}B_y(x)$ and the plasma velocity is of the form $v= - k x \hat{x} + k y \hat{y}$, k being a constant, and in which the magnetic field vanishes at the center of the current sheet, at x=0, and is antisymmetric, i. e., $B_y(x)=-B_y(-x)$. In his work, Parker postulated the stagnation point flow pattern, $v= - k x \hat{x} + k y \hat{y}$, but did not consider the momentum equation for the plasma. Sonnerup and Priest [1975] then showed that, with a proper choice of the pressure distribution, Parker's solution in fact satisfies the incompressible MHD equations exactly. They went on to develop exact solutions for three-dimensional (3D) MHD stagnation point flows in which the magnetic field lines are still straight and parallel to the current sheet, but can have different directions. In Sonnerup and Priest's symmetric solutions, the flow is irrotational, and consequently, assuming constant viscosity, the net viscous force per unit volume vanishes identically. They also formulated the general 3D viscous MHD stagnation point flow problem in which the two opposing plasmas may have different properties, such as density , viscosity, resistivity, and inflow speed. However, no solutions were presented. Recently, Gratton et al. [1988, 1990] presented a new exact analytic solution (as well as certain numerical solutions) of the 2D incompressible viscous and resistive MHD equations in connection with stagnation point flows. However, Sonnerup and Phan [1990] argued that the Gratton et al. solutions, while mathematically correct and intrinsically interesting, do not represent flow behavior acceptable for the symmetric (under the transformation $x \Rightarrow -x$) magnetic field annihilation problem. Even more recently, Besser et al. [1990] presented a generalization of the Sonnerup and Priest 2D solution. Their generalization consists of adding a term to the plasma stream function which allows the construction of flow patterns with an arbitrary angle of flow incidence.

The present paper describes what we believe to be the most general family of exact solutions to the problem of 2D steady-state incompressible MHD stagnation point flow with field annihilation at a plane current sheet. Resistive and viscous effects are included. These solutions describe both symmetric and asymmetric flows toward the current sheet at arbitrary angles of incidence and with an arbitrary amount of divergence or convergence in the incident flow. The magnetic field lines are confined to a plane parallel to the current sheet, but are no longer required to be straight. Because of the former property, the solutions therefore still represent magnetic annihilation with no reconnection. It is this restriction on the magnetic field that allows one to obtain simple exact solutions to the MHD stagnation point flow problem. The 2D solutions presented here are far more general than those obtained previously: they include the configurations discussed by Parker [1973], Sonnerup and Priest [1975], Gratton et al.[1988, 1990], and Besser et al. [1990] as special cases. The 3D case will be dealt with in a separate paper.

In section 2, the formulation of the MHD stagnation point flow problem is presented. We first find the most general functional form of the velocity and the magnetic field under the restriction that the magnetic field have no component perpendicular to the current sheet. We then show the system of equations, and the procedure for solving these equations for the stagnation point flow problem. Section 3 contains analytic solutions for the flow and fields in the limits $Re \Rightarrow 0$ and $Re \Rightarrow \infty$, Re being the viscous Reynolds number. Some analytic and numerical solutions for the more general case of finite Re are also presented. In section 4, we consider the case where the two colliding plasmas have different density, viscosity, and conductivity. In section 5, we assess the influence of viscosity on the flow and field distributions. Possible application of results obtained from this study to the Earth's magnetopause is also discussed.

2. BASIC EQUATIONS AND ASSUMPTIONS

The MHD equations governing the motion of an incompressible plasma are

$$\nabla \cdot \mathbf{v} = 0 \tag{1}$$

$$\rho \frac{\partial \mathbf{v}}{\partial t} + \rho(\mathbf{v} \cdot \nabla \mathbf{v}) = -\nabla p + \mathbf{j} \times \mathbf{B} + \eta \nabla^2 \mathbf{v} \tag{2}$$

$$\nabla \cdot \mathbf{B} = 0 \tag{3}$$

$$\nabla \times \mathbf{B} = \mu_0 \mathbf{j} \tag{4}$$

$$\mathbf{j} = \sigma (\mathbf{E} + \mathbf{v} \times \mathbf{B}) \tag{5}$$

$$\nabla \times \mathbf{E} = -\frac{\partial \mathbf{B}}{\partial t} \tag{6}$$

where $\mathbf{B}$, $\mathbf{j}$, $\mathbf{E}$, $\mathbf{v}$, ρ and p are the magnetic field, electrical current density, electric field, and the plasma velocity, density and pressure, respectively. Also, η is the dynamic viscosity and σ is the electrical conductivity, both of which are assumed, along with ρ, to be uniform in the each of the flow regions $x<0$ and $x>0$, for simplicity.

Equations (3), (4), (5) and (6) can be combined to form the induction equation

$$-\frac{\partial \mathbf{B}}{\partial t} + \nabla \times (\mathbf{v} \times \mathbf{B}) + \frac{\nabla^2 \mathbf{B}}{\mu_0 \sigma} = 0 \tag{7}$$

We now assume the flow and fields to be independent of the coordinate z, i.e., $\partial/\partial z \equiv 0$. (The electric potential and the plasma pressure are allowed to vary linearly with z). The magnetic field is assumed to be confined to the yz plane, i.e., $B_x = 0$. To satisfy $\nabla \cdot \mathbf{B} = 0$, the field component B_y can depend only on x, whereas B_z can depend on x as well as y. In addition, the field components can depend on time, t. Thus the total magnetic field may be written as

$$\mathbf{B} = \hat{y}\, B_y(x,t) + \hat{z}\, B_z(x,y,t) \tag{8}$$

It then follows from the x component of the induction equation (7) that, for $B_y \neq 0$, the velocity v_x must be independent of the y coordinate.

To satisfy the incompressible-flow condition, $\nabla \cdot \mathbf{v} = 0$, the most general form of solution for the plasma velocity is

$$\mathbf{v} = \hat{x}\, v_x(x,t) + \hat{y}\, [-v_x'(x,t)\, y + g(x,t)] + \hat{z}\, v_z(x,y,t) \tag{9}$$

where a prime denotes partial differentiation of any function of x and t only with respect to x. The form of the y component of the velocity given by (9) (but without time dependence) was used by Besser et al.[1990] in their study of flow patterns which have arbitrary angles of flow incidence.

By use of the forms of **B** and **v** given by (8) and (9), and by cross differentiation of the x and y components of the momentum equation (2) to eliminate the pressure, setting the coefficients of like powers of y to zero, one obtains the following equations for $v_x(x,t)$ and $g(x,t)$:

$$-\rho \partial v_x''/\partial t + \eta\, v_x^{iv} - \rho\, v_x\, v_x''' + \rho\, v_x'\, v_x'' = 0 \tag{10}$$

$$\rho \partial g'/\partial t - \eta\, g''' + \rho\, v_x\, g'' - \rho\, v_x''\, g = 0 \tag{11}$$

Equations (10) and (11) may be integrated once to give

$$- \rho \partial v_x'/\partial t + \eta v_x''' - \rho v_x v_x'' + \rho v_x'^2 = K_1(t) \tag{12}$$

$$\rho \partial g/\partial t - \eta g'' + \rho v_x g' - \rho g v_x' = K_2(t) \tag{13}$$

respectively. Here $K_1(t)$ and $K_2(t)$ are constants of integration which may depend on time. Equations (10) and (12) with $\partial/\partial t=0$ were first given by K. Hiemenz in his thesis at Göttingen in 1911 (see, e.g., Schlichting, [1968]) while equations (11) and (13) have been obtained by Besser et al. [1990]. Gratton et al.[1988] pointed out that temporally varying flows and fields can be incorporated, although, to date, no such flows have been examined in detail.

The z component of the momentum equation, with $p= p_1(x,y,t) + p_2(t)z$, reduces to

$$\frac{\partial v_z}{\partial t} - \eta \left(\frac{\partial^2 v_z}{\partial x^2} + \frac{\partial^2 v_z}{\partial y^2} \right) + \rho\, v_x \frac{\partial v_z}{\partial x} - \rho\, (v_x' y - g) \frac{\partial v_z}{\partial y} - \frac{B_y}{\mu_0} \frac{\partial B_z}{\partial y} + p_2 = 0 \tag{14}$$

where $p_2(t)$ is a function of time only.

The momentum equation (2) may also be integrated to yield the pressure distribution

$$p + (B_y^2 + B_z^2)/2\mu_0 + \rho\, v_x^2/2 - \eta\, v_x' + K_1 y^2/2 + K_2\, y - p_2 z + \rho \partial/\partial t \left(\int v_x dx \right) = K_3(t) \tag{15}$$

where $K_3(t)$ is again a constant of integration.

The x component of the induction equation is identically satisfied while the y and z components become

$$\frac{\partial B_y}{\partial t} - \frac{B_y''}{\mu_0 \sigma} + v_x B_y' + v_x' B_y = 0 \tag{16}$$

and

$$\frac{\partial B_z}{\partial t} - \frac{1}{\mu_0 \sigma}\left(\frac{\partial^2 B_z}{\partial x^2} + \frac{\partial^2 B_z}{\partial y^2}\right) + v_x \frac{\partial B_z}{\partial x} - (v_x'y - g)\frac{\partial B_z}{\partial y} - B_y \frac{\partial v_z}{\partial y} = 0 \tag{17}$$

As mentioned already, in these equations a prime denotes partial differentiation with respect to the coordinate x.

The equations (10), (11), (14), (15), and (17) constitute a set of coupled equations with unknowns $v_x(x,t)$, $g(x,t)$, $v_z(x,y,t)$, $B_y(x,t)$, $B_z(x,y,t)$, and $p(x,y,t)$. In the remainder of this paper, we consider only time independent flow, i.e., the time derivatives in equations (10) to (17) are dropped, and the quantities K_1, K_2, K_3 and p_2 are taken to be constants independent of time. The procedure for solving the set of equations is then as follows: Equation (10) is not coupled to the other equations and may be solved for $v_x(x)$ first. Solutions of $g(x)$ and $B_y(x)$ are subsequently obtained from equations (11) and (16). The coupled partial differential equations describing $v_z(x,y)$ and $B_z(x,y)$ can then be solved as discussed in section 3.2. Finally, the plasma pressure p is obtained by use of equation (14), with K_1 and K_2 given by expressions (12) and (13).

In the next two sections, we shall obtain families of solutions of equations (10) to (17) for the problem of MHD stagnation point flow at a current sheet. For this purpose, it is convenient to render equations (10) to (17) nondimensional by introducing the following dimensionless variables:

$$x^* = x/L$$

$$y^* = y/L$$

$$z^* = z/L$$

$$v_x^* = v_x/v_{A0}$$

$$v_z^* = v_z/v_{A0}$$

$$g^* = g/v_{A0}$$

$$B_y^* = B_y/B_0$$

$$B_z^* = B_z/B_0$$

$$p^* = p/(B_0^2/2\mu_0)$$

$$p_2^* = p_2/(B_0^2/2\mu_0 L)$$

$$\rho^* = \rho/\rho_0$$

$$\eta^* = \eta/\eta_0$$

$$\sigma^* = \sigma/\sigma_0$$

$$K_1^* = K_1/(\rho_0 V_{A0}^2/L^2)$$

$$K_2^* = K_2/(\rho_0 V_{A0}^2/L)$$

$$K_3^* = K_3/(B_0^2/2\mu_0)$$

In these expressions, L, B_0, ρ_0, η_0, σ_0, and $v_{A0} = B_0/(\mu_0\rho_0)^{1/2}$ are the characteristic length, magnetic field, plasma density, dynamic viscosity, electrical conductivity, and Alfvén speed, respectively. In section 3, where we solve for flow and field profiles, 'upstream' conditions for v and **B** are imposed along the $x=\pm L$ boundary, i.e., at $x^*=\pm 1$.

Equations (10) to (17) may be written in terms of the above dimensionless variables as

$$(\eta^*/Re)v_x^{*iv} - \rho^* v_x^* v_x^{*'''} + \rho^* v_x^{*'} v_x^{*''} = 0 \qquad (10^*)$$

$$(\eta^*/Re)g^{*'''} - \rho^* v_x^* g^{*''} + \rho^* v_x^{*''} g^* = 0 \qquad (11^*)$$

$$(\eta^*/Re)v_x^{*'''} - \rho^* v_x^* v_x^{*''} + \rho^* v_x^{*'2} = K_1^* \qquad (12^*)$$

$$- (\eta^*/Re)g^{*''} + \rho^* v_x^* g^{*'} - \rho^* g^* v_x^{*'} = K_2^* \qquad (13^*)$$

$$\frac{\eta^*}{Re}\left(\frac{\partial^2 v_z^*}{\partial x^{*2}} + \frac{\partial^2 v_z^*}{\partial y^{*2}}\right) - \rho^* v_x^* \frac{\partial v_z^*}{\partial x^*} + \rho^* (v_x^{*'} y^* - g^*) \frac{\partial v_z^*}{\partial y^*} + B_y^* \frac{\partial B_z^*}{\partial y^*} - \frac{p_2^*}{2} = 0 \qquad (14^*)$$

$$p^* + B_y^{*2} + B_z^{*2} + \rho^* v_x^{*2} - (2\eta^*/Re) v_x^{*'} + K_1^* y^{*2} + 2K_2^* y^* - p_2^* z^* = K_3^* \qquad (15^*)$$

$$(\sigma^* Rm)^{-1} B_y^{*''} - v_x^* B_y^{*'} - v_x^{*'} B_y^* = 0 \qquad (16^*)$$

$$\frac{1}{\sigma^* Rm}\left(\frac{\partial^2 B_z^*}{\partial x^{*2}} + \frac{\partial^2 B_z^*}{\partial y^{*2}}\right) - v_x^* \frac{\partial B_z^*}{\partial x^*} + (v_x^{*'} y^* - g^*) \frac{\partial B_z^*}{\partial y^*} + B_y^* \frac{\partial v_z^*}{\partial y^*} = 0 \qquad (17^*)$$

where $Re = v_{A0} L \rho_0 / \eta_0$ and $Rm = v_{A0} L \mu_0 \sigma_0$ are the viscous and magnetic Reynolds' numbers, respectively, based on the reference density, viscosity, conductivity, and Alfvén speed. A prime now denotes differentiation with respect to x^*.

3. SOLUTIONS

In this section, the two colliding plasmas are assumed to have the same density ρ, viscosity η, and electrical conductivity σ. In this case, we set ρ^*, η^*, and σ^* to one in equations (10*) to (17*). The section contains two parts. In part 1, exact analytic solutions for $v_x^*(x^*)$, $g^*(x^*)$ and $B_y^*(x^*)$ are first obtained for the limiting cases of $Re \Rightarrow 0$ and $Re \Rightarrow \infty$, and for various inflow boundary conditions. Analytic and numerical solutions for the finite Re case will then be presented. Differences between these solutions will be discussed. In part 2, solutions for $v_z^*(x^*, y^*)$ and

$B_z^*(x^*,y^*)$ in the form of power series in y^* are assumed, as a result of which, the partial differential equations (14*) and (17*) become a set of ordinary differential equations. It is shown that this set can be truncated at any desired power of y^*. Two simple examples are given to illustrate the procedure for obtaining solutions of v_z^* and B_z^*.

3.1. Solutions for $v_x^*(x^*)$, $g^*(x^*)$, and $B_y^*(x^*)$

The general expression for B_y^* in term of v_x^* may be found by integrating equation (16*), the result being

$$B_y^*(x^*) = B_y^*(0)\, I(x^*) + B_y^{*\prime}(0)\, I(x^*) \int^{x^*} I^{-1}(t)\, dt \tag{18}$$

where $$I(\xi) = \exp\left(Rm \int^{\xi} v_x^*(s)ds\right)$$

In what follows, we first present the solutions for v_x^*, g^*, and B_y^* for the limiting cases of $Re \Rightarrow 0$ and $Re \Rightarrow \infty$. We then go on to obtain sample numerical solutions for chosen finite values of Re.

3.1.a. $Re \Rightarrow 0$ In this limit, equations (10*) and (11*) reduce to

$$v_x^{*iv} = 0$$

and

$$g^{*\prime\prime\prime} = 0$$

with general solutions

$$v_x^* = a_1 x^{*3} + b_1 x^{*2} + c_1 x^* + d_1$$

$$g^* = a_2 x^{*2} + b_2 x^* + c_2$$

here a_1, a_2, b_1, b_2, c_1, c_2, and d_1 are constant coefficients determined by inflow boundary conditions. Many symmetric and asymmetric flow patterns can be generated by varying the seven coefficients. For flows patterns that are symmetric about the $x^*=0$ plane, the corresponding solutions are

$$v_x^* = \{[M_A + v_x^{*\prime}(\pm 1)]x^{*3} - [3M_A + v_x^{*\prime}(\pm 1)]x^*\}/2 \qquad (19)$$

and

$$g^* = g^*(\pm 1)\, x^2$$

here M_A is the Alfvén Mach number at $x^*=\pm 1$. With $g^* \equiv 0$, the quantity $v_x^{*\prime}(\pm 1)$ fixes the angle of plasma inflow at $x^*=y^*=\pm 1$. Flow toward the stagnation point, located at $x^*=y^*=0$, is referred to as divergent (convergent) if $v_x^{*\prime}(\pm 1)$ is less (greater) than zero. If $v_x^{*\prime}(\pm 1) < -3M_A$, there are three stagnation points located along the x^* axis at $x^*_1 = 0$ and at $x^*_{2,3} = \pm[3M_A + v_x^{*\prime}(\pm 1)]/[M_A + v_x^{*\prime}(\pm 1)]$. In this case, the velocity v_x^* in the region $x^*_2 > x^* > x^*_3$ is in a sense opposite to that of the inflow at greater $|x^*|$ values. As will be shown later, this behavior occurs only at low values of Re and then only when the inflow is greatly divergent. Figure 1a and figure 2 show the v_x^* profiles and the streamlines, respectively, for values of $v_x^{*\prime}(\pm 1)$ ranging from $-4M_A$ to $+3M_A$, with $M_A=1$, to illustrate the flow patterns just described. It should be noted that when $v_x^{*\prime}(\pm 1) = -M_A$, expression (19) reduces to $v_x^* = -M_A x^*$, which is the standard stagnation-point flow utilized by Parker [1973] and by Sonnerup and Priest [1975]. In the

standard stagnation-point flow solution, the plasma flow is irrotational. This is no longer the case when $v_x^{*\prime}(\pm 1) \neq -M_A$.

An example of the construction of flow patterns which are asymmetric about $x^*=0$ is shown in Figure 3 for the entire range of the viscous Reynolds number. These flows satisfy the following boundary conditions:

$$\begin{aligned} &\underline{\text{At } x^*=-1:} \quad && v_x^*(-1) = M_A \\ & && v_x^{*\prime}(-1) = 0 \\ &\underline{\text{At } x^*=+1:} \quad && v_x^*(+1) = -\pi M_A/2 \\ & && v_x^{*\prime\prime}(+1) = 0 \end{aligned} \tag{20}$$

This set of boundary conditions corresponds to the situation where the plasma flow incident on the current sheet, from the left boundary, is at right angle to that boundary (at $x^*=-1$), whereas the plasma flow incident from the right boundary is irrotational at $x^*=+1$. The amount of vorticity in the flow region therefore varies with position, but is asymmetric about $x^*=0$. In the limit $Re \Rightarrow 0$, the solution of (10*) which satisfies the above boundary conditions is found to be

$$v_x^* = M_A \left[(\pi+2)(x^{*3}-3x^{*2}-9x^*) + (22-5\pi)\right]/32 \tag{21}$$

The curves in Fig. 3a and 3b which correspond to (21), with $M_A=1$, are labeled by "crosses". The corresponding flow pattern is shown in Figure 3c. Flow patterns for other values of Re are discussed in sections 3.1b and 3.1c.

A nonzero function $g^*(x^*)$ introduces asymmetry in the flow pattern. The a_2 term causes asymmetry between the regions $y^*>0$ and $y^*<0$, while the b_2 term produces asymmetry between the regions $x^*>0$ and $x^*<0$. This case is discussed further in section 3.1c.

We turn now to a discussion of the magnetic field B_y. Figure 4a shows the odd solutions of B_y^* as a function of x^*, corresponding to the v_x^* distributions shown in Fig. 1a, for Rm=10. The magnetic pile-up effect is observed for all cases, the effect being more important for divergent flow. For convergent flow, the magnetic field first decreases before piling up as the plasmas move toward and into the current sheet, centered at $x^*=0$.

In Figure 5a, the even solutions of B_y^* as a function of x^* are shown for the same cases as in Fig. 1. It is noted that for $v_x^{*\prime}<-3M_A$, i.e., when flow reversal in v_x^* is present, the magnetic field exhibits extrema at $x^*\neq 0$. These extrema occur at locations where the reverse flow is a maximum. This behavior can easily be understood by examining the z component of the Ohm's law. As will be shown presently, these extrema disappear at high Re values.

3.1.b $Re \Rightarrow \infty$ In this limit, equations (10*) and (11*) reduce to

$$v_x^* v_x^{*'''} - v_x^{*\prime} v_x^{*''} = 0$$

$$v_x^* g^{*''} - v_x^{*''} g^* = 0$$

These equations can be integrated to give either

$$v_x^* = A_1 x^* + B_1$$

or

$$v_x^* = A_1 \sin a_5 x^* + B_1 \cos a_5 x^*$$

or

$$v_x^* = A_1 \sinh a_5 x^* + B_1 \cosh a_5 x^*$$

and

$$g^* = v_x^* \left[A_2 + B_2 \int^{x^*} (v_x^*)^{-2} \, dx^* \right]$$

where A_1, B_1, A_2, B_2 and a_5 are constants of integration.

For flows that are anti-symmetric about $x^*=0$, so that $v_x^*(-x^*)=-v_x^*(x^*)$, the form of the solution then depends on the value of $v_x^{*\prime}(\pm 1)$ in the following way:

For $v_x^{*\prime}(\pm 1) = -M_A$:

$$v_x^* = -M_A \, x^*$$

$$g^* = a_3 \, x^* + b_3$$

For $v_x^{*\prime}(\pm 1) < -M_A$:

$$v_x^* = a_4 \sin(a_5 x^*) \tag{22}$$

$$g^* = a_6 \sin(a_5 x^*) + b_4 \cos(a_5 x^*)$$

For $v_x^{*\prime}(\pm 1) > -M_A$:

$$v_x^* = a_7 \sinh(a_8 x^*) \tag{23}$$

$$g^* = a_9 \sinh(a_8 x^*) + b_5 \cosh(a_8 x^*)$$

where the a's and b's are constants determined by the specific values of $v_x^{*\prime}(x^*)$ at $x^*=\pm 1$. Note that the standard stagnation-point flow solution for v_x^* again appears for $v_x^{*\prime}(\pm 1)=-M_A$. Unlike the $Re \Rightarrow 0$ case, for $Re \Rightarrow \infty$ the only stagnation point within $-1<x^*<1$ is that located at the origin. Figure 1b shows v_x^* profiles for the same boundary condition as that used in Figure 1a. Finally, it

is noted that, as a_5 and a_8 approach zero, expressions (22) and (23) approach the standard stagnation-point flow.

In the limit Re⇒∞, the solution of (10*) which satisfies the asymmetric boundary conditions (20) is given by

$$x^* \le 0: \qquad v_x^* = M_A \sin(\pi x^*/2) \tag{24}$$

$$x^* \ge 0: \qquad v_x^* = -\pi M_A x^*/2$$

The curves corresponding to (24), with $M_A=1$, are labeled by "diamonds" in Figures 3a and 3b. The flow pattern is shown in Figure 3d.

Figures 4b and 5b show the odd and even solutions for B_y^* as a function of x^* for Re⇒∞. The qualitative features seen in the Re⇒0 case are still present here, with the exception that only one extremum, which always occurs at $x^*=0$, is observed in the even solution. This is because no flow reversal of the type shown in Figure 2d can occur for Re⇒∞.

3.1.c Finite Re

For finite Re, equations (10*) and (11*) can be integrated numerically to obtain solutions for $v_x^*(x)$ and $g^*(x)$, subject to specific boundary conditions. Examples of velocity and magnetic field profiles are shown in Figures 1c, 1d, 4c, 4d, 5c, and 5d. An examination of Figure 1 shows that the velocity profiles, $v_x^*(x^*)$, for Re=100 and Re ⇒ ∞ are nearly indistinguishable. Thus for flows with large viscous Reynolds number, the influence of viscosity is very small.

As mentioned already, the standard stagnation point flow, $v_x^* = -M_A\, x^*$, is the solution of (10*) that satisfies the particular boundary condition of $v_x^{*\prime}(\pm 1) = -M_A$, and has a flow pattern that is symmetric about $x^*=0$. For this flow, which is irrotational, the net viscous force per unit volume vanishes identically. Regardless of the value of Re, viscosity therefore has no effects on the

velocity profile, $v_x^*(x^*)$. The viscous force is nonzero in symmetric flows for boundary condition $v_x^{*\prime}(\pm 1) \neq -M_A$. However, it is noted that the velocity distributions, $v_x^*(x^*)$, corresponding to the boundary condition $v_x^{*\prime}(\pm 1)=0$ differ from each other by no more than 0.02 M_A in the entire range of values of the viscous Reynolds number. Thus the distribution of the x component of the velocity in this case is determined almost entirely by the boundary conditions, the influence of viscosity being very small. For flows toward the current sheet which have large amount of divergence from, or convergence toward the stagnation point, the behavior at low Re differs substantially from that at high Re, as can be seen is Figure 1.

The numerical solutions of (10*) for Re=1 and 100 which satisfy the asymmetric boundary condition (20) are labeled by "squares" and "circles", respectively, in Figures 3a and 3b. It is noted that the velocity profiles, $v_x^*(x^*)$, for Re=100 and $Re \Rightarrow \infty$ are almost identical. This again indicates that, even in flows which are asymmetric about $x^*=0$, the flow patterns at high Re values are determined almost entirely by the boundary conditions and not by the viscosity.

With the standard stagnation point solution, $v_x^* = -M_A x^*$, the general expression for $g^*(x)$ is found to be

$$g^*(x^*) = c_1 \left[\sqrt{\pi Q}\, x^* \operatorname{erf}\left(\sqrt{Q}\, x^*\right) + e^{-Qx^{*2}}\right] + c_2 x^* + c_3 \tag{25}$$

where $Q = ReM_A/2$. An expression equivalent to equation (25) was given by Besser et al.[1990] in terms of the Kummer function. For other more general v_x^* solutions, equation (11*) is still a linear equation for g^*; it can be integrated once to give

$$Re^{-1} g^{*\prime\prime} - v_x^* g^{*\prime} + v_x^{*\prime} g^* = \text{constant}$$

but further integration is most conveniently done numerically. Examples are shown in Figure 6 for $Re=10^6$ and Rm=10, with the flow, v_x^*, satisfying the boundary condition $v_x^{*\prime}(\pm 1)=0$. These flow patterns are similar to, but somewhat more complex than those obtained by Besser et al. [1990].

To investigate the influence of the viscosity on $g^*(x^*)$, we examine the solution for $g^*(x^*)$ given by (25). The odd solution for g^*, i.e., the term c_2x^*, is formally independent of the viscosity. The non-constant part of the even solution for g^*, i.e., the term proportional to c_1, on the other hand, is a function of the viscous Reynolds number. It is noted that this term is approximately quadratic in x^* near $x^*=0$, while at large $|x^*|$ it is proportional to $|x^*|$. The distance away from $x^*=0$ where the c_1 term starts to behave essentially as $|x^*|$ is of the order of $(ReM_A)^{-1/2}$. Thus for flows with large viscous Reynolds number, the even solution for $g^*(x^*)$ can be approximated by $g^*(x^*)\approx \alpha|x^*|+\beta$ over most of the flow region, α and β being constants which depend on boundary conditions, but not on the viscosity. Thus, for large Re the effects of viscosity on g^* are limited to a thin layer at $x^*=0$.

Since it is the magnetic Reynolds number, Rm, and the velocity distribution, $v_x^*(x^*)$, but not $g^*(x^*)$, that determine the magnetic field B_y^*, via the induction law, the magnetic field profiles, B_y^*, are also nearly independent of viscosity, except in strongly divergent or convergent flows with viscous Reynolds number of the order of unity or smaller. On the other hand, as will be shown in section 3.2, the z component of the magnetic field, B_z^*, may depend on $g^*(x^*)$. Thus in flows where the characteristic resistive length is comparable to or smaller than the characteristic viscous length, the influence of the viscosity on the B_z^* distribution may be important in flows which are asymmetric about $y^*=0$.

An asymmetric exact solution of equation (10) in the form $v_x=U_0(1-\exp(\pm\rho U_0x/\eta))$, was found by Gratton et al.[1988]; comments on the relevance of this solution and on the importance of viscosity can be found in Sonnerup and Phan [1990] and in Gratton et al [1990].

3.2 Solutions for $v_z^*(x^*,y^*)$ and $B_z^*(x^*,y^*)$

We look for solutions of equations (14*) and (17*) of the form

$$v_z^* = \sum_{n=0}^{\infty} v_n(x^*)\, y^{*n} \tag{26}$$

and

$$B_z^* = \sum_{n=0}^{\infty} B_n(x^*)\, y^{*n} \tag{27}$$

where n is an integer. Substituting these expressions into equations (14*) and (17*), and equating coefficients of like powers of y*, we obtain the following coupled ordinary differential equations

$$Re^{-1}v_n''-v_x^*v_n'+nv_x^{*\prime}v_n = -(n+1)B_y^*B_{n+1}+(n+1)g^*v_{n+1}-(n+1)(n+2)v_{n+2}+\delta_{n0}p_2^*/2 \tag{28}$$

$$Rm^{-1}B_n''-v_x^*B_n'+nv_x^{*\prime}B_n = -(n+1)B_y^*v_{n+1}+(n+1)g^*B_{n+1}-(n+1)(n+2)B_{n+2} \tag{29}$$

where $\delta_{n0}=1$ for $n=0$ and $\delta_{n0}=0$ for all other n values.

In practice, this form of solution is useful only if the series can be truncated to a finite number of terms. Examination of equations (28) and (29) shows that the inhomogeneous parts of the equations, which are collected on their right-hand sides, involve only terms of higher order. The series (26) and (27) can therefore be truncated at will.

To lowest order where $v_z^*(x^*)=v_0(x^*)$, and $B_z^*(x^*)=B_0(x^*)$, equations (28) and (29) reduce to

$$(1/Re)v_0'' - v_x^*\, v_0' = p_2^*/2$$

$$(1/Rm)B_0'' - v_x^* B_0' = 0$$

with solutions

$$v_0(x^*) = v_0(0) + \int^{x^*} ds \left(k_1 H(s) + \frac{1}{2} p_2 \, Re \, H(s) \int^{s} H^{-1}(t) \, dt \right) \tag{30}$$

and

$$B_0(x^*) = B_0(0) + k_2 \int^{x^*} dt \, I(t) \tag{31}$$

where $H(\xi) = \exp\left(Re \int^{\xi} v_x^*(s) ds \right)$

$I(\xi) = \exp\left(Rm \int^{\xi} v_x^*(s) ds \right)$

and k_1 and k_2 are constants of integration.

Expression (30), with velocity profile $v_x^* = -M_A x^*$ and $p_2^* = 0$ was given by Besser et al.[1990]. Expression (31), with the same velocity profile, was first given by Sonnerup and Priest [1975]. Figure 7 shows the odd solutions of B_0 (or v_0 with $p_2^* = 0$) as a function of x^*, corresponding to the various v_x^* distributions shown in Fig. 1.

If, in addition, we allow $B_1(x^*)$ to be nonzero, i.e., $B_z^* = B_0(x^*) + y B_1(x^*)$, then equations (28) and (29) produce 3 coupled differential equations for v_0, B_0, and B_1:

$$Re^{-1} v_0'' - v_x^* v_0' = - B_y^* B_1 + p_2^*/2 \tag{32}$$

$$Rm^{-1} B_0'' - v_x^* B_0' = g^* B_1 \tag{33}$$

$$Rm^{-1} B_1'' - v_x^* B_1' + v_x^{*\prime} B_1 = 0 \tag{34}$$

For $v_x^* = -M_A x^*$, the solution of (34) is given by

$$B_1 = c_1 \left[\sqrt{\pi W}\, x^* \operatorname{erf}(\sqrt{W}\, x^*) + \frac{1}{P(x^*)} \right] + c_2 x^* \tag{35}$$

Equations (32) and (33) can subsequently be integrated to yield

$$v_0 = c_3 \operatorname{erf}(\sqrt{Q}\, x^*) + c_4 - Re \int^{x^*} \frac{ds}{J(s)} \left[\int^{s} dt\, J(t) \left(B_y^* B_1 - \frac{p_2^*}{2} \right) \right] \tag{36}$$

$$B_0 = c_5 \operatorname{erf}(\sqrt{W}\, x^*) + c_6 + Rm \int^{x^*} \frac{ds}{R(s)} \left[\int^{s} dt\, R(t)\, g^* B_1 \right] \tag{37}$$

where $W = RmM_A/2$, $Q = ReM_A/2$, $R(\xi) = \exp(W \xi^2)$, and $J(\xi) = \exp(Q \xi^2)$. In section 5, equations (35) to (37) are used to model plasma flow with field annihilation along the flank magnetopause.

4. DISCONTINUITY IN DENSITY, VISCOSITY, AND CONDUCTIVITY

Thus far we have described stagnation point flow in which the colliding plasmas have the same density, viscosity, and electrical conductivity. In a situation where the two plasmas have different properties, solutions for the plasma flow and electromagnetic field in the two media have to be properly matched at the interface separating them. The interface conditions are that the velocity, the tangential electromagnetic field components, and the shear stresses as well as the normal stresses be continuous. Choosing the plane $x^*=0$ to coincide with the interface, the

continuity requirement for the three components of the velocity lead to the following conditions at the interface:

$$v_x^{*I}(0^-) = v_x^{*II}(0^+) = 0 \tag{38}$$

$$\frac{dv_x^{*I}}{dx^*}(0^-) = \frac{dv_x^{*II}}{dx^*}(0^+) \equiv v_x^{*\prime}(0) \tag{39}$$

$$g^{*I}(0^-) = g^{*II}(0^+) \equiv g^*(0)$$

$$v_z^{*I}(0^-,y^*) = v_z^{*II}(0^+,y^*) \equiv v_z^*(0,y^*)$$

where the superscripts I and II denote the plasmas occupying the regions $x<0$ and $x>0$, respectively. The continuity requirements for the tangential components of the electromagnetic field result in the conditions:

$$B_y^{*I}(0^-) = B_y^{*II}(0^+) \equiv B_y^*(0) \tag{40}$$

$$B_z^{*I}(0^-,y^*) = B_z^{*II}(0^+,y^*) \equiv B_z^*(0,y^*) \tag{41}$$

$$\frac{1}{\sigma^{*I}}\frac{dB_y^{*I}}{dx^*}(0^-) = \frac{1}{\sigma^{*II}}\frac{dB_y^{*II}}{dx^*}(0^+)$$

$$\frac{1}{\sigma^{*I}}\frac{dB_z^{*I}}{dx^*}(0^-, y^*) = \frac{1}{\sigma^{*II}}\frac{dB_z^{*II}}{dx^*}(0^+, y^*)$$

The balance of shear stresses at the interface leads to

$$\eta^{*I} \frac{d^2 v_x^{*I}}{dx^{*2}}(0^-) = \eta^{*II} \frac{d^2 v_x^{*II}}{dx^{*2}}(0^+)$$

$$\eta^{*I} \frac{dg^{*I}}{dx^*}(0^-) = \eta^{*II} \frac{dg^{*II}}{dx^*}(0^+)$$

$$\eta^{*I} \frac{dv_z^{*I}}{dx^*}(0^-) = \eta^{*II} \frac{dv_z^{*II}}{dx^*}(0^+)$$

Finally, the normal stress must be the same on both sides of the interface which leads to

$$p^{*II}(0^+,y^*,z^*) - p^{*I}(0^-,y^*,z^*) = 4\,(\eta^{*II} - \eta^{*I})\, v_x^{*\prime}(0) / Re \qquad (42)$$

where conditions (39), (40), and (41) have been used. The last condition indicates that the plasma pressure will usually be discontinuous across the interface if $\eta^{*I} \neq \eta^{*II}$. This pressure discontinuity is balanced by a discontinuity in the viscous normal stress.

By use of expression (15) and the matching conditions (38) - (41), the left-hand side of (42) may be evaluated to give

$$p^{*II}(0^+,y^*,z^*) - p^{*I}(0^-,y^*,z^*) = 2(\eta^{*II} - \eta^{*I}) v_x^{*\prime}(0)/Re - y^{*2}(K_1^{*II} - K_1^{*I}) - 2y^*(K_2^{*II} - K_2^{*I}) + z^*(p_2^{*II} - p_2^{*I}) + K_3^{*II} - K_3^{*I} \qquad (43)$$

Since the right-hand side of equation (42) is independent of y^* and z^*, the coefficients of y^*, y^{*2}, and z^* in (43) are required to vanish identically. This leads to 3 additional matching conditions, namely

$$K_1^{*I} = K_1^{*II} \tag{44}$$

$$K_2^{*I} = K_2^{*II}$$

$$p_2^{*I} = p_2^{*II}$$

The relation between the K_3^* values in the two plasmas is found by substituting (43) into (42), the result being

$$K_3^{*I} = K_3^{*II} + 2(\eta^{*I}-\eta^{*II})v_x'(0)/Re$$

In what follows, we show two examples of the interaction between plasmas of different properties. For simplicity, we shall restrict the discussion to the situation where the two incident plasma flows are irrotational, i.e.,

$$v_x^{*I}(-\infty) \Rightarrow -\gamma^I x^*$$

$$v_x^{*II}(+\infty) \Rightarrow -\gamma^{II} x^*$$

where γ^I and γ^{II} are positive constants. The matching condition (44) then leads to

$$\rho^{*I} (\gamma^I)2 = \rho^{*II} (\gamma^{II})2 \tag{45}$$

In the first example, the two colliding plasmas have the same dynamic viscosity and electrical conductivity, but their densities are different from each other. Figures 8 shows the x and y components of the velocity, together with the y component of the magnetic field for Re=1, 10, and 100, and Rm=1, based on the properties of plasma I. The density, dynamic viscosity, and electrical conductivity ratios of the two plasmas are $\rho^{*II}/\rho^{*I}=10$, $\eta^{*II}/\eta^{*I}=1$, and $\sigma^{*II}/\sigma^{*I}=1$,

respectively. From equation (45) it can then be deduced that $\gamma^{*II}/\gamma^{*I}=(10)^{-1/2}$. It should be noted that a viscous layer appears near the interface, located at $x^*=0$. The nondimensional width of the boundary layer is of the order of the viscous length $\lambda_v^*=\lambda_v/L=(\eta^*/\rho^*\gamma^*Re)^{1/2}$, as expected. Inside this layer, a smooth joining occurs of the asymptotic inviscid solutions, namely $v_x^{*I}(x^*) = \gamma^I x^*$ for $x^*<0$ and $v_x^{*II}(x^*) = \gamma^{II} x^*$ for $x^*>0$. An examination of the magnetic field profile, $B_y^*(x^*)$, shows that extrema in the profiles occur at a distance comparable to the resistive length $\lambda^*_r=\lambda_r/L=(\sigma^*\gamma^*Rm)^{-1/2}$. Finally, as expected, the magnetic field profiles are less sensitive to the viscosity at large viscous Reynolds number.

In the second example, in addition to the discontinuity in density across the interface, the dynamic viscosity and the electrical conductivity are now also discontinuous. Figure 9 shows the velocity and magnetic profiles for Re=Rm=1, based on the properties of plasma I. The density, dynamic viscosity, and electrical conductivity ratios of the two plasma are $\rho^{*II}/\rho^{*I}=10$, $\eta^{*II}/\eta^{*I}=0.01$, and $\sigma^{*II}/\sigma^{*I}=0.1$, respectively. In this case, the viscous normal stress, the plasma pressure, and the z component of the electrical current are discontinuous across the interface, as can be seen from the abrupt change in slopes at $x^*=0$ of the $v_y^*(x^*,y^*)/y^*$ and $B_y^*(x^*)$ curves.

In this section, we have only discussed situations where the two incident plasmas are irrotational. But it should be expected, from the discussion in section 3, that, except in strongly divergent or convergent flows with low viscous Reynolds number, the effect of viscosity is confined to a narrow boundary layer.

5. DISCUSSION AND CONCLUSION

In sections 2 and 3 of this paper, we have presented exact solutions of two-dimensional steady-state stagnation point flows at a current sheet. The physical process described consists of magnetic annihilation without reconnection. Resistive and viscous effects are included in the analysis. The effects of resistivity on the flow and field have been discussed extensively by others (see for example Sonnerup and Priest [1975] and Gratton et al.[1988]) and need not be explored further here. On the other hand, in our view, the role of viscosity in determining the flow and field configurations is less clear. It has been argued that a defect of the types of flow discussed by Sonnerup and Priest [1975] is the fact that the viscous forces are zero in those flows [Gratton et al., 1988; 1990; Besser et al.,1990]. These authors suggest that viscous effects are important in stagnation point flows having nonzero vorticity, even in astrophysical applications where the viscous Reynolds number, Re, is usually high. In this paper, we have examined flow with nonzero vorticity incident on the current sheet at an arbitrary angle and having an arbitrary amount of divergence or convergence. We have explored the behavior of these flows in the entire range of Reynolds numbers. When the two colliding plasmas have the same density and viscosity, it is found that the viscous effects are important only in strongly divergent and strongly convergent flows with viscous Reynolds number of the order of one or smaller. We have also examined the situation where the two colliding plasmas have different density, viscosity and conductivity. It is found that the viscous effects are important only in a boundary layer, in the vicinity of the interface, of width comparable to the viscous length. For many astrophysical applications, the viscous Reynolds number is high and the effect of viscosity is therefore confined to a narrow layer.

As a second point of discussion, we note that solutions for v_z^* and B_z^* of the form shown in section 3.2 may be used to model the dawn and dusk portions of the Earth's magnetopause where magnetic field annihilation (or reconnection at a very low rate) may take place in combination with a strong external magnetosheath flow component at right angle to the magnetic field. A schematic drawing of the dawn magnetopause is shown in Figure 10. In this figure, the correspondence is shown between the (x,y,z) coordinate system used in this paper and the standard geocentric solar magnetospheric (X_{GSM}, Y_{GSM}, Z_{GSM}) system, commonly used to discuss magnetospheric configurations and phenomena. We have used solutions of the form (35), (36) and (37) to describe the flow and magnetic field in a situation where the x component (the Y_{GSM} component) of the electric current becomes large as $x \Rightarrow -\infty$ and vanishes as $x \Rightarrow +\infty$. The region $x<0$ corresponds to the magnetosheath and the region $x>0$ to the magnetosphere. In the former region, the main component of the current is along x with a smaller component along y; in the later, the current is gradually deflected to become more or less magnetic-field aligned. Both j_x and j_y vanish deep in the magnetosphere. This behavior of the current is shown schematically in Fig. 10 along with the bending of the magnetic field lines into parabolas with vertices facing downstream in the magnetosphere and upstream in the magnetosheath, bending that results from the presence of the current component j_x. On the magnetospheric side, the parabolas become increasingly obtuse, i.e., the field lines become increasingly straight, with increasing distance from the magnetopause; on the magnetosheath side they become increasingly acute. We note that the field-aligned currents on the magnetospheric side have been chosen to have the sense of the observed so-called Region 1 currents.

Figure 11a shows velocity profiles for the flow along the negative z axis (the $-X_{GSM}$ axis) for different values of the pressure gradient, $\partial p^*/\partial z^* = p_2^*$, along the magnetopause. It is seen that a pressure drop in the flow direction ($p_2^*>0$) generates a minimum in the velocity profile on the magnetosheath side of the current sheet, whereas a pressure rise in the flow direction generates a

region of reversed (sunward) flow on the magnetosphere side. The z component of the magnetic field, divided by y, is shown in Fig. 11b and the main field component, B_y, is shown in Fig. 11c as a function of x. The B_y component reverses sign across the magnetopause, corresponding to southward magnetic field in the magnetosheath. Finally, Fig. 11d shows the "field-aligned" current j_y, divided by y, as a function of x. This current component approaches a constant value deep in the magnetosheath and approaches zero deep in the magnetosphere.

It should not be inferred from the previous discussion that we believe our MHD solutions with flow along z to be directly applicable to the Earth's magnetopause. This is not the case: we realize that the incompressible MHD model is not capable of describing many important effects in the flow of the plasma along the magnetopause. However, the model calculations may nevertheless have merit as illustrations of the kind of flow and field configurations that might arise.

Finally, we note that many of the results presented in this paper can be generalized to three-dimensional flows of the type considered by Sonnerup and Priest [1975] in which a flow component, v_z, along the z axis is included which is proportional to z. The most general version of these flows and their associated magnetic fields will be discussed in a separate paper.

Acknowledgments. The research was supported by the Air Force Geophysics Laboratory under contract F19628-87-K-0026 and by the National Science Foundation, Atmospheric Sciences Division, under grant ATM-8807645 to Dartmouth College.

REFERENCES

Besser, B. P., H. K. Biernat, R. P. Rijnbeek, Planar MHD stagnation point flows with velocity shear, Planetary and Space Science, 38, 411, 1990.

Gratton, F. T., M. F. Heyn, H. K. Biernat, R. P. Rijnbeek, and G. Gnavi, MHD stagnation point flows in the presence of resistivity and viscosity, J. Geophys. Res., 93, 7318, 1988.

Gratton, F. T., G. Gnavi, M. F. Heyn, H. K. Biernat, and R. P. Rijnbeek, Pressure drive and viscous dragging: a reply, J. Geophys. Res., 95, 261, 1990.

Parker, E. N., Comment on the reconnection rate of magnetic fields, J. Plasma Phys., 9, 49, 1973.

Sonnerup, B. U. Ö., and E. R. Priest, Resistive MHD stagnation point flows at a current sheet, J. Plasma Phys., 14, 283, 1975.

Sonnerup, B, U, Ö., and T. D. Phan, Comment on "MHD stagnation point flows in the presence of resistivity and viscosity" by Gratton et al., J. Geophys. Res., 95, 259, 1990.

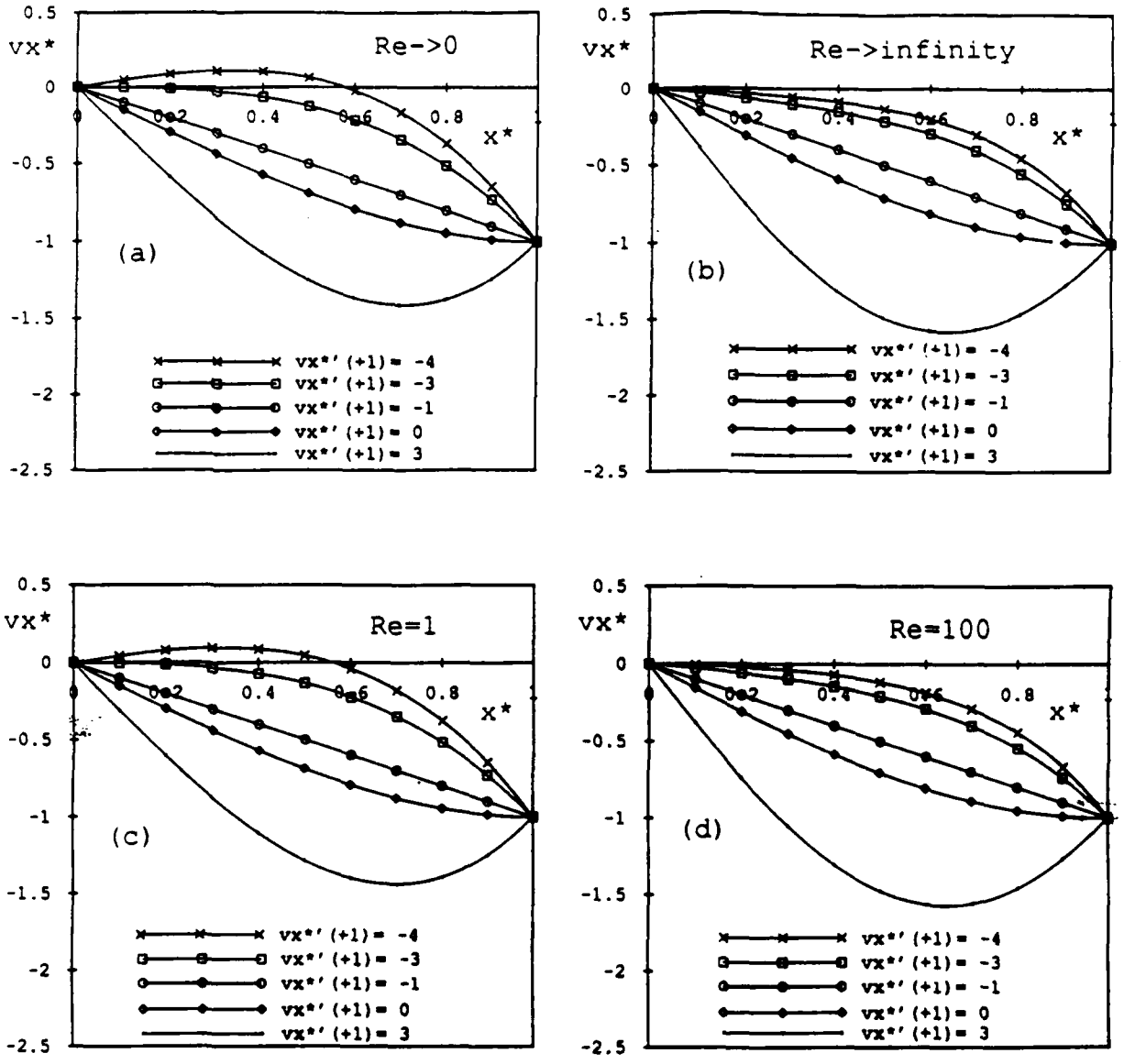

Fig. 1. Distributions of the x component of the velocity for $M_A(\pm 1)=1$, $v_x^{*\prime}(\pm 1)=3,0,-1,-3$, and -4, and for (a) Re⇒0, (b) Re⇒∞, (c) Re=1, (d) Re=100. Note the flow reversals when $v_x^{*\prime}(1)$ <-3 in the low Re cases (parts a and c). Only half of the symmetric flow region is shown.

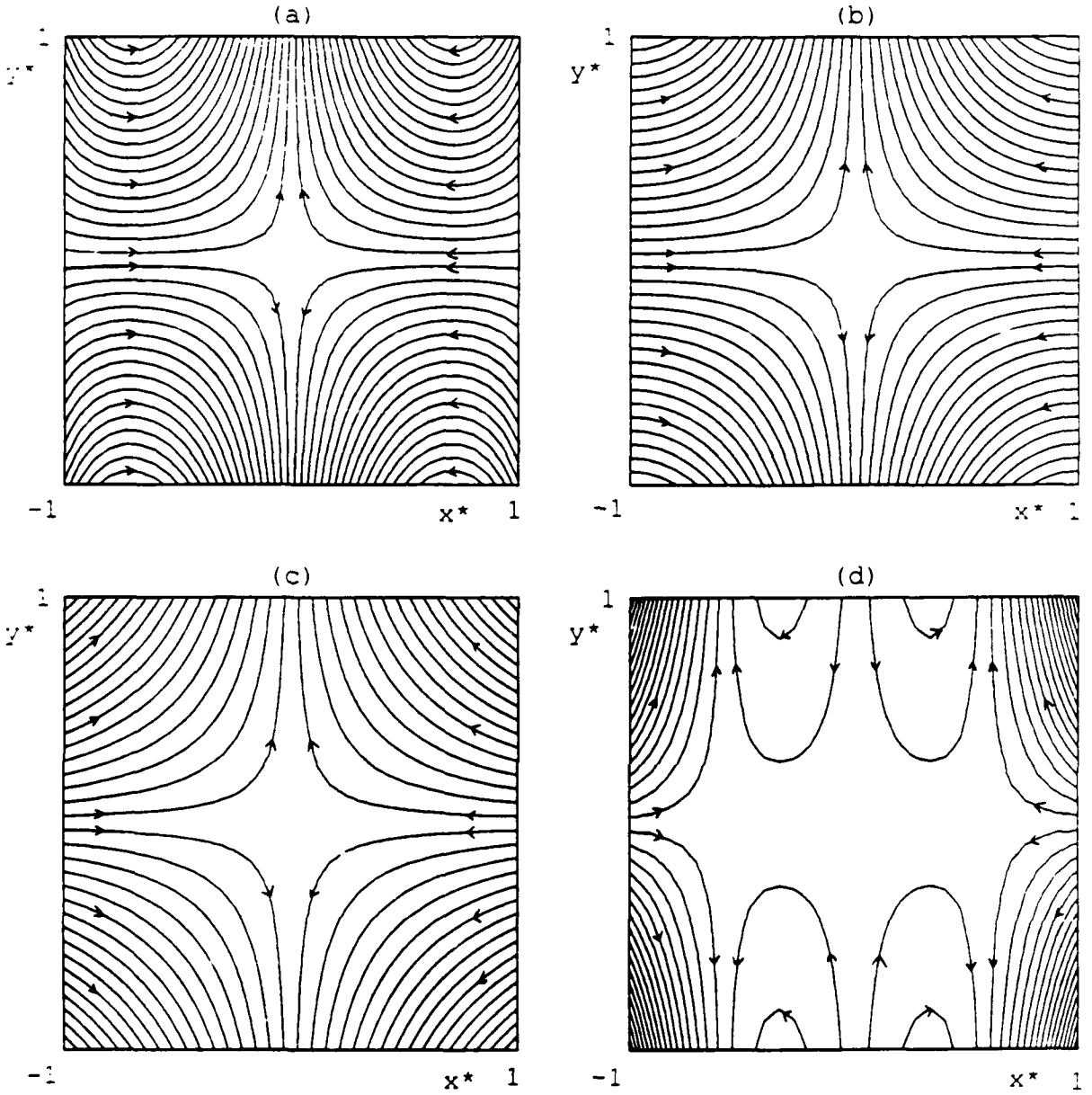

Fig. 2. Streamlines in the x-y plane for symmetric flows in the vicinity of the stagnation point, for the limiting case of Re⇒0, and for (a) $v_x^{*\prime}(\pm 1)=3$, (b) $v_x^{*\prime}(\pm 1)=0$, (c) $v_x^{*\prime}(\pm 1)=-1$, and (d) $v_x^{*\prime}(\pm 1)=-4$. Flow reversal occurs when $v_x^{*\prime}(1)<-3$. (see fig. 2d)

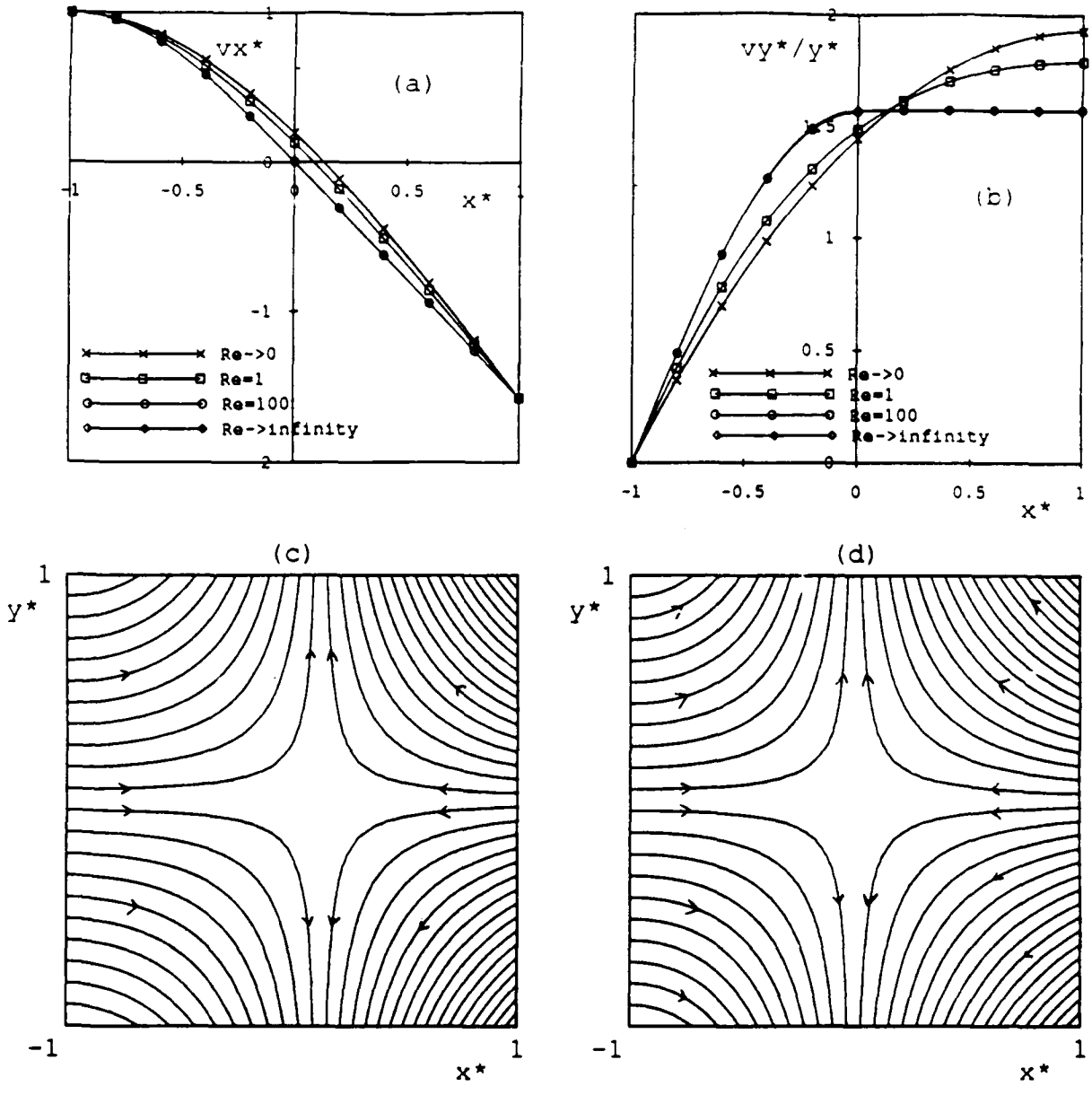

Fig. 3. Distributions of the (a) x component, and the (b) y component of the velocity for M_A=1, $v_x^*(-1)=1$, $v_x^{*\prime}(-1)=0$, $v_x^{*\prime}(1)= -\pi M_A/2$, and $v_x^{*\prime\prime}(1)=0$, and for Re=0, 1, 100, and ∞. Streamlines are shown for (c) Re$\Rightarrow$0, and (d) Re$\Rightarrow\infty$ cases.

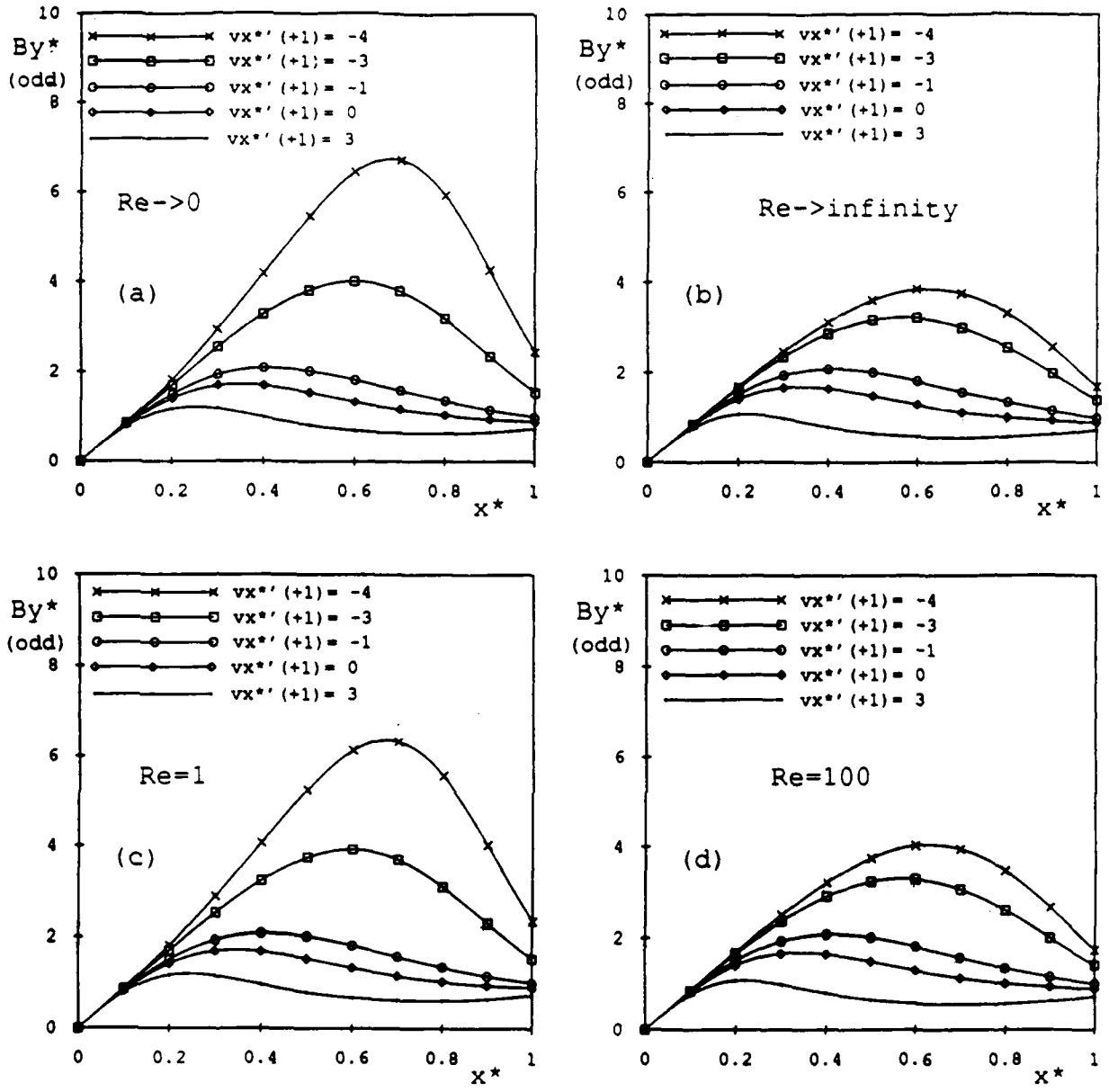

Fig. 4. Odd solutions of the magnetic field B_y^* vs x^* for Rm=10, and for the same cases as in fig. 1. Note that the magnetic pile-up effect is more important for divergent flows.

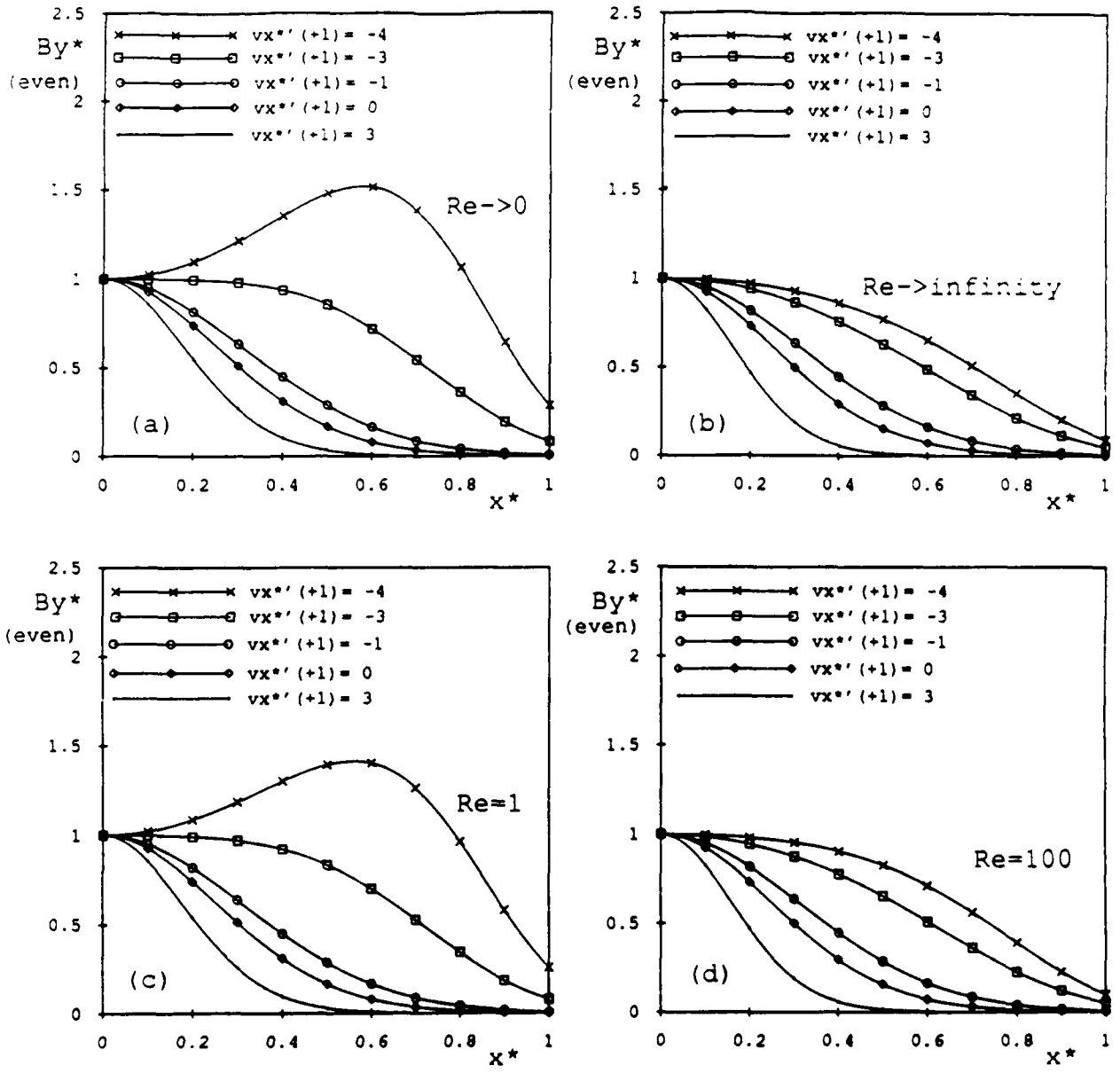

Fig. 5. Even solutions of the magnetic field B_y^* vs x^* for Rm=10, and for the same cases as in fig. 1. Note the magnetic field extrema at $x^* \neq 0$ in low Re cases. The extrema occur at the locations where the reverse flow is maximum.

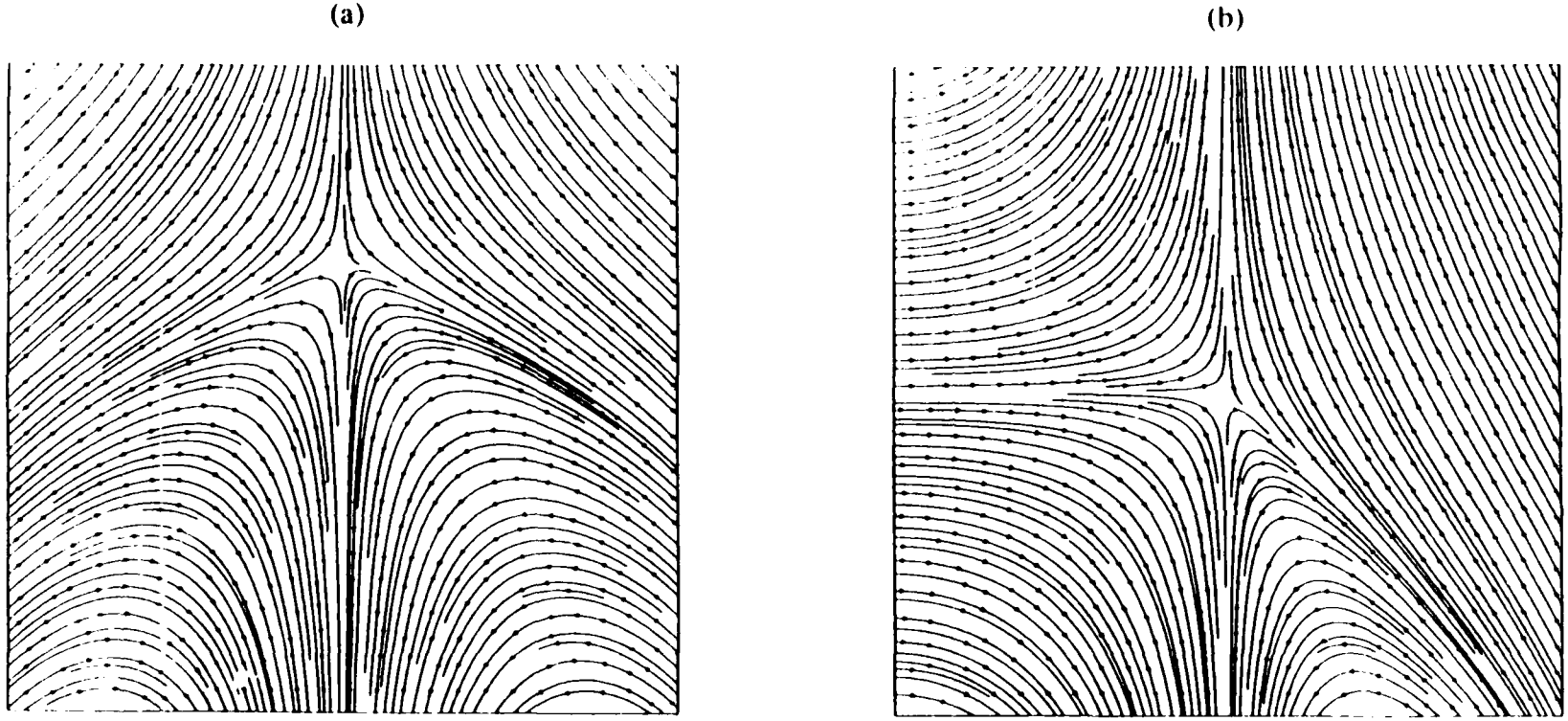

Fig. 6. Streamlines in the x-y plane for $Re=10^6$, Rm=100, $v_x^{*\prime}(1)=0$, and for (a) $g^*(\pm 1)=1$, $g^{*\prime}(-1)=-1$, and (b) $g^*(-1)=g^{*\prime}(-1)=0$, $g^*(1)=1$.

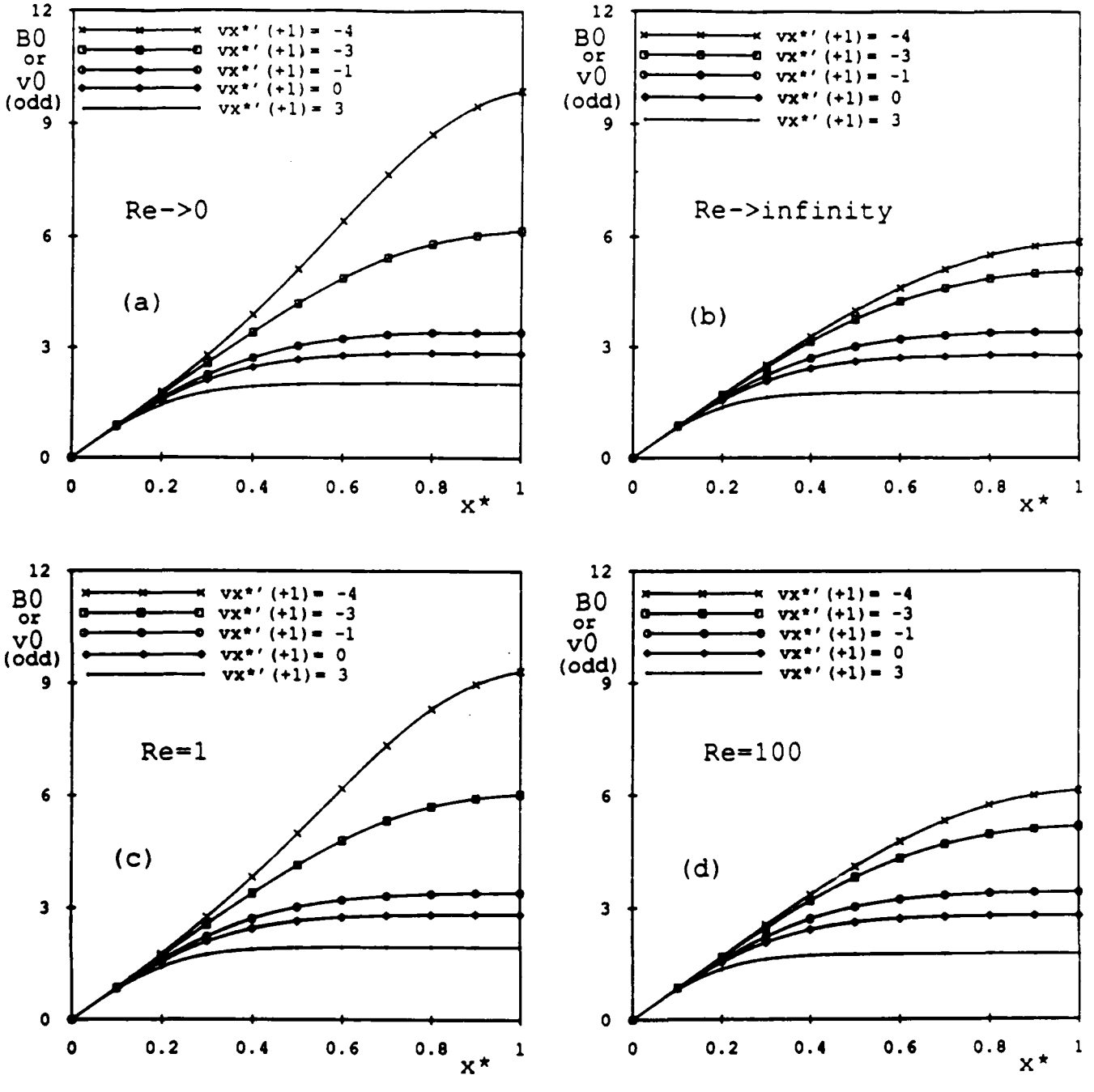

Fig. 7. Odd solutions of B_0 or v_0 (for $p_2^*=0$) (lowest order solutions of B_z^* and v_z^*) vs x^* for the same cases as in fig. 1.

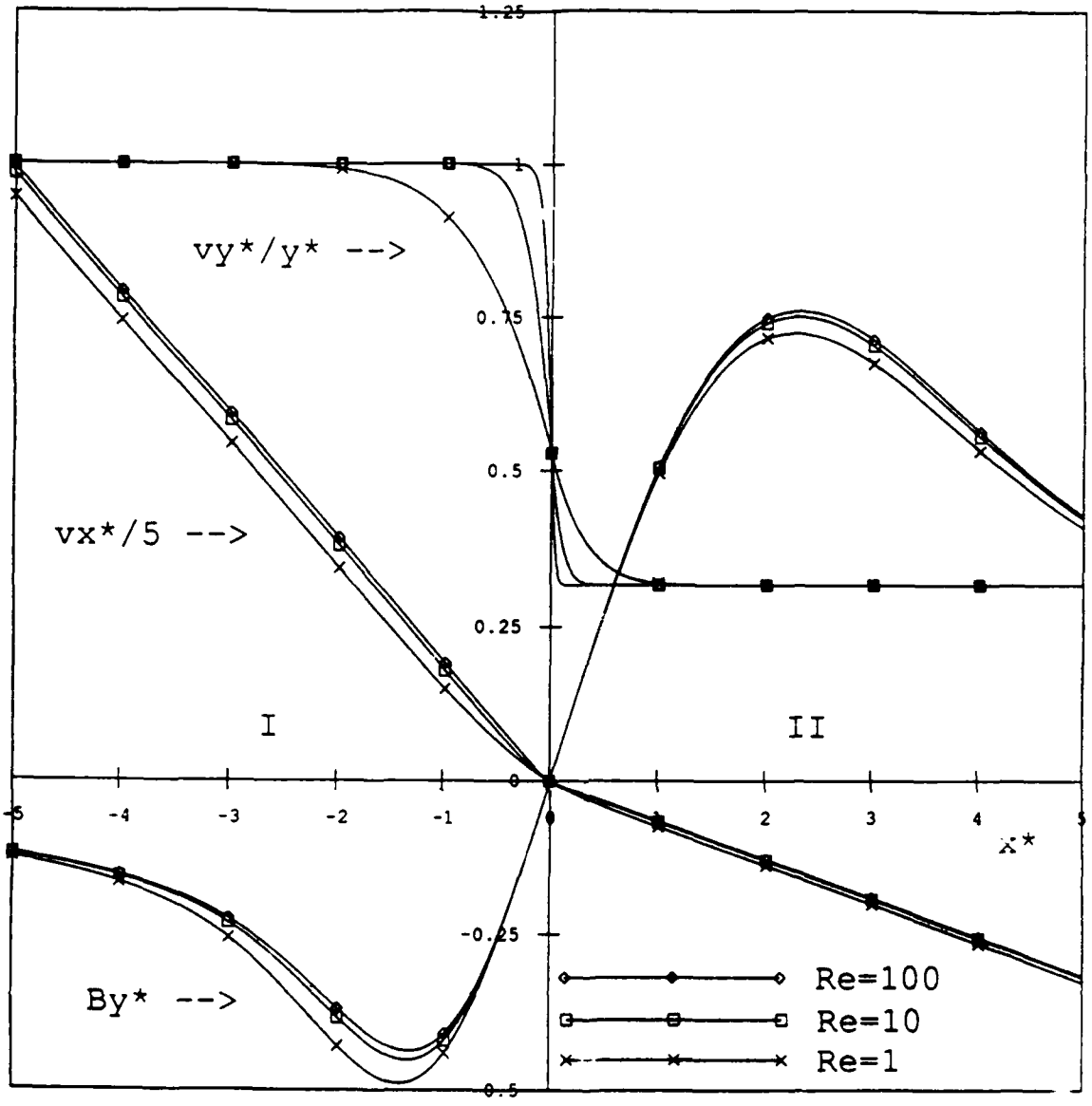

Fig. 8. Distributions of $v_x^*(x^*)$, $v_y^*(x^*,^*)/y^*$, and $B_y^*(x^*)$ for Re=1, 10, 100, and Rm=1, based on the properties of plasma I. Density, dynamic viscosity, and electrical conductivity ratios are: $\rho^{*II}/\rho^{*I}=10$, $\eta^{*II}/\eta^{*I}=1$, and $\sigma^{*II}/\sigma^{*I}=1$.

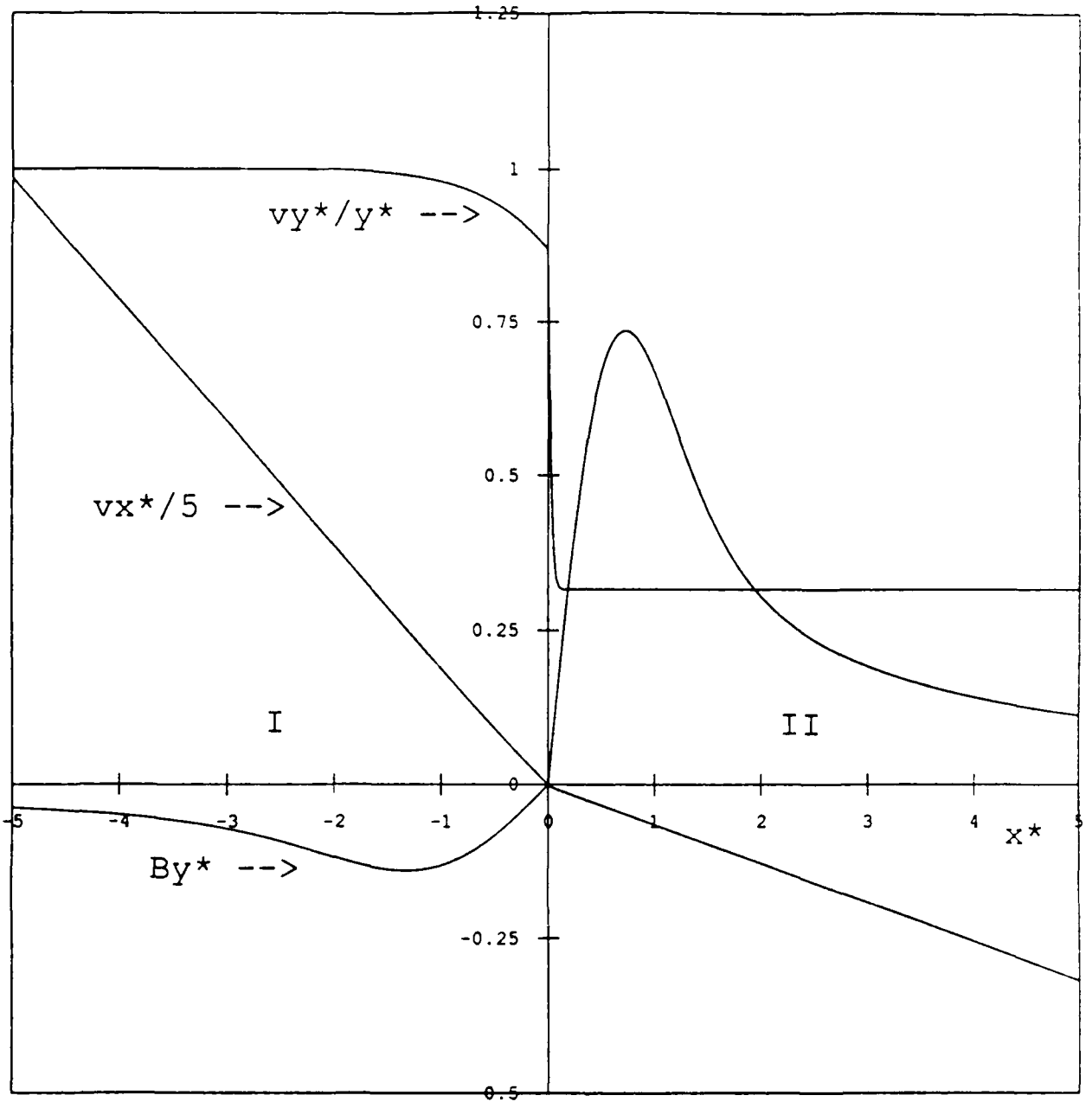

Fig. 9. Distributions of $v_x^*(x^*)$, $v_y^*(x^*,^*)/y^*$, and $B_y^*(x^*)$ for Re=Rm=1, based on the properties of plasma I. Density, dynamic viscosity, and electrical conductivity ratios are: $\rho^{*II}/\rho^{*I}=10$, $\eta^{*II}/\eta^{*I}=0.01$, and $\sigma^{*II}/\sigma^{*I}=0.1$.

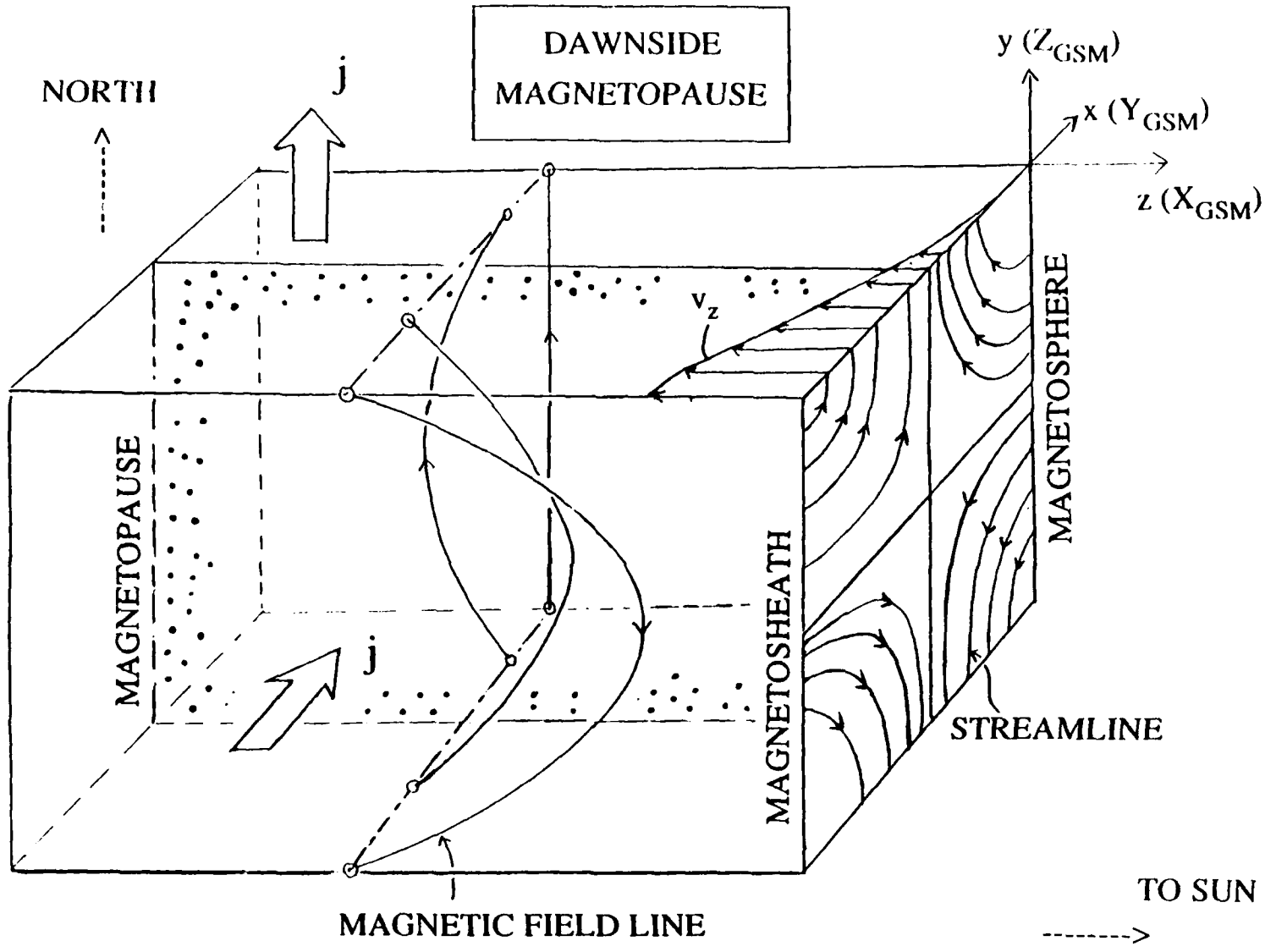

Fig. 10. Schematic drawing of the dawn magnetopause. See text for the description.

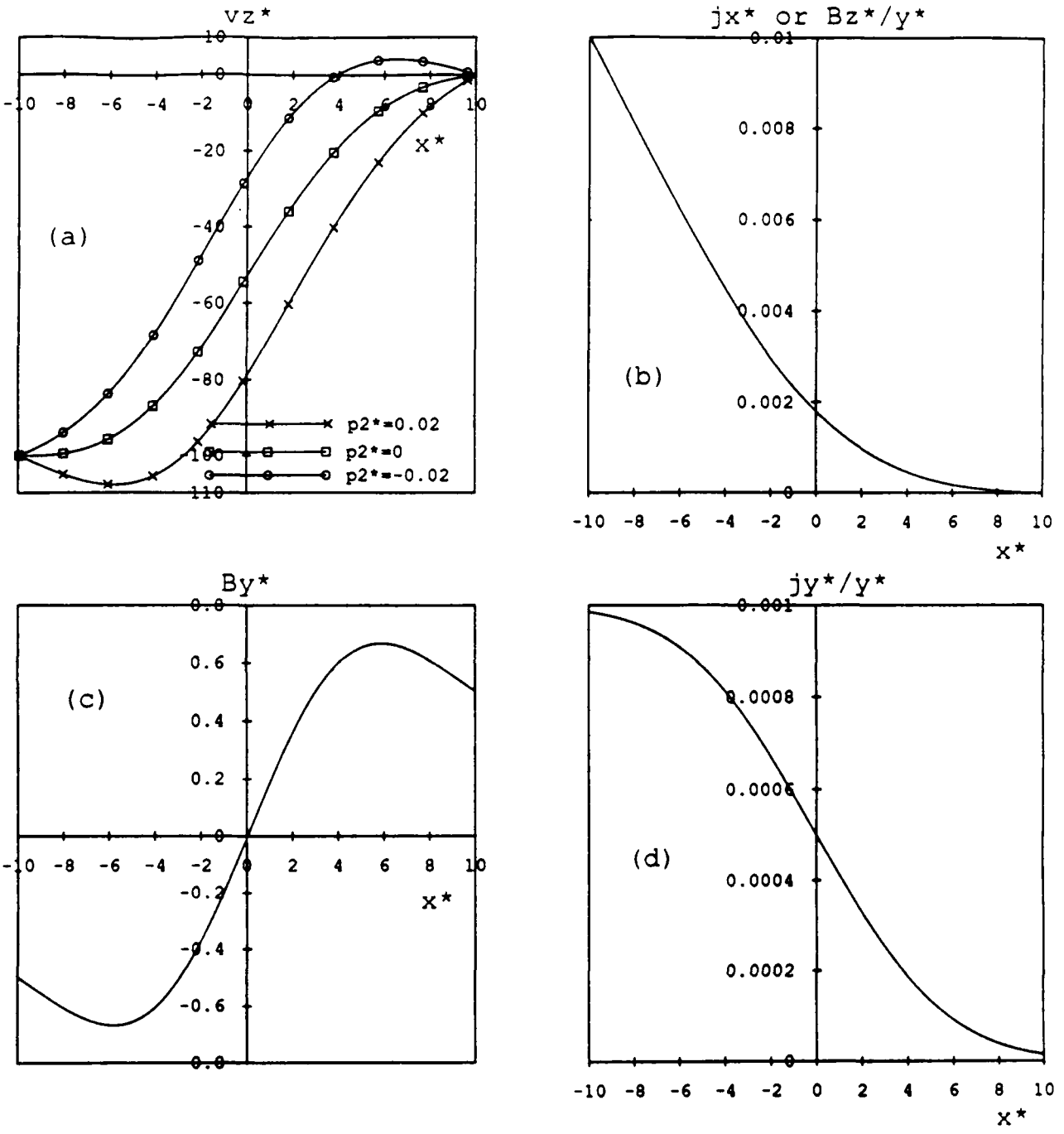

Fig. 11. Plasma flow and magnetic field distributions at the dawn-side magnetopause for Re=Rm=100. (a) Velocity profiles for the flow along the -z axis (the $-X_{GSM}$ axis) for pressure gradient p_2^*= -0.02, 0, and +0.02, (b) current j_x^* or B_z^*/y^* profile, (c) main field By* profile, and (d) current j_y^* profile.

STEADY MAGNETIC FIELD RECONNECTION

B. U. Ö. Sonnerup, J. Ip, and T.-D. Phan

Thayer School of Engineering, Dartmouth College, Hanover, New Hampshire

Abstract. A brief overview is presented of steady two dimensional magnetic field reconnection, with emphasis on recent developments. First, comments are made on difficulties in arriving at a satisfactory rigorous definition of the reconnection phenomenon which retains the traditional topological aspects of the magnetic field as an integral part. Analytical models of magnetic field annihilation and magnetic field reconnection are then reviewed with emphasis on the description of flux pile up as well as on the structure of exit jets and of vortex layers forming at magnetic separatrices. In particular, a new exact analytic incompressible MHD solution, illustrating flux pile up in the inflow, is presented. A brief discussion is then given of numerical simulation results. Finally, comments are made on the importance of two-fluid effects in the immediate vicinity of the reconnection site, in the so-called diffusion region.

1. Introduction

The classical concept of magnetic field reconnection in a highly conducting plasma is illustrated in Figure 1. Plasma elements in magnetic cell #1, linked together by a strong magnetic field, B_1, move slowly to the right with speed $v_1 = E_0/B_1$. At the same time, plasma elements in magnetic cell #2, linked together by a strong but oppositely directed field, B_1, move slowly to the left, again with speed $v_1 = E_0/B_1$. The motion occurs as a result of the reconnection electric field, E_0, directed out of the plane of the paper, and the speed of motion is small because B_1 is large (in a 2D steady state, E_0 is the same everywhere, as a consequence of Faraday's law). An encounter and subsequent relinking of pairs of oppositely directed magnetic field lines and the plasma located on them occurs at the X-type magnetic null point at the center of the figure. The relinking is made possible by finite electrical resistivity, which serves to break the frozen magnetic-field condition in a small volume, called the diffusion region, around the null point. The result of the relinking is that reconnected magnetic field lines and plasma elements of different origin (cells #1 and 2) leave together at a high speed $v_2 = E_0/B_2$ in magnetic cells #3 and 4. The speed v_2 is large because the magnetic field B_2 is weak. In this sense, reconnection may be thought of as a process that converts, on a continuous or intermittent basis, the high magnetic energy and low plasma kinetic energy in cells #1 and 2 to a state of low magnetic energy and high plasma kinetic energy in cells #3 and 4. In addition, realistic treatments of the process indicate that the thermal energy of the plasma is also increased as it enters the exit flow cells #3 and 4. The pairwise symmetry of cells #1 and 2 and #3 and 4 in the figure is not required and the process may operate also in the presence of a "guide" magnetic field, $B_\parallel$, perpendicular to the plane of the figure.

As indicated in Figure 1, an analogy exists between reconnection and some of the interactions between solar and magnetospheric physicists sought at the present meeting. The reconnection electric field that drives the two research communities together at Bermuda is provided by conference organizers E.R. Priest and C.T. Russell in the solar and the magnetospheric cells, #1 and 2 respectively, while the reconnection process itself is brought about by certain activities of the third conference organizer, L.C. Lee, in the diffusion region (Hamilton). We know that merely pushing the two research communities together does not guarantee that strong interaction and relinking will occur. The same holds true for differently magnetized plasma regions: magnetic reconnection between them often occurs only reluctantly and at low rates although in special circumstances, poorly understood at present, the process is thought to proceed rapidly, even explosively.

Magnetic reconnection is expected to play an important role in flux rope physics. As illustrated in Figure 2, it can be responsible for: (a) the generation of flux ropes via the tearing instability in the presence of a guide magnetic field, $B_\parallel$, along the current; (b) the coalescence of flux ropes via the coalescence instability; (c) the relinking and

Geophysical Monograph 58

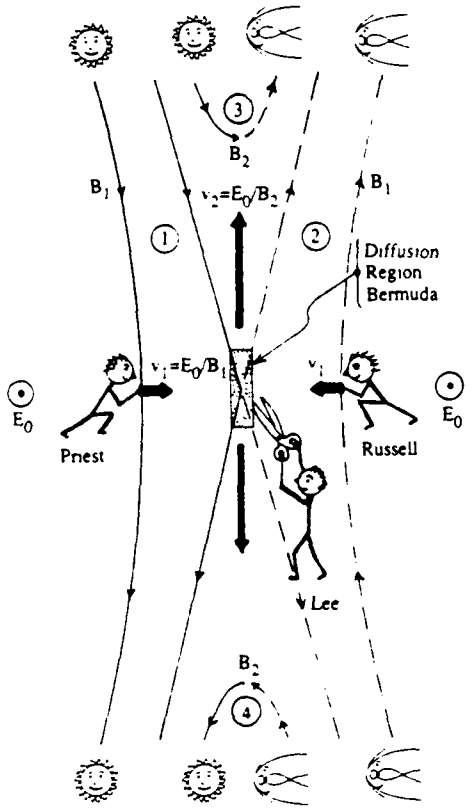

Fig. 1. Schematic drawing showing basic aspects of the magnetic field reconnection process.

unlinking of flux ropes; and (d) the restructuring of a flux rope via the internal kink mode.

In this paper, a brief discussion is presented of certain aspects of steady or quasi-steady reconnection; dynamic aspects are dealt with in the review by Schindler and Otto (1989; this conference); turbulent aspects are discussed by Lysak and Song (1989; this conference). The paper is organized as follows. We first comment briefly on the definition of reconnection, an area where certain important developments have occurred recently. We then summarize the main properties of existing 2D analytical models of reconnection, including a recent unification of those models provided by Priest and Forbes (1986). Numerical simulations are then examined which have brought to light new and, in part, unexpected features of the reconnection process, among them the formation of vortex layers at magnetic separatrices. Finally, we comment briefly on the physical processes in the diffusion region which may allow reconnection to occur even in a collisionless plasma. This outline of the paper has substantial similarities to that of a recent review article on steady state reconnec-

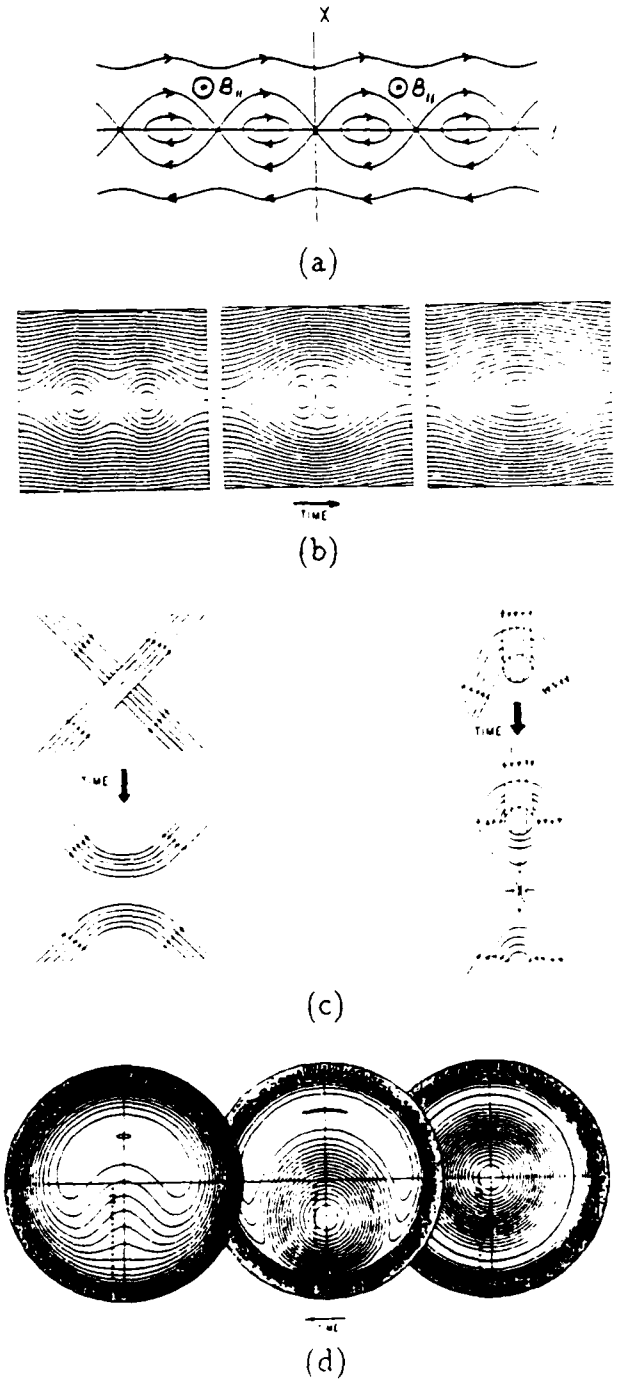

Fig. 2. Role of reconnection in flux rope physics (*a*) Flux ropes generated by tearing instability in the presence of a guide field, $B_{\parallel}$; (*b*) coalescence of flux ropes [after Pritchett and Wu, 1979]; (*c*) relinking and unlinking of flux ropes; (*d*) rearrangement of internal flux rope structure by the internal kink instability [from Park et al., 1984].

tion Sonnerup, 1988; hereafter referred to as Paper I. For that reason, the present account is brief and from time to time the reader will be referred to the earlier article for details.

2. Definition

One of the first formal definitions of reconnection was provided by Vasyliunas [1975] who stated that "magnetic field line merging, or reconnection, is the process whereby plasma flows across a surface that separates regions containing topologically different magnetic field lines. The magnitude of the plasma flow is a measure of the merging rate." The separating surface referred to in the definition is called a separatrix: the field lines forming the X in Figure 1 delineate two such surfaces orthogonal to the plane of the figure. Later, the working group on reconnection at the Coolfont Workshop [Butler and Papadopoulos, 1984] agreed on a slightly different, but for practical purposes equivalent definition: "magnetic field reconnection occurs in a plasma whenever an electric field, $E_\parallel \equiv E_0$ in Figure 1c, is present along a magnetic separator, i.e., along a line of intersection of two separatrix surfaces which divide space into different magnetic cells...". The separator in Figure 1 is a straight line through the center point of the X and at right angles to the plane of the figure; it is often referred to as the X line.

Both of the above definitions are based on topological properties of the magnetic field, namely, the separatrices and the separator. Except in special cases, such as the purely 2D case with $B_\parallel \equiv 0$, these properties cannot be ascertained locally but require reference to null points in the magnetic field, points that may be located at large distances from the place where reconnection is being observed or examined. The importance of these nulls has been discussed recently by Greene [1988]. An illustration of magnetic cells, separatrix surfaces, separators and null points is shown in Figure 3 where a cross section is depicted of the field configuration obtained by superposition of a dipole field and a uniform field at right angles to the dipole moment vector. Two X type magnetic null points (see Dungey [1963] for a precise definition) are located at X_1 and X_2 in the plane of the figure. They are connected by a circular [Yeh, 1976] field line that lies in a plane perpendicular to that of the figure. Note that this special field line is located at the intersection of separatrix surfaces that separate three distinct magnetic cells. Thus it comprises the separator in this configuration. At an arbitrarily chosen point on the separator, there is a nonvanishing value, $B_\parallel$, of the parallel magnetic field in general; only at X_1 and X_2 is that field absent. At such an arbitrary location, it does not seem possible to uniquely identify a field line as being the separator without following it in both directions to assure that one ultimately reaches points X_1 and X_2. In the same way, identification

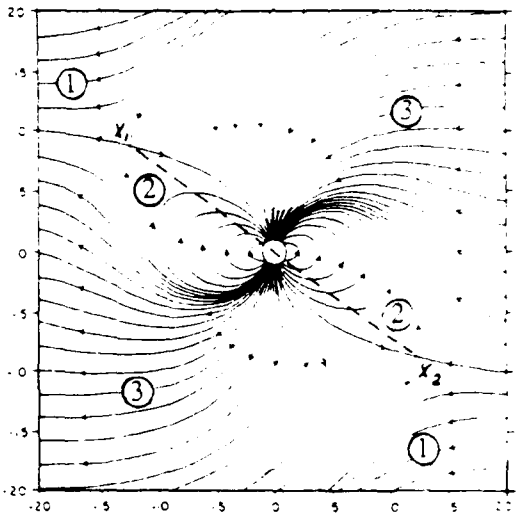

Fig. 3. Magnetic field lines in the meridional plane containing the null points X_1 and X_2 for a uniform horizontal field superimposed on a vertical 3D dipole. Dashed line is the separator circle, viewed edge on (after Cowley, 1973).

of a separatrix surface cannot be done locally but requires an excursion along two neighboring field lines located in the presumed separatrix surface until those two lines meet at X_1 or at X_2. Two dimensional configurations such as the one shown in Figure 1, but with an added transverse constant field component, $B_\parallel$, or toroidal configurations such as tokamaks, have the further difficulty that no null points exist which can form the basis for a unique definition of separator and separatrices. Similar difficulties may arise in many space applications of reconnection, e.g., in plasmoid formation in the geomagnetic tail.

A local definition of reconnection, i.e., a definition that does not depend on finding, possibly distant, null points in the **B** field would be desirable since it seems somewhat questionable whether the local dynamics associated with the reconnection process could be controlled by these distant nulls. An attempt to provide such a local definition that retains the topological aspects of the field consists of examining the local magnetic field topology in a plane perpendicular to a chosen field line, as discussed in some detail in Paper I (see also Podgorny [1986] and Priest and Forbes [1989]). If the field topology in that plane is hyperbolic, then the field line is a potential separator line. However, it turns out that this procedure does not provide a unique separator; typically, entire regions in space will contain potential separator field lines (e.g., in the field $B_x = ay$; $B_y = bx$; $B_z = B_0$, all field lines display the required hyperbolic topology). In Figure 1, say, reconnection then ceases to be localized at the origin when $B_\parallel \neq 0$

but occurs in the entire diffusion region, i.e., wherever the electric field has a component along **B**.

The difficulties described above can be circumvented by adopting a more general definition of reconnection that does not involve the topology of the magnetic field at all. Thus Axford [1984] described reconnection as "a localized breakdown of the requirement for 'connection' of elements of fluid at one time on a common magnetic field line." Such breakdown by necessity involves the presence, in a localized region, of an electric field component along **B**. More recently, this idea has been pursued in detail by Schindler et al. [1988] and Hesse and Schindler [1988] who define what they call 'general magnetic reconnection' (GMR) as "the breakdown of magnetic connection due to a localized nonidealness." They have established that such breakdown occurs if and only if the quantity

$$\mathbf{U} \equiv \mathbf{B} \times [\nabla \times (\mathbf{E} + \mathbf{v} \times \mathbf{B})] \neq 0 \,. \tag{1}$$

This broader definition includes all cases, such as the ones depicted in Figures 1 and 2, which we have traditionally associated with the term reconnection, but also cases that are rather different. An example of GMR that does not involve the usual hyperbolic field topology is shown in Figure 4 where a flux rope configuration for which

$$\left.\begin{aligned} \mathbf{B} &= \hat{\phi}\mu_0\sigma_2\omega B_0 R^3/8h + \hat{\mathbf{z}}B_0 \\ p &\simeq p_0 - \mu_0(\sigma_2\omega B_0)^2 R^6/96h^2 \end{aligned}\right\} \tag{2}$$

is depicted. Here B_0 and p_0 are constants representing the uniform axial magnetic field and the plasma pressure on the flux tube axis ($R = 0$), respectively. Pressure variations due to fluid motion are neglected. In region 1, i.e., for $z < 0$, the electrical conductivity is assumed infinite and there is no plasma motion so that $\mathbf{v}_1 = \mathbf{E}_1 = 0$. In region 3, i.e., for $z > h$, the conductivity is again infinite

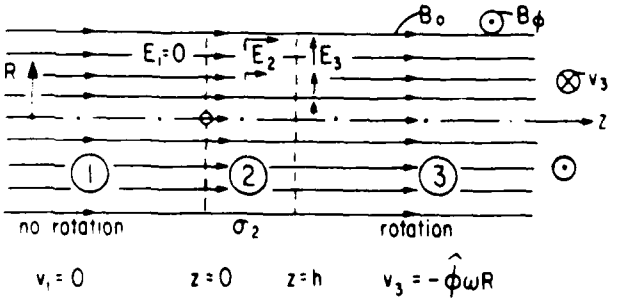

Fig. 4 Flux rope having a twisted magnetic field, (B_ϕ, B_z), given by equation (2). The plasma in region 1 is infinitely conducting and stationary; the plasma in region 3 is also infinitely conducting but is in solid body rotation about the z axis. General reconnection occurs in region 2 where the conductivity is finite

but this portion of the flux rope is in solid-body rotation at angular rate ω about its axis so that

$$\left.\begin{aligned} \mathbf{v}_3 &= -\omega R\hat{\phi} \\ \mathbf{E}_3 &= \omega R B_0 \hat{\mathbf{R}} \end{aligned}\right\} \tag{3}$$

In the intervening region 2, $h > z > 0$, the conductivity, σ_2, is large but finite and the plasma velocity and the electric field are

$$\left.\begin{aligned} \mathbf{v}_2 &= -(z/h)\omega R\hat{\phi} \\ \mathbf{E}_2 &= (z/h)\omega R B_0 \hat{\mathbf{R}} + (\omega R^2/2h)B_0\hat{\mathbf{z}} \end{aligned}\right\} \tag{4}$$

The electric field is curl free everywhere, as required, but there is a positive volume charge density in region 2 as well as positive and negative surface charges at $z = 0$ and at $z = h$, respectively, so that this region has the appearance of an electrical double layer plus a net charge. There is an electric field component along **B** in region 2 and the quantity $\mathbf{U}_2 = (\omega R/h)B_0^2\hat{\mathbf{R}} \neq 0$ so that, according to the Schindler et al. definition, reconnection does indeed take place throughout region 2 (except at $R = 0$) as a result of the localized resistive nature of the plasma in that region.

The type of behavior illustrated in Figure 4 is particularly relevant to this conference because it would allow a segment of a strongly twisted flux rope to untwist itself, thereby releasing magnetic energy, a mechanism that has been discussed by P. Carlqvist [1969] in connection with solar flares. But at the same time, we point out that the nature and dynamics of this type of reconnection appears rather different from those of the configuration in Figure 1. Thus the wisdom of using the same name for both cases may be questioned. At present, we tend to prefer the more traditional, topologically based definitions even though they have certain shortcomings. To quote Supreme Court Justice Potter Stewart (in Jacobellis v. Ohio, 1964) "I shall not today further attempt to define the kinds of material I understand to be embraced within that shorthand description; and perhaps I could never succeed in intelligibly doing so. But I know it when I see it, ..."

3 Magnetic Field Annihilation Models

In the usual reconnection configuration, magnetic flux is transported from two magnetic cells (cells #1 and 2 in Figure 1) into two other cells (#3 and 4 in Figure 1) in which the magnetic field lines are differently connected. In the special case of field annihilation the angle occupied by the two exit cells (#3 and 4), which is also the angle between the separatrices, has been collapsed to zero which means that antiparallel magnetic flux is carried from cells #1 and 2 towards the current sheet (the yz plane) separating them where the flux is resistively annihilated. The

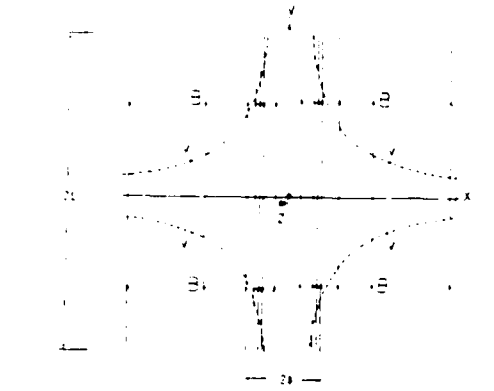

(a)

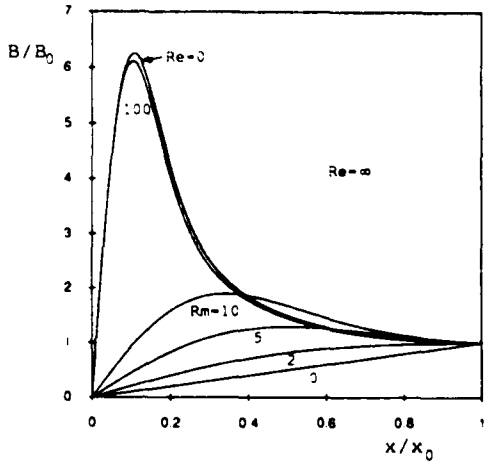

(b)

Fig. 5. Magnetic field annihilation (Sweet-Parker like) models. (*a*) Stagnation point flow [after Sonnerup and Priest, 1975]; (*b*) magnetic field profiles from equation (11) for flow between two fluid emitting walls at $x = \pm x_0$ where $\mathbf{v} = \mp\hat{\mathbf{x}}U_0$.

resulting field annihilation configuration is shown in Figure 5a. In this figure, plasma inflow occurs from the left and right in broad regions (length = $2L$) and with a small velocity $v_1 = E_0/B_1$ that exactly equals the diffusion velocity $1/\mu_0\sigma\delta$, based on the electrical conductivity, σ, in the current sheet and on the half width, δ, of the sheet. Outflow in the $\pm y$ direction occurs in the narrow region (thickness = 2δ) occupied by the current sheet. The outflow along the y axis is accelerated from $v_y = 0$ at the stagnation point (at $x = y = 0$) to $v_y = v_2 = B_1/\sqrt{\mu_0\rho} \equiv v_{A1}$ at the "exit" sections, $y = \pm L$, where the plasma pressure is assumed to be the same as in the inflow, i.e., $p_2 = p_1$.

The acceleration along the current sheet is effected by the pressure gradient, $\partial p/\partial y$, associated with the excess pressure, $p_0 = p_1 + B_1^2/2\mu_0$, at the stagnation point. The key formula describing this model, due to Sweet [1958] and Parker [1957, 1963], is

$$M_{A1} \equiv v_1/v_{A1} = S_1^{-1/2} \tag{5}$$

where $v_{A1} = B_1/\sqrt{\mu_0\rho_1}$ is the Alfvén speed in the inflow and $S_1 \equiv \mu_0\sigma v_{A1}L$ is the Lundquist number based on the length L of the current sheet. This formula is easily obtained from mass conservation and Bernoulli's equation along with Ampère's and Ohm's laws, as reviewed in Paper I. The Alfvén Mach number M_{A1} is a commonly used nondimensional measure of the reconnection rate. Since the Lundquist number is very large in most cosmic applications, mainly on account of assumed large values of L, the predicted reconnection rate is very small. However larger rates can be achieved if the plasma can find a way to generate an effective scale much smaller than L, the overall size of the reconnection configuration in the y direction or to generate a smaller value of v_{A1}. This is exactly what is assumed to happen in the Petschek model and other reconnection models, to be discussed presently. Note however that a decrease in v_{A1}, while increasing M_{A1}, in fact leads to a decrease in the actual inflow speed, v_1, as well as in the reconnection electric field, E_0.

The configuration discussed above incorporates the basic assumption of uniform flow and field conditions in the upstream regions. This is not necessarily what will occur: the velocity v_∞ and magnetic field B_∞ far upstream may differ from those (v_1 and B_1) immediately adjacent to the current sheet, as long as $E_0 = -v_1B_1 = -v_\infty B_\infty$ remains constant. For incompressible flow we may thus rewrite equation (5) in the form

$$M_{A\infty} = \frac{v_\infty}{v_{A\infty}} = \frac{B_1}{B_\infty}\,\frac{1}{\sqrt{\mu_0\sigma v_{A\infty}L}} \tag{6}$$

If we think of $v_{A\infty}$ and L as fixed, then an increase in v_∞ (or equivalently E_0) means an increase in $M_{A\infty}$: this can only be accomplished by increasing B_1/B_∞, an effect referred to as flux pile up. An important consequence of the above is that the upstream measure of the reconnection rate, $M_{A\infty}$, is different from the reconnection rate, M_{A1}, evaluated adjacent to the diffusion region, namely

$$M_{A1} = M_{A\infty}(B_\infty/B_1)^{3/2} \tag{7}$$

Thus, flux pile up corresponds to $M_{A1} < M_{A\infty}$. Furthermore, for fixed L, an increase in $M_{A\infty}$ by a factor k, say, simply leads to an increase in B_1/B_∞ by the same factor and an associated decrease of M_{A1} by a factor $k^{1/2}$.

The flux pile up effect is a prominent feature of the 2D MHD stagnation point flow depicted in Figure 5a and

studied by Parker [1973] as well as by Sonnerup and Priest [1975]. The latter authors demonstrated that exact solutions of the incompressible MHD equations could be obtained for the type of straight field-line configuration shown in Figure 5a when the flow field is of the form $v_x = -k_1 x$; $v_y = k_2 y$; $v_z = k_3 z$ with $(-k_1 + k_2 + k_3) = 0$. These solutions are reviewed in Paper I. Here we discuss instead a new exact 2D field annihilation solution where a somewhat different flow configuration is used, namely unidirectional uniform inflow $\mathbf{v} = \mp U_0 \hat{\mathbf{x}}$ at two upstream boundaries $x = \pm x_0$ (this set of boundary conditions was brought to our attention by M. F. Heyn in a private communication). This solution, along with the stagnation point flows mentioned above, are members of a general class of 2D and 3D field annihilation solutions in which the magnetic field lines remain straight and parallel to the current sheet. The viscous momentum equation governing the velocity field (here assumed two dimensional for simplicity) is given by

$$R_e^{-1} f''' = f'^2 - f f'' + \kappa \tag{8}$$

where $v_x = -U_0 f(s)$, $v_y = U_0 (y/x_0) f'(s)$ and the constant $\kappa \equiv (x_0^2/\rho U_0^2 y)(\partial p/\partial y)$. Also, $R_e \equiv U_0 x_0/\nu$ is the viscous Reynolds number, based on the ordinary newtonian kinematic viscosity, ν, and a prime denotes differentiation with respect to the variable $s \equiv x/x_0$. Equation (8), with the boundary conditions $f = f'' = 0$ at $s = 0$ and $f = 1$, $f' = 0$ at $s = \pm 1$, has simple solutions both for $R_e \to \infty$ and for $R_e \to 0$:

$$\left.\begin{aligned} f &= \sin \pi s/2 \\ \kappa &= -\pi^2/4 \end{aligned}\right\} \quad R_e \to \infty \tag{9}$$

$$\left.\begin{aligned} f &= (3s - s^3)/2 \\ \kappa &= -3/R_e \end{aligned}\right\} \quad R_e \to 0 \tag{10}$$

The corresponding magnetic field profiles, obtained from Ohm's law, are given by

$$B_y = (E_0 R_m / U_0) e^{-R_m I(s)} \int_0^s e^{R_m I(\tilde{s})} d\tilde{s} \tag{11}$$

where $R_m \equiv \mu_0 \sigma U_0 x_0$ is the magnetic Reynolds number and

$$I(s) \equiv \int_1^s f(\tilde{s}) d\tilde{s}$$

The relation between the reconnection electric field, E_0, and the magnetic field, B_0, at $x = \pm x_0$ is

$$B_0 = (E_0 R_m / U_0) \int_0^1 e^{R_m I(\tilde{s})} d\tilde{s}$$

The pressure distribution is given by a Bernoulli-type formula:

$$p = p_0 - \frac{\rho}{2}(v_x^2 + v_y^2) - B_y^2/2\mu_0 \tag{12}$$

A plot of the magnetic field, B_y, given by equation (11) is shown in Figure 5b for several different values of the magnetic Reynolds number but with $R_e = \infty$. The flux pile-up effect is clearly evident in this diagram for $R_m = 5$, 10, and 100. In fact, the pile up becomes infinite as $R_m \to \infty$.

A second point to note is that the influence of finite R_e on these results is minimal, as shown by comparison of the curve for $R_m = 100$ labelled $R_e = 0$ with the curve for $R_m = 100$ having $R_e = \infty$. The reason for this small difference is that the two velocity distributions $v_x = -U_0 f(s)$ given by equations (9) and (10) for $R_e = \infty$ and $R_e = 0$, respectively, differ by only 2% in the region $0 \le |s| \le 1$. Since it is v_x that enters the term $\mathbf{v} \times \mathbf{B}$ in Ohm's law, the influence of the viscous Reynolds number on the magnetic field is correspondingly weak. Thus it is evident that the viscous forces (which vanish identically in the stagnation point flows discussed by Sonnerup and Priest [1975]) play no important role in these symmetric MHD flows toward a current sheet other than that of changing the pressure gradient κ. This latter effect would modify the Sweet-Parker formula, equation (5): on the basis of approximate calculations, Park et al. [1984] conclude that viscous effects reduce the value of M_{A1} by a factor $(1 + \mu_0 \sigma \nu)^{-1/4}$. Note, however, that this result cannot be general since it does not apply to the stagnation point flows mentioned above.

It should be added that the exact solutions discussed above are valid only for incompressible flow. In that limit, time-dependent versions can also be generated (e.g., Gratton et al., 1988]. For the compressible case, no exact solutions have been found: it appears that the field lines cannot remain straight and parallel to the yz plane in that case. On the other hand, the case of self-similar decay of a one-dimensional current sheet in a compressible medium has been treated [Kirkland and Sonnerup, 1979].

4. Magnetic Field Reconnection Models

As mentioned already, the principal difficulty in applying the Sweet-Parker formula to cosmic reconnection problems lies in the small reconnection rates obtained for L values comparable to the overall size of a cosmic region in which the reconnection occurs. Perhaps the only way to avoid this difficulty is to assume that the field and flow geometries will adjust themselves automatically in such a fashion that a much smaller effective length, a^*, say, is established and replaces L in equation (5). This is the idea developed by Petschek [1964] who proposed the reconnec-

tion configuration shown in Figure 6a. In this geometry, the Sweet-Parker current sheet, or some refinement of it to allow a magnetic field component $B_x(y)$ to develop gradually as $|y|$ increases, still applies near the origin, in a diffusion region of size $2y^* \times 2x^*$. (Priest and Cowley [1975] have shown that, assuming analytic behavior near $x = y = 0$, $B_x \sim y^3$ in incompressible resistive flow.) In the outflow wedges, the flow in Petschek's model has speed $v_2 \simeq B_1/\sqrt{\mu_0\rho}$ regardless of the reconnection rate; the acceleration of most of the plasma to this velocity cannot be achieved by a pressure gradient $\partial p/\partial y$ (only the plasma flowing through the diffusion region is accelerated in this fashion). Rather Maxwell stresses, concentrated in pairs of standing slow shocks (near the switch-off condition) are responsible for the acceleration.

The qualitative behavior of Petschek's reconnection configuration, as the reconnection rate, $M_{A\infty}$, increases is as follows.

- The outflow speed remains approximately

$$v_2 = B_{1\infty}(\mu_0\rho)^{-1/2}$$

but the angle θ_2 between the slow shocks increases.

- At the same time, the length, $2y^*$, of the diffusion region decreases. The width, $2x^*$, of that region also decreases but rather less rapidly so that the diffusion region becomes smaller and more square in shape as the reconnection rate increases.

The magnetic field and the flow speed, measured at points on the x axis outside the diffusion region, are nearly independent of x for small reconnection rates. However, as $M_{A\infty}$ increases, the field weakens and the flow speed toward the diffusion region increases near $|x| = x^*$. As pointed out by Vasyliunas [1975], this behavior is ascribable to fast-mode expansion in the inflow; it is the opposite of the flux pile up described in the previous section and it leads to $M_{A1} > M_{A\infty}$ where M_{A1} is the Alfvén Mach number measured at $|x| = x^*$. According to Petschek [1964], the field weakening at $|x| = x^*$ limits the reconnection rate to a maximum value given by the formula (as corrected by Vasyliunas [1975])

$$M_{A\infty}^{max} \simeq \frac{\pi}{8}\{\ln(2M_{A\infty}^{max})S_\infty\}^{-1} \qquad (13)$$

At this maximum rate, M_{A1} is expected to be of order unity.

An important point to note is that Petschek's maximum reconnection rate depends on the upstream Lundquist number, S_∞, only logarithmically. Thus the formula (13) predicts maximum rates that far exceed those obtained from the Sweet-Parker formula (5). It is noted

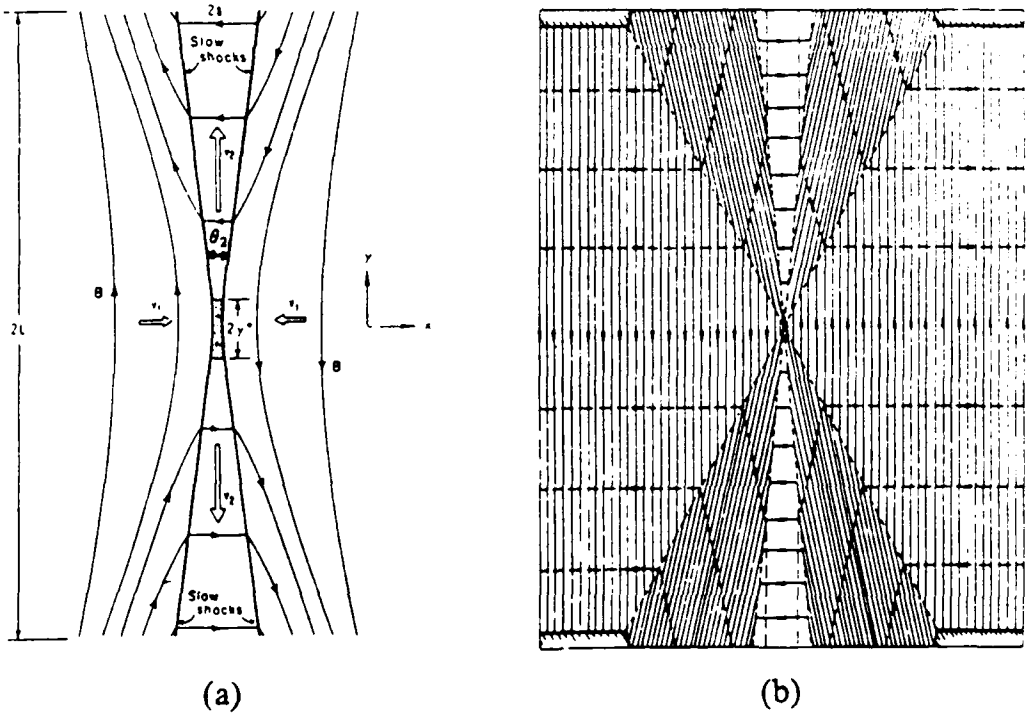

Fig. 6. Reconnection models containing standing slow mode waves. (*a*) Petschek's model [from Petschek, 1964]; (*b*) Sonnerup's model [from Vasyliunas, 1975].

that Petschek employed small perturbation analysis in arriving at equation (13) even though the deviations from the unperturbed state, which consists of oppositely directed uniform magnetic fields in the regions $x > 0$ and $x < 0$, are not small. Thus the formula for the upper limit $M_{A\infty}^{max}$ must be considered approximate.

Petschek's [1964] discussion of the above reconnection configuration also contained the observation that, in incompressible flow, the addition of a constant magnetic field, $B_z = B_{\parallel}$, is allowed without any important change in the analysis or the behavior of the system. In the same paper, Petschek also dealt with the compressible case but only for antiparallel fields; the addition of a B_z component is now not trivial since B_z by necessity is a function of x and y in compressible flow. Nevertheless, such a component is not expected to have a critical influence on the reconnection process, at least not in the MHD limit.

A special case of asymmetric reconnection, applicable to the earth's magnetopause, was discussed by Levy et al. [1964]; more realistic versions of this case have been produced recently [Heyn et al., 1985; Biernat et al., 1989], including a time-dependent model that may be relevant to the formation of flux transfer events and associated flux ropes on the dayside magnetopause [Biernat et al., 1987].

There exists another type of solution to the incompressible reconnection problem that consists entirely of a set of standing slow-mode waves separating wedges of uniform flow and field [Sonnerup, 1970]. This solution is shown in Figure 6b. It is exact exterior to the diffusion region; in the latter, only approximate analysis is available. A basic property of this model is the appearance of slow-mode rather than fast-mode expansion in the inflow. However, the slow-mode expansion is unrealistically confined to a set of standing waves upstream of Petschek's slow shocks and no expansion is present on the x axis so that $M_{A1} = M_{A\infty}$. The maximum reconnection rate in this case is found to be $M_{A1} = (1+\sqrt{2})$. At the maximum rate, conditions are the same in the inflow and outflow wedges so that no energy conversion takes place. More generally, it is believed (but has never been rigorously proved) that values of the Alfvén number, M_{A1}, in the inflow adjacent to the diffusion region, of order unity represent the maximum reconnection rate possible in any reconnection configuration of the general type described in Figure 6.

Approximate compressible, symmetric as well as asymmetric versions of this model have been given by Yang and Sonnerup [1976;1977] who also pointed out the possibility of fast-mode termination shocks in the exit flow wedges. An exact solution in which all slow-mode waves were replaced by rotational discontinuities has been discussed by Hameiri [1978]. In the latter solution, the magnetic field magnitude is constant everywhere and no conversion of energy from magnetic field to plasma occurs, except in the diffusion region.

Recently, Priest and Forbes [1986] have produced a unified linear perturbation theory of steady 2D reconnection which provides insight into the interrelationship between the various reconnection models discussed above. These authors started with an unperturbed stationary state in which the magnetic field is uniform and directed to the right in the upper half of a square box and uniform but directed to the left in the lower half of that box. A concentrated current sheet separates the two halves. A small electric field, E_0, is then introduced to drive the plasmas in the two halves of the box toward each other; the perturbation procedure used can be viewed as an expansion in powers of this field or, equivalently, in powers of the reconnection rate. The method of expansion is equivalent to the perturbation analysis performed by Petschek [1964]. To lowest order, the expansion leads to a Poisson equation for the perturbation magnetic vector potential in which the nonhomogeneous term, the perturbation current, is a function only of the coordinate perpendicular to the current sheet. Therefore this current in fact can be specified as a boundary condition. The equation is solved by separation of variables and a large variety of solutions, the nature of which depends on the boundary conditions, are possible. The most interesting aspect of the analysis is that it allows, for the first time, a systematic insight into the role played by the boundary conditions in determining the nature of the plasma inflow toward the current sheet. The diffusion region as well as the outflow wedges, the latter being extremely narrow on account of the assumed small reconnection rate, are not treated in detail but have the same character as in the original Petschek calculation. Behavior in the inflow ranging from slow-mode compression to fast-mode and slow-mode expansion and, in the extreme, to flux pile up can be readily generated. Petschek's configuration is included among the solutions as is the case of pure slow-mode expansion, although this expansion occurs in a distributed manner rather than being concentrated into the standing waves shown in Figure 6b. Even the Sweet-Parker solution and the case of stagnation point flow, with its associated extreme flux pile up, can be identified. Illustrations of the type of field and flow maps obtained from the analysis are shown in Figure 7.

The structure of the outflow regions associated with reconnection cannot be obtained from linear analysis. Recently, this problem has been studied in detail by use of the boundary layer approximation [Sonnerup and Wang, 1987]. In this manner a family of self similar incompressible solutions describing the flow and field in such reconnection layers was obtained. The layers, which are nondissipative, are bounded by two slow-mode standing waves in which all the dissipation is concentrated. One member of the family of solutions has precisely the same structure as that assumed in Petschek's analysis; other members cor-

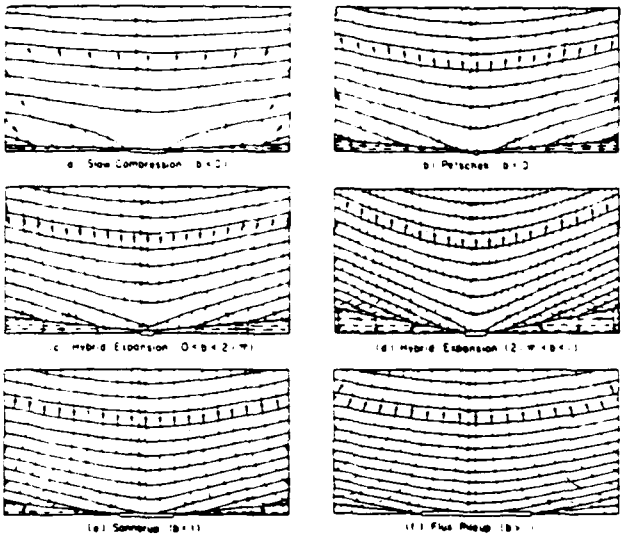

Fig. 7. Magnetic field lines (solid lines) and streamlines (dashed lines) resulting from small perturbation analysis by Priest and Forbes for magnetic Reynolds number = 500, based on inflow conditions and box size. Rectangle at bottom of each frame shows size of diffusion region. The quantity b measures the current density in the inflow [from Priest and Forbes, 1986]

respond to different overall reconnection geometries, e.g., reconnection at a Y type magnetic null. In this latter case, it appears that the reconnection layer, rather than being wedge shaped, can have a constant thickness. An example of this type of layer is shown in Figure 8. An

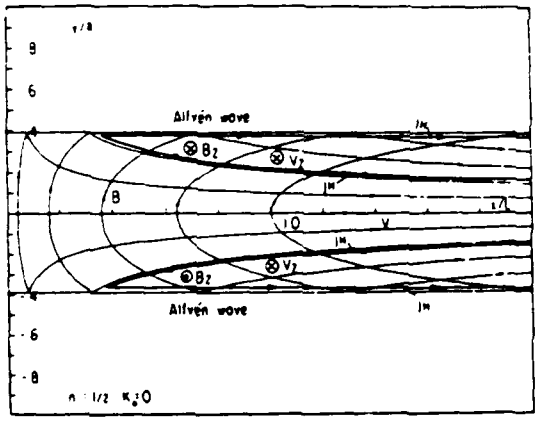

Fig. 8. Magnetic field and streamlines in a self similar incompressible reconnection layer having width independent of x. By interchange of field lines and streamlines, a vortex layer surrounding a magnetic separatrix is obtained. Also shown are Hall current loops, j_H, in the xy plane and associated transverse components, B_z and v_z, of field and flow [from Sonnerup and Wang, 1987].

interesting feature of the reconnection layer solutions is that, in the nondissipative equations describing them, the magnetic field and the velocity field appear in an essentially symmetrical fashion. Therefore these two fields can be interchanged so that the magnetic field lines in Figure 8 become the streamlines and vice versa. If this is done, one finds that plasma flow across a magnetic separatrix appears to be associated with sharp bends in the streamlines, i.e., with the presence of a layer of strong vorticity, centered at the location of the separatrix. The role played by these magnetic separatrix layers and by the reconnection layer is shown schematically in Figure 9 for the case of reconnection at a Y type magnetic null point. It is expected that separatrix layers could occur also in other reconnection configurations, including the usual Petschek geometry. However, the linear analysis performed by Petschek [1964] and by Priest and Forbes [1986] does not permit of such layers. Thus it is not clear that the results of these linear analyses are meaningful, except for very small reconnection rates. In particular, it is not clear that linear analysis can be used to properly predict the maximum reconnection rate, as was done in obtaining equation (13).

The physical reason for the appearance of separatrix layers has been given, e.g., by Soward and Priest [1986] and Schindler and Birn [1987]. As reviewed in detail in Paper I, these layers occur because of the large increase in flux-tube cross section that occurs near a magnetic null point as a tube is convected toward the null. Plasma must flow along the magnetic field toward the weak field region, in order to fill the void and, at least for incompressible flow, this effect will be strong as long as the diffusion region (where the frozen-field condition becomes invalid) is small.

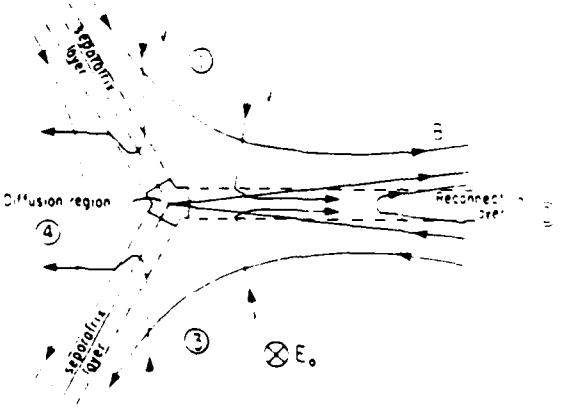

Fig. 9. Schematic drawing of reconnection configuration at a Y-type magnetic null showing how the reconnection layer/separatrix layer solution in Figure 8 would arise [from Sonnerup and Wang, 1987].

5. Numerical Simulations

A fairly large number of numerical simulations of 2D reconnection have been performed to date. These have been reviewed in detail by Forbes and Priest [1987]. Here we mention only three important features of these simulations.

The first point to be made is that it appears fairly difficult to set up boundary conditions such that the precise Petschek configuration emerges, including fast-mode expansion in the inflow. The main feature of Petschek's model, namely the appearance of Alfvénic exit flow jets wedged between slow shocks is seen in a number of driven as well as spontaneous numerical reconnection experiments [e.g., Sato, 1979; Ugai, 1988] but the inflow often has features associated with slow-mode rather than fast-mode expansion. Fast mode termination shocks in the exit flow have been seen in several simulations [e.g., Ugai, 1988].

The second item to be mentioned is that for certain classes of boundary conditions, e.g., those used by Biskamp [1986] and Lee and Fu [1986a,b] the reconnection configuration depends on the reconnection rate in a manner that is exactly opposite from the Petschek model: both the length $2y^*$ and the width $2x^*$ of the diffusion region increase with increasing reconnection rate in these simulations. Increasing reconnection rate also leads to an increasing amount of flux pile up in the inflow. Although it is clear from the work of Priest and Forbes [1986] that this behavior is somehow associated with the particular boundary conditions used in these simulations, a convincing physical explanation for the scaling ($x^* \sim M_{A\infty}$; $y^* \sim M_{A\infty}^{-1}$) observed by Biskamp is not available. And the question of whether real reconnection events occurring on the sun or in the earth's magnetosphere have boundary conditions that will lead to Petschek-like or current-sheet like (Sweet-Parker like plus flux pile up) configurations remains unanswered. However, we note that in a number of geometries where the exit flow is impeded, long diffusion regions, i.e., Sweet-Parker-like behavior seems to be preferred. This appears to be the case in tokamak simulations [Park et al., 1984], in magnetic island coalescence simulations [Pritchett and Wu, 1979], and in simulations of decaying 2D MHD turbulence [Biskamp and Welter, 1989]. The tearing mode also becomes active in such long layers, for $y^*/x^* \geq 10$, say, [Lee and Fu, 1986b; Biskamp, 1986; Biskamp and Welter, 1989].

The third point to be made is that the incompressible simulations of driven reconnection by Biskamp, and to some extent those by Lee and Fu, show strong vortex layers at the magnetic separatrices, much as discussed in the previous section. The outflow wedges between these separatrices are much wider than in the Petschek model and the flow speed there is only a fraction of the Alfvén speed, V_{A1}.

Field and flow maps, taken from the work of Lee and Fu [1986b] and illustrating the behavior described above are shown in Figure 10.

6. Two Fluid Effects

The MHD description of the reconnection process used up to this point in the paper is expected to be adequate, even in the case of a collisionless plasma, provided the characteristic scale sizes for change in plasma flow and field are much larger than the relevant inner plasma scales, viz., the ion and electron inertial lengths, c/ω_{pi} and c/ω_{pe}, and gyroradii, R_{Li} and R_{Le}. If that condition is satisfied the half width, x^*, of the diffusion region will be of the order of the resistive length $\lambda_r = (\mu_0 \sigma_r)^{-1}$, as discussed in section 3. The above condition for use of the MHD description in the diffusion region is then equivalent to the statement that the resistive length must be substantially larger than the inner plasma scales. Note that the resistive length can be nonzero even in a collisionless plasma if microinstabilities are present in the diffusion region to generate a finite effective electrical conductivity. If the resulting value of λ_r is comparable to λ_i and/or R_{Li} but remains much larger than λ_e and R_{Le}, then the MHD description should be improved by inclusion of the Hall

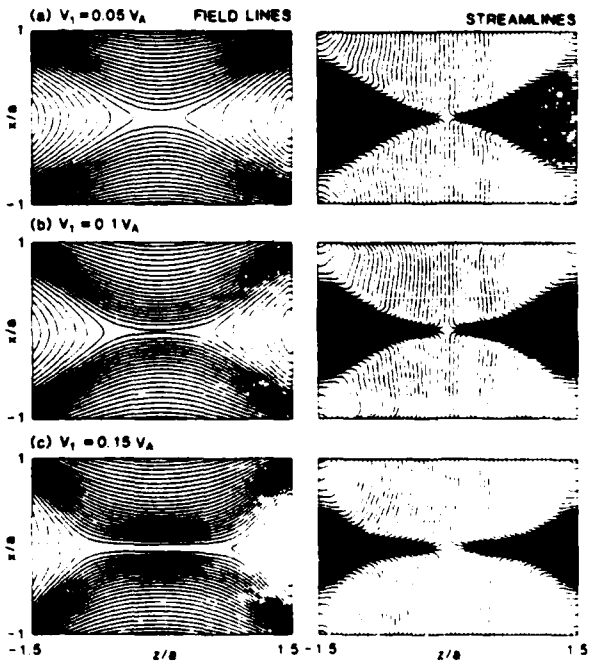

Fig. 10. Formation of a long current sheet as the reconnection rate V_i/V_{A1} (evaluated at $x/a = \pm 1$) increases in incompressible MHD simulation by Lee and Fu. Note also vortex layers at the magnetic separatrices [from Lee and Fu, 1986b].

current term, $\mathbf{j} \times \mathbf{B}/ne$, in Ohm's law so that it has the form

$$(\mathbf{E} - \mathbf{v} \times \mathbf{B}) = \mathbf{j}/\sigma + \mathbf{j} \times \mathbf{B}/ne - \frac{1}{ne} \nabla p_e \qquad (14)$$

as well as by inclusion of an improved version of the ion pressure tensor in the momentum equation to incorporate the effects of finite ion gyroradii (if R_{Li} is comparable to λ_e and λ_i). Neither of these effects has been dealt with in much quantitative detail to date but the role of the Hall term may be understood qualitatively as follows (see also Sonnerup [1979]). If $\nabla \times (\mathbf{j} \times \mathbf{B}/ne)$, with $\mathbf{j} = \hat{\mathbf{z}} j(x, y)$ and $\mathbf{B}$ taken from the MHD solution, vanishes identically, as it does for the field annihilation solutions discussed in section 3, then Hall currents in the xy plane need not flow. The Hall term can then be exactly cancelled by a Hall electric field, provided the boundary conditions permit of the presence of the corresponding Hall potential. If not, Hall currents will flow. A quantitative example of this situation, referring, not to the diffusion region but to a reconnection layer of width comparable to λ_i, is shown in Figure 8. In this particular MHD configuration $\nabla \times (\mathbf{j} \times \mathbf{B}/ne) = 0$ but the condition of constant potential along the slow shocks that form the boundaries of the layer leads to the two Hall current loops in the xy plane shown in the figure. These currents, $\mathbf{j}_H$, are seen to flow along the streamlines but in the opposite sense to the bulk plasma flow. They close by flowing outward along the slow shocks (labelled "Alfvén waves" in the figure). We expect that a set of four such Hall current loops (two in each outflow region) would also be present in the diffusion region but no rigorous analysis producing such loops has been performed. The point we want to emphasize is that such loops will lead to a nonuniform magnetic field component, $B_z(x, y)$, as well as flow, $v_z(x, y)$, in the z direction. There will also be associated electric field components E_x and E_y which were not present in the MHD model. Thus the actual electromagnetic field configuration in the diffusion region and outflow regions would be far more complicated than that indicated in Figure 1.

If the resistive length becomes comparable to, or smaller than λ_e and/or R_{Le}, additional terms, namely the electron inertial terms and the full electron stress tensor, $\mathbf{P}_e$, come into play in Ohm's law which now becomes [e.g., Rossi and Olbert, 1970]

$$\mathbf{E} + \mathbf{v}_e \times \mathbf{B} = \mathbf{j}/\sigma - (1/ne)\nabla \cdot \mathbf{P}_e + (m_e/ne^2)[\partial \mathbf{j}/\partial t + \nabla \cdot (\mathbf{vj} + \mathbf{jv})] \qquad (15)$$

In this version of Ohm's law, the terms $\mathbf{v} \times \mathbf{B}$ and $\mathbf{j} \times \mathbf{B}/ne$ which appear separately in (14) have been combined to form $\mathbf{v}_e \times \mathbf{B}$, where $\mathbf{v}_e$ is the electron fluid velocity. It is then seen that unfreezing of the electron fluid from the magnetic field must be accomplished by one or more terms on the right-hand side of (15). If the first of these terms is unable to do this, or is unable to do it alone, then either the off-diagonal electron stress tensor terms or the electron inertial terms must come into play. It can be shown [Sonnerup, 1979] that the latter terms are unable to provide the unfreezing in 2D steady-state cases (their role in 3D stagnation point flows with magnetic field annihilation has been examined by Sonnerup [1979]). That leaves the off-diagonal (gyroviscous) terms in the electron stress tensor. The importance of these terms to collisionless reconnection was first discussed by Vasyliunas [1975].

If terms such as electron gyroviscosity or electron inertia are required to unfreeze the magnetic field from the electrons, then the diffusion region must contain a substructure at the separator of scale size λ_e and/or R_{Le}. This would add further complexity to the electromagnetic structure of the diffusion region. More detailed discussion of two-fluid phenomena in the diffusion region is provided in Paper I. Here we add one more comment: because of an ongoing controversy in magnetospheric physics concerning antiparallel ($B_\parallel = 0$) merging versus so-called component ($B_\parallel \neq 0$) merging, it would be particularly important to evaluate how the unfreezing provided by the three terms on the right-hand side of equation (15) is influenced by the presence of a guide magnetic field, $B_\parallel$, in the z direction.

Questions and Answers

Zelenyi: What can be the maximum potential reconnection rate (and what are the corresponding boundary conditions) for the two counterstreaming plasma flows with antiparallel magnetic fields with a given Mach number and a given resistivity?

Sonnerup: In my view, the maximum reconnection rate, M_{AI}, evaluated in the inflow region immediately outside the diffusion region, is of order unity. This result is given for the unified theory provided by Priest and Forbes (1986) and also in the self-similar MHD reconnection geometry (Sonnerup, 1970) where the value $M_{AI} = 1 + \sqrt{2}$ was obtained.

Atkinson: In a paper to be given on Thursday, I will be presenting a model which proposes that the Alfvén waves you discussed propagate to the ionosphere and become auroral arcs. I will also present experimental observations which strongly support the idea that there is a one-to-one relationship between arcs and X-lines.

Sonnerup: I shall be very interested in hearing about these new results.

Schindler: I should like to explain why there is a close relationship between the configuration that you referred to as a "double-layer" and more conventional reconnection fields. Consider a situation where the electric field is parallel to the magnetic field, varying in the perpendicular direction such that $\nabla \times \mathbf{E} \neq 0$.

Then there is a time-dependent magnetic field component which has the effect of magnetic shear. The whole process may be described as relaxation of the shear, similar to classical resistive instabilities that are conventionally seen as reconnection processes.

Sonnerup: The electric field that was shown in my example is curl-free, so that I do not see that this comment is applicable.

Greene: Why should a separator be a local quantity? One can imagine that behavior is forced to be two-dimensional by Alfvén waves traveling along the separator. Thus, the two-dimensionality might depend on the nonlocal behavior of Alfvén waves.

Sonnerup: The nonlocal effects you describe could be operative, in particular, in a low-β and low Mach number plasma. But when one considers the actual behavior of the magnetic field in the magnetopause, one finds it to be extremely complicated and often turbulent. In such circumstances, it is hard for me to believe that null points located on the flanks of the magnetosphere could dictate the behavior of the reconnection process near the subsolar point. In my view, such null points would be simply blown downstream by the magnetosheath flow. On the other hand, a magnetic null point trapped in the cusp can probably influence reconnection occurring along a reconnection line originating in the cusp and extending downstream in the manner observed in the 3-D numerical simulations performed by Fedder and Lyon (this conference). In that case, the steady-state induction equation,

$$\mathbf{v} \cdot \nabla \left(\frac{\mathbf{B}}{\rho} \right) = \frac{\mathbf{B}}{\rho} \cdot \nabla \mathbf{v}$$

leads to the generation of a true magnetic null line originating in the cusp as proposed a number of years ago by Nancy Crooker (1979). It should be added that magnetic null points do not occur in the tearing mode when a magnetic field component along the current is present. Thus, a separator line cannot be identified by first finding the magnetic nulls. Yet, we would like to consider tearing of this type as a form of reconnection.

Forbes: Can the vorticity layers along the separatrices be considered as discontinuities? If so, what determines their thickness, and what type of discontinuities are they?

Sonnerup: Yes, I think they could be considered as discontinuities, but they are of a new type different from either shocks or rotational and tangential discontinuities. The vortex layers are two-dimensional and, consequently, they are not included in the usual set of one-dimensional discontinuities. I believe their strength and thickness are determined non-locally, by the field geometry and the effectiveness of field-line diffusion near the magnetic null point.

Acknowledgments. The research was supported by the National Science Foundation, Atmospheric Sciences Division, under grant ATM-8807645, and by the Air Force Geophysics Laboratory, under contract F19628-87-K0026.

References

Axford, W. I., Magnetic reconnection, in *Magnetic Reconnection in Space and Laboratory Plasmas*, *Geophys. Monogr. Ser.*, vol. 30, edited by E. W. Hones, Jr., pp. 1-8, AGU, Washington, D.C., 1984.

Biernat, H. K., M. F. Heyn, and V. S. Semenov, Unsteady Petschek reconnection, *J. Geophys. Res.*, *92*, 3392-3396, 1987.

Biernat, H. K., M. F. Heyn, R. P. Rijnbeek, V. S. Semenov, and C. Farrugia, The structure of reconnection layers: Application to the earth's magnetopause, *J. Geophys. Res.*, *94*, 287-298, 1989.

Biskamp, D., Magnetic reconnection via current sheets, *Phys. Fluids*, *29*, 1520-1531, 1986.

Biskamp, D., and H. Welter, *Dynamics of Decaying Two-Dimensional Magnetohydrodynamic Turbulence*, Max-Planck-Inst. f. Plasmaphysik, Report IPP 6/279, to appear, *Phys. Fluids B*, *1*, 1989.

Butler, D. M., and K. Papadopoulos, eds., *Solar Terrestrial Physics: Present and Future*, NASA Ref. Publ. 1120, 1984.

Carlqvist, P., Current limitation and solar flares, *Solar Phys.*, *7*, 377-392, 1969.

Cowley, S. W. H., A qualitative study of the reconnection between the earth's magnetic field and an interplanetary magnetic field of arbitrary orientation, *Radio Sci.*, *8*, 903-913, 1973.

Dungey, J. W., The structure of the exosphere or adventures in velocity space, in *Geophysics: The Earth's Environment*, edited by C. De Witt, J. Hieblot, and L. Le Beau, Gordon and Breach, New York, p. 503, 1963.

Forbes, T. G., and E. R. Priest, A comparison of analytical and numerical models for steadily driven magnetic reconnection, *Revs. Geophys.*, *25*, 1583-1607, 1987.

Gratton, F. T., M. F. Heyn, H. K. Biernat, R. P. Rijnbeek, and G. Gnavi, MHD stagnation point flows in the presence of resistivity and viscosity, *J. Geophys. Res.*, *93*, 7318-7324, 1988.

Greene, J. M., Geometrical properties of three-dimensional reconnecting magnetic fields with nulls, *J. Geophys. Res.*, *93*, 8583-8590, 1988.

Hameiri, E., Compressible magnetic field reconnection, *J. Plasma Phys.*, *22*, 245-256, 1979.

Hesse, M., and K. Schindler, A theoretical foundation of general magnetic reconnection, *J. Geophys. Res.*, *93*, 5559-5567, 1988.

Heyn, M. F., H. K. Biernat, V. S. Semenov, and I. V. Kubyshkin, Dayside magnetopause reconnection, *J. Geophys. Res.*, *90*, 1781-1785, 1985.

Kirkland, K. B., and B. U. Ö. Sonnerup, Self-similar resistive decay of a current sheet in a compressible plasma, *J. Plasma Phys.*, *22*, 289-302, 1979.

Lee, L. C., and Z. F. Fu, A simulation study of mag-

netic reconnection: Transition from a fast-mode to a slow-mode expansion. *J. Geophys. Res.*, *91*, 4551-4556, 1986*a*.

Lee, L. C. and Z. F. Fu, Multiple x-line reconnection, 1, A criterion for the transition from a single x-line to a multiple x-line reconnection, *J. Geophys. Res.*, *91*, 6807-6815, 1986*b*.

Levy, R. H., H. E. Petschek, and G. L. Siscoe, Aerodynamic aspects of the magnetospheric flow, *AIAA J.*, *2*, 2065-2076, 1964.

Lysak, R. L., and Y. Song, Formation of flux ropes by turbulent reconnection, *This Conference*, 1989.

Park, W., D. A. Monticello, and R. B. White, Reconnection rates of magnetic fields including the effects of viscosity, *Phys. Fluids*, *27*, 137-149, 1984.

Parker, E. N., Sweet's mechanism for merging magnetic fields in conducting fluids, *J. Geophys. Res.*, *62*, 509-520, 1957.

Parker, E. N., The solar flare phenomenon and the theory of reconnection and annihilation of magnetic fields, *Astrophys. J., Suppl. Ser.*, *8*, 177-212, 1963.

Parker, E. N., Comments on the reconnection rate of magnetic fields, *J. Plasma Phys.*, *9*, 49-63, 1973.

Petschek, H. E., Magnetic field annihilation, *NASA Spec. Publ., NASA-SP-50*, pp. 425-439, 1964

Podgorny, A. I., *A Longitudinal Magnetic Field in the Vicinity of a Singular Line*, Lebedev Phys. Inst., Preprint 358, Moscow, 1986.

Priest, E. R., and S. W. H. Cowley, Some comments on magnetic-field reconnection, *J. Plasma Phys.*, *14*, 271-282, 1975.

Priest, E. R., and T. G. Forbes, New models for fast steady state magnetic reconnection., *J. Geophys. Res.*, *91*, 5579-5588, 1986.

Priest, E. R., and T. G. Forbes, Steady magnetic reconnection in three dimensions, *Solar Physics*, *119*, 211-214, 1989.

Pritchett, P. L., and C. C. Wu, Coalescence of magnetic islands, *Phys. Fluids*, *22*, 2140-2146, 1979.

Rossi, B., and S. Olbert, *Introduction to the Physics of Space*, McGraw-Hill, New York, p. 348, 1970.

Sato, T., Strong plasma acceleration by slow shocks resulting from magnetic reconnection, *J. Geophys. Res.*, *84*, 7177-7189, 1979.

Schindler, K., and J. Birn, On the generation of field-aligned plasma at the boundary of the plasma sheet, *J. Geophys. Res.*, *92*, 95-103, 1987

Schindler, K., M. Hesse, and J. Birn, General magnetic reconnection, parallel electric fields, and helicity, *J. Geophys. Res.*, *93*, 5547-5557, 1988.

Schindler, K., and A. Otto, Resistive instability, *This Conference*, 1989.

Sonnerup, B. U. Ö., Magnetic field re-connexion in a highly conducting incompressible fluid, *J. Plasma Phys.*, *4*, 161-174, 1970.

Sonnerup, B. U. Ö., Magnetic field reconnection, in *Solar System Plasma Physics*, vol. III, edited by L. T. Lanzerotti, C. F. Kennel, and E. N. Parker, pp. 46-108, North-Holland, Amsterdam, 1979.

Sonnerup, B. U. Ö., On the theory of steady state reconnection, *Computer Phys. Comm.*, *49*, 143-159, 1988.

Sonnerup, B. U. Ö., and E. R. Priest, Resistive MHD stagnation-point flows at a current sheet, *J. Plasma Phys.*, *14*, 283-294, 1975.

Sonnerup, B. U. Ö., and D.-J. Wang, Structure of reconnection layers in incompressible MHD, *J. Geophys. Res.*, *92*, 8621-8633, 1987.

Soward, A. M.,and E. R. Priest, Magnetic field-line reconnection with jets, *J. Plasma Phys.*, *35*, 333-350, 1986.

Sweet, P. A., The neutral point theory of solar flares, in *Electromagnetic Phenomena in Cosmical Physics*, edited by B. Lehnert, p. 123, Cambridge University Press, New York, 1958.

Ugai, M., MHD simulations of fast reconnection spontaneously developing in a current sheet, *Computer Phys. Comm.*, *49*, 185-192, 1988.

Vasyliunas, V. M., Theoretical models of magnetic field line merging, *Rev. Geophys.*, *13*, 303-336, 1975.

Yang, C.-K., and B. U. Ö. Sonnerup, Compressible magnetic field reconnection: a slow wave model, *Astrophys. J.*, *206*, 570-582, 1976.

Yang, C.-K., and B. U. Ö. Sonnerup, Compressible magnetopause reconnection, *J. Geophys. Res.*, *82*, 699-703, 1977.

Yeh, T., Day-side reconnection between a dipolar geomagnetic field and a uniform interplanetary field, *J. Geophys. Res.*, *81*, 2140-2144, 1976.

Appendix 6

JOURNAL OF GEOPHYSICAL RESEARCH, VOL. 95, NO. A1, PAGES 259-260, JANUARY 1, 1990

Comment on "MHD Stagnation Point Flows in the Presence of Resistivity and Viscosity" by F. T. Gratton, M. F. Heyn, H. K. Biernat, R. P. Rijnbeek, and G. Gnavi

B. U. Ö. SONNERUP AND T. D. PHAN

Thayer School of Engineering, Dartmouth College, Hanover, New Hampshire

In a recent article, *Gratton et al.* [1988] have presented a new exact analytical solution of the two-dimensional incompressible viscous and resistive MHD equations which they claim to be relevant to the magnetic field annihilation problem in stagnation point flow at an electric current sheet, a problem studied earlier by *Sonnerup and Priest* [1975]. They have also discussed the possible application of their solution to the problem of magnetic field annihilation near the stagnation point at the subsolar magnetopause. It is the purpose of our comment to demonstrate that the Gratton et al. solution, while mathematically correct and intrinsically interesting, does not represent flow behavior acceptable for the field annihilation problem, either in its symmetric form or in the asymmetric version thought to occur at the magnetopause.

Gratton et al. have found the velocity field

$$v_x = (U_o^2/\nu)xe^{\pm U_o y/\nu}$$
$$v_y = \pm U_o(1 - e^{\pm U_o y/\nu}) \tag{1}$$

to satisfy the laws of mass and momentum conservation, including viscous effects represented by the kinematic viscosity ν. In these formulas, the upper and lower signs refer to $y < 0$ and $y > 0$, respectively. An attractive feature of this velocity distribution is that it yields parallel flow, at speed U_o, toward the current sheet, located at $y = 0$, as y, the coordinate perpendicular to the current sheet, approaches $\pm\infty$. At $y = 0$ it yields flow along the $\pm x$ direction, i.e., flow parallel to the current sheet and directed away from the stagnation point which is located at $x = y = 0$. This parallel flow has a speed that increases linearly with increasing distance, $|x|$, from the stagnation point. The Gratton et al. solution differs in a fundamental way from the velocity field

$$v_x = k_1 x$$
$$v_y = -k_1 y \tag{2}$$

employed by Sonnerup and Priest. The difficulty with the Gratton et al. solution lies in the cusplike behavior of the velocity distribution $v_x(x, y)$ when plotted as a function of y for any fixed x value. This behavior, shown in Figure 1, implies that the fluids on the two sides of the plane $y = 0$ exert a viscous drag force (directed toward the origin, $x = 0$) on that plane, of magnitude $2\rho\nu|\partial v_x/\partial y|$. We do not see how this type of behavior can be relevant to any realistic version of the magnetic field annihilation problem. Rather, it appears to us that one half of the Gratton et al. solution, for $y > 0$ say, corresponds to the flow that would be generated in a viscous plasma for example by "upwelling" of some massive and nearly solid material from the region $y < 0$ toward the plane $y = 0$, with deflection of its motion to be purely horizontal (parallel to the plane $y = 0$) at $y = 0$ and given by $v_x = (U_o^2/\nu)x$. This motion of the "solid" at $y = 0$ would viscously entrain the plasma occupying the region $y > 0$ via a tangential viscous stress $\rho\nu\partial v_x/\partial y$, causing it to move in the manner described by the Gratton et al. solution. However, we cannot think of any actual situation in which this type of flow would be important.

As is evident from the discussion of asymmetric annihilation configurations in section 4 of the Gratton et al. paper, its authors are aware that certain conditions must be applied to the stresses at the interface, $y = 0$, which separates the two halves of the flow problem. However, for the tangential stresses this condition is incorrectly stated as $\sigma_{xy}(y = 0^+) = -\sigma_{xy}(y = 0^-)$, the correct version being $\sigma_{xy}(y = 0^+) = +\sigma_{xy}(y = 0^-)$. In a solution that is symmetric about the plane $y = 0$ in the sense that $v_x(y) = v_x(-y)$, $v_y(y) = -v_y(-y)$, the correct condition leads to $\partial v_x/\partial y = 0$ at $y = 0$.

The basic viscous momentum equation governing the velocity field is found by Gratton et al. to be

$$\nu f''' = f'^2 - ff'' + \kappa \tag{3}$$

where $v_x = xf'(y)$, $v_y = -f(y)$ and κ is a constant which can be shown to represent a pressure gradient $\partial p/\partial x$. One may ask whether this equation possesses acceptable solutions of the general type discussed by Gratton et al., i.e., solutions that have a similar asymptotic behavior as $|y| \to \infty$ but where, in addition, the stress condition $\partial v_x/\partial y = 0$ is satisfied at $y = 0$, which requires $f''(0) = 0$. It is evident that solutions of this type have $f'(\pm\infty) = f''(\pm\infty) = f'''(\pm\infty) = 0$ so that the constant $\kappa = 0$; this is the κ value used by Gratton et al., and it implies that the flow is not driven by pressure gradients in the impressed flow at large $|y|$ values. For $\kappa = 0$, we may integrate equation (3) from $y = 0$ to $y = \infty$, employing partial integration to deal with the term ff''. The result is

$$\nu[f''(\infty) - f''(0)] = 2\int_0^\infty f'^2 dy - [f(\infty)f'(\infty) - f(0)f'(0)] \tag{4}$$

The boundary conditions described above are such that all of the boundary terms vanish, leaving only the integral in (4), which has a nonnegative integrand. It follows that no nontrivial solution of the required type exists. This result is

Paper number 89JA01601.
0148-0227/90/89JA-01601$02.00

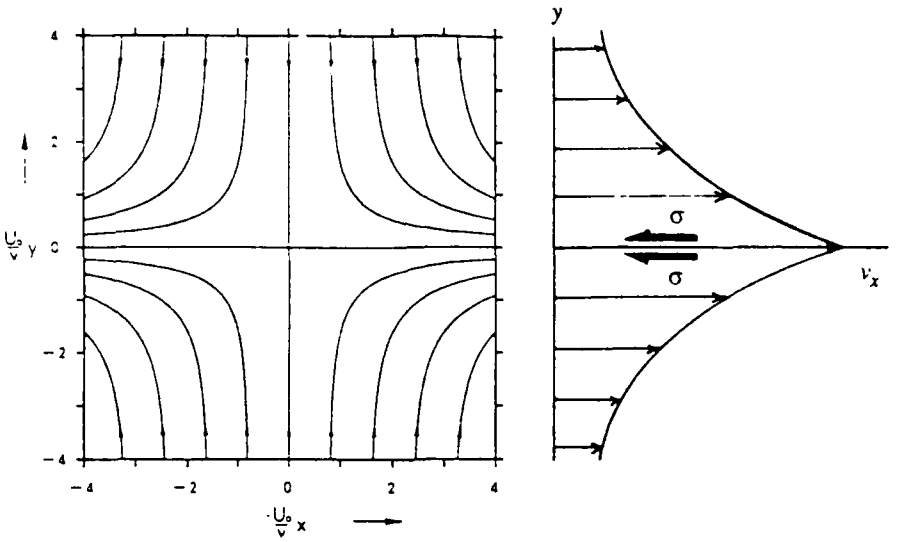

Fig. 1. Velocity distribution $v_x(y)$ at a fixed x value in the flow discussed by *Gratton et al.* [1988]. The direction of the shear stresses, σ, transmitted from the fluid to the plane $y = 0$ is shown by heavy arrows.

not surprising, for without a pressure gradient at large $|y|$ values or a shear stress at $y = 0$ to drive the flow, no motion will occur.

In order to obtain solutions of equation (3), which represent pressure-driven rather than viscously entrained stagnation point flow, one needs to abandon the flow behavior at large $|y|$ values assumed by Gratton et al. and replace it with behavior appropriate to two-dimensional pressure-driven stagnation point flow, i.e., $v_x = k_1 x$ for large $|y|$. One then finds $\kappa = -k_1^2$ in (3). The only solution of that equation that also satisfies $v_y = 0$, $\partial v_x/\partial y = 0$ at $y = 0$ can be shown to be $f = k_1 y$, which is the stagnation point flow described by (2) and used by *Sonnerup and Priest* [1975]. We believe that this is the flow behavior to be expected in pressure-driven magnetic field annihilation. It is important to realize that this pressure-driven solution does not "lead to the neglect of the viscous term" as stated by Gratton et al. Rather, the situation is that for this symmetric flow the net viscous force per unit volume vanishes identically, as it does for any irrotational incompressible flow of a Newtonian fluid. In more detail, the Newtonian viscous shear stresses, $\sigma_{xy} = \sigma_{yx}$, vanish identically in the flow given by (2). But the viscous normal stresses, σ_{xx} and σ_{yy}, do not vanish, and the viscous dissipation per unit volume is also nonzero.

Even in the case of pressure-driven MHD stagnation point flow, the viscous forces may enter in a nontrivial manner as a result of a lack of symmetry between the plasma and flow in the two regions $y > 0$ and $y < 0$. This problem was discussed briefly by *Sonnerup and Priest* [1975], who derived a set of coupled ordinary differential equations describing general three-dimensional viscous MHD stagnation point flows. These equations reduce to equation (3) in the special case of two-dimensional flow. It may be added that the latter equation is also well known in ordinary viscous fluid mechanics. It was derived, and solved numerically, by K. Hiemenz in his thesis at Göttingen in 1911 for the case of stagnation point flow at a solid stationary wall [e.g., *Schlichting*, 1968]. The Hiemenz solution could be used to describe magnetic field annihilation in viscous resistive MHD stagnation point flow at a solid stationary wall.

The response by *Gratton et al.* [this issue] to the above comments has not led us to make any changes in those comments, but it has prompted the following additional remarks. As is evident from the previous paragraph, we fully agree with those authors that viscous forces (and associated vorticity) may become important under asymmetric plasma and flow conditions. However, we do not believe that asymmetric solutions of the type described in Figures 2 and 3 of the response, i.e., solutions for which the pressure gradient term is absent ($\kappa = 0$ in equation (3)), are relevant to flow near the subsolar magnetopause stagnation point.

Acknowledgement. The research was supported by the National Science Foundation, Atmospheric Sciences Division, under grant ATM-8807645 and by the Air Force Geophysics Laboratory under contract F19628-87-K-0026 to Dartmouth College.

REFERENCES

Gratton, F. T., M. F. Heyn, H. K. Biernat, R. P. Rijnbeek, and G. Gnavi, MHD stagnation point flows in the presence of resistivity and viscosity, *J. Geophys. Res.*, *93*, 7318, 1988.

Gratton, F. T., G. Gnavi, M. F. Heyn, H. K. Biernat, and R. P. Rijnbeek, Pressure drive and viscous dragging: A reply, *J. Geophys. Res.*, this issue.

Schlichting, H., *Boundary Layer Theory*, pp. 87-92, McGraw-Hill, New York, 1968.

Sonnerup, B. U. Ö., and E. R. Priest, Resistive MHD stagnation point flows at a current sheet, *J. Plasma Phys.*, *14*, 283, 1975.

T. D. Phan and B. U. Ö. Sonnerup, Thayer School of Engineering, Dartmouth College, Hanover, NH 03755.

(Received October 25, 1988;
revised June 28, 1989;
accepted June 28, 1989.)

Appendix 7

JOURNAL OF GEOPHYSICAL RESEARCH, VOL. 94, NO. A6, PAGES 6539-6551, JUNE 1, 1989

On the Structure of Resistive MHD Intermediate Shocks

L.-N. HAU AND B. U. Ö. SONNERUP

Thayer School of Engineering, Dartmouth College, Hanover, New Hampshire

An overview is presented of the resistive steady state structure of intermediate MHD shocks, i.e., shocks that effect a transition from super-alfvénic to sub-alfvénic flow. The results are presented in terms of magnetic hodograms in which the two components of the magnetic field tangential to the shock surface are plotted against each other. By performing fixed-point analysis in this plane, at the possible upstream and downstream states of these shocks, and by solving the one-dimensional, steady state, resistive, nonviscous MHD equations numerically, it is found that three basic types of hodogram topology exist, describing the resistive intermediate shock structure. These topologies are characterized by the normal flow speed (in the shock frame) relative to the fast-wave speed and the sound speed at the upstream and downstream states. Fast-mode and slow-mode shocks are contained within these hodograms as well. In brief summary, it is found that all intermediate shocks that have an upstream normal flow speed, v_{x1}, less than the local small-amplitude fast-mode wave speed, c_{f1}, and a downstream normal flow speed, v_{x2}, greater than the local small-amplitude slow-mode wave speed, c_{s2}, have a unique magnetic structure consisting mainly of a rotation of the tangential magnetic field, accompanied by a more or less pronounced change in field magnitude. This type of shock is called a subfast ($v_{x1} < c_{f1}$) weak ($v_{x2} > c_{s2}$) intermediate shock. A subfast strong intermediate shock has $v_{x1} < c_{f1}$ and $v_{x2} < c_{s2}$ instead. Its magnetic structure is found to be nonunique and the shock thickness depends on this structure. When the upstream normal flow speed exceeds c_{f1}, the shock is said to be superfast ($v_{x1} > c_{f1}$). The structures of both weak ($v_{x2} > c_{s2}$) and strong ($v_{x2} < c_{s2}$) superfast intermediate shocks are found to be nonunique. When the intermediate shock involves a transition from supersonic ($v_{x1} > c_1$) to subsonic ($v_{x2} < c_2$) conditions, the resistive intermediate shock structure usually contains a discontinuous substructure consisting of a gas dynamic shock in which dissipation processes other than resistivity, namely, viscosity and/or heat conductivity, are dominant. However, in certain cases a continuous, purely resistive transition from supersonic to subsonic flow is possible.

1. Introduction

Conventionally, magnetohydrodynamic (MHD) shock waves are classified as slow, intermediate or fast according to their propagation speeds relative to the slow, intermediate and fast small-amplitude MHD wave speeds [e.g., *Anderson*, 1962; *Kantrowitz and Petschek*, 1966]. For these shock modes, the upstream and downstream velocity components, v_{x1} and v_{x2}, normal to the shock and measured in a frame of reference moving with it, are, respectively, greater than and less than the slow, the intermediate, and the fast small amplitude wave speeds, a property that allows each shock mode to be generated by steepening of finite amplitude waves. In this regard, fast and slow shocks may be viewed as pure modes in the sense that the process of steepening to form these structures involves only the properties of the corresponding linear mode. On the other hand, the intermediate-mode shock is a hybrid mode for which the steepening process depends not only on the properties of the linear intermediate mode but also on those of the slow mode and, in some cases, the fast mode. A nonlinear purely intermediate wave in a loss-free medium, called a rotational discontinuity (RD), does not steepen. It propagates exactly at the normal component of the Alfvén speed, c_{ax}, and leaves the thermodynamic state of the plasma unchanged, its only effect being a rotation, without change of magnitude, of the component of the magnetic field tangential to the shock front by an arbitrary angle, $\Delta\phi$, and a corresponding rotation of the tangential velocity component. This rotation property means that in general an RD does not obey the so-called coplanarity theorem, valid for all three shock modes, according to which the shock normal, $\boldsymbol{e}_x$, and the field vectors $\boldsymbol{B}_1$ and $\boldsymbol{B}_2$ on the two sides of the shock lie in one plane. Fast and slow shocks have $\Delta\phi = 0$ while intermediate shocks (IS) have $\Delta\phi = \pi$. In other words, fast and slow shocks do not reverse the sense of the tangential component of $\boldsymbol{B}$, whereas the intermediate shock does. It is noted that the RD is a purely nondissipative structure and therefore does not exist (or, equivalently, must be infinitely thick) in a dissipative medium.

As mentioned above, an IS propagates at a super-alfvénic speed, so that it will overtake upstream intermediate-mode waves (Alfvén waves; RDs) propagating in the same direction. Similarly, the normal flow speed behind an IS is sub-alfvénic so that the IS is always overtaken by such waves in the downstream region. Therefore upstream and downstream intermediate-mode waves tend to become incorporated into the IS structure. However, as discussed by *Kantrowitz and Petschek* [1966], a difficulty then arises, since the IS must obey coplanarity whereas intermediate-mode waves such as RDs in general do not obey that condition. This dilemma led Kantrowitz and Petschek, and others, to conclude that the IS must be an extraneous structure which in interacting with any noncoplanar intermediate wave will disintegrate rapidly, principally into an RD and a slow shock. On this basis, intermediate shocks which had been studied in some detail in the fifties and sixties [e.g., *Shercliff*, 1960] were rejected as unphysical and were essentially forgotten, at least by the space physics community. However, recently *Wu* [1987, 1988*a*, *b*] has undertaken to reexamine the behavior of ISs and RDs by use of numerical simulation, based on the resistive or resistive/viscous MHD equations. In brief, he has demonstrated (1) that a nonlinear plane-polarized transverse MHD wave can steepen to form an IS; (2) that, with appropriate initial conditions, all four types of ISs, described by *Shercliff* [1960], can be generated and appear stable; (3) that, in the interaction between a noncoplanar

Paper number 89JA00296.
0148-0227/89/89JA-00296$05.00

RD and an IS described above, a long time may elapse before the disintegration predicted by *Kantrowitz and Petschek* [1966] takes place, this time being longer the smaller the deviation of the field rotation $\Delta\phi$ in the RD from 0; (4) that, in the presence of dissipation, an RD having $\Delta\phi = \pi$ evolves into a "neighboring" class of IS while for $\Delta\phi \neq \pi$ it evolves into a new slowly time dependent IS-like structure which however does not obey the usual Rankine Hugoniot conditions and which, in particular, violates coplanarity.

In light of the above mentioned new results, Wu has proposed that time-dependent and, in some cases, time-independent ISs rather than RDs may be at hand in a variety of space plasma situations such as in the solar wind or at the earth's magnetopause during reconnection events [e.g., *Sonnerup et al.*, 1987]. However, the relevance of the one-fluid dissipative MHD equations to these applications remains open to question. For example, in recent collisionless hybrid-code particle simulations, *Lee et al.* [1989] have found RDs to be stable and some ISs to evolve into RDs, i.e., behavior opposite to that reported by Wu. Nevertheless, the structure and evolution of ISs in the MHD description has become a topic of intrinsic interest and fundamental importance as a result of Wu's work.

In this paper, we examine the steady state structure of intermediate shocks in a purely resistive MHD medium (which is the simplest case from a mathematical view point), as well as certain aspects of their relationship to rotational discontinuities. The purpose of our study is to present an overview of the structure of steady state resistive ISs, which we believe will provide a useful complement to Wu's dissipative MHD simulations and to an earlier incomplete study of the intermediate shock structure by *Bickerton et al.* [1971]. (Indeed, some of our conclusions can be deduced from a careful study of the set of simulation results reported in Wu's papers.) The paper is organized as follows. In section 2, the MHD jump conditions and the different types of ISs are reviewed; in section 3 different types of steady state intermediate shock structures are obtained. Section 4 contains a summary and discussion of the results.

2. MHD Jump Relations

Using standard notation, the one-dimensional, steady state nonviscous MHD conservation laws ($\partial/\partial y = 0$; $\partial/\partial z = 0$; B_x = constant) can be integrated once and written as follows:

$$\rho v_x = \rho_1 v_{x1} \tag{1}$$

$$\rho v_x^2 + p + \frac{B^2}{2\mu_o} = \rho_1 v_{x1}^2 + p_1 + \frac{B_1^2}{2\mu_o} \tag{2}$$

$$\rho v_x v_t - \frac{1}{\mu_o} B_x B_t = \rho_1 v_{x1} v_{t1} - \frac{1}{\mu_o} B_{x1} B_{t1} \tag{3}$$

$$\frac{\gamma}{\gamma-1}\frac{p}{\rho} + \frac{v^2}{2} = \frac{\gamma}{\gamma-1}\frac{p_1}{\rho_1} + \frac{v_1^2}{2} \tag{4}$$

Furthermore, Ohm's law may be written as

$$\boldsymbol{E} + \boldsymbol{v}\times\boldsymbol{B} = \frac{\eta}{\mu_o}\nabla\times\boldsymbol{B} \tag{5}$$

In these equations, the subscript t denotes the two components of a vector tangential to the shock and η is the electrical resistivity. Also, the quantities denoted by subscripts 1, and 2 represent the upstream (ahead of the shock) and downstream (behind the shock) conditions, respectively. Note that the energy equation (4) is written in a frame of reference moving with the discontinuity and sliding along it in such a manner that $\boldsymbol{E} = 0$ outside the shock and $\boldsymbol{E} = \boldsymbol{e}_x E_x$ within the shock. In this so called deHoffmann-Teller frame, which will be used throughout this paper, the plasma flow velocity $\boldsymbol{v}$ is parallel to $\boldsymbol{B}$ on both sides of the shock. The above equations will be used in two different ways: (1) to obtain shock jump conditions, and (2) to obtain a set of ordinary differential equations for steady state shock structures.

In this section, we review the jump relations, which relate the uniform properties on both sides of a stationary time independent shock front. The derivation of these relations is straightforward and may be found, e.g., in *Anderson* [1962] or *Jeffrey and Taniuti* [1964], although in a form somewhat different from that employed here. Regardless of the resistivity and/or other dissipative processes within the shock, the normal Alfvén numbers $A_x = v_x(\mu_o\rho)^{0.5}/B_x$ on the two sides of a discontinuity are found to be related by the following equation:

$$A_{x1}^2 = \left[A_{x2}^2\left(\frac{\gamma-1}{\gamma}\left(\frac{\gamma+1}{\gamma-1} - \tan^2\theta_1\right)(A_{x2}^2-1)\right)^2\right.$$

$$\left. + \tan^2\theta_1\left(\frac{\gamma-1}{\gamma}A_{x2}^2 - 1\right)(A_{x2}^2 - 2)\right) - \frac{\beta_1}{\cos^2\theta_1}(A_{x2}^2 - 1)^2\Big] /$$

$$\left[\frac{\gamma-1}{\gamma}\frac{(A_{x2}^2-1)^2}{\cos^2\theta_1} - A_{x2}^2\tan^2\theta_1\left(\frac{\gamma-1}{\gamma}A_{x2}^2 - 1\right)\right] \tag{6}$$

where β_1 is the upstream ratio of plasma pressure to magnetic pressure, $\beta_1 = p_1/(B_1^2/2\mu_o)$, and θ_1 is the angle between the shock normal, $\boldsymbol{e}_x$, and the upstream magnetic field vector. The curve describing the relationship between A_{x1}^2 and A_{x2}^2 given by this equation is shown in Figure 1 for two sets of parameter values (β_1, θ_1). We shall refer to these curves as shock curves. They have several noteworthy properties. First, they always intersect the 45° line $A_{x1}^2 = A_{x2}^2$ at three points. These are labeled *s*, *i*, and *f* in the diagram and they represent small amplitude slow, intermediate, and fast MHD waves, respectively. Second, portions of the shock curve located below the 45° line are unphysical because they yield an entropy decrease across the shock.

Slow-mode shocks (SS) lie on the branch of the shock curve above the 45° line that starts at point *s* and goes upwards until the condition $A_{x1}^2 = 1$ is reached. This latter point is denoted by *so* in the diagram and corresponds to the strongest possible slow shock, also called a switch-off shock. It has the property that the tangential component of the magnetic field is switched off by the shock, yielding $\boldsymbol{B}_2 = \boldsymbol{e}_x B_x$.

As one continues from point *so* upward and to the right along the shock curve, one enters the intermediate-shock (IS) portion of the curve for which $A_{x1}^2 > 1$ and $A_{x2}^2 < 1$ and for which the tangential component of $\boldsymbol{B}_2$ is now antiparallel to that of $\boldsymbol{B}_1$. It can be shown that between *so* and the maximum point on the shock curve, the flow speed v_{x2} downstream of the intermediate shock is always less than the local slow wave speed, $v_{x2} < c_{s2}$. In this regime the IS is said to be (downstream) "subslow," or "strong." At the maximum point, labeled *cs* in the diagram, the downstream flow is "critical slow" ($v_{x2} = c_{s2}$). Continuing from

this point downward and to the right along the shock curve, one enters the (downstream) "superslow," or "weak," parameter region of the IS for which $v_{x2} > c_{s2}$. This region extends to the point *i* where $A_{x1}^2 = A_{x2}^2$ which represents the endpoint of the IS branch of the shock curve. It is also the location of purely intermediate waves (RDs) which have $|B_1| = |B_2|$ and arbitrary angle rotations, $\Delta\phi$, of the tangential field. The slope of the shock curve at the point *i* is always equal to −1. From the discussion above and from the behavior of the shock curve, it is evident that for one and the same upstream condition an intermediate shock can generate two different downstream states: one of these is subslow and corresponds to a strong IS, the other is superslow and corresponds to a weak IS.

Finally, the fast-shock (FS) portion of the shock curve starts at point *f* and extends upward and to the right above the 45° line. It will not be discussed further in this paper. However, we note that for some, but not all parameter values the fast-mode propagation speed can be less than the intermediate shock speed. An example of this situation is provided by the shock curve labeled $\beta_1 = 0.1$, $\theta_1 = 26.57°$ in the diagram, for which the maximum point *cs* has a larger value of A_{x1}^2 than does the point *f*. The portion of the IS branch located above *f* is termed (upstream) "superfast" and the portion below *f* is termed "subfast." The two points labeled *cf* on the IS branch correspond to fast critical conditions upstream of the IS, i.e., $v_{x1} = c_{f1}$.

The values of the Alfvén numbers A_{x1}^2 and A_{x2}^2 at the maximum point (the critical-slow point *cs*) on the IS branch of the shock are shown in Figure 2 as a function of β_1 and $\tan\theta_1$. In Figure 2*a* a curve separating superfast and subfast upstream conditions at the point *cs* is also shown, allowing one to identify the parameter regime in which upstream superfast ISs can occur. As an example, for conditions typical of the magnetopause ($\beta_1 \geq$ 1, $\tan\theta_1 \geq 5$, say), all ISs are subfast and have values of A_{x1}^2 restricted to a rather narrow range above unity, $1 \leq A_{x1}^2 < 1.1$, say. The downstream Alfvén number, A_{x2}^2, has a much broader range: Figure 2*b* indicates that, in the example above, the weak IS branch occupies the approximate range $0.85 < A_{x2}^2 < 1$ from which one can estimate the strong IS range to be, very approximately, $0.7 < A_{x2}^2 < 0.85$. Thus substantial deviations from the RD condition $A_{x1}^2 = A_{x2}^2 = 1$ could in principle occur; in particular, A_{x2}^2 could be substantially less than unity, if the magnetopause contained a strong IS rather than an RD.

By use of the relationship (6) between A_{x1}^2 and A_{x2}^2, the changes in tangential magnetic field, B_t, in the angle, θ, between the magnetic field and the shock normal, in the density, ρ, and in

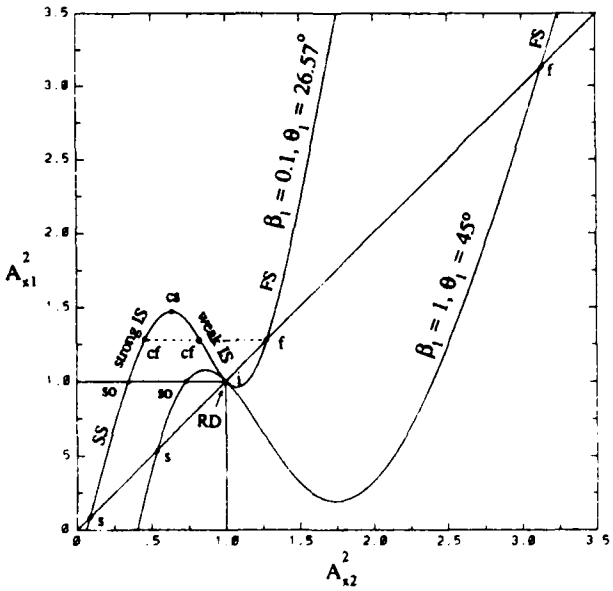

Fig. 1. Shock curves showing the relationship between upstream (A_{x1}^2) and downstream (A_{x2}^2) normal Alfvén numbers ($A_x^2 \equiv v_x^2\mu_0\rho/B_x^2$) for two sets of values of $\beta_1 = p_1 2\mu_0/B_1^2$ and angle θ_1 between shock normal and field vector B_1. Slow shocks (SS) occur between points *s* and *so*; strong (subslow) intermediate shocks (IS) occur between points *so* and *cs*; weak (superslow) ISs occur between points *cs* and *i*; rotational discontinuities (RD) occur at point *i*; fast shocks (FS) occur above the point *f*. The portion of the IS branch (if any) above the line *cf-cf-f* is called superfast; the portion below that line is called subfast.

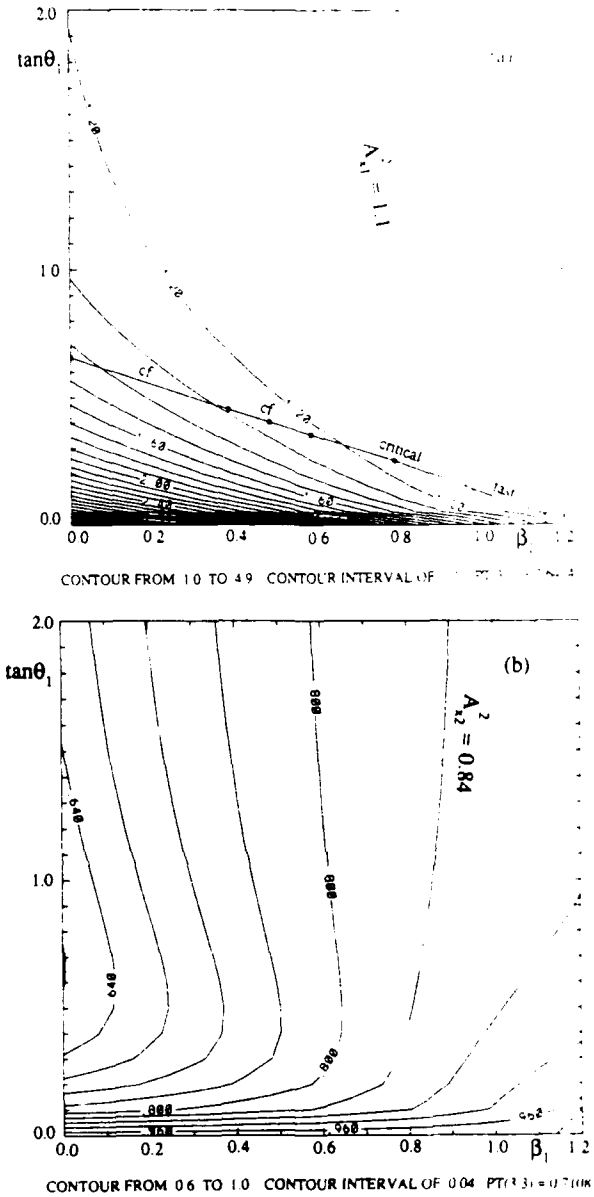

Fig. 2. Location of the critical-slow (*cs*) point in Figure 1, as a function of β_1 and $\tan\theta_1$. The coordinates A_{x1}^2 and A_{x2}^2 of point *cs* are shown as contours of (*a*) constant A_{x1}^2 and (*b*) constant A_{x2}^2 in the β_1 - $\tan\theta_1$ plane. In part 2*a* of the figure, the region below the curve labeled "critical fast" (*cf*) permits of superfast intermediate shocks. Above that curve, only subfast intermediate shocks are possible.

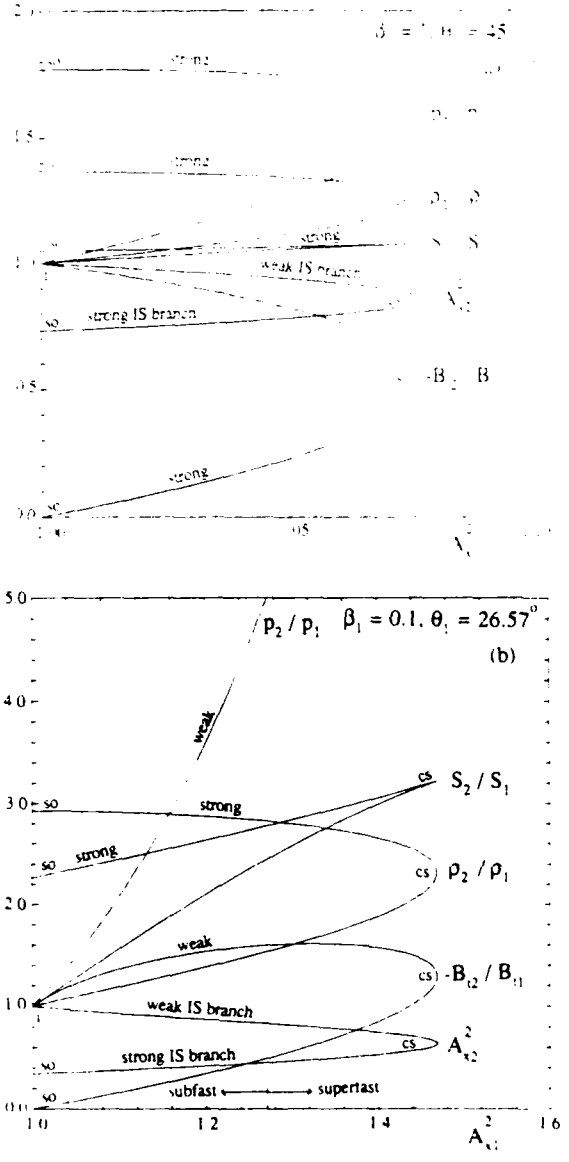

Fig. 3. The pressure ratio p_2/p_1, density ratio ρ_2/ρ_1, entropy ratio S_2/S_1, tangential magnetic field ratio $-B_{t2}/B_{t1}$, and A_{x2}^2 as a function of A_{x1}^2 for intermediate shock with (*a*) $\beta_1 = 1$ and $\theta_1 = 45°$ and (*b*) $\beta_1 = 0.1$ and $\theta_1 = 26.57°$.

the plasma β value can be calculated from the following further jump conditions which are readily obtained from equations (1)-(5):

$$\frac{B_{t2}}{B_{t1}} = \frac{\tan\theta_2}{\tan\theta_1} = \frac{(A_{x1}^2 - 1)}{(A_{x2}^2 - 1)} \tag{7}$$

$$\frac{\rho_2}{\rho_1} = \frac{A_{x1}^2}{A_{x2}^2} \tag{8}$$

$$A_{x2}^2 + \frac{(\beta_2+1)}{2\cos^2\theta_2} = A_{x1}^2 + \frac{(\beta_1+1)}{2\cos^2\theta_1} \tag{9}$$

It is not possible here to present a complete graphical overview of the changes in these quantities across intermediate shocks for all values of β_1 and θ_1. Figure 3 shows results for the (β_1, θ_1) values used in Figure 1, in a format similar to that used by *Lee et al.* [1989]. In this diagram, the IS branch of the shock curve is also shown for convenient reference along with the locations of the switch off shock (*so*), the rotational discontinuity (*i*) and the (downstream) critical-slow (*cs*) point. It is seen that p_2/p_1 and ρ_2/ρ_1 have maxima for the switch-off shock where $A_{x1}^2 = 1$ and $B_{t2}/B_{t1} = 0$. In this sense, the switch-off shock represents the strongest possible slow or intermediate shock. However, it is noted that for the IS the entropy ratio, S_2/S_1, is a maximum at the extremum of the shock curve, i.e., at the point *cs*. It is further seen that the ratios of downstream to upstream pressure, density, and entropy are always greater for the (downstream) subslow IS branch than for the superslow branch. Thus it is also appropriate to label the former the strong and the latter the weak IS branch. We shall adopt this notation in the remainder of the paper. The weak IS branch has its end point (*i*) at $A_{x1} = A_{x2} = 1$, where $p_2/p_1 = \rho_2/\rho_1 = S_2/S_1 = 1$ and $B_{t2}/B_{t1} = -1$. This is the behavior of a rotational discontinuity with $\Delta\phi = \pi$.

The curve for $-B_{t2}/B_{t1}$ in Figure 3*a* is such that $|B_{t2}| < |B_{t1}|$ for the entire IS branch, which in this example is purely subfast. Since a decrease in $|B|$ is a characteristic of the slow compressive mode, all ISs in this figure can be viewed as hybrids of mainly intermediate-mode rotation and slow-mode compression with the later being more dominant on the strong branch than on the the weak branch. This interpretation will be verified and discussed further in section 3 of the paper. A different type of behavior is evident in Figure 3*b* where the portion of the diagram to the right of $A_{x1}^2 = 1.272$ represents upstream superfast conditions. It is seen that in this case the entire weak IS branch, as well as a small portion of the strong IS branch (near the *cs* point), has $|B_{t2}| > |B_{t1}|$. In such cases it is clear that fast-mode compression, which leads to an increase in $|B|$, is also involved, along with intermediate mode rotation and perhaps slow-mode compression. Furthermore, the fast-mode effect dominates the slow-mode one on the entire weak IS branch as well as on part of the strong IS branch. Again, these effects will be discussed further in section 3.

The information concerning IS jump conditions given in the preceding paragraphs can be found, at least qualitatively, in the existing literature. The following additional property of ISs appears to be little known: for chosen A_{x1}, the downstream state of the weak (superslow) IS solution can also serve as the upstream state for a slow shock that propagates at exactly the same speed and that has exactly the same downstream state as the strong (subslow) IS. This relationship between the weak and the strong IS solutions at the same A_{x1} will be clarified in the next section.

3. Equilibrium Intermediate Shock Structure

3.1. *Differential Equations*

In this section, we discuss the one-dimensional, steady state, resistive MHD equations which describe the shock structure. With the assumption of uniform resistivity, equations (1)-(5) can be simplified to the following form:

$$A_{x1}^2\lambda_{r1}\frac{dB_y}{dx} = (A_x^2 - 1)B_y - (A_{x1}^2 - 1)B_{y1} \tag{10}$$

$$A_{x1}^2\lambda_{r1}\frac{dB_z}{dx} = (A_x^2 - 1)B_z - (A_{x1}^2 - 1)B_{z1} \tag{11}$$

$$A_x^2 = \frac{\gamma}{\gamma+1}\left(A_{x1}^2 + \frac{\beta_1+1}{2\cos^2\theta_1} - \frac{B^2}{2B_x^2}\right) \pm \left\{\left(\frac{\gamma}{\gamma+1}\right)^2\right.$$

$$\left(A_{x1}^2 + \frac{\beta_1+1}{2\cos^2\theta_1} - \frac{B^2}{2B_x^2}\right)^2 + \left(\frac{\gamma-1}{\gamma+1}\right)\left(\frac{B^2}{B_x^2}+2(A_{x1}^2-1)\tan\theta_1\frac{B_z}{B_x}\right.$$

$$\left.\left. + (A_{x1}^2-1)^2\tan^2\theta_1 - 1 - \frac{A_{x1}^2}{\cos^2\theta_1}\left(A_{x1}^2 + \frac{\gamma}{\gamma-1}\beta_1\right)\right]\right\}^{0.5} \quad (12)$$

where $\lambda_{r1} = \eta/\mu_0 v_{x1}$ is the resistive length. As before, variables with subscript 1 represent upstream conditions. For the upstream state, we further assume $B_{y1} = 0$. However, the equations remain valid if the subscript 2, representing the downstream conditions, is used in place of the subscript 1. Equations (10)-(12) describe the resistive structure, not only of ISs, but of fast and slow shocks (for which we may put $B_y \equiv 0$) and RDs as well. In particular, they imply that RDs, which have the properties $A_x = A_{x1} = A_{x2} = 1$, have finite thickness only in the case of zero resistivity. On the other hand, for all MHD resistive shocks the thickness is seen to be proportional to $\lambda_{r1}A_{x1}^2$. However, as is evident from the equations, this proportionality does not describe the complete dependence of the shock thickness on A_{x1}. In particular, for A_x^2 near unity the factor $(A_x^2 - 1)$ on the right-hand side of the equations tends to make the shock thickness much larger than λ_{r1}.

The following comments should be made concerning the plus or minus sign in equation (12). In the vicinity of the upstream state ($A_x = A_{x1}$; $B_{z1} = B_1$; $B_{y1} = 0$) only one of the signs will give $A_x^2 = A_{x1}^2$. Similarly, in the vicinity of a downstream state ($A_x = A_{x2}$; $B_{z2} = B_2$; $B_{y2} = 0$) only one of the signs will give $A_x = A_{x2}$. It can be shown directly from equation (12) that the criterion for choosing the sign is as follows: the plus sign and the minus sign are to be used, respectively, for A_x^2 greater than and less than $\gamma\beta/2\cos^2\theta$ or, equivalently, for $v_x^2 > c^2$ and $v_x^2 < c^2$ where $c^2 = \gamma p/\rho$. When the signs needed are the same for the upstream and the downstream state (i.e., when v_{x1} and v_{x2} are both supersonic or both subsonic), or, to borrow a mathematical term, when these two states are located on the same Riemann sheet in the complex B_t plane, a purely resistive transition from the upstream to the downstream state exists. When the signs are opposite for the upstream and downstream states, i.e., since the case $v_{x1} < c_1$ and $v_{x2} > c_2$ does not occur, when the shock involves a transition from supersonic to subsonic flow, it usually contains a substructure in which dissipative processes other than resistivity, e.g., viscosity and/or heat conduction, dominate (although in special cases a purely resistive transition from supersonic to subsonic flow is possible, as we shall see). Since these additional dissipative processes are not described by our basic equations, such a substructure will appear as a discontinuous jump from one Riemann sheet to the other. Such jumps constitute regular gas dynamic shocks and they leave the magnetic field and the tangential velocity components unchanged. It is a matter of straightforward algebra to show, from the basic conservation laws, that a transition from the supersonic (plus) Riemann sheet to the subsonic (minus) Riemann sheet, at a fixed value of the field vector, B, leads to the usual gasdynamic jump conditions. It should be pointed out that the calculations shown in this paper are valid under the assumption that the viscous scale length is much smaller than the resistive length.

3.2. *Fixed-Point Analysis*

The set of equations (10)-(12) represents a two-dimensional autonomous nonlinear system [e.g., *Hochstadt*, 1964]. The upstream and downstream states are the fixed points of the system. The character of the fixed points in terms of nodal or saddle-point behavior can be obtained by studying the response of equations (10)-(12) to small perturbations about the fixed points. Linearization of these equations around the upstream state, say, leads to

$$\frac{\eta A_{x1}^2}{\mu_0 v_{x1}}\frac{d(\delta B_y)}{dx} = (A_{x1}^2 - 1)\delta B_y \equiv K_y\,\delta B_y \quad (13)$$

$$\frac{\eta A_{x1}^2}{\mu_0 v_{x1}}\frac{d(\delta B_z)}{dx} = \frac{A_{x1}^2\,(v_{x1}^2 - c_{f1}^2)(v_{x1}^2 - c_{s1}^2)}{v_{x1}^2\,(v_{x1}^2 - c^2)}\,\delta B_z \equiv K_z\,\delta B_z \quad (14)$$

As before, the subscript 1 can be replaced by 2 for the downstream point. The second of these equations was first derived by *Coroniti* [1970] in his study of slow and fast shocks; it is in fact valid for all resistive shocks. The first equation is not needed for fast and slow shocks, since they permit a shock structure with $B_y \equiv 0$ (however, to prove that $B_y = 0$ in fact is the only possibility, one needs it).

We first review the nature of the fixed points for different values of the coefficients (eigenvalues) K_y and K_z on the right-hand sides of equations (13) and (14). Four possibilities exist. First, if both K_y and K_z are positive the point examined is an unstable node. By unstable is meant that infinitesimal deviations δB_y and/or δB_z lead to exponential growth of B_y and/or B_z away from their values at the fixed point. Second, if both K_y and K_z are negative the point is a stable node instead. Third, if K_y is positive and K_z negative we have a saddle point that is unstable (in the sense described above) to deviations δB_y and stable to deviations δB_z. Finally, for K_y negative and K_z positive we have a saddle point that is stable to deviations δB_y and unstable to deviations δB_z.

Next, let us examine the nature of the upstream fixed point for intermediate shocks. First, since $A_{x1}^2 > 1$, we know that K_y is positive. The constant K_z is also positive both for the subfast subsonic case and for the superfast (and therefore by necessity supersonic) case. In these two cases the upstream point is therefore an unstable node. This means that an infinite number of solutions to equations (10)-(12) exist where B_y and B_z, in different proportions, start to deviate from their initial upstream values as x increases. In the subsonic case the node is located on the minus Riemann sheet; in the supersonic case it is located on the plus sheet. For the subfast supersonic case, we have $K_z < 0$ so that the upstream point is a saddle point located on the plus Riemann sheet and stable to perturbations δB_z; unstable to perturbations δB_y. Therefore any continuous solution for the subfast supersonic case must start out from the point $B_y = 0$ $B_z = B_{z1}$ with $\delta B_z = 0$ and $\delta B_y \neq 0$. In other words, the solution must start as a pure field rotation. A second possibility is that the solution is discontinuous at the upstream point and starts with a gas dynamic shock which provides a transition to subsonic (but still super-alfvénic) conditions. Following this gas dynamic substructure, a purely resistive part of the shock structure will occur.

We turn now to an examination of the two possible downstream states for an intermediate shock: the subslow and the superslow cases. For both, we have $A_{x2}^2 < 1$ and therefore $K_y < 0$. For the subslow or strong IS case, the flow must also by necessity be

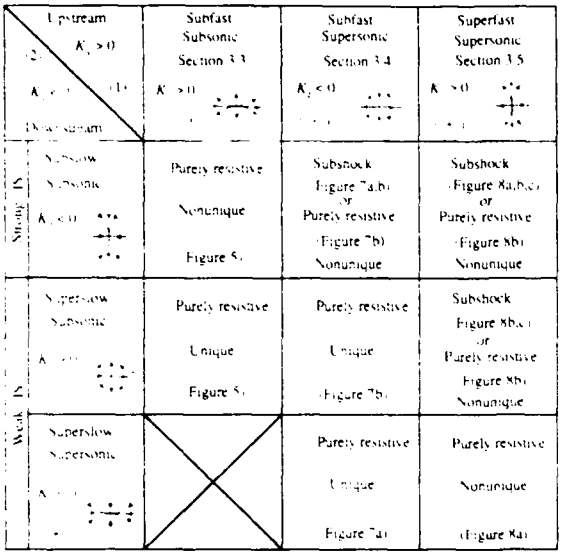

Fig. 4. Matrix showing possible intermediate shock conditions and structures. K_y and K_z are coefficients defined by equations (13) and (14). The symbols plus and minus refer to the supersonic and subsonic Riemann sheets. Nature of upstream and downstream fixed points (nodes or saddle points) are shown schematically.

subsonic so that $K_z < 0$. Thus the subslow downstream point is always a stable node located on the minus Riemann sheet. An infinite number of solutions exist that approach the downstream stable node exponentially as $x \to \infty$. For the case of superslow downstream conditions, the flow may either be subsonic or supersonic. In the latter case, $K_z < 0$ and we again have a stable node but now on the plus Riemann sheet; in the former case, $K_z > 0$ and we have a saddle point on the minus sheet, stable to approach along the B_y axis and unstable to approach along the B_z axis.

The preceding discussion is summarized in the matrix, shown in Figure 4. In most cases, purely resistive IS structures require the upstream and downstream points to be located on the same Riemann sheet. It is seen that there are four such cases: (1) For subfast subsonic upstream conditions the strong IS, i.e., the (downstream) subslow subsonic case is purely resistive and the structure is expected to be nonunique because an unstable and a stable node can be connected by an infinite number of paths in the $B_y B_z$ plane. (2) For the same upstream conditions, the weak IS, i.e., the superslow but subsonic case, also has a purely resistive structure, which is expected to be unique, except for the sign of B_y, because only two paths from the upstream unstable node lead into the downstream saddle point from the stable directions. (3) For the case of subfast but supersonic upstream conditions, only the weak IS structure is located entirely on one Riemann sheet and then only when the downstream flow remains supersonic. For the same reason as in the previous case, a unique structure is expected. (4) For superfast (and therefore supersonic) upstream conditions, it is again only the weak IS with supersonic downstream conditions that is located entirely on one Riemann sheet. This time an unstable upstream node is connected to a stable downstream node; this connection is expected to be nonunique.

For the remaining positions in the matrix shown in Figure 4, a transition from one Riemann sheet to the other must occur at some location in the shock structure. As pointed out already, such a transition is usually achieved by means of an ordinary viscous/heat conductive gasdynamic shock which is to be treated as a discontinuity in the present purely resistive theory. Another possibility, to be discussed further below, is that a smooth purely resistive transition from supersonic to subsonic conditions occurs. One location in the matrix is excluded altogether, on the basis that a shock cannot achieve a transition from subsonic to supersonic flow.

From the discussion above, it may appear that the equations (10)-(12) have three fixed points corresponding to the upstream state and the two downstream states of the IS. In fact, as we shall see, there is a fourth fixed point which corresponds either to the upstream or the downstream state of a fast shock. In the former case, this point is an unstable node on the supersonic (plus) Riemann sheet and it also serves as the upstream state of superfast ISs; in the latter case it is either a saddle on the plus sheet with stable approach along the B_z axis or it is an unstable node on the minus sheet.

We now discuss in quantitative detail the nature of the tangential magnetic field behavior in resistive intermediate shocks. The results to be presented were obtained by numerical integration of equation (10) and (11). They will be displayed in terms of magnetic hodograms, i.e., plots of B_z versus B_y. In these plots, the upstream and downstream states have $B_y = 0$.

3.3. *Subfast Subsonic Upstream Flow*

In this case, which comprises the second column of the matrix in Figure 4, the minus sign has to be used in equation (12) for the three relevant fixed points, because the upstream state and the two downstream states of the IS are all subsonic. Thus we may confine our attention to the hodogram in the subsonic (minus) Riemann sheet (the other sheet will be discussed in section 3.5). Figures 5*a*-5*d* show such hodograms in the case where $\beta_1 = 1$, and $\theta_1 = 45°$ for which all ISs are subfast and subsonic. As discussed previously, this means the upstream and the strong-IS (subslow) downstream states are nodal points and the weak-IS (superslow) downstream state is a saddle point. We start by examining the magnetic hodogram in Figure 5*b*. It is seen in this figure that the strong-IS transition is nonunique: it can be achieved not only with $B_y = 0$ (i.e., going along the vertical axis in the diagram) but also along an infinite number of other trajectories which have $B_y \neq 0$, leading from the upstream point, labeled 1 to the strong-IS downstream state, labeled 2*s*. The node structure of points 1 and 2*s* is evident in the figure. It is also seen that $|B_y|$ cannot become arbitrarily large in the strong-IS transition. There exists an outer bounding trajectory which leads along a nearly circular arc, from the upstream point to the weak-IS downstream state, labeled 2*w*, and is followed by a straight-line segment upward along the vertical axis to the strong-IS downstream state. As mentioned in section 2, the transition $2w \to 2s$ consists of a slow shock. It is also clear that the outer bounding trajectory is the only possible transition from the upstream state to the weak-IS downstream state. Thus, except for the sign of B_y, the resistive structure of the weak IS is unique whereas the nonunique strong IS structure is bounded as follows: at one extreme it can be viewed as a weak-IS field rotation followed by a slow shock; at the other extreme it has no field rotation at all ($B_y = 0$). In between these extremes, a strong-IS structure follows the weak-IS curve some distance away from the upstream point (1) and then starts to deviate toward the strong-IS downstream state (2*s*). Along the weak-IS trajectory, there is a small decrease in field magnitude, produced by slow mode compression but the main effect is a field rotation. (For the

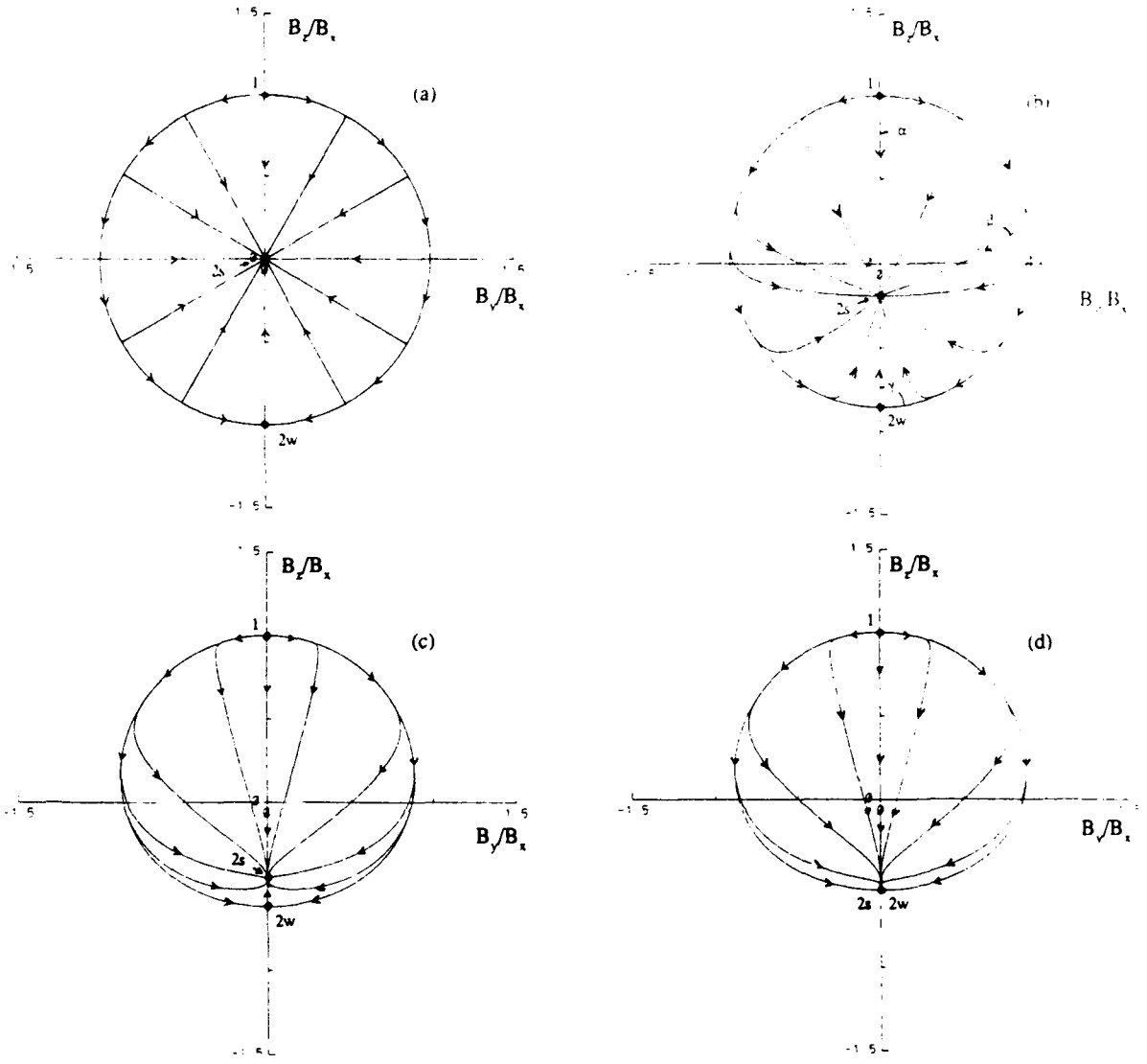

Fig. 5. Magnetic field hodograms in the minus Riemann sheet for subfast subsonic upstream normal flow, shown for $\beta_1 = 1$ and $\theta_1 = 45°$ and (*a*) $A_{x1}^2 = 1$; (*b*) $A_{x1}^2 = 1.0428$; (*c*) $A_{x1}^2 = 1.0745$; (*d*) $A_{x1}^2 = 1.0765$. For detailed discussion, see section 3.3. In part 5*a* the weak IS transition, $1 \rightarrow 2w$, corresponds to a rotational discontinuity and the strong IS transition, $1 \rightarrow 2s$, to a switch-off shock or to a rotational discontinuity followed by a switch-off shock. In part 5*d* the downstream flow is critical slow (*cs*).

case shown in Figure 5*b*, this trajectory is described with good approximation as an arc of a circle with its center at $B_y = 0$, $B_z = (B_{z1} + B_{z2})/2$.) Thus, this leading-edge portion of the strong-IS shock can be said to be dominated by the intermediate wave mode. On the other hand, its trailing edge portion involves field rotation accompanied by a substantial net decrease in field magnitude so that the slow mode compression in this part of the structure is strong.

The separation of intermediate and slow mode effects in the strong IS becomes perfect in the limit as $A_{x1} \rightarrow 1$, i.e., for the switch-off shock. The hodogram for this case, shown in Figure 5*a*, has a purely circular weak-IS trajectory corresponding to RD behavior, followed (for a strong IS) by purely radial slow-mode field decrease to the point 2*s* at the origin. However, as pointed out already, the RD portion of the structure will in fact be infinitely thick. Thus the only switch-off shock structure having a finite thickness is that for which $B_y = 0$. It is for this reason that the switch-off shock is classified as a slow shock rather than as an intermediate one.

It is also noted that those solutions on the strong IS branch which have $B_y \equiv 0$ do not involve the intermediate mode at all but represent simply an extension of the slow-mode shock branch into the super-alfvénic regime.

In terms of the properties of the fixed point 2*s* in Figure 5, it is noted that, for the switch-off shock in part 5*a* of the figure, this point is degenerate in the sense that the two eigenvalues, K_y and K_z, characterizing the solution near the point [e.g., *Hochstadt*, 1964] are equal, giving the appearance of an axisymmetric sink at the origin. In Figure 5*b* the behavior at point 2*s* appears nearly the same because the two eigenvalues are close but not identical. The usual nondegenerate node behavior which has two principal and orthogonal asymptotic directions of approach (or departure) of the trajectories is always evident for the upstream point (1). In Figure 5*c* which has a larger value of A_{x1} than Figure 5*b*, this

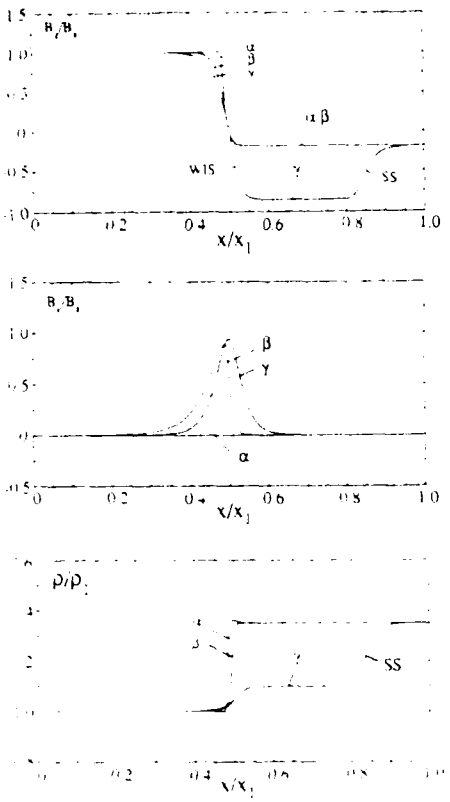

Fig. 6. Spatial structure of strong and weak intermediate shocks with subfast subsonic upstream flow. Tangential magnetic field components B_z and B_y, and plasma density ρ are given as a function of distance, x, normal to the shock. The three curves shown in each panel correspond to the hodogram traces labeled α, β, and γ in Figure 5*b*. The curves α and β represent strong (downstream subslow) intermediate shocks (which have nonunique structure); the curve γ represents the special case of a strong IS composed of a weak IS (WIS, which has unique structure) followed by a slow shock (SS). The reference value ρ_1 is the upstream density and $x_1 = 500\,\eta/\mu_0 v_{A1}$.

behavior is evident at point 2*s* as well. It implies that the trailing edge of a subfast strong IS usually involves pure slow-mode expansion or compression, the only exception being the one trajectory that enters point 2*s* at right angles to the B_z axis. Figure 5*d* shows the limiting case where the strong and weak intermediate shocks coincide (2*s* = 2*w*), i.e., the (downstream) critical-slow case, for which A_{x1} has its maximum allowed value. The noncircular nature of the weak-IS trajectory is evident in both Figure 5*c* and 5*d*.

The thickness of the strong intermediate shock depends on its hodogram trajectory. The situation is illustrated in Figure 6 which shows B_z, B_y and ρ as a function of x for the hodogram trajectories labeled α, β, and γ in Figure 5*b*. The smallest thickness is obtained when $B_y \equiv 0$ (curve α). For hodograms extending to increasingly large $|B_y|$ values, the corresponding shock thickness also becomes increasingly large (curve β) and reaches a maximum for the outer bounding trajectory (curve γ). As pointed out already, this latter case consists of a weak IS followed by a slow shock. The slow shock may in fact be placed at an arbitrary location downstream of the weak IS. The case shown in Figure 6 has $A_{x1}^2 = 1.0428$: as $A_{x1}^2 \to 1$, the thickness of the weak IS approaches infinity. In this limit the weak IS becomes an RD.

As mentioned already, a subfast strong IS with $B_y \equiv 0$ (curve α in Figure 6) involves only the slow mode. As B_z decreases from its initially positive value to zero within such a shock, the density, shown in the third panel of Figure 6, is seen to increase, as expected in slow-mode compression. This density increase is followed by a small decrease as B_z reverses sign and increases in magnitude to its final negative value. This latter behavior corresponds to slow-mode expansion at the trailing edge of the shock structure.

3.4. *Subfast Supersonic Upstream Flow*

As indicated in the third column of the matrix in Figure 4, the upstream state in this case is a saddle point located on the plus Riemann sheet, and the strong IS downstream state is a stable node on the minus Riemann sheet. For the weak IS case, there are two possibilities which we discuss separately.

First, for certain parameter values, the downstream flow may remain supersonic in which case the downstream state is a stable node, also on the plus Riemann sheet so that a purely resistive weak IS exists. Trajectories on this sheet are shown as dashed lines in Figure 7*a* (for $\beta_1 = 0.5$, $\theta_1 = 26.57°$ and $A_{x1}^2 = 1.0546$). It is seen that only a single (approximately circular) trajectory connects the upstream saddle point with the downstream weak IS stable node, yielding again a unique weak-IS structure. The plus sheet also contains an unstable node and associated trajectories. These features are not shown in the figure but will be discussed in section 3.5. Trajectories on the minus Riemann sheet are shown by solid lines in Figure 7*a*. They emerge at the edge of a forbidden region in the B_yB_z plane, in which the square root in equation (12) is imaginary (at this edge, shown by the dash-dotted curve in the figure, the normal flow is sonic, $v_x = c$), and converge toward the strong IS downstream stable node. Transition from the plus sheet to the minus sheet is achieved by a gas dynamic shock (which leaves B_y and B_z unchanged). The transition point can be located anywhere on the approximately circular trajectory on the plus sheet from point 1 to point 2*w* (an example, denoted by *gs*, is shown in the figure). If it occurs immediately at the upstream edge (point 1) of the shock layer, the strong IS shock has $B_y \equiv 0$; if it occurs at point 2*w*, the strong IS has the appearance of a weak IS followed by a slow shock where the latter has a regular gas dynamic subshock at its upstream edge.

The second possibility is that the weak IS downstream flow is subsonic and corresponds to a saddle point located on the minus Riemann sheet (see matrix in Figure 4). An example of this situation is shown in Figure 7*b* (for $\beta_1 = 0.5$, $\theta_1 = 26.57°$ and $A_{x1}^2 = 1.1471$) where, as before, trajectories in the plus sheet are shown as dashed lines and those on the minus sheet as solid lines (as in Figure 7*a*, we have not shown an additional unstable node on the plus sheet and its associated trajectories; these features will be dealt with in section 3.5). In this case, the weak IS structure is again unique but there is now a smooth supersonic-subsonic transition at a sonic point ($v_x = c$), denoted by *sp* in the figure. This point is located where the trajectory out of the upstream saddle (point 1 on the plus sheet) and the trajectory into the downstream saddle (point 2*w* on the minus sheet) both reach, and are tangent to the boundary of the forbidden region. The strong IS structure remains nonunique and there are cases both with and without a gas dynamic shock. Such a shock, denoted by *gs* in the figure, can occur anywhere between points 1 and *sp* along the trajectory out of the upstream point. On the other hand, if this trajectory is followed all the way to the sonic point, *sp*, and perhaps some distance beyond it toward the point 2*w*, purely resistive strong IS structures are obtained.

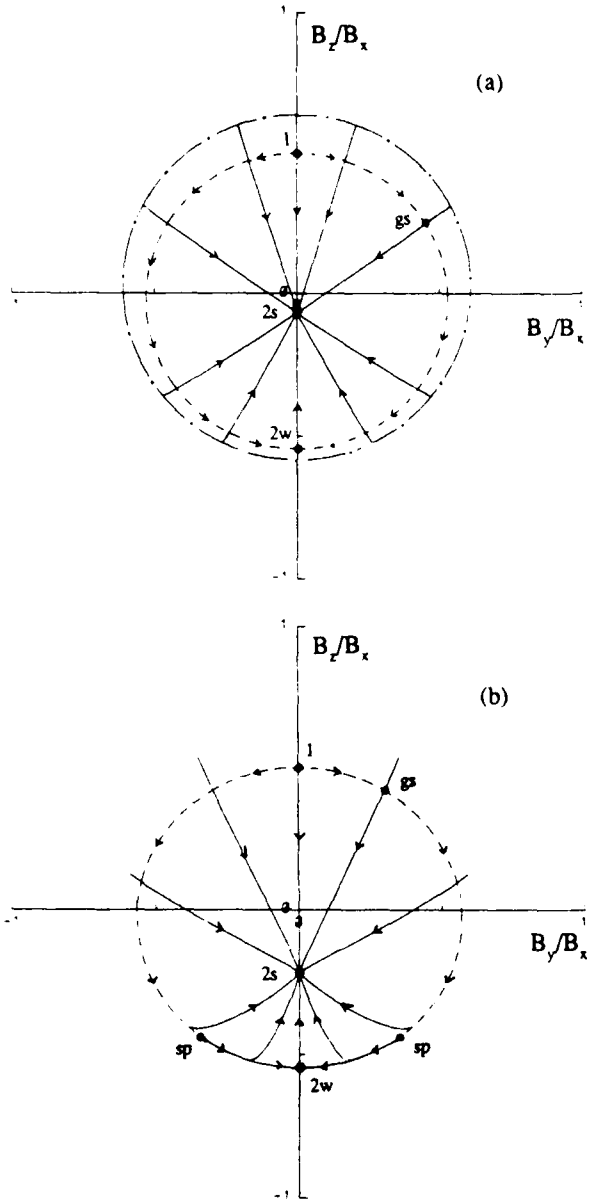

Fig. 7. Magnetic field hodograms for subfast supersonic upstream normal flow. Dashed curves are trajectories on the plus Riemann sheet; solid lines lie on the minus sheet. For detailed discussion, see section 3.4. Case 7*a*, with $\beta_1 = 0.5$, $\theta_1 = 26.57°$, $A_{x1}^2 = 1.0546$, has supersonic downstream state for the weak IS. For the strong IS, a gas dynamic shock (*gs*) provides transition from the plus to the minus sheet. The inner edge of the forbidden region is shown by the dash-dotted line. Case 7*b*, with $\beta_1 = 0.5$, $\theta_1 = 26.57°$, $A_{x1}^2 = 1.1471$, has subsonic downstream state for the weak IS. For the weak IS the supersonic-subsonic transition is continuous and occurs at the sonic point, *sp*. For the strong IS, a gas dynamic shock (*gs*) may occur anywhere between points 1 and *sp*. Another possibility is a continuous transition at point *sp*.

3.5 *Superfast Upstream Flow*

In this case, the upstream state is an unstable nodal point located on the plus Riemann sheet. For the downstream state, the situation is the same as the previous case, i.e., the strong IS downstream state is a stable node on the minus Riemann sheet, while there are two possibilities for the weak IS: its downstream state may be a stable node on the plus sheet or it may be a saddle point, stable to approach along the B_y direction, on the minus sheet. The former case is illustrated in Figure 8*a*, which is the same as Figure 7*a* but with the upstream fast-mode nodal point, 1*f* (on the plus sheet) and its associated trajectories shown. It is now this point that serves as the upstream point for the superfast intermediate shocks as well as for the regular fast shock. It has $\beta_{1f} = 0.4523$, $\theta_{1f} = 6.05°$, $A_{x1f}^2 = 1.2578$. These parameter values are such that the downstream state, 2*f*, of the fast shock remains supersonic. Any of the trajectories out of the node point 1*f* can be followed to the weak IS downstream state 2*w*. Included is the special case where the weak IS consists of a resistive fast shock transition from 1*f* to 2*f* (2*f* is the same as point 1 in Figure 7*a*), followed by a subfast-supersonic weak IS in which the flow remains supersonic ($v_{x2} > c_2$) and for which the hodogram trajectory consists of the unique path connecting point 1 to point 2*w*. At the other extreme is the special case where a direct transition along the B_z axis from 1*f* to 2*w* occurs. Thus the weak IS structure is now nonunique. The strong IS structure is also nonunique: one may follow any of the trajectories in the plus sheet out of point 1*f* and then make a transition, by means of a gas dynamic shock, *gs*, to the minus sheet in which one then follows one of the trajectories into the point 2*s*. At one extreme, the strong superfast IS structure may consist of the path 1*f*-2*f*-2*w*-2*s* with a gas dynamic shock to achieve a transition from the plus sheet to the minus sheet located at the point 2*w*. In this special case, the superfast strong IS consists of a resistive fast shock, followed by a subfast, supersonic purely resistive weak IS, followed by a slow shock with a viscous subshock at its upstream edge. At the other extreme, the superfast strong IS may consist of a direct transition along the B_z axis from 1*f* to 2*s* with a gas dynamic shock located somewhere between, or possibly at one or the other of these two points. Or it may cosist of a direct transition, along the B_z axis from 1*f* to 2*w*, followed by a slow shock from 2*w* to 2*s*, the latter having a viscous subshock at location 2*w*.

We now turn now to the second case mentioned above, where the downstream state for the weak IS is a saddle point on the subsonic (minus) Riemann sheet. This case is illustrated in Figure 8 for two situations. In Figure 8*b* the normal flow downstream of the fast shock remains supersonic ($v_{x2f} > c_{2f}$). This figure is the same as Figure 7*b* but with the upstream fast-shock nodal point, 1*f* (on the plus sheet) and its associated trajectories shown. The conditions at point 1*f* are: $\beta_{1f} = 0.4738$, $\theta_{1f} = 13.57°$, $A_{x1f}^2 = 1.3048$. In Figure 8*c* the normal flow downstream of the fast shock is subsonic ($v_{x2f} < c_{2f}$). This figure is the same as Figure 5*b* but with the supersonic (plus) Riemann sheet, which contains the upstream fast-shock nodal point, 1*f*, supplied. In this case, the conditions at point 1*f* are: $\beta_{1f} = 0.2586$, $\theta_{1f} = 1.74°$, $A_{x1f}^2 = 2.4129$. We discuss Figures 8*b* and 8*c* separately.

In Figure 8*b*, the superfast weak intermediate shock is nonunique and can correspond to any trajectory emerging from the upstream point 1*f*. There are two classes of such trajectories: those that reach sonic conditions, $v_x = c$, at the point, *sp*, and those that reach $v_x = c$ at the boundary of the forbidden region away from that point. For the former class, purely resistive weak IS structures exist with the supersonic-subsonic transition occurring at *sp*. For the latter class, that transition occurs in a gas dynamic shock, *gsw*, located where the trajectory in the plus sheet crosses the short segment of trajectory in the minus sheet between the points *sp* and 2*w*. The strong IS is also nonunique: again one can follow any trajectory emerging from point 1*f* in the plus sheet until it crosses one of the trajectories into point 2*s* in the minus

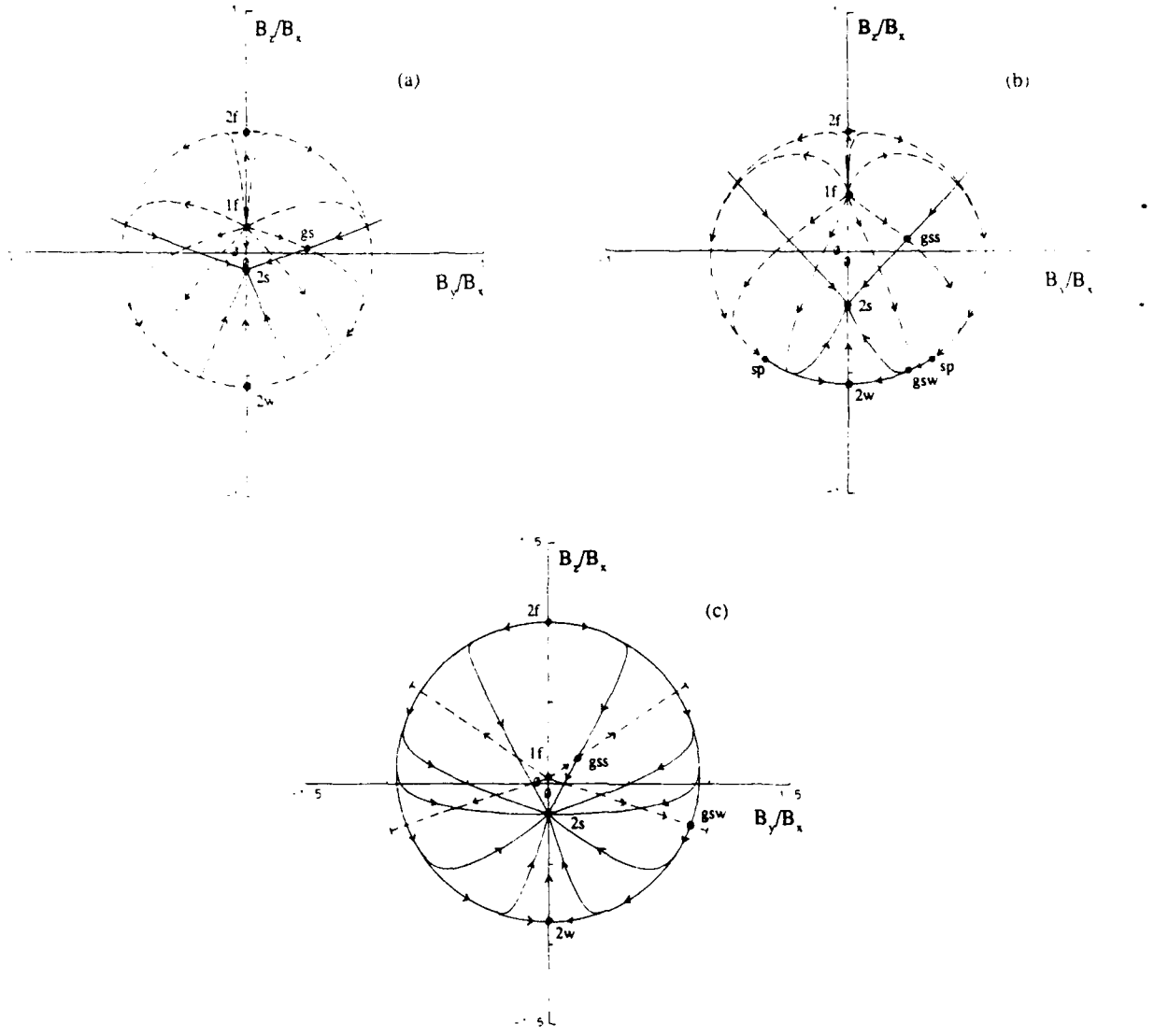

Fig. 8. Magnetic field hodograms for superfast (and therefore supersonic) upstream normal flow. Dashed curves are trajectories on the plus Riemann sheet; solid lines lie on the minus sheet. For detailed discussion, see section 3.5. Case 8*a* is identical to Figure 7*a* but with the fast-shock upstream node, 1*f*, on the plus Riemann sheet shown. This node has $\beta_{1f} = 0.4523$, $\theta_{1f} = 6.05°$, $A_{x1f}^2 = 1.2578$, and serves as the upstream state for the superfast weak and strong intermediate shocks. Case 8*b* is identical to Figure 7*b* but again with the node, 1*f*, on the plus sheet, shown. This node has $\beta_{1f} = 0.4738$, $\theta_{1f} = 13.57°$, $A_{x1f}^2 = 1.3048$, and again serves as the upstream state for the ISs. Case 8*c* is identical to Figure 5*b* but now with the plus Riemann sheet and the node 1*f* added. This node has $\beta_{1f} = 0.2587$, $\theta_{1f} = 1.74°$, $A_{x1f}^2 = 2.4129$.

sheet. At the crossing point, a gas dynamic shock, *gss*, brings the solution from the supersonic to the subsonic Riemann sheet. In this case too, purely resistive structures with a continuous supersonic-subsonic transition are possible and occur for all trajectories passing through point *sp*.

In Figure 8*c*, all shocks having their upstream conditions defined by point 1*f* must contain a gas dynamic subshock as part of their structure. For the fast-shock transition 1*f*-2*f* (2*f* is the same as point 1 in Figure 5*b*), this substructure must occur at the trailing edge, i.e., at point 2*f*, since this point is an unstable node. Both the weak and the strong IS have nonunique structures. In one extreme, the weak IS consists of a fast shock with a viscous subshock at its downstream edge, followed by a unique subfast subsonic weak IS along the outer bounding trajectory from point 1 to point 2*w*. In this same extreme, the strong IS has the same structure, followed by a purely resistive slow shock transition 2*w*-2*s*. In the other extreme, the weak IS has $B_y \equiv 0$ and is described by a trajectory from 1*f* to 2*w* on the plus sheet along the B_z axis, followed by a gas dynamic shock at 2*w* to bring the solution from the plus sheet to the minus sheet where point 2*w* is located. The strong IS, in this extreme, may be obtained either by adding a resistive slow shock at the downstream edge of the weak IS just described, or by direct transition from 1*f* to 2*s* along the B_z axis, with a gas dynamic shock located somewhere between these two points (or at one or the other of them). In between these extreme cases, weak IS structures all have a gas dynamic shock, *gsw*, located somewhere on the outer bounding trajectory connecting points 1 and 2*w*; strong IS structures have their gas dynamic shock, *gss*, located somewhere inside that bounding trajectory, at the intersection between a trajectory emerging from point 1*f* in the

plus sheet and a trajectory terminating at point 2*s* in the minus sheet, as illustrated in the figure.

4. Summary and Discussion

The principal defining property of an intermediate MHD shock (IS) is that it produces an abrupt transition from super-alfvénic to sub-alfvénic flow. The magnetic fields on the two sides of the shock obey the coplanarity theorem, i.e., the two field vectors and the shock normal vector lie in one plane, but in contradistinction to the better known fast and slow MHD shocks, the sense of the tangential magnetic field reverses across an intermediate shock. In this paper, we have examined the steady state structure of intermediate shocks by use of the resistive nonviscous MHD equations. The results may be summarized as follows.

1. When the upstream normal flow velocity, v_{x1}, in the shock frame is less than the local small-amplitude fast-mode MHD wave propagation speed, c_{f1}, as well as less than the local sound speed, c_1, the magnetic structure of weak ($v_{x2} > c_{s2}$) and strong ($v_{x2} < c_{s2}$) intermediate shocks is described by a hodogram having the topology shown in Figure 8*c* (see also Figure 5) (the downstream normal flow speed and small-amplitude slow-mode MHD wave propagation speed are denoted by v_{x2} and c_{s2}, respectively). The weak IS has a unique structure which involves a deviation of the magnetic field from coplanarity within the shock layer. The tangential field behavior consists mainly of a rotation by 180° accompanied by a more or less pronounced change in field magnitude. The strong IS has a nonunique structure which in one extreme satisfies coplanarity and in the other extreme looks like a weak IS followed by a slow shock.

2. When $c_{f1} > v_{x1} > c_1$, two hodogram topologies are possible, namely that shown in Figure 8*a* (or Figure 7*a*) when $v_{x2} > c_2$ for the weak IS, and that shown in Figure 8*b* (or Figure 7*b*) when $v_{x2} < c_2$ for the weak IS. As in the previous case, the weak IS has a unique structure, the strong IS does not.

3. When $v_{x1} > c_{f1}$, all three hodogram topologies in Figure 8 are possible. When the downstream normal flow speed, v_{x2f} of a fast shock (having the same upstream state as the IS) is subsonic, the hodogram topology is that shown in Figure 8*c*. In the case where v_{x2f} is supersonic instead, the hodogram topology is that shown in Figure 8*a* when the downstream state of the weak IS is supersonic, $v_{x2} > c_2$, and is that shown in Figure 8*b* when the downstream state of the weak IS is subsonic, $v_{x2} < c_2$. Both weak and strong ISs have nonunique structures.

4. The three hodogram topologies in Figure 8 are the only ones that occur (except for transition cases between them).

5. Intermediate resistive shocks that involve a transition from supersonic to subsonic values of the normal flow speed usually contain a discontinuity consisting of a regular gas dynamic shock in which dissipation processes other than resistivity, namely, viscosity and heat conductivity are dominant. However, in special cases, it appears that a continuous purely resistive transition from supersonic to subsonic flow, i.e., a transition without a gas dynamic subshock, can occur.

6. The overall thickness of resistive shocks is proportional to $A_{x1}^2\lambda_{r1}$ where A_{x1} is the Alfvén number based on the upstream normal flow speed, $A_{x1}^2 \equiv v_{x1}^2\mu_o\rho_1/B_{x1}^2$, and λ_{r1} is the resistive length, $\lambda_{r1} \equiv \eta/\mu_o v_{x1}$. However, the complete dependence of shock thickness on A_{x1} is more complicated. For example, the weak IS shock thickness approaches infinity as A_{x1} approaches unity. When the shock structure is nonunique, the shock thickness is usually greater the greater the deviation of the magnetic field from coplanarity within the shock layer.

Several comments should be made about these results. First, we have found a large number of possible equilibrium structures for resistive intermediate shocks. We have not examined the stability of all, or most of these equilibria. Numerical simulations by *Wu* [1987, 1988*a*, *b*], as well as a few simulations that we have undertaken ourselves indicate that at least some of these structures are indeed stable, but a complete survey of the stability properties is not available at present. In particular, the stability of cases involving a smooth purely resistive transition from supersonic to subsonic normal flow needs to be examined, along with cases where this transition is effected by a gas dynamic subshock having a nonunique location within the overall shock structure.

Another remaining task is to map out the regions in parameter space in which the three different types of hodogram topology occur. The relevant parameter space is three dimensional and is defined by the upstream plasma beta, $\beta_1 = p_1\, 2\mu_o/B_1^2$, the upstream angle, θ_1, between shock normal and magnetic field, and the upstream normal Alfvén number $A_{x1}^2 \equiv v_{x1}^2\mu_o\rho_1/B_{x1}^2$. With the exception of the limited information provided in Figure 2, such an overview is not at hand. However, for any chosen set of parameters, the conditions given in items (1)-(3) above can be used in a straightforward manner to establish the relevant hodogram topology.

It should be noted that the three hodogram classes in Figure 8 also incorporate fast and slow resistive shocks. In particular, we have recovered the well known result for such shocks that when a transition from supersonic to subsonic normal flow is required, this transition is effected by a gas dynamic subshock located at the upstream edge of a slow-shock layer and at the downstream edge of a fast-shock layer [*Coroniti*, 1970; *Kennel and Edmiston*, 1988]. The only case not contained in the main part of the paper is that of switch-on shocks. However, since such shocks are close neighbors to the intermediate shocks, they are discussed briefly in the appendix.

Finally, we emphasize that we do not claim that resistive intermediate-shock structures are necessarily directly relevant to space plasma applications such as the magnetopause (during reconnection) or the solar wind. In these applications, effects other than classical electrical resistivity are likely to be important and perhaps to dominate the structure of these shocks. In particular, dispersive effects generated by the Hall term in Ohm's law should be included, as in the early study by *Bickerton et al.* [1971]. Nevertheless, as has been the case for fast and slow shocks, the development of our understanding of structure can profitably use the resistive MHD limit as a starting point. Furthermore, many numerical simulations of magnetospheric and space plasma phenomena such as reconnection are based on the resistive MHD description. The results provided in this paper should prove useful for the identification of field-reversing shock structures that may arise in such simulations. For example, it follows from Figure 5 that only strong, not weak subfast intermediate shocks can occur in two-dimensional simulations where the magnetic field and flow vectors are confined to the simulation plane.

Appendix

In the special case where the shock propagates exactly along the upstream magnetic field, $\theta_1 = 0$, the shock curve, defined by equation (6), reduces to the straight line given by

$$A_{x1}^2 = \frac{\gamma+1}{\gamma-1} A_{x2}^2 - \frac{\gamma}{\gamma-1}\beta_1 \qquad \text{(A1)}$$

plus the portion of the line $A_{x2}^2 = 1$ for which A_{x1}^2 lies between unity and the value $(\gamma+1)/(\gamma-1) - \gamma\beta_1/(\gamma-1)$. The situation is shown in Figure A1 from which it is clear that the intermediate shock branch exists only for $\beta_1 < 2/\gamma$ and that it then has a triangular shape. The downstream superslow (weak) branch of this IS curve is the vertical line at $A_{x2}^2 = 1$ located between $A_{x1}^2 = 1$ and the tip of the triangle at $A_{x1}^2 = (\gamma+1)/(\gamma-1) - \gamma\beta_1/(\gamma-1)$, although this portion of the shock curve can also be viewed as part of the fast-shock branch. The downstream-subslow (strong) branch of the IS curve is the portion of the line given by equation (A1) located between $A_{x1}^2 = 1$ and $A_{x1}^2 = (\gamma+1)/(\gamma-1) - \gamma\beta_1/(\gamma-1)$.

The weak IS branch corresponds to so-called switch-on shocks for which the downstream state has $A_{x1}^2 = 1$ and a nonzero tangential magnetic field B_{t2}. The magnitude of this field can be obtained by putting $A_x^2 = A_{x2}^2 = 1$ and $\theta_1 = 0$ in equation (12):

$$\frac{B_2^2}{B_x^2} = 1 + \frac{B_{t2}^2}{B_x^2} = \gamma[(\beta_1 - 1) + (2-\beta_1)A_{x1}^2 - \frac{\gamma-1}{\gamma}A_{x1}^4] \quad \text{(A2)}$$

It can be shown from this formula that the two end points of the weak IS branch have $B_2^2/B_x^2 = 1$ (i.e., no tangential field is generated) and that a maximum value of B_2^2/B_x^2 occurs at $A_{x1}^2 = \gamma(2-\beta_1)/2(\gamma-1)$ and is given by

$$(\frac{B^2}{B_x^2})_{max} = \frac{\gamma}{\gamma-1}(1 - \beta_1 + \frac{\gamma\beta_1^2}{4}) \quad \text{(A3)}$$

It is seen that this maximum value is largest for $\beta_1 = 0$.

The structure of resistive switch-on shocks can be obtained from equations (10)-(12). From the first two of these equations, with $B_{x1} = 0$, it is seen that the magnetic hodogram will consist of purely radial straight lines through the origin. Thus unless a rotational discontinuity is added at its trailing edge, the switch-on shock has a purely coplanar structure and does not involve the intermediate mode. For this reason, it is most appropriately classified as a fast shock.

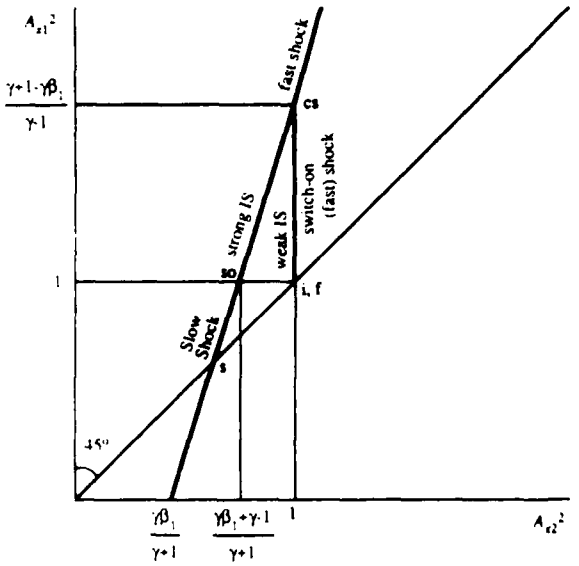

Fig. A1. Shock curve for the case $\theta_1 = 0$. Switch-on shocks occur along vertical portion of the shock curve at $A_{x2}^2 = 1$ in the range $1 < A_{x1}^2 < (\gamma+1-\gamma\beta_1)/(\gamma-1)$.

The structure of a resistive switch-on shock involves a gas-dynamic subshock located at the downstream edge of the shock layer, whenever a supersonic to subsonic transition of the normal flow is required, as discussed by *Bleviss* [1960]. As an example, for $\gamma = 5/3$ and $\beta_1 = 0$ one can show that a purely resistive structure of the switch-on shock occurs only in the range $1 \le A_{x1}^2 \le 1.708$, whereas the entire possible range for the switch-on shock in this case is $1 \le A_{x1}^2 \le 4$.

The strong IS branch for $\theta_1 = 0$ also coincides with a portion of the fast-shock branch. If the corresponding shocks are viewed as fast shocks, they are ordinary gas dynamic shocks in which the magnetic field remains equal to $B_x e_x$ throughout the shock structure and where the structure is determined entirely by viscosity and heat conductivity. However, if they are viewed as ISs instead, another possibility, pointed out by *Kantrowitz and Petschek* [1966], exists: such a shock can be composed of a switch-on shock followed by a switch-off shock traveling at the same speed. This possibility exists because the downstream Alfvén number for the former shock is $A_{x2} = 1$ which is also the required upstream Alfvén number for a switch-off shock (more generally, we have pointed out that the downstream state for any weak IS is also the upstream state for a slow shock propagating at the same speed as the weak IS and producing the same downstream state as the strong IS mode). It would also be possible to insert a rotational discontinuity, with an arbitrary angle of rotation, $\Delta\phi$, of the tangential magnetic field, between the switch-on and the switch-off shock, in which case the strong IS hodogram would have the appearance of a segment of pie. However, for finite resistivity this RD would have infinite thickness. For further discussion of switch-on shocks, the reader is referred to *Kennel and Edmiston* [1988].

Acknowledgments. We thank one of the referees for drawing our attention to the thesis at MIT by J. E. Anderson, published in monograph form [*Anderson*, 1962], which contains discussion of shock curves and of fixed-point analysis somewhat similar to that given in our paper. The research was supported by the National Science Foundation, Atmospheric Sciences Division, under grants ATM-8507192 and ATM-8807645, and by the Air Force Geophysics Laboratory under grants F19628-87-K-0026 and F19628-87-K-0038 to Dartmouth College.

The editor thanks R. Blandford and K. B. Quest for their assistance in evaluating this paper.

REFERENCES

Anderson, J. E., *Magnetohydrodynamic Shock Waves*, MIT Press, 1962.

Bickerton, R. J., L. Lenamon, and R. V. W. Murphy, The structure of hydromagnetic shock waves, *J. Plasma Phys.*, *5*, 177, 1971.

Bleviss, Z. O., A study of the structure of the magnetohydrodynamic switch-on shock in steady plane motion, *J. Fluid Mech.*, *9*, 49, 1960.

Coroniti, F. V., Dissipation discontinuities in hydromagnetic shock waves, *J. Plasma Phys.*, *4*, 265, 1970.

Hochstadt, H., *Differential Equations, a Modern Approach*, p. 256, Dover, New York, 1964.

Jeffrey, A., and T. Taniuti, *Non-Linear Wave Propagation*, Academic, San Diego, Calif., 1964.

Kantrowitz, A. R., and H. E. Petschek, MHD characteristics and shock waves, in *Plasma Physics in Theory and Application*, edited by W. B. Kunkel, MaGraw-Hill, New York, 1966.

Kennel, C. F., and J. P. Edmiston, Switch-on shocks, *J. Geophys. Res.*, *93*, 11,363, 1988.

Lee, L. C., L. Huang, and J. K. Chao, On the stability of rotational discontinuities and intermediate shocks, *J. Geophys. Res.*, in press, 1989.

Shercliff, J. A., One-dimensional magnetogasdynamics in oblique fields, *J. Fluid Mech.*, *9*, 481, 1960.

Sonnerup, B. U. Ö., I. Papamastorakis, G. Paschmann, and H. Lühr, Magnetopause properties from AMPTE/IRM observations of the convection electric field: Method development, *J. Geophys. Res.*, *92*, 12,137, 1987.

Wu, C. C., On MHD intermediate shocks, *Geophys. Res. Lett.*, *14*, 668, 1987.

Wu, C. C., The MHD intermediate shock interaction with an intermediate wave: Are intermediate shocks physical?, *J. Geophys. Res.*, *93*, 987, 1988*a*.

Wu, C. C., Effects of dissipation on rotational discontinuities, *J. Geophys Res.*, *93*, 3969, 1988*b*.

L.-N. Hau and B. U. Ö. Sonnerup, Thayer School of Engineering, Dartmouth College, Hanover, NH 03755.

(Received October 14, 1988;
revised February 3, 1989;
accepted February 7, 1989.)

Appendix 8

The Structure of Resistive-Dispersive Intermediate Shocks

L.-N. HAU AND B.U.Ö. SONNERUP

Thayer School of Engineering, Dartmouth College, Hanover, New Hampshire

The structure of intermediate shocks is studied on the basis of the resistive, nonviscous two-fluid equations. Electron inertia effects are neglected so that the generalized Ohm's law contains only the Hall current and the electron pressure terms in addition to the usual resistive term and the electric field. As for the case of purely resistive MHD, reported recently by Hau and Sonnerup (Journal of Geophysical Research, 94, 6539, 1989), fixed-point analysis is performed to examine the nature of the magnetic structure near the upstream and downstream states of the intermediate shock. The one-dimensional, steady-state, resistive Hall MHD equations are then integrated numerically to generate complete shock structures which are presented in the form of magnetic hodograms. These hodograms describe fast and slow shocks in addition to intermediate shocks. As expected, the calculations show that the main effect of Hall currents is to remove the symmetry between left-hand and right-hand polarized shock structures found in the purely resistive case and sometimes to convert the smooth shock transitions obtained from the resistive MHD model into transitions that incorporate oscillatory standing wave-train structures at their upstream and/or downstream edge. The magnetic structure in the plane of the shock near the possible upstream and downstream states of the intermediate shock, which in the case of purely resistive MHD is either a node or a saddle, can be either a node, a saddle or a spiral point, the latter corresponding to a standing wave train, when the Hall term is included. As a result, the number of possible types of magnetic hodogram topology increases from 3 in the resistive case, to a total of 20. However, it appears that the constraints provided by the shock jump conditions make certain of these topologies unattainable: only 13 of the 20 cases have been found and are reported in the paper. The relationship between small amplitude dispersive waves in the flow upstream or downstream of a shock and the nature of the corresponding fixed point is also discussed.

1. Introduction

The subject of intermediate shocks, i.e., shocks that effect a transition from superalfvénic to subalfvénic flow and that reverse the magnetic field component tangential to the shock, has been reopened recently, as a result of the numerical MHD simulation results of *Wu* [1987; 1988*a*,*b*]. One of the peculiarities of the intermediate shock (IS), obtainable directly from the MHD jump conditions, is that for one and the same upstream condition, the IS can have two different downstream states: one of these is subslow ($v_{x2} < c_{s2}$) corresponding to what is termed a "strong" IS, the other is superslow ($v_{x2} > c_{s2}$) corresponding to a "weak" IS. When the upstream flow is subfast, i.e., $v_{x1} < c_{f1}$, the latter is also referred to as an Alfvén shock [e.g., *Jeffrey and Taniuti*, 1964]. Here v_x is the flow velocity component perpendicular to the shock, measured in the shock frame, and the subscripts 1 and 2 denote conditions upstream and downstream of the shock, respectively. Also, c_f and c_s are the fast and slow wave-mode speeds in a direction perpendicular to the shock. It can be shown that the two IS downstream states also satisfy the jump conditions of a slow shock (SS) propagating at the same speed as, and behind the weak IS . Similarly, one can show that the downstream state of a fast shock can also serve as the upstream state of an intermediate shock propagating at the same speed as, and behind the fast shock.

By performing fixed-point analysis of the behavior of the magnetic field components tangential to the shock surface at the possible upstream and downstream states of intermediate shocks and by solving the one-dimensional, steady-state, resistive, nonviscous MHD equations numerically, *Hau and Sonnerup* [1989] (hereafter referred to as Paper I) have studied the structure of purely resistive ISs. Their results can be summarized as follows. (1) There exist three basic types of magnetic hodogram topology, describing the resistive IS structure; slow-mode and fast-mode shocks are contained within these hodograms as well. These topologies are characterized by the normal flow speed, v_x, (in the shock frame) relative to the fast-wave speed (c_f) and the sound speed (c) at the upstream and downstream states. (2) All subfast weak ISs, i.e., all ISs which have an upstream normal flow velocity, v_{x1}, less than the upstream small-amplitude fast-mode wave speed, c_{f1}, perpendicular to the shock ($v_{x1} < c_{f1}$) and a downstream normal flow speed, v_{x2}, greater than the downstream small-amplitude slow-mode wave speed, c_{s2}, perpendicular to the shock ($v_{x2} > c_{s2}$), have a unique magnetic structure (except for the sense of polarization) consisting mainly of a rotation of the tangential magnetic field, accompanied by a more or less pronounced change in field magnitude. (3) On the other hand, all subfast strong ISs (i.e., $v_{x1} < c_{f1}$ and $v_{x2} < c_{s2}$) have nonunique magnetic structure. (4) The structures of both superfast weak ISs ($v_{x1} > c_{f1}$ and $v_{x2} > c_{s2}$) and superfast strong ISs ($v_{x1} > c_{f1}$ and $v_{x2} < c_{s2}$) are nonunique. (5) When the IS involves a transition from supersonic to subsonic conditions, the purely resistive IS structure usually contains a discontinuous substructure consisting of an ordinary gasdynamic shock in which dissipation processes other than resistivity, viz., viscosity and heat conductivity, are dominant. However, in certain special cases, shock structures containing a continuous, purely resistive transition from supersonic to subsonic flow appear possible, although the stability of such structures has not been established.

The overview of possible resistive MHD IS structures, described above, is useful in some respects, e.g., for the identification of field-reversing shocks in MHD numerical simulations of reconnection (see *Scholer*, [1989]). However,

effects other than the electrical resistivity are usually important in space plasmas and therefore should be included. In this paper, we will use a nonviscous resistive two-fluid model to study the dispersive structure of intermediate shocks. However, for simplicity, we shall neglect the electron inertia terms in the generalized Ohm's law, leaving the Hall current term as its only important new feature. We refer to this plasma description as resistive Hall MHD.

Even though viscous effects and heat conduction are expected to be important dissipative mechanisms in many intermediate shocks, there are several reasons for not including these effects at the present time. To gain physical insight, we find it desirable to add the various processes that operate in the shock one by one. In this manner, one can come to appreciate the role played by each individual process as it is added to the analysis. From this standpoint, the simplest dissipation mechanism to incorporate is ordinary electrical resistivity. This was done in Paper I. The logical next step is to add dispersion effects. This is done in the present paper by inclusion of the Hall term in Ohm's law. Viscosity and heat conductivity should be ultimately included as well but it is noted that these effects lead to added complexity in the mathematical structure of the problem, namely a change from a second order to a sixth order system so that six, rather than two eigenvalues are obtained at each fixed point. As pointed out above, and discussed further in Paper I, the case of small but finite viscosity and heat conductivity can in fact be understood rather well without actually including these effects in the analysis: when these dissipation coefficients are small compared to the resistivity, they tend to be important only in narrow substructures of the shock. These substructures show up as discontinuities in the purely resistive as well as in the resistive-dispersive shock structure. They are in fact ordinary gasdynamic shocks and the role played by viscosity and heat conductivity in them is well understood. Finally, we note that the correct form of the viscous and heat conduction terms in the equations describing a collisionless magnetized plasma remains open to debate. For this reason, it is not a simple matter to incorporate these effects in a realistic fashion. Although a similar statement can be made about electrical resistivity effects in a collisionless plasma, the simple constant resistivity to be used in this paper should be sufficient to capture most of the essential features of resistive shocks.

The effect of Hall currents on the intermediate shock structure was also considered in the early work by *Bickerton et al.* [1971] and in the recent study by *Kennel et al.* [1989]. Some of the results to be presented here are similar to those reported in these papers. However, direct quantitative comparison is not possible (except in cases where resistive dissipation dominates) since, unlike these studies, our analysis does not include viscous and heat conduction terms. Our work is more complete than that of Bickerton et al. in the sense that we present a catalog of all allowed hodogram topologies; it is more general than the work of Kennel et al. in the sense that it is not restricted to small shock amplitudes or small angles, θ_1, between the shock normal and the upstream magnetic field. By performing numerical two-fluid simulations (including electron inertia) in which viscosity and heat conductivity were the dominant transport coefficients, *Lyu and Kan* [1989] recently found that an initial discontinuity, which satisfies the jump condition of a subfast, subsonic weak IS and which has a smooth field rotation with either the right-hand or the left-hand polarization, evolves to an S-shaped hodogram structure with upstream right-hand polarization and downstream left-hand polarization. On the basis of their results, Lyu and Kan suggest that the S-shaped hodograms with a net rotation angle of the tangential magnetic field component of 180°, occasionally observed at the magnetopause [*Berchem and Russell*; 1982*a*], may correspond to Alfvén shocks, i.e., to subfast weak intermediate shocks. However, it will be shown here that, at least in resistive Hall MHD, S-shaped hodograms may occur not only for the weak but also for the strong IS.

The paper is organized as follows. In sections 2 and 3, we will present the basic equations and discuss the magnetic structure near the upstream and the downstream states of ISs by performing fixed-point analysis. In addition to a node and a saddle, which are the only possibilities in resistive MHD, the magnetic structure in the B_yB_z plane (the coordinates y and z are tangential to the shock) at a stationary point can now also be a spiral, owing to the effect of Hall currents. The actual shock structure will depend, not only on the upstream plasma beta value, β_1, shock angle, θ_1, and Alfvén number, A_{x1}, but also on one additional parameter, namely h, the ratio of electron gyrofrequency to collision frequency. Using the same type of analysis as in Paper I, all allowed types of magnetic behavior near the upstream and downstream states of ISs have been identified. In section 4, the results are presented in terms of magnetic hodograms, in which the two tangential components of the magnetic field, B_y and B_z, are plotted against each other. Discussion of the physical meaning of the different types of fixed points is contained in section 5. A summary of the results is given in section 6.

2. Basic Equations

In the usual notation, the one-dimensional, steady state, nonviscous conservation laws can be written as follows:

$$\rho v_x = \rho_1 v_{x1} \tag{1}$$

$$\rho v_x^2 + p + \frac{B^2}{2\mu_o} = \rho_1 v_{x1}^2 + p_1 + \frac{B_1^2}{2\mu_o} \tag{2}$$

$$\rho v_x v_t - \frac{1}{\mu_o} B_x B_t = \rho_1 v_{x1} v_{t1} - \frac{1}{\mu_o} B_{x1} B_{t1} \tag{3}$$

$$\frac{\gamma}{\gamma-1}\frac{p}{\rho} + \frac{v^2}{2} = \frac{\gamma}{\gamma-1}\frac{p_1}{\rho_1} + \frac{v_1^2}{2} \tag{4}$$

where the subscript t denotes the two components of a vector tangential to the shock and the quantities denoted by subscript 1 represent the upstream condition. Note that equation (4) is written in the deHoffmann-Teller frame which has $\boldsymbol{E} = 0$ outside the shock and $\boldsymbol{E} = \boldsymbol{e}_x E_x$ within the shock. The pressure, p, in (2) and (4), which is assumed scalar for simplicity, is the sum of electron and ion pressure; quasi-charge neutrality is assumed; the electron mass is neglected and, in (4), the ratio of specific heats, $\gamma = 5/3$, is assumed to be the same for electrons and ions, i.e., the ions are

assumed monoatomic. Also, the electric stress $\varepsilon_0 E^2/2$ is assumed negligible compared to the magnetic stress $B^2/2\mu_0$.

To this set of equations must be added the generalized Ohm's law

$$E + v\times B = \eta j + \frac{1}{ne} j\times B - \frac{1}{ne}\nabla p_e \qquad (5)$$

in which electron inertial terms have been neglected, leaving only the resistive term, ηj, the Hall term, $j\times B/ne$, and the electron pressure term, $-(\nabla p_e)/ne$, on the right hand side (n and e are the number density and the magnitude of the electron charge, respectively). In principle, an equation for the electron pressure, p_e, should be supplemented for the closure of equations (1)-(5). However, the electron pressure term appears only in the normal (x) component of (5) which is an auxiliary equation for E_x, the normal component of the electric field. This field component cannot be determined unless an equation of state for the electrons is provided but the magnetic and plasma structure of the shocks does not depend on E_x.

It can be shown that the two tangential components of equation (5) together with equations (1)-(4) can be reduced to the following:

$$A_{x1}^2\lambda_{r1}(1+h^2)\frac{dB_y}{dx} = (A_x^2-1)(B_y-hB_z)+(A_{x1}^2-1)(hB_{z1}-B_{y1}) \quad (6)$$

$$A_{x1}^2\lambda_{r1}(1+h^2)\frac{dB_z}{dx} = (A_x^2-1)(B_z+hB_y)-(A_{x1}^2-1)(hB_{y1}+B_{z1}) \quad (7)$$

in which B_{y1} can be put equal to zero without loss of generality and, for $B_{y1} = 0$,

$$A_x^2 = \frac{\gamma}{\gamma+1}(A_{x1}^2 + \frac{\beta_1+1}{2\cos^2\theta_1} - \frac{B^2}{2B_x^2}) \pm \{(\frac{\gamma}{\gamma+1})^2$$

$$(A_{x1}^2 + \frac{\beta_1+1}{2\cos^2\theta_1} - \frac{B^2}{2B_x^2})^2 + (\frac{\gamma-1}{\gamma+1})(\frac{B^2}{B_x^2} + 2(A_{x1}^2-1)\tan\theta_1\frac{B_z}{B_x}$$

$$+ (A_{x1}^2-1)^2\tan^2\theta_1 - 1 - \frac{A_{x1}^2}{\cos^2\theta_1}(A_{x1}^2 + \frac{\gamma}{\gamma-1}\beta_1)]\}^{0.5} \qquad (8)$$

As in Paper I, equations (1)-(8) remain valid if the subscript 2, representing the downstream conditions, is used in place of the subscript 1. In equations (6)-(8), A_x, λ_{r1}, β_1, and θ_1 are the normal Alfvén number, v_x/v_{Ax} where $v_{Ax} = (B_x^2/\mu_0\rho)^{0.5}$; the resistive length, $\eta/\mu_0 v_{x1}$; the ratio of particle to magnetic pressure, $2\mu_0 p_1/B_1^2$; and the angle between the shock normal and the upstream magnetic field vector, respectively. In addition, the Hall parameter, h, defined as $B_x/ne\eta$, which comes from the Hall current term in Ohm's law, appears in equations (6) and (7) but not in equation (8). The value $h = 0$ represents the resistive MHD limit. It is also evident that the Hall current term plays no role in perpendicular shocks (i.e., the case where $B_x = 0$). Note that h can also be written as the ratio of electron gyrofrequency, ω_{cex}, based on B_x, to electron collision frequency, $\eta ne^2/m_e$, or as the ratio of ion inertial length, $\lambda_i = v_{Ax}/\omega_{cix}$, to Alfvén resistive length, λ_{Ar}, the latter defined as $\eta/\mu_0 v_{Ax}$. Finally, it is emphasized that, for constant η, h is inversely proportional to the density and therefore is not constant across the shock. By use of mass conservation, one may write $h/h_1 = A_x^2/A_{x1}^2$.

Equation (8) is identical to equation (12) of Paper I. For supersonic (subsonic) flow, the plus (minus) sign in front of the square root has to be used. Corresponding to these two signs, the B_yB_z plane can be considered to consist of two Riemann sheets: the supersonic (plus) and the subsonic (minus) sheet. These two sheets come together at a certain closed curve encircling the origin in the B_yB_z plane. On this curve, the square root in equation (8) is zero and the flow is sonic. Outside it, the square root is imaginary: we refer to this region as the forbidden region, since no real hodogram trajectories exist there. The bounding curve itself is referred to as the edge of the forbidden region or simply the forbidden curve. In principle, a smooth transition from one Riemann sheet to the other, i.e., a smooth transition from subsonic to supersonic flow, or vice versa, can occur at points on the forbidden curve. However, it is easy to show that only hodogram trajectories that reach the forbidden curve (from the inside) at grazing incidence can effect such transitions: trajectories intersecting at a finite angle are unacceptable because the subsonic and supersonic trajectories can be shown to have the same slope as well as the same direction at the forbidden curve. If the shock involves a net transition from supersonic to subsonic conditions (the reverse does not occur), the resistive or resistive-dispersive shock usually contains a discontinuity, representing an ordinary gasdynamic shock, in which dissipation processes other than resistivity, i.e., viscosity and heat conduction, are dominant. Such a discontinuity produces an abrupt jump from the plus to the minus sheet, without change of B_y and B_z. In reality, this substructure has a finite width, of the order of the characteristic viscous or heat conductive scale. These scales become vanishingly small as the viscosity and heat conductivity go to zero. However, as mentioned above and as discussed in detail in Paper I, in certain cases, such as when the upstream state is subfast and supersonic while the downstream state of the weak IS is subsonic, a continuous, purely resistive transition from supersonic to subsonic flow is possible. It will be shown in this paper that this property also exists for resistive-dispersive ISs. The calculations in Paper I further indicated that when the signs in equation (8), applicable for the upstream and downstream states of an IS are the same, i.e., when both states are either subsonic or supersonic, a purely resistive transition from the upstream to the downstream state always exists. As we shall see in section 4, in resistive Hall MHD certain cases can be found where no purely resistive-dispersive shock structure connects two such states.

Remarks should be made concerning two general properties that can be easily deduced from equations (1)-(8). It is well known that equations (3) and (5), applied as jump conditions from one side of a discontinuity to the other, give rise to either the coplanarity condition, $(B_1\times B_2)\cdot e_x = 0$, or to the conditions $v_{x1}^2 = v_{Ax1}^2$ and $v_{x2}^2 = v_{Ax2}^2$, i.e., $A_{x1}^2 = A_{x2}^2 = 1$. In the former case which applies to all shocks, if $B_{y1} = 0$ is assumed, then it follows from the coplanarity condition that $By_2 = 0$. In the latter case, it can be further shown that $p_2 = p_1$, $\rho_2 = \rho_1$ and $B_2 = B_1$ so that $v_{x1} = v_{x2}$. This type of nondissipative discontinuity is called a rotational discontinuity. In the presence of finite resistivity, it can be kept nondissipative only by making its width infinite, i.e., in practice it does not exist [*Wu*, 1988*b*]. In ordinary MHD with

zero resistivity, its width is arbitrary and the quantities ρ, v_x, p, and B^2 remain strictly constant throughout the structure. When the Hall term is included, the zero-resistivity case has $\lambda_{r1} = 0$ and $h = \infty$ but $\lambda_{r1}h = \lambda_i/v_{Ax1}$. For $A_{x1}{}^2 = 1$, equations (6)-(8) then yield $A_x{}^2 = A_{x1}{}^2 = 1$ and $dB_y/dx = dB_z/dx = 0$. In other words, one may conclude that within the framework of the nonresistive Hall MHD model, the rotational discontinuity has infinite thickness, i.e., it does not exist.

3. Fixed Point Analysis

Although the detailed shock structure will be obtained by integrating equations (6)-(8) numerically, an overall picture of the magnetic structure is most conveniently obtained by performing fixed-point analysis near the upstream and downstream states. Linearization of the equations around an upstream state (or, by replacing the subscript 1 by 2, around a downstream state) leads to the following equations:

$$\frac{\eta A_{x1}^2}{\mu_o v_{x1}}(1+h_1^2)\frac{d(\delta B_y)}{dx} = K_{y1}\delta B_y - h_1 K_{z1}\delta B_z \qquad (9)$$

$$\frac{\eta A_{x1}^2}{\mu_o v_{x1}}(1+h_1^2)\frac{d(\delta B_z)}{dx} = K_{z1}\delta B_z + h_1 K_{y1}\delta B_y \qquad (10)$$

$$K_{y1} = A_{x1}^2 - 1 \qquad (11)$$

$$K_{z1} = \frac{A_{x1}^2(v_{x1}^2-c_{f1}^2)(v_{x1}^2-c_{s1}^2)}{v_{x1}^2(v_{x1}^2-c_1^2)} \qquad (12)$$

where δB_y and δB_z are the small deviations of B_y and B_z, respectively, from their upstream (or downstream) values. As before, c_f, c_s, and c are the propagation speeds, in the direction of the shock normal, of small-amplitude fast waves, slow waves and sound waves, respectively. The nature of a fixed point depends on the value of the two eigenvalues of equations (9)-(10), which are

$$\lambda_\pm = \frac{(K_{y1}+K_{z1}) \pm \sqrt{(K_{y1}-K_{z1})^2 - 4h_1^2 K_{y1}K_{z1}}}{2K_1} \qquad (13)$$

where

$$K_1 = \frac{\eta A_{x1}^2}{\mu_o v_{x1}}(1+h_1^2) \qquad (14)$$

Three possibilities exist. First, if the two eigenvalues, λ_+ and λ_-, are real and positive, the point examined is an unstable node. If they are real and negative, it is a stable node. Second, if λ_+ and λ_- are real and have the opposite sign, the point is a saddle instead. Finally, if the eigenvalues are complex conjugates, we have a spiral point. The spiral point is unstable when the real part is positive and stable when it is negative. The relationship between saddle points, nodes and spiral points and the properties of small amplitude waves in the regions upstream and downstream of a shock is discussed in section 5. Here, we merely emphasize that, assuming upstream conditions correspond to $x \to -\infty$ and downstream conditions to $x \to +\infty$, unstable behavior, i.e., exponential growth with increasing x, is the behavior normally required upstream of a shock. Stable behavior corresponds to exponential decay with increasing x and is required downstream of a shock.

Before examining the nature of the fixed points for ISs, we shall review the values of K_y and K_z at the possible upstream and downstream states of an IS. For the purpose of this discussion, we suppress the subscript 1 (or 2) on K_y, K_z, K and h. As seen from equations (11) and (12), and as discussed in detail in Paper I, at the upstream state K_y is always positive. Therefore, we have $K_yK_z > 0$ for subfast subsonic ($v_{x1} < c_1 < c_{f1}$) as well as superfast ($v_{x1} > c_{f1}$) ISs, while $K_yK_z < 0$ for subfast, supersonic ($c_1 < v_{x1} < c_{f1}$) ISs. At the two possible downstream states of ISs, namely the subslow (and therefore subsonic) case and the superslow case, corresponding to the strong and the weak IS, respectively, K_y is always negative. Therefore, at the downstream state we have $K_yK_z > 0$ for subslow (strong) ISs and for superslow (weak), supersonic ISs, and $K_yK_z < 0$ for superslow (weak) but subsonic ISs. It is seen from equation (13) that the two eigenvalues are always real and have the opposite sign for $K_yK_z < 0$; in that case the fixed point therefore is a saddle. However, for the case $K_yK_z > 0$, the two eigenvalues are either real having the same sign so that the magnetic structure is a node, if $(K_y-K_z)^2 > 4h^2K_yK_z$, or they are complex conjugates and the magnetic structure is a spiral, if $(K_y-K_z)^2 < 4h^2K_yK_z$. For the latter case, it can be further shown that, for $B_x > 0$, i.e., for B_x in the direction of the (positive) flow component v_x across the shock, the trajectory in the B_yB_z plane spirals counterclockwise with increasing x for the upstream state of an IS and clockwise for the downstream state. In the MHD limit ($h = 0$), the two eigenvalues become K_y/K and K_z/K; these are always real so that the magnetic structure is a node for $K_yK_z > 0$ and a saddle for $K_yK_z < 0$.

In Paper I, we used this fixed-point analysis to find all allowed types of magnetic structure at the upstream and downstream states of an IS. The results were summarized in a 3×3 matrix (see Figure 4 of Paper I) in which the columns represent the three possible upstream states (subfast subsonic; subfast supersonic; superfast) and the rows represent the three possible downstream states (subslow; superslow subsonic; superslow supersonic). The same matrix representation can be used in the present case and is shown in Figure 1*a*. However, depending on the value of the Hall parameter, h, more than one type of upstream and downstream fixed-point structure is now possible in each of the basic matrix elements so that many more topologies of the B_yB_z hodogram exist than for $h = 0$. Note that the element in the lower left-hand corner of the matrix is unphysical because it represents a net shock transition from subsonic to supersonic flow.

As can be seen from the matrix, there are three fixed points: the upstream state and the strong and weak downstream states of the IS. However, as discussed in Paper I, there is in fact a fourth fixed point in the B_yB_z plane, which corresponds either to the upstream or the downstream state of a fast shock depending on whether the upstream state of ISs is subfast or superfast. In the former case, this fourth fixed point is a node or a spiral on the supersonic (plus) Riemann sheet and it represents the upstream state of a fast shock. Furthermore, in this case the downstream state of the fast shock is

also the upstream state of ISs so that a subfast IS can propagate immediately behind the fast shock and at exactly the same speed. The combination of a fast shock and an IS propagating in this manner constitutes a special case of the superfast IS. In the latter case, this fourth fixed point can be either a saddle on the supersonic (plus) sheet or a node or a spiral on the subsonic (minus) sheet: the upstream state of ISs in this case is the same as the upstream state of a fast shock. In addition, as mentioned earlier, the weak and strong downstream states of the IS also satisfy the jump condition of a slow shock so that the four fixed points can be identified as the upstream and downstream states of fast and slow shocks. Following the notation given by Germain [1960], the upstream and the downstream states of a fast shock are then referred to as points 1 and 2, respectively, while the upstream and downstream states of a slow shock correspond to points 3 and 4, respectively. In this notation, the possible sh s are: 1→2 (fast shock), 3→4 (slow shock), 1→3 (superfast wea S), 1→4 (superfast strong IS), 2→3 (subfast weak IS), and 2→4 (subfast strong IS). It is evident that the B_yB_z hodograms to be generated will contain, not only the structure of ISs, but also the structure of fast and slow shocks. Note that the notation used here for labelling the four fixed points is different from that in Paper I, in which the weak and strong downstream states of the IS (or, equivalently, the upstream and downstream states of the slow shock) are denoted by 2*w* and 2*s*, respectively, while the upstream and downstream states of the fast shock are labelled 1*f* and 1, respectively. Note also that we will continue to use the subscript 1 and 2 to denote the upstream and downstream states of any particular shock. For example, for a slow shock the subscript 1 refers to fixed point 3 and the subscript 2 to fixed point 4.

In the first column of the matrix in Figure 1*a*, where the IS upstream state is subsonic (and therefore subfast), the three fixed points, corresponding to the upstream and the two downstream states of an IS, are all on the same Riemann sheet, namely the subsonic, or minus sheet. Since the upstream state (point 2) as well as the downstream subslow IS state (point 4) can be either a node or a spiral and since the downstream superslow IS state (point 3) is always a saddle, one might expect that four types of magnetic hodogram topology should exist in this column. However, if the fixed point on the plus sheet, representing the upstream state of a fast shock (point 1), which can be either a node or a spiral, is also considered, there exist 8 possible magnetic hodogram topologies. One of these topologies, in which the upstream state of the IS is a node, the strong-IS downstream state is a node, the weak-IS downstream state is a saddle, and the upstream state of the fast shock is a node, corresponds to the resistive MHD limit (Figure 8*c* in Paper I).

When the upstream state is subfast and supersonic, corresponding to the second column of the matrix in Figure 1*a*, the upstream point of the IS (point 2) is always a saddle (on the supersonic sheet); the downstream state, however, can be either a node or a spiral on the subsonic sheet for the strong IS (point 4) and it can be a node, a spiral, or a saddle for the weak IS (point 3) depending on whether the downstream state is supersonic or subsonic. We therefore expect 6 possible types of magnetic hodogram topology in this column. However, if the fourth fixed point, which is again the upstream state of the fast shock (point 1) and can be either a node or a spiral on the plus sheet is considered, there are 12 allowed magnetic hodogram topologies in this column. Two of these correspond to the MHD limit: (1) when the downstream state of the strong and the weak IS are, respectively, a node and a saddle point (as mentioned earlier, the upstream state of the IS is always a saddle) and the upstream state of the fast shock is a node (Figure 8*b* in Paper I); (2) when the two downstream states of the IS as well as the upstream state of the fast shock are all nodes (Figure 8*a* in Paper I).

For the last column of the matrix where the upstream state of the intermediate shock is superfast (and therefore supersonic), corresponding to point 1, it would appear from the matrix that there are two possible structures for the upstream state, i.e., a node or a spiral point, while the situation for the strong and the weak IS downstream states is the same as in the previous column. Thus the combination of possible structures of these three fixed points would appear to constitute another 12 types of magnetic hodogram topology. However, if one includes the fourth point, i.e., the downstream state of the fast shock (point 2) which can be either subfast and subsonic (a node or a spiral) or subfast and supersonic (a saddle), the situation is in fact identical to the previous two columns. In the last column of the matrix, one would therefore expect 10 hodograms in each subcolumn for a total of 20. But these 20 hodogram topologies are exactly the same as the 8+12 cases found in the two first columns.

Another way to account for the 20 types of magnetic hodogram topology is by distributing the four fixed points on the plus and minus sheets, as illustrated in the matrix in Figure 1*b*. Since the 4 fixed points, namely the upstream state of the fast shock (point 1), the downstream state of the fast shock (point 2), the downstream state of the weak IS (point 3), and the downstream state of the strong IS (point 4), cannot all be on the plus (supersonic) or minus (subsonic) sheet, there are only three possible ways to distribute these 4 fixed points on the plus and minus sheets. First, one of the four fixed points is on the plus sheet and the other three are on the minus sheet; in this case, point 1 must be on the plus sheet. Second, two fixed points, 1 and 2, are on the plus sheet and the other two, 3 and 4, are on the minus sheet. Finally, three fixed points are on the plus sheet and one on the minus sheet. In the case, point 4 must be on the minus sheet. For the first row of the matrix, point 1 on the plus sheet as well as points 2 and 4 on the minus sheet can be either nodes or spiral points while point 3 is a saddle on the minus sheet: one therefore expects 8 possible magnetic topologies in this row. The same accounting procedure can be applied to the second and the last row of the matrix, yielding 4 and 8 possible cases, respectively. The three rows together therefore produce 20 possible cases, in agreement with our previous accounting. However, as we shall see, some of these 20 cases may not be realizable. In the last column of the matrix in Figure 1*b* we show the cases which have been found. In this column, the letters, *n*, *sa*, and *s* stand for node, saddle and spiral point, respectively: the sequence of letters describes the four fixed points in the order 1, 2, 3 and 4. It is seen that only 13 of the 20 possible hodograms have been found.

When the fixed point 2 is located on the subsonic Riemann sheet it is either a node or a spiral point (Figure 1*b*, first row) and furthermore it is always an unstable node or spiral. Unstable behavior is appropriate, and provides the required egress from point 2 when it serves as the upstream state of an IS. But stable

rather than unstable behavior is required when it serves as the downstream state of a fast shock. Thus the unstable node or spiral behavior is not directly relevant to the latter case where, in the resistive-dispersive model, access to the downstream fixed point is achieved via a gasdynamic subshock at the trailing edge of the fast shock. This subshock leads to an abrupt drop of the solution curve from the supersonic Riemann sheet into the fixed point, 2, on the subsonic sheet. If finite bulk viscosity is included to permit resolution of the viscous subshock structure, the order of the system is increased from two to three. In that case, one eigenvector provides a direction of stable approach to the fixed point 2 which is utilized when this point serves as the downstream state of a fast shock. The unstable node or spiral behavior remains in the plane containing the other two eigenvectors to provide egress from point 2 when it serves as the upstream state of an IS. It is this latter behavior that is used to characterize point 2 in the purely resistive-dispersive model discussed in this paper. Specifically, a fast shock characterized as an *s-s* transition in Figure 1 (see also Figure 5) in fact has spiral behavior of the B field only at its upstream edge: the downstream edge consists of a viscous subshock.

A similar situation arises when the fixed point 3 is located on the supersonic sheet, in which case it is a node or a spiral (Figure 1*b*, column 3), and furthermore, it is always a stable node or spiral. Stable behavior is appropriate when point 3 serves as the downstream state of a weak intermediate shock but not when it serves as the upstream state of a slow shock. In the latter case, the node or spiral behavior is not directly relevant because egress from point 3 occurs abruptly via a viscous subshock located immediately at the upstream edge of the total slow shock structure. Thus, even though a slow shock transition characterized as *s-s* is given in Figure 1 (and in Figure 14) such a shock does not display a spiral B field at its upstream edge. Instead, that edge consists of a viscous subshock.

We have not been able to produce a simple physical explanation for the absence of certain hodogram topologies but we have found the following empirical rule to be consistent with all cases reported here: in the resistive-dispersive model, shocks that involve fast-mode compression ($|B_{t2}| > |B_{t1}|$) cannot have an upstream node and a downstream spiral point whereas shocks that involve slow-mode compression ($|B_{t2}| < |B_{t1}|$) cannot have an upstream spiral point and a downstream node. Fast-mode compression occurs in all fast shocks and in all superfast weak intermediate shocks. Thus the cases (*n-s-sa-n*) and (*n-s-sa-s*) are excluded from row one and the cases (*n-sa-s-n*) and (*n-sa-s-s*) are excluded from row 3 of Figure 1*b*. Similarly, slow-mode compression occurs in all slow shocks as well as in all subfast strong intermediate shocks. Thus the cases (*n-sa-s-n*) and (*s-sa-s-n*) are excluded from row 3 and the cases (*n-s-sa-n*) and (*s-s-sa-n*) are excluded from row 1 on Figure 1*b*. In this accounting, the cases (*n-s-sa-n*) and (*n-sa-s-n*) appear twice so that only 6 of the 7 missing cases have been accounted for. It can be shown that the final missing case (*n-n-sa-s*), in row one of Figure 1*b*, would contain a superfast strong intermediate shock for which $|B_{t2}| > |B_{t1}|$, with an upstream (point 1) node and a downstream (point 4) spiral, behavior that is again excluded by our empirical rule.

One final, unrelated matter is that certain downstream plasma and magnetic field states may be forbidden because the corresponding upstream state would have unphysical parameter values. For exampe, it is possible to choose plasma conditions at point 2 in such a way that point 1 has a negative plasma pressure. In such a case, point 2 is not an acceptable downstream state for a fast shock but it remains a valid upstream state for a weak or strong intermediate shock.

4. HODOGRAMS

In this section, we show the behavior of the tangential magnetic field in resistive-dispersive ISs quantitatively. The results were obtained by numerical integration of equations (6)-(8); they are displayed in terms of magnetic hodograms in which B_y and B_z are plotted against each other. For convenient comparison with the resistive MHD cases in Paper I, the results are classified on the basis of the normal flow speed relative to the small-amplitude fast-wave and the sound speed at the upstream state of the shock, as in the matrix in Figure 1*a*. For the calculations shown in the following, B_x is in the direction of v_x and in each figure the trajectories on the plus (supersonic) and minus (subsonic) sheets are denoted by the dashed and solid lines, respectively. For subfast ISs (the first and second columns of the matrix in Figure 1*a*), the structure of the fourth fixed point, i.e., the upstream state of the fast shock, denoted by 1 in the hodograms, which can be either a node or a spiral, will also be shown, even though its character does not affect the hodogram topology of the subfast IS. The reason for showing this fourth fixed point is that it also serves as the upstream state of superfast ISs (the last column of the matrix in Figure 1*a*), as discussed further in section 4.3 (in examining sections 4.1 and 4.2 which deal with subfast ISs, the reader may focus attention on the hodogram traces emerging from point 2). Also, in Figure 1*b* and in the text following, the fixed points will always be listed in the order 1; 2; 3; 4. As an example, the list *n-n-sa-n* refers to the case where the points 1, 2 and 4 are nodes while 3 is a saddle point. As in Paper I, all calculations are performed with constant η and with $\gamma = 5/3$.

4.1. *Subfast Subsonic Upstream Flow*

In this case, which comprises the first column of the matrix in Figure 1*a* or the first row of the matrix in Figure 1*b* with point 2 as the upstream state of ISs, the three fixed points corresponding to the upstream and the two downstream states of the IS are all in the subsonic (minus) Riemann sheet. As shown in Figure 1*b*, the upstream (point 2) and the strong-IS downstream (point 4) states can be either a node or a spiral point while the weak-IS downstream (point 3) state is always a saddle point so that four hodogram topologies are possible. In principle, each of these contains two possible subcases when the fourth fixed point, 1, on the plus sheet, i.e., the upstream state of the fast shock, is considered. However, in reality we have only been able to find four of the 8 subcases. The missing cases are (*n-n-sa-s*), (*n-s-sa-s*), (*n-s-sa-n*) and (*s-s-sa-n*). For the hodograms shown in Figures 2-5, the upstream (point 2) conditions used are: $\beta_1 = 1$, $\theta_1 = 45^o$ and $A_{x1}{}^2 = 1.0428$.

Case (*i*): *n-n-sa-n*. We start by examining the case where the upstream state of the fast shock (1) and of the intermediate shock (2) are nodes, whereas the weak-IS downstream state (3) is a saddle point (as it is in this entire subsection) and the strong-IS

downstream state (4) is a node. The hodogram shown in Figure 2, for which h_1 = 0.012, is topologically the same as the purely resistive MHD case in Figure 8c of Paper I. It is seen that the two hodograms are in fact very similar, the difference being the absence of precise symmetry between right-hand and left-hand polarized traces in the hodogram when the upstream Hall parameter, h_1, is different from zero. There are an infinite number of trajectories connecting the upstream (point 2) and the strong-IS downstream state (4), but only two trajectories connecting point 2 and the weak-IS downstream state (3). Detailed discussion of this type of hodogram is given in section 3.3 of Paper I.

Case (*ii*): *s-n-sa-n*. Increasing h_1 to 0.1 leads to the case where the upstream state of the fast shock (point 1) is converted from a node to a spiral while the other three fixed points are the same as in the previous case. It is seen from Figure 3 that, except for the weak counterclockwise (right-hand) spiral structure at point 1, the magnetic-field behavior is the same as in the previous case.

Case (*iii*): *s-n-sa-s*. By further increasing the Hall parameter to h_1 = 1, we obtain the case where the strong-IS downstream state (point 4) is converted from a node to a spiral point, as shown in Figure 4, while the other three fixed points are the same as in case (ii). It is seen that the two trajectories connecting points 2 and 3 are asymmetric, an effect that is also present but is is less pronounced in Figures 2 and 3 and is completely absent in the purely resistive case. The hodograms in the minus sheet are similar to those in Figures 2 and 3 in that there still exists an infinite number of transitions connecting points 2 and 4. The only difference is the spiral structure of point 4 in Figure 4 which leads to a clockwise (left-hand) twisting of the trajectories in the B_yB_z plane near that point.

Case (*iv*): *s-s-sa-s*. By increasing the Hall parameter still further, we obtain the case where the upstream fast and intermediate shock states as well as the strong-IS downstream states are all spiral points while the weak-IS downstream state (point 3) remains a saddle. Unlike the previous cases, in which purely resistive-dispersive transitions exist between the three fixed points, 2, 3 and 4, on the minus sheet, in the present case a continuous transition between 2 and 4 or 2 and 3 does not exist if the counterclockwise twisting at the upstream point 2 becomes too strong. At one extreme, illustrated in part (*a*) of Figure 5 where h_1 = 3.33, there still exist nonunique smooth transitions between points 2 and 4, bounded by the two trajectories connecting points 2 and 3; at another extreme, illustrated by part (*b*) of the figure where h_1 = 10, the spiral curves out of point 2 and the two curves into the saddle point 3 all terminate at the boundary of the forbidden region where the square root in equation (9) becomes zero and the flow is sonic. Thus there is no continuous connection between the upstream and the downstream states. However, it is seen that the transition from points 2 to 3 can be achieved via a smooth subsonic-supersonic transition at the sonic point, denoted by *sp* in the figure, followed by a trajectory on the supersonic sheet to the position of a gasdynamic subshock, *gsw*1 or *gsw*2, where a jump from the plus sheet to the minus sheet occurs, followed by a trajectory on the latter sheet into point 3. For the strong IS (2→4), the transition can be achieved by an infinite number of trajectories, e.g., along the one just described followed by a slow shock from point 3 to point 4, or along 2-*sp*-*gss*-4. Note that the trajectories into and out of the point *sp* are tangential to the forbidden curve at that point in both Riemann sheets.

Between the two extremes in parts (*a*) and (*b*) of Figure 5, many possibilities exist: three examples are shown in parts (*c*), (*d*) and (*e*). As seen in part (*c*) where h_1 = 5.715, the curve into the left side of the saddle point, 3, reaches the forbidden region at grazing incidence at the sonic point *sp*, while the curve into the right side of 3 remains entirely on the minus sheet. In this case, there still exists an infinite number of spiral curves connecting points 2 and 4. Slightly increasing h_1 to 6.64 leads to the case shown in part (*d*), in which the left-hand curve into point 3 terminates at the forbidden edge while the right-hand curve into that point barely reaches the forbidden region at grazing incidence (at point *sp*). The transition between 2 and 3 along the left curve can be achieved by including a subsonic-supersonic transition at *sp* and a viscous subshock (denoted by *gsw*) in the structure, i.e., along 2-*sp*-*gsw*-3. For the strong IS (2→4), there still exists an infinite number of discontinuous transitions, such as along 2-*sp*-*gss*-4; while the only smooth transition is composed of a S-shaped curve connecting 2 and 3, followed by a slow shock described by the spiral curve between points 3 and 4. Between the two cases in parts (*c*) and (*d*) of Figure 5, one of the curves connecting points 2 and 4 passes the sonic point, *sp*, at grazing incidence, as illustrated in part (*e*) (where h_1 = 5.814). The right trajectory into point 3 remains on the minus sheet but the left trajectory emerges at the forbidden curve and is disconnected from the upstream state. In this case, the purely resistive-dispersive shock structure connecting points 2 and 4 can be achieved by an infinite number of curves bounded on one side by the S-shaped trajectory connecting the upstream state and the right side of the weak-IS downstream point, 3, and on the other side by the curve connecting 2 and 4 and passing through the point *sp*. As in part (*d*) of the figure, the transition between points 2 and 3 or points 2 and 4 can also be achieved by including a smooth subsonic-supersonic transition followed by a viscous subshock and a trajectory on the subsonic sheet into 3 or 4.

4.2. *Subfast Supersonic Upstream Flow*

As shown in the second column of the matrix in Figure 1*a*, the upstream IS state in this case is always a saddle point located on the plus Riemann sheet and the strong-IS downstream state is a either node or a spiral on the minus Riemann sheet. For the weak-IS downstream state, there are three possibilities. For certain parameter values, the downstream flow may remain supersonic in which case the downstream state is a node or a spiral, also on the plus Riemann sheet; the other possibility is that the weak IS downstream flow is subsonic and corresponds to a saddle point located on the minus Riemann sheet. This column therefore contains 6 cases. If the fourth fixed point, 1, is also considered, this section can be viewed to comprise the second and third rows of the matrix in Figure 1*b* (with point 2 as the upstream state of ISs) with a total of 12 possible hodogram topologies: of these, the combinations (*n-sa-s-s*), (*n-sa-s-n*) and (*s-sa-s-n*), all in the third row, have not been found.

Case (*v*): *n-sa-sa-n*. A sample hodogram for this case is shown in Figure 6, for which the upstream parameter values are β_1 = 0.5, θ_1 = 26.57°, $A_{x1}{}^2$ = 1.1471 and h_1 = 0.2. The hodogram topology is the same as that in Figure 8*b* of Paper I but the asymmetry of the hodogram trajectories generated by the Hall current effect is

evident. As discussed in section 3.4 of Paper I, the weak IS (2→3) has its upstream and downstream states on different Riemann sheets. Nevertheless, two shock-free trajectories connect these two states with a smooth supersonic-subsonic transition at the two points *sp*. For the strong IS (2→4) there are infinitely many trajectories connecting the upstream and the downstream state; some but not all of these contain a gasdynamic subshock (*gss*) which can occur anywhere between points 2 and *sp* along the two trajectories out of the upstream point.

Case (*vi*): *s-sa-sa-n*. Using $\beta_1 = 0.255$, $\theta_1 = 40.89^o$, $A_{x1}{}^2 = 1.1425$ and $h_1 = 0.25$, we obtain the case where point 1 becomes a spiral while the other points remain the same as in the previous case. The hodogram is shown in Figure 7. It is seen that Figures 6 and 7 are similar, the only difference being the change of the fast-shock upstream state (1) from a node to a spiral point.

Case (*vii*): *n-sa-sa-s*. By use of the same upstream conditions as in Figure 6 but with $h_1 > 0.323$, we obtain the case where the strong-IS downstream state (4) becomes a spiral while the other fixed points remain the same as in Figure 6. The hodogram shown in Figure 8 is for $h_1 = 0.345$. It is seen that the spiral structure at point 4 is so weak that the hodogram in Figure 8 is very similar to Figures 6 and 7. In particular, there still exist two smooth supersonic-subsonic transitions from point 2 to 3 at the sonic points, *sp*.

Case (*viii*): *s-sa-sa-s*. By slightly increasing the Hall parameter h_1 but with the same upstream conditions as in the previous case, we obtain the case where point 1 is converted to a spiral point, as shown in Figure 9. We have found several possible transitions between two states on different Riemann sheets. At one extreme, shown in part (*a*) of Figure 9, the magnetic hodogram topologies are similar to the purely resistive case in that there still exist two smooth supersonic-subsonic transitions from point 2 to 3 at the sonic points, *sp*, while the transitions from 2 to 4 may or may not contain a subshock (*gss*). Another possibility is that one of the two transitions from 2 to 3 involves a discontinuity in the form of a viscous subshock, as illustrated in part (*b*) of Figure 9: here the dashed curve out of left-hand side of the saddle point 2 intersects the solid curve into the right-hand side of the saddle point 3 at *gsw* where a subshock occurs, while the trajectory out of the right-hand side of point 2 still connects smoothly to 3 at the sonic point, *sp*. For the strong IS (2→4), there are again cases both without and with a gasdynamic subshock, *gss*. The subshock can occur anywhere between points 2 and *sp* along the right trajectory or between points 2 and *gsw* along the left trajectory out of point 2. For the magnetic topologies shown in parts (*c*) and (*d*) of the figure, the transition from point 2 to point 3 can occur only by including a viscous subshock either at point *gsw*1 or at point *gsw*2, whereas for the strong-IS (2→4), a viscous subshock, *gss*, can occur at the intersection between either of the two curves out of point 2 on the plus sheet and any of the spiral curves on the minus sheet converging to point 4.

Case (*ix*): *n-sa-n-n*. We turn now to cases where point 3 is supersonic. By using the parameters: $\beta_1 = 0.5$, $\theta_1 = 26.57^o$, $A_{x1}{}^2 = 1.0546$ and $h_1 < 0.085$, we obtain configurations of the type shown in Figure 10 (where $h_1 = 0.067$), which are topologically the same as Figure 8*a* in Paper I. As discussed in section 3.4 of that paper, there exist two trajectories between points 2 and 3, both of which are located on the supersonic Riemann sheet, and an infinite number of curves connecting points 2 and 4, in all of which a discontinuous viscous subshock, *gss*, is included in the overall shock structure.

Case (*x*): *s-sa-n-n*. Using the parameters: $\beta_1 = 0.24$, $\theta_1 = 38.66^o$, $A_{x1}{}^2 = 1.1316$ and $h_1 = 0.25$, one finds the case where point 1 is converted to a spiral point while the other fixed points remain the same as in the previous case. It is seen from Figure 11 that except for the weak spiral structure at point 1, the magnetic topology is the same as in Figure 10.

Case (*xi*): *n-sa-n-s*. With the same upstream conditions as in case (ix) (Figure 10) but with a larger value of h_1, we obtain the case in which the strong-IS downstream state (4) becomes a spiral while the other fixed points remain the same. The case shown in Figure 12 is for $h_1 = 0.125$. The basic features of Figure 12 are similar to those in Figures 10 and 11 (see also Figure 8*a* of Paper I) in the sense that there are two trajectories between points 2 and 3 and an infinite number of transitions from 2 to 4; in the latter case, a viscous gasdynamic shock (*gss*) is required to complete the shock transition.

Case (*xii*): *s-sa-n-s*. Increasing h_1 still further leads to the case where point 1 becomes a spiral point while the others remain the same as in the previous case. As indicated in Figure 13 (in which $h_1 = 1$), the asymmetry of the hodogram becomes more evident but otherwise the basic hodogram structure is similar to that in Figure 12.

Case (*xiii*): *s-sa-s-s*. Further increasing the Hall parameter ($h_1 > 1.54$) but otherwise with the same upstream parameters as in Figures 10, 12 and 13, one finds a structure where the upstream state of the fast shock as well as the strong and the weak IS downstream states are all spiral points. This case is similar to case (iv) in the following respect: despite the fact that the upstream and the weak-IS downstream states are both on the supersonic sheet, there exists no smooth purely resistive-dispersive transition between these two states in certain cases. We discuss various possibilities below. The case shown in part (*a*) of Figure 14 (where $h_1 = 3.33$) is similar to Figure 13 in that two smooth transitions between points 2 and 3 exist; the main difference is that in Figure 14, due to the clockwise spiral structure of point 3, the left trajectory out of point 2, which connects to point 3, is S-shaped. Part (*b*) of Figure 14, in which $h_1 = 10$, shows that if the spiral structure at point 3 is so strong that the two curves leaving the upstream saddle point as well as the spiral trajectories into the point 3 all terminate at the edge of the forbidden zone then there is no purely resistive-dispersive transition between these two states. However, the transition from points 2 to 3 can be completed via a gas dynamic shock located either at point *gsw*1 or at point *gsw*2, which effects a jump from the plus to the minus sheet, along with a subsonic trajectory to the sonic point *sp* where a smooth transition back to the supersonic sheet occurs, followed by a supersonic trajectory into point 3. Unlike the weak IS (2→3), the transition from the upstream to the downstream state of the strong IS can be achieved by an infinite number of paths, such as along 2-*gss*-4. Also included are two trajectories passing the sonic point: 2-*gsw*1-*sp*-4 and 2-*gsw*2-*sp*-4. Between the two cases shown in parts (*a*) and (*b*) of Figure 14, intermediate magnetic hodogram topologies exist. An example is shown in part (*c*) of the figure where the right-hand trajectory out of point 2 terminates at the edge of the forbidden region, while the

left-hand trajectory out of 2 is tangential to that edge at the sonic point *sp*. It is further seen that one of the spiral trajectories into the strong-IS downstream state (4) also passes the sonic point. Therefore, despite the fact that points 2 and 4 are located on different Riemann sheets, a smooth supersonic-subsonic transition between these two states is possible. As in part (*b*) of Figure 14, the trajectory in the minus sheet between points *gsw* and *sp* can also be used to achieve a transition between points 2 and 3 that includes a gasdynamic subshock.

4.3. *Superfast Supersonic Upstream Flow*

As discussed earlier, the cases in this section include all three rows of the matrix in Figure 1*b* and yield a total of 20 possible hodogram topologies. In the hodograms presented in the previous two subsections, we have included the structure near the upstream state of the fast shock, i.e., near point 1. This point now also serves as the upstream state of the superfast IS. The present subsection therefore contains all magnetic hodograms displayed earlier, with point 2 representing the downstream state of the fast shock rather than the upstream state of the IS. In the following, we discuss the hodograms shown earlier in the context of the matrix in Figure 1*b*. Since in the limit of resistive MHD, the hodograms in each row of that matrix correspond to Figure 8*c*, 8*b* and 8*a* of Paper I, we shall classify those in each row as type I, type II and type III, respectively. It is also of interest to note from the matrix in Figure 1*b* that a certain symmetry exists between hodograms of type I (those contained in the first row of the matrix) and type III (those included in the third row). Specifically, the eight possible hodogram topologies in the third row are the same as those obtained from the first row by reversing the sequence of the four fixed points (or, equivalently, by flipping the hodogram around the B_y axis) and interchanging the solid (subsonic) and the dashed (supersonic) curves in the corresponding hodograms. In Paper I, this type of symmetry therefore exists between Figure 8*c* and Figure 8*a*.

Type I. This case comprises the first row of the matrix in Figure 1*b* where point 1, representing the upstream state of superfast ISs, is on the plus sheet while the other three fixed points are on the minus sheet. This case therefore includes the hodogram topologies in Figures 2, 3, 4 and 5. It is seen that in all of these, an infinite number of transitions exists for both strong and weak superfast ISs. However, unlike the purely resistive MHD case (Figure 8*c* of Paper I), in which a viscous subshock is always required to complete the transition from the supersonic upstream state to the two subsonic downstream IS states, in certain cases, illustrated in parts (*c*), (*d*) and (*e*) of Figure 5, a smooth supersonic-subsonic transition at a sonic point *sp* is possible. Figure 5*c* serves as an example of this behavior: the transition between 1 and 3 can be achieved either by a single continuous trajectory along 1-*sp*-3 or by an infinite number of discontinuous transitions such as the one along 1-*gs*-3. Similarly, for the strong IS, the transition can be a continuous one along 2-*sp*-4 or it can be discontinuous, a special case of which is 2-*gs*-3-4.

Type II. In this case, point 1, the upstream state of superfast ISs, and point 2 are on the plus sheet while points 3 and 4 are on the minus sheet. As indicated in the second row of the matrix in Figure 1*b*, this case includes the hodograms in Figures 6, 7, 8 and 9. It is seen that, as for Type I, there exists an infinite number of transitions connecting the upstream state and the two downstream states of the IS. Furthermore, there are cases both with and without a smooth supersonic-subsonic transition at the sonic point *sp*. In the former cases, the hodogram topology is similar to the purely resistive MHD case (Figure 8*b* of Paper I) in that all of the trajectories out of point 2 are tangential to the forbidden curve at the sonic point; in the latter cases, illustrated in parts (*b*), (*c*) and (*d*) of Figure 9, the spiral structure of point 1 is so strong that the trajectories out of it become disconnected from those into the downstream states: a gasdynamic subshock is then required to complete the transition.

Type III. This type of hodogram corresponds to the case where point 4 is on the minus sheet while the other three fixed points are all on the plus sheet, as illustrated in Figures 10-14 and in the third row of the matrix in Figure 1*b*. This case is of particular interest for the following reason: despite the fact that the upstream superfast IS state, 1, and the weak-IS downstream state are on the same Riemann sheet, in certain cases, no smooth transition exists between these two states. As shown in part (*b*) of Figure 14, an infinite number of transitions between points 1 and 3 can be achieved via a gasdynamic shock, which can occur anywhere between points *gsw*1 and *gsw*2 along that particular trajectory in the subsonic sheet that reaches the sonic point *sp*. In certain cases, illustrated in part (*c*) of Figure 14, a smooth supersonic-subsonic transition between points 1 and 4 along the trajectories 1-2-*sp*-4 coexists with the supersonic-sonic-supersonic transition between points 1 and 3 along the trajectory 1-2-*sp*-3.

5. Discussion

Fixed-point analysis of the type employed in this paper consists of establishing the properties of time-independent small-amplitude spatial perturbations around the upstream or downstream state of a shock. But these properties must coincide with those of small-amplitude waves standing in the upstream or downstream regions. In Hall MHD, such waves are governed by the dispersion relation [*Stringer*, 1963; *Formisano and Kennel*, 1969]

$$(\omega^2-k^2v_A^2\cos^2\theta)[\omega^4-(c^2+v_A^2)\omega^2k^2+c^2v_A^2k^4\cos^2\theta]$$

$$-\lambda_i^2k^4\omega^2v_A^2(\omega^2-k^2c^2)\cos^2\theta = 0 \qquad (15)$$

where the quantity $\lambda_i \equiv (m_i/\mu_0 ne^2)^{0.5}$ in front of the dispersive term is the ion inertial length; c is the speed of sound; v_A is the Alfvén speed and θ is the angle between the propagation vector and the magnetic field. The fast mode described by this relation has the following properties. (1) Its phase and group speeds increase monotonically with increasing wave number, k. For $k \to 0$ both speeds approach the MHD fast-mode speed, c_f. For $k \to \infty$ both speeds approach infinity. (2) For all finite wave lengths, the mode displays anomalous dispersion, i.e., the group speed exceeds the phase speed. (3) The mode is right-handed. Similarly, the slow mode has the following properties. (1) Its phase and group speeds decrease monotonically with increasing wave number. For $k \to 0$ both speeds approach the MHD slow-mode speed, c_s. For $k \to \infty$ both speeds approach zero. (2) For all finite wave lengths, the mode displays ordinary dispersion, i.e., the phase speed exceeds the group speed. (3) The mode is left-handed. Finally, the intermediate mode has the property (1) that its phase and group speed both approach the MHD intermediate wave

speed, $v_{Ax} = v_A\cos\theta$, as $k \rightarrow 0$, while for $k \rightarrow \infty$ both speeds remain finite and approach the sound speed, c. (2) The polarization and dispersion properties are different for $c > v_A\cos\theta$ and $c < v_A\cos\theta$, i.e., for $\beta > (2/\gamma)\cos^2\theta$ and $\beta < (2/\gamma)\cos^2\theta$. In the former case, the intermediate mode is right-handed and has anomalous dispersion; in the latter case it is left-handed and has ordinary dispersion. (3) For $c = v_A\cos\theta$, the mode is longitudinal and nondispersive. These properties of the three modes are illustrated by the dispersion curves in Figure 15.

As shown quantitatively in the Appendix, the occurrence of saddle points, nodes and spiral points in the fixed-point analysis is related to the above small-amplitude wave properties as follows. If none of the three modes can phase stand in the upstream or downstream flow, i.e., if the phase speed cannot be equal to the plasma flow speed there, then the corresponding fixed point is a saddle point. If one of the modes can phase stand, the fixed point is either a node or a spiral point. It is a node for sufficiently small h values and a spiral for larger h. The former instance corresponds to the case of an overdamped system where resistive dissipation effects dominate dispersion effects; the latter case represents underdamped behavior, and the critical h value at which a node is converted to a spiral point corresponds to critical damping. A right-handed (left-handed) spiral point corresponds to a right-hand (left-hand) polarized wave mode. Finally, as pointed out, e.g., by *Kennel et al.* [1985], a wave standing at the upstream edge of a shock must always have anomalous dispersion otherwise wave energy cannot be transported from the main shock into the upstream region where it is dissipated, in the present case by Ohmic heating. This situation corresponds to an unstable spiral point (or, for small h_1 values, an unstable node). Similarly, a wave standing at the downstream edge of a shock must always have ordinary dispersion in order to allow wave energy to escape and be dissipated downstream. This situation corresponds to a stable spiral point (or, for small h_2 values, a stable node).

Equipped with this information, we may now reexamine the results obtained in sections 3 and 4. First, we note that, at a sufficiently short wave length, the small-amplitude fast-mode wave can always phase stand upstream of a fast shock or a superfast intermediate shock. For this reason, point 1 in the Figures is always either a node (for small h_1) or a spiral point (for sufficiently large h_1) but never a saddle. Furthermore, the fast mode always has anomalous dispersion, as required for it to be generated at the upstream edge of the shock. Similarly, at a sufficiently short wavelength, a small-amplitude slow-mode wave can always phase stand downstream of a slow shock or a strong intermediate shock. For this reason point 4 in Figures is always a node or a spiral, never a saddle. Furthermore, the slow mode always has ordinary dispersion and thus can be generated at the downstream edge of a shock.

At the downstream state of a fast shock (point 2 in the Figures), which is also the upstream state of the subfast intermediate shock, the plasma flow is subfast but superalfvénic and therefore superslow. It is evident from the dispersion relation that only the intermediate mode can phase stand in such a flow and then only if the flow speed falls between the MHD intermediate wave speed, $v_A\cos\theta$, and the sound speed, c. Since the flow is superalfvénic, this is never the case when $c < v_A\cos\theta$, i.e., when $\beta < (2/\gamma)\cos^2\theta$. When $\beta > (2/\gamma)\cos^2\theta$, it will occur only when the flow is subsonic. Thus, when point 2 falls on the supersonic Riemann sheet it must always be a saddle point. When it falls on the subsonic Riemann sheet (which requires $\beta > (2/\gamma)\cos^2\theta$), it is either a node or a spiral point. As seen in Figure 1*b*, this is indeed the case. Furthermore, since the intermediate mode has anomalous dispersion (and is right-handed) for $\beta > (2/\gamma)\cos^2\theta$, the node or spiral point is always unstable indicating that, for sufficiently large h_1, a right-handed standing intermediate wave train can be generated at the upstream edge of a subfast subsonic intermediate shock but never at the downstream edge of a fast shock. As mentioned already, it is for this reason that a resistive fast shock having a subsonic downstream state must contain a viscous subshock at its trailing edge: in the resistive-dispersive model, this subshock provides the only possible access to the unstable node or spiral point representing the downstream state.

The remaining fixed point represents the upstream state of the slow shock or the downstream state of the weak intermediate shock (point 3 in Figures). The plasma flow is subalfvénic but superslow so that only the intermediate mode can phase stand in the flow and then only if the flow speed falls between c and $v_A\cos\theta$. Since the flow is subalfvénic, this is never the case when $c > v_A\cos\theta$, i.e., when $\beta > (2/\gamma)\cos^2\theta$. When $\beta < (2/\gamma)\cos^2\theta$, it will occur only when the flow is supersonic. Thus, when point 3 falls on the subsonic Riemann sheet, it is always a saddle. When it falls on the supersonic Riemann sheet, it is either a node (for small h_1) or a spiral point (for sufficiently large h_1). As seen in Figure 1*b*, this is indeed the case. Furthermore, since the intermediate mode has ordinary dispersion (and is left handed) for $\beta < (2/\gamma)\cos^2\theta$, the node or spiral point is always stable, indicating that, for sufficiently large h_1, a left-handed standing intermediate wave train can be generated at the downstream edge of a weak intermediate shock for which the downstream flow is supersonic but never at the upstream edge of a slow shock. It is for this reason that a resistive slow shock having a supersonic upstream state must contain a viscous subshock at its leading edge: in the resistive-dispersive model, this subshock provides the only possible path of departure from the the stable node or spiral point representing the upstream state.

In summary, the properties of small amplitude waves in resistive Hall MHD lead us to conclude the following. (1) For sufficiently large Hall parameter h_1, a fast shock will have a right-handed oscillatory wave train at its upstream edge but never a standing small-amplitude wave train at its downstream edge; if the downstream state is subsonic, a viscous subshock will appear at the downstream edge. (2) For sufficiently large Hall parameter, a slow shock will have a left-handed oscillatory wave train at its downstream edge but never a standing small-amplitude wave train at its upstream edge; if the upstream flow is supersonic, a viscous subshock will appear at the upstream edge. (3) Superfast intermediate shocks will have an upstream right-handed wave train in the same circumstances as the fast shock; subfast subsonic intermediate shocks will also have a right-handed upstream standing wave train for sufficiently large h_1 values whereas subfast supersonic intermediate shocks will not. (4) Strong intermediate shocks will have a downstream left-handed standing wave train in the same circumstances as a slow shock; weak intermediate shocks will have a left-handed downstream standing wave for sufficiently large h_1 values when the downstream flow is

supersonic but not when it is subsonic. (5) It follows from (3) and (4) that certain strong as well as weak intermediate shocks may have a right-handed wave standing at the upstream edge and a left-handed wave standing at the downstream edge of the shock.

Note that conclusions (1) and (2) are not new but are restatements of earlier and by now well-known results [e.g., *Kennel et al.*, 1985; *Coroniti*, 1970; 1971; *Bickerton et al.*, 1971]. Note also that the above conclusions do not depend on the dissipation mechanisms operating in the shock but only on the properties of small-amplitude dispersive waves. Thus we expect the upstream and downstream behavior of shocks which incorporate small viscous dissipation and heat conductivity to be essentially the same as for the purely resistive case, with the exception that viscous subshocks will acquire a finite width (for large viscosity the latter may become the width of the entire shock).

As mentioned earlier, fixed-point analysis indicates the possible existence of a total of 20 different hodogram topologies for shocks in resistive Hall MHD. However, the constraints imposed by the jump conditions appear to restrict the actual number to 13, or at least, our numerical search of parameter space, has produced only 13 of the 20 cases. The missing cases, as well as the 13 cases that have been found, are consistent with the rule that an upstream node and a downstream spiral point cannot occur for a shock that produces a net fast-mode compression ($|B_{t2}| > |B_{t1}|$)whereas an upstream spiral and a downstream node cannot occur for a shock that produces a net slow mode compression ($|B_{t2}| < |B_{t1}|$). This rule is known from previous studies to be valid for fast and slow shocks and four of the missing 7 hodogram topologies can be accounted for by noting that they contain forbidden fast or slow shocks. The remaining three missing cases (as well as two of the four cases accounted for already) contain intermediate shocks that are forbidden by the rule. In the context of small-amplitude standing waves, the rule implies that the h value at critical damping is always lower upstream than downstream of a shock that generates net fast mode compression and always lower downstream than upstream of a shock that generates net slow mode compression. From the behavior of damped oscillations in simple mechanical or electrical systems (e.g., an LR circuit), one can further infer that the h value at critical damping will be lower the shorter the wavelength of the phase standing wave. Beyond that, no physical explanation for the rule can be obtained from the small amplitude wave analysis alone; the shock jump conditions appear to be involved in an intrinsic manner.

6. Summary

In this paper, we have examined the steady-state structure of intermediate shocks as well as fast and slow shocks by use of the resistive nonviscous Hall MHD equations. It is evident from the fixed point analysis in section 3, as well as from the calculations reported in section 4, that for a sufficiently large upstream Hall parameter, h_1, defined as the ratio of the ion inertial length to the Alfvén resistive length, the magnetic hodogram topology may become very different from that obtained for the purely resistive MHD case which corresponds to the limit $h_1 = 0$; in that limit, all fixed points are either nodes or saddle points, as discussed by *Hau and Sonnerup* [1989] whereas for $h_1 \neq 0$ spiral points my also occur. Specifically, we have found the following:

(1) For sufficiently large h_1 value, a nodal fixed point in the $B_y B_z$ plane is converted to a spiral point with the sense of the electron (right-hand) polarization at the upstream state of a fast or an intermediate shock and the ion (left-hand) polarization at the downstream state of an intermediate or a slow shock. Both weak and strong intermediate shocks may in some cases have an upstream right-hand and a downstream left-hand spiral point, representing phase standing wave trains of the intermediate mode, or, downstream of a strong intermediate shock, of the slow mode.

(2) Thirteen distinct hodogram topologies (some of which have several subcases) of a total of 20 possible cases have been found, describing resistive-dispersive fast, slow and intermediate shocks in Hall MHD, compared to only 3 topologies for $h_1 = 0$. Seven cases that are allowed in the fixed-point analysis appear to be missing as a result of constraints imposed by the shock jump conditions.

(3) The spiral structure associated with certain fixed points does not affect one of the basic results obtained by *Hau and Sonnerup* [1989] from the purely resistive MHD model: there still exists an infinite number of transitions for all strong ISs as well as for all superfast weak ISs, while only two transitions exist for the subfast weak IS.

(4) Unlike the MHD case, a purely resistive transition between two supersonic or two subsonic states of an intermediate shock may not always exist. In such cases, the transition can still be achieved via a discontinuity in the form of a viscous gasdynamic subshock along with a smooth subsonic-supersonic transition at a sonic point.

(5) The relationship between small amplitude dispersive waves in the flow upstream or downstream of a shock and the nature of the corresponding fixed point has been established.

(6) For fast and slow shocks, which are also contained in the hodograms presented here, our findings are in complete agreement with the previous studies by *Coroniti* [1970; 1971], *Bickerton et al.* [1971] and many others. In the limit of resistive MHD, i.e., for $h_1 = 0$, the upstream state of a fast shock is always an unstable node while the downstream state can be either an unstable node or a saddle point [*Hau and Sonnerup*; 1989]. For the slow shock, the situation is reversed, namely the upstream state can be either a stable node or a saddle point but the downstream state is always a stable node. Inclusion of the Hall effect with sufficiently large h_1 values leads to the conversion of the fast-mode upstream node to a right-handed unstable spiral point and of the slow-mode downstream node to a left-handed stable spiral point. In addition, when the downstream fast-mode state is a subsonic unstable node for $h_1 = 0$, conversion of this point to an unstable right-handed spiral point may occur; for both $h_1 = 0$ and $h_1 \neq 0$ this state can be reached only via a viscous subshock at the trailing edge of the fast shock structure. Thus, spiral behavior of the magnetic field does not occur at the downstream edge of a fast-mode shock. Similarly, when the upstream slow-mode state is a supersonic stable node for $h_1 = 0$, conversion of this point to a stable left-handed spiral point may occur; for both $h_1 = 0$ and $h_1 \neq 0$, departure from this state occurs via a viscous subshock at the upstream edge of the slow shock structure. Thus, spiral behavior of the magnetic field does not occur at the upstream edge of a slow-mode shock. Unlike the intermediate shock, there always exists a purely resistive-dispersive transition between upstream and downstream states

located on the same Riemann sheet. Unlike the intermediate shocks, the fast and slow-mode shock structures are unique for given upstream parameter values, both when $h_1 = 0$ and when $h_1 \neq 0$. Figure 1*b* indicates 5 possible hodogram topologies (*n-n*; *s-n*; *s-s*; *n-sa*; *s-sa*) for the fast-mode shock but the cases *s-n* and *s-s* are not distinct since for both access to the downstream state occurs via a viscous trailing-edge subshock. Similarly, formally there are 5 possible hodogram topologies (*sa-n*; *sa-s*; *n-n*; *n-s*; *s-s*) for the slow-mode shock but the cases *n-s* and *s-s* are not distinct since for both egress from the upstream state occurs via a viscous leading-edge subshock.

Finally, we note that no systematic attempt has been made to identify and delineate the regions in parameter space in which the 13 different hodogram topologies arise, to examine the dynamic stability of the various intermediate shock structures described by these hodograms, or to work out spatial profiles of quantities such as density, temperature, magnetic field and velocity.

APPENDIX

The dispersion relation for small-amplitude waves in Hall MHD, i.e, quation (15), can be rewritten as follows:

$$\left(\frac{\omega^2}{k^2} - v_A^2 cos^2\theta\right)\left[\frac{\omega^4}{k^4} - (c^2+v_A^2)\frac{\omega^2}{k^2} + c^2 v_A^2 cos^2\theta\right]$$

$$- \lambda_i^2 k^2 \frac{\omega^2}{k^2} v_A^2 \left(\frac{\omega^2}{k^2} - c^2\right) cos^2\theta = 0 \qquad \text{(A1)}$$

If a wave can stand in the upstream or downstream flow, then its phase speed must be equal to the plasma flow speed there, i.e., $\omega/k = v_x$. Furthermore, it can be easily shown that $c^2 + v_A{}^2 = c_f{}^2 + c_s{}^2$ and $c^2 v_A{}^2 cos^2\theta = c_f{}^2 c_s{}^2$ so that, together with the definition $A_x = v_x / v_A cos\theta$, equation (A1) becomes

$$(A_x^2 - 1)\frac{(v_x^2 - c_f^2)(v_x^2 - c_s^2)}{v_x^2 (v_x^2 - c^2)} - \lambda_i^2 k^2 = 0 \qquad \text{(A2)}$$

Writing (A2) in terms of the quantities K_y and K_z, defined in equations (11) and (12), yields

$$k^2 = \frac{K_y K_z}{A_x^2 \lambda_i^2} \qquad \text{(A3)}$$

Equation (A3) clearly indicates that for the case $K_y K_z < 0$, i.e., when the fixed point examined is a saddle, none of the three wave modes can phase stand in the upstream or downstream flow, or, equivalently, the phase speed cannot be equal to the plasma flow speed there. For the case $K_y K_z > 0$, i .e., when the fixed point examined is either a node or a spiral point, (A3) gives the corresponding wavelength of the standing wave train.

Acknowledgments. The research was supported by the National Science Foundation, Atmospheric Sciences Division, under grant ATM-8807645, and by the Air Force Geophysics Laboratory under contracts F19628-87-K-0026 and F19628-87-K-0038 to Dartmouth College.

REFERENCES

Berchem, J. W., and C. T. Russell, Magnetic field rotation through the magnetopause: ISEE 1 and 2 observations, *J. Geophys. Res.*, *87*, 8139, 1982a.

Bickerton, R. J., L. Lenamon, and R. V. W. Murphy, The structure of hydromagnetic shock waves, *J Plasma Phys.*, *5*, 177, 1971

Coroniu, F. V., Dissipation discontinuities in hydromagnetic shock waves, *J. Plasma Phys.*, *4*, 265, 1970.

Coroniti, F. V., Laminar wave-train structure of collisionless magnetic slow shocks, *Nucl. Fusion*, *11*, 261, 1971.

Formisano, V., and C. F. Kennel, Small amplitude waves in high β plasmas, *J Plasma Phys.*, *3*, 55, 1969.

Germain, P., Shock waves and shock wave structures in magneto fluid dynamics, *Rev. Mod. Phys.*, *32*, 951, 1960.

Hau, L.-N., and B. U. Ö. Sonnerup, On the structure of resistive Hall intermediate shocks, *J Geophys Res.*, 94, 6539, 1989

Jeffrey, A., and T. Taniuu, *Non-Linear Wave Propagation*, Academic, San Diego, Calif., 1964.

Kennel, C. F., J. P. Edmiston, and T. Hada, A quarter century of collisionless shock research, in *Collisionless Shocks in the Heliosphere: A Tutorial Review*, *Geophys. Monogr. Ser.*, vol. 34, edited by R. G. Stone and B. T. Tsurutani, p. 1, AGU, Washington, D. C., 1985.

Kennel, C. F., R. D. Blandford, and C. C. Wu, Structure and evolution of small amplitude intermediate shock waves, *Phys. Fluids*, *2*, 253, 1990

Lyu, L.-H, and J. R. Kan, Structures of Alfvén Shocks: S-shaped magnetic hodogram observed at the magnetopause, *Geophys. Res. Lett.*, *16*, 349, 1989.

Scholer, M., Asymmetric time-dependent and stationary magnetic reconnection at the dayside magnetopause, *J. Geophys. Res.*, *94*, 15099, 1989.

Stringer, T. E., Low-frequency waves in an unbounded plasma, *Plasma Phys J. Nucl. Energy, Part C*, *5*, 89, 1963.

Wu, C. C., On MHD intermediate shocks, *Geophys. Res. Lett.*, *14*, 668, 1987.

Wu, C. C., The MHD intermediate shock interaction with an intermediate wave: Are intermediate shocks physical?, *J. Geophys. Res.*, *93*, 987, 1988a.

Wu, C. C., Effects of dissipation on rotational discontinuities, *J Geophys Res.*, *93*, 3969, 1988b.

L.-N. Hau and B. U. Ö Sonnerup, Thayer School of Engineering, Dartmouth College, Hanover, NH 03755.

Cases	Supersonic ("+") Sheet	Subsonic ("−") Sheet	Hodograms
8	Point 1: node or spiral	Point 2: node or spiral Point 3: saddle Point 4: node or spiral	Fig 2 (n-n-sa-n) Fig 3 (s-n-sa-n) Fig 4 (s-n-sa-s) Fig 5 (s-s-sa-s)
4	Point 1: node or spiral Point 2: saddle	Point 3: saddle Point 4: node or spiral	Fig 6 (n-sa-sa-n) Fig 7 (s-sa-sa-n) Fig 8 (n-sa-sa-s) Fig 9 (s-sa-sa-s)
8	Point 1: node or spiral Point 2: saddle Point 3: node or spiral	Point 4: node or spiral	Fig 10 (n-sa-n-n) Fig 11 (s-sa-n-n) Fig 12 (n-sa-n-s) Fig 13 (s-sa-n-s) Fig 14 (s-sa-s-s)

(b)

Upstream / Downstream			Subfast Subsonic ("−") (Point 2) Section 4.1		Subfast Supersonic ("+") (Point 2) Section 4.2	Superfast Supersonic ("+") (Point 1) Section 4.3	
			node	spiral	saddle	node	spiral
Strong IS (Point 4)	Subslow Subsonic ("−")	node	Fig 2,3		Fig 6,7 Fig 10,11	Fig 2,6,10	Fig 3,7,11
		spiral	Fig 4	Fig 5	Fig 8,9 Fig 12,13 Fig 14	Fig 8,12	Fig 4,5,9 Fig 13,14
Weak IS (Point 3)	Superslow Subsonic ("−")	saddle	Fig 2,3 Fig 4	Fig 5	Fig 6,7 Fig 8,9	Fig 2,6,8	Fig 3,4,5 Fig 7,9
	Superslow Supersonic ("+")	node			Fig 10,11 Fig 12,13	Fig 10,12	Fig 11,13
		spiral			Fig 14		Fig 14

(a)

Fig. 1. Matrices showing possible shock states based on (*a*) the nature of the upstream and downstream flow for intermediate shocks or (*b*) on the fixed-point location on the supersonic and subsonic Riemann sheets. Notation: 1, 2 and 3, 4 denote fast-shock and slow-shock upstream and downstream conditions, respectively; the possible intermediate shocks (IS) are: 1→3 (superfast weak), 1→4 (superfast strong), 2→3 (subfast weak) and 2→4 (subfast strong). The fixed points (*n* = node, *sa* = saddle point and *s* = spiral point) are listed in the order 1, 2, 3, 4. Missing hodograms are: (*n-n-sa-s*), (*n-s-sa-s*), (*n-s-sa-n*) and (*s-s-sa-n*) in row 1 of part (*b*); (*n-sa-s-s*), (*n-sa-s-n*) and (*s-sa-s-n*) in row 3 of part (*b*).

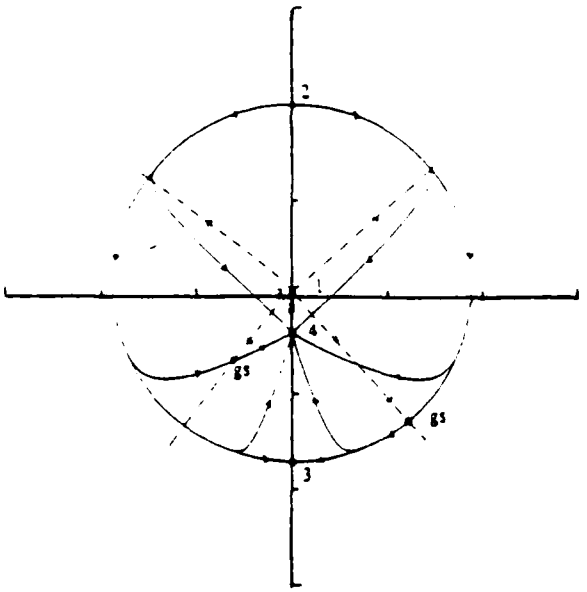

Fig. 2. Magnetic field hodogram for case (i) of section 4 (*n-n-sa-n*), where the fast-shock upstream state, 1, and downstream state, 2, as well as the strong-IS downstream state, 4, are all nodes while the weak-IS downstream state, 3, is a saddle. Point 2 serves as the upstream state of a subfast IS while point 1 can also be the upstream state of a superfast IS. Dashed curves are trajectories on the *supersonic (plus) Riemann sheet*; solid lines lie on the subsonic (minus) sheet. In the superfast IS, the supersonic-subsonic transition occurs in a gasdynamic subshock (*gs*). Plasma parameters at point 2 are: $\beta_1 = 1$, $\theta_1 = 45^o$, $A_{x1}^2 = 1.0428$, and Hall parameter (the ratio of electron gyrofrequency to collision frequency), $h_1 = 0.012$.

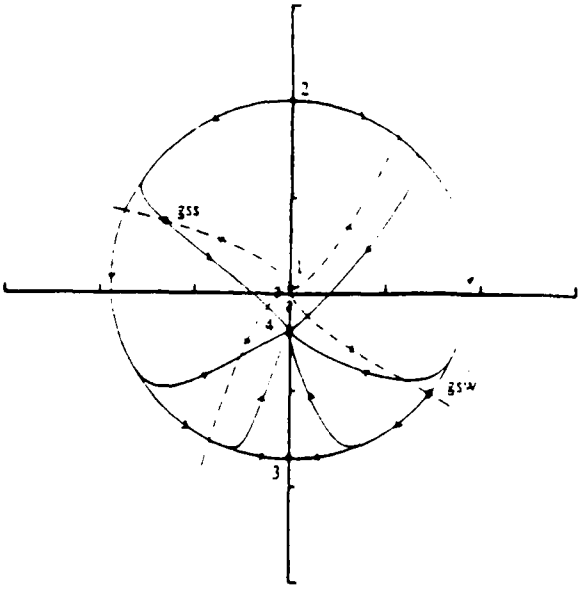

Fig. 3. Hodogram for case (ii) of section 4 (*s-n-sa-n*), where point 1 is converted from a node to a spiral point while points 2, 3 and 4 remain the same as in Figure 2. Supersonic-subsonic transition occurs in a gasdynamic subshock, denoted by *gsw* and *gss* for the weak and *strong superfast* intermediate shock, respectively. Parameters at point 2 are the same as in Figure 2, except that $h_1 = 0.1$.

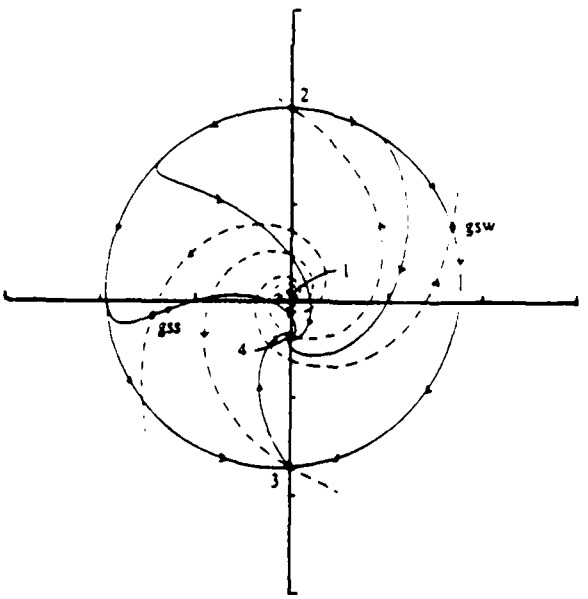

Fig. 4. Hodogram for case (iii) of section 4 (*s-n-sa-s*), where points 1 and 4 are spiral points, point 2 is a node and point 3 is a saddle point. Parameters at point 2 are the same as in Figures 2 and 3, except that $h_1 = 1$.

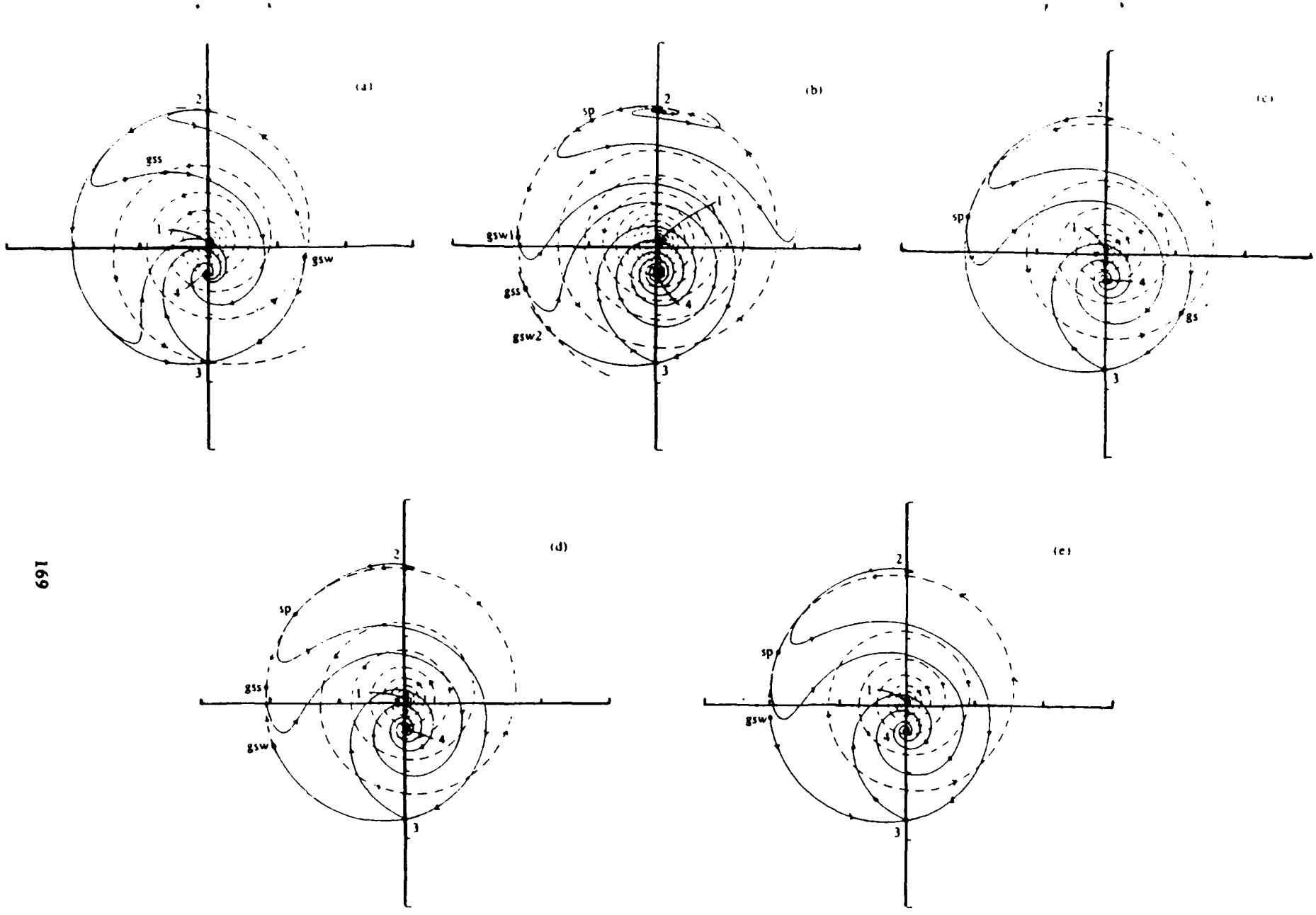

Fig. 5. Hodograms for case (iv) of section 4 (s-s-sa-s), where points 1, 2 and 4 are all spiral points while point 3 remains a saddle point. Parameters at point 2 are the same as in Figures 2, 3 and 4, except that A_1 = 3.33, 10, 5 715, 6.64 and 5 814 in parts (a)-(e), respectively.

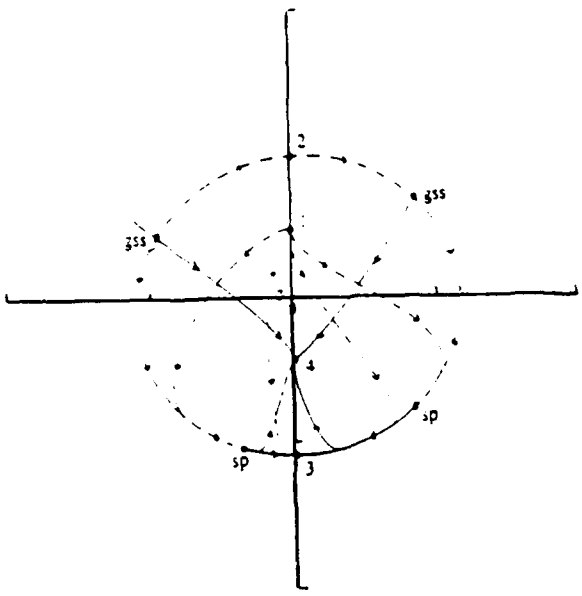

Fig. 6. Hodogram for case (v) of section 4 (*n-sa-sa-n*), where points 2 and 3 are saddle points while points 1 and 4 are nodes. Parameters at point 2 are: $\beta_1 = 0.5$, $\theta_1 = 26.57^{\circ}$, $A_{x^2} = 1.1471$ and $h_1 = 0.2$. The symbol *sp* denotes the point where smooth supersonic-subsonic transition is possible; the point *gss* is a gasdynamic subshock, which serves as part of the transition between the IS upstream state (which can be at point 1 or 2), and the strong-IS downstream state (4).

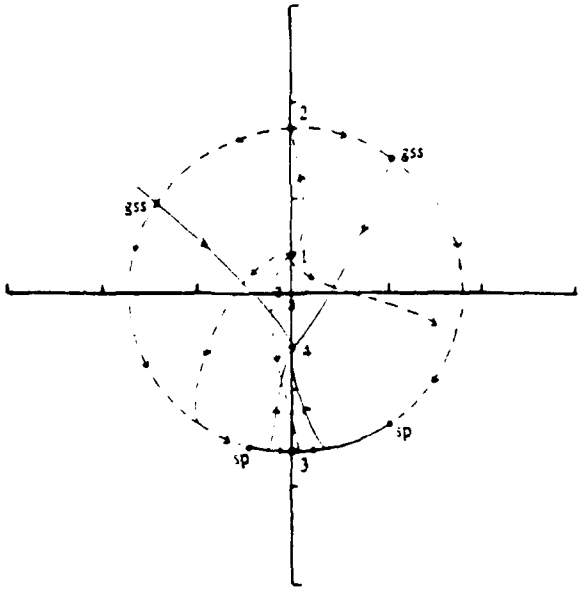

Fig. 7. Hodogram for case (vi) of section 4 (*s-sa-sa-n*), where point 1 is converted from a node to a spiral point while points 2, 3 and 4 remain the same as in Figure 6. Parameters at point 2 are: $\beta_1 = 0.255$, $\theta_1 = 40.89^{\circ}$, $A_{x1}{}^2 = 1.1425$ and $h_1 = 0.25$.

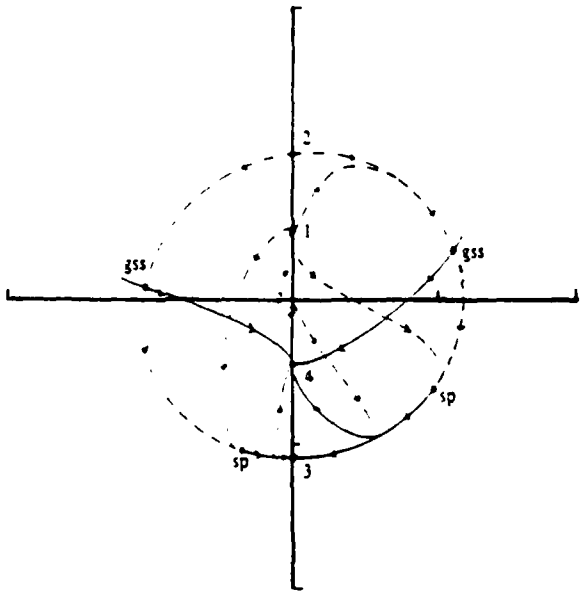

Fig. 8. Hodogram for case (vii) of section 4 (*n-sa-sa-s*), where point 1 is a node, point 4 is a spiral point while points 2 and 3 are both saddle points. Parameters at point 2 are the same as in Figure 6, except that $h_1 = 0.345$.

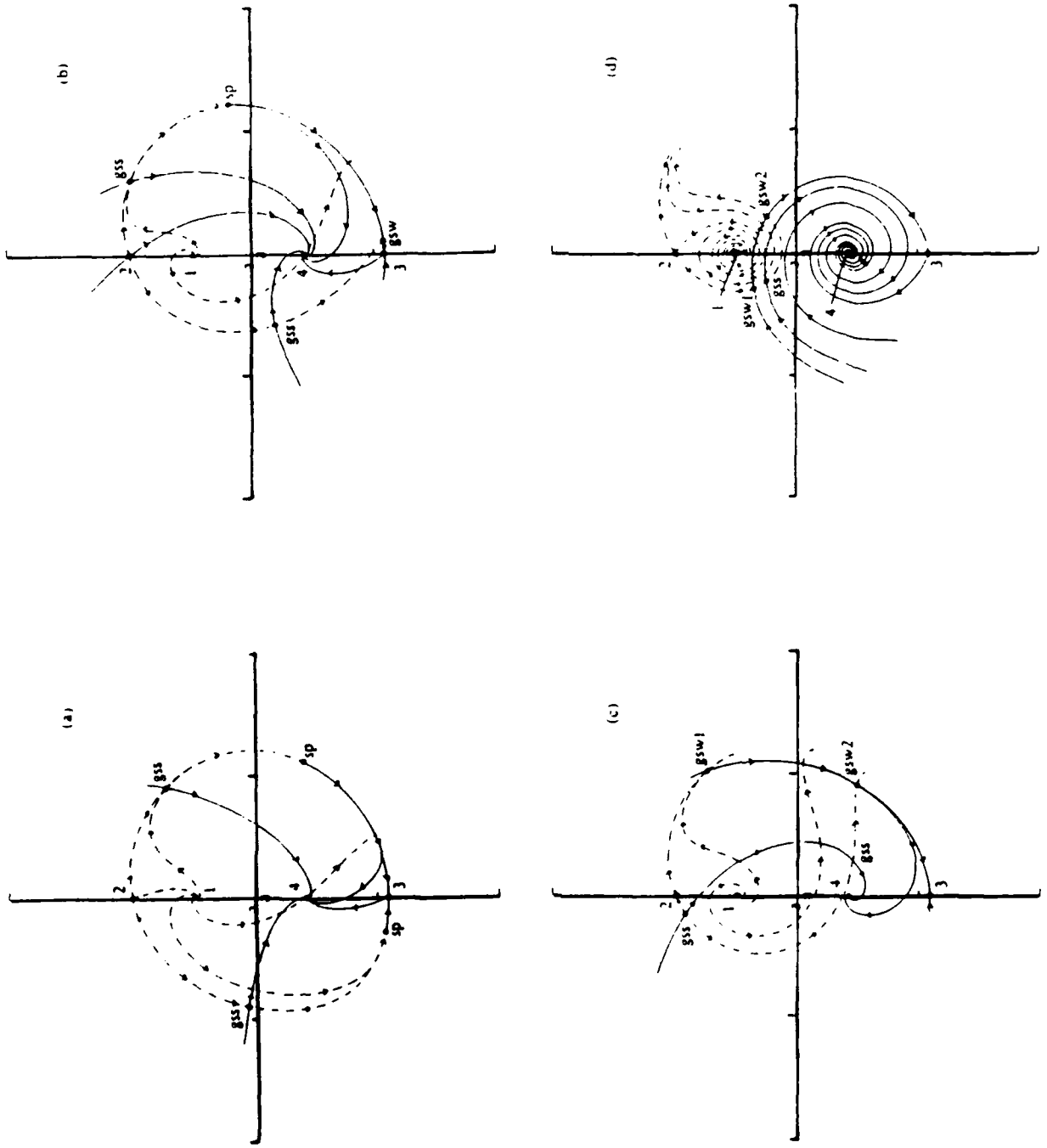

Fig. 9. Hodograms for case (viii) in section 4 ($s_1 = s_2 = s_3 = s$), where point 1 is convected from a node to a spiral point while points 2, 3 and 4 remain the same as in Figure 8. Plasma parameters at point 2 are the same as in Figure 8, except that $A_1 = 0.667, 1.25, 2$ and 10 in parts (*a*)-(*d*), respectively.

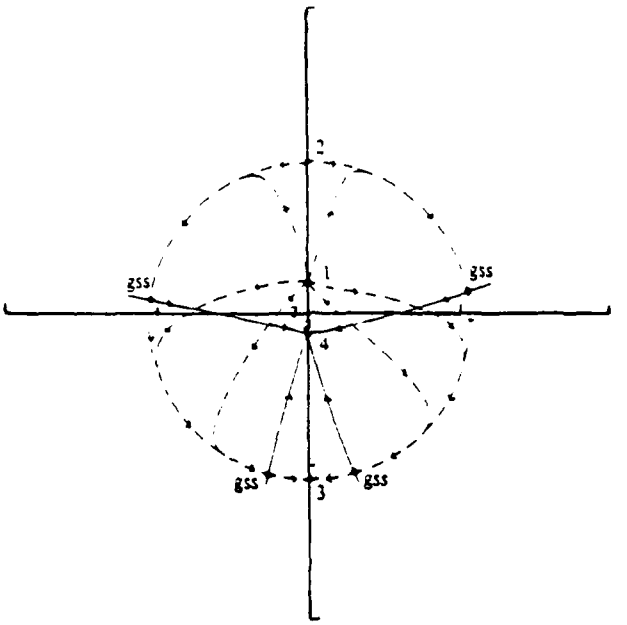

Fig. 10. Hodogram for case (ix) of section 4 (*n-sa-n-n*), where points 1, 3 and 4 are all nodes while point 2 is a saddle point. Parameters at point 2 are: β_1 = 0.5, $\theta_1 = 26.57^{\circ}$, $A_{x1}{}^2 = 1.0546$ and $h_1 = 0.067$.

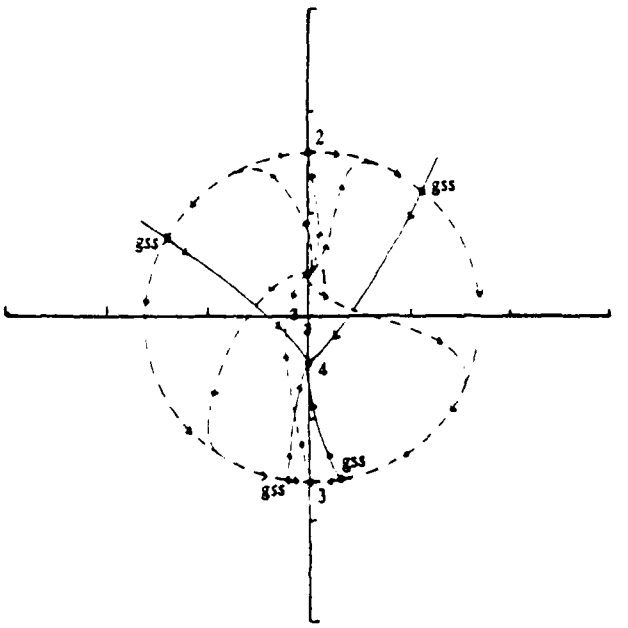

Fig. 11. Hodogram for case (x) of section 4 (*s-sa-n-n*), where point 1 is converted form a node to a spiral point while the other three fixed points remain the same as in Figure 10. Plasma conditions at point 2 are: $\beta_1 = 0.24$, $\theta_1 = 38.66^{\circ}$, $A_{x1}{}^2 = 1.1316$ and $h_1 = 0.25$.

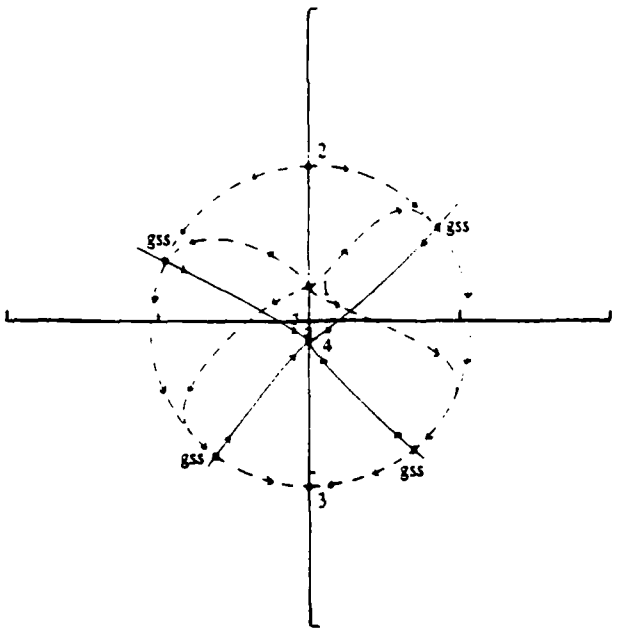

Fig. 12. Hodogram for case (xi) in section 4 (*n-sa-n-s*), where points 1 and 3 are nodes, point 2 is a saddle and point 4 is a spiral. Parameters at point 2 are the same as in Figure 10, except that $h_1 = 0.125$.

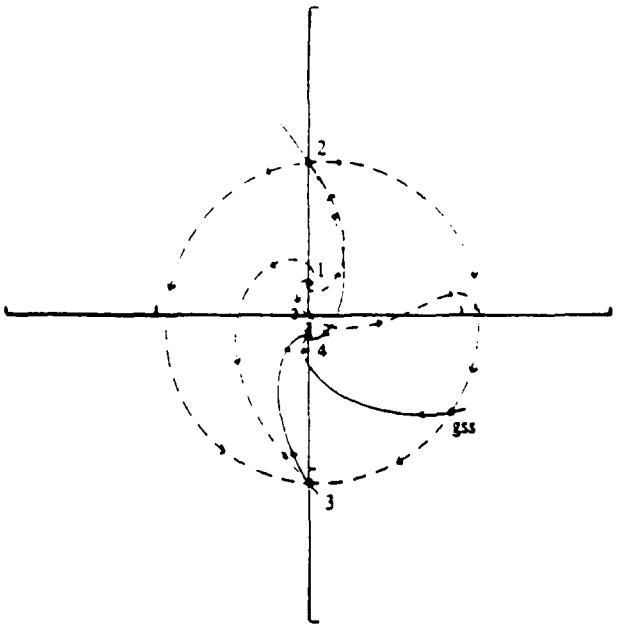

Fig. 13. Hodogram for case (xii) in section 4 (*s-sa-n-s*), where point 1 is converted from a node to a spiral while points 2, 3 and 4 are the same as in Figure 12. Parameters at point 2 are the same as in Figure 12, except that $h_1 = 1$.

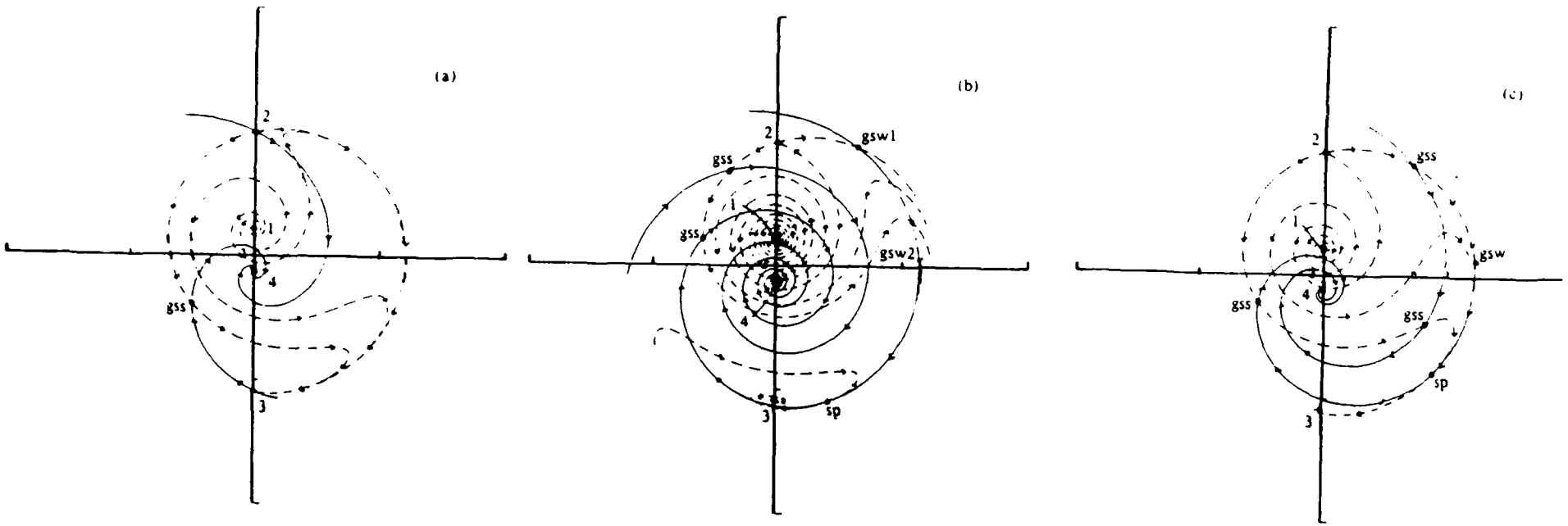

Fig. 14. Hodograms for case (xiii) in section 4 (*s-sa-s-s*), where points 1, 3 and 4 are all spiral points while point 2 is a saddle point. Parameters at point 2 are the same as in Figure 13, except that h_1 = 3.33, 10 and 4.728 in parts (a)-(c), respectively.

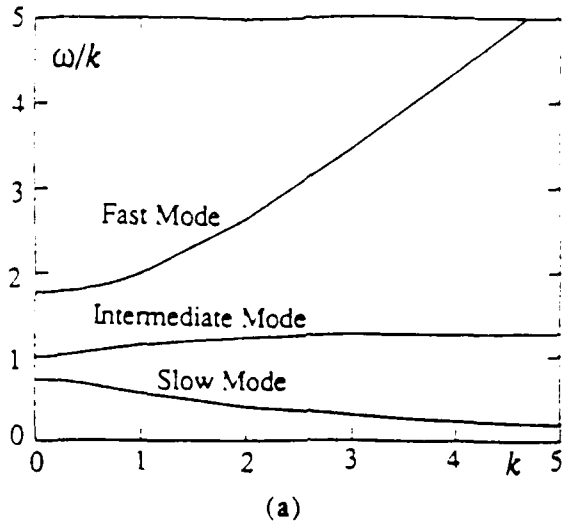

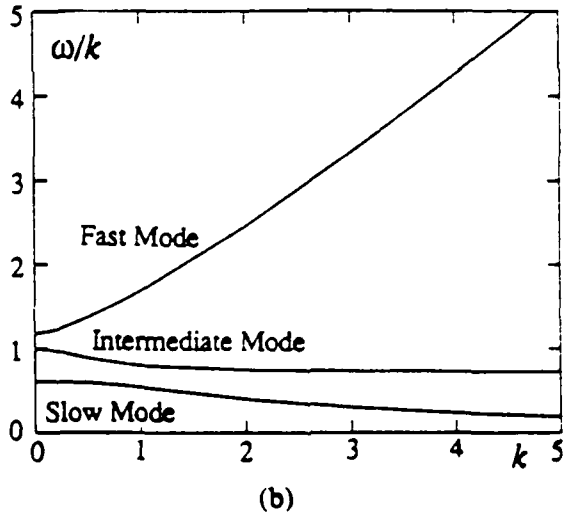

Fig. 15. Dispersion relation (phase speed, ω/k, versus wave number, k) for small amplitude waves (*a*) for $\beta > (2/\gamma)\cos^2\theta$ ($\gamma = 5/3$; $\beta = 1$; $\theta = 45^{\circ}$); (*b*) for $\beta < (2/\gamma)\cos^2\theta$ ($\gamma = 5/3$; $\beta = 0.5$; $\theta = 26.57^{\circ}$). Positive (negative) slope of the dispersion curve corresponds to group speed greater (smaller) than the phase speed.

JOURNAL OF GEOPHYSICAL RESEARCH, VOL. 95, NO. A7, PAGES 10,541–10,557, JULY 1, 1990

The Magnetopause for Large Magnetic Shear: Analysis of Convection Electric Fields From AMPTE/IRM

B. U. Ö. SONNERUP

Thayer School of Engineering, Dartmouth College, Hanover, New Hampshire

I. PAPAMASTORAKIS[1] AND G. PASCHMANN

Max-Planck-Institut für extraterrestrische Physik, Garching, Federal Republic of Germany

H. LÜHR

Institut für Geophysik und Meteorologie, Technische Universität, Braunschweig, Federal Republic of Germany

A number of magnetopause crossings by the AMPTE/IRM spacecraft, which exhibited large shear in the magnetic field, were studied recently by Paschmann et al. (1986) in order to assess the presence or absence of reconnection processes at the dayside magnetopause. In the present article, eleven of these crossings are reanalyzed by use of methods described by Sonnerup et al. (1987). Although only eight of the cases lend themselves to this more detailed analysis procedure, the results derived when the analysis is successful are considerably more detailed and quantitative than those obtained previously. Four such cases are documented in detail in the paper. For these events it was possible to derive accurate vectors, **n**, normal to the magnetopause. It was also possible to place bounds on the values of average magnetic field and flow velocity components along **n** as well as on the average electric field tangential to the magnetopause and on the velocity of the magnetopause itself along **n** and therefore on the magnetopause thickness. It is particularly noteworthy that in two crossings (on September 4, 1984) it was possible to place lower bounds of 2.8 mV/m and 0.5 mV/m on the tangential (reconnection) electric field and corresponding lower bounds on normal flow and field. In a third crossing (September 8, 1984), located about 1 R_E north of the subsolar point, evidence is deduced, indicating that the observed plasma acceleration along the magnetopause had a large temporal component, caused by a tangential gradient in the total pressure, in addition to the usual convective component caused by the Maxwell shear stresses. Finally, in the fourth crossing (October 19, 1984), large magnetic shear was present but, in agreement with a conclusion reached by Paschmann et al. (1986), the analysis shows that no evidence for reconnection was present and that the magnetopause had the properties of a tangential discontinuity. This case provides convincing evidence that the mere existence of a deHoffmann-Teller frame of reference in which the flow is field aligned (an excellent fit of the data to such a frame could be performed in this case) does not guarantee that the magnetopause is a rotational discontinuity. The remaining events analyzed by use of the new procedure demonstrate that the methodology sometimes fails, or yields unconvincing results, even when there is considerable evidence, in the form of accelerated plasma flows, that some form of reconnection is in progress.

1. INTRODUCTION

Recently, *Paschmann et al.* [1986], hereafter referred to as paper 1, have surveyed the features of 21 passes by the AMPTE/IRM spacecraft through the magnetopause region in which large magnetic shear was observed to be present. In that study, special attention was paid to the presence or absence of the large plasma velocity enhancements in the magnetopause/boundary-layer region that are believed to signify the occurrence of reconnection at the magnetopause, such enhancements having been reported earlier on the basis of observations from the ISEE 1 and 2 spacecraft [*Paschmann et al.*, 1979; *Sonnerup et al.*, 1981; *Gosling et al.*, 1982;1986]. The main finding in paper 1 is that the presence of large magnetic shear is not a sufficient condition for the occurrence of velocity enhancements having directions and magnitudes that are in approximate agreement with the so-called Walén relation. The latter relation is valid across rotational discontinuities and it is assumed that the main magnetopause structure during reconnection consists of a rotational discontinuity, as in the classical model proposed by *Levy et al.* [1964]. Thus the principal conclusion of paper 1 is that the presence of large magnetic shear is not a sufficient condition for the occurrence of reconnection in the subsolar magnetopause region. Rather it appears that velocity enhancements approximately compatible with the Walén relation occurred only when the plasma beta value ($\beta \equiv 2\mu_0 p/B^2$) in the adjacent magnetosheath was less than about 2. For larger β values, the velocity enhancements, if any, amounted to only a small fraction of the change in Alfvén velocity, indicating that the Walén relation, $\Delta v = \pm \Delta v_A$, was poorly satisfied. Here, Δv denotes the difference between the locally measured plasma velocity

[1] Permanent affiliation is Physics Department, University of Crete, Heraklion, Greece.

Paper number 90JA00228.
0148-0227/90/90JA-00228$05.00

at some point within the magnetopause/boundary layer region and the plasma velocity measured during a reference interval in the magnetosheath, immediately preceding (for an inbound crossing) or following (for an outbound crossing) the magnetopause data interval. Similarly, Δv_A is the corresponding difference between the locally measured magnetic field, converted to a local Alfvén velocity, and the Alfvén velocity in the reference interval. The positive and negative signs in the Walén relation correspond to plasma flow across the discontinuity that is parallel and antiparallel to the normal magnetic-field component, respectively. In the context of the standard subsolar reconnection model [*Levy et al.*, 1964], the positive and negative signs correspond to crossings north and south of the reconnection site, respectively.

A new framework for examination of various features of the magnetopause, including its orientation, normal motion and acceleration as well as its adherence to the Walén relation, has been reported by *Sonnerup et al.* [1987], hereafter referred to as paper 2, who applied the new methods to one of the magnetopause crossings (September 4, 1984, 1500:42–1501:51 UT) discussed in paper 1. Plasma velocity enhancements on that day have also been studied by *Johnstone et al.* [1986] using data from the AMPTE/UKS spacecraft. Certain portions of the new methodology have also been found useful in the study of magnetopause flux transfer events (FTEs) [*Papamastorakis et al.*, 1989], hereafter referred to as paper 3. In the present paper, the new procedures will be applied to the remaining eleven crossings that were discussed in detail in paper 1, with the objective of testing the new methods further, as well as obtaining improved information about the orientation, motion and structure of the magnetopause during these events.

In brief, the new analysis is based on the convection electric field, $\mathbf{E}_c = -\mathbf{v} \times \mathbf{B}$, computed from measured local plasma velocities, $\mathbf{v}$, and magnetic fields, $\mathbf{B}$. It is found that for many (but by no means all) magnetopause crossings, this electric field can be nearly removed by transformation to a moving frame of reference, called the deHoffmann-Teller (HT) frame, which follows the magnetopause in its motion normal to itself and also slides in the local magnetopause tangent plane in such a manner that the individual plasma velocity vectors observed in the HT frame are as nearly field-aligned as the data set permits.

Unless the plasma velocity is constant, or nearly constant, it is by no means a trivial property of a magnetopause data set to possess a good HT frame, for its existence implies that the component of each measured velocity vector, $\mathbf{v}$, perpendicular to the simultaneously measured magnetic field vector, $\mathbf{B}$, is equal to the component of the constant velocity of motion, $\mathbf{v}_{HT}$, of the HT frame perpendicular to the same field. However, an HT frame does exist for the data on two sides of any thin one-dimensional and time-independent current sheet which has a nonzero normal magnetic field component, such as a shock [*deHoffmann and Teller*, 1950] or a rotational discontinuity. Furthermore, a thin tangential discontinuity with uniform, but different field and flow on its two sides also has an HT frame [*Paschmann*, 1985]. But for thick current sheets where the data consist of $\mathbf{v}$ and $\mathbf{B}$ measurements mostly within the layer itself, further restrictions are needed: the intrinsic normal electric field, i.e., the electric field normal to the current sheet, evaluated in an HT frame obtained from exterior data, must cancel the normal electron pressure term, $(\nabla p_e)/ne$; the resistive and dispersive terms, $\eta \mathbf{j}$ and $\mathbf{j} \times \mathbf{B}/ne$, as well as the electron inertia terms in Ohm's law must all be small compared to $\mathbf{v} \times \mathbf{B}$. These additional conditions are expected to be fulfilled for a rotational discontinuity of thickness much greater than the ion gyroradius. They may or may not be satisfied by a tangential discontinuity so that one cannot in general use the existence of an HT frame for a thick discontinuity to conclude that it must be a rotational discontinuity. This point will be illustrated in one of the events to be analyzed here. For internally sampled shock structures which have a substantial intrinsic electric field, one would not expect an HT frame to exist, although certain weak intermediate shocks [*Wu*, 1987; *Hau and Sonnerup*, 1989] may in practice be indistinguishable from rotational discontinuities in this regard. As discussed in paper 3, an FTE structure moving along the magnetopause may also have an HT frame.

It has been shown in paper 2 that in some cases the fit between $-\mathbf{v} \times \mathbf{B}$ and $-\mathbf{v}_{HT} \times \mathbf{B}$ can be improved substantially by assuming the HT frame to be in a state of accelerated motion relative to the spacecraft, i.e., by writing $\mathbf{v}_{HT} = \mathbf{v}_{HTo} + \mathbf{a}_{HT} \cdot t$, where both the initial HT velocity, $\mathbf{v}_{HTo}$ and the (constant) frame acceleration, $\mathbf{a}_{HT}$, are determined from a least squares fitting procedure. The components of $\mathbf{v}_{HTo}$ and of $\mathbf{a}_{HT}$ perpendicular to the magnetopause represent the initial normal velocity and the average normal acceleration of the magnetopause itself. The components tangential to the magnetopause represent the motion of the HT frame in the magnetopause tangent plane which is needed to bring about a field-aligned plasma flow in that frame. The physical significance of the tangential acceleration is discussed at a later point in our paper.

Finally, we note that, by use of the HT frame, the Walén relation can be written in the convenient form

$$(\mathbf{v} - \mathbf{v}_{HT}) = \pm \mathbf{v}_A \tag{1}$$

indicating that in this frame the flow is field-aligned and Alfvénic. As discussed in the Appendix, the existence of an HT frame and the validity of the Walén relation are interrelated properties of steady quasi one-dimensional MHD discontinuities when (and only when) the normal magnetic field component is nonzero.

It should be added that, even for rotational discontinuities, strict agreement with the Walén relation, (1), is expected only for sufficiently thick, one-dimensional and time-independent structures; all of these conditions are usually not met at the magnetopause. An additional difficulty is the fact that the AMPTE/IRM plasma instrument cannot discriminate between different ion species. It is usually assumed that the particles are protons. But even a small admixture of heavier ions such as O^+ will influence the mass density and thus the calculated Alfvén velocity significantly. By use of the relation

$$\rho(1 - \alpha) = \text{const} \tag{2}$$

which is valid across any ideal rotational discontinuity and is also approximately valid within such a discontinuity, provided it is much thicker than the ion gyroradius, it was argued in paper 1 that the effective ion mass within the magnetopause and boundary layer can often be significantly larger

than in the magnetosheath reference interval. In equation (2), $\rho = \sum n_i m_i$ is the total mass density, summed over all species, and α is the total locally measured plasma pressure anisotropy factor, $\alpha \equiv (p_\parallel - p_\perp)\mu_0/B^2$, which can be shown to depend only weakly on the mass composition, as discussed in paper 1. Thus the problem of the unknown mass composition in calculating the Alfvén velocity was overcome in papers 1 and 2 (a similar procedure was used in paper 3) by writing

$$v_A \equiv \mathbf{B}\sqrt{(1-\alpha)/\mu_0\rho} = \mathbf{B}(1-\alpha)/\sqrt{\mu_0\rho_1(1-\alpha_1)} \quad (3)$$

where ρ_1 and α_1 refer to the magnetosheath reference interval in which the plasma composition is assumed known. The same method will be employed here and, for simplicity, it will be assumed initially that the magnetosheath plasma consists exclusively of protons and electrons. Possible corrections to that assumption will then be discussed.

The paper is organized as follows. In section 2, we summarize briefly the nature of the data and data analysis procedures used in the study. In section 3, we present detailed results for four AMPTE/IRM magnetopause crossings, contained in paper 1, along with our interpretation and discussion of those results. We also mention briefly the results from the other crossings discussed in detail in paper 1. In section 4, a summary of our findings is given, along with concluding remarks.

2. Data Analysis Methods

The observations presented in this paper were obtained in the Fall of 1984, with the 3D plasma instrument and the magnetometer onboard the AMPTE/IRM spacecraft. A brief summary of the features of the plasma instrument is given in paper 1; more details are provided in *Paschmann et al.* [1985]. The magnetometer has been described by *Lühr et al.* [1985].

The data used directly in the analysis consist of measured ion number density, n, flow velocity vector, $\mathbf{v}$, magnetic field, $\mathbf{B}$, and pressure anisotropy factor, $\alpha = (p_\parallel - p_\perp)\mu_0/B^2$. These quantities were obtained every spin period, i.e., approximately every 4.4 s. The magnetic field data has much higher time resolution (32 samples/s) but only spin averages synchronized with the plasma measurements were used in the study.

The data reduction procedures are described in detail in paper 2. Depending on the quality of the data and the event, the analysis can be carried through one or more of three levels of increasing complexity, as summarized below.

2.1. *Level A*

A (constant) velocity, $\mathbf{v}_{HT}$, of the deHoffmann-Teller frame is determined by minimization of the quadratic form

$$D = \frac{1}{N}\sum_{m=1}^{N} |(\mathbf{v}^m - \mathbf{v}_{HT}) \times \mathbf{B}^m|^2 \quad (4)$$

where the superscript m is used to denote the N individual pairs of velocity and magnetic field vectors in the data set for the magnetopause crossing. This set is chosen to include points within the current-layer structure as well as some points on the two sides of the layer. The relative residual D/D_0, where D_0 is obtained from (4) with $\mathbf{v}_{HT} = 0$, is a measure of the quality of the fit between what we call the HT electric field, $\mathbf{E}_{HT} \equiv -\mathbf{v}_{HT} \times \mathbf{B}$, and the measured convection electric field, $\mathbf{E}_c = -\mathbf{v} \times \mathbf{B}$, with a small value of D/D_0 indicating a high-quality fit. A visual representation of the fit is also provided in a single scatter plot of the three components of $\mathbf{E}_c$ versus the corresponding components of $\mathbf{E}_{HT}$, using an arbitrary cartesian coordinate system, in our case the GSE system, denoted by (X, Y, Z) in the paper. It can be shown that in such a scatter plot the correlation coefficient, but not the regression line slope, depends weakly on the choice of coordinate system; since the correlation coefficients given in the paper are used only for comparison of fits using the same coordinate system but different levels of analysis, this is not a serious problem. Changes in regression line slope as well as correlation coefficient also occur when the electric fields $\mathbf{E}_c$ and $\mathbf{E}_{HT}$ are transformed to a frame of reference moving with the magnetopause. Again, these effects are usually negligibly small.

We emphasize that $\mathbf{E}_{HT}$ is not the electric field in the HT frame. The latter field is $(\mathbf{E}_c - \mathbf{E}_{HT})$ and $\mathbf{v}_{HT}$ has been determined from (4) in such a way that its magnitude-square, averaged over the data set, has been minimized. Except for singular cases, this determination of $\mathbf{v}_{HT}$ is unique. Furthermore, the component of $\mathbf{v}_{HT}$ perpendicular to the magnetopause represents the motion of that layer perpendicular to itself, although, as discussed more in detail below, the vector normal to the magnetopause is usually not precisely known. The component of $\mathbf{v}_{HT}$ tangential to the magnetopause represents the sliding motion of the HT frame along the layer, needed to make the flow in the HT frame as field aligned as the data set permits.

The agreement of the data with the Walén relation can now be tested by use of a scatter diagram in which each of the three components of $(\mathbf{v}^m - \mathbf{v}_{HT})$ is plotted against the corresponding component of the Alfvén velocity, $\mathbf{v}_A^m = \mathbf{B}^m(1-\alpha^m)/\sqrt{\mu_0\rho_1(1-\alpha_1)}$. Here ρ_1 and α_1 are the mass density and pressure anisotropy, evaluated in a suitable reference interval in the adjacent magnetosheath in which, initially at least, we assume the plasma ions to consist only of protons. Good agreement requires not only that the data points fall on or near a straight regression line through the origin but also that the slope of that line be unity. Slopes greater than unity should not occur since they would imply a particle mass less than the proton mass in the reference interval. Slopes that are moderately less than unity can perhaps be explained by assuming the presence of acceptable amounts of alpha particles or other heavier ions in the magnetosheath reference interval.

It is noted that, in contrast to the version of the Walén test employed in paper 1, the present test is independent of the plasma velocity in the reference interval. Since that velocity often fluctuates a great deal, the new version of the Walén test is far less sensitive to the choice of reference interval.

As a third step, one performs variance analysis on the convection electric field $\mathbf{E}_c' = -(\mathbf{v} - u_n\mathbf{n}) \times \mathbf{B}$ where u_n is an assumed velocity of the magnetopause normal to itself. The velocity $\mathbf{v}' \equiv (\mathbf{v} - u_n\mathbf{n})$ represents the plasma flow in a frame of reference moving with the magnetopause. The normal vector, $\mathbf{n}$, is identified with the maximum variance eigenvector, $\mathbf{i}_c$, for the field $\mathbf{E}_c'$ and must therefore be obtained by iteration of the variance analysis in which the

initial guess for $\mathbf{n}$ is usually taken to be the maximum variance eigenvector obtained for $u_n = 0$. It is our experience that the normal vector obtained in this manner is usually a far better estimate of the true normal direction than that provided by the magnetic-field minimum-variance direction (for a discussion of the minimum-variance method, see *Sonnerup and Cahill* [1967]). However, the normal vector thus obtained does depend somewhat on the choice of magnetopause velocity, u_n. A diagram of important quantities such as the average normal magnetic field, $\bar{\mathbf{B}} \cdot \mathbf{n}$, and flow component, $\bar{\mathbf{v}}' \cdot \mathbf{n}$, as well as the average tangential electric field component, $\bar{\mathbf{E}}'_c \times \mathbf{n}$, versus u_n can now be prepared and usually shows linear behavior of all these quantities. We therefore refer to such a plot as a linear diagram. As discussed in paper 2, an allowable range, but not a unique value for the magnetopause velocity, u_n, can be inferred from such a diagram.

Finally, the third step can be repeated by use of $\mathbf{E}'_{HT} = -(\mathbf{v}_{HT} - u_n\mathbf{n}) \times \mathbf{B}$ in place of $\mathbf{E}'_c$ and a second linear diagram can be prepared. Close agreement between the linear diagrams obtained from $\mathbf{E}'_c$ and from $\mathbf{E}'_{HT}$ indicates that no need exists to proceed to the next level of analysis, to be described below. Hodogram plots of $\mathbf{E}'_c$ and $\mathbf{E}'_{HT}$ can also be generated and compared to provide a visual three-dimensional picture of the agreement between these two vectors.

We have already mentioned that the maximum variance eigenvectors $\mathbf{i}_c$ or $\mathbf{i}_{HT}$, evaluated at one's best estimate of the magnetopause normal speed, u_n, may serve as predictors of the true magnetopause normal, $\mathbf{n}$. However, in many cases where a good HT frame exists, the minimum variance directions, $\mathbf{k}_c$ and $\mathbf{k}_{HT}$, for the convection and HT electric fields, $\mathbf{E}'_c$ and $\mathbf{E}'_{HT}$, respectively, are far more accurately determined than $\mathbf{i}_c$ and $\mathbf{i}_{HT}$. Where that is the case, these $\mathbf{k}$ vectors are usually also nearly aligned and, at the correct u_n, should be good tangent vectors to the magnetopause. If the maximum-variance eigenvector, $\mathbf{i}_B$, of the magnetic field is also well determined, in the sense that the eigenvalue ratio $\lambda_{B_i}/\lambda_{B_j} \gg 1$, then $\mathbf{i}_B$ is also a good tangent vector. Therefore, if $\mathbf{i}_B$ forms a substantial angle with $\mathbf{k}_c$ and $\mathbf{k}_{HT}$, a preferred predictor of the magnetopause normal is the vector $\tilde{\mathbf{i}}$ in the orthonormal triad given by

$$\tilde{\mathbf{k}} = (\mathbf{k}_c + \mathbf{k}_{HT})/|\mathbf{k}_c + \mathbf{k}_{HT}|$$
$$\tilde{\mathbf{i}} = (\mathbf{i}_B \times \tilde{\mathbf{k}})/|\mathbf{i}_B \times \tilde{\mathbf{k}}| \qquad (5)$$
$$\tilde{\mathbf{j}} = \tilde{\mathbf{k}} \times \tilde{\mathbf{i}}$$

(If the vector $\mathbf{i}_B$ is not accurately determined, or if it forms only a small angle with $\tilde{\mathbf{k}}$, or if $\mathbf{k}_c$ and $\mathbf{k}_{HT}$ are widely different, it may be preferable to use $\bar{\mathbf{i}}$, the re-normalized average of $\mathbf{i}_c$ and $\mathbf{i}_{HT}$, as the predicted normal vector. In that case, an orthogonal triad, $\tilde{\mathbf{i}}$, $\tilde{\mathbf{j}}$, $\tilde{\mathbf{k}}$, is formed by putting $\tilde{\mathbf{j}}$ equal to the renormalized version of the vector $(\mathbf{k}_c + \mathbf{k}_{HT}) \times \bar{\mathbf{i}}$ and $\tilde{\mathbf{k}} = \tilde{\mathbf{i}} \times \tilde{\mathbf{j}}$.)

2.2. *Level B*

If the agreement between the linear diagrams based on $\mathbf{E}'_c$ and $\mathbf{E}'_{HT}$ needs to be improved, one may attempt to include a constant acceleration of the HT frame by writing

$$\mathbf{v}_{HT} = \mathbf{v}_{HTo} + \mathbf{a}_{HT}t \qquad (6)$$

where $t = 0$ corresponds to the first data point in the interval at which time $\mathbf{v}_{HT} = \mathbf{v}_{HTo}$. The expression (6) for $\mathbf{v}_{HT}$ can now be substituted into (4) and a new minimization can be performed to obtain $\mathbf{v}_{HTo}$ as well as $\mathbf{a}_{HT}$. The remainder of the steps performed at level A may then be repeated with the proviso that u_n is replaced by u_{no}, the normal magnetopause speed at $t = 0$. If the two linear diagrams now show satisfactory agreement, the data analysis can be stopped and interpretation of the results can be undertaken. Included in the latter process is a check to see whether the normal component of $\mathbf{a}_{HT}$ has an acceptable magnitude. In particular, it is noted that u_{no} should be chosen so that $u_n \equiv u_{no} + \mathbf{a}_{HT} \cdot \mathbf{n}t$ does not reverse its sign during the crossing. Also, one can check whether an improvement in the agreement with the Walén relation has been obtained by inclusion of $\mathbf{a}_{HT}$. An improvement, relative to level A, in the agreement between the convection electric field, $\mathbf{E}_c$, and the *HT* electric field, $\mathbf{E}_{HT}$, must occur, since this is the basis for the determination of $\mathbf{a}_{HT}$. This improvement can be seen in a scatter plot of the components of the two fields

$$\mathbf{E}''_c = -(\mathbf{v} - \mathbf{a}_{HT}t - u_{no}\mathbf{n}) \times \mathbf{B}$$
$$\mathbf{E}''_{HT} = -(\mathbf{v}_{HTo} - u_{no}\mathbf{n}) \times \mathbf{B} \qquad (7)$$

which are fields referred to a frame of reference moving with the magnetopause at speed $(u_{no} + \mathbf{a}_{HT} \cdot \mathbf{n}t)$, directed along $\mathbf{n}$, and at the same time moving along the magnetopause with velocity $t\mathbf{n} \times (\mathbf{a}_{HT} \times \mathbf{n})$. In preparing such a scatter plot, the vector $\mathbf{n}$ is replaced by $\tilde{\mathbf{i}}$. The component along $\mathbf{n}$ of the plasma velocity, $\mathbf{v}'' \equiv (\mathbf{v} - \mathbf{a}_{HT}t - u_{no}\mathbf{n})$, in this *moving frame of reference*, now represents the actual flow of plasma across the magnetopause so that, in the usual model of magnetopause reconnection, one expects $\bar{\mathbf{v}}'' \cdot \mathbf{n} \leq 0$.

2.3. *Level C*

If the coincidence between the two linear diagrams obtained at level B is still judged unsatisfactory, it is desirable to attempt one further step in the analysis procedure, by use of what is referred to as the Final Method in paper 2. This method is described in detail in section 3 of that paper. We do not repeat those rather complicated details here but simply note that in some cases the procedure fails to converge which means that the analysis cannot be carried beyond level B. In other cases the Final Method fails to yield an overall improvement in the linear diagrams or it leads to unreasonable values of the acceleration and an associated substantial deterioration in the agreement between the electric fields $\mathbf{E}''_c$ and $\mathbf{E}''_{HT}$, defined by (7). However, there are also instances (see, e.g., paper 2) where it leads to acceptable accelerations and little change in the agreement between $\mathbf{E}''_c$ and $\mathbf{E}''_{HT}$. We also note that the analysis at level C is such that $\mathbf{k}_c \equiv \mathbf{k}_{HT}$ at a chosen reference value of the initial normal magnetopause speed, u_{no}.

3. Analysis of Events

3.1. *September 4, 1984: First Crossing*

This inbound magnetopause crossing, the first of three on the September 4 inbound pass of the satellite, occurred on the afternoon side (1530 LT) of the magnetosphere at substantial southern latitude (−25° GSM). The second crossing on this pass was discussed in paper 2, the third crossing is

treated in the next subsection. Three flux-transfer events in the magnetosheath, preceding the three crossings were discussed in paper 3. The first crossing has a rather long duration (1441:32–1444:08) and exhibits an extremely complicated magnetic structure. This structure is shown in Figure 1 in the usual hodogram form. Since the ratio of intermediate to minimum variance of the **B** field is not large ($\lambda_{Bj}/\lambda_{Bk} = 1.7$), the minimum variance eigenvector $\mathbf{k}_B$ is not a useful predictor of the magnetopause normal vector, **n**. In fact $\mathbf{k}_B$ forms an angle of 120° with our best normal vector prediction (given in Table 1) for this case. On the other hand, the maximum to intermediate eigenvalue ratio, $\lambda_{Bi}/\lambda_{Bj} = 7$, is fairly large, indicating that the maximum variance eigenvector $\mathbf{i}_B$ should be approximately tangential to the magnetopause (see paper 2).

The measured plasma velocity vectors during this crossing are also highly variable and the convection electric field $\mathbf{E}_c = -\mathbf{v} \times \mathbf{B}$ displays a complicated structure as well. Nevertheless, the minimum variance direction, $\mathbf{k}_c$, for the $\mathbf{E}_c$ data is extremely well defined, the ratio of intermediate to minimum eigenvalue being about 27, and furthermore the average value of $\mathbf{E}_c''$ along $\mathbf{k}_c$ is nearly zero, as shown in Figure 2*b*. As discussed in paper 2, these properties of $\mathbf{E}_c$ are a strong indication that a good deHoffmann-Teller frame may exist. Therefore, in spite of the complicated structure of the magnetopause, this event lends itself to the analysis developed in paper 2; in fact the calculation can be carried through level C, although, as will be seen below, the results at level B are of higher quality than those at level C. Pertinent results of the analysis at all three levels are given in Table 1. First, it is seen that even when the acceleration,

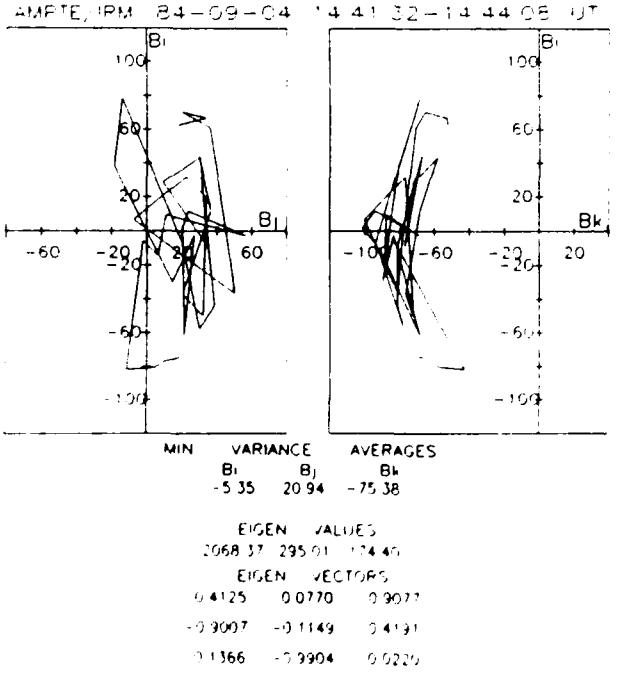

Fig. 1. Magnetic structure during magnetopause crossing on September 4, 1984, 1441:32–1444:08 UT, shown in hodogram form. The quantities B_i, B_j, and B_k are the field components along the maximum, intermediate, and minimum variance eigenvectors i, j, and k, respectively. Also given are the average values (nT) and the variances (= the eigenvalues λ_i, λ_j, λ_k (nT)^2) of those components, and the GSE (*XYZ*) components of i, j, and k.

TABLE 1. Derived Magnetopause Parameters on September 4, 1984, 1441:32–1444:08 UT

Parameter[a]	Level A	Level B	Level C
		deHoffmann – Teller Frame	
$\mathbf{v}_{HTo}$, km/s	-189,298,-65	-151,268,-80	-130,217,-84
$\mathbf{a}_{HT}$, km/s^2	0	-0.51,0.50,0.32	-0.57,0.76,0.38
D/D_o	0.044	0.030	0.040
		Magnetopause Motion	
u_{no}^b, km/s	20	40	40
$\mathbf{a}_{HT} \cdot \mathbf{i}$, km/s^2	0	-0.28	-0.21
		Magnetopause Normals (x10^4)	
$\mathbf{i}_c^c$	7714,5082,-3829	7908,5184,-3253	7841,5312,-3209
$\mathbf{i}_{HT}^c$	7897,4865,-3737	7916,4839,-3730	7780,5110,-3656
$\mathbf{i}$	7765,4912,-3946	7824,4804,-3963	7731,4974,-3935
$\mathbf{n}_{mod}^d$		(8360,5480,-170)	
		Electric Field Correlation[e]	
Slope	1.022 ± 0.022	1.017 ± 0.021	1.130 ± 0.026
Correlation coefficient	0.978	0.981	0.977
		Walén Correlation[e,f]	
Slope	-0.756 ± 0.040	-0.782 ± 0.030	-0.660 ± 0.033
Correlation coefficient	-0.899	-0.937	-0.907

[a] Vectors are given in terms of (*X*, *Y*, *Z*) components in GSE.
[b] Magnetopause reference speed used for normal vector calculations, electric field correlations, and for calculation at level C.
[c] Maximum variance direction of $\mathbf{E}_c''$ or $\mathbf{E}_{HT}''$.
[d] From *Fairfield* [1971].
[e] Regression line constrained to pass through the origin.
[f] Magnetosheath reference interval (1438:45–1441:30 UT) has $n_1 = 63$ cm^{-3}; $\alpha_1 = -0.08$; effective mass $m^*(1 - \alpha^*)/(1 - \alpha_1) = 1.50$.

$\mathbf{a}_{HT}$, is zero (level A) a good correlation exists between $\mathbf{E}_c'$ and $\mathbf{E}_{HT}'$. It improves slightly when $\mathbf{a}_{HT} \neq 0$ at level B but a substantial decrease in the relative residual, D/D_o, does occur. At level C, the correlation coefficient and D/D_o are about the same as at level A. The correlation at level B is shown as a scatter plot in Figure 2*a* for $u_{no} = 40$ km/s (a choice to be discussed further below), and as a superposition of $\mathbf{E}_c''$ and $\mathbf{E}_{HT}''$ hodograms (in the coordinate system $\mathbf{i}, \mathbf{j}, \mathbf{k}$ defined by (5)) in Figure 2*b*. The vectors $\mathbf{i}$ at the different levels of analysis are given in Table 1 along with the vectors $\mathbf{i}_c$ and $\mathbf{i}_{HT}$ which may serve as alternate predictors of **n**. Comparison of these vectors provides insight into the level of uncertainty in the normal vector prediction.

The Walén correlation at level B, where the correlation coefficient is significantly larger than at levels A and C (see Table 1), is shown in Figure 3. It is seen that the slope of the regression line is negative, as expected from the standard reconnection model for a crossing at substantial southern latitudes. The magnitude of the slope, 0.78 ± 0.03, indicates that, assuming all particles in the magnetosheath reference interval to be protons, the field-aligned flow speeds in the deHoffmann-Teller frame were on average only 78% of the local Alfvén speeds. This discrepancy could perhaps be explained by assuming that in addition to the expected presence of some 5% alpha particles, heavier ions, e.g., 3%

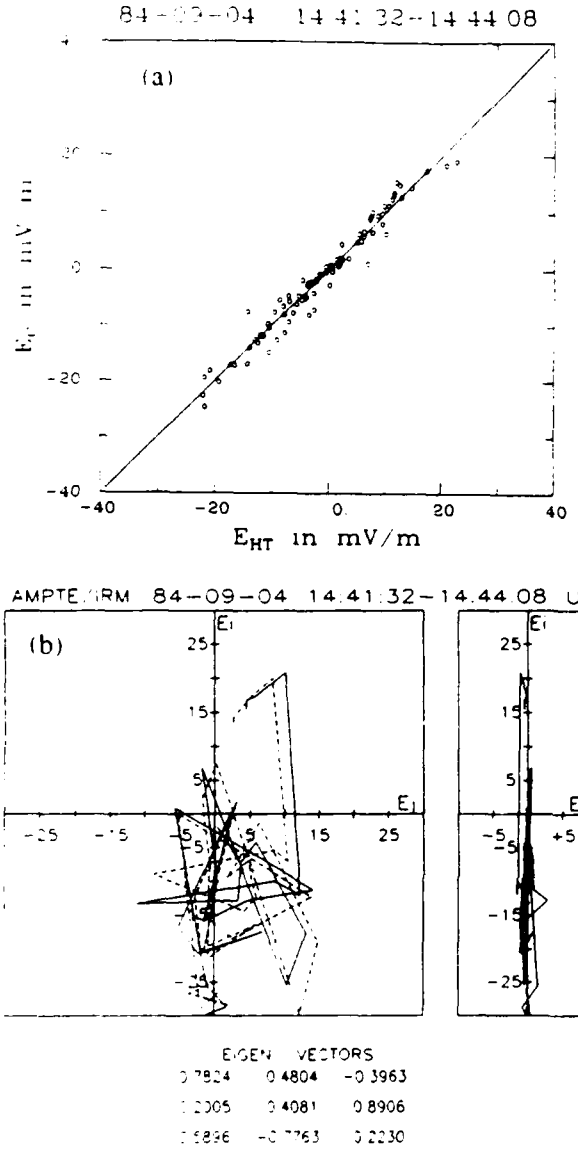

Fig. 2. Electric structure during magnetopause crossing on September 4, 1984, 1441:32–1444:08 UT. Relationship between the two electric fields $\mathbf{E}_c''$ and $\mathbf{E}_{HT}''$, defined by equations (7) with u_{no} and a_{HT} from level B of the analysis, is shown (*a*) as a scatter plot and (*b*) as a superposition of hodograms for $\mathbf{E}_c''$ (solid line) and $\mathbf{E}_{HT}''$ (dashed line), using components along the unit vectors $\hat{\mathbf{i}}$, $\hat{\mathbf{j}}$, $\hat{\mathbf{k}}$ defined by equations (5). Parameters are provided in Table 1.

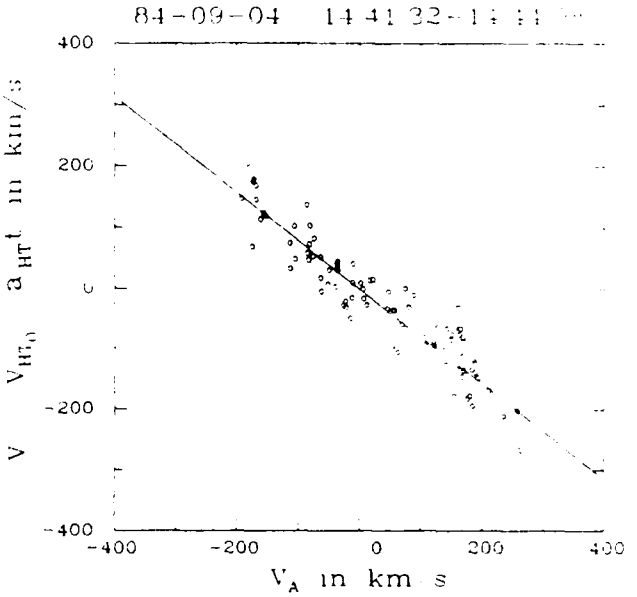

Fig. 3. Walén correlation for magnetopause crossing on September 4, 1984, 1441:32–1444:08 UT, with v_{HT_0} and a_{HT} from level B of the analysis. Parameters are provided in Table 1.

O^+ by number) were present in the magnetosheath reference interval. It is further noted that, for this crossing, the ratio of effective ion mass in the magnetopause to that in the reference interval, calculated from equation (2) as described in paper 1, was 1.50, suggesting that the population of heavy ions in the magnetopause itself may have been even larger (e.g., 8.7% O^+ by number). If such was indeed the case, it would be unreasonable to assume that none of these heavy ions would migrate into the adjacent magnetosheath during a reconnection event. In this context it is noted that the boundary layer region inside the magnetopause has been observed occasionally to have O^+ number densities as high as 50% [*Fuselier et al.*, 1989], although only for northward interplanetary magnetic field. On the other hand, we have not discovered any indications in the measured particle distributions that a separate species with different flow behavior was present. In our view, it is therefore entirely possible that, because of the complicated three-dimensional and presumably time-dependent magnetopause structure in this event, the actual average flow speed in the HT frame was in fact some 20% less than the Alfvén speed and that equation (2) was not applicable between the magnetosheath reference interval and the magnetopause. However, it should be pointed out that equation (2) does appear to be relevant within the magnetopause itself: its use there to cast the Alfvén velocity into the form $\mathbf{B}^m(1-\alpha^m)/\sqrt{\mu_o\rho_1(1-\alpha_1)}$ leads to an improvement of the Walén correlation coefficient by about 5% relative to the value obtained by use of $v_A = \mathbf{B}^m\sqrt{(1-\alpha^m)/\mu_o\rho^m}$. (As before, the superscript m denotes individual measurements in the data set obtained during a magnetopause crossing.)

We turn finally to a discussion of the acceleration and of the linear diagram for this event. The latter is shown in Figure 4 at analysis level B. The calculated acceleration is rather small and it does not change a great deal from level B to level C. Furthermore, the normal component, $\mathbf{a}_{HT}\cdot\hat{\mathbf{i}} = -0.28$ km/s^2, is small, as might be expected for a crossing of long duration. It is also negative, indicating that the magnetopause was slowing down in its outward motion, as one would expect if that motion were initiated in an impulsive manner prior to the encounter of the spacecraft with the magnetopause. The time plot for this pass, provided in paper 1, suggests that the magnetopause ultimately came to a near halt when its inner edge reached the spacecraft because the latter then remained immersed in the magnetopause/boundary layer region for about 15 min before the motion was reversed to produce the second magnetopause encounter (analyzed in paper 2). It is for the above reason we believe that the initial normal velocity u_n of the mag-

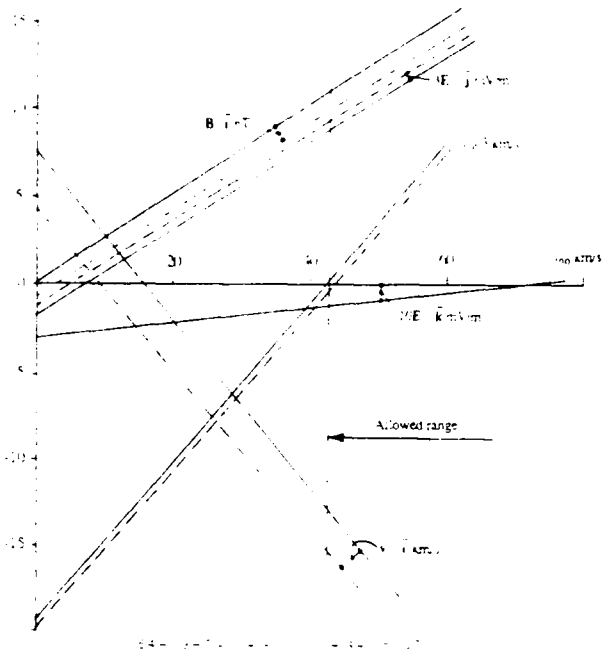

Fig. 4. Linear diagram, at analysis level B, for magnetopause crossing on September 4, 1984, 1441:32–1444:08 UT. Solid lines correspond to the vector system ($\mathbf{i}_c$, $\mathbf{j}_c$, $\mathbf{k}_c$) and the electric field $\tilde{\mathbf{E}}_c''$ from equations (7); dashed lines correspond to the vector system ($\mathbf{i}_{HT}$, $\mathbf{j}_{HT}$, $\mathbf{k}_{HT}$) and the electric field $\tilde{\mathbf{E}}_{HT}''$. Note that $\tilde{\mathbf{E}}_{HT}'' \cdot \mathbf{k}_{HT} \equiv 0$. Allowed range for u_{no} is such that $u_{ne} \geq 0$. Parameters are provided in Table 1.

netopause was in the vicinity of 40 km/s. This is the value used in Table 1 and in Figure 2. It is seen from the linear diagram in Figure 4 that for $u_{no} \simeq 43$ km/s the velocity of the magnetopause at the end of the data interval, u_{ne}, has been reduced to zero. Thus, strictly speaking, only values of u_{no} greater than 43 km/s are allowed. This corresponds to a magnetopause thickness of not less than $d = 3350$ km. It is also seen from the figure that the average normal magnetic field component was positive, as expected for a southern hemisphere crossing, and that its magnitude was at least 10 nT. Similarly, the average normal flow speed was negative, as expected, and had magnitude of at least 13 km/s. The tangential (reconnection) electric field $\mathbf{E}'' \cdot \mathbf{j}$ was at least 2.8 mV/m while the component of $\mathbf{E}''$ along $\mathbf{k}$ was very small. It is also seen in the linear diagram that, at level B, the solid lines, derived from $\mathbf{E}_c''$, and the corresponding dashed lines, derived from $\mathbf{E}_{HT}''$, are parallel but do not coincide exactly. At level C, they are forced to intersect at the reference velocity $u_{no} = 40$ km/s, but are then no longer parallel but form angles of up to 5°. We take this latter feature of the linear diagram as a further indication that the analysis at level C yields results that are less believable than those at level B. The behavior described here should be compared to the case reported in paper 2 where analysis at level C brought about a nearly exact coincidence of solid and dashed lines.

Finally, it is seen in Table 1 that considerable scatter exists in the various normal vector predictions at levels A, B, and C. For this reason, we do not believe that the normal vector determination in this event has the same high quality as for the second magnetopause crossing on September 4 analyzed in paper 2. We note, for example, that the $\mathbf{i}$ vector (at level B) in the present crossing forms an angle of 11.6° with the normal vector predicted in paper 2. Nevertheless, it is remarkable that the normal vector we have obtained is such that the average normal magnetic field, $\bar{\mathbf{B}} \cdot \mathbf{i}$, and the normal flow, $\bar{\mathbf{v}}'' \cdot \mathbf{i}$, both have their expected sign and reasonable magnitudes.

3.2. *September 4, 1984: Third Crossing*

This final inbound crossing of the magnetopause was relatively rapid (1504:19–1505:24 UT) and was the result of an outward magnetopause motion that probably started impulsively shortly before the encounter. The results from this encounter are presented in the same format as in section 3.1, the only difference being that the results for level C are not given. The reason for omitting the level C results is that, relative to level B, a large change in acceleration and an attendant substantial increase in D/D_o as well as a decrease in electric-field and Walén correlation coefficients occurred. Use of the results from level B rather than those from level A is justified on the basis of a substantial improvement in the linear diagram.

The following comments should be made on this case. First, as can be seen in Figure 5, the magnetic structure of this magnetopause crossing was relatively simple, the $B_i B_j$ hodogram showing a tangential field rotation of the type expected for a classical rotational discontinuity. The B_k component is positive, suggesting a positive value of the normal magnetic field, but has a large variance ($\lambda_{Bj}/\lambda_{Bk} = 1.7$). Therefore the vector $\mathbf{k}_B$ does not provide a reliable normal vector prediction. On the other hand, $\lambda_{Bi}/\lambda_{Bj} = 16.9$ so that $\mathbf{i}_B$ should be a good tangent vector.

The correlation between $\mathbf{E}_c''$ and $\mathbf{E}_{HT}''$ (at level B) is excellent as shown in Figure 6 and in Table 2. The Walén correlation diagram, Figure 7, also shows much less scatter than for the first crossing on September 4. The slope of

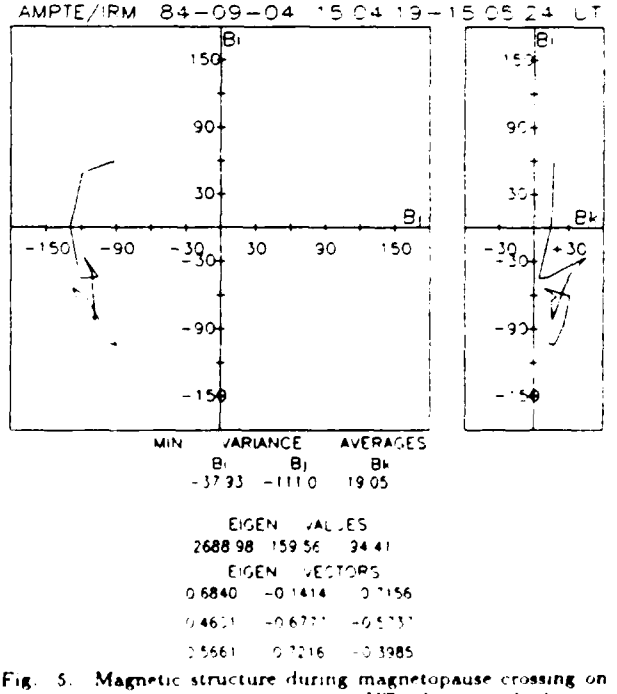

Fig. 5. Magnetic structure during magnetopause crossing on September 4, 1984, 1504:19–1505:24 UT, shown in hodogram form. For explanation of symbols, see Figure 1.

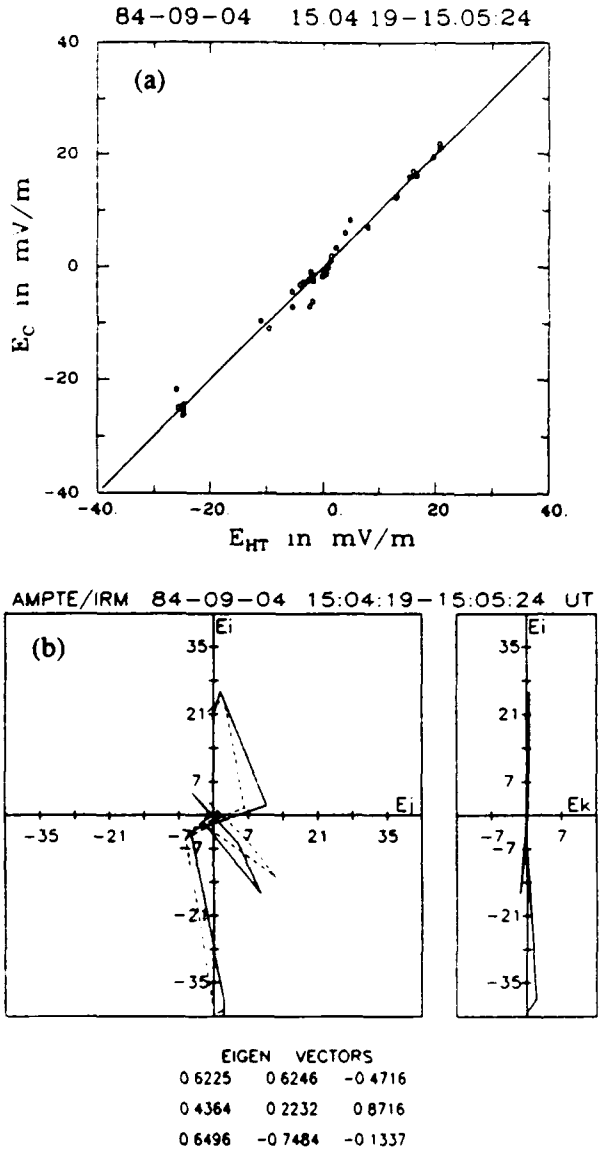

Fig. 6. Electric structure during magnetopause crossing on September 4, 1984, 1504:19–1505:24 UT, with u_{no} and a_{HT} from level B of the analysis, shown (*a*) as a scatter plot and (*b*) as a superposition of hodograms, as explained in Figure 2. Parameters are provided in Table 2.

TABLE 2. Derived Magnetopause Parameters on September 4, 1984, 1504:19–1505:24 UT

Parameter[a]	Level A	Level B	Level C
	deHoffman – Teller Frame		
v_{HTo}, km/s	-315,360,16	-256,348,53	
a_{HT}, km/s^2	0	-0.92,-1.42,-2.08	
D/D_o	0.032	0.011	
	Magnetopause Motion		
u_{no}^b, km/s	15	30	
$a_{HT} \cdot \bar{i}$, km/s^2	0	-0.48	
	Magnetopause Normals ($\times 10^4$)		
i_c^c	5875,6107,-5309	5997,6186,-5076	
i_{HT}^c	6207,6069,-4964	6172,6150,-4908	
$\bar{i}$	6209,6279,-4694	6225,6246,-4716	
n_{mod}^d		(8440,5350,-190)	
	Electric Field Correlation[e]		
Slope	1.017 ± 0.030	1.008 ± 0.021	
Correlation coefficient	0.983	0.992	
	Walén Correlation[e,f]		
Slope	-1.101 ± 0.028	-0.840 ± 0.038	
Correlation coefficient	-0.987	-0.965	

[a–e]For explanation, see Table 1.
[f]Magnetosheath reference interval (1503:30–1504:16 UT) has $n_1 = 92$ cm^{-3}; $\alpha_1 = -0.11$; effective mass $\overline{n^m(1-\alpha^m)}/n_1(1-\alpha_1) = 1.41$.

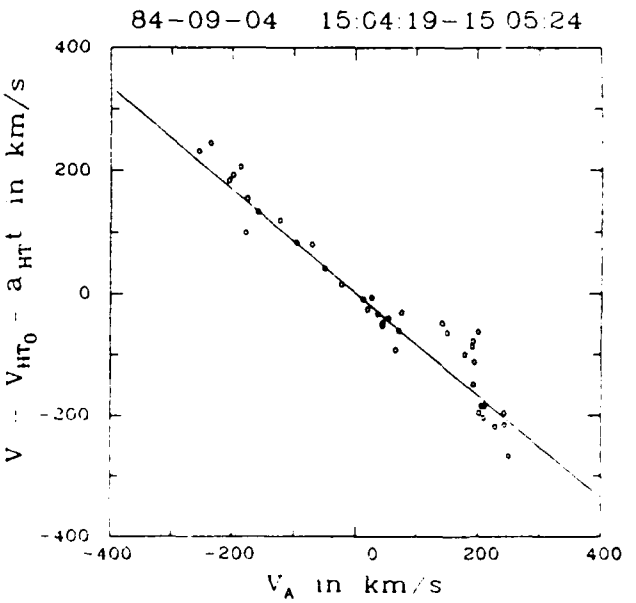

Fig. 7. Walén correlation for magnetopause crossing on September 4, 1984, 1504:19–1505:24 UT, with v_{HTo} and a_{HT} from level B of the analysis. Parameters are provided in Table 2.

the regression line is again negative, as expected south of a reconnection site. The magnitude of the slope, 0.81, could be accounted for by an admixture of 5% alpha particles and 2.6% O^+ in the reference interval (1503:30–1504:16 UT). It is noted that in the adjacent reference interval (1502:00–1502:16 UT) for the second crossing, an admixture of 3.5% alpha particles and no oxygen would account for the slope discrepancy in that crossing (see paper 2). For the present crossing, the effective ion mass in the magnetopause predicted from (2) was 1.42 times the effective ion mass in the reference interval which would be accounted for by a magnetopause ion composition of 5% alpha particles and 7% oxygen.

The linear diagram (at level B) for this crossing is shown in Figure 8. It is first noticed that, as in the previous case, corresponding lines from $\mathbf{E}_c''$ and from $\mathbf{E}_{HT}''$ data are parallel but do not coincide exactly. Second, all of the sets of parallel lines intersect the u_{no} axis in the vicinity of $u_{no} = 20 - 25$ km/s. The magnetopause is again decelerating (see Table 2) and only for $u_{no} > 25$ km/s is u_{no}, the normal velocity of the magnetopause at the end of the crossing, positive.

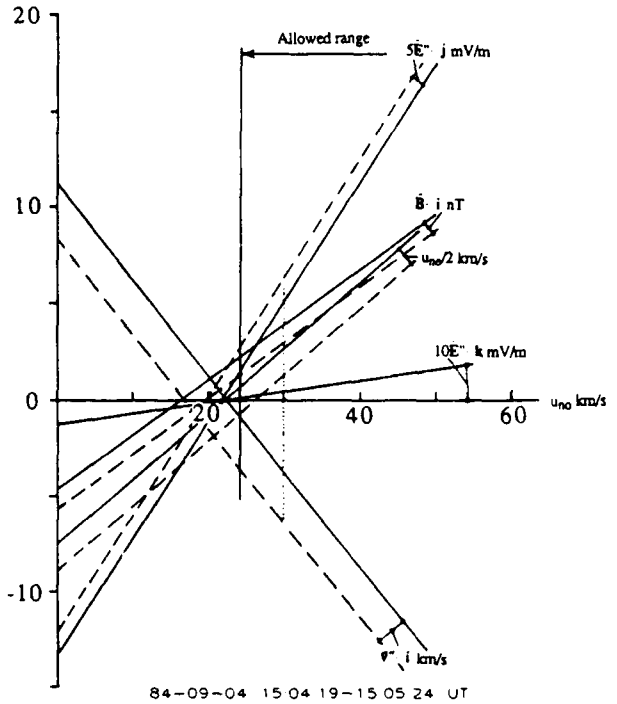

Fig. 8. Linear diagram, at analysis level B, for magnetopause crossing on September 4, 1984, 1504:19–1505:24 UT, in the same format as Figure 4. Parameters are provided in Table 2.

as required to avoid reversal of the motion. In this case, the lower bound on $\bar{B} \cdot \bar{i}$, $\bar{E}'' \cdot \bar{j}$ and $v'' \cdot \bar{i}$ is approximately zero and the lower bound on the magnetopause thickness is 810 km at $u_{no} \simeq 25$ km/s. For larger u_{no} values $\bar{B} \cdot \bar{i}$ and $\bar{E}'' \cdot \bar{j}$ are positive and $v'' \cdot \bar{i}$ is negative, as was the case in the previous two crossings. However, at the end of the third magnetopause crossing, the magnetopause velocity was probably small, because the spacecraft remained in the boundary layer or in the innermost portion of the magnetopause structure for 3–4 min beyond the end of the data analysis interval. For this reason, we have chosen $u_{no} = 30$ km/s for the data presentation in Table 2 and in Figure 6. If this value is approximately correct, then the reconnection rate, measured by the tangential electric field, or the normal magnetic field, was small but nonzero during this crossing.

3.3. *September 8, 1984: First Crossing*

This outbound crossing, the first of a set of three during this outbound pass, occurred near local noon (1140 LT) at slightly northern latitude (7.5° GSM). It was again a relatively rapid crossing (1444:01–1445:02 UT) and was the result of an inward motion of the magnetopause past the spacecraft. The analysis has been carried through level C and, as we shall see, it is an example where the inclusion of a large acceleration, a_{HT}, appears necessary. The linear diagrams from E_c and E_{HT} data which show rather poor agreement at level A are brought into nearly perfect coincidence at level C. Basic results from the three levels of analysis are summarized in Table 3 and (at level C) in Figures 9–12. The following comments should be made.

First, the magnetic field structure of this magnetopause crossing, shown in Figure 9, was relatively simple and not unlike that of an ideal rotational discontinuity with a negative normal magnetic field, B_k. However, the minimum-variance eigenvector, k_B, is at best a fair predictor of the normal direction ($\lambda_{B_j}/\lambda_{B_k} = 5.9$) whereas the maximum-variance eigenvector, l_B, should be an excellent tangent vector ($\lambda_{B_i}/\lambda_{B_j} = 22.5$).

TABLE 3. Derived Magnetopause Parameters on September 8, 1984, 1444:01–1445:02 UT

Parameter[a]	Level A	Level B	Level C
		deHoffmann – Teller Frame	
v_{HTo}, km/s	34,286,74	173,443,-252	210,474,-306
a_{HT}, km/s^2	0	-1.67,0.09,5.79	-2.20,0.33,6.52
D/D_o	0.040	0.022	0.024
		Magnetopause Motion	
u_{no}^b, km/s	-5	0	0
$a_{HT} \cdot \bar{i}$, km/s^2	0	-0.04	-0.32
		Magnetopause Normals (x10^4)	
i_c^c	9643,-2303,2269	9426,-2271,2447	9319,-2353,2762
i_{HT}^c	9491,-1944,2478	9398,-2168,2640	9321,-2371,2736
$\bar{i}$	9420,-2070,2640	9394,-2144,2675	9318,-2344,2770
n_{mod}^d		(9940,-990,520)	
		Electric Field Correlation[e]	
Slope	1.020 ± 0.035	1.015 ± 0.028	0.984 ± 0.027
Correlation coefficient	0.971	0.986	0.987
		Walén Correlation[e,f]	
Slope	0.414 ± 0.024	0.924 ± 0.019	1.038 ± 0.021
Correlation coefficient	0.941	0.993	0.993

[a–e]For explanation, see Table 1.
[f]Magnetosheath reference interval (1444:58–1445:42 UT) has $n_1 = 13$ cm^{-3}; $\alpha_1 = -0.10$; effective mass $n^m(1-\alpha^m)/n_1(1-\alpha_1) = 1.17$.

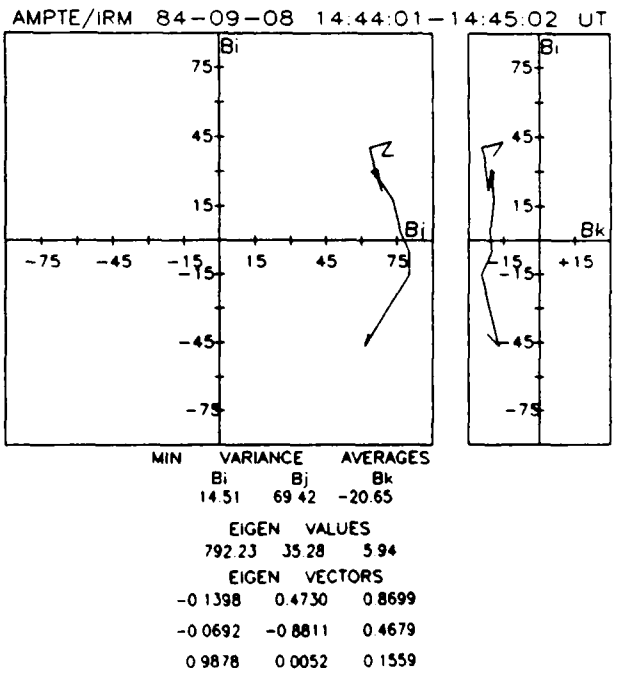

Fig. 9. Magnetic structure during magnetopause crossing on September 8, 1984, 1444:01–1445:02 UT, shown in hodogram form. For explanation of symbols, see Figure 1.

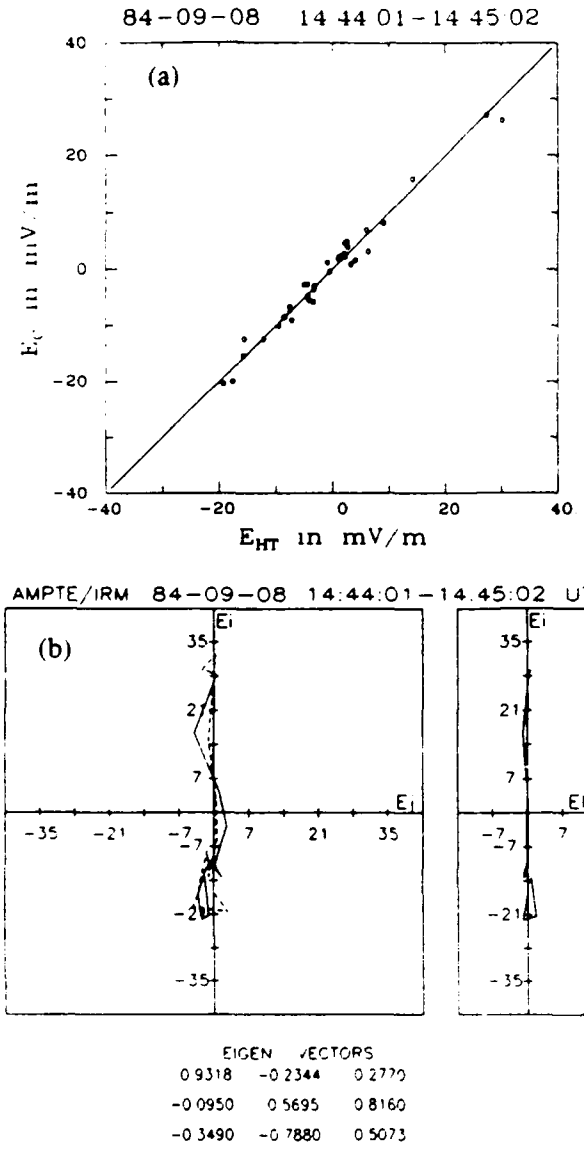

Fig. 10. Electric structure during magnetopause crossing on September 8, 1984, 1444:01–1445:02 UT, with u_{no} and a_{HT} from level C of the analysis, shown (*a*) as a scatter plot and (*b*) as a superposition of hodograms as explained in Figure 2. Parameters are provided in Table 3.

The correlation between E_c'' and E_{HT}'' at level C, shown in Figure 10, is very good, although certain discrepancies are evident in the two hodograms shown in Figure 10*b*. The Walén correlation is shown without acceleration (level A) in Figure 11*a* and with acceleration (level C) in Figure 11*b*. It is seen that in both cases the regression line has a positive slope, as expected for a crossing north of an equatorial reconnection site. However, for $a_{HT} = 0$ the slope of the regression line is only 0.41. To account for such a slope in association with a rotational discontinuity, one would have to assume an admixture of 5% alpha particles, say, plus 31% O^+ in the reference interval and 5% alpha particles plus 38% O^+ in the magnetopause interval. As mentioned earlier, such high concentrations of oxygen cannot be excluded entirely. However, those ions would be of magnetospheric origin and would be expected to have properties of their distribution function that are significantly different from those of the regular magnetosheath plasma. In particular, they would be flowing across the magnetopause in a direction opposite to the magnetosheath protons. With oxygen present in such high concentrations, a noticeable influence on the measured distribution functions should therefore be at hand. We have found no such effects in the data for September 8. Furthermore, the data scatter in Figure 11*b* is considerably less than in Figure 11*a*, indicating that inclusion of the acceleration improves, not only the $E_c'' - E_{HT}''$ correlation (as it must), but also the Walén correlation. For these reasons, we find the results with $a_{HT} \neq 0$ more likely to be correct than those with $a_{HT} = 0$. The Walén regression-line slope in Figure 11*b* is 1.038 ± 0.021. While formally this result

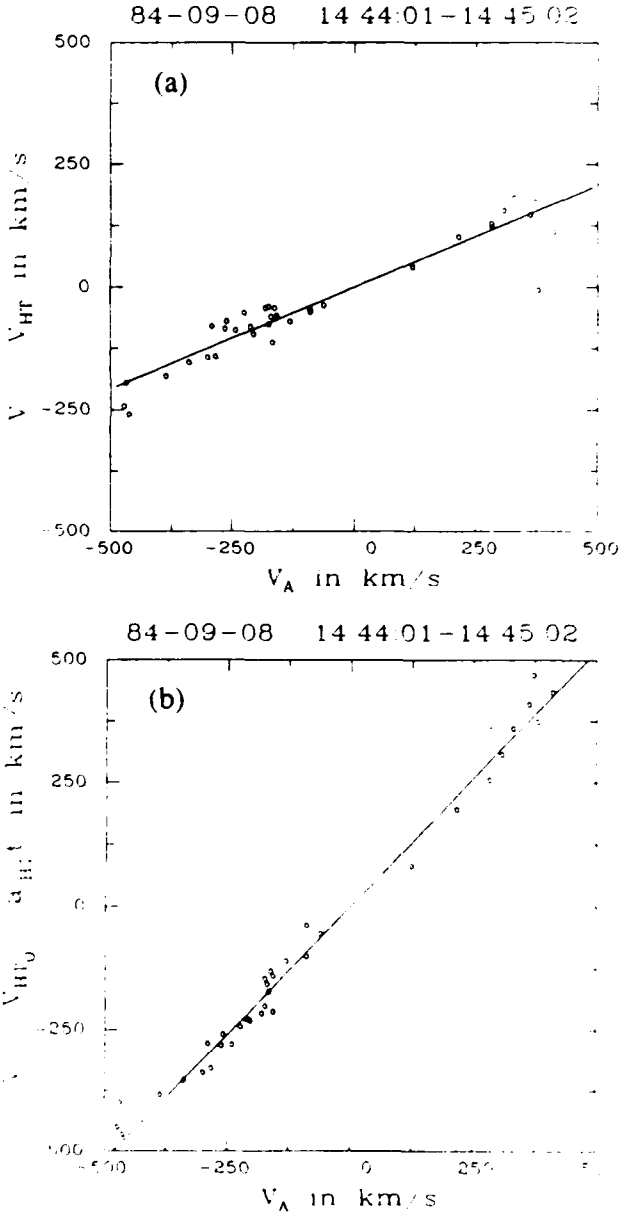

Fig. 11. Walén correlation for magnetopause crossing on September 8, 1984, 1444:01–1445:02 UT: (*a*) with v_{HT} from level A of the analysis and (*b*) with v_{HT_o} and a_{HT} from level C of the analysis. Parameters are provided in Table 3.

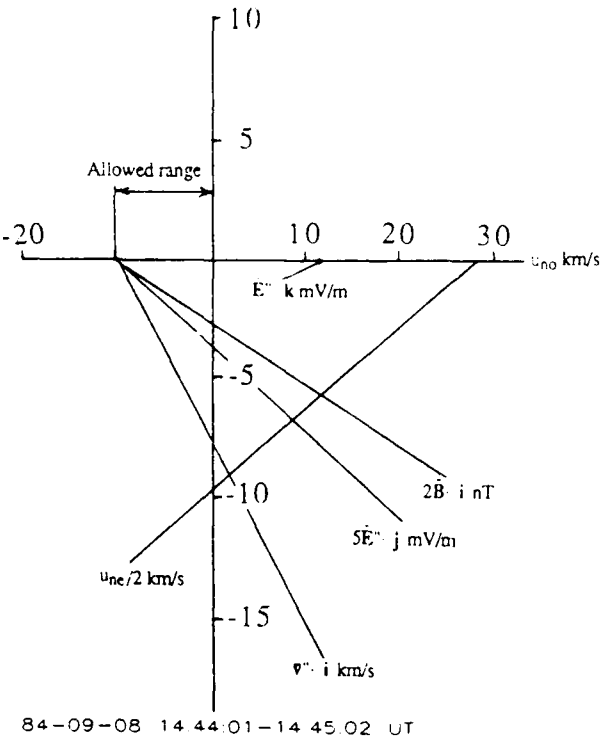

Fig. 12. Linear diagram, at analysis level C, for magnetopause crossing on September 8, 1984, 1444:01-1445:02 UT, in the same format as Figure 4. Solid and dashed lines coincide in this case. The allowed range for u_{no} is determined by the requirements $u_{no} \leq 0$ and $\bar{v}'' \cdot \hat{i} \leq 0$. Parameters are provided in Table 3.

would correspond to an effective ion mass about 2% less than the proton mass, m_p, in the reference interval (and an effective mass of $1.15m_p$ (5% alpha) in the magnetopause interval) we find that such a discrepancy easily falls within the expected uncertainties of this type of analysis. For example, it is seen in Table 3 that at level B of the calculation the Walén regression-line slope is 0.924, i.e., less than unity.

The large change in Walén regression-line slope between level A and level C (or B) of the analysis is caused by a large tangential (northward) component of $\mathbf{a}_{HT}$ which causes mainly a rotation of the $\mathbf{v}_{HT}$ vector from its initial duskward-southward direction to a final duskward-northward direction with an associated decrease in $|\mathbf{v}_{HT}|$ from 600 to 500 km/s. It has been pointed out to us (J. Scudder, private communication, 1986) that the Walén relation should not be expected to hold in an accelerating frame. If it is nevertheless found to be valid, as in the present case, we argue that the effective inertia force present in such a frame must be exactly counterbalanced by a tangential force other than that associated with the Maxwell shear stresses in a one-dimensional current sheet. One possible such force would be a gradient in the total pressure, $P_\perp = p_\perp + B^2/2\mu_o$, in the north-south direction associated with a higher value of $P_\perp$ on the equatorward side of the spacecraft. In the spacecraft frame, this gradient drives a nonsteady, northward-accelerating plasma flow such that $\partial \mathbf{v}/\partial t (= \mathbf{a}_{HT}) = -(1/\rho)\nabla P_\perp$. In this frame, each of the individual velocity vectors, measured as the spacecraft traverses the magnetopause, refers to a different dynamic state of the system. However, when those vectors are used to test the Walén relation in a nonaccelerating frame, the tacit (but incorrect) assumption is made that they refer to one and the same state; it is for this reason that the Walén relation appears poorly satisfied in Figure 11*a*. On the other hand, in the accelerating HT frame, the plasma flow is approximately steady. In this frame, $\mathbf{a}_{HT} = -(1/\rho)\nabla P_\perp$ and, furthermore, the Maxwell shear stresses are balanced by the convective change of tangential momentum as a plasma element crosses the magnetopause, exactly as required by the Walén relation (see Figure 11*b*).

To provide an analytical basis for the above explanation, the steady state nonviscous MHD equations in an accelerating (HT) frame of reference have been written down in the appendix, under the assumption that the flow is field aligned in that frame, as was the case for the September 8 event. If the flow occurs in a narrow current layer having a small but nonvanishing normal magnetic field component and having the property that changes across the layer occur on a length scale that is much less than the characteristic length scale for changes along the layer, then it is shown that (except perhaps in certain exceptional cases) the flow in the HT frame must be Alfvénic and that the gradient in total pressure, $(p_\perp + B^2/2\mu_o)$, must balance the effective inertia term associated with $\mathbf{a}_{HT}$, exactly as described above. Note that Alfvénic field-aligned flow means that the Walén relation is satisfied, as was indeed found to be the case for this event. Thus, the physical explanation of $\mathbf{a}_{HT}$ outlined in the previous paragraph is a reasonable one, at least for the September 8 crossing. However, many different types of temporal and spatial variations in the magnetopause layer may manifest themselves in the data analysis by yielding a nonzero $\mathbf{a}_{HT}$ vector. For this reason, we cannot prove that our explanation is unique. And we do not claim that it is necessarily applicable to other events where $\mathbf{a}_{HT} \neq 0$.

The linear diagram (at level C) for this event is shown in Figure 12. It is seen that the lines derived from $\mathbf{E}_c''$ and $\mathbf{E}_{HT}''$ data have been brought into virtually exact coincidence. It is also seen that u_{no} is restricted to the range $-10 \leq u_{no} \leq 0$ km/s; the corresponding range for the magnetopause thickness is $580 < d < 1100$ km. At $u_{no} = 0$ the normal magnetic field, $\bar{B} \cdot \hat{i}$, the normal flow speed, $\bar{v}'' \cdot \hat{i}$ and the tangential electric field, $\bar{E}'' \cdot \hat{j}$, have their maximal values, -1.2nT, -7.5 km/s, and $+0.7$ mV/m, respectively. Note that both $\bar{B} \cdot \hat{i}$ and $\bar{v}'' \cdot \hat{i}$, although small, have their expected signs. Note also that these two quantities along with $\bar{E}'' \cdot \hat{j}$ all decrease as u_{no} becomes negative and reach zero simultaneously at $u_{no} = -10$ km/s. At that value of u_{no}, the magnetopause should be interpreted as a tangential discontinuity. However, as argued above, we expect a small negative normal magnetic field component to be present so that the observed velocity changes are generated as a combined effect of pressure forces and Maxwell stresses. For this reason, we have selected $u_{no} = 0$ as the reference value of the normal magnetopause speed in Table 3 and in Figure 10.

3.4. *October 19, 1984: Ninth Crossing*

This outbound crossing, the last of a set of nine during this outbound pass, occurred on the prenoon side of the magnetosphere (0930 LT) at substantial northern latitude ($+18.4°$ GSM). It was again a relatively rapid traversal (0518:20-0519:26 UT) and was the result of a final inward motion of

the magnetopause past the spacecraft during this pass. The analysis had to be stopped at level B since no convergence was obtained in the iterative procedure used in level C. Furthermore, only a small decrease in the residual D/D_o and no improvement in the $\mathbf{E}_c - \mathbf{E}_{HT}$ correlation was obtained by allowing for an acceleration $\mathbf{a}_{HT}$ at level B. The linear diagrams at level B were better than those at level A in the sense that corresponding lines from $\mathbf{E}_c''$ and $\mathbf{E}_{HT}''$ were brought closer together. However, one unacceptable feature, not present at level A, appeared: the normal flow was positive in the entire range of allowable u_{no} values. Thus we decided that the optimal results for this event were at level A. These results are summarized in Table 4 and in Figures 13-16.

TABLE 4. Derived Magnetopause Parameters on October 19, 1984, 0518:20–0519:26 UT

Parameter[a]	Level A	Level B	Level C
	deHoffmann – Teller Frame		
$\mathbf{v}_{HTo}$, km/s	-123,-223,75	-102,-204,21	
$\mathbf{a}_{HT}$, km/s^2	0	-0.62,-0.54,0.88	
D/D_o	0.012	0.010	
	Magnetopause Motion		
u_{no}^b, km/s	-5	-5	
$\mathbf{a}_{HT} \cdot \hat{\mathbf{i}}$, km/s^2	0	-0.25	
	Magnetopause Normals (x10^4)		
$\mathbf{i}_c^c$	9015,-4312,370	9012,-4254,822	
$\mathbf{i}_{HT}^c$	8911,-4503,558	9036,-4173,969	
$\hat{\mathbf{i}}$	8989,-4178,1323	9024,-4214,896	
$\hat{\mathbf{i}}$	8963,-4408,466		
$\mathbf{n}_{mod}^d$		(8640,-5020,310)	
	Electric Field Correlation[e]		
Slope	1.007 ± 0.016	1.004 ± 0.016	
Correlation coefficient	0.994	0.994	
	Walén Correlation[e,f]		
Slope	0.054 ± 0.263	0.180 ± 0.04	
Correlation coefficient	0.140	0.640	

[a–e]For explanation, see Table 1.
[f]Magnetosheath reference interval (0519:30–0520:00 UT) has $n_1 = 18$ cm^{-3}; $\alpha_1 = -0.15$; effective mass $\overline{n^m(1-\alpha^m)}/n_1(1-\alpha_1) = 0.60$.

The magnetic structure of the crossing is shown in Figure 13. The structure is not unlike certain magnetopause structures observed by OGO 5 [*Sonnerup and Ledley*, 1979]. The minimum variance analysis of the B field yields extremely well separated eigenvalues indicating that the minimum-variance eigenvector should be a good predictor of the magnetopause normal and that the maximum-variance eigenvector should be a good tangent vector. It also appears that the average normal magnetic field component $\bar{B}_k$ may have been close to zero. We shall return to this point presently.

The correlation between $\mathbf{E}_c'$ and $\mathbf{E}_{HT}'$, at level A, is shown in Figure 14. It is seen to be excellent, with a correlation coefficient of 0.994. On the other hand, the Walén correlation, shown in Figure 15, is very poor, with a correlation coefficient of 0.140 and a slope of 0.054. It is clear that the Walén relation (or anything resembling it) is not satisfied in this case. Since little systematic flow remains in the HT frame, it appears instead that the detailed structures of the magnetopause current sheet were carried past the spacecraft in a frozen manner by the tangential plasma flow. As mentioned in connection with the September 8 case, and as discussed in the appendix, the existence of a good HT frame for a quasi one-dimensional current sheet having a nonvanishing normal magnetic field component implies that the Walén relation should be satisfied in the sheet. We therefore believe that no normal magnetic field component was present, i.e., that the magnetopause was a tangential discontinuity on this occasion. This belief is reinforced by the fact that no relation should be satisfied in the sheet. We therefore believe that no normal magnetic field component was present, i.e., that the magnetopause was a tangential discontinuity on this occasion. This belief is reinforced by the fact that no significant velocity enhancements occurred in this crossing (see paper 1).

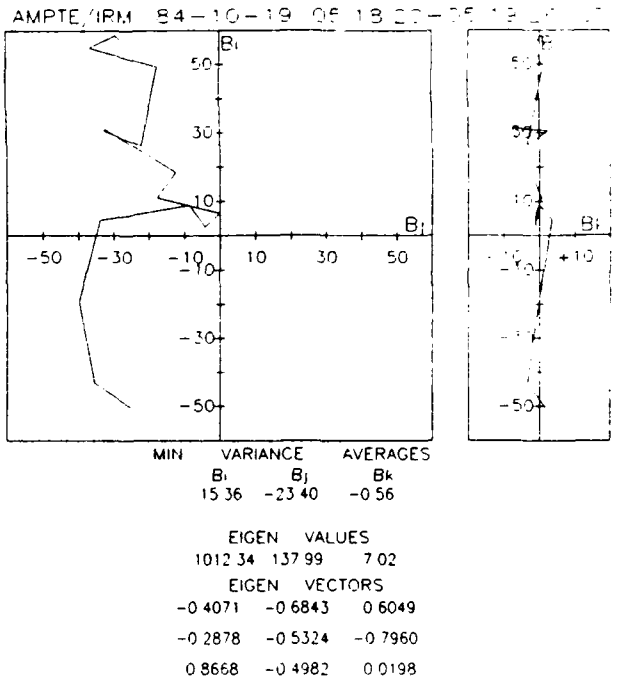

Fig. 13. Magnetic structure during magnetopause crossing on October 19, 1984, 0518:20–0519:26 UT, shown in hodogram form. For explanation of symbols, see Figure 1.

The linear diagram, shown in Figure 16 (at level A), is relatively poor in the sense that corresponding lines, derived from $\mathbf{E}_c'$ and $\mathbf{E}_{HT}'$ data, while parallel, do not coincide. Their slopes are also small, causing a substantial uncertainty in the intercepts with the u_{no} axis. Nevertheless, if the renormalized version, $\hat{\mathbf{i}}$, of the vector $(\mathbf{i}_c + \mathbf{i}_{HT})/2$ is used as a predictor of the magnetopause normal (the $\mathbf{k}_c$ vector is poorly determined for this case so that $\hat{\mathbf{i}}$ rather than $\hat{\mathbf{j}}$ is used as the optimal normal vector), the average intercepts are well defined and are found to be u_{no} =-2 km/s, -4 km/s, and -5 km/s, for the normal magnetic field, the normal flow velocity and (using the average of $\mathbf{E}_c'$ and $\mathbf{E}_{HT}'$), the tangential electric field, respectively. Since we have already concluded that the magnetopause was a tangential

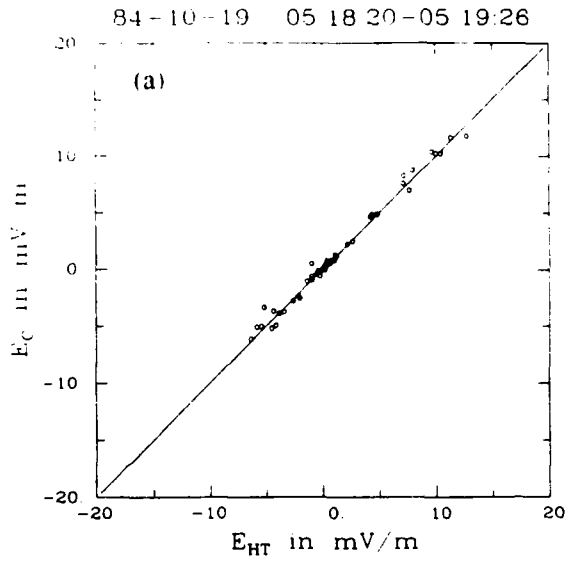

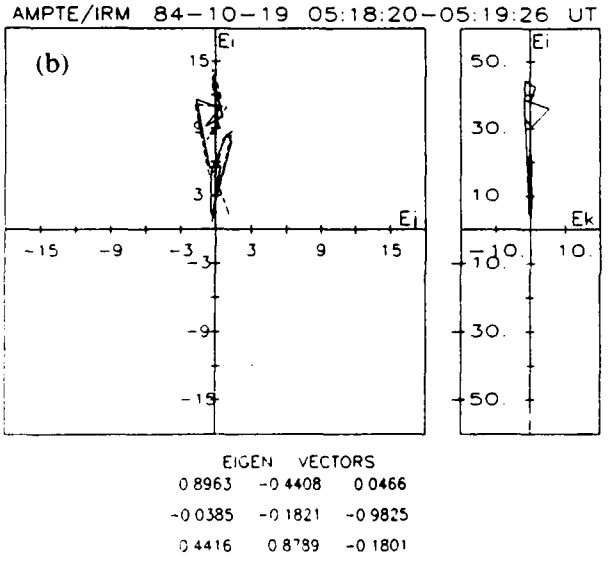

Fig. 14. Electric structure during magnetopause crossing on October 19, 1984, 0518:20–0519:26 UT, with u_{no} and a_{HT} from level A of the analysis, shown (*a*) as a scatter plot and (*b*) as a superposition of hodograms as explained in Figure 2, with the exception that the coordinate axes are $\bar{\mathbf{I}}$, $\bar{\mathbf{J}}$, $\bar{\mathbf{K}}$ rather than $\bar{\mathbf{i}}$, $\bar{\mathbf{j}}$, $\bar{\mathbf{k}}$. Parameters are provided in Table 4.

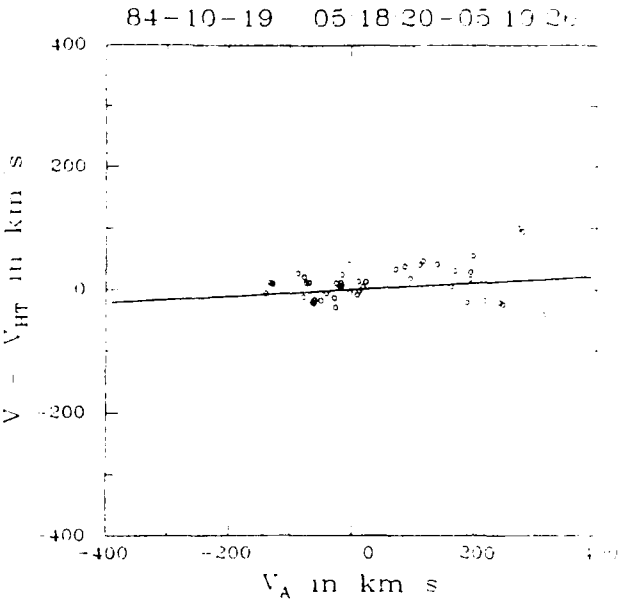

Fig. 15. Walén correlation for magnetopause crossing on October 19, 1984, 0518:20–0519:26 UT, with $\mathbf{v}_{HT}$ from level A of the analysis. Parameters are provided in Table 4.

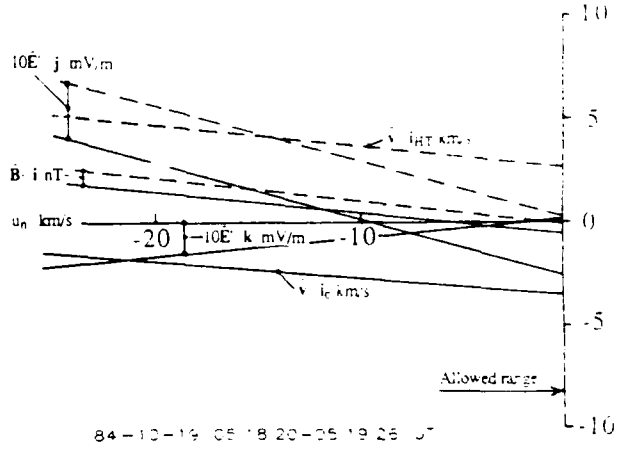

Fig. 16. Linear diagram, at analysis level A, for magnetopause crossing on October 19, 1984, 0518:20–0519:26 UT. As in Figure 4, solid and dashed lines correspond to the vector triads ($\mathbf{i}_c$, $\mathbf{j}_c$, $\mathbf{k}_c$) and ($\mathbf{i}_{HT}$, $\mathbf{j}_{HT}$, $\mathbf{k}_{HT}$), respectively. However, since $\mathbf{a}_{HT} \equiv 0$ at analysis level A, the electric fields are $\mathbf{E}'_c \equiv -(\mathbf{v} - u_n\mathbf{i}_c) \times \mathbf{B}$ and $\mathbf{E}'_{HT} \equiv -(\mathbf{v}_{HT} - u_n\mathbf{i}_{HT}) \times \mathbf{B}$. Allowed u_n range is determined by the condition $u_n \leq 0$. Parameters are provided in Table 4.

discontinuity, these results indicate that the magnetopause was moving inward with a speed of ~ 4 km/s so that the duration of the event, 66 s, can be translated into a magnetopause thickness of 260 km.

It should be noted that the various estimates for the normal vector that could be used in this case all are very close. The vectors $\mathbf{i}_c$ and $\mathbf{i}_{HT}$ (at $u_{no} = -5$ km/s) each deviate from $\bar{\mathbf{I}}$ by less than 0.5°; the angle between $\bar{\mathbf{I}}$ and $\bar{\mathbf{i}}$ is 4.2° and the angle between $\bar{\mathbf{I}}$ and $\mathbf{k}_B$ is 4.0°. The vector $\mathbf{k}_B$ can also be rotated slightly so that the average magnetic field along it is exactly zero; the angle between $\bar{\mathbf{I}}$ and this corrected vector is 3.5°. Further, the angle between $\bar{\mathbf{I}}$ and $\mathbf{i}_B$ is 88°, indicating that $\mathbf{i}_B$ is a rather accurate tangent vector to the magnetopause. However, even small angular discrepancies can produce inconsistent results. For example, the projection of the average velocity vector along $\mathbf{k}_B$, which one might reasonably adopt as the true normal direction, yields a flow component of +8 km/s "normal" to the magnetopause, an unacceptable result since it is known that the magnetopause was moving inward past the spacecraft. Finally, it is noted that the angle between $\bar{\mathbf{I}}$ and the *Fairfield* [1971] normal is only 4.3°.

3.5. *Other Cases*

In addition to the four magnetopause encounters discussed in detail in this paper, we have attempted to reana-

TABLE 5. Summary of Magnetopause Parameters (AMPTE/IRM, 1984)

GSM latitude Local time	September 4 -25.0° 1530			September 8 +7.5° 1140	October 19 +18.4° 0930	August 30 +1.8° 1230		October 9 -10.5° 1305	
Crossing	1	2[a]	3	1	9	2	3	1	4
Direction	SH→SP	SP→SH	SH→SP	SP→SH	SP→SH	SH→SP	SP→ SH	SP→SH	SH→SP
Analysis level	B	C	B	C	A	A	A	B	B
$\mathbf{E}''_c/\mathbf{E}''_{HT}$ Correlation coefficient[b]	0.981	0.994	0.992	0.987	0.994	0.992	0.978	0.977	0.989
D/D_o	0.030	0.011	0.011	0.024	0.012	0.010	0.026	0.045	0.025
Walén Correlation coefficient	-0.937	-0.985	-0.965	0.993	0.140	0.715	.535	-0.627	-0.881
Walén regression Line slope	-0.78	-0.94	-0.84	1.04	0.05	0.20	0.29	-0.38	0.73
u_{no} (km/s) Range	$\geq$43	$\geq$-97 $\leq$-88	$\geq$24	$\geq$-10 $\leq$0	$\leq$0	$\geq$0	$\geq$-15 $\leq$0	$\geq$ -90 $\leq$0	$\geq$11
Reference	40	-90	30	0	-5	0	0	10	20
d (km)	$\geq$3350	$\geq$3040 $\leq$3640	$\geq$780	$\geq$580 $\leq$1100	~260	-	$\leq$390	$\geq$370 $\leq$3520	$\geq$315
B_n (nT)	$\geq$10	$\geq$0 $\leq$2.4	$\geq$1.9	$\geq$-1.3 $\leq$0	~0	$\leq$-1.3	$\geq$-3.1 $\leq$0	$\geq$0 $\leq$3.0	$\geq$8.0
v''_n (km/s)	$\leq$-13	$\geq$-5 $\leq$0	$\leq$-2	$\geq$-8 $\leq$0	~0	$\leq$-3	$\geq$-2 $\leq$0	$\geq$-16 $\leq$0	$\leq$-7
$\lvert\tilde{\mathbf{E}}''_t\rvert$ (mV/m)	$\geq$2.8	$\geq$0 $\leq$1.1	$\geq$0.5	$\geq$0 $\leq$0.8	~0	$\geq$0.2	$\leq$0.8	$\geq$0 $\leq$2.0	$\geq$3.0
$\lvert\mathbf{a}_{HT}\rvert$ (km/s^2)	0.8	1.6	2.7	6.9	-	-	-	3.0	1.0
$\mathbf{a}_{HT}\cdot\mathbf{n}$ (km/s^2)	-0.3	1.3	-0.5	-0.3	-	-	-	-0.6	-0.2
Angle: $(\mathbf{n};\mathbf{n}^c_{mod})$[b]	22.9°	11.9°	29.7°	15.5 °	4.3°	16.3°	4.9°	13.0°	3.1°

[a]From paper 2.
[b]Evaluated at reference value of u_{no}.
[c]Model normal, $\mathbf{n}_{mod}$, from *Fairfield* [1971].

lyze seven more of the crossings dealt with in paper 1, in the same manner. Included were the two remaining crossings on the September 8, 1984, outbound pass: in neither case was it possible to find a good deHoffmann-Teller frame. For the middle crossing (1446:51–1449:23 UT) this is perhaps not surprising since there are indications that the reconnection site may have moved past the spacecraft during the crossing (see paper 1). We have also attempted to analyze the three crossings on August 30, 1984, discussed in paper 1. The first of these crossings did not yield an acceptable HT frame; the second and third crossings were analyzed at levels A and B but did not show convergence at level C. Furthermore, the results at level A, which are summarized in Table 5, were judged more reliable than those at level B. The Walén correlation was poor (correlation coefficients 0.51 and 0.53) and the Walén regression line slopes much too small. From these results, one might be tempted to conclude that these current layers were tangential discontinuities. However, since large velocity enhancements were present in these two crossings we do not believe such a conclusion to be correct. Rather the situation may have been that these events had a too complicated structure (including reflected magnetosheath ions, as discussed in paper 1) to lend themselves to the detailed analysis attempted here. Finally, two crossings on October 9, discussed in paper 1, were studied. The first of these (1419:51–1420:26 UT) was analyzed through level B. A fairly good deHoffmann-Teller frame was found but the Walén correlation was only −0.63. The second crossing (1424:22–1425:19 UT) could be analyzed through level C although the results at level B were judged more acceptable. The results are summarized in Table 5. An excellent HT fit could be made (correlation coefficient = 0.989); the Walén correlation was less good (correlation coefficient = 0.881) with a regression line slope of -0.73. With the simpler analysis method and Walén test employed in paper 1, both of these crossings appeared to be good reconnection cases. However, as discussed in detail in that paper, both had complicated, possibly strongly time-variable structures. This may explain why they give marginal results in the present, more detailed analysis.

4. SUMMARY

In this paper, we have analyzed four magnetopause crossings in detail, and discussed several others briefly, using the methodology developed in paper 2. The principal element of this methodology is the determination of an optimal deHoffmann-Teller (HT) frame in which the convection electric field $\mathbf{E}_c = -\mathbf{v} \times \mathbf{B}$ has been transformed to zero as nearly as the data permit. An initial velocity, $\mathbf{v}_{HTo}$, of this frame as well as its acceleration, $\mathbf{a}_{HT}$, is determined, although in some cases the physical meaning of the latter remains in doubt. A summary of our findings is given in Table 5, which, for completeness, also includes the crossing studied in paper 2.

In general terms, we have found that many, but by no means all magnetopause crossings possess a reasonably good HT frame. The acceleration of the HT frame obtained from the analysis should be taken seriously only if it leads to a substantial decrease in the relative residual, D/D_o, associated with the determination of $\mathbf{v}_{HTo}$ and $\mathbf{a}_{HT}$ and/or an increase in the correlation coefficient between the convection electric field and the HT electric field, $-\mathbf{v}_{HT} \times \mathbf{B}$. This is not always the case but when it is, the component of $\mathbf{a}_{HT}$ along the magnetopause normal is interpreted as the acceleration of that layer in its motion normal to itself. The physical interpretation of the tangential components of $\mathbf{a}_{HT}$ is less clear and can vary from event to event.

The method has yielded magnetopause normal vectors which we believe to be rather accurate in some cases. It has also yielded components of magnetic field and flow normal to the magnetopause, as well as an electric field component, E_t, tangential to the magnetopause, that have the expected signs and reasonable magnitudes. The range of these quantities and of the magnetopause thicknesses (more precisely, the data interval thicknesses), d, are given in Table 5. Note in particular that in one case a lower limit on E_t of 2.8 a value in the range 1.7–2.8 mV/m.

The Walén relation has been tested for all of the crossings in Table 5 and was found to be satisfied in a reasonably accurate way only in the second and third crossing on September 4 and in the September 8 crossing. In the first crossing on September 4, the Walén correlation was convincing but the slope of the regression line was some 20% too small. Except for the extremely complicated two- or three-dimensional magnetic structure of this crossing, we have no simple and convincing explanation for this deviation from the ideal Walén formula. A principal source of uncertainty in the Walén test is the actual plasma composition, which was not measured. On the whole, our study of the three crossings on September 4 nevertheless confirms their interpretation in paper 1 as reconnection events. In the September 8 case, excellent agreement with the Walén relation was achieved, but only after a substantial acceleration of the HT frame tangential to the magnetopause was incorporated in the analysis. In accordance with the theory developed in the appendix, we interpret this acceleration in terms of the presence of a gradient in the total pressure $(p_\perp + B^2/2\mu_o)$ along the magnetopause, this gradient being responsible for a temporal change, $\partial \mathbf{v}/\partial t$, of the plasma velocity in the magnetopause region. This effect would set into northward accelerated motion plasma and magnetic structures located equatorward of the spacecraft, thus causing them to move toward and past the spacecraft (which was located $\sim 1 R_E$ north of the GSM equatorial plane). A similar acceleration may have been responsible for the motion, suggested in paper 1, of the reconnection site itself past the spacecraft during the second magnetopause encounter on September 8, which occurred only 2 min after the crossing analyzed here. Thus our results add strength to the interpretation of the September 8 events in terms of reconnection. The final event in Table 5, the October 19 case, is interpreted as a tangential discontinuity, both here and in paper 1. It provides convincing evidence that the mere existence of a good HT frame does not guarantee that the magnetopause structure was that of a rotational discontinuity.

The analysis of magnetopause data employed here (and in paper 2) is considerably more detailed than that used in paper 1. The advantage gained thereby is that the reconnection hypothesis can be tested in a more quantitative and therefore more objective manner and that precise information about the magnetopause normal vector, as well as approximate information about magnetopause thickness and reconnection electric field can be obtained. Another advantage is that the new version of the Walén test depends on the choice of reference interval only via the square root of the average density and pressure anisotropy in that interval. On the other hand, the older, more primitive analysis in paper 1 also depends linearly on the plasma velocity in the reference interval and therefore is rather sensitive to the choice of that interval. The disadvantage of the new analysis is that only relatively few events have sufficiently simple structure to permit such detailed analysis. The failure of a particular magnetopause crossing, in which substantial velocity enhancements are measured, to lend itself to the more advanced analysis procedure should not be construed to mean that the event could not or should not be interpreted in terms of reconnection. Rather, it may simply mean that the basic assumptions underlying the analysis, namely those of a time-stationary (in the HT frame) quasi-one-dimensional magnetopause structure, were not at hand to a sufficient extent to allow the analysis to proceed.

APPENDIX

We show that for a steady, quasi-one-dimensional MHD current sheet having a nonzero normal magnetic field component, B_z, the existence of an accelerating deHoffmann-Teller (HT) frame, in which the flow is field aligned, implies the validity of the Walén relation in the accelerating frame as well as a balance of the total pressure force and the inertia term, $\rho \mathbf{a}_{HT}$ in the sheet. By steady is meant that the flow and field configuration appears time independent in the accelerating HT frame; by quasi-one-dimensional is meant that derivatives, $\partial/\partial x$, across the layer scale as $1/\delta$ while derivatives, $\partial/\partial y$ and $\partial/\partial z$, along the layer scale as $1/L$ where $\delta \ll L$. Viscous stresses and finite resistivity are both assumed unimportant.

The steady state momentum equation in the HT frame, which is assumed to have acceleration, $\mathbf{a}_{HT}$, can be written as

$$\nabla \cdot [\rho \mathbf{v}\mathbf{v} - (1-\alpha)\mathbf{B}\mathbf{B}/\mu_o] = -\nabla P_\perp - \rho \mathbf{a}_{HT} \qquad \text{(A1)}$$

where the total pressure $P_\perp \equiv (p_\perp + B^2/2\mu_o)$ is the sum of perpendicular plasma pressure and magnetic pressure and $\alpha \equiv (p_\parallel - p_\perp)\mu_o/B^2$ is the pressure anisotropy factor. Since

the flow is assumed to be field-aligned in this frame of reference, we may write

$$\mathbf{v} = (v_x/B_x)\mathbf{B} \tag{A2}$$

so that (A1) can be rearranged to the form

$$\mathbf{B}\cdot\nabla[(A^2-1)(1-\alpha)\mathbf{B}/\mu_o] = -\nabla P_\perp - \rho\mathbf{a}_{HT} \tag{A3}$$

Here $A^2 \equiv \mu_o\rho v_x^2/B_x^2(1-\alpha) = \mu_o\rho v^2/B^2(1-\alpha)$ is the Alfvén number of the flow in the HT frame.

We now examine the x component of (A3) which represents the momentum balance normal to the current sheet. Assuming (A^2-1) to be at most of order unity and ρa_{HTx} to be at most of the same size as $\partial P_\perp/\partial x$, we then find

$$-\partial P_\perp/\partial x - \rho a_{HTx} \simeq O(B_o^2\delta/\mu_o L^2) \tag{A4}$$

where $B_y \sim B_z \sim B_o$ and (from $\nabla\cdot\mathbf{B}=0$) $B_x \sim (B_o\delta/L)$. Neglecting terms of order δ^2/L^2 we may thus replace the x momentum conservation by

$$\partial P_\perp/\partial x = -\rho a_{HTx} \tag{A5}$$

We further assume ρa_{HTx} to be independent of x. Since $\mathbf{a}_{HT}$ is taken to be constant in the data analysis procedure used in the paper, this assumption means that the mass density, ρ, is assumed independent of x. This was approximately the case for the September 8 event but, more generally, in cases where substantial systematic variations of ρ with x are present, we suggest that the acceleration should perhaps be determined by assuming $\rho\mathbf{a}_{HT}$ rather than $\mathbf{a}_{HT}$ to be constant.

Equation (A5) can now be integrated to give

$$P_\perp(x,y,z) = P_{\perp o}(y,z) - \rho a_{HTx}x \tag{A6}$$

and, when this result is substituted into the y and z components, i.e., the tangential components of (A3), there results

$$\begin{aligned}\mathbf{B}\cdot\nabla[(A^2-1)(1-\alpha)B_y/\mu_o] &= \\ -\partial P_{\perp o}/\partial y + x\partial(\rho a_{HTx})/\partial y - \rho a_{HTy} & \\ \mathbf{B}\cdot\nabla[(A^2-1)(1-\alpha)B_z/\mu_o] &= \\ -\partial P_{\perp o}/\partial z + x\partial(\rho a_{HTx})/\partial z - \rho a_{HTz} &\end{aligned} \tag{A7}$$

But the ratio of the second to the third term on the right-hand sides of (A7) is of order $(\delta/L)(a_{HTx}/a_{HTy,z})$ and can be neglected, in particular since the tangential component of $\mathbf{a}_{HT}$ is often considerably larger than the normal component. Thus we obtain

$$\begin{aligned}\mathbf{B}\cdot\nabla[(A^2-1)(1-\alpha)B_y/\mu_o] &= -\partial P_{\perp o}/\partial y - \rho a_{HTy} \\ \mathbf{B}\cdot\nabla[(A^2-1)(-\alpha)B_z/\mu_o] &= -\partial P_{\perp o}/\partial z - \rho a_{HTz}\end{aligned} \tag{A8}$$

An important property of these approximate equations is that their right-hand sides are independent of x, the coordinate across the layer, whereas their left-hand sides contain B_y and B_z, both of which vary rapidly with x. On the other hand, since we have assumed ρ to be independent of x, only small variations of the factor $(A^2-1)(1-\alpha)$ with x should occur. Except perhaps for special cases, the only way the left-hand sides of (A8) can be independent of x is by having $A^2 = 1$, so that they are zero. But $A^2 = 1$ means that the Walén relation is satisfied in the accelerating HT frame, as was indeed the case for the September 8 crossing, and also that

$$\begin{aligned}\partial P_{\perp o}/\partial y &= -\rho a_{HTy} \\ \partial P_{\perp o}/\partial z &= -\rho a_{HTz}\end{aligned} \tag{A9}$$

These equations then show that the components of $\mathbf{a}_{HT}$ tangential to the current sheet are generated by changes in total perpendicular pressure along the sheet.

One should not conclude from the above that satisfaction of the Walén relation is an unavoidable consequence of the existence of a good HT frame. If the current sheet has no normal magnetic field component, or if any of the other assumptions leading to (A9), e.g., those of stationarity or quasi-one-dimensionality, are seriously violated, it is entirely possible to find a good HT frame but poor or no agreement with the Walén relation. An example of this situation is the October 19, 1984, event discussed in the paper.

Acknowledgments. The research of Bengt Sonnerup was supported by the National Science Foundation, Atmospheric Sciences Division, under grant ATM-8807045 and by the Air Force Geophysics Laboratory under contract F19628-87-K-0026 to Dartmouth College.

The Editor thanks R. Elphic and N. Omidi for their assistance in evaluating this paper.

REFERENCES

deHoffmann, F., and E. Teller, Magneto-hydrodynamic shocks, *Phys. Rev.*, *80*, 692-703, 1950.

Fairfield, D. H., Average and unusual locations of the Earth's magnetopause and bow shock, *J. Geophys. Res.*, *76*, 6700-6716, 1971.

Fuselier, S. A., D. M. Klumpar, W. K. Peterson, and E. G. Shelley, Direct injection of ionospheric O^+ into the dayside low latitude boundary layer, *Geophys. Res. Lett.*, *16*, 1121-1124, 1989.

Gosling, J. T., J. R. Asbridge, S. J. Bame, W. C. Feldman, G. Paschmann, N. Sckopke, and C. T. Russell, Evidence for quasi-stationary reconnection at the dayside magnetopause, *J. Geophys. Res.*, *87*, 2147-2158, 1982.

Gosling, J. T., M. F. Thomsen, S. J. Bame, and C. T. Russell, Accelerated plasma flows at the near-tail magnetopause, *J. Geophys. Res.*, *91*, 3029-3041, 1986.

Hau, L.-N., and B. U. Ö. Sonnerup, On the structure of resistive MHD intermediate shocks, *J. Geophys. Res.*, *94*, 6539-6551, 1989.

Johnstone, A. D., D. J. Rogers, A. T. Coates, M. F. Smith, and D. J. Southwood, Ion acceleration during steady-state reconnection at the dayside magnetopause, in *Ion Acceleration in the Magnetosphere and Ionosphere, Geophys. Monogr. Ser.*, vol. 38, edited by T. Chang, pp. 136-140, AGU, Washington, D. C., 1986.

Levy, R. H., H. E. Petschek, and G. L. Siscoe, Aerodynamic aspects of the magnetospheric flow, *AIAA J.*, *2*, 2065-2076, 1964.

Lühr, H., N. Klöcker, W. Oelschlägel, B. Häusler, and M. Acuña, The IRM flux-gate magnetometer, *IEEE Trans. Geosci. Remote Sens.*, *GE-23*, 259-261, 1985.

Papamastorakis, I., G. Paschmann, W. Baumjohann, B. U. Ö. Sonnerup, and H. Lühr, Orientation, motion and other properties of flux transfer event structures on September 4, 1984, *J. Geophys. Res.*, *94*, 8852-8866, 1989.

Paschmann, G., Comment on "Electric field measurements at the magnetopause 1. Observation of large convective velocities at rotational magnetopause discontinuities," by T. L. Aggson, P. J. Gambardella, and N. C. Maynard, *J. Geophys. Res.*, *90*, 7629-7630, 1985.

Paschmann, G., B. U. Ö. Sonnerup, I. Papamastorakis, N. Sckopke, G. Haerendel, S. J. Bame, J. R. Asbridge, J. T. Gosling, C. T. Russell, and R. C. Elphic, Plasma acceleration at the

Earth's magnetopause: Evidence for reconnection, *Nature*, *282*, 243-246, 1979.

Paschmann, G., H. Loidl, P. Obermayer, M. Ertl, R. Laborenz, N. Sckopke, W. Baumjohann, C. W. Carlson, and D. W. Curtis, The plasma instrument for AMPTE IRM, *IEEE Trans. Geosci. Remote Sens.*, *GE-23*, 262-266, 1985.

Paschmann, G., I. Papamastorakis, W. Baumjohann, N. Sckopke, C. W. Carlson, B. U. Ö. Sonnerup, and H. Lühr, The magnetopause for large magnetic shear: AMPTE/IRM observations, *J. Geophys. Res.*, *91*, 11,099-11,115, 1986.

Sonnerup, B. U. Ö., and L. J. Cahill, Magnetopause structure and attitude from Explorer 12 observations, *J. Geophys. Res.*, *72*, 171-183, 1967.

Sonnerup, B. U. Ö., and B. G. Ledley, Electromagnetic structure of the magnetopause and boundary layer, in *Magnetospheric Boundary Layers, ESA SP-148*, edited by B. Battrick, pp. 401-411, European Space Agency, Paris, 1979.

Sonnerup, B. U. Ö., G. Paschmann, I. Papamastorakis, N. Sckopke, G. Haerendel, S. J. Bame, J. R. Asbridge, J. T. Gosling, and C. T. Russell, Evidence for magnetic field reconnection at the earth's magnetopause, *J. Geophys. Res.*, *86*, 10,049-10,067, 1981.

Sonnerup, B. U. Ö., I. Papamastorakis, G. Paschmann, and H. Lühr, Magnetopause properties from AMPTE/IRM observations of the convection electric field: Method development, *J. Geophys. Res.*, *92*, 12,137-12,159, 1987.

Wu, C. C., On MHD intermediate shocks, *Geophys. Res. Lett.*, *14*, 668-671, 1987.

H. Lühr, Institut für Geophysik und Meteorologie der Technischen Universität Carolo-Wilhelmina, 3300 Braunschweig, Federal Republic of Germany.

I. Papamastorakis and G. Paschmann, Max-Planck-Institut für Physik und Astrophysik, Institut für extraterrestrische Physik, 8046 Garching, Federal Republic of Germany.

B. U. Ö. Sonnerup, Thayer School of Engineering, Dartmouth College, Hanover, NH 03755.

(Received November 3, 1989;
accepted January 15, 1990.)

Appendix 10

THE MAGNETOPAUSE AND BOUNDARY LAYER FOR SMALL MAGNETIC SHEAR: CONVECTION ELECTRIC FIELDS AND RECONNECTION

G. Paschmann[1] · B. Sonnerup[2] , I. Papamastorakis[1,3] W. Baumjohann[1], N.Sckopke[1], and H. Lühr[4]

Abstract. Convection electric fields, $E_C = -V_p \times B$, measured during a magnetopause/boundary layer encounter at low latitude by the AMPTE/IRM spacecraft, are shown to yield an accurate determination of the magnetopause normal vector, N, even though the magnetic shear across the magnetopause was small. The average plasma velocity along N is used to estimate a boundary layer thickness of about 1.3 R_E . Analysis of E_C in the magnetopause itself reveals the existence of a deHoffmann-Teller frame in which the flow is nearly field aligned. The field-aligned flow is also found to be approximately Alfvénic, indicating that the magnetopause was a rotational discontinuity; this is interpreted as a signature that magnetic-field reconnection was occurring somewhere on the magnetopause.

1. Introduction

The properties of the earth's magnetopause under conditions of large magnetic shear have been studied extensively over the past 25 years. Early investigations [Cahill and Amazeen, 1963; Sonnerup and Cahill, 1967; Aubry et al., 1971; Ledley, 1971] were based on magnetic field data alone. An unambiguous identification of the magnetopause is difficult in such circumstances, unless the magnetic field displays a large rotation, i.e., large shear, as the observing spacecraft passes from one side of the magnetopause to the other. Even when such is the case, it is occasionally difficult to distinguish true magnetopause crossings from traversals of interplanetary magnetic discontinuities that have become draped over the magnetosphere by the magnetosheath flow. More recent studies [Mozer et al., 1979; Berchem and Russell, 1982; Aggson et al., 1983; Gosling et al., 1986, 1990; Paschmann et al., 1986; Sonnerup et al., 1981, 1987, 1990] have made use of data from electric-field probes, fast plasma analyzers and energetic-particle detectors on board the ISEE and AMPTE spacecraft in addition to magnetometer data, thereby greatly enhancing the possibility of identifying the magnetopause unambiguously and of studying its properties, orientation and dynamics. In particular, analysis of the convection electric field during magnetopause crossings with large magnetic shear has been shown to yield accurate magnetopause normal vectors, N, [Sonnerup et al., 1987, 1990] as well as quantitative evidence for the occurrence of magnetic field reconnection. To date, the case of moderate to low magnetic shear has not been studied in the same detail, the reason being that it has been thought difficult or impossible to derive good N vectors from the data. Furthermore, the signatures of reconnection in the form of plasma jetting would be weak or absent. But even when the shear is observed to be weak locally, reconnection may be globally important: because of draping of the interplanetary magnetic field (IMF) around the magnetosphere, unobserved regions of high shear and strong reconnection signatures may exist elsewhere on the magnetopause surface.

In this letter we show that an excellent N vector can be obtained even for low magnetic shear, provided a region of boundary layer plasma and flow with substantial velocity gradients is present inside the magnetopause. We also show that convincing evidence for magnetic connection across the magnetopause (and thus for reconnection) can be obtained even for low magnetic shear. Finally, we show how the N vector, along with measured plasma velocities, can be used to estimate the actual boundary layer thickness and density profile.

2. Data Description

The data employed in our study were obtained on December 29, 1984, with the 3D plasma instrument [Paschmann et al., 1985] and the magnetometer [Lühr et al., 1985] on board the AMPTE/IRM spacecraft during an inbound pass of the spacecraft through the morningside magnetopause (local time: 0815 h) at a moderate southern GSM latitude of -10.5°. An overview of relevant observations is shown in Figure 1 during a 20 minute period surrounding the magnetopause and containing measurements during a brief period of the magnetosheath (on the left) as well as during an extended period of the low-latitude boundary layer (LLBL, on the right) on the magnetospheric side of the magnetopause. Conditions in the magnetosphere proper, inside the LLBL, appear briefly at around 1818:40 UT near the right-hand edge of the diagram but the spacecraft reenters the LLBL almost immediately and then does not return to the magnetosphere proper until 1840 UT.

We have identified the center of the magnetopause (MP) to be located at 1804:58 UT with an approximate duration of 40s. In the order of the various panels in Figure 1, the following signatures of the magnetopause are evident. Although there is little signficant change in the measured proton number density, N_p, the energetic electron number density $N_{2e}(40>E>2$ keV) increases rapidly from very small values in the magnetosheath toward an intermediate level characteristic of the LLBL; the full magnetospheric level can be seen briefly in the interval 1818-1819 UT. The parallel and perpendicular proton temperatures, $T_{p\|}$ and $T_{p\perp}$, both increase across the MP but the former more rapidly than the latter so that a change occurs from $T_{p\perp}>T_{p\|}$ in the magnetosheath to $T_{p\perp}\sim T_{p\|}$ in the LLBL. There is also a pronounced increase in the electron temperatures $T_{e\|}$ and $T_{e\perp}$ with an associated change from approximate isotropy in the magnetosheath to $T_{e\|}>T_{e\perp}$ in the LLBL. A well defined decrease in the plasma flow speed, V_p, occurs as the spacecraft crosses the MP and there are associated small changes in the LMN elevation angle, λ_{vp}, and azimuth angle, φ_{vp}, of the flow vector. Note in particular the change from flow toward the MP ($\lambda_{vp}<0$) in the magnetosheath to flow more nearly parallel to it, but on the average slightly outward ($\lambda_{vp}\geq 0$), in the LLBL. Finally, the magnetic field magnitude, B, exhibits little net change from one side of the MP to the other but has a small minimum during the MP crossing. There are associated modest changes in field direction, in particular in the azimuth angle, φ_B. The LLBL, which adjoins the MP, exhibits substantial structure, much of which may have been caused by inward-outward oscillatory motion of the MP with a period of 60-120 sec or by a modulation of the layer thickness. Apart from these effects, the boundary layer density decreases gradually over a period of about 13 minutes to its magnetospheric level, seen at 1818-1819 UT.

Two further comments are required concerning Figure 1. First, our identification of the MP, which we consider to be unambiguous, is not based solely, or even principally, on the changes in magnetic field and flow velocity that occur there. Such changes can be observed frequently in the magnetosheath. Rather, it is the appearance of energetic electrons in association with marked changes in the thermal properties of the plasma that permits the identification to be made. In particular, in a study of many passes of the spacecraft through the MP, we have found the 'cigar-shaped' electron distribution functions ($T_{e\|}>T_{e\perp}$) that appear at the MP on an inbound pass, say, and then persist inside it for a period of time to be a common and unambiguous signature of boundary-layer plasma.

[1] Max-Planck-Institut für Physik und Astrophysik, Garching, F.R.G.
[2] Dartmouth College, Hanover, NH.
[3] University of Crete and Research Centre of Crete, Heraklion, Greece.
[4] Technische Universität Braunschweig, F.R.G.

The second comment is that the zero level of the elevation angles, λ_{vp} and λ_B, depends sensitively upon the choice of the magnetopause normal vector **N**. The **N** vector used in Figure 1 is the maximum-variance eigenvector, $\mathbf{i}_c$, of the convection electric field, $\mathbf{E}_c = -(\mathbf{V}_p - \mathbf{N}V_n)\times\mathbf{B}$, calculated from measured plasma velocities and magnetic fields and evaluated in a frame of reference travelling with the average outward speed, V_n = 10.8 km/s, of the plasma during the boundary layer interval 1805:17-1818:37 UT. This vector has GSE components **N** = (0.7551,-0.6343,-0.1660) and deviates by only 4.5° from the Fairfield model normal [Fairfield, 1971]; it has the advantage over the latter that it leads to a smaller average normal magnetic field (B_n = +0.3 nT versus +4.9 nT) during the same time interval. With either normal, an inward plasma flow, i.e., a flow towards the MP is present in the magnetosheath in a 4-minute period preceding the MP encounter (a tailward rotation of **N** by more than 8° would be needed to reverse this flow). This inward plasma motion has an average speed of $\bar{V}_n$ = -38 km/s during the magnetosheath interval (1801:00-1804:37 UT) but it decreases toward zero near the end of that interval, just before the MP encounter. The inward flow appears incompatible with the observed fact that the magnetopause moved outward past the spacecraft around 18:04:58 UT, unless one assumes that plasma could flow across the MP or (and) that **N** was directed more tailward during the magnetosheath interval than during the boundary layer interval. Plasma motion across the magnetopause would require it to have been a rotational discontinuity (RD) rather than a tangential discontinuity (TD). In order to reach the spacecraft, this RD would have propagated outward, against the inward magnetosheath flow, at a speed greater than that flow. There may also have been a change in **N** but even so, we show below that data taken within the MP structure itself indicate RD rather than TD structure.

3. Magnetopause Structure

In practice, it is essentially impossible to check whether a low-shear magnetopause is an RD or a TD on the basis of magnetic field data alone. However, when plasma measurements are also available, as in the present case, two properties can be checked: (i) the existence of a moving frame of reference, the so-called deHoffmann-Teller (HT) frame, in which the plasma flow is field aligned (an HT frame must exist for an RD; it may or may not exist for a TD); and (ii) the requirement for the RD, also referred to as the Walén relation, that the flow be Alfvénic in this moving frame. We have examined these two features by use of the simplest version of the analysis (i.e., assuming zero acceleration of the HT frame) described in Sonnerup et al. [1987]. According to this analysis, the velocity, $\mathbf{V}_{HT}$, of the HT frame is determined from a least-squares fit between the convection electric field, $\mathbf{E}_c = -\mathbf{V}_p\times\mathbf{B}$, and the electric field $\mathbf{E}_{HT} = -\mathbf{V}_{HT}\times\mathbf{B}$. Figure 2 shows a scatter plot of the three GSE components of $\mathbf{E}_c$ versus the corresponding components of $\mathbf{E}_{HT}$. The correlation coefficient in this diagram, cc = +0.989, is sufficient to justify the conclusion that an HT frame exists. This frame moves relative to the spacecraft with velocity $\mathbf{V}_{HT}$ = (-85, -3, -378) km/s (GSE components). The relationship between the measured velocity components and the corresponding measured Alfvén velocity components $\mathbf{V}_A = \mathbf{B}[1-\alpha)/\mu_0\rho]^{1/2}$, α being the pressure anisotropy and ρ the mass density (based on the assumption that all measured particles are protons), is shown in the scatter plot in Figure 3. Again, the correlation between $(\mathbf{V}-\mathbf{V}_{HT})$ and $\mathbf{V}_A$ is not perfect (cc = +0.986). But a correlation is clearly present and furthermore the regression line slope, s = +0.832, is sufficiently close to unity so that, allowing for experimental uncertainties including the possible presence of heavier ions, the flow could indeed have been Alfvénic in the HT frame. Furthermore, with an assumed inward flow of plasma across the MP, the positive slope signifies the presence of an inward directed component of **B** across the MP.

It is noted that the existence of an HT frame does not in itself indicate that the magnetopause must have been an RD. As pointed out by Paschmann [1985], and as established observationally by use of the AMPTE/IRM data [Sonnerup et al., 1990], TDs may also have excellent HT frames. However, for a TD there is no a-priori reason why the flow should be Alfvénic when viewed in the HT frame. Even for a TD, Alfvénic flow could of course arise, purely accidentally so to speak. But for an RD, the tangential stress balance requires the flow always to be Alfvénic in the HT frame. We conclude, not only that the data during the magnetopause crossing are consistent with the RD structure and therefore consistent with the interpretation outlined at the end of the previous section, in which the magnetopause propagated outward against an inward magnetosheath flow component, but also that the consistency of those data with the Walen relation would be purely coincidental in the TD interpretation.

Because of the small magnetic and flow shear across the MP, the minimum variance direction for **B** and the maximum variance direction for $\mathbf{E}_c$ during the short MP interval fail to provide consistent and credible **N** vectors. Therefore, we initially assume that the **N** vector derived from LLBL data (see Section 2) applies to the MP as well. We then find $V_n = \bar{\mathbf{V}}\cdot\mathbf{N}$ = -11 km/s, $V_{HTn} = \mathbf{V}_{HT}\cdot\mathbf{N}$ = +9.5 km/s, $V_{An} = \bar{\mathbf{V}}_A\cdot\mathbf{N}$ = -17 km/s, and $B_n = \bar{\mathbf{B}}\cdot\mathbf{N}$ = -1.8 nT during the magnetopause crossing. Note that V_{HTn} represents the motion of the MP along **N**. This velocity has the correct sign, corresponding to outward motion, but is too small (it yields an MP thickness of only 20 km), presumably due to a small error in **N**. The plasma flows inward across the magnetopause with speed $V_n - V_{HTn}$ = -11.5 km/s as expected, but this flow speed is smaller than V_{An}, again indicating possible errors. The normal field B_n is negative as expected from the positive regression line slope in Figure 3. A rotation of **N** by only 1.5°, to the new orientation (.7494,-0.6342,-0.1899), leads to V_n = -9.9 km/s, V_{HTn} = 10 km, V_{An} = -27.5 km/s, and B_n = -2.8nT, corresponding to a more reasonable MP thickness of 390 km (≅4 ion inertial lengths) and flow across the MP at 72% of the normal Alfvén speed. In light of the imperfect correlations in Figures 2 and 3, and the general uncertainties in measured plasma velocities and mass densities, this lauer discrepancy should not be considered significant.

If the MP were a TD instead, one would expect $\mathbf{B}\cdot\mathbf{N}_{TD} = 0$ and $(\bar{\mathbf{V}}-\mathbf{V}_{HT})\cdot\mathbf{N}_{TD} = 0$ which gives $\mathbf{N}_{TD}$ = (0.4514, -0.8363, -0.3115): such a large deviation from the model normal seems unlikely. For example, it would lead to an increase of the variance in B_n from 4.2 $(nT)^2$ (using **N**) to 7.6 $(nT)^2$ (using $\mathbf{N}_{TD}$). Also, the magnetopause velocity would be 82 km/s and the corresponding MP thickness 3200 km, which must be considered unusually large.

4. Discussion

Three conclusions emerge from the present study:

(1) The maximum-variance direction of the convection electric field, $\mathbf{E}_c = -\mathbf{V}\times\mathbf{B}$, during the boundary layer crossing discussed here appears to provide an excellent estimate of the average direction normal to the magnetopause. This result has been confirmed by examination of other cases where a substantial boundary layer, but only small magnetic shear across the magnetopause, was observed.

(2) Even magnetopause structures having small magnetic and velocity shear may display the rotational discontinuity structure that has been associated with magnetic connection across the magnetopause and therefore presumably with reconnection. To date, we have found one additional example (November 10, 1984, 0929:45-0942:50 UT) in the AMPTE/IRM data set of the type of magnetopause properties discussed here; there may be more cases where local temporal and spatial variations obscure those properties. Low magnetic shear across the equatorial magnetopause may occur, not only for northward or nearly northward interplanetary magnetic field (IMF) but, as a result of field draping around the magnetosphere, also when the IMF has other orientations, e.g., when it lies more nearly in the ecliptic plane. Yet, the large thickness of the LLBL observed in this event is most conveniently explained in terms of a northward IMF and reconnection above the cusps, as shown by the insert in Figure 3 [from Cowley, 1981]. Through this process, layers of magnetosheath plasma and magnetic flux are continuously added to the frontside LLBL.

(3) There is evidence in Figure 1 of quasiperiodic outward/inward motion of the LLBL past the spacecraft with time periods in the range 60-120 s. If such motion did occur, the actual thickness of the layer can be estimated as the product of its duration (800 s) and the average measured outward plasma velocity in the LLBL (10.8 km/s), the result being a thickness of ~1.3 R_E. We have also attempted to deconvolve the radial oscillatory motion and the measured temporal density profile in the top panel of Figure 1 in order to obtain a true spatial density profile. This is done by associating each sampled density Np_k at time t_k with a distance along the magnetopause normal given by

$$y_k = \Delta t \sum_{i=1}^{k} V_{ni}$$

where V_{ni} is the normal plasma velocity at time t_i and Δt is the time between samples. The result of this process is shown in Figure 4. There is considerable scatter in this plot but one can nevertheless discern a smooth average density profile that has a modest negative slope, starting at the magnetopause and extending over most of the thickness of the LLBL with a steeper negative slope near the magnetospheric edge of the layer. Such a profile would not be generated by a purely diffusive process unless the diffusion coefficient is a decreasing function of distance from the magnetopause. Eddy diffusivity in the outer part of the layer could perhaps lead to the observed density profile.

Acknowledgment. Research of B.S. was supported by the National Science Foundation, Atmospheric Sciences Division, under Grant ATM 8807645 and by the Air Force Geophysics Laboratory under Contract F19628-87-K-0026 to Dartmouth College.

References

Aggson, T. L., P. J. Gambardella, and N.C. Maynard, Electric field measurements at the magnetopause 1. Observation of large convective velocities at rotational magnetopause discontinuities, *J. Geophys.Res.*, 88, 10,000, 1983.

Aubry, M. P., M. G. Kivelson, and C. T. Russell, Motion and structure of the magnetopause, *J. Geophys. Res.*, 76, 673, 1971.

Berchem, J., and C. T. Russell, The thickness of the magnetopause current layer: ISEE 1 and 2 observations, *J. Geophys. Res.*, 87, 2108, 1982.

Cahill, L. J., Jr., and P. G. Amazeen, The boundary of the geomagnetic field, *J. Geophys. Res.*, 68, 1835, 1963.

Cowley, S. W. H., Magnetospheric and ionospheric flow and the interplanetary magnetic field, in *The Physical Basis of the Ionosphere in the Solar-Terrestrial System*, p. 4-1, AGARD-CP, NATO, Neuilly-sur-Seine, 1981.

Fairfield, D. H., Average and unusual locations of the Earth's magnetopause and bow shock, *J. Geophys. Res.*, 76, 6700, 1971.

Gosling, J. T., M. F. Thomsen, S. J. Bame and C. T. Russell, Accelerated plasma flows at the near-tail magnetopause, *J. Geophys. Res.*, 91, 3029, 1986.

Gosling, J. T., M. F. Thomsen, S. J. Bame, R. C. Elphic and C. T. Russell, Plasma flow reversals at the dayside magnetopause and the origin of asymmetric polar cap convection, *J. Geophys. Res.*, 95, 8073, 1990.

Ledley, B. G., Magnetopause attitudes during Ogo 5 crossings, *J. Geophys Res.*, 76, 6736, 1971.

Lühr, H., N. Klöcker, W. Oelschlägel, B. Häusler, and M. Acuña, The IRM flux-gate magnetometer, *IEEE Trans. Geosci. Remote Sens.*, GE-23, 259, 1985.

Mozer, F. S., R. B. Torbert, U. V. Fahleson, C.-G. Fälthammar, A. Gonzalone, A. Pedersen, and C. T. Russell, Direct observation of a tangential electric field component at the magnetopause, *Geophys. Res. Lett.*, 6, 305, 1979.

Paschmann, G., Comment on "Electric field measurements at the magnetopause 1. Observation of large convective velocities at rotational magnetopause discontinuities," by T. L. Aggson, P. J. Gambardella, and N. C. Maynard, *J. Geophys. Res.*, 90, 7629, 1985.

Paschmann, G. H. Loidl, P. Obermayer, M. Ertl, R. Laborenz, N. Sckopke, W. Baumjohann, C. W. Carlson, and D. W. Curtis, The plasma instrument for AMPTE IRM, *IEEE Trans. Geosci. Remote Sens.*, GE-23, 262, 1985.

Paschmann, G., I. Papamastorakis, W. Baumjohann, N. Sckopke, C. W. Carlson, B. U. Ö. Sonnerup, and H. Luhr, The magnetopause for large magnetic shear: AMPTE/IRM observations, *J. Geophys. Res.*, 91, 11,099, 1986.

Russell, C. T., and R. C. Elphic, ISEE observations of flux transfer events at the dayside magnetopause, *Geophys. Res. Lett.*, 6, 33, 1979.

Sonnerup, B. U. Ö., and L. J. Cahill, Magnetopause structure and attitude from Explorer 12 observations, *J. Geophys. Res.*, 72, 171, 1967.

Sonnerup, B. U. Ö., G. Paschmann, I. Papamastorakis, N. Sckopke, G. Haerendel, S. J. Bame, J. R. Asbridge, J. T. Gosling, and C. T. Russell, Evidence for magnetic field reconnection at the Earth's magnetopause, *J. Geophys. Res.*, 86, 10,049, 1981.

Sonnerup, B. U. Ö., I. Papamastorakis, G. Paschmann, and H. Lühr, Magnetopause properties from AMPTE/IRM observations of the convection electric field: Method development, *J. Geophys. Res.*, 92, 12,137, 1987.

Sonnerup, B. U. Ö., I. Papamastorakis, G. Paschmann, and H. Lühr, The magnetopause for large magnetic shear: Analysis of convection electric fields from AMPTE/IRM, *J. Geophys Res.*, 95, 10,541, 1990.

W. Baumjohann, G. Paschmann, and N. Sckopke, Max-Planck-Institut für Physik und Astrophysik, Institut für extraterrestrische Physik, 8046 Garching, Federal Republic of Germany.

H. Lühr, Institut für Geophysik und Meteorologie der Technischen Universität Carolo-Wilhelmina, 3300 Braunschweig, Federal Republic of Germany.

I. Papamastorakis, Physics Department, University of Crete, Heraklion, Greece.

B. Sonnerup, Thayer School of Engineering, Dartmouth College, Hanover, NH 03755.

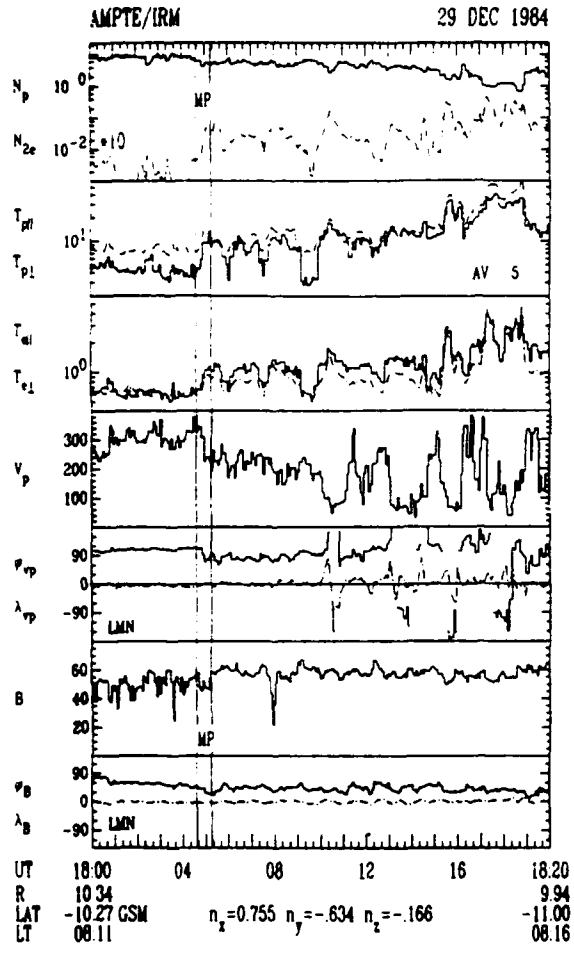

Fig. 1. AMPTE/IRM measurements during inbound pass through the magnetopause/boundary-layer region on December 29, 1984: proton number density, $N_p(cm^{-3})$ and energetic electron number density, N_{2e}(multiplied by 100; cm^{-3}; 40>E>2 keV); parallel and perpendicular proton and electron temperatures, $T_{p\parallel}$, $T_{p\perp}$ and $T_{e\parallel}$, $T_{e\perp}$ (10^6K); plasma bulk flow speed, V_p (kms^{-1}), azimuth angle, φ_{vp}, and elevation angle, λ_{vp} (degrees); magnetic field, B(nT), azimuth angle, φ_B, and elevation angle, λ_B (degrees). The angles φ and λ refer to the boundary normal coordinate system LMN [Russell and Elphic, 1979] with λ=0 in the magnetopause tangent plane and λ>0 indicating an outward pointing component; φ=0 along the +L axis and φ=90° along the +M axis. In each panel, the bar-graph (solid) trace corresponds to the upper symbol (N_p, $T_{p\parallel}$, etc.) and the dash-dot trace to the lower symbol.

Fig. 4. Deconvolved ion density profile for the boundary layer on December 29, 1984, 1804.33-1818:28

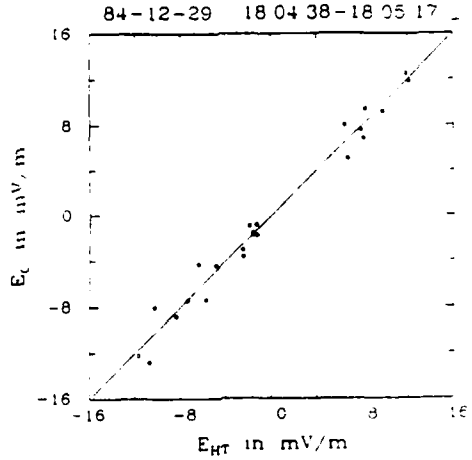

Fig. 2. Scatterplot for magnetopause data interval of GSE components of convection electric field $E_c = -V_p \times B$ versus corresponding components of the deHoffmann-Teller electric field $E_{HT} = -V_{HT} \times B$, with V_{HT} = (-85, -3,-378) kms^{-1}. Correlation coefficient is 0.989.

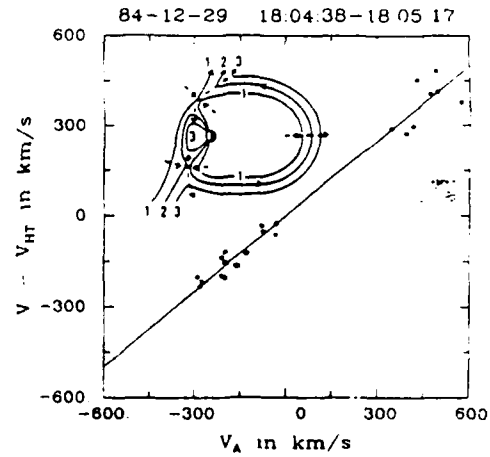

Fig. 3. Scatter plot of GSE components of $(V_p - V_{HT})$ versus corresponding components of the Alfvén speed $V_A = B[(1-\alpha)\mu_{oo}\rho]^{1/2}$ for magnetopause data interval. Agreement with Walén relation corresponds to a regression line slope $s = \pm 1$. The regression line slope obtained is $s = +0.832$ with correlation coefficient +0.986. Insert from Cowley [1981].

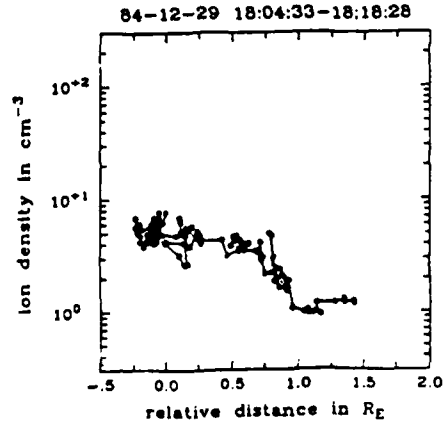

Appendix 11

Adv. Space Res. Vol. 8, No. 9–10, pp. (9)263–(9)272, 1988
Printed in Great Britain.

0273-1177/88 $0.00 + .50

EXPERIMENTAL TESTS OF FTE THEORIES

B. U. Ö. Sonnerup

Thayer School of Engineering, Dartmouth College, Hanover, NH 03755, U.S.A.

ABSTRACT

A brief overview is presented of a number of qualitative geometrical models as well as simulation models of flux transfer events (FTEs) and an attempt is made to identify critical observational tests that would help discriminate between these models. These tests are concerned with flux tube orientation, speed, and structure. Available single and multiple spacecraft observations are discussed in the context of these tests. Particular attention is given to the problem of determining flux-tube orientation and speed from a single spacecraft.

1. INTRODUCTION

The phrase "flux transfer event," or FTE for short, is used to refer to a set of observations, near the magnetopause, of short-lived abnormal deflections in the magnetic field, in many cases accompanied by associated characteristic signatures in the plasma and energetic particle properties. For events observed inside the magnetopause, the main plasma signature is the presence of magnetosheath-like plasma in the event; for observations outside the magnetopause, the main signature is a slightly depressed plasma density and the occurrence of magnetospheric-like energetic particles streaming along the magnetic field. Since their discovery in 1978 by Russell and Elphic /1,2,3/, FTEs have attracted an unusual amount of attention and have come to play a singularly important role in a conceptual picture of the solar-wind magnetosphere interaction that is shared by many workers in magnetospheric physics. In this picture, FTEs represent a time-dependent and perhaps patchy form of magnetic-field reconnection which may be the dominant mechanism whereby the cross-magnetospheric electric potential is generated and magnetic flux is transferred from closed field lines in the front lobe of the magnetosphere to open field lines which are deposited in, and added to the geomagnetic tail flux.

A great deal of data analysis has been performed to establish the main observational features of FTEs in terms of occurrence statistics as well as in terms of the geometrical features and structure of individual events. Simultaneously, several different theoretical models have started to emerge. These models are either of a qualitative geometrical nature or they are based on numerical simulations which have been performed, for the most part in two space dimensions and time. It is not the purpose of this paper to review all of this work in detail. Rather we shall focus attention on a few critical observational tests which need to be performed to help identify the most promising model or models and which may perhaps guide the development of new different or more detailed models. These tests are concerned with *in situ* measurements at the magnetopause. Observations concerning FTE signatures in the ionosphere are potentially important as well but, in the author's view, are more likely to provide supportive evidence rather than unambiguous critical tests of different FTE models.

The paper is organized as follows. In sections 2 and 3 we review briefly the properties of the original Russell-Elphic geometrical model of an FTE as well as the main features of several more recent, mainly two-dimensional models. In section 4 we discuss critical observational tests which are concerned with local FTE flux-tube orientation, motion, and structure. In section 5 we provide an illustration, from the recent work of Papamastorakis et al. /4/, of the determination of flux-tube orientation and speed by use of data from a single spacecraft (AMPTE/IRM). Section 6 deals with the relationship, proposed by Saunders et al. /5,6/, between magnetic twist in FTE flux tubes and Alfvén waves. Finally, section 7 contains a brief summary and comments on future multiple spacecraft studies.

2. THE RUSSELL-ELPHIC MODEL

The potential importance of FTEs was generally recognized and accepted almost instantly after their discovery, in part perhaps owing to the highly suggestive name "flux transfer event" assigned to the observational syndrome by Russell and Elphic, in part owing to an equally suggestive and creative cartoon drawn by these authors to represent the magnetic field geometry associated with this syndrome. This cartoon, a modernized version of which is reproduced in Figure 1, shows an elbow-shaped flux tube crossing the magnetopause. It has at least four important implications (of which however only the first can be considered as being reasonably firmly established observationally): (i) that the FTE signature is caused by an elongated object, such as a tube, rather than by a short one such as a nodule on the magnetopause; (ii) that the magnetosheath part of an FTE flux tube ultimately extends out into the solar wind and that the magnetospheric part ultimately reaches the ionosphere, thus providing direct magnetic connection between a patch in the ionosphere and the solar wind; (iii) that, very approximately, the flux

tube has a cross section that is a more or less deformed circle or semicircle, leading to an ionospheric footprint of similar shape; (iv) that magnetic tension in the elbow-shaped tube causes it to accelerate polewards which in turn leads to a gradual straightening of the elbow. This latter effect means that the two arms of the flux tube away from the elbow form an angle with the ambient field, causing the latter to be draped around the tube. However, the draping effect may be relatively weak along the two arm parts of the tube whereas it is strong near the elbow. Indeed, as the tube sweeps past a spacecraft this draping produces the characteristic bipolar signature in B_N, the magnetic field component normal to the magnetopause, that led to the discovery of the FTE syndrome in the first place. It was soon realized from encounters with the actual FTE flux tube that the field in that tube must itself be twisted, as shown in Figure 1, in order to account for the observed magnetic signature and for the persistent presence of a maximum of the total pressure, $P = p+B^2/2\mu_0$, in the tube /7,8/. This twisted field may be incorporated into the Russell-Elphic model in an *ad-hoc* manner. Observational evidence that it may be associated with an Alfvèn wave travelling in the tube has been discussed by Saunders et al. /5,6/ and will be considered further in section 6.

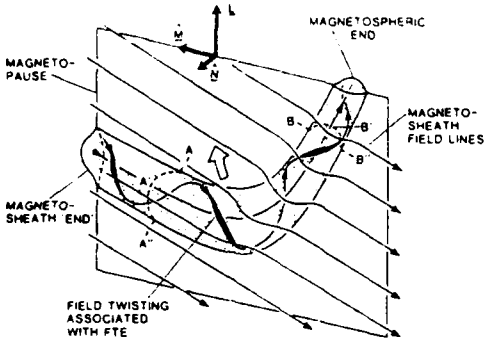

Fig. 1. Russell-Elphic model of flux transfer event (from Saunders et al. /6/).

An added implication of the Russell-Elphic model is that the FTE flux tube has been produced by reconnection that switches on and off in a fairly narrow longitude segment, creating pairs of elbow-shaped flux tubes, one tube in the northern hemisphere, as illustrated in Figure 1, and its mirror image in the southern hemisphere as shown in Figure 2. Indeed, FTEs with mirror image B_N signatures are seen in the two hemispheres: the source region for an FTE flux-tube pair statistically appears to be in the equatorial region /9/. Other important observational indications that FTEs involve reconnection are the fact that they are seen only for southward IMF and the fact that enhanced plasma flow speeds are often seen, usually near the trailing (equatorial) edge of the events. This latter observation suggests that active reconnection may be occurring on the equatorward side of the flux tube /2,7/. There are also observations /10/ of electron heat fluxes to support this latter contention.

Finally, it has been assumed from the beginning /2/ that the FTE flux tube is convected away from its point of generation more or less with the velocity of the ambient magnetosheath plasma. It has been argued /11/ that, as a result of a force balance between Maxwell stresses in the elbow and Maxwell stresses produced by magnetopause field lines being pushed ahead of, and wrapped around the FTE flux tube (see Figure 2), such flux tubes of small cross section will indeed be convected with the ambient plasma whereas tubes larger than a certain critical size will move poleward more rapidly and will involve reconnection of magnetopause field and FTE flux-tube field as well as magnetopause field with itself. Another consequence of pushing the magnetopause field out of the way is the generation of field-aligned currents in the FTE tube, currents that have the sense needed to generate the observed field twist /11/.

Because of its intrinsically three-dimensional and time-dependent nature, few attempts have been made to provide an internally consistent mathematical description of the plasma dynamics associated with the Russell-Elphic model, or to establish whether this kind of flux-tube configuration would tend to be generated spontaneously at the dayside magnetopause (a recent 3D simulation by Sato et al. /12/ showed a more longitude-extended structure). Thus the model, while qualitatively predictive of a number of geometrical features of FTEs, does not provide quantitative predictions concerning field and plasma. However, it must be said that, on the qualitative level, it has been remarkably successful in either accounting for, or being able to accommodate, a large number of observations. Owing to this success, the Russell-Elphic model remained unchallenged as representing the proper FTE geometry until 1985, when Lee and Fu proposed their so-called multiple X-line model. That model and others that have followed are summarized briefly in the next section.

3. TWO DIMENSIONAL MODELS

The Lee-Fu multiple X line model /13,14/ is the outcome of a two-dimensional simulation of the tearing mode as it may occur at the nose of the magnetopause, i.e., in the presence of a stagnation-point like flow. A recent global version of this simulation by Shi et al. /15/, in which a magnetized incompressible plasma flows past a two-dimensional dipole, is reproduced in Figure 3(a). Magnetic islands are formed, grow, and are ejected in the poleward direction with a velocity that approximately equals the magnetosheath Alfvén speed evaluated at the subsolar point. Lee and Fu /13/ proposed that, with the addition of a field component B_y perpendicular to the plane of the figure, such magnetic islands become FTE flux tubes imbedded in the magnetopause and containing a helical magnetic field (the latter having the actually observed sense of helicity). Connection of such a tube to the

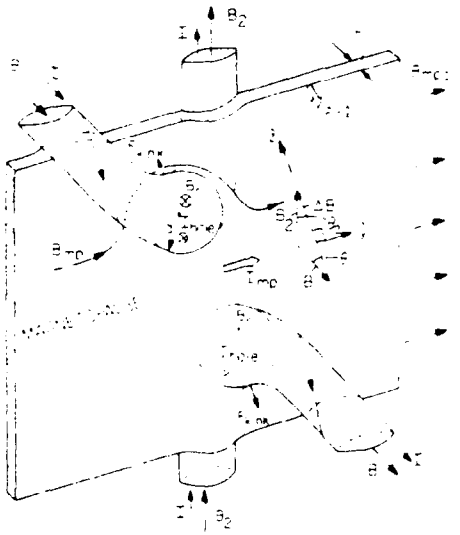

Fig. 2. A pair of FTE elbow-shaped flux tubes. Wrapping of magnetopause field B_{mp} around the elbow is shown (from Sonnerup /11/).

magnetosheath field and to the magnetospheric field would occur on the dawn side and dusk side as illustrated in Figure 3(b). The establishment of this connection is not described by the simulations (but the 3D simulation by Sato et al. /12/ suggests that the process for providing such connection may be fully three dimensional and rather complicated). It is of course possible to argue that the basic geometry of an FTE at the center of the "elbow" is as shown in Figure 3(a) but that the longitude extent of the portion of the FTE tube that is imbedded in the magnetopause is much more limited than in Figure 3(b). In that case, however, 2D simulation ceases to be quantitatively valid and it is not clear that the model is then significantly different from the Russell-Elphic one. One also loses a key prediction of the 2D geometry: that a spacecraft located somewhere on the frontside magnetopause will encounter *all* FTEs, which is an attractive explanation for their observed high frequency of occurrence.

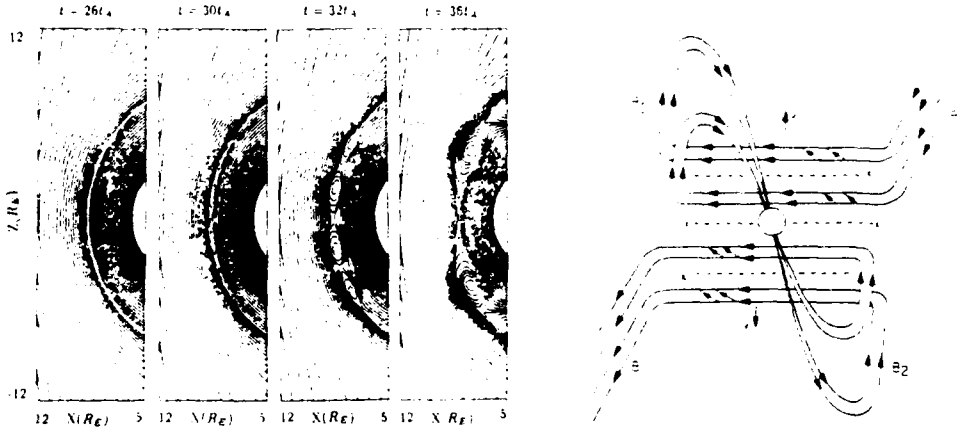

Fig. 3(a). Simulation of two-dimensional incompressible MHD flow past a dipole, showing the formation of multiple X lines and magnetic islands (from Shi et al. /15/). (b) FTE flux tubes (view towards the sun) in Fu-Lee multiple X line reconnection model (from Sonnerup /11/).

Careful examination of the magnetic field map in the Fu and Lee as well as the Shi et al. simulations /14,15/ shows the presence not only of magnetic islands but also of layers of magnetic flux located between islands and penetrating the magnetopause. This feature has not been emphasized by the Alaska group but it forms the essential ingredient in the recent 2D simulation model by Scholer /16,17/ as well as in the qualitative model discussed by Southwood et al. /18/. These authors propose to interpret FTEs in terms of ongoing but time-variable reconnection in some longitude segment on the front-side magnetopause. They argue that periods of increased reconnection rate lead to the formation of a pair of bulges in the magnetopause, much like magnetic islands, except that there is no intrinsic need for X lines away from the equator. These bulges are carried pairwise toward the north and the south cusp regions essentially with the Alfvén speed. Analysis of 2D time-dependent reconnection by Biernat et al. /19/ in the MHD description and by Owen and Cowley /20/ in the collisionless case also predicts ejection velocities of this size. This

result is not surprising since the exit flow speed in standard steady-state reconnection models is of the order of the Alfvén speed regardless of the reconnection rate.

The most important suggestion concerning FTE geometry made by Scholer and by Southwood et al. is that it is the open flux layer between two magnetic islands rather than an island itself that provides the magnetic coupling between the magnetosheath and the magnetosphere in an FTE event. This layer has the same longitude extent as that of the overall reconnection event. Thus its ionospheric footprint may be in the form of a band extended in longitude rather than in the form of a more or less circular patch. The field in the center of the bulge, i.e., if multiple X lines do occur as in the Alaska simulations, the field in the flux tube produced by a magnetic island plus a B_y component need not have the connection to the magnetosheath at one end and to the magnetosphere on the other, indicated in the Lee-Fu model and shown in Figure 3(b). Instead, this field may be connected at both ends to the magnetopause field or perhaps even at both ends to the magnetosheath field or to the magnetosphere field. Connection to the magnetopause field is proposed in a recent paper by Scholer /17/ as a mechanism whereby a high B field* is generated in the core of an FTE and whereby a drag force on the bulge is generated, similar to that discussed by Sonnerup /11/. Such a drag force would slow down the poleward speed of an FTE bulge to values that could be considerably less than the Alfvèn speed expected in 2D models. It would render invalid other quantitative predictions obtained from 2D simulations as well. For short elbows, the Scholer /17/ geometry returns roughly to the Russell-Elphic situation as modified by Sonnerup /11/. However, it is different in some important respects, in particular, the FTE flux tube would be ribbon shaped rather than tubular, the ribbon being linked by a bundle of stretched magnetopause field lines which would form the core of the FTE bulge. The process whereby twist is generated in the band might include the effect discussed by Wright /21/ as well as perhaps velocity shear /18/. Both of these are different from the mechanism proposed in /11/.

Both the Scholer and Southwood et al. geometry and that described by Sonnerup /11/ imply a layered structure of the FTE and there is evidence in the data /22,23,24/ that some such layering may be present.

It may be added that recent 2D simulations by Liu and Hu /25/ and by LaBelle-Hamer et al. /26/ concerning the interaction of the Kelvin-Helmholtz (KH) instability with reconnection (the tearing mode) at the magnetopause have led to yet another 2D FTE model in which the FTE bulge is a rolled-up vortex and its associated rolled up magnetic field. Such a model also entails a layered FTE structure. However, detailed comparison with observations will have to await more precise predictions concerning this structure from the simulation experiments.

4. OBSERVATIONAL TESTS

As is evident from the widely different nature of the various theoretical models described above, the most important unfinished experimental task in FTE research is to establish the overall geometry of FTE flux tubes and their motion on the magnetopause. It is of particular importance to determine to what extent, if at all, FTEs can be understood quantitatively in terms of two-dimensional models and simulations. Three specific questions will be addressed here: (i) what is the orientation of the FTE flux tube or bulge in an individual event and what is the statistical distribution of orientations as a function of local time and perhaps latitude; (ii) what is the velocity of motion of the flux tube or bulge along the magnetopause and perpendicular to the tube (bulge) axis; (iii) is the FTE signature produced by a tube that is pressed against one side or the other of the magnetopause current layer causing an indentation in that layer or is the flux tube an integral part of the magnetopause itself, describable as a latitudinally localized growth of its thickness (caused by enhanced reconnection) which produces a longitudinally extended bulge on the outer as well as the inner surface of the magnetopause layer? We now discuss briefly how these questions relate to the various theoretical models.

(i) Flux-tube orientation

In the multiple X line model of Lee and Fu as well as in the time-variable reconnection models of Scholer and Southwood et al., one would expect most or all FTE tubes or bulges encountered on the day-side magnetopause to have their orientation approximately along the magnetopause net current (this is precisely the case in the Fu-Lee as well as the Scholer simulations). For equal strengths of the magnetospheric field and the magnetosheath field, the FTE axis would then bisect the angle between the two fields. This type of result has recently been reported by Elphic and Southwood /27/ who examined nearly simultaneous observations from ISEE and AMPTE/UKS of an array of FTEs in the northern and in the southern hemisphere, and were able to determine the flux-tube or bulge orientations by minimum-variance analysis of the magnetic field, as discussed further in section 5. As these authors point out, their result is compatible with the Lee-Fu model (or indeed the more recent models by Scholer and by Southwood et al.) but it could also correspond to pairs of Russell-Elphic flux tubes sampled at, or near the elbow. Only in a statistical sense is the prediction of the Russell-Elphic model different: when many events are observed at the day-side magnetopause and are analyzed to yield the flux-tube direction, there ought to be a substantial probability of encountering either the magnetospheric arm or the magnetosheath arm of an elbow-shaped flux tube. The former arm would be more closely oriented along the magnetospheric field and the latter more closely along the magnetosheath field. However, this type of statistics must be done with care: as pointed out already, the elbow events are likely to have a larger magnetic draping signature, on average, than arm events. Therefore, there may be a built-in bias in favor of detecting elbow events.

The Lee-Fu model has a flux tube topology that is similar to the Russell-Elphic model but with the elbow flattened and extended over a substantial longitude segment. In such a geometry, only elbow encounters are expected near local noon whereas, for positive interplanetary B_y component, as shown in Figure 3(b), one would expect to see magnetospheric-arm FTEs on the afternoon and dusk side in the northern hemisphere and on the morning side and dawn side in the southern hemisphere. Similarly, for $B_y>0$ one would see magnetosheath-arm FTEs on the

* An increase in field strength also occurs in a purely two-dimensional model, as a result of plasma compression and an associated increase in B_y near the center of a magnetopause island or bulge.

morning (dawn) side in the northern hemisphere and on the afternoon (dusk) side in the southern hemisphere. For $B_y<0$ the reverse would hold.

It is noted that the Scholer and Southwood et al. models must also have some kind of three-dimensional structure at the morning and evening ends of the bulge in the magnetopause caused by the main flux transfer event. The exact nature of these effects is not known but it clearly depends on how the field lines in the core of the FTE bulge are connected.

Undertaking a statistical study of the type outlined here is a major task which is made extremely difficult by the fact that determination of flux tube orientation in general requires multiple spacecraft observations of one and the same flux tube or bulge. The only realistic hope is that the method, utilized by Elphic and Southwood /27/ and discussed further in section 5, which requires only magnetic data from a single spacecraft, can be used in a sufficient number of cases to provide the required statistics.

(ii) Flux-tube velocity

Based on the previous description of various FTE models, it would appear that experimental determination of the velocity of an FTE flux tube or bulge perpendicular to its axis, together with the direction of the axis, would provide a critical test of the two-dimensional aspect of these models even if only a few events are studied. As pointed out already, models which invoke ongoing reconnection with a modulation of the reconnection rate and which are basically two-dimensional, should show FTE bulge ejection away from the principal reconnection region in the equatorial plane with a speed comparable to the Alfvén speed. On the other hand, the Russell-Elphic configuration and any other configuration where the tube has to push its way through the magnetopause field would show velocities that are comparable to, but for large flux tubes perhaps somewhat greater than the surrounding magnetosheath flow speeds /11/; these are generally substantially smaller than the Alfvén speed on the frontside magnetopause. Finally, with reference to the recent models by Liu and Hu /25/ and LaBelle-Hamer et al. /26/, the process of generating Kelvin-Helmholtz vortices requires these vortices to move at a speed less than the ambient magnetosheath flow speed. This would also be the case if the FTE signatures were produced by nothing more than a simple wave on the magnetopause, travelling past the observing spacecraft.

In general, the determination of the orientation and speed of a planar front requires the use of three probes in a triangular configuration, well separated and located near the magnetopause. With luck, a few such events may be found when the Cluster spacecraft become operational. However, in this case too it turns out that data from a single spacecraft may yield the desired information, provided a good deHoffmann-Teller frame, i.e., a frame in which the plasma flow is aligned with the magnetic field, can be found for an FTE structure. An efficient method for determining the velocity of this frame has been described recently by Sonnerup et al. /28/ who applied the method to a quasisteady reconnection event. The application to an FTE is illustrated in section 5.

Once the perpendicular flux-tube speed has been determined, one can convert the duration of the FTE into a characteristic scale size along the magnetopause but transverse to the FTE axis.

(iii) Flux-tube structure

In order to examine whether an FTE is caused by a swelled-up part of the magnetopause itself (a bulge), as in the Lee-Fu model or the Scholer and Southwood et al. models, or whether it is caused by a flux tube pressed against one side or the other of the magnetopause current layer, it would be of particular value to examine data from two radially separated spacecraft, located near to, but on opposite sides of the magnetopause. Observations of this kind have in fact been made by Farrugia et al. /29/, who referred to them as "Two-Regime FTEs." These authors discuss two events where ISEE1 and 2 were located in the required manner. They found one case to be consistent with an encounter with the magnetospheric arm of a Russell-Elphic type flux tube. This tube was penetrated by the spacecraft in the magnetosphere but was sensed remotely also by the adjoining magnetosheath spacecraft. The magnetosheath effect was assumed to be caused by the indentation of the inner magnetopause surface and the corresponding bulging of the outer magnetopause surface caused by the flux tube. However, the evidence is not conclusive: the magnetopause could have bulged on both sides with the magnetospheric spacecraft penetrating the bulge on the magnetospheric side and the magnetosheath spacecraft sensing the bulge on the magnetosheath side remotely.

The second case reported by Farrugia et al. /29/ and interpreted by them as an encounter with the magnetosheath arm of a Russell-Elphic type FTE flux tube may have been more conclusive. Here it appears that the magnetospheric spacecraft briefly sampled the flux tube itself and, in doing so, passed through the magnetopause on the way into and out of the tube. This type of behavior would not be compatible with the FTE flux tube being part of the magnetopause itself.

Most importantly, observations of "two-regime" events rule out the aforementioned interpretation of FTEs in terms of a simple travelling wave, since such a wave would not generate the observed simultaneous B_N signature on both sides of the magnetopause. However, rolled-up KH vortices /25,26/ cannot be excluded in this manner.

Another critical observation relating to the internal structure of an FTE bulge is that of enhanced plasma flow speeds concentrated to the equatorward portion of an FTE bulge travelling past a spacecraft /1/. These enhanced flow speeds are likely to be associated with reconnection. However, in a two-dimensional model with continuously ongoing reconnection at a time-modulated reconnection rate, the whole FTE structure should be moving with the Alfvén speed and one would expect flow-speed enhancement throughout the time that the spacecraft is located inside the FTE structure, not just during the latter part of its residence time in the tube. It would therefore seem that this asymmetry of the flow speed enhancements is an indication that the poleward motion of the FTE structure occurs with a velocity that is substantially less than the flow speeds generated by the reconnection process (i.e., the Alfvén speed). This is the situation for the Russell-Elphic model and for Scholer's model /17/ when drag generated by

pushing the magnetopause field out of the way is included. However, it remains unclear whether the trailing-edge flow-speed enhancement is generated by reconnection between magnetospheric and magnetosheath fields in the equatorial plane, as in Scholer's model, or by reconnection away from the equatorial plane, perhaps as proposed by Sonnerup /11/ in the context of the Russell-Elphic model. In both cases, a layered FTE structure is predicted in which the reconnection-heated and accelerated plasma occupies an outer layer where the magnetic field magnitude may be also depressed, surrounding an FTE core which is occupied by plasma of magnetosheath (or, in Scholer's case, magnetopause) origin. These predictions may have a direct bearing on the crater-like FTE signatures in the magnetosphere reported by LaBelle et al. /22/ and on the similar structures reported by the AMPTE/UKS group /23,24/.

Another clue related to the flow-speed enhancements is that they are seen both in magnetospheric and in magnetosheath events (although perhaps somewhat more frequently in the latter). This is expected in Sonnerup's /11/ configuration but it is less clear what to expect if the FTE is simply a manifestation of a burst of high reconnection rate in an ongoing reconnection event in which magnetosheath and magnetospheric fields continually become interconnected. In quasisteady reconnection, the accelerated plasma appears in the magnetopause and on the magnetospheric side of the magnetopause but not on the magnetosheath side of it. It is not clear why this asymmetry should be lost if the reconnection rate is suddenly increased. In the numerical simulations /14,16/ symmetry appears to be at hand but this may be due to a failure to build into the calculations the intrinsic plasma and magnetic-field asymmetry that usually exists across the real magnetopause.

Finally, we comment on the ribbon-like nature of the flux tube that connects the magnetosheath and the magnetosphere in a model of Scholer's type. This band is wrapped around a core of magnetic field and plasma of magnetopause origin. Since the overall diameter of an FTE bulge may be fairly large, 1-2 R_E say, it would seem that escaping energetic magnetospheric particles should be mainly confined to this band. Thus, a spacecraft penetrating all the way into the deep core of such an FTE should see a burst (or at least an enhancement) of streaming such particles during entry into and exit from the FTE structure whereas they should be more or less absent during the traversal of the core itself. Evidence of this type should be looked for: none of the 15 FTEs examined by Paschmann et al. /7/, using ISEE data, showed this behavior (although only the energetic-particle density, not the streaming, was examined). In the Southwood et al. scenario, all of the field lines in the FTE bulge provide connection between the magnetosheath and the magnetosphere so that the entire FTE may contain streaming energetic particles. However, even in that case, one may expect the fluxes to be most intense near the surface of the bulge where field lines first become connected.

5. EXAMPLE

In this section the process of obtaining FTE flux-tube orientation and velocity from single spacecraft data is illustrated. The analysis to be presented is discussed in more detail in a recent paper by Papamastorakis et al. /4/. The method is based on two assumptions: (i) that the magnetic field sampled in the event has a constant component along the flux tube axis; (ii) that a frame of reference, the deHoffmann-Teller frame, exists in which the plasma flow sampled in the event is aligned with the magnetic field. Both of these assumptions are also made in a recent theoretical study of the external-field draping region by Farrugia et al. /30/ and both can be verified by use of magnetic field and plasma velocity measurements. From examination of a few AMPTE/IRM events the impression has been gained that assumption (i) is likely to work well only in the draping region whereas (ii) may work also in the interior of at least some events.

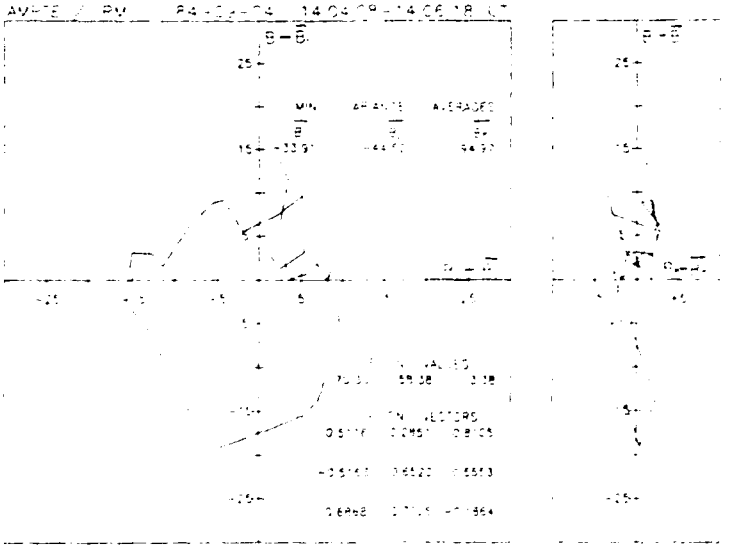

Fig. 4. Magnetic field hodograms for FTE observed by AMPTE/IRM on 4 Sep 1984. The average field B has been subtracted (from Papamastorakis et al. /4/).

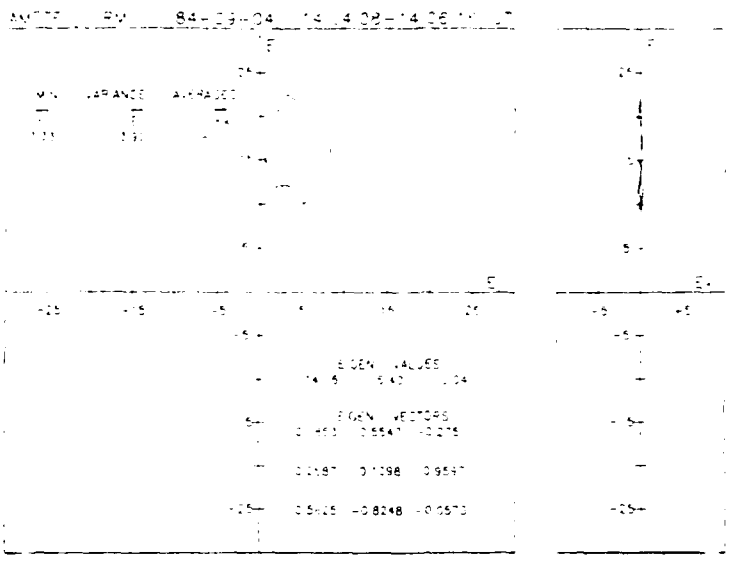

Fig. 5. Hodograms of convection electric field, $\mathbf{E_c} = -\mathbf{v}\times\mathbf{B}$ in Fig. 5 (from Papamastorakis et al. /4/).

Figure 4 shows the result, in the usual hodogram form, of minimum variance analysis of the magnetic field in a weak magnetosheath FTE event in which the AMPTE/IRM spacecraft sampled the field draping but did not penetrate the FTE flux tube. The ratio of the intermediate to the minimum variance is 58.4/3.4, indicating that a good minimum variance direction (**k**) has been obtained. This direction should be identified with the direction of the flux-tube or bulge axis. The average field component along this axis is seen to be -95nT. The roughly circular hodogram representing the field components perpendicular to the minimum variance direction is what is expected from a model of the type discussed by Farrugia et al. /30/. For the semicircular tube cross section (of radius a, say) used by these authors, one can further deduce a satellite "impact parameter" of about 1.4a in this case.

The axis determination described above is identical to that used by Elphic and Southwood /27/ who examined 13 cases and found 8 of these to have the ratio of intermediate to minimum variance greater than 10. The existence of a good minimum-variance direction in these FTEs provides convincing evidence that they are produced by distant encounters with an elongated rather than a nodular structure.

We now analyze the convection electric field $\mathbf{E_c} = -\mathbf{v}\times\mathbf{B}$ in the manner discussed in Sonnerup et al. /28/. Minimum variance analysis on $\mathbf{E_c}$ yields the results in Figure 5. It is seen that the electric field component in the minimum variance (**k**) direction is nearly zero and that it has a very small variance. This is usually an indication that a good deHoffmann-Teller transformation velocity, $\mathbf{v}_{HT}$, exists ($\mathbf{v}_{HT}$ is expected to be parallel to **k**). Least squares fitting as described in /28/ was used to determine this velocity. The three components of the resulting electric field $\mathbf{E}_{HT} = -\mathbf{v}_{HT}\times\mathbf{B}$ are found to have a correlation coefficient of 0.990 with the corresponding components of $\mathbf{E_c}$, which demonstrates that a good deHoffmann-Teller frame has been found.

Figure 6 shows the orientation and magnitude, in a plane tangential to the magnetopause, of the magnetospheric and magnetosheath fields, of the net magnetopause current, of the flux-tube axis, of the deHoffmann-Teller velocity, and of the magnetosheath flow velocity. The FTE occurred in the magnetosheath around 15.40 LT and -1.1° GSE latitude. It had the signature of a southern hemisphere event. It is seen that the flux-tube axis is tilted by a substantial angle away from the net magnetopause current vector and towards the external field. Yet it also deviates substantially from the latter field. Furthermore, the component of $\mathbf{v}_{HT}$ perpendicular to the flux tube axis is only about 35 km/s, in the southerly direction. The magnetosheath flow speed, on the other hand, has a perpendicular component of about 70 km/s, in the northerly direction. Thus it is clear that this portion of the FTE structure is not convected with the magnetosheath flow. Furthermore, we note that the opposite sense of motion of the FTE bulge and the magnetosheath plasma is also present in Scholer's simulations /16/*. As shown in the figure, the magnetosheath plasma velocity in the deHoffmann-Teller frame, $\mathbf{v}_{shHT}$, is 235 km/s and is approximately field-aligned as expected. It should be compared to an Alfvén speed of 290 km/s in the magnetosheath. The correlation coefficient between the three components of ($\mathbf{v}$-$\mathbf{v}_{HT}$) and the corresponding components of the local Alfvén velocity was 0.998 but the magnitudes of the former were only 81% of the corresponding Alfvén speed components. Thus the Walén relation was not exactly satisfied. Nevertheless, given the uncertainties in the data and in the analysis, one cannot exclude the possibility that this FTE had the basic properties expected from 2D models in which ongoing bursty reconnection is responsible for the creation of the FTE. In this context, it is noted that this FTE preceded by about 50 minutes the quasisteady reconnection event discussed by Sonnerup et al. /28/. On the other hand, the results are not consistent with the FTE being caused by wave motion on the magnetopause or by rolled-up KH vortices for which one would expect motion of the magnetopause bulge in the same direction as the ambient magnetosheath flow.

* It is presumably a result of the fast-mode expansion, characteristic of the inflow regions of a Petschek-like reconnection geometry, as discussed by Vasyliunas /31/.

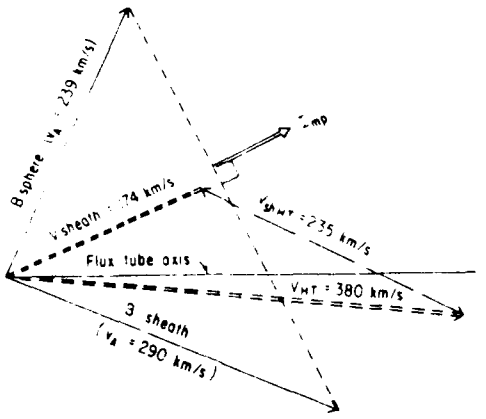

Fig. 6. Relative orientation of flux tube axis, magnetospheric and magnetosheath fields, magnetosheath flow velocity and deHoffmann-Teller (HT) transformation velocity, v_{HT}, for FTE in Figs. 4 and 5. Magnetic fields are drawn in Alfvén speed units. Note that the magnetosheath velocity in the HT frame is nearly antiparallel to $\mathbf{B}_{sheath}$ and has magnitude equal to about 80% of the magnetosheath Alfvén speed (from Papamastorakis et al. /4/).

The FTE signature analyzed here had a duration of 130 sec. With a perpendicular component of v_{HT} of 35 km/s, this time translates to a transverse FTE dimension of 4550 km along the magnetopause.

It would seem that analysis of the type described here, carried out on a number of events observed at different local times, should cast a great deal of light on the geometry and dynamics of FTEs.

6. ALFVEN WAVE IN FTE TUBE

Although detailed documentation was not provided, Saunders et al. /5,6/ have reported one FTE where the Walén relation, $\mathbf{b}_\perp = B_0\mathbf{v}_\perp/A_0$, A_0 being the Alfvén speed, was satisfied for the components $\mathbf{b}_\perp$ and $\mathbf{v}_\perp$ of magnetic field and plasma velocity perpendicular to the main field B_0. It is not known if this is a common property of FTEs, but it appears that there is now a fairly widespread belief that the magnetic field twist in FTEs and its associated flux-tube aligned current are propagated along the arms of the tube, thought of as having the Russell-Elphic geometry, away from a source region where the tube crosses the magnetopause. It would seem important to examine the Walén relation in FTE flux tubes for a substantial number of events to see whether the finding by Saunders et al. has general validity. However, as is evident from the example in section 5 (and as stressed by Farrugia et al. /30/), approximate satisfaction of the Walén relation is not an unambiguous indicator of an Alfvén wave propagation in the FTE tube. It could simply indicate that a deHoffmann-Teller frame exists in which the flow is field aligned, with speed equal to, or near the Alfvén speed. Here we point out that the twist-Alfvén wave idea may be in conflict with well documented observations /7/ of a substantial increase of total pressure, $(p+B^2/2\mu_0)$, in the interior of FTEs. This pressure increase is due mainly to the magnetic term. This point is illustrated by considering a flux tube of circular cross section containing a propagating twist-Alfvén wave. With the tube axis along z and with the assumptions $\partial/\partial z = 0$ and $\partial/\partial\phi = 0$ (axial symmetry), the magnetic field and the plasma velocity may be written as $\mathbf{B} = \mathbf{e}_z B_z(R)+\mathbf{e}_\phi B_\phi(R)$ and $\mathbf{v} = \mathbf{e}_z v_z(R)+\mathbf{e}_\phi v_\phi(R)$, respectively. For this configuration, we can show that the momentum equation for the plasma reduces to a radial force balance of the form

$$d(p+B^2/2\mu_0)/dR = \rho(v^2_\phi - B^2_\phi/\mu_0\rho)/R \qquad (1)$$

In the Alfvénic case we have $v^2_\phi = B^2_\phi/\mu_0\rho$, the result being that the total pressure $P = p+B^2/2\mu_0$ is constant over the tube cross section. This result arises because the magnetic hoop stres. $B^2_\phi/\mu_0 R$, used by Paschmann et al. /7/ to account for the excess values of P in FTEs, is exactly counterbalanced by the centrifugal force $\rho v^2_\phi/R$.

On the basis of the above argument, it seems somewhat doubtful** that the FTE field twist is generally the result of a propagating Alfvén wave in a flux tube of the Russell-Elphic type. It seems more likely that we are simply dealing with a flux-tube aligned current as envisaged by Paschmann et al. /7/. We may additionally ask whether the configuration might be a force-free one. For the cylindrical geometry described above, the force-free condition $\mathbf{j}\times\mathbf{B} = 0$ becomes

$$d(B^2/2\mu_0)/dR = - B^2_\phi/\mu_0 R \qquad (2)$$

and the radial force balance, equation (1), reduces to

$$dp/dR = \rho\, v^2_\phi/R \qquad (3)$$

In such a situation the plasma pressure would increase and the magnetic pressure decrease with increasing radius R. However, if the Walén relation holds, the total pressure would still remain constant.

** However, one can perhaps not entirely exclude the possibility of a wave-guide like mode in which $v^2_\phi < B^2_\phi/\mu_0\rho$.

7. SUMMARY

In this paper the author has discussed, in a general way, some observational tests that he believes would be of help in discriminating between a number of existing models of FTEs. The main objective has been to determine the local orientation and speed of an FTE flux tube. It will be difficult to obtain statistical information concerning these quantities if they have to be determined from time-of-passage measurements from three widely separated spacecraft, all simultaneously located near the magnetopause. For this reason, special emphasis was placed on the possibility of finding orientation and speed from a single spacecraft. Although a few such determinations have been reported, the information available to date is not sufficient to unambiguously select or reject any particular model or models. Indeed, one should be alert to the possibility that, in reality, more than one type of FTE geometry may occur.

When the four Cluster spacecraft begin to deliver data, a vast new set of possibilities for detailed examination of FTE orientation, structure and dynamics will open up. In the context of determination of the flux-tube orientation, the method discussed in this paper required the magnetic field to have a constant component along the flux-tube axis during the FTE traversal. This may be a realistic assumption for distant encounters but, on account of the field-strength maximum at the center of an FTE tube, probably not for penetrating ones. When Cluster data become available, one may be able to determine the flux-tube orientation by use of the requirement $\mathbf{k}_\parallel \bullet \nabla \mathbf{B} = 0$ where $\mathbf{k}_\parallel$ is a unit vector along the tube axis. This set of three scalar equations has a nontrivial solution only if the determinant of the matrix $\partial B_i/\partial x_j$ vanishes. The determinant will be readily obtainable from the Cluster data so that this condition (along with the condition that the matrix have zero trace) can be checked throughout an FTE encounter. If it is well satisfied, many determinations of the flux-tube orientation will be obtained for each event, by solving the equations $\mathbf{k}_\parallel \bullet \nabla \mathbf{B} = 0$ for each individual time of measurement.

One important current question in FTE research concerns the significance of observed streaming magnetospheric-like energetic particles in magnetosheath FTEs /32,33/. Do such observations provide unambiguous evidence for magnetic connection across the magnetopause, as has been generally assumed, or could they be accounted for in terms of particle leakage across the magnetopause without the presence of magnetic connection /34/? Since a clear and generally accepted answer to this question does not seem to be available at present, continued detailed studies of the energetic-particle signatures in FTEs are of extreme importance.

Finally, a comment should be made about numerical simulations of FTEs. In order for these simulations to be maximally helpful, they should be used to generate artificial data that represent the measurements made by one or more "spacecraft" passing through the FTE structure. Comparison of such artificial data with real observations should prove most illuminating.

ACKNOWLEDGMENT

The research was supported by the Air Force Geophysics Laboratory under contract F19628-87-K-0026, by the National Science Foundation, Atmospheric Sciences Division, under grants ATM-8507192 and ATM-8807645, and by the National Aeronautics and Space Administration under grant NAGW-1169 to Dartmouth College.

REFERENCES

1. C. T. Russell and R. C. Elphic, Initial ISEE magnetometer results: magnetopause observations, Space Sci. Rev. 22, 681 (1978)

2. C. T. Russell and R. C. Elphic, ISEE observations of flux transfer events at the dayside magnetopause, Geophys. Res. Lett. 6, 33 (1979)

3. R. C. Elphic and C. T. Russell, ISEE-1 and -2 observations of the magnetopause, in: Magnetospheric Boundary Layers, ed. B. Battrick, ESA SP-148, Noordwijk, Netherlands 1979, p.51.

4. I. Papamastorakis, G. Paschmann, W. Baumjohann, B. U. Ö. Sonnerup, and H. Lühr, Orientation, motion and other properties of FTE structures on September 4, 1984, J. Geophys. Res. to be submitted (1988)

5. M. A. Saunders, C. T. Russell, and N. Sckopke, Flux transfer events: scale size and interior structure, Geophys. Res. Lett. 11, 131 (1984)

6. M. A. Saunders, C. T. Russell, and N. Sckopke, A dual-satellite study of the spatial properties of FTEs., in: Magnetic Reconnection in Space and Laboratory Plasmas, ed. E. W. Hones, Jr., Geophys. Monogr. Ser. 30, Am. Geophys. Union, Washington, DC 1984, p. 145.

7. G. Paschmann, G. Haerendel, I. Papamastorakis, and N. Sckopke, Plasma and magnetic field characteristics of magnetic flux transfer events, J. Geophys. Res. 87, 2159 (1982)

8. S. W. H. Cowley, The causes of convection in the Earth's magnetosphere, Rev. Geophys. Space Phys. 20, 531 (1982)

9. C. T. Russell, J. Berchem, and J. G. Luhmann, On the source regions of flux transfer events, Adv. Space Res. 5, 363 (1985)

10. J. D. Scudder, K. W. Ogilvie, and C. T. Russell, The relation of flux transfer events to magnetic reconnection, in: Magnetic Reconnection in Space and Laboratory Plasmas, ed. E. W. Hones, Jr., Geophys. Monogr. Ser. 30, Am. Geophys. Union, Washington, DC 1984, p. 153.

11. B. U. Ö. Sonnerup, On the stress balance in flux transfer events, J. Geophys. Res. 92, 8613 (1987)

12. T. Sato, T. Shimada, M. Tanaka, T. Hayashi, and K. Watanabe, Formation of field-twisting flux tubes on the magnetopause and solar wind particle entry into the magnetosphere, Geophys. Res. Lett. 13, 801 (1986)

13. L. C. Lee, and Z. F. Fu, A theory of magnetic flux transfer at the Earth's magnetopause, Geophys. Res. Lett. 12, 105 (1985)

14. Z. F. Fu, and L. C. Lee, Simulation of multiple X-line reconnection at the dayside magnetopause, Geophys. Res. Lett. 12, 291 (1985)

15. Y. Shi, C. C. Wu, and L. C. Lee, A study of multiple X line reconnection at the dayside magnetopause, Geophys. Res. Lett. 15, 295 (1988)

16. M. Scholer, Magnetic flux transfer at the magnetopause based on single X line bursty reconnection, Geophys. Res. Lett. 15, 291 (1988)

17. M. Scholer, Strong core magnetic fields in magnetopause flux transfer events, Geophys. Res. Lett. 15, 748 (1988)

18. D. J. Southwood, C. J. Farrugia, and M. A. Saunders, What are flux transfer events?, Planet. Space Sci. 36, 503 (1988)

19. H. K. Biernat, M. F. Heyn, and V. S. Semenov, Unsteady Petschek reconnection, J. Geophys. Res. 92, 3392 (1987)

20. C. J. Owen, and S. W. H. Cowley, Simple models of time-dependent reconnection in a collision-free plasma with an application to substorms in the geomagnetic tail, Planet. Space Sci. 35, 451 (1987)

21. A. N. Wright, The evolution of an isolated reconnected flux tube, Planet. Space Sci. 35, 813 (1987)

22. J. LaBelle, R. A. Treumann, G. Haerendel, O. H. Bauer, G. Paschmann, W. Baumjohann, H. Lühr, R. R. Anderson, H. C. Koons, and R. H. Holzworth, AMPTE IRM observations of waves associated with flux transfer events in the magnetosphere, J. Geophys. Res. 92, 5827 (1987)

23. R. P. Rijnbeek, C. J. Farrugia, D. J. Southwood, M. W. Dunlop, W. A. C. Mier-Jedrzejowicz, C. P. Chaloner, D. S. Hall, and M. F. Smith, A magnetic boundary signature within flux transfer events, Planet. Space Sci. 35, 871 (1987)

24. C. J. Farrugia, R. P. Rijnbeek, M. A. Saunders, D. J. Southwood, D. J. Rogers, M. F. Smith, C. P. Chaloner, D. S. Hall, P. J. Christiansen, and L. J. Wooliscroft, A multi-instrument study of flux transfer event structure, J. Geophys. Res. 93, in press (1988)

25. Z. X. Liu, and Y. D. Hu, Local magnetic reconnection caused by vortices in the flow field, Geophys. Res. Lett. 15, 752 (1988)

26. A. L. Labelle-Hamer, Z. F. Fu, and L. C. Lee, A mechanism for patchy reconnection at the dayside magnetopause, Geophys. Res. Lett. 15, 152 (1988)

27. R. C. Elphic, and D. J. Southwood, Simultaneous measurements of the magnetopause and flux transfer events at widely separated sites by AMPTE UKS and ISEE 1 and 2, J. Geophys. Res. 92, 13,666 (1987)

28. B. U. Ö. Sonnerup, I. Papamastorakis, G. Paschmann, and H. Lühr, Magnetopause properties from AMPTE/IRM observations of the convection electric field: method development, J. Geophys. Res. 92, 12,137 (1987)

29. C. J. Farrugia, D. J. Southwood, S. W. H. Cowley, and R. P. Rijnbeek, Two-regime flux transfer events, Planet. Space Sci. 35, 737 (1987)

30. C. J. Farrugia, R. C. Elphic, D. J. Southwood, and S. W. H. Cowley, Field and flow perturbations outside the reconnected field line region in flux transfer events: theory, Planet. Space Sci. 35, 227 (1987)

31. V. M. Vasyliunas, Theoretical models of magnetic field line merging, Revs. Geophys. Space Phys. 13, 303 (1975)

32. M. Scholer, D. Hovestadt, F. M. Ipavich, and G. Gloeckler, Energetic protons, alpha particles and electrons in magnetic flux transfer events, J. Geophys. Res. 87, 2169 (1982)

33. T. W. Speiser, and D. J. Williams, Magnetopause modeling: flux transfer events and magnetosheath quasi-trapped distributions, J. Geophys. Res. 87, 2177 (1982)

34. D. G. Sibeck, R. W. McEntire, A. T. Y. Lui, R. E. Lopez, S. M. Krimigis, R. B. Decker, L. J. Zanetti, and T. A. Potemra, Energetic magnetospheric ions at the dayside magnetopause: leakage or merging?, J. Geophys. Res. 92, 12,097 (1987)

JOURNAL OF GEOPHYSICAL RESEARCH, VOL. 94, NO. A7, PAGES 8852-8868, JULY 1, 1989

Orientation, Motion, and Other Properties of Flux Transfer Event Structures on September 4, 1984

I. PAPAMASTORAKIS,[1] G. PASCHMANN, AND W. BAUMJOHANN

Max-Planck-Institut für extraterrestrische Physik, Garching, Federal Republic of Germany

B. U. Ö. SONNERUP

Thayer School of Engineering, Dartmouth College, Hanover, New Hampshire

H. LÜHR

Institut für Geophysik und Meteorologie, Technische Universität, Braunschweig, Federal Republic of Germany

Three flux transfer events (FTEs), observed by the AMPTE/IRM spacecraft in the southern hemisphere magnetosheath are studied by use of variance analysis of measured magnetic fields, B, and convection electric fields, $\mathbf{E}_c = -\mathbf{v} \times \mathbf{B}$, with the objective of determining the orientation and motion of the flux tube or magnetopause bulge causing the FTE signature. These FTEs preceded a series of magnetopause crossings during which the high plasma flow speeds, characteristic of quasi-steady reconnection, were present. The main results are as follows: (1) For each FTE, a moving so-called deHoffmann-Teller (HT) frame of reference can be found, in which the local plasma velocities are nearly antiparallel to the local B vectors and have magnitudes in the range 70%–90% of the local nominal Alfvén speed (assuming all measured ions to be protons). The velocities of motion, v_{HT}, of the HT frames for all three events, and for two subsequent magnetopause crossings, are sufficiently similar so that a single HT frame orders the data in this manner for one full hour. (2) In the first FTE, the spacecraft appears to have sampled fields and flow around a moving tube or elongated magnetopause bulge. The tube orientation and motion (given by the component of v_{HT} perpendicular to the tube axis) could be determined along with impact parameter ($\ell \simeq 1.4a$), tube diameter ($2a \simeq 8000$ km), and, with reasonable assumptions, tube length ($L > 20{,}000$ km). The tube was found to move southward past the spacecraft, consistent with the observed negative-positive signature in the component of B along the magnetopause normal. The ambient magnetosheath plasma moved in the opposite direction. (3) For the second and third FTEs, which were close encounters ($\ell/a < 1$), the tube orientation and therefore its motion could not be reliably determined. (4) On the whole, the observations are consistent with ongoing magnetopause reconnection with a time-modulated reconnection rate that leads to repeated ejection of bulges in the magnetopause from the reconnection site.

1. INTRODUCTION

The phrase "flux transfer event," or FTE for short, is commonly used to refer to a set of observations, near the magnetopause, of a bipolar pulse in the magnetic-field component normal to the magnetopause [*Russell and Elphic*, 1979], and associated characteristic signatures in the time records of measured plasma and energetic particle properties [e.g., *Paschmann et al.*, 1982; *Scholer et al.*, 1982]. The use of this phrase in the literature should not be construed to mean that, for each observed event, an unambiguous demonstration has been made, or can be made, that magnetic connection was present between the magnetosheath and the magnetosphere, i.e., that in some local region magnetic flux crossed the magnetopause. Rather, the term FTE has become a generally accepted and convenient name for an observational syndrome that merits study in its own right, regardless of whether the name is an appropriate one or not.

Since the discovery of FTEs about 10 years ago [*Russell and Elphic*, 1978], the idea of sporadic and patchy magnetic connection across the magnetopause has gained wide acceptance and forms an integral part of a conceptual picture of the solar wind-magnetosphere interaction that is shared by many workers in magnetospheric physics. In this picture, FTEs represent a time-dependent, perhaps patchy form of magnetic field reconnection which may be the dominant mechanism whereby the cross-magnetospheric potential is generated and magnetic flux is transferred from closed field lines in the magnetospheric front lobe to open field lines that are deposited in the geomagnetic tail.

A number of geometrical and quantitative models have been proposed to account for FTEs [*Russell and Elphic*, 1978; 1979; *Lee and Fu*, 1985; *Sonnerup*, 1987; *Scholer*, 1988*a*, *b*; *Southwood et al.*, 1988; *LaBelle-Hamer et al.*, 1988; *Liu and Hu*, 1988]. Although a fairly large number of observational studies of individual events has been undertaken, there is no consensus at present as to which of these models, if any, provides an acceptable explanation for the observed features of FTEs. In our view, there is a need to establish, directly from the observations, certain basic geometrical and kinematic properties of FTEs before an informed choice between models can be made. The present paper represents a step in that direction. As a vehicle for the study, we use three FTEs in the magnetosheath which

[1] Also at Physics Department, University of Crete, and Research Center of Crete, Heraklion, Greece.

Paper number 89JA00198.
0148-0227/89/89JA-00198$05.00

preceded the quasi-steady reconnection events observed by the AMPTE/IRM spacecraft on September 4, 1984. On this inbound pass of the spacecraft, the basic signatures of reconnection, principally the appearance of high-speed flows, were observed [*Paschmann et al.*, 1986] during each of three magnetopause traversals that occurred within a time span of about 30 min. The second of these crossings has been analyzed in considerable detail by *Sonnerup et al.* [1987], who made use of convection electric fields, $\mathbf{E}_c = -\mathbf{v} \times \mathbf{B}$, calculated from measured plasma velocities, $\mathbf{v}$, and magnetic fields, $\mathbf{B}$, to determine the magnetopause orientation, normal speed, and acceleration, and to confirm the validity of the Walén relation in the magnetopause current sheet. As part of this activity, it was shown that a moving so-called deHoffmann-Teller (HT) frame of reference could be found in which the plasma flow was nearly antiparallel to the magnetic field and in which therefore the convection electric field was nearly zero. A convenient methodology for finding the velocity, $\mathbf{v}_{HT}$, and acceleration, $\mathbf{a}_{HT}$, of this frame was developed.

In the present article, we show that the study of convection electric fields provides important insights into the properties of some FTEs as well. In particular, we find that, for each of the three events on September 4, 1984, that form the object of our study, a good deHoffmann-Teller frame exists. Furthermore, we find that the Walén relation, which in this frame has its fundamental form, requiring the field-aligned flow to be Alfvénic, i.e., $\mathbf{v} - \mathbf{v}_{HT} = \pm \mathbf{v}_A$, $\mathbf{v}_A$ being the local Alfvén velocity, is approximately, but not exactly, satisfied in these FTEs. (In other frames of reference, the Walén relation is usually written in terms of velocity differences: $\Delta \mathbf{v} = \pm \Delta \mathbf{v}_A$.) These two results have important implications for the kind of geometrical and physical models that may account for the observations.

Further observational information may be obtained in the case of models that invoke an elongated flux tube or elongated bulge in the magnetopause to account for the characteristic FTE signature. If the axis of elongation can be determined, then the component of the deHoffmann-Teller velocity perpendicular to the axis represents the motion of the FTE tube or bulge normal to itself. This velocity component may be used, together with the event duration, to estimate the bulge diameter. Furthermore, by comparison with the corresponding component of the ambient plasma velocity, one can decide whether the FTE tube is convected with the ambient plasma or moves relative to it. However, determination of the orientation of a flux tube is not a simple matter and may usually not be possible from single spacecraft measurements. An exception is the case where the magnetic field component parallel to the tube axis remains constant throughout the event. In that case, the tube orientation corresponds to the minimum-variance direction of the magnetic field, a fact that has been used recently by *Elphic and Southwood* [1987] in order to estimate a total of 13 FTE tube orientations. This method will be used here also.

The paper is organized as follows. In section 2 we present the basic observed features of the three FTEs in terms of the temporal variations of magnetic field, plasma velocity, plasma density and pressure, and energetic particle density. In section 3, the results of minimum variance analysis of magnetic field and convection electric field are presented along with the determination of the velocity of the deHoffmann-Teller frame, $\mathbf{v}_{HT}$, and the test of the Walén relation. Section 4 contains discussion and interpretation of the results in terms of various proposed FTE models. A summary of our main conclusions is given in section 5.

2. DATA PRESENTATION

An overview of data gathered during the September 4, 1984, inbound pass of AMPTE/IRM through the magnetopause region may be found in *Paschmann et al.* [1986], along with a brief description of the plasma and magnetic field instrumentation and the data reduction procedures. The FTE and magnetopause encounters occurred on the afternoon side of the magnetosphere at about 1540 UT, and in the southern hemisphere, at $-1.2°$ GSE, $-25°$ GSM latitude, and at a geocentric distance of about 8.5 R_E. A detailed plot of relevant plasma and magnetic field data for the time period 1400–1440 UT is shown in Figure 1. Three FTEs are identified in the diagram, although it appears plausible that several additional small events may have occurred. The first of these events has the classical bipolar signature in the normal magnetic field component, here expressed in terms of the elevation angle, λ_B, of the magnetic field relative to a suitable magnetopause tangential surface. The angle λ_B is zero when the field lies in that surface and is $+90°$ when it is directed along the outward-pointing magnetopause normal, N. The azimuth angle φ_B is $0°$ and $+90°$ when the field lies in the first or fourth quadrant of the LN plane and the MN plane, respectively, of the standard boundary-normal coordinate system, LMN, introduced by *Russell and Elphic* [1979]. The negative-positive bipolar signature, seen in Figure 1 for FTE 1, is characteristic of the southern hemisphere. The second and third events have more complicated negative-positive-negative λ_B signatures. The total pressure, $P = p + B^2/2\mu_o$, rises somewhat in the middle of each event, mainly on account of an increase in the magnetic pressure. The plasma density remains nearly constant throughout the first FTE for which also the magnetic and other signatures are relatively weak. For the other two events, the density shows several minima within the main structure. Large increases in plasma velocity and in the flux of energetic ions are present in the centers of these two events.

The first FTE appears to have the basic properties expected in a distant encounter with an FTE tube or bulge where the main observable effects are associated with the draping of magnetic field around the tube or bulge, and associated flow deflections, somewhat in the manner described by *Farrugia et al.* [1987]. The second and third FTEs have complicated and not entirely typical signatures, which nevertheless indicate that the spacecraft may have penetrated the tube or bulge and sampled its complex internal structure. While the signatures of the first event could perhaps have been caused by a ripple on the magnetopause, travelling past the spacecraft, rather than by a moving flux tube or bulge, detailed structural features, as well as the appearance of high-speed flows in the second and third event, would not readily fit such an interpretation.

The magnetopause normal used in Figure 1 and later figures was obtained in two steps. First we constructed a normal from the cross product of $\mathbf{v}$ and $\mathbf{B}$, averaged over an adjacent quiet magnetosheath interval (1422–1426 UT), assuming that $\mathbf{v}$ and $\mathbf{B}$ are (nearly) tangential to the magnetopause. This normal, however, produced slight asym-

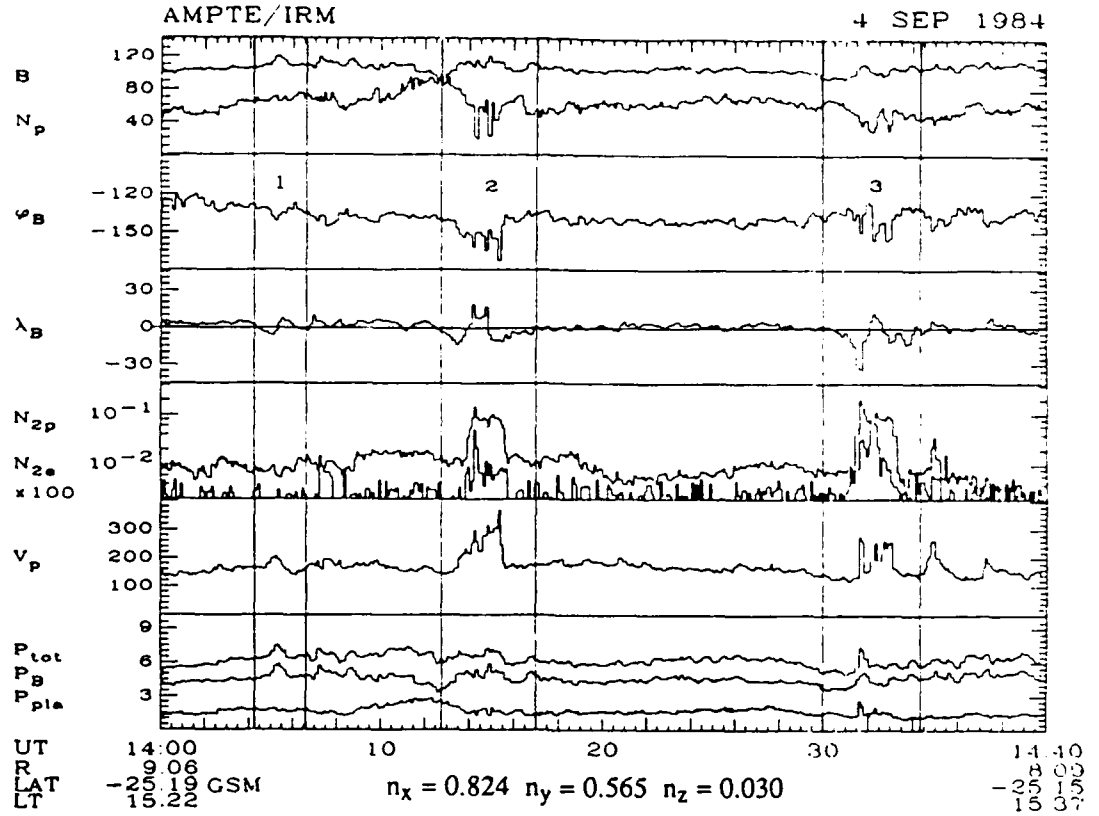

Fig. 1. Overview of measurements during three flux transfer events on September 4, 1984. The AMPTE/IRM spacecraft was in the magnetosheath during the time interval shown, 1400–1440 UT. Starting at the top of the figure, the quantities shown are magnetic-field magnitude, B (nT); measured ion number density, $N_P(\mathrm{cm}^{-3})$; magnetic-field azimuth and elevation angles, φ_B° and λ_B°, in LMN system (see text); number density of energetic ions ($40 > E_p > 9$ kV) and electrons ($30 > E_e > 1.8$ kV), N_{2p} and $100 * N_{2e}(\mathrm{cm}^{-3})$; plasma bulk speed V_P(km/s); total pressure $P_{tot} \equiv P = p + B^2/2\mu_o$, magnetic pressure, $P_B = B^2/2\mu_o$, and plasma pressure $P_{pla} \equiv p$ (all in nPa). The quantities n_x, n_y and n_z represent the GSE components of the magnetopause normal vector used (see text).

metries in the bipolar λ_B signature. To remove this asymmetry, we rotated the normal by 4° around the M axis. The resulting normal vector has the GSE components given in Figure 1 and agrees rather well with the *Fairfield* [1971] normal ($n_x = 0.843$, $n_y = 0.538$, $n_z = -0.018$). On the other hand, there is an 11° discrepancy with the normal determined by *Sonnerup et al.* [1987] for the magnetopause crossing at 1500:42 UT. Deviations of this size or more are not surprising in light of the likely presence of large scale undulations of the magnetopause. They are not in any way critical for the analysis to follow.

3. Data Analysis

The data from each of the three FTEs will be treated in an identical manner. Minimum variance analysis will be performed on the magnetic field data as well as on the convection electric-field data, $\mathbf{E}_e = -\mathbf{v} \times \mathbf{B}$, obtained from the measured 3D velocities and magnetic fields once every 4.3 s. As we shall see, the results of the latter analysis usually indicates whether or not a good deHoffmann-Teller (HT) frame exists. The velocity, $\mathbf{v}_{HT}$, of this frame relative to the spacecraft frame is determined by use of the least squares procedure described in section 2.4 of *Sonnerup et al.* [1987]. According to that procedure, $\mathbf{v}_{HT}$ is determined by minimization of the quantity

$$D = \frac{1}{N} \sum_{m=1}^{N} |(\mathbf{v}^m - \mathbf{v}_{HT}) \times \mathbf{B}^m|^2$$

where the superscript m denotes the N individual data points used in the analysis. The relative residual, D/D_o, is the value of D for the optimal value of $\mathbf{v}_{HT}$ divided by its value for $\mathbf{v}_{HT} = 0$. This residual serves as a measure of the quality of the fit.

The acceleration of the HT frame is also determined, as discussed by Sonnerup et al., but is found to be relatively small for the events under study. For this reason, acceleration effects are not incorporated in the results given here.

The next step in the analysis procedure is to perform minimum-variance analysis on what we refer to as the deHoffmann-Teller electric field, $\mathbf{E}_{HT} = -\mathbf{v}_{HT} \times \mathbf{B}$, and to examine the correlation between the components of $\mathbf{E}_e$ and the corresponding components of $\mathbf{E}_{HT}$. Finally, the relationship between the velocity components measured in the deHoffmann-Teller frame (in which $\mathbf{v}' = \mathbf{v} - \mathbf{v}_{HT}$) and the corresponding components of the Alfvén velocity is exam-

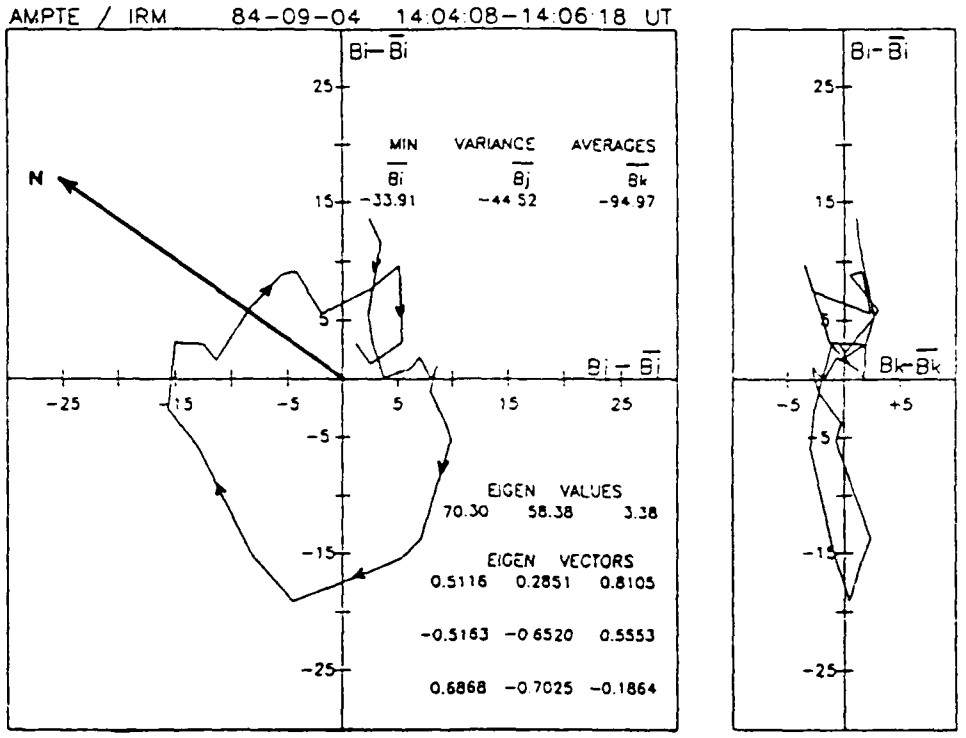

Fig. 2. Hodogram representation of the magnetic field for FTE 1. Average field components, $\bar{B}_i$, $\bar{B}_j$, and $\bar{B}_k$, (in nT) along the maximum variance, intermediate variance, and minimum variance axes (eigenvectors), $\mathbf{i}_B$, $\mathbf{j}_B$, and $\mathbf{k}_B$, have been subtracted from the measured field. The corresponding variances (eigenvalues), λ_{iB}, λ_{jB}, and λ_{kB} (in $(nT)^2$) are given in the figure along with the eigenvectors, $\mathbf{i}_B$ (first row), $\mathbf{j}_B$ (second row), and $\mathbf{k}_B$ (third row), in the GSE coordinate system.

ined with the objective of testing to what extent the Walén relation, $\mathbf{v} - \mathbf{v}_{HT} = \pm \mathbf{v}_A$, is satisfied.

3.1. *FTE 1*

The results of the minimum-variance analysis of the magnetic field for the data interval 1404:08–1406:18 UT are shown in Figure 2 in the usual hodogram form, where the maximum, intermediate, and minimum variance directions are denoted by $\mathbf{i}_B$, $\mathbf{j}_B$, and $\mathbf{k}_B$, respectively, the corresponding variances being λ_{iB},λ_{jB}, and λ_{kB}. Note that the average field components along the three axes have been subtracted in the hodograms. It is seen from the large value of the ratio $\lambda_{jB}/\lambda_{kB} = 58.4/3.4$, as well as from the relatively unsystematic nature of the variations in the field component $\mathbf{B}_k$ (shown in the hodogram on the right), that a fairly reliable minimum-variance direction, $\mathbf{k}_B$, is at hand. In the next section, this direction will be used as a predictor of the axis of the flux tube or bulge causing the magnetic field deflection. The major component of the magnetic field, −95 nT, is along $\mathbf{k}_B$. The hodogram on the left in Figure 2 shows the behavior of the magnetic-field components B_i and B_j in the plane perpendicular to $\mathbf{k}_B$ (the average values of these components are −34 nT and −44.5 nT, respectively). In this plane, we have also shown the approximate orientation of the vector, N, normal to the magnetopause. The looped hodogram trace is then seen to represent the presence of a negative normal magnetic field component, B_N, in the first half and a positive B_N in the second half of the event, as well as the occurrence of a maximum in the field magnitude near the center of the event.

Hodograms representing the convection electric field, $\mathbf{E}_c = -\mathbf{v} \times \mathbf{B}$, in the eigenvector system $(\mathbf{i},\mathbf{j},\mathbf{k})$ of the corresponding variance matrix are shown in Figure 3*a*. The most striking feature in these diagrams is the existence of an extremely well defined minimum-variance direction, k. The ratio of intermediate variance to minimum variance, $\lambda_j/\lambda_k = 6.4/0.04$, is very large and the electric-field component along k, as well as the fluctuations in that component, are both extremely small. These features provide an indication that an excellent deHoffmann-Teller frame should exist for this data set and that the transformation velocity $\mathbf{v}_{HT}$ to this frame should be closely aligned with the k vector. As mentioned above, we have determined this transformation velocity by finding the best least squares fit between $\mathbf{E}_c$ and $\mathbf{E}_{HT} \equiv -\mathbf{v}_{HT} \times \mathbf{B}$, the result being $\mathbf{v}_{HT}$ = (−218, 313, 8) km/s with a relative residual $D/D_o = 0.010$. Here, and in the remainder of the paper, all vector components are given in the GSE coordinate system, XYZ. The direction of this $\mathbf{v}_{HT}$ vector deviates from the $-\mathbf{k}$ direction by only 2°. The electric field $\mathbf{E}_{HT}$ is the field that would be present in the spacecraft frame if a perfect deHoffmann-Teller frame had existed. Thus, $\mathbf{E}_{HT}$ can be thought of as a predictor of the field $\mathbf{E}_c$. The results of minimum-variance analysis on $\mathbf{E}_{HT}$ are shown in Figure 3*b*. It is seen that a striking similarity does in fact exist between hodograms representing the fields $\mathbf{E}_c$ and $\mathbf{E}_{HT}$. Note that the $\mathbf{v}_{HT}$ vector also happens to be nearly aligned with $\mathbf{k}_B$, the angle between the two being

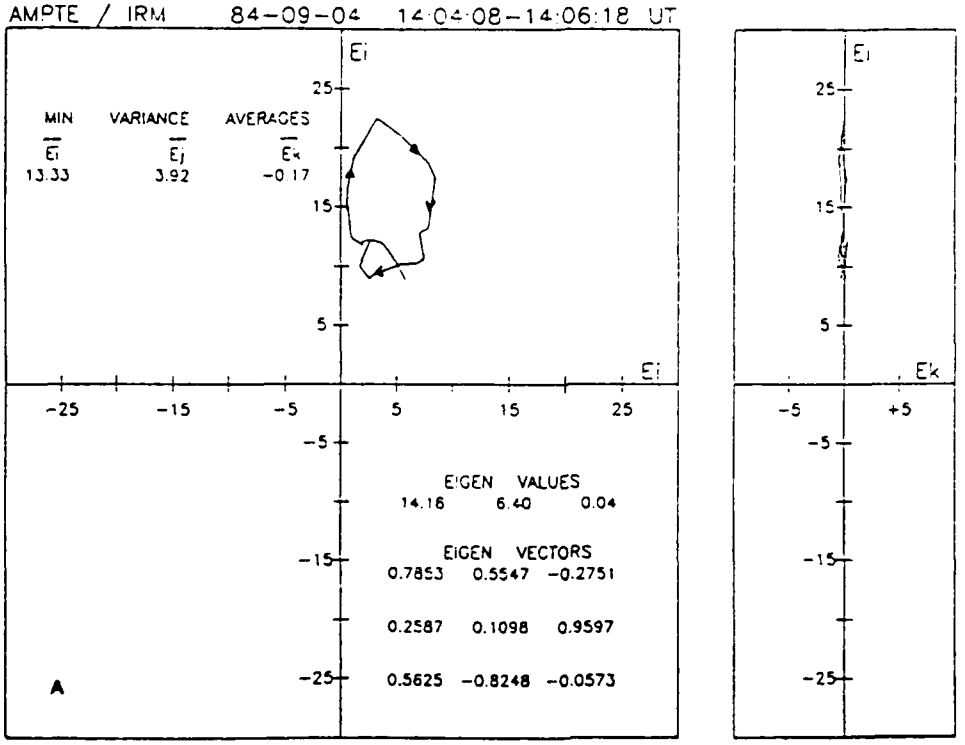

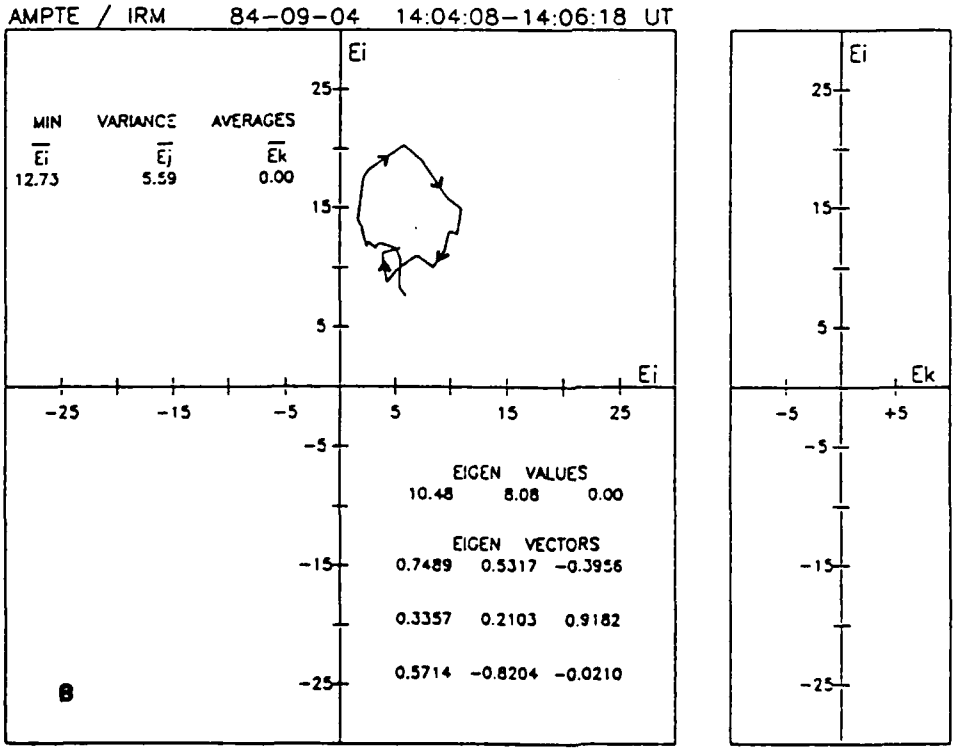

Fig. 3. Hodogram representation of (a) convection electric field, $\mathbf{E}_c = -\mathbf{v} \times \mathbf{B}$, and (b) deHoffmann-Teller (HT) electric field, $\mathbf{E}_{HT} = -\mathbf{v}_{HT} \times \mathbf{B}$ (both in mV/m), for FTE 1. The transformation velocity $\mathbf{v}_{HT}$ has GSE components (−218, 313, 8) km/s. Same format as in Figure 2, except that average values of the field components have not been subtracted. The similarity between the $\mathbf{E}_c$ and $\mathbf{E}_{HT}$ hodograms indicates that a good HT frame exists. Note that in 3b the right-hand hodogram trace has $\mathbf{E}_{HT} \cdot \mathbf{k} \equiv 0$.

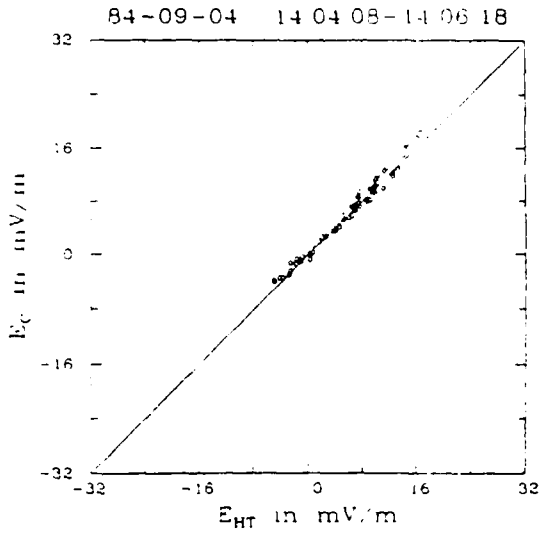

Fig. 4. Relationship between the three GSE components of the convection electric field, $\mathbf{E}_c = -\mathbf{v} \times \mathbf{B}$, and the corresponding components of the deHoffmann-Teller electric field, $\mathbf{E}_{HT} = -\mathbf{v}_{HT} \times \mathbf{B}$ for FTE 1. The solid line shown passes through the origin and has unit slope: it represents the ideal relationship. The actual regression line, constrained to pass through the origin, and based on orthogonal distances, has slope = 1.045 ± 0.011 and correlation coefficient = 0.990.

only 13°, so that the (i,j) plane in Figure 3 is tilted relative to the $i_B j_B$ plane in Figure 2 by only 13°. It is then clear that there exists a simple explanation for the loop-shaped electric hodogram in the (i,j) plane: we have $E_{HTi} = v_{HT} B_j$ and $E_{HTj} = -v_{HT} B_i$, indicating that the electric field loop is a simple (but somewhat distorted) image of the magnetic loop on the left in Figure 2. In general, the $E_i E_j$ hodogram of $\mathbf{E}_{HT}$ represents the behavior of the component of $\mathbf{B}$ perpendicular to $\mathbf{v}_{HT}$. The new information it contains, beyond that provided by the B hodograms, consists of the direction and magnitude of the transformation velocity $\mathbf{v}_{HT}$.

The relationship between the three components of $\mathbf{E}_c$ and the corresponding components of $\mathbf{E}_{HT}$ is shown in a scatter plot in Figure 4. It is seen that the data points are gathered in a narrow band around the ideal 45° line. This remarkably accurate agreement of $\mathbf{E}_{HT}$ with $\mathbf{E}_c$ constitutes one of our main experimental results. It will be discussed further in section 4.

The relationship between the components of the plasma velocity, $(\mathbf{v} - \mathbf{v}_{HT})$, in the deHoffmann-Teller frame, and the corresponding components of a nominal Alfvén velocity, $\mathbf{v}_{Ae} = \mathbf{B}(1-\alpha)^{1/2}(\mu_o n m_p)^{-1/2}$, is shown in Figure 5. Note that in calculating $\mathbf{v}_{Ae}$ we have used the individual measured B vectors but average values of measured pressure anisotropy, $\alpha = (p_\parallel - p_\perp)\mu_o/B^2$, and of measured number density, n, during the event and that we have assumed all particles to be protons (mass = m_p). Thus the diagram shows the relationship between $(\mathbf{v} - \mathbf{v}_{HT})$ and $\mathbf{B}$, the latter expressed as a nominal Alfvén velocity, rather than between $(\mathbf{v} - \mathbf{v}_{HT})$ and the local value of $\mathbf{v}_A$ as required in the true local Walén relation. However, for FTE 1 the difference between the nominal and the true Walén relation is very small.

Four items should be noted in Figure 5. First, an excellent linear relationship exists between the components of $(\mathbf{v} - \mathbf{v}_{HT})$ and the corresponding components of $\mathbf{v}_{Ae}$. The regression line shown has been constrained to pass through the origin but it is evident that the data are consistent with this behavior. This result requires not only that the vectors $\mathbf{v} - \mathbf{v}_{HT}$ are nearly aligned with the vectors $\mathbf{B}$ but, additionally, that the magnitudes of the two vectors are proportional, with a fixed constant of proportionality, throughout the event. Second, the data are seen to be clustered in two groups; the ordinary correlation coefficient is misleading in such circumstances and is therefore not given in the figure. The reason for the clustering is that, in the coordinate system used, none of the three velocity components is near zero. Third, the negative slope of the correlation line shown in the figure indicates that, in the deHoffmann-Teller frame, the flow is antiparallel to the magnetic field. This is also the flow direction expected and observed in quasisteady reconnection events south of the reconnection line and it is, indeed, the flow direction found in the magnetopause encounters on this pass discussed by *Paschmann et al.* [1986] and *Sonnerup et al.* [1987]. The fourth point to be made is that the slope of the regression line is −0.816, i.e., its magnitude is somewhat less than the value of unity required by the nominal Walén relation. Perfect agreement with that relation could be achieved by assuming the presence of 5% alphas and 2% oxygen ions (by number). Alternatively, the actual situation may have been that the plasma contained only lesser amounts of heavy ions and that the field-aligned flow speed was somewhat less than the actual Alfvén speed.

3.2. *FTE 2*

The results of the analysis of this event are presented in Figures 6–9, in the same format as before. The data interval used is 1412:22–1417:00 UT. As is seen in Figure 6, the magnetic structure in this case is complicated; in particular, the minimum-variance direction k_B should be considered a far less reliable predictor of the flux-tube axis than in the previous event.

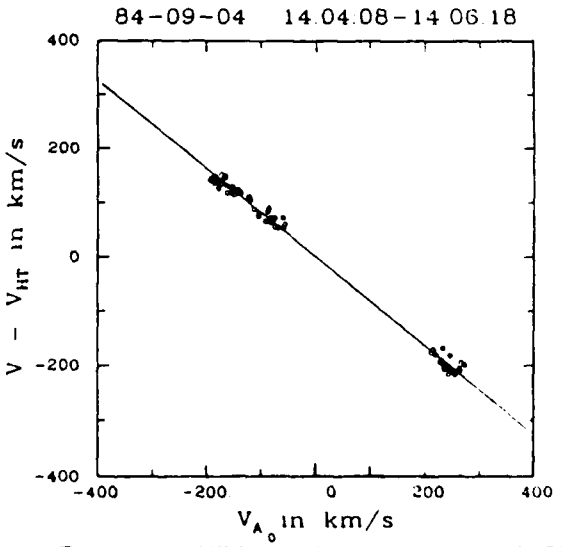

Fig. 5. Test of nominal Walén relation, $\mathbf{v} - \mathbf{v}_{HT} = \pm \mathbf{v}_{Ae}$ for FTE 1. Nominal Alfvén velocities, $\mathbf{v}_{Ae}$, are calculated from measured local magnetic fields, using average values of pressure anisotropy, $\bar{\alpha} = -0.09$, and number density, $\bar{n} = 68$ cm^{-3}, during the event, and assuming all measured ions to be protons. The regression line passing through the origin and based on orthogonal distances has slope = -0.816 ± 0.007.

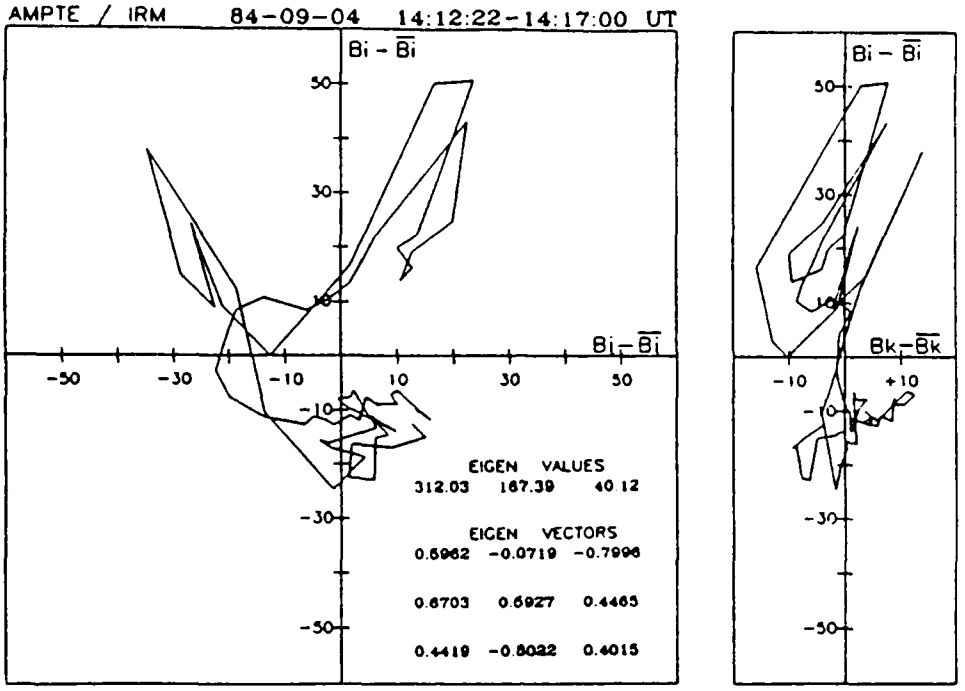

Fig. 6. *Hodogram representation of magnetic field for FTE 2. Same format as in Figure 2.*

In spite of the complicated magnetic structure, the $\mathbf{E}_c$ hodogram on the right in Figure 7*a* shows a nearly vanishing k component of the field, with a small variance, an indication that a good deHoffmann-Teller frame may again exist. The velocity of this frame is found to be $\mathbf{v}_{HT}$ = (-226, 321, -14) km/s, which is rather similar to the result for the first event, except that the relative residual, $D/D_o = 0.033$, is larger. Results of the minimum-variance analysis on $\mathbf{E}_{HT} = -\mathbf{v}_{HT} \times \mathbf{B}$ are shown in Figure 7*b*. Comparison of the left-hand hodogram in Figure 7*b* to that in Figure 7*a* gives a visual impression of the correlation between $\mathbf{E}_c$ and $\mathbf{E}_{HT}$ (the relationship of the former to the left-hand **B** hodogram in Figure 6 is also evident). The scatter plot of the components of these two fields is shown in Figure 8. Again, the data points are well clustered around the ideal 45° line although the scatter is somewhat larger than for FTE 1.

The nominal Walén correlation for FTE 2 is shown in Figure 9. The data points are seen to cluster around a regression line of slope -0.860 through the origin, a result that is quantitatively consistent with the nominal Walén relation only if one assumes, as for FTE 1, a small amount of heavier ions in the plasma. In our view, it is more likely that the flow speed in the HT frame was in fact somewhat less than the nominal Alfvén speed (which is again based on average density and pressure anisotropy during the event).

3.3. *FTE 3*

This event is presented in Figures 10–13, in the same format as before. The data interval used is 1430:01–1434:09 UT. As can be seen from Figure 10, the magnetic field structure is again complicated and is quite different from that seen in FTE 2. As in that case, the $\mathbf{k}_B$ vector should be considered a rather unreliable predictor of the flux-tube axis. The $\mathbf{E}_c$ hodogram on the right in Figure 11*a* again shows very small variance in the k direction although the average $\mathbf{E}_c$ component does not vanish, as was nearly the case in FTEs 1 and 2. Nevertheless, a fairly good deHoffmann Teller frame appears to exist, moving with velocity $\mathbf{v}_{HT}$ = (-206, 285, -2) km/s (relative residual $D/D_o = 0.041$). Note that this $\mathbf{v}_{HT}$ is similar to the corresponding velocities for FTEs 1 and 2. The results of minimum-variance analysis on $\mathbf{E}_{HT} = -\mathbf{v}_{HT} \times \mathbf{B}$ are shown in Figure 11*b* which exhibits substantial similarities to the $\mathbf{E}_c$ data in Figure 11*a*. The correlation between the two sets of electric-field components remains good as illustrated in Figure 12. Finally, the nominal Walén correlation for this event is shown in Figure 13. The scatter in the data is substantial but, as in the previous two cases, a regression line through the origin provides a good fit. The slope of this line, -0.729, indicates that a significant number of heavier ions (e.g., 5% oxygen) would have to have been present in order for the nominal Walén relation to be satisfied. Alternatively, and more likely, the field-aligned flow speed may in fact have been less than the nominal Alfvén speed.

3.4. *General Comments*

In studying the Walén relation, we have also tried to use the actual local Alfvén speed, based on individual measured, rather than average, values for the pressure anisotropy, α, and number density, n, but retaining the assumption that all measured particles were protons. For FTE 1, in which the measured number density was nearly constant throughout the event, the resulting correlation differs little from the one shown in Figure 5, but for FTE 2 and, in particular, FTE 3 the scatter in the data increases substantially. This effect is caused by the large fluctuations in n, evident in Figure 1. The improved correlation, when a constant number density is used, indicates that, rather than the proportionality between $\mathbf{v} - \mathbf{v}_{HT}$ and $\mathbf{v}_A$ predicted by the true local

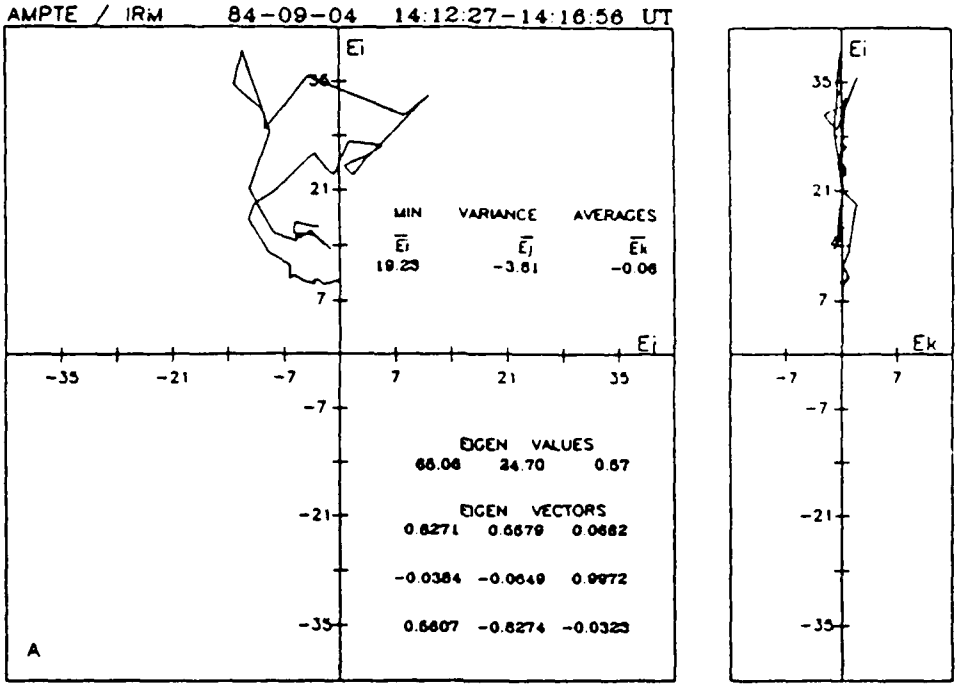

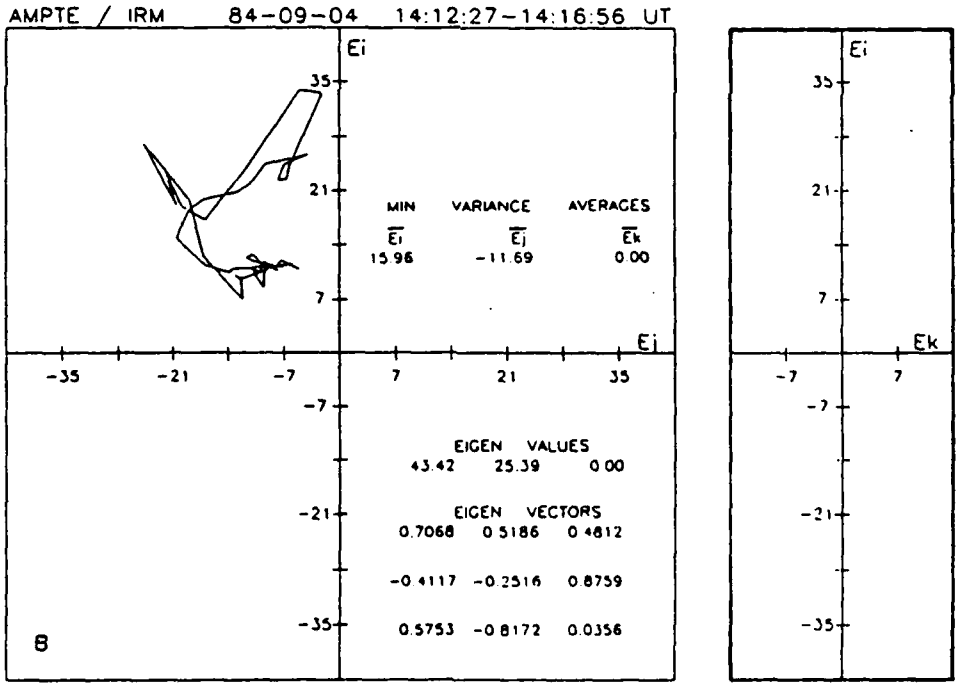

Fig. 7. Hodogram representation of (*a*) convection electric field, $\mathbf{E}_c$, and (*b*) deHoffmann-Teller electric field, $\mathbf{E}_{HT}$, for FTE 2. Same format as in Figure 3. The transformation velocity $\mathbf{v}_{HT}$ has GSE components (−226, 321, −14) km/s.

Walén relation, a linear relationship between $\mathbf{v} - \mathbf{v}_{HT}$ and $\mathbf{B}$ was a fundamental property of these FTEs. However, one cannot exclude the possibility that there may have been an anticorrelation between number density and effective particle mass with a higher proportion of heavy ions where the number density was low so that $\mathbf{B}$ and $\mathbf{v}_A$ were directly proportional. In this latter context, we have noted that the data scatter in the Walén diagrams decreases slightly in all three events, below what is shown in Figures 5, 9, and 13, if the nominal Alfvén velocity, $\mathbf{v}_{A_o}$ is replaced by $\mathbf{B}(1-\alpha)$, using

local measured values of the pressure anisotropy. As pointed out in *Paschmann et al.* [1986], the combination $\mathbf{B}(1-\alpha)$ arises directly from the tangential stress balance across a one-dimensional discontinuity. Furthermore, in a thick rotational discontinuity the relationship $\rho(1-\alpha) = \text{const}$ holds so that, by elimination of ρ, the instantaneous Alfvén velocity $\mathbf{v}_A = \mathbf{B}(1-\alpha)^{1/2}(\mu_o\rho)^{-1/2}$ is directly proportional to $\mathbf{B}(1-\alpha)$. For this reason, $\mathbf{B}(1-\alpha)$ is an appropriate variable to use in testing the Walén relation in the magnetopause itself. As pointed out by *Paschmann et al.* [1986], it has the advantage over $\mathbf{v}_A$ itself of being far less prone to uncertainties caused by the presence of heavy ions in the plasma. However, it is not clear whether its use is justified for FTEs since they are not one dimensional structures.

A second general comment concerns the existence of deHoffmann-Teller frames for each of the three events. We have already noted that the velocities, $\mathbf{v}_{HT}$, obtained for these events are rather similar. They also do not deviate much from the $\mathbf{v}_{HT}$, obtained by *Sonnerup et al.* [1987] for the second magnetopause crossing, at 1501 UT, on this pass. Thus it is natural to ask whether an acceptable common deHoffmann-Teller transformation velocity $\mathbf{v}_{HT}$ can be found for the entire pass. We have used our least-squares procedure to obtain $\mathbf{v}_{HT}$ = (-237, 319, -25) km/s (with a relative residual $D/D_o = 0.071$) for the one-hour interval 1403:02–1502:56 UT. The scatter plot of $\mathbf{E}_c$ versus $\mathbf{E}_{HT}$ and the Walén correlation are shown in Figures 14*a* and 14*b*. The correlation in both diagrams is impressive, given the long data interval used. In the former figure, the correlation coefficient is 0.960; in the latter it is 0.968 with a regression line slope of -0.866. Some data clustering of the type evident in Figures 5, 9, and 13 is present in Figure 14*b* also. However, the spread in the points is now sufficient to make the correlation coefficient a useful indicator of the quality of the fit. This result is similar to that reported by *Aggson et al.* [1983] for a 15-min period of ISEE 1 magnetosheath/magnetosphere data.

4. DATA INTERPRETATION

4.1. *FTE 1*

As is evident from Figure 2, the magnetic field in the first FTE exhibits rather well organized behavior. For this reason we start with the interpretation of this event. It is first noted that the magnetic field and flow behave in a manner that is in substantial qualitative agreement with a simple model of magnetic field draping over, and steady field aligned flow past a flux tube of semicircular cross section, proposed by *Farrugia et al.* [1987], and shown qualitatively in Figure 15. The key assumptions used by those authors is that of a current-free magnetic field and an associated irrotational, field-aligned, incompressible flow, $\mathbf{v} = C\mathbf{B}$, where C is a constant. In this model, the component of $\mathbf{B}$ (and of $\mathbf{v}$) along the cylinder axis remains constant. Thus, the variance in this field component is zero; for this reason, we tentatively identify the minimum-variance direction, $\mathbf{k}_B$, for the magnetic field with the flux-tube axis. The shape of the magnetic-field hodogram in a plane perpendicular to this axis, i.e., the $(\mathbf{i}_B, \mathbf{j}_B)$ plane in Figure 2, predicted by the Farrugia et al. model can be shown to be that of a "cardioid," with its size determined by the "impact parameter," ℓ/a, a being the cylinder radius and ℓ the distance of the spacecraft trajectory above the cylinder axis, as shown in the figure. On the basis of this model and the size of the field loop in the hodogram on the left in Figure 2, we estimate an impact parameter of about 1.4, as shown in Figure 15. However, it is noted that the left-hand hodogram in Figure 2 does not have the precise shape of a cardioid, indicating that the actual flux tube or bulge over which the measured magnetic field is draped does not have a semicircular cross section or, more realistically, the cross section associated with any of the field-line surfaces draped over a semicircular object. Other cross sections, and corresponding hodogram traces, can be generated in a straightforward manner by use of potential theory. For example, it is easy to show that a circular hodogram shape is obtained if the two-dimensional dipole used to produce the circular cylinder is replaced by a line current.

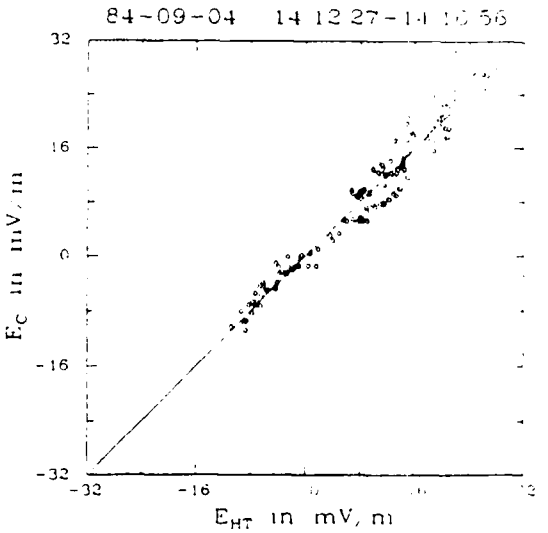

Fig. 8. Relationship of components of $\mathbf{E}_c$ and $\mathbf{E}_{HT}$ for FTE 2. Actual regression line through the origin has slope 1.016 ± 0.015 and correlation coefficient = 0.971.

The actual measured magnetic field vectors are also shown in two projections in Figure 15. It is clear from this figure

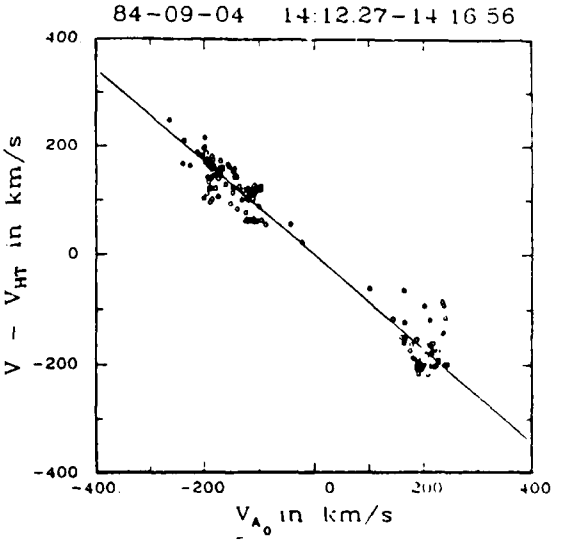

Fig. 9. Test of nominal Walén relation for FTE 2. Nominal Alfvén velocities, $\mathbf{v}_{A_0}$, are based on $\bar{\alpha} = -0.06$ and $\bar{n} = 64$ cm^{-3}. The regression line passing through the origin has slope $= -0.860 \pm 0.015$.

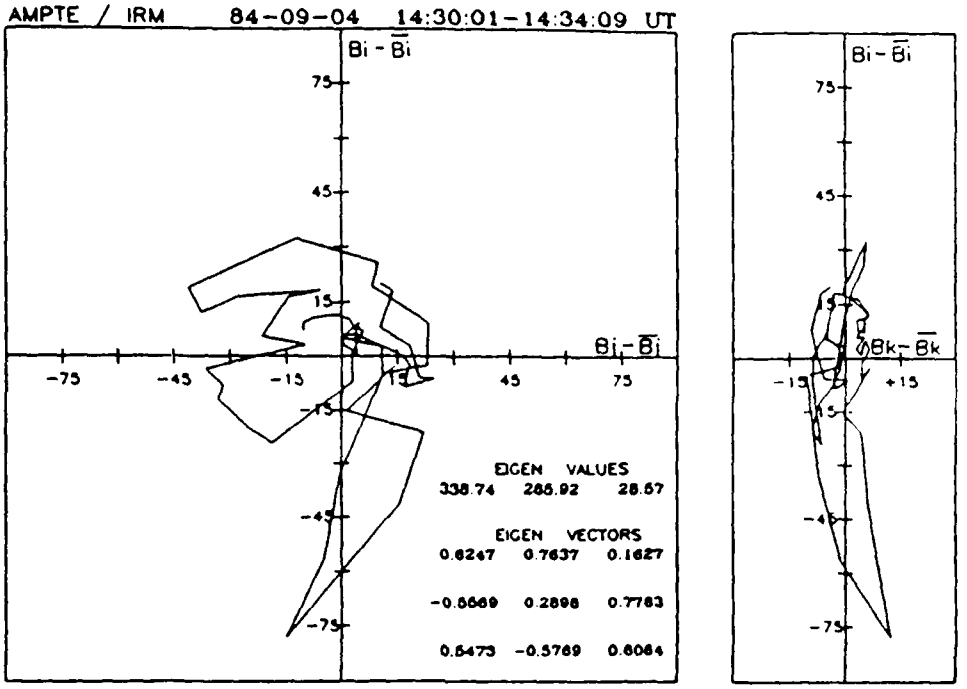

Fig. 10. Hodogram representation of magnetic field for FTE 3. Same format as in Figure 2.

that the flux tube direction does not coincide with the ambient magnetosheath field direction or with the field direction at the center of the event.

A second key assumption in the model by *Farrugia et al.* [1987] is that a frame of reference exists in which the flow is field-aligned. Since we have found an excellent deHoffmann Teller frame for this event, this assumption can be considered experimentally verified. Furthermore, with the assumptions made by Farrugia et al., it follows from the equations of motion that the magnitude of the velocity must be proportional to the magnetic field, with the constant of proportionality, C, independent of position and time. This result is verified in Figure 5.

The additional feature in Figure 5, namely that the flow speed is as high as 82% of the nominal Alfvén speed, is not predicted by the Farrugia et al. model, in which the flow speed can be chosen arbitrarily. If the mass composition was such that the actual Alfvén speed was only 82% of the nominal values used in Figure 5, then the event can be considered to be a nonlinear multidimensional Alfvén wave of the type discussed by *Walén* [1944]. It is noted that in such a case the total pressure, $P = p + B^2/2\mu_o$, should be constant throughout the event. As can be seen in Figure 1, this is not the case. The total pressure is higher in the center of the event by about 1.1 nPa. This amounts to 22% of the dynamic pressure, $\varrho v_A^2/2$, associated with the Alfvén speed at the center of the event, thus providing evidence that the actual flow speed there was about 11% less than the Alfvén speed. This calculation remains somewhat uncertain because the measured plasma pressure also depends to some extent on the actual mass composition, although much less so than the mass density [*Paschmann et al.*, 1986]. A further unexplained feature is that the plasma pressure does not display the minimum at the center of the event that would be expected from Bernoulli's equation in irrotational flow. This is perhaps an indication that the external flow may have been somewhat rotational, contrary to one of the assumptions made in the Farrugia et al. model.

We turn now to a discussion of the orientation of the flux-tube axis (or, more precisely, the $\mathbf{k}_B$ vector) and the deHoffmann-Teller velocity vector, $\mathbf{v}_{HT}$, relative to each other and relative to the magnetospheric and magnetosheath magnetic fields as well as the ambient magnetosheath plasma flow speed. A diagram showing the location of the projections of these vectors in a plane tangential to the magnetopause (the LM plane) is given in Figure 16*a*. The vectors are nearly, but not exactly, perpendicular to the chosen magnetopause normal vector N. For example, the vectors $\mathbf{k}_B$ and $\mathbf{v}_{HT}$ form angles of 79.9° and 90.5°, respectively, with N. Figure 16*a* shows that the flux-tube direction does not coincide with either the direction of the net magnetopause current, $\mathbf{I}_{mp}$, as in the simulations by *Fu and Lee* [1985] or *Scholer* [1988*a*], or with the magnetosheath field direction. Rather the axis falls halfway between these two directions. It is also seen that the flux tube moves in the southward direction with a velocity of about 63 km/s which is the component of $\mathbf{v}_{HT}$ perpendicular to $\mathbf{k}_B$ (the component of $\mathbf{v}_{HT}$ along the tube axis has no physical significance other than that of representing the motion of the HT frame along the tube axis required to make the flow field aligned). On the other hand, the ambient magnetosheath plasma flow velocity, $\mathbf{v}_{sh}$, has a component perpendicular to the tube axis that is directed northeastward and has a magnitude of about 45 km/s. Although this flow direction is unusual, given the location of the event relative to the subsolar point, it could perhaps be explained in terms of the fast-mode expansion present in the inflow regions of the Petschek reconnection model [*Vasyliunas*, 1975] and in the recent simulations by

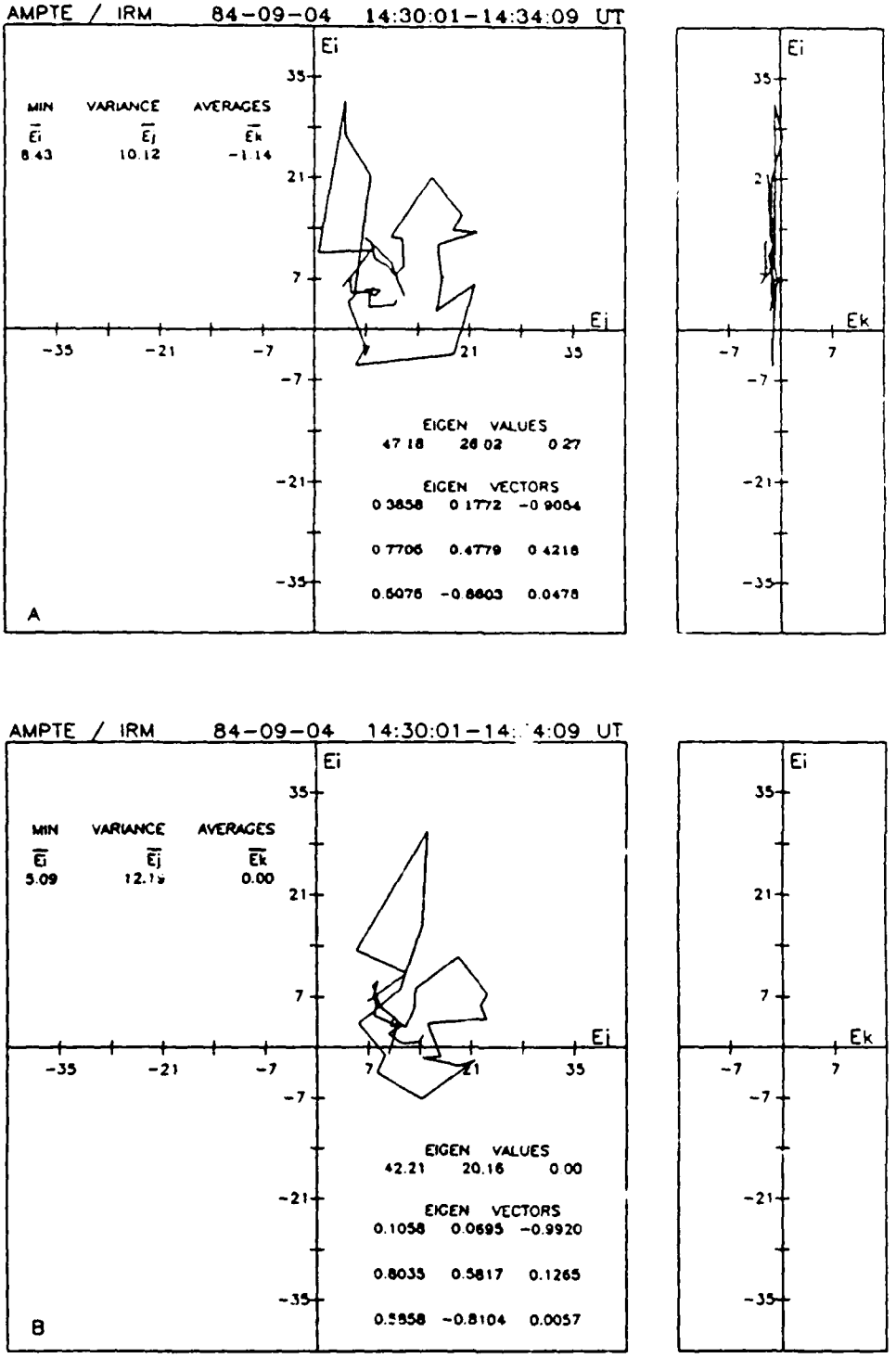

Fig. 11. Hodogram representation of (*a*) convection electric field, $\mathbf{E}_c$, and (*b*) the Hoffmann-Teller electric field, $\mathbf{E}_{HT}$, for FTE 3. Same format as in Figure 3. The transformation velocity $\mathbf{v}_{HT}$ has GSE components (−206, 285, −2) km/s.

Scholer [1988a]. However, regardless of the explanation for the magnetosheath flow direction, an important conclusion from Figure 16*a* is that the flux tube is not convected with the ambient flow. Rather, it moves southward relative to the magnetosheath plasma with a speed that is about 82% of the nominal Alfvén speed, based on the component of the magnetosheath magnetic field perpendicular to the tube axis. Furthermore, although there is some uncertainty concerning the actual flux-tube orientation, it is clear that the axis could not be located south of the $\mathbf{v}_{HT}$ vector for then the tube would be moving northward which would yield an incorrect B_N signature.

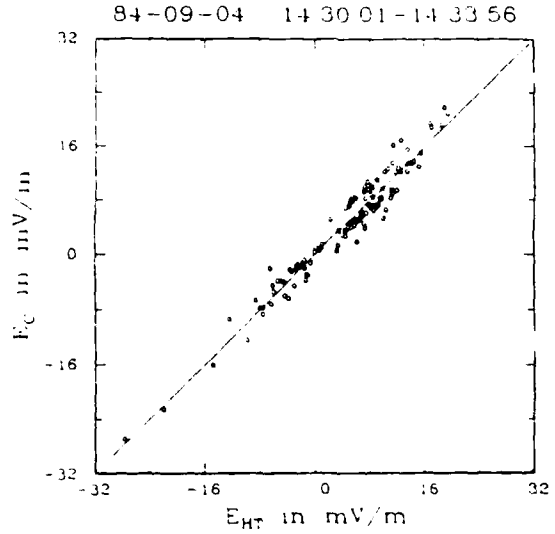

Fig. 12. Relationship of components of $\mathbf{E}_c$ and $\mathbf{E}_{HT}$ for FTE 3. Actual regression line through the origin has slope 1.019 ± 0.019 and correlation coefficient = 0.971.

Motion of FTE flux tubes relative to the ambient magnetosheath plasma has been invoked by *Daly et al.* [1984] in discussing certain anomalous FTEs observed by the ISEE spacecraft. However, to our knowledge the case discussed here provides the first quantitative experimental determination, from a single spacecraft, of such relative motion.

Finally, the component of $\mathbf{v}_{HT}$ perpendicular to the tube axis, 63 km/s (relative to the spacecraft), can be used together with the duration of the event, $\Delta t = 130$ s, to estimate a distance along the magnetopause of about 8,000 km, which one may expect to be comparable to the diameter of the flux tube or bulge causing the magnetic and flow deflections. An FTE tube diameter of the order of 1 R_E has been reported by *Saunders et al.* [1984] from ISEE 1 and 2 observations. Thus the value 8,000 km is reasonable, although it

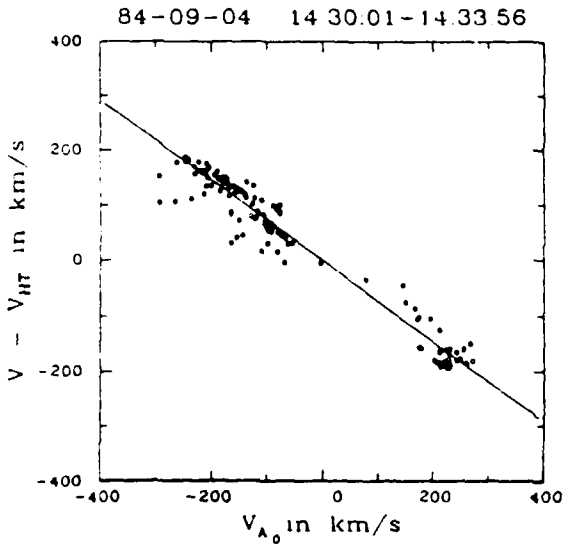

Fig. 13. Test of nominal Walén relation for FTE 3. Nominal Alfvén velocities, $\mathbf{v}_{A_0}$, are based on $\bar{\alpha} = -0.04$ and $\bar{n} = 53$ cm^{-3}. The regression line passing through the origin has slope $= -0.729 \pm 0.015$.

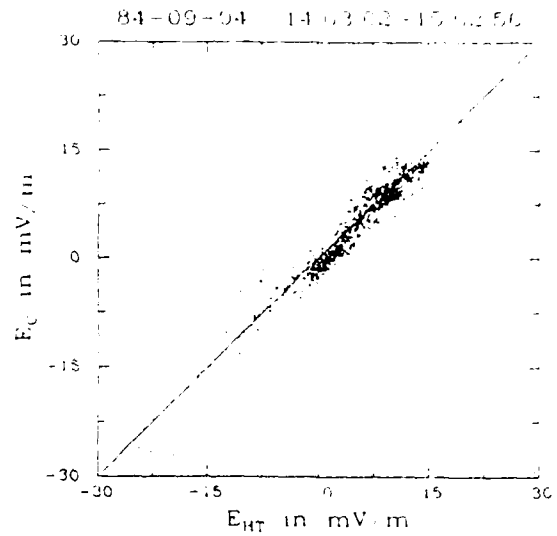

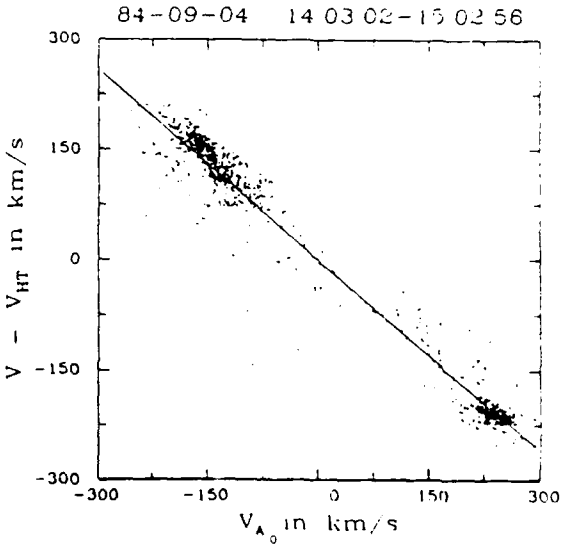

Fig. 14. (*a*) Relationship of corresponding components of $\mathbf{E}_c$ and $\mathbf{E}_{HT}$ for a 1 hour data interval which includes the three FTEs as well as two magnetopause crossings. Actual regression line through the origin has slope 1.038 ± 0.007 and correlation coefficient = 0.960. (*b*) Test of nominal Walén relation for the same interval. Nominal Alfvén velocities, $\mathbf{v}_{A_0}$, are based on $\bar{\alpha} = -0.05$ and $\bar{n} = 59$ cm^{-3}. The regression line passing through the origin has slope $= -0.866 \pm 0.005$, and correlation coefficient = 0.968.

may be in error by as much as a factor 2, owing to uncertainties in the flux-tube speed, 63 km/s. These uncertainties are caused by possible errors in the flux-tube and normal vector orientations. A characteristic length along the flux-tube axis is more difficult to obtain: if the entire flux tube were moving along its axis, $\mathbf{k}_B$, with speed $\mathbf{v}_{sh} \cdot \mathbf{k}_B$, a plausible assumption, then the actual tube length would have been at least $|\mathbf{v}_{sh} \cdot \mathbf{k}_B| \, \Delta t = 19,800$ km.

4.2. *FTEs 2 and 3*

The vectors $\mathbf{k}_B$ and $\mathbf{v}_{HT}$ for these two events are shown in Figure 16*b*. As mentioned already, and as is evident from Figure 16, the $\mathbf{v}_{HT}$ vectors are similar for all three events. They also agree rather well with the $\mathbf{v}_{HT}$ vector (−294, 320, −69) km/s for the magnetopause crossing at 1501 UT [*Son-*

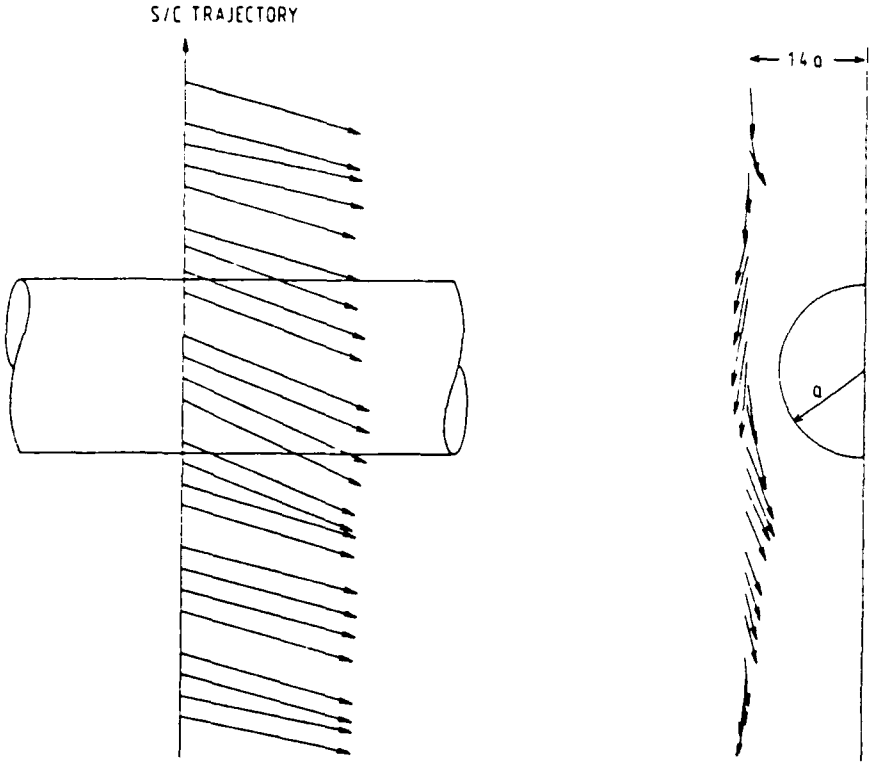

Fig. 15. Comparison between measured magnetic-field vectors in FTE 1 and a model by *Farrugia et al.* [1987] representing a potential magnetic field outside a diamagnetic semicylinder. An impact parameter $\ell/a \simeq 1.4$ can be deduced from the model.

nerup et al., 1987]. For the $\mathbf{k}_B$ vectors, the situation is rather different. As can be seen in Figure 16*b*, these vectors now lie closer to the magnetosheath field direction and well south of the $\mathbf{v}_{HT}$ vectors, thus implying northward flux-tube motion with a speed normal to the flux tube axis comparable to the magnetosheath flow component normal to the tube. In other words, if one believes that the $\mathbf{k}_B$ vectors represent the actual flux-tube axes, then the tubes would be convected more or less with the magnetopause plasma. For FTE 3, where the $\mathbf{k}_B$ vector is south of the magnetosheath field vector, the B_N draping signature would then remain the basic negative-positive excursion characteristic of the southern hemisphere, but for FTE 2 the B_N signature would be reversed. In reality, both events have an unusual negative-positive-negative B_N signature that is difficult to account for in terms of simple field-line draping around a flux tube, unless one assumes, either that the sense of motion of the flux tube reversed itself during the event, or that the spacecraft encountered flux tubes that were detached from the magnetopause. We are not able to provide a definite resolution of the dilemma posed by the unusual $\mathbf{k}_B$ orientations found for FTEs 2 and 3 and the unusual B_N signatures associated with those two events. However, it should be remembered that for FTEs 2 and 3 the spacecraft is likely to have penetrated the actual flux tubes providing magnetic connection between the magnetosheath and the magnetosphere across the magnetopause. Within such tubes, azimuthal electrical currents may be present, causing systematic variations in the axial magnetic field so that the minimum variance direction, $\mathbf{k}_B$, no longer coincides with the flux tube axis. In the extreme case of a central encounter (impact parameter = 0) with such a flux tube, the vector $\mathbf{k}_B$ is in fact perpendicular to the tube axis. Axial currents, if present, will influence the B_N signature. In other words, a priori one should not expect the Farrugia et al. draping model to be fully applicable to FTEs 2 and 3.

It should be added that the existence of a good deHoffmann-Teller frame and a convincing correlation between the components of $(\mathbf{v} - \mathbf{v}_{HT})$ and the corresponding components of B, with the flow speed amounting to a large fraction of the nominal Alfvén speed, are important properties of FTEs 2 and 3 that remain valid regardless of the resolution of the above dilemma. Furthermore, the fact that the flow in the deHoffmann-Teller frame is antiparallel to the B field, as was the case in FTE 1, indicates that any explanation of the B_N signature that invokes motion of a reconnection line past the spacecraft is not viable.

5. SUMMARY AND DISCUSSION

The main observational results of this study can be summarized in four points.

1. We have shown that for each of the three adjacent southern hemisphere magnetosheath FTEs studied here, a moving frame of reference (the deHoffmann-Teller frame) can be found, in which the plasma flow is aligned, or nearly aligned with the magnetic field. For each case, we have obtained a reliable value for the velocity, $\mathbf{v}_{HT}$ of this frame. We have also found that a common value of $\mathbf{v}_{HT}$ provides a good de Hoffman-Teller frame during a full hour of observations including the three FTEs as well as two magnetopause crossings.

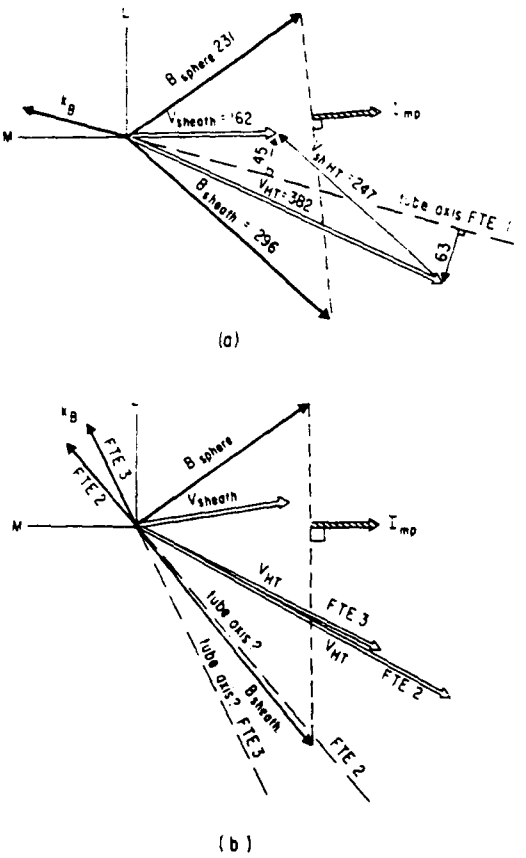

Fig. 16. Plot of flux tube axis (represented by the minimum variance direction, $\mathbf{k_B}$, of **B**), magnetic field vectors, and velocity vectors (relative to the spacecraft) in the magnetopause tangent (LM) plane: (*a*) for FTE 1; (*b*) for FTEs 2 and 3. The tube axis is reliably determined for FTE 1 but is uncertain for FTEs 2 and 3. The magnetic-field vectors $\mathbf{B}_{sheath}$ and $\mathbf{B}_{sphere}$ are shown as Alfvén speeds (based on average density and pressure anisotropy in the magnetosheath reference interval, 1403:30–1404:00 UT for FTE 1, and 1417:00– 1430:00 UT for FTEs 2 and 3). Numbers given in the diagram are in units of km/s. Also shown is the direction of the net magnetopause current, I_{mp}. The vector $\mathbf{v}_{shHT}$ in part 16*a* represents the magnetosheath flow velocity as observed in the deHoffmann-Teller frame of FTE 1.

2. We have shown that, for each of the three events separately, as well as for the combined FTE magnetopause event, the velocity components measured in the deHoffmann-Teller frame were proportional to the corresponding magnetic field components, with one and the same constant of proportionality for all three components. Furthermore, this constant has a large negative value, indicating, not only that the flow in this frame was antiparallel to the magnetic field, as expected for a southern hemisphere reconnection event, but also that the flow speed was a large fraction (0.73–0.86) of the nominal Alfvén speed.

3. For the first FTE we have demonstrated that substantial agreement exists between the observations and a simple model [*Farrugia et al.*, 1987] for irrotational plasma flow along a potential magnetic field that is draped around a diamagnetic cylinder of circular cross section. An impact parameter of 1.4 was obtained. For this event, a reasonably reliable estimate of the orientation of the cylinder has been obtained. The cylinder axis falls halfway between the direction of the net magnetopause current and the ambient magnetosheath field. The motion of the cylinder perpendicular to itself can be determined and is found to be southward, in agreement with the observed B_N signature. Furthermore, the cylinder is not convected with the ambient magnetosheath plasma but moves relative to it with a speed that is at least 82% of the Alfvén speed, based on the magnetic field component perpendicular to the cylinder axis. A cylinder diameter of the order of 8,000 km and, with reasonable assumptions, a cylinder length of not less than about 20,000 km can also be inferred.

4. For the second and third FTE, the observations indicate that the cylinder or bulge causing the event was penetrated by the spacecraft. The internal structure of these events was complicated and the prediction of cylinder orientation much more uncertain. Taken at face value, the orientations obtained would provide evidence that the tube axis may have been closer to the direction of the ambient magnetosheath magnetic field, in which case the FTE flux tube or bulge would also have been convected approximately with the magnetosheath plasma flow. The unusual B_N signature for these two FTEs remains unexplained.

We now discuss these results briefly in the context of several different FTE models. An important question is whether the first event, FTE 1, could have been simply a bipolar Alfvén wave pulse, unrelated to reconnection, rather than the signature of an FTE flux tube or bulge moving past the spacecraft in such a way that no penetration but only distant sensing of field and flow perturbations occurred. We cannot exclude this possibility completely, although there is some evidence in the total pressure increase during the event to indicate that the flow speed in the deHoffmann Teller frame was not the full Alfvén speed. Furthermore, the similar values of v_{HT} for the three FTEs and for the adjoining magnetopause at 1501 UT suggest that they were all part of the same dynamic event. It is then logical to interpret the first event as a distant encounter with an FTE tube or bulge and the second and third events as penetrating encounters with subsequent tubes moving past the spacecraft. Furthermore, it is not attractive to interpret FTE 1 in terms of distant sensing of a Kelvin-Helmholtz surface wave on the magnetopause, because its propagation direction is then not readily accounted for. Neither would it be reasonable to interpret FTEs 2 and 3 in terms of radial magnetopause motion, causing the spacecraft to become briefly immersed in the magnetopause current layer during ongoing reconnection, because the large B_N signatures in these two events would then not be accounted for. Furthermore, the behavior of the other field components is not the same as in the subsequent first magnetopause encounter at 1441 UT.

At present, the most satisfactory explanation for the three FTEs appears to be in terms of models where continually ongoing reconnection, with periodic and strong time modulation of the reconnection rate, occurs somewhere north of the observation site and causes large bulges in the magnetopause to travel southward past the spacecraft. Such models have been discussed by *Lee and Fu* [1985], *Biernat et al.* [1987], *Scholer* [1988*a*, *b*], and *Southwood et al.* [1988]. This type of model fits well with the existence of a common deHoffmann-Teller frame for all three FTEs and two subsequent magnetopause crossings during which reconnection signatures were present. The fact that the flow velocities in the deHoffmann-Teller frame were antiparallel to the

magnetic field and had magnitudes approaching the Alfvén speed for all three FTEs, as well as for the magnetopause crossings, provides strong support for the notion that reconnection was going on continually north of the spacecraft for at least one hour during this pass. The orientation of the flux tube or bulge during the first FTE and its motion relative to the ambient plasma are features consistent with the above mentioned models rather than with encounters with the magnetosheath arm of an isolated elbow-shaped flux tube of the type proposed by *Russell and Elphic* [1978, 1979] although an encounter with the elbow itself remains a possibility. The situation for FTEs 2 and 3 remains unclear, owing to the uncertain determination of flux tube orientation. Finally, we note that many different types of FTE flux-tube geometries may perhaps occur at different times and in different locations on the magnetopause so that one should not exclude the possibility that other FTEs display geometrical and kinematic properties rather different from those deduced here.

Acknowledgments. The work of W.B. was supported by the Deutsche Forschungsgemeinschaft through a Heisenberg fellowship. Research at Dartmouth College was supported by the National Science Foundation, Atmospheric Sciences Division, under grant ATM-8807645, and by the Air Force Geophysics Laboratory, under grant F19628-87-K-0026.

The Editor thanks P. W. Daly and M. F. Heyn for their assistance in evaluating this paper.

REFERENCES

Aggson, T. L., P. J. Gambardella, and N. C. Maynard, Electric field measurements at the magnetopause, 1, Observations of large convective velocities at rotational magnetopause discontinuities, *J. Geophys. Res.*, *88*, 10,000–10,010, 1983.

Biernat, H. K., M. F. Heyn, and V. S. Semenov, Unsteady Petschek reconnection, *J. Geophys. Res.*, *92*, 3392–3396, 1987.

Daly, P. W., M. A. Saunders, R. P. Rijnbeek, N. Sckopke, and C. T. Russell, The distribution of reconnection geometry in flux transfer events using energetic ion, plasma and magnetic data, *J. Geophys. Res.*, *89*, 3843–3854, 1984.

Elphic, R. C., and D. J. Southwood, Simultaneous measurements of the magnetopause and flux transfer events at widely separated sites by AMPTE/UKS and ISEE 1 and 2, *J. Geophys. Res.*, *92*, 13,666–13,672, 1987.

Fairfield, D. H., Average and unusual locations of the Earth's magnetopause and bow shock, *J. Geophys. Res.*, *76*, 6,700–6,716, 1971.

Farrugia, C. J., R. C. Elphic, D. J. Southwood, and S. W. H. Cowley, Field and flow perturbations outside the reconnected field line region in flux transfer events: Theory, *Planet. Space Sci.*, *35*, 227–240, 1987.

Fu, Z. F., and L. C. Lee, Simulation of multiple *X* line reconnection at the dayside magnetopause, *Geophys. Res. Lett.*, *12*, 291–294, 1985.

LaBelle-Hamer, A. L., Z. F. Fu, and L. C. Lee, A mechanism for patchy reconnection at the dayside magnetopause, *Geophys. Res. Lett.*, *15*, 152–156, 1988.

Lee, L. C., and Z. F. Fu., A theory of magnetic flux transfer at the Earth's magnetopause, *Geophys. Res. Lett.*, *12*, 105–108, 1985.

Liu, Z. X., and Y. D. Hu, Local magnetic reconnection caused by vortices in the flow field, *Geophys. Res. Lett.*, *15*, 752–755, 1988.

Paschmann, G., G. Haerendel, I. Papamastorakis, N. Sckopke, S. J. Bame, J. T. Gosling, and C. T. Russell, Plasma and magnetic field characteristics of magnetic flux transfer events, *J. Geophys. Res.*, *87*, 2159–2168, 1982.

Paschmann, G., I. Papamastorakis, W. Baumjohann, N. Sckopke, C. W. Carlson, B. U. Ö. Sonnerup, and H. Lühr, The magnetopause for large magnetic shear: AMPTE/IRM observations, *J. Geophys. Res.*, *91*, 11,099–11,115, 1986.

Russell, C. T., and R. C. Elphic, Initial ISEE magnetometer results: Magnetopause observations, *Space Sci. Rev.*, *22*, 681–715, 1978.

Russell, C. T., and R. C. Elphic, ISEE observations of flux transfer events at the dayside magnetopause, *Geophys. Res. Lett.*, *6*, 33–36, 1979.

Saunders, M. A., C. T. Russell, and N. Sckopke, Flux transfer events: Scale size and interior structure, *Geophys. Res. Lett.*, *11*, 131–134, 1984.

Scholer, M., Magnetic flux transfer at the magnetopause based on single *X* line bursty reconnection, *Geophys. Res. Lett.*, *15*, 291–294, 1988*a*.

Scholer, M., Strong core magnetic fields in magnetopause flux transfer events, *Geophys. Res. Lett.*, *15*, 748–751, 1988*b*.

Scholer, M., D. Hovestadt, F. M. Ipavich, and G. Gloeckler, Energetic protons, alpha particles, and electrons in magnetic flux transfer events, *J. Geophys. Res.*, *87*, 2169–2175, 1982.

Sonnerup, B. U. Ö., On the stress balance in flux transfer events, *J. Geophys. Res.*, *92*, 8613–8620, 1987.

Sonnerup, B. U. Ö., I. Papamastorakis, G. Paschmann, and H. Lühr, Magnetopause properties from AMPTE/IRM observations of the convection electric field: Method development, *J. Geophys. Res.*, *92*, 12,137–12,159, 1987.

Southwood, D. J., C. J. Farrugia, and M. A. Saunders, What are flux transfer events?, *Planet. Space Sci.*, *36*, 503–506, 1988.

Vasyliunas, V. M., Theoretical models of magnetic field line merging, 1, *Rev. Geophys.*, *13*, 303–336, 1975.

Walén, C., On the theory of sunspots, *Ark. Mat. Astron. Fys.*, *30A(15)*, 1–87, 1944.

W. Baumjohann, G. Paschmann, and I. Papamastorakis, Max-Planck-Institut für extraterrestrische Physik, D-8046 Garching, Federal Republic of Germany.

B. U. Ö. Sonnerup, Thayer School of Engineering, Dartmouth College, Hanover, NH 03755.

H. Lühr, Institut für Geophysik und Meteorologie, Technische Universität Braunschweig, Mendelsohnstr. 3a, D-3300 Braunschweig, Federal Republic of Germany.

(Received September 26, 1988;
revised January 17, 1989;
accepted January 30, 1989.)